

Michael L. Mains · Brandon J. Dilworth *Editors*

Topics in Modal Analysis & Testing, Volume 8

Proceedings of the 37th IMAC, A Conference and
Exposition on Structural Dynamics 2019



Conference Proceedings of the Society for Experimental Mechanics Series

Series Editor

Kristin B. Zimmerman, Ph.D.
Society for Experimental Mechanics, Inc.,
Bethel, CT, USA

More information about this series at <http://www.springer.com/series/8922>

Michael L. Mains • Brandon J. Dilworth
Editors

Topics in Modal Analysis & Testing, Volume 8

Proceedings of the 37th IMAC, A Conference and Exposition
on Structural Dynamics 2019

Editors

Michael L. Mains
Mechanical and Materials Engineering
College of Engineering and Applied Sciences
Faculty Advisor, Bearcat Motorsports
University of Cincinnati
Cincinnati, OH, USA

Brandon J. Dilworth
Lincoln Laboratory
Massachusetts Inst of Technology
Lexington, MA, USA

ISSN 2191-5644 ISSN 2191-5652 (electronic)
Conference Proceedings of the Society for Experimental Mechanics Series
ISBN 978-3-030-12683-4 ISBN 978-3-030-12684-1 (eBook)
<https://doi.org/10.1007/978-3-030-12684-1>

© Society for Experimental Mechanics, Inc. 2020

This work is subject to copyright. All rights are reserved by the Publisher, whether the whole or part of the material is concerned, specifically the rights of translation, reprinting, reuse of illustrations, recitation, broadcasting, reproduction on microfilms or in any other physical way, and transmission or information storage and retrieval, electronic adaptation, computer software, or by similar or dissimilar methodology now known or hereafter developed.

The use of general descriptive names, registered names, trademarks, service marks, etc. in this publication does not imply, even in the absence of a specific statement, that such names are exempt from the relevant protective laws and regulations and therefore free for general use.

The publisher, the authors, and the editors are safe to assume that the advice and information in this book are believed to be true and accurate at the date of publication. Neither the publisher nor the authors or the editors give a warranty, express or implied, with respect to the material contained herein or for any errors or omissions that may have been made. The publisher remains neutral with regard to jurisdictional claims in published maps and institutional affiliations.

This Springer imprint is published by the registered company Springer Nature Switzerland AG.
The registered company address is: Gewerbestrasse 11, 6330 Cham, Switzerland

Preface

Topics in Modal Analysis & Testing represents one of eight volumes of technical papers presented at the 37th IMAC, A Conference and Exposition on Structural Dynamics, organized by the Society for Experimental Mechanics and held in Orlando, Florida, January 28–31, 2019. The full proceedings also include volumes on Nonlinear Structures & Systems; Dynamics of Civil Structures; Model Validation and Uncertainty Quantification; Dynamics of Coupled Structures; Special Topics in Structural Dynamics & Experimental Techniques; Rotating Machinery, Optical Methods & Scanning LDV Methods; and Sensors and Instrumentation, Aircraft/Aerospace, Energy Harvesting & Dynamic Environments Testing.

Each collection presents early findings from experimental and computational investigations on an important area within structural dynamics. *Topics in Modal Analysis* represents papers on enabling technologies for modal analysis measurements and applications of modal analysis in specific application areas.

The organizers would like to thank the authors, presenters, session organizers, and session chairs for their participation in this track.

Cincinnati, OH, USA
Lexington, MA, USA

Michael L. Mains
Brandon J. Dilworth

Contents

1	Modern Modal Testing: A Cautionary Tale	1
	James C. Akers, Kim D. Otten, Joel W. Sills, and Curtis E. Larsen	
2	Vibration Testing of Laparoscopic Surgical Instruments Under Varying Grip Pressures	9
	Andrew R. Hutchins, Sabino Zani Jr., Roberto J. Manson, and Brian P. Mann	
3	Combined Qualification Vibration Testing and Fixed Base Modal Testing Utilizing a Fixed Based Correction Method	13
	James P. Winkel, Vicente J. Suárez, and James C. Akers	
4	Pressure Stiffened Modal Correlation of a Cylindrical Pressure Vessel	31
	Emily A. Jewell and Isam Yunis	
5	Pretest Analysis for Modal Survey Tests Using Fixed Base Correction Method	39
	Peter Kerrian and Kevin L. Napolitano	
6	Fixing Degrees of Freedom of an Aluminum Beam by Using Accelerometers as References	53
	Kevin L. Napolitano	
7	Signal Reconstruction from Mobile Sensors Network Using Matrix Completion Approach	61
	Soheil Sadeghi Eshkevari and Shamim N. Pakzad	
8	All Vibration Is a Summation of Mode Shapes	77
	Brian Schwarz, Patrick McHargue, Jason Tyler, and Mark Richardson	
9	Modal Testing Using the Slinky Method	93
	Brian Schwarz, Patrick McHargue, and Mark Richardson	
10	Numerical and Experimental Modal Analysis of a Cantilever Beam Axially Loaded by a Tendon Which Is Attached in a Single Spanwise Location	107
	Vaclav Ondra and Branislav Titurus	
11	Designing a Modal Test Plan Based on Finite Element Method Results	117
	Yan Cao and Liu Jinming	
12	Maximizing the Quality of Shape Extractions from Base Shake Modal Tests	123
	Kevin L. Napolitano	
13	New Approaches to Inverse Structural Modification Theory Using Random Projections	127
	Prasad Cheema, Mehrisadat M. Alamdari, and Gareth A. Vio	
14	Modal Analysis of Wind Turbine Blades with Different Test Setup Configurations	143
	E. Di Lorenzo, S. Manzato, B. Peeters, V. Ruffini, P. Berring, P. U. Haselbach, K. Branner, and M. M. Luczak	
15	Modal Excitation of Circular Rotating Structures Using an Innovative Electromagnetic Device	153
	Thomas Hoffmann, Martin Jahn, Lars Panning-von Scheidt, and Jörg Wallaschek	

16	Modal Analysis of a 7 DoF Sweet Pepper Harvesting Robot	163
	Tobias F. C. Berninger, Sebastian Fuderer, and Daniel J. Rixen	
17	Characterizing Dynamics of Additively Manufactured Parts	171
	Gary Adkins, Clayton Little, Peter Meyerhofer, Garrison Flynn, and Kyle Hammond	
18	How Linear Is a Linear System?	185
	D. Roettgen, B. Pacini, and B. Moldenhauer	
19	An Interpolation Algorithm to Speed Up Nonlinear Modal Testing Using Force Appropriation	193
	Michael Kwarta, Matthew S. Allen, and Joseph J. Hollkamp	
20	Estimating Applied Loads and Response Accelerations on a Dynamic System Using Vibration Data	197
	Eren Koçak, Caner Gençoğlu, Bülent Acar, and Kenan Gürses	
21	Analysis of Coupling Relationship Between Car-Body and Flexible Hanging Equipment	209
	Xiaoning Cao, Xiugang Wang, Qin tao Guo, Ai qin Tian, Shaoqing Liu, Wei Xue, and Jiancai Zou	
22	Imager-Based Characterization of Viscoelastic Material Properties	215
	Howard Brand, Tia Kauppila, Kayla Wielgus, Bridget Martinez, Nathan Miller, Trevor Tippetts, Yongchao Yang, and David Mascareñas	
23	Development and Validation of Data Processing Techniques for Aircraft Ground Vibration Testing	225
	Silvia Vettori, Emilio Di Lorenzo, Bart Peeters, and Antonio Carcaterra	
24	Structural Health Monitoring with Self-Organizing Maps and Artificial Neural Networks	237
	Onur Avci, Osama Abdeljaber, Serkan Kiranyaz, and Daniel Inman	
25	A Novel Technique to Extract the Modal Damping Properties of a Thin Blade	247
	T. Mace, J. Taylor, and C. W. Schwingshackl	
26	Finite Element Model Updating of the UCF Grid Benchmark Connections Using Experimental Modal Data	251
	Milad Mehrkash and Erin Santini-Bell	
27	Structural Health Monitoring on Industrial Structures Using a Combined Numerical and Experimental Approach	263
	Fabian Keilpflug, Robert Kamenzky, Daniel J. Alarcón, Tarun Teja Mallareddy, and Peter Blaschke	
28	Validation of Automatic Modal Parameter Estimator on a Car Body-in-White	279
	N. Gioia, Pieter-Jan Daems, and J. Helsen	
29	Modal Analysis of Rotating Tires in Stationary and Rotating Frames of Reference	285
	Mohammad Albakri and Pablo Tarazaga	
30	Combining Machine Learning and Operational Modal Analysis Approaches to Gain Insights in Wind Turbine Drivetrain Dynamics	293
	N. Gioia, P. J. Daems, T. Verstraeten, P. Guillaume, and J. Helsen	
31	Modal Test-Analysis Correlation Using Left-Hand Eigenvectors	301
	Robert N. Coppelino	
32	A Theoretical Study on the Generation and Propagation of Traveling Waves in Strings	311
	Isil Anakok, V. V. N. Sriram Malladi, and Pablo A. Tarazaga	
33	Shaping the Frequency Response Function (FRF) of a Multi-Degree-of-Freedom (MDOF) Structure Using Arrays of Tuned Vibration Absorbers (TVA)	317
	Campbell R. Neighborgall, Karan Kothari, V. V. N. Sriram Malladi, Pablo Tarazaga, Sai Tej Paruchuri, and Andrew Kurdila	
34	Experimental Study on Tire Vibrations and Induced Noise	327
	Sterling McBride, Seyedmostafa Motaharibidgoli, Mohammad Albakri, Ricardo Burdisso, Pablo Tarazaga, and Corina Sandu	

35 On the Adaptive Vibration Suppression on a Flexible Spatial Structure	333
Oscar A. Garcia-Perez, Luis G. Trujillo-Franco, and Gerardo Silva-Navarro	
36 Evaluation of the Human-Structure-Soil Interaction on a Two-Wheel Tractor Using Modal Analysis Techniques	341
E. Velazquez-Miranda, G. Silva-Navarro, J. Bory-Reyes, O. A. Garcia-Perez, and L. G. Trujillo-Franco	
37 Reproducible Modal Testing Using a Flexure-Based Impact Excitation System	349
Shivang Shekhar and O. Burak Ozdoganlar	
38 Modal Analysis and Characterization of Mounting Cart Used for Testing in the Combined Environment Acoustic Chamber	353
Melissa A. Hall	
39 Effects of Sensor Count on Damping Estimates from Operational Modal Analysis	357
Esben Orlowitz	
40 Ambient Vibration Tests and Modal Response Analysis of an Old Age High-Rise Building in Downtown Vancouver, Canada	365
M. Motamedi, C. E. Ventura, P. Adebar, and R. A. Murugavel	
41 System Identification of a Full Scale Wood Frame Building Specimen Subjected to Shake Table Tests	369
M. Motamedi and C. E. Ventura	
42 Estimating Rotor Suspension Parameters from Runout Data	373
Brian Damiano	



Chapter 1

Modern Modal Testing: A Cautionary Tale

James C. Akers, Kim D. Otten, Joel W. Sills, and Curtis E. Larsen

Abstract Over the past 50 years, great advances have happened in both analytical modal analysis (i.e., finite element models and analysis) and experimental modal analysis (i.e., modal testing) in aerospace and other fields. With the advent of more powerful computers, higher performance instrumentation and data acquisition systems, and powerful linear modal extraction tools, today's analysts and test engineers have a breadth and depth of technical resources only dreamed of by our predecessors. However, some observed recent trends indicate that hard lessons learned are being forgotten or ignored, and possibly fundamental concepts are not being understood. These trends have the potential of leading to the degradation of the quality of and confidence in both analytical and test results. These trends are a making of our own doing, and directly related to having ever more powerful computers, programmatic budgetary pressures to limit analysis and testing, and technical capital loss due to the retirement of the senior demographic component of a bimodal workforce. This paper endeavors to highlight some of the most important lessons learned, common pitfalls to hopefully avoid, and potential steps that may be taken to help reverse this trend.

Keywords Analytical modal analysis · Bimodal workforce · Experimental modal analysis · Finite element analysis · Finite element model · Lessons learned · Modal testing · Retirement

1.1 Introduction

Analytical modal analysis (i.e., finite element modelling and analysis) and experimental modal analysis (i.e., modal testing) have advanced greatly over the past 50 years. Today's powerful computers, high performance instrumentation and data acquisition systems (DAQ's), and powerful linear modal extraction tools can provide today's modal test/analysis engineer the technical resources needed to competently tackle most, if not all, linear structural issues. However, even with this breadth and depth of technical resources, today's modal test/analysis engineer is still only as good as their technical expertise. For us "seasoned veterans" this technical expertise was gained during the course of 30+ years of working and study in the aerospace field and through the exceptional mentoring we received from many senior knowledgeable professionals. It was through this exceptional mentoring that we were able to leverage the expertise of the "seasoned veterans" that came before us and avoid making many poor (and quite frankly simple/unwise) mistakes. It is said "Good judgement comes from experience, and experience comes from bad judgement [1]." Unfortunately, or maybe fortunately, organizations do not have the luxury of being able to allow their engineers to make bad judgements. That said, recent trends observed in both individual engineers and in engineering organizations indicate the hard lessons learned over the past 50 years are being forgotten or ignored, and possibly fundamental concepts are not being understood. These troubling trends have the potential of leading to the degradation in the quality of and confidence in both analytical and test results and increase risk to the project. If this happens the credibility and efficacy of our engineering profession will come into question and missions may potentially suffer.

To some extent, these problems are a making of our own doing. With the advent of modern portable high power computers and user friendly automated software, it is relatively easy for a novice engineer to generate a computer aided-design (CAD) model of a structure, auto mesh it to generate a finite element model (FEM), and perform static and modal analysis

J. C. Akers (✉) · K. D. Otten
NASA Glenn Research Center, Cleveland, OH, USA
e-mail: james.c.akers-1@nasa.gov

J. W. Sills
NASA Johnson Space Center, Houston, TX, USA

C. E. Larsen
Department of Engineering, Texas Christian University, Fort Worth, TX, USA

(i.e., compute stresses, strains, modal frequencies, and mode shapes). Also a novice engineer can collect test data (i.e., force, acceleration, and strain time histories), post process it, and extract modal parameters (i.e., modal frequencies, mode shapes, and modal damping). In a work force where there are ample seasoned engineering professionals helping to guide and mentor less experienced novice engineers to avoid common pitfalls and reinforce the underlying engineering theoretical concepts, these modern capabilities are a true asset. Even in organizations that have a bimodal workforce where there are mostly very seasoned and very novice engineers, ample mentoring can help to make up for the shortfall of not having many, if any, mid-career engineers. However in organizations where the current and foreseeable programmatic budgetary pressures are limiting the amount of analysis and testing, combined with their technical capital loss due to the retirement of their senior seasoned professionals, which curtails much needed mentoring, the early career novice engineers are left “not knowing what they don’t know”. While the focus of this paper is on aerospace engineers performing modal/vibration testing or performing analysis with FEM’s, the concerns discussed here apply to many engineering disciplines. The goal of this paper is to provide early career novice engineers with some key concepts to help avoid the most common pitfalls, and to provide both them and everyone in their organization potential steps for ensuring their organization’s technical expertise remains viable and the aerospace engineering profession remains vibrant and relevant.

1.2 Pitfall #1: Confusing Computer Jockeys and Engineers

As engineers we must understand the key fundamental physics based concepts that underpin our analysis and testing and realize that software and hardware are tools, not crutches to make up for our lack of understanding. We must be able to not only provide results, but be able to verify and validate those results. Being able to make “simple back of the envelope calculations” is of paramount importance to provide sanity checks. This is even more critical in today’s work environment where engineers are increasingly operating as an “army of one” and the double checks and fact checking that occurred in the past are happening less and less frequently, if at all. If you can draw the free body diagram of a single degree of freedom (SDOF) oscillator, derive its equation of motion, solve for its impulse response function, solve for the frequency response function, be able to plot these functions and understand them, you are 90% of the way to understanding most vibration problems. The old adage “Keep It Simple and Straightforward” (KISS) is as relevant today as in the past. Start simply in your analysis/testing and only add complexity as needed. Don’t confuse complexity for sophistication. Many times the most sophisticated solution method is the simplest. Remember, we went to the Moon on FEM’s having only centerline grid points and beam elements, more commonly referred to as “ball-stick models.” The Saturn V launch vehicle was initially modeled in this manner during the Apollo program [2, 3]. Somehow million degree of freedom (DOF) FEM’s were not required (and neither was the Internet).

1.3 Pitfall #2: Too Much Blind Faith in FEM’s

“All MODELS ARE WRONG BUT SOME ARE USEFUL [4].” This blind faith is the direct result of having extremely powerful computers allowing relatively novice engineers to generate CAD models that look exactly like the hardware and in turn using auto mesh features to generate FEM’s that look exactly like the hardware. “Pretty pictures do not a good model make.” This has led some decision makers to believe that accurate CAD models and FEM’s can be accomplished with inexperienced (a.k.a. inexpensive) engineers. This is simply not true. A finely meshed FEM does not guarantee it accurately captures the structural characteristics (i.e., load paths) of the actual hardware. It only means the same modelling assumptions have been made many, many, many times and if these assumptions are incorrect then the resulting FEM will still be inaccurate. Also there is a current trend of using the stress FEM as the loads FEM. The stress FEM has very fine meshing to accurately capture the intricacies of stress fields around joints and fasteners. The loads FEM does not require as fine a meshing since it is intended to capture the structural dynamic properties and needs to allow reasonable modal analysis run times. The validity of CAD models and FEM’s is highly dependent upon the proficiency and experience of the engineer generating them. The engineer generating the FEM needs to use the appropriate elements instead of simply relying on auto-meshing that picks element types based upon ease of meshing instead of the behavior of the underlying structure. Similarly, the FEM automatic single point constraint (AUTOSPC) feature should be avoided so the engineer is forced to understand what DOF are constrained and unconstrained in the FEM and why. Remember that until a FEM has been “grounded” to test data (i.e., correlated to static and modal test data), its accuracy/validity is uncertain. Incorporation of static test results into a FEM correlation to obtain the correct stiffness is half the battle—never forget the dynamic side of the equation

(i.e., square root (k/m)). For modal testing pretest analysis, this means having a healthy skepticism of the FEM accuracy and always incorporating margin into test preparations (e.g., skewing shakers to help ensure that all Target Modes will be adequately excited, instrumentation at the boundary to verify the boundary conditions during testing, using engineering judgement along with such tools as iterative kinetic energy to select instrumentation locations).

1.4 Pitfall #3: Confusing Being Busy with Being Productive

Avoid confusing being busy with being productive. People naturally want to feel that they are making progress towards reaching their end goal and it is natural to assume that if they are busy doing something instead of being “idle”, then they are surely making progress. Not true. Take the necessary time to plan, prioritize, and define the objectives, goals, and success criteria of the task. This will allow you to focus your time and resources to give you the highest probability of successfully completing your task. Note there are no certainties and you must realize that you do not control everything. Hence, we can only speak of probabilities and likelihoods of success.

1.5 Pitfall #4: Avoid Rushing to Analyze

It is very tempting when first given a model or data to want to jump right in and start performing your analysis. See Pitfall #3. However, it is important to perform “sanity checks” on any models or data prior to performing any analysis in order to avoid working for weeks only to discover it was all for naught because of either a faulty model or corrupted data. Be skeptical of FEM’s provided to you and perform your own standard model checks, especially if the previous FEM analysis resides in a different version of software than you are using because default settings can change [5]. Be sure the FEM has been validated to match the CAD or as-built hardware. A FEM is not valid just because it has been “correlated” to modal parameters extracted from a modal test or results from a static stiffness test. Taking the time to match the FEM to the CAD or as-built hardware is absolutely critical for accurately capturing the load paths and being able to predict internal loads [6]. Moreover, when the FEM matches the CAD or as-built hardware, 90–95% of the model correlation effort is achieved. If the FEM does not accurately represent the CAD or as-built hardware, the model correlation effort, while being inaccurate, most likely will also be extremely difficult and time consuming and probably lead to unmet requirements and schedule constraints. Be sure you understand the units the FEM is in and the data units. Even though it is the twenty-first century, many FEM’s generated and used by US companies still have mass in units of slinches and slugs and acceleration data can be in units of in/s^2 or g ’s. Don’t forget frequencies can be in units of rad/s or Hz . When doing your checks, if you are off by a factor of 9.8, this is probably an acceleration units issue and if you are off by a factor of 6.3 (i.e., 2π), this is probably a frequency units issue.

Similarly be skeptical of data provided to you, and if possible, perform time-domain and frequency domain data quality checks as appropriate. Ask questions to the entity providing the data for proof of its validity. For example, if time history data has been supplied and has either been clipped or is in the noise floor of the data acquisition system that was used to record it, blindly post processing it into spectra will lead to very misleading spectra, which is not self-evident.

Take time throughout your analysis to perform intermediate checks. With today’s software it is very easy to plot results and generate tabular listings, which provide quick and insightful checking methods. For example if you are filtering time histories, be sure to compare the frequency response function of the filter to the Power Spectral Density (PSD) computed on broadband random white noise that has been passed through it to verify the filter. It is very easy in to design filters that have very tight passbands, but are numerically unstable. It is of critical importance to be able to compute “back of the envelope” calculations for providing at least cursory sanity checks of analytical results. Some technical references to consider are listed in [7–24]. Documenting these intermediate and final checks constitute the important portion of your analysis report that verifies the validity of your analysis results. At the end of the day, it is your name and reputation that is on the line, and it only takes one or two bad analyses to give you a negative reputation in your organization, which can be very hard to overcome.

1.6 Pitfall #5: Avoid Rushing to Test

Setting up a modal test and performing it, can be both a very exhilarating and stressful time. It involves physical exertion (e.g., moving shakers, mounting accelerometers, running cabling, being in an unfamiliar locale), upper management and programmatic personnel being present to “witness” the testing (i.e., looking over your shoulder, being in a fish bowl), and having a very limited time window to accomplish it. Because of this, it is very natural to want to start collecting data as quickly as possible, and in turn to start extracting modal parameters as quickly as possible. However, as with analysis, it is important to take time to verify the test setup and the validity of the data being collected. Be sure the DAQ has anti-aliasing filtering engaged and operating. With the advent of faster and faster computers, a common misconception going around is that you can sample so fast that aliasing is no longer an issue. Not true. Aliasing will always be present whatever the sampling rate is and once the recorded time histories have been corrupted by aliasing it is impossible to correct them. Take the time to perform time-domain and frequency-domain data quality checks during testing to verify the health of the channels and validity of the test setup.

Time domain checks should include visual inspection of the time histories, looking for data dropouts, digitization error (i.e., full scale setting of the DAQ set too high), clipping (i.e., full scale setting of the DAQ set too low), adequately capturing peaks in the frequency range of interest, and impulsive spikes indicating rattling and/or impacting taking place. Computing standard statistics such as mean, standard deviation, kurtosis, and crest factor on random excitation test runs provide a quick and useful check to determine if nonlinear behavior is present [25]. Keep in mind that crest factors (i.e., peak divided by standard deviation) during vibration testing can reach as high as 5 or more. However, extremely high crest factors and kurtosis may indicate impulsive spikes in the time histories of channels going bad or measuring significant rattling/impacting in the test article. It is important to monitor channels in real time as they are being acquired to check for underflow, overflow, excessive mean, signal drift, and impulsive spikes. If the DAQ generates an automatic channel fault log (i.e., dead channel, overflow, underflow, etc.) take advantage of this important feature.

Frequency domain checks should include verifying the drive point frequency response function (FRF) has the expected phase angle behavior (i.e., for a force to acceleration FRF if the accelerometer has the same orientation as the load cell the phase angle stays between -180° and -360° over the desired frequency range). Check the input excitation force PSD and compare the response PSD's to their ambient background levels to verify the excitation has sufficient frequency bandwidth and level. Check the coherence plots to verify there are linear relationships between input excitation forces and responses confirming the adequacy of the input excitation force level. Check the FRF for excessive hashiness, indicating either too low an input excitation force level and/or nonlinear behavior in the test article. Are the FRF resonance peaks symmetric and well-shaped or are they tipped to the right or left (i.e., “shark fin” pattern) that indicates nonlinear behavior in the test article? PSD or Fast Fourier Transform (FFT) waterfall plots (also called spectrograms) are a very useful tool for determining if test article is behaving nonlinearly or its structural dynamics are time varying, which may indicate degradation of its structural health (i.e., damage is occurring). Keep in mind that PSD or FFT waterfall plots computed on sine sweep data may have subharmonic or super harmonic components that are due to the nonlinear behavior of the input excitation. While electrodynamic shakers can be predominantly linear, as they are driven to higher force levels they will also become nonlinear due to large displacement of their alignment flexures. Hydraulic shakers, which have the advantage of being able to provide higher force levels at lower cost than electrodynamic shakers, typically have significantly higher nonlinear behavior than electrodynamic shakers given the same drive signal. However, pre-distorting a hydraulic shaker's drive signal can significantly reduce the amount of total harmonic distortion in the force it generates.

Be sure to instrument the support structure the test article is mounted to in order to verify/measure the test boundary conditions. This is true for both modal and vibration testing. While floors, strongbacks, slip tables, and expander heads may be very stiff, they typically do exhibit some flexing or rigid body motion during testing. Without this boundary condition information, deflections in the support structure cannot be seen in the extracted test mode shapes and any subsequent FEM model correlation will erroneously attribute support structure flexibility/dynamics to the test article.

Acquiring ambient background levels at least at the beginning and end of each test day, and prior to each new test configuration (e.g., moving of shakers or accelerometers, reconfiguring the test article) is vital in being able to understand the ambient background level and to verify the health of the test setup. Having the ambient background level will also help determine minimum input excitation levels, which avoids wasting time performing modal testing with input excitation levels being too low. Keep in mind that if the response signals are in the noise floor, no amount of averaging is going to clean them up. Many times high ambient background levels are due to florescent lighting, heating, ventilation, and air conditioning (HVAC) running, and pumps and motors operating in adjacent rooms. Turning these off or testing when they are not in operation can significantly drop the ambient background levels. This is why many modal tests, since they need to measure very low level responses, are conducted during off-shift hours and/or on weekends.

Once a preliminary set of FRF have been computed, if possible extract an operating deflection shape at a frequency well below the lowest resonance peak frequency and animate this with your Test Display Model (TDM). This provides a quick visual check that the accelerometers have been setup correctly (i.e., location, orientation, sensitivity). It is strongly recommended that all of these checks be done at the start of the modal test to verify the validity of the entire test setup. If these checks are not first completed, typically what happens is that errors are discovered a few at a time over the course of several test runs. This in turn quickly leads to a bookkeeping headache of having to go back, if possible, and correct not only the original test data, but all of the post processed results generated from that corrupted test data (i.e., FRF, mode shapes, etc.).

Perform low level random or sine sweep characterization test runs before and after any high level modal or vibration testing to monitor the structural health of the test article. This is necessary in order to be able to determine if observed shifts in the FRF resonance peaks at different input excitation levels is due to a permanent change in the test article (e.g., damage, settling) or is due to nonlinear behavior (e.g., joints breaking free and slipping). These pre and post characterization test runs also answer the important question of whether the modal/vibration test affected the structural health/characteristics of the test article.

When performing a modal hammer survey, start with the softest hammer tip and only go onto stiffer/harder tips if needed to obtain the desired frequency bandwidth. Stiffer/harder tips excite higher frequencies and more strongly excite nonlinearities in the test article, which degrades the FRF, and produces responses with higher peak responses, which eats up dynamic range on the DAQ.

1.7 Pitfall #6: Lack of Documentation

For both the analyst and test engineer it is vital to keep a running log of your work. For the analyst this can be a running summary memo that documents your daily work, which should include the models used, the results generated, file locations, and important findings. For the test engineer this can be a test log, which includes the data acquisition and post processing parameters, channel table, test run log, and file locations. Photo document (including labels) as you go throughout the test. There is NO excuse with the proliferation of excellent digital cameras and cell phone cameras to NOT have an abundance of photographic evidence. Generating quick look memos/reports after each major testing phase helps to keep all stakeholders informed as to testing status/progress. Start writing the draft of the test report and test presentation as you go during the test so that key results, lessons learned, and key insights are captured. These drafts should be 90% complete by the end of the test. It is very difficult to remember details sometimes even days later, let alone weeks after a test has wrapped up. For both the analyst and test engineer, this documentation forms the foundation of your personal technical encyclopedia of technical knowledge and accomplishments, which you can draw and build upon as your career progresses. You typically will encounter many similar tasks throughout your career, and your technical encyclopedia will be an invaluable asset to you.

1.8 Pitfall #7: Designing Only for Design Loads

Hardware needs to be designed for all of the environments it will be exposed to, which includes not only design loads (i.e., maximum expected flight environment (MEFL)), but also testing loads, which in the case of vibration qualification testing may be MEFL +3 dB [26]. Ideally the associated upper test tolerance (e.g., for random vibration testing the acceleration PSD test tolerance is +3 dB) should also be included in the design so that if the achieved test level exceeds the nominal test level, which often occurs, testing does not need to be suspended while an analytical assessment of the hardware is made. In addition the hardware needs to be designed so that it can be mounted for testing, which means discussions with the test lab and the designer of the test fixturing. Many times the test fixture is nothing more than an adapter plate that goes from the bolt-hole pattern of the hardware to the bolt-hole pattern of the slip table/expander head of the facility shaker. For more complicated test fixturing, verify the test fixture does not introduce unwanted dynamics during testing (i.e., the integrated hardware and fixture have modes different from the fixed-base hardware over the test frequency range). Modes introduced by the test fixture have two detrimental effects. First, is that these modes may produce narrowband vibration environments that significantly exceed what the hardware can withstand. Second, is that the test fixture acts as a lowpass filter and attenuates the vibration environment the hardware sees above the frequencies of these modes and therefore leads to under testing. For force limited vibration testing, the hardware mounting tabs need to not only meet stiffness requirements, but also need to be of sufficient size to properly interface with the load cells used to measure the total amount of force going into the test article.

1.9 Pitfall #8: Modal Analysis Not Accounting for Out-of-Band Dynamics

Residual vectors, or equivalently a mode acceleration approach, need to be included in any analysis until they are shown to be unnecessary to account for structural dynamics that lie out-of-band the frequency band of interest. Not accounting for structural dynamics either below or above the frequency range of interest can lead to wildly inaccurate FEM results. In modal testing pretest analysis where initial shaker locations and orientations are selected, residual vectors are needed to account for potentially significant compliance in the test article at the shaker drive points. Not including residual vectors can erroneously lead the modal test engineer to over predict how well the target modes will be excited and therefore lead to poorly choosing the initial modal shaker locations and orientations, which in turn will lead to major changes in the shaker setups during the modal test and possibly not being able to meet schedule or excite all target modes.

If possible, consider the real environments used to derive the design loads. Do the real environments have significant frequency content outside the frequency range of the design loads? Is the type of design load conservative with respect to the time-domain characteristics of the real environments (i.e., is the environment random and stationary or is it transient)? Does the analysis produce results that are conservative enough, but not too conservative, to account for out-of-band energy and differences between the real environment type and that of the design loads?

1.10 Pitfall #9: Asking for Help or Seeking Advice Is a Sign of Weakness

A common misconception is that asking for help or advice is a sign of weakness and incompetence. Not true. No one knows everything, especially newer and less experienced engineers. Even the more experienced “seasoned” engineers fall into this category, but they typically understand what questions to ask. Always understand that you “do not know what you don’t know”. Asking colleagues to look over your work or asking for advice is an expected and welcomed behavior in a healthy organization. Senior engineers want to share their experience, knowledge, and insights. Unfortunately, due to current and foreseeable budgetary pressures, novice engineers are many times not being paired directly with senior engineers leading to the novice engineers not having a naturally occurring “apprenticeship” period early in their careers. Therefore, unfortunately the burden falls on the novice engineers to actively seek out the advice of their senior colleagues. Apprenticeship is important and needs to once again become a norm in engineering. Make that connection!

1.11 Pitfall #10: Stove Piping: Separating Analysts and Test Engineers

This is quite a common practice that leads to tension and potential disconnects between the analysis and testing groups/personnel, diminishes the technical prowess/capability of the organization, and adds risk to programs. Having analysts supporting testing provides them with the much needed access to the actual hardware and the ability to gain a deeper appreciation/understanding for the assumptions/simplifications they have incorporated into their FEM. It also provides analysts the opportunity to see firsthand the challenges the test engineer faces conducting vibration/modal testing (e.g., mounting instrumentation and shakers, obtaining valid/quality test data, extracting modal parameters, etc.) The analyst also gains insight into the fundamental structural dynamic characteristics of the hardware in its test configuration. Likewise, test engineers performing analysis gain an appreciation of the work that went into generating the FEM’s, particularly the assumptions about joints and connections, which heavily influence the modal characteristics. The test engineers also gain insight into the challenges associated with the complexity and sophistication of the analytical work. I encourage you, if given the opportunity, to do both test and analysis work. It will only make you a more experienced and knowledgeable engineer and technically strengthen your organization.

Another related poor practice is not having interdisciplinary teams (i.e., “Tiger Teams”) incorporated into programs, particularly at their start. Tiger Teams cover all aspects of a piece of hardware including: design, analysis, testing, operation, and decommissioning. This unfortunate practice is again partly due to current budgetary pressures and the misconception that Tiger Teams are more costly. While it is true that Tiger Teams may cost more during the initial phase of a program, they actually reduce the overall program cost by helping to ensure a good initial design and a well laid out plan for the subsequent analysis, testing, operation, and decommissioning are developed. Starting with a poor initial design can be very costly to remedy, especially the later in the program its shortfalls are identified. If you are presented with an opportunity to serve on a Tiger Team, do so! This will help you develop the ability to effectively communicate and work with other disciplines, which is critical to both a program’s and organization’s success.

1.12 Pitfall #11: Test Is a Four Letter Word

Due to a combination of current budgetary pressures and decision makers becoming less technically knowledgeable, there is tremendous schedule pressure to reduce the amount of analysis and especially the amount of testing. A common misconception is that testing increases a program's cost, which is not accurate [27]. However, because a test has a well-defined resource allocation (i.e., cost, personnel, and schedule), this makes it very easy for decision makers to believe that cutting testing will save the program time and money. Unfortunately testing provides information about the hardware that is simply not available from unverified and unvalidated FEM's. Hence the residual risk in the FEM, which many times is not well understood, must be carried along and typically results in having to incorporate higher uncertainty factors. Many times these high uncertainty factors in turn lead to predicted negative structural margins, which leads to redesign or de-scoping the hardware's performance.

If possible, piggyback "mini-modal" hammer or base drive modal tests onto existing planned component and subassembly vibration tests to gain insight early in the program. Not only will this allow these FEM's to be test correlated, but it serves as a vital check on the design and identifies problems early when they are less costly and time consuming to fix. Always try to implement the philosophy of build from the foundation UP, not from the final configuration top DOWN. However, be careful of not falling prey to "tests of opportunity" and the "something is better than nothing" approach, where short cuts are taken due to lack of funding and schedule resulting in tests being poorly planned and executed. Decision makers may see "tests of opportunity" providing risk reduction to the program, when in reality their results may be at best confusing and most likely misleading.

Because of this current environment, engineers need to not only communicate to decision makers the *who, what, when, and where*, but most importantly be able to succinctly explain why the modal or vibration test is needed and the value they bring to the program in terms of reducing risk (i.e., increasing confidence the system will satisfactorily perform given the program's risk profile). Risk, schedule, and cost is the language of decision makers and engineers need to be comfortable and proficient in talking in these terms. Being able to succinctly convey essential concepts in easily understandable language is critical to the success of both you, your organization, and the project/program you are working on. Be able to advocate for the "right" test and to convey the associated risk with a "test of opportunity". Always have a "30 second elevator" speech in the back of your mind ready to go. You can be pulled into high level meetings at a moment's notice, and none of the attendees may have any technical knowledge in your area.

1.13 Pitfall #12: Unrealistic Success Criteria

Whether it be for an analysis task or for a modal/vibration test, if at all possible define the success criteria at the very beginning and get agreement from all stakeholders. Along with the success criteria identify the receivables, task scope, task schedule (i.e., milestones), and the deliverables. For modal pretest analysis the success criteria includes proper selection of the Target Modes, excitation methods (i.e., shaker and hammer) and locations, test DOF set (i.e., ASET-NASTRAN analysis set of constrained boundary DOF) and the associated TDM, types of instrumentation, DAQ other computer resources, and the format the modal test results will be delivered to the customer. If modal shakers will be used, this also includes the coordination of how these shakers will be supported/suspended during the modal test, which many times is the most challenging aspect of any modal test. Always leave a little margin in the test schedule (i.e., success oriented) because no test goes exactly according to plan and tasks always take longer than expected. A too aggressive test schedule can result in needing to support long testing hours, which leads to increased stress, which leads to sleep deprivation, which leads to the test team making mistakes, which leads to testing delays, which leads back to long testing hours. Not a good situation.

Sometimes there really are no firm requirements. You have been called in by the Customer, who only knows that they have a problem, but they don't know the cause nor have they seen it before, but need it fixed rapidly. If possible acquire data during operation when the problem is occurring. Be mindful the cause of the problem may be spatially and/or temporally separated from the part that is failing. In the case of electronic components, even though failure occurred during a vibration fatigue test, the cause of the failure can be due damage incurred during the preceding thermal test [20, 21].

Many times the Customer has a testing requirement levied upon them from a company or program, but they themselves do not fully understand nor appreciate the effort needed to meet this requirement. As the test engineer, you provide that vital role of "technical requirements translator" informing the Customer of the type and scope of testing that is required and how this fits into the overall test/analysis program requirements. Be sure to account for this in your work estimate, because this can take significant time (e.g., need to support review panels and technical meetings).

Modal testing extremely large hardware may also require a forced response analysis to ensure the selected excitation method and locations can produce response levels throughout the test article that are "significantly" above the ambient

background. The ambient background is a combination of the ambient vibration levels in the test article, sensor and DAQ noise and signal drift, and the ambient electromagnetic environment. As stated earlier in Pitfall #5, this may require performing the modal test during off-shift hours and/or on weekends. It may also require using a greater number of exciters (e.g., modal shakers), larger exciters, or instrumentation that is more sensitive. Understanding both the ambient background and the test article's modal damping characteristics are critical in this assessment.

In all pretest analysis, there needs to be a healthy dose of skepticism and some conservatism added because the pretest analysis is based upon an uncorrelated FEM and assuming perfect test boundary conditions. The selection of the test DOF needs to be done judiciously and sparingly because more instrumentation does not guarantee better self-orthogonality (ORTHO)/cross-orthogonality (XORTHO), in fact in many cases it causes significant degradation. Also more instrumentation requires longer installation and removal time, more effort during testing to keep them healthy and functioning, extra cost to purchase/rent the extra instrumentation and the associated DAQ channels, and incurs the extra burden of handling larger sized files. Always, as a final check of the selected test DOF, display the Target Modes (i.e., select modes of interest that contain the fundamental characteristics of the test article needed to achieve a well-correlated FEM) with the TDM. The TDM should only contain the grid points where instrumentation is installed. If the TDM display of the Target Modes does not make intuitive sense, then the test DOF set (i.e., ASET) needs to be further revised.

1.14 Conclusion

The advancements made in both analytical and experimental modal analysis in the aerospace field is beyond amazing. This is an exciting time for college students studying to go into and new engineers entering this field. This paper, by identifying 12 specific pitfalls, will hopefully serve as a guide to both groups to help ensure they have a successful career by pointing out some of the most common pitfalls and misconceptions. Well informed, their energy, enthusiasm, and drive will lead to the aerospace engineering profession remaining viable, vibrant, and relevant.

References

1. Brown, R.M.: *Alma Mater*. Random House Publishing Group, New York (2001)
2. Grimes, P.J., McTigue, L.D., Riley, G.F., Tilden, D.L.: *Advancements in Structural Dynamic Technology Resulting from Saturn V Programs*. NASA-CR-1539, Volume I (1970)
3. Grimes, P.J., McTigue, L.D., Riley, G.F., Tilden, D.L.: *Advancements in Structural Dynamic Technology Resulting from Saturn V Programs*. NASA-CR-1539, Volume II (1970)
4. Box, G.E.P.: Robustness in the strategy of scientific model building. In: Launer, R.L., Wilkinson, G.N. (eds.) *Robustness in Statistics*. Academic Press, New York (1979)
5. Rose, T.: Your model is wrong. NESC Loads & Dynamics Technical Discipline Team Face to Face (2018)
6. Kabe, A.: Mode survey tests and mode shape orthogonality checks. NESC Loads & Dynamics Technical Discipline Team Face to Face (2018)
7. Avallone, E.A., Baumeister III, T.: *Marks' Standard Handbook for Mechanical Engineers*, 9th edn. McGraw-Hill, New York (1987)
8. Bayer, W.H.: *CRC Standard Mathematical Tables*, 24th edn. CRC Press, Boca Raton, FL (1974)
9. Beer, F.P., Johnston Jr., E.R.: *Mechanics of Materials*. McGraw-Hill, New York (1981)
10. Bendat, J.S., Piersol, A.G.: *Engineering Applications of Correlation and Spectral Analysis*. John Wiley & Sons, New York (1980)
11. Bendat, J.S., Piersol, A.G.: *Random Data: Analysis and Measurement Procedures*, 2nd edn. John Wiley & Sons, New York (1986)
12. Blevins, R.D.: *Formulas for Natural Frequency and Mode Shape*. Krieger Publishing, Malabar, FL (1995)
13. Craig Jr., R.R., Kurdila, A.J.: *Fundamentals of Structural Dynamics*, 2nd edn. John Wiley & Sons, New York (2006)
14. Ewins, D.J.: *Modal Testing: Theory, Practice and Application*, 2nd edn. Research Studies Press LTD., Philadelphia, PA (2000)
15. Greenwood, D.T.: *Principles of Dynamics*. Prentice-Hall, Englewood Cliffs, NJ (1965)
16. Harris, C.M.: *Shock and Vibration Handbook*, 3rd edn. McGraw-Hill, New York (1987)
17. Horn, R.A., Johnson, C.R.: *Matrix Analysis*. Cambridge University Press, Cambridge (1991)
18. McConnell, K.G.: *Vibration Testing Theory and Practice*. John Wiley & Sons, New York (1995)
19. Oppenheim, A.V., Willsky, A.S.: *Signals & Systems*, 2nd edn. Prentice Hall, Englewood Cliffs, NJ (1997)
20. Steinberg, D.S.: *Vibration Analysis for Electronic Equipment*, 3rd edn. John Wiley & Sons, New York (2000)
21. Steinberg, D.S.: *Preventing Thermal Cycling and Vibration Failures in Electronic Equipment*. John Wiley & Sons, New York (2001)
22. University of Massachusetts: Lowell "Modal Space". <https://www.uml.edu/Research/SDASL/Education/Modal-Space.aspx>
23. Wirsching, P.R., Paez, T.L., Ortiz, K.: *Random Vibrations: Theory and Practice*. John Wiley & Sons, New York (1995)
24. Young, W.C.: *Roark's Formulas for Stress and Strain*, 6th edn. McGraw-Hill, New York (1989)
25. Bendat, J.S.: *Nonlinear Systems Techniques and Applications*. John Wiley & Sons, New York (1998)
26. NASA-STD-7001B. *Payload Vibroacoustic Test Criteria*, 11 Nov 2017
27. Juranek, J.B., Wright, C.P.: *Improving Efficiency in Space Vehicle Assembly, Integration, and Test (AI&T)*. 30th Aerospace Testing Seminar, March 2017



Chapter 2

Vibration Testing of Laparoscopic Surgical Instruments Under Varying Grip Pressures

Andrew R. Hutchins, Sabino Zani Jr., Roberto J. Manson, and Brian P. Mann

Abstract Many devices use vibration to provide sensory cues to a human user. In applications, such as smart phones, the vibratory sensory cue is somewhat simple and needs only to exceed a known threshold to signal the user; however, applications that require an individual to control or manipulate an instrument while being given a vibratory sensory cue must also consider the excitation, whose primary purpose is to provide vibrotactile feedback, which can alter the user's ability to properly control or maneuver the instrument. Another consideration for many handheld instruments is that a user's grip pressure can drastically alter the instrument's dynamic response. To this end, predicting the instrument's response is made difficult, because the relationships between grip pressure and the equivalent interfacial damping and stiffness is complex. To address this research gap, this paper explores the idea of performing experimental vibration tests on a laparoscopic instrument while being held at varying grip pressures. This research is motivated by the idea of providing vibratory feedback through laparoscopic surgical instruments. A gap in the literature exists in understanding how surgeon grip characteristics impact the optimal frequency for which this excitation should be supplied. Results from this study indicate that excitation frequencies should be greater than 175 Hz for both weak and strong grip configurations. Lower frequencies result in a larger amplitude response at the instrument tip for all grip pressures, which could result in patient harm as the instrument tip oscillates uncontrollably.

Keywords Laparoscopic surgery · Haptic interface · Grip force · Vibrotactile feedback · Vibration testing

2.1 Introduction

The number of minimally invasive surgical cases worldwide (ex. laparoscopic surgery) continue to increase as these procedures have added benefits such as less post-operative pain, faster recovery, lower morbidity rates, and less trauma [1]. One of the primary drawbacks associated with laparoscopic surgery is the lack of haptic feedback to surgeons that is relied upon during open surgery techniques (i.e. tissue palpation). The design of laparoscopic instrumentation limits the amount of haptic feedback, particularly tactile feedback. To address this concern, there have been attempts at adding haptic capabilities to laparoscopic instruments; however, an important step before simply adding vibrotactile capabilities to surgical instrumentation is to study the fundamental vibration response of the instrument from various types of excitation. This is essential as the instrument tip should be located at a node, while the handle at an anti-node to ensure that the tip is not moving uncontrollably inside of the patient and that the surgeon can perceive the feedback, respectively. To address this research gap, this study involved a vibration test of a laparoscopic instrument while being held at varying grip pressures and simultaneously being excited by a vibrating motor located at the instrument handle. Grip forces were measured by using a series of force sensors attached to the instrument handle and the instrument response was measured at both the handle and at the instrument tip using uniaxial accelerometers. Results from this study have implications, not only in surgery, but also for many hand-held tools or instruments with haptic interfaces.

A. R. Hutchins (✉) · B. P. Mann

Department of Mechanical Engineering and Materials Science, Duke University Pratt School of Engineering, Durham, NC, USA
e-mail: andrew.hutchins@duke.edu

S. Zani Jr. · R. J. Manson

Department of Surgery, Duke University Medical Center, Duke University, Durham, NC, USA

2.2 Background

Much research and medical device development has addressed the need of adding haptic capabilities to laparoscopic surgery instrumentation. Most of this prior work, however, has primarily focused on either surgeon perception of added haptics [2] or performance of surgeons at tasks with haptic interfaces added to instrumentation during training [3, 4]. Some prior research has investigated the impact of adding pneumatic actuators at the instrument handle to communicate instrument jaw contact force to the surgeon [5]. In this study, the authors found that novice surgeons greatly reduced their average and peak gripping force when the pneumatic actuators were activated. These foundational studies provide evidence that the addition of haptics in laparoscopic surgery could expedite surgeon learning and result in useful technologies that could be implemented into live procedures but fail to investigate the mechanics of laparoscopic instrumentation under vibratory excitation.

As full control of surgical instrumentation is essential in providing optimal patient care, surgical tools equipped with haptic interfaces should be designed in such a manner that the instrument tips are located at nodes when vibrotactile feedback is activated. Likewise, to maximize human perception from a signal, instrument handles should be at anti-nodes. To this end, experimental vibration tests should be performed for all surgical instruments that have haptic interfaces to better understand the impact of varying grip pressures on tip and handle response.

2.3 Analysis

The experimental setup included an Endo Dissect laparoscopic surgery instrument (Medtronic plc, Dublin, Ireland), a 2.7 mm vibrating motor, five FlexiForce™ sensors (Tekscan, Inc., Boston, MA), and two piezoelectric accelerometers (Handle: J352C34, Tip: 352C42, PCB Piezotronics, Inc., Depew, NY). The FlexiForce™ sensors were calibrated using a handheld force gauge (DFG35-10, Omega Engineering, Norwalk, CT). Data acquisition for the force sensors and accelerometers was made using a National Instruments USB-6251 and MATLAB 2018B. Figure 2.1 shows an image of the Endo Dissect with the force sensors, vibrating motor, and accelerometers affixed to the instrument. The force sensors were attached at contact points along the instrument handle to measure the contact force of each finger. An electronically controlled resistance box (ohmSOURCE OS-250, IET Labs, Inc., Westbury, NY) was connected in series with the vibrating motor and was used to control the motor frequency.

The instrument amplitude response was measured at both the handle and tip under varying motor frequencies and grip pressures for 10 s at each iteration. Frequency responses at the tip and handle were then extracted from the Fast Fourier Transform of the accelerometer data, along with the voltage amplitude at those frequencies. Finally, the amplitude responses of the tip and handle were compared (Fig. 2.2) to determine the frequency ranges where a small response occurs at the tip, but a somewhat larger response occurs at the handle, i.e. to ensure vibrotactile feedback.

In observing Fig. 2.2, it can be seen that for frequencies greater than 175 Hz the amplitude at the tip is lower than that of the handle. This finding indicates that for laparoscopic surgical instruments with a haptic interface, the vibratory motor should rotate at these higher frequencies to ensure that the tip of the instrument is static while the handle is vibrating.

Figure 2.3 illustrates the gripping forces for each of the contact points on the instrument handle as a function of the motor frequency. The weak grip configuration resulted in a more consistent gripping force for each finger, while the strong grip configuration was more unpredictable. Further tests are warranted for testing gripping pressures of surgeons to determine the distribution of contact pressure from each finger along the instrument handle and how varying gripping styles impact the frequency response at the instrument tip and handle. Preliminary results from Figs. 2.2 and 2.3 indicate that the tip and handle

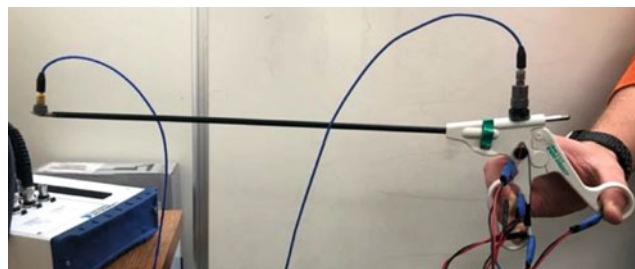


Fig. 2.1 Experimental setup of the Endo Dissect with five FlexiForce™ A101 sensors attached at the handle, a vibrating motor attached at the handle, and two PCB Piezotronics accelerometers attached at the handle and tip

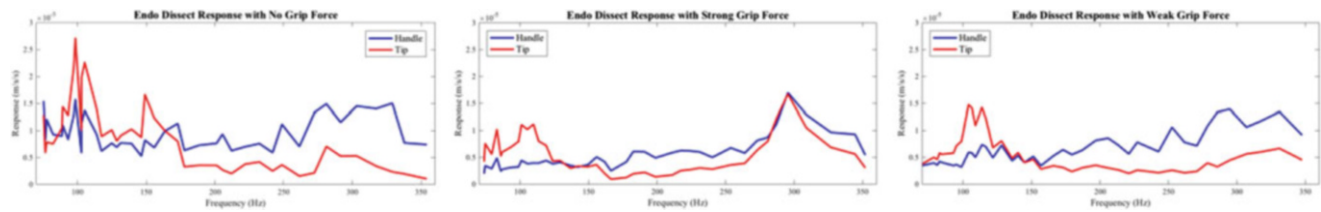


Fig. 2.2 Normalized amplitude response vs. vibration motor frequency plots for the instrument tip and handle response at varying grip pressures. Response is normalized by the squared frequency to ensure constant amplitude across frequency sweeps

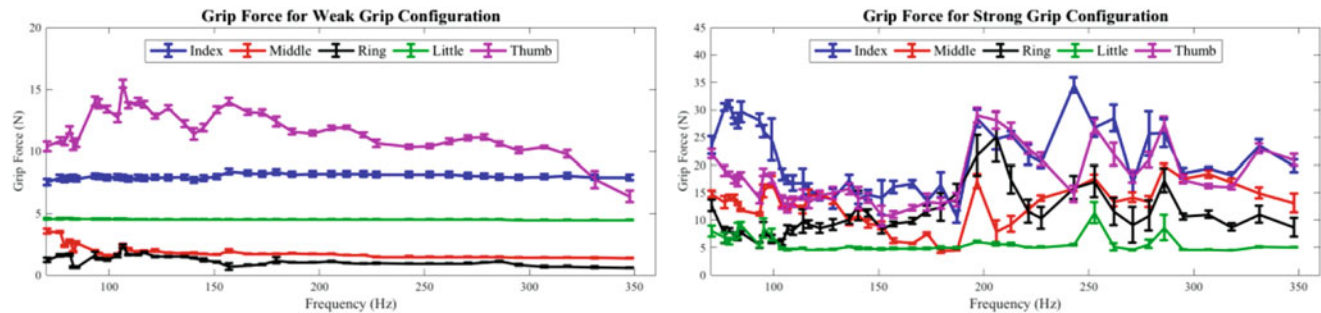


Fig. 2.3 Average contact force from each finger for the weak and strong grip trials across all frequencies tested. Error bars indicate standard deviations

responses are comparable regardless of grip pressure; however, as indicated near 285 Hz in the strong grip configuration, a larger-amplitude response may be a factor to consider when holding the instrument with an increased grip force.

2.4 Conclusion

This study involved vibration tests on a laparoscopic surgical instrument held at varying grip pressures and excited by a motor with a rotating mass imbalance. Results from this study indicate that lower frequencies should be avoided when providing excitation to laparoscopic instruments to ensure that handle response exceeds tip response, leading to an increase in instrument control and providing an decreased risk to patients. Further work is being completed to test excitation waveforms with the plan to train a neural network to alter the motor frequency in real-time using grip pressure. Additionally, we will be testing the grips of multiple surgeons at to determine the optimal grip configuration and motor frequency combination.

Acknowledgements We would like to acknowledge the Department of Mechanical Engineering & Materials Science at Duke University and the Department of Surgery at Duke University Medical Center for providing the necessary funding to support this research.

References

- Berguer, R., Forkey, D., Smith, W.: Ergonomic problems associated with laparoscopic surgery. *Surg. Endosc.* **13**(5), 466–468 (1999)
- Koehn, J.K., Kuchenbecker, K.J.: Surgeons and non-surgeons prefer haptic feedback of instrument vibrations during robotic surgery. *Surg. Endosc.* **29**(10), 2970–2983 (2015)
- Panait, L., Akkary, E., Bell, R.L., Roberts, K.E., Dudrick, S.J., Duffy, A.J.: The role of haptic feedback in laparoscopic simulation training. *J. Surg. Res.* **156**(2), 312–316 (2009)
- Basdogan, C., Ho, C.H., Srinivasan, M.A.: Virtual environments for medical training: graphical and haptic simulation of laparoscopic common bile duct exploration. *IEEE/ASME Trans. Mechatronics.* **6**(3), 269–285 (2001)
- Wottawa, C.R., Cohen, J.R., Fan, R.E., Bisley, J.W., Culjat, M.O., Grundfest, W.S., Dutson, E.P.: The role of tactile feedback in grip force during laparoscopic training tasks. *Surg. Endosc.* **27**(4), 1111–1118 (2013)



Chapter 3

Combined Qualification Vibration Testing and Fixed Base Modal Testing Utilizing a Fixed Based Correction Method

James P. Winkel, Vicente J. Suárez, and James C. Akers

Abstract Vibration testing spaceflight hardware is a vital, but time consuming and expensive endeavor. Traditionally modal tests are performed at the component, subassembly, or system level, preferably free-free with mass loaded interfaces or fixed base on a seismic mass to identify the fundamental structural dynamic (modal) characteristics. Vibration tests are then traditionally performed on single-axis slip tables at qualification levels that envelope the maximum predicted flight environment plus 3 dB and workmanship in order to verify the spaceflight hardware can survive its flight environment. These two tests currently require two significantly different test setups, facilities, and ultimately reconfiguration of the spaceflight hardware. The vision of this research is to show how traditional fixed-base modal testing can be accomplished using vibration qualification testing facilities, which not only streamlines testing and reduces test costs, but also opens up the possibility of performing modal testing to untraditionally high excitation levels that provide for test-correlated finite element models to be more representative of the spaceflight hardware's response in a flight environment. This paper documents the first steps towards this vision, which is the comparison of modal parameters identified from a traditional fixed-based modal test performed on a modal floor and those obtained by utilizing a fixed based correction method with a large single-axis electrodynamic shaker driving a slip table supplemented with additional small portable shakers driving on the slip table and test article. To show robustness of this approach, the test article chosen is a simple linear weldment, whose mass, size, and modal parameters couple well with the dynamics of the shaker/slip table. This paper will show that all dynamics due to the shaker/slip table were successfully removed resulting in true fixed-base modal parameters, including modal damping, being successfully extracted from a traditional style base-shake vibration test setup.

Keywords Modal testing · Pretest analysis · Model updating · Base-shake · Environmental testing · Fixed base

3.1 Introduction

Testing spaceflight hardware is a vital, but time consuming and expensive endeavor. Traditional dynamic test methods presently require two separate tests; the first, a modal test performed on a seismic mass, and the second, a flight level verification test performed on a shaker table. The vision of this research is to combine two separate structural dynamic tests required for space hardware verification into one, which would allow performing modal testing to untraditionally high excitation levels that could approach flight levels.

Several different methods have been proposed to extract fixed base modes from structures mounted on shake tables [1–9]. Authors of this paper were able to be involved with utilizing one of these methods developed by ATA Engineering, which utilizes the shake table accelerations as references when calculating the Frequency Response Functions (FRFs) [8, 9]. It is the intent of this research to start where these two papers left off and further advance utilization of these methods.

Currently only the first stage of a multi-phase research effort has been completed. This paper discusses the test setup, trade studies performed prior to the testing on the shaker table, describing the challenges and lessons learned thus far, and finally disclosing the plan for completing the remaining two phases of the research effort. In the next phase, the primary objective will be to process all the data collected in the first phase and formulate a test plan that incorporates any necessary changes. In the third and final phase, the plan will be to carry out high level vibration testing and extracting fixed based modal parameters from this same test.

J. P. Winkel (✉) · V. J. Suárez · J. C. Akers
NASA Glenn Research Center, Cleveland, OH, USA
e-mail: james.winkel@nasa.gov

3.2 Simple Beam Pathfinder Study

As a pathfinder to verify that the methodology of using accelerations as references to remove base motion was being properly implemented, a simple free-free beam was used [10]. The setup of this simple free-free beam involved a 2" square 6061-T6 aluminum hollow rectangular cross-section beam that was 87" long and had a wall thickness of 0.125" thick. As shown in Fig. 3.1, the beam was suspended from a 1 ton overhead crane hanging over 12 ft. above the top of the beam. A thin nylon string was used directly tied to the top of the beam. In between the string and the chain of the hoist, a rubber bungee cord was added to isolate any modes from the crane influencing the beam as well as lower the rigid body suspension modes of the beam to frequencies much lower than the flexible body mode frequencies to simulate a free-free boundary condition.

The beam was divided into six equal sections and seven uniaxial accelerometers were placed along the beam in each of the two lateral beam directions. A single uniaxial accelerometer was placed at the top of the beam oriented in the axial direction to be able to measure motion along the beams axial direction. This totaled up to 15 channels of accelerometer data for the test. A small impact hammer with a white vinyl tip was utilized for the excitation. A total of ten impacts were collected at each of the 15 accelerometer measurement locations.

The method was exercised to verify that the modal parameters of this simple beam with the following three restrained boundary conditions: pinned at one end, pinned at both ends, and pinned at the ends as well as in the middle, could be extracted from its free-free modal hammer survey. A finite element model (FEM) was generated utilizing 2D beam elements with a total four boundary conditions, the free-free boundary conditions of the test and the three restrained boundary conditions. The first four FEM modal frequencies and mode shapes of the four boundary conditions were computed and compared to the modes extracted using the fixed-base method and are shown in Fig. 3.2.

Time histories were post processed into frequency response functions (FRF) by concatenating the impact hammer data into one long time history file depending upon the specific locations needed to extract the desired boundary condition. For example, in simulating the boundary condition of the beam being pinned at both ends, the impact time histories for the X (lateral) directions at both end location were concatenated together. Then the time histories were post processed using drive point accelerations at those impact locations as references. The Hv FRF method was utilized due to the fact that the noise level on the reference accelerometer and response accelerometer was equal in magnitude. Comparisons of the FEM and extracted fixed-base frequencies and a visual inspection of the FEM and extracted fixed-base mode shapes was performed and are shown in Fig. 3.2. Figure 3.3 illustrates the cross orthogonality comparison between the FEM and test results for these different boundary conditions. This study verified that a fixed-base correction technique, in this specific case using drive point accelerometers as references, could be used somewhat effectively to extract modal parameters for different boundary conditions from a free-free modal test. It was definitely more difficult to extract clean modes shapes when the boundary conditions the test data was being corrected to became more complicated. Thus, when trying to simulate the pinned-pinned condition, while the deformation shapes and frequencies appeared to be correct, the cross-orthogonality was not as clean. More work is planned to be done using this data to help make more significant conclusions. It is the hope that prior to using any other fixed based correction techniques on the shaker slip table, these techniques can first be applied to this simple free-free beam data.

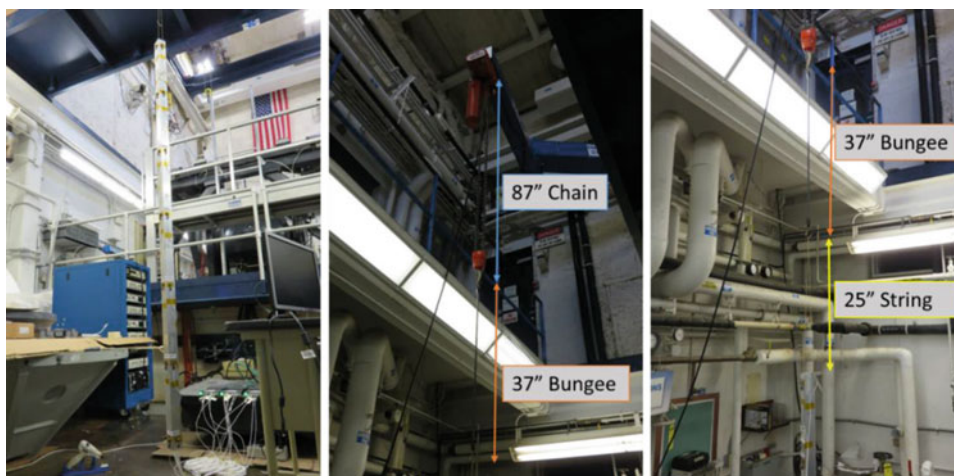


Fig. 3.1 Simple beam pathfinder setup

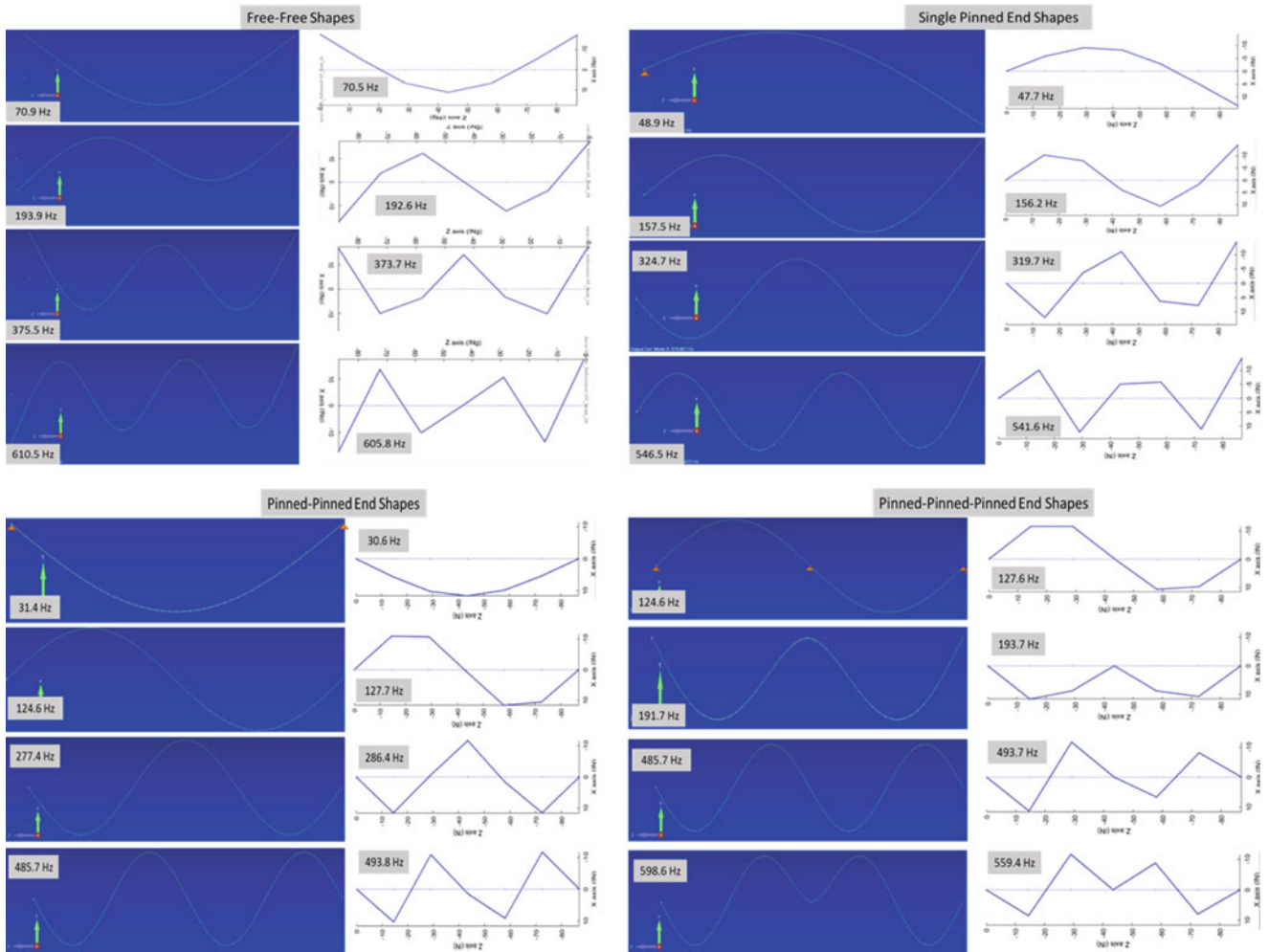


Fig. 3.2 Simple beam pathfinder fixed based correction mode shape and frequency comparison

There were a few challenges encountered with the setup of this pathfinder study that if it were redone would be avoided. The test article had a symmetric square cross-section meaning that there were two lateral bending modes at each resonant frequency, which were aligned with the axes of the cross-section and therefore occurring in orthogonal planes to each other. The closely spaced and highly similar mode shapes made it much more difficult to extract the modes cleanly. The second was that running all the accelerometer cables taped down the length of the beam created a significant amount of mass loading and additional damping. This study is far from being fully completed and the hope is to spend more time with this data going forward.

3.3 Test Article Selection

For the first stage of this research, development of an appropriate test article along with all the infrastructure needed to perform the modal testing was the first step. Initially, it was planned that a test article would be designed and fabricated that would meet the following requirements: simple design and fabrication, behave linearly, have sufficient weight to influence the current shaker table dynamics, and have its fundamental lowest frequency modes in the same frequency range as most aerospace structures. Shortly into the process, it became clear that meeting all these requirements would be cost prohibitive and would exceed the first stage schedule constraints. As a compromise, an existing magnesium bookend used in the dynamics lab was chosen because it would meet the first three requirements. However, unfortunately its lowest fundamental

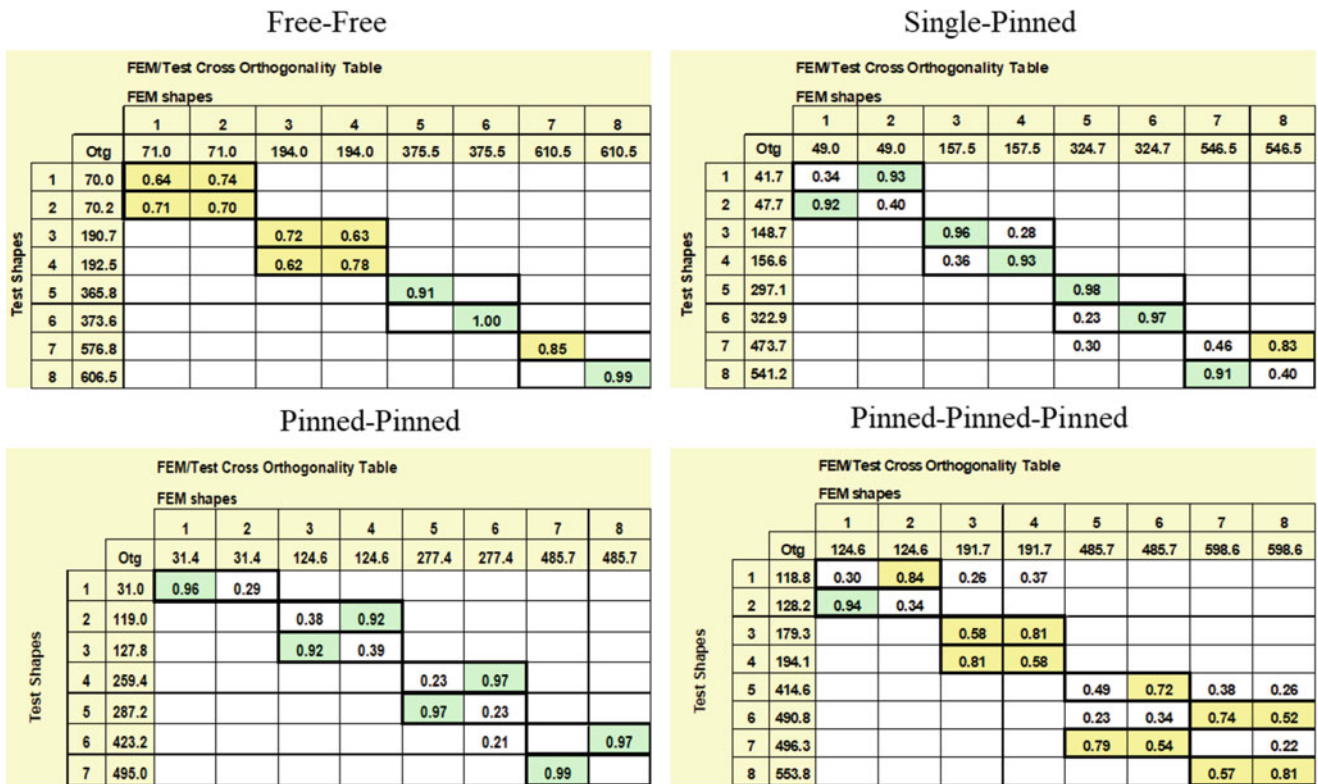


Fig. 3.3 Simple beam pathfinder fixed based correction cross-orthogonality comparison

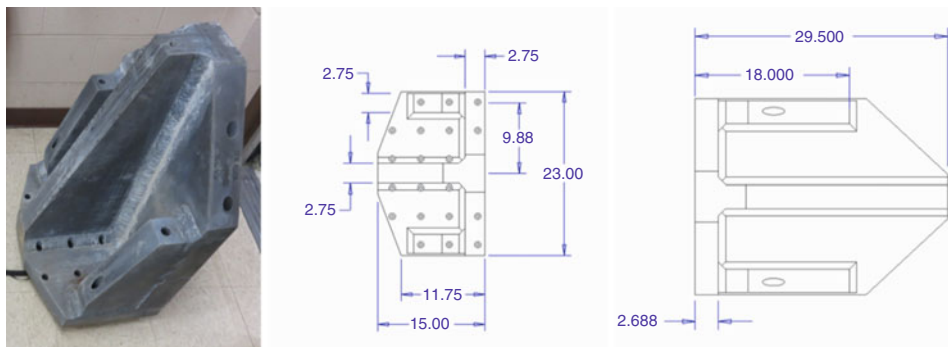


Fig. 3.4 Selected test article

modes are significantly higher in frequency than typical aerospace test articles. At the time it was felt that this limitation would not be an issue for the first stage of this research effort.

The magnesium bookend weighed 217 lb and was expected to behave extremely linear since it was a fully welded magnesium structure. The bookend utilized 3/8 in. diameter fasteners in a 4 in. x 4 in. square hole pattern to hold it down to the floor. More detailed information on the article can be seen in Fig. 3.4.

3.4 FEM Construction and Sensor Pretest Trade Study

A FEM of this magnesium bookend was created to support this research effort. Three different FEMs of the bookend were generated using three different modeling techniques traditionally utilized in modeling aerospace structures. The first, and most simple, modelling technique was to model the bookend using 2D shell elements over the entire bookend, which is typically done in aerospace loads FEMs, and is shown in Fig. 3.5 and will be referred to throughout this paper as the Simple

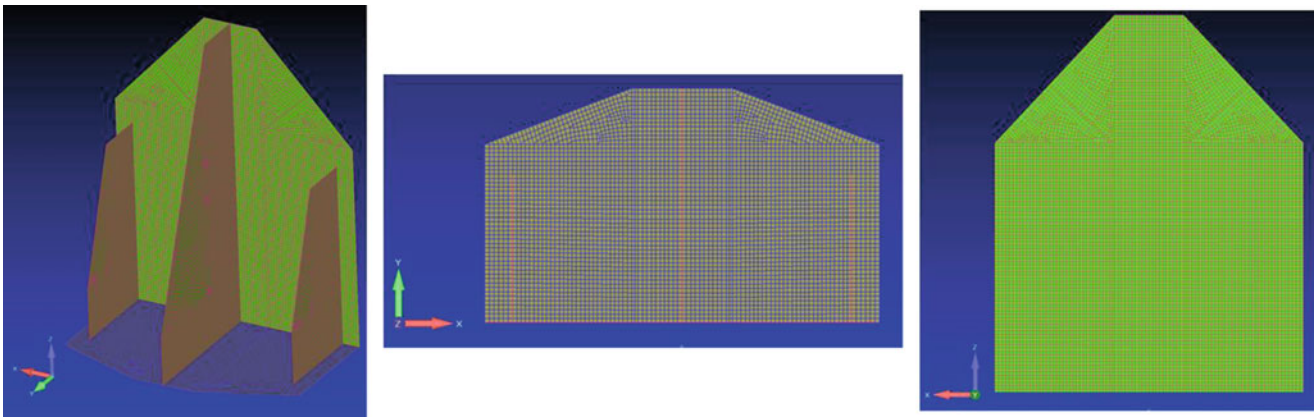


Fig. 3.5 Simple 2D shell FEM

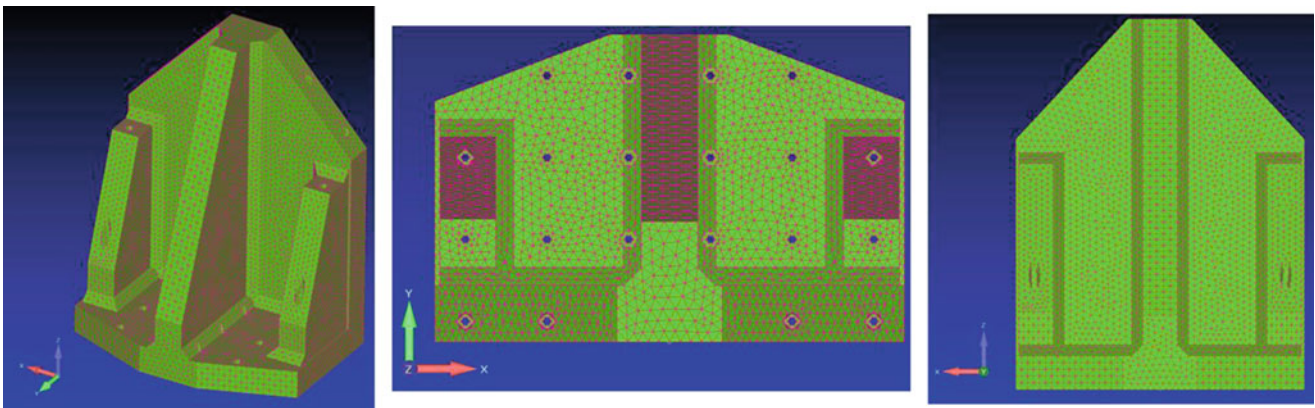


Fig. 3.6 Solid 3D FEM

2D Shell FEM. The advantages of this type of FEM are it is the simplest FEM to generate, analyze, modify, and it has the shortest solution run times. The disadvantage of this modeling technique is that simple features such as holes and welds are not taken into account and there is a lot of duplication of mass at the joints, which was especially the case due to the extreme thickness of the plates.

The second modelling technique utilized was to automesh the CAD representation of the bookend using 3D solid tetrahedral elements, which has the advantage that very fine detail can be accurately captured. The obvious disadvantages of this technique is that solution run times are significantly longer and trying to modify or troubleshoot the FEM can be extremely cumbersome given the number of elements and nodes that are internal to the outer surface and not easily sorted out. The bookend FEM utilizing this second modelling technique is shown in Fig. 3.6 and will be referred to as the Solid 3D FEM.

The final modelling technique used is a hybrid approach where the starting point was the simple 2D shell FEM and then making modifications to eliminate the overlapping elements at joints and adding in more detail to capture details such as holes and welds. Element offsets and RBE2 spider elements are utilized to make this added detail possible. The advantages of this modeling technique is it allows for the increased accuracy of the mass distribution and stiffness changes without going to the full extreme of solid elements. However, the disadvantage is it is the most difficult and time consuming FEM to create. The bookend FEM utilizing this third modelling technique is shown in Fig. 3.7 and will be referred to throughout this paper as the Complex 2D Shell FEM.

At this point, the reader may be wondering why three different FEMs were created for this research. It was done as a side study to allow test engineers to be able to investigate which finite element modeling technique would most closely match the real dynamics of the bookend. In the process of finding out the answer to this, test engineers could also look into which FEM modeling technique would be the most efficient to utilize in modal pretest analyses which are done to see how many accelerometers are required to independently capture the target modes. Modal pretest analysis was performed utilizing a customized set of MATLAB-based test DOF selection tools that draw extensively upon ATA Engineering's IMAT[®] software

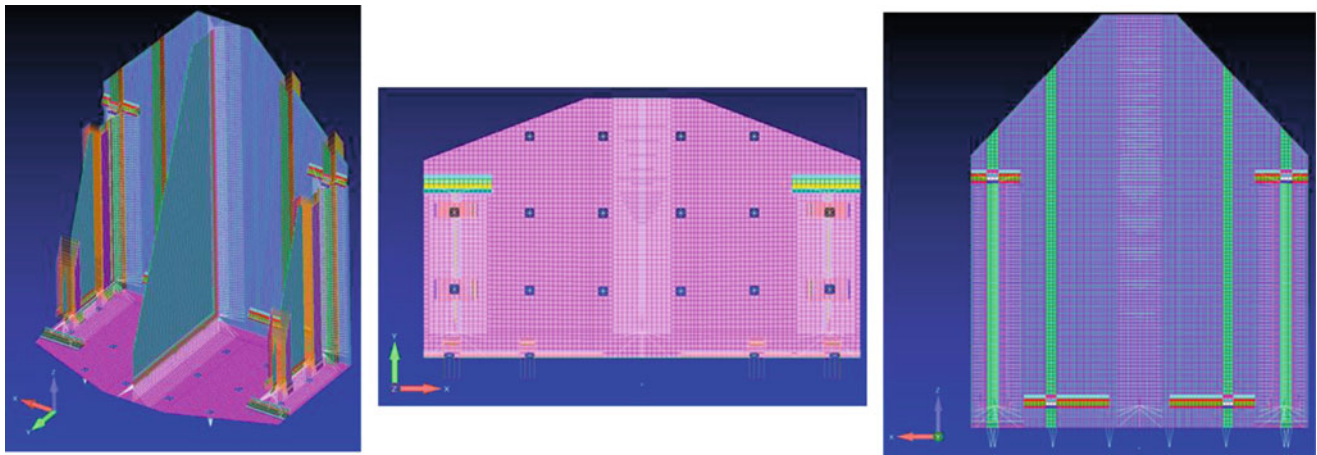


Fig. 3.7 Complex 2D shell FEM

	Simple 2D Shell FEM		Complex 2D Shell FEM		Solid 3D FEM	
Bungee Rigid Body Modes	1	0.01	1	0.01	1	0.01
	2	0.01	2	0.01	2	0.01
	3	0.54	3	0.57	3	0.57
	4	0.65	4	0.69	4	0.68
	5	0.88	5	0.92	5	0.92
	6	3.01	6	3.15	6	3.16
Flexible Body Modes	7	550.63	7	664.26	7	674.87
	8	873.31	8	1063.78	8	1062.85
	9	1017.38	9	1233.64	9	1224.02
	10	1365.89	10	1566.31	10	1551.27
	11	1484.67	11	1693.15	11	1701.22
	12	1682.40	12	1894.11	12	1884.98
	13	1697.19	13	2135.53	13	2114.22
	14	1864.67	14	2190.85	14	2196.15
	15	1898.74	15	2375.30	15	2384.07

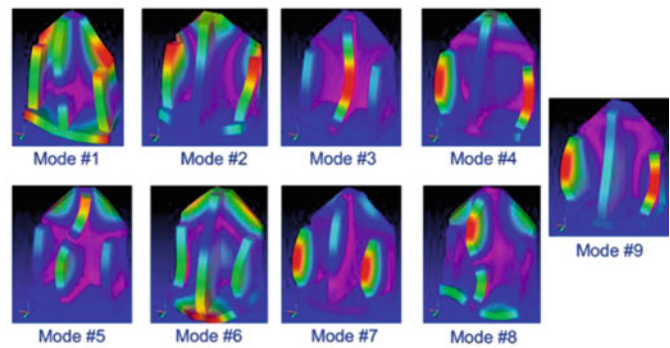


Fig. 3.8 FEM modal frequencies and shape profiles

packages. A simple CBUSH spring was attached to the top of the bookend representing the test verified axial stiffness of a bungee cord that would be used to hold the bookend suspended in the subsequent modal survey. The first nine elastic body modes for each FEM (i.e. the six rigid body suspension modes were excluded) were used as target modes in these pretest analyses (Fig. 3.8).

An initial set 34 test DOF was utilized the pretest analysis of each FEM. This set was based upon engineering judgement to give the pretest analysis a good starting point for capturing the shape and mass distribution of the target mode set. The Iterative Residual Kinetic Energy (IRKE) was utilized to identify additional test DOF resulting in a total of 2500 test DOF. Then a down selection algorithm created by ATA engineering was utilized to incrementally remove test DOF to achieve a minimal test DOF set that met the following criteria (numbered by designated importance):

1. <5% frequency difference between TAM and FEM for target modes
2. <5% on off diagonal of the Self-Orthogonality Matrices
3. >90% on the diagonal values and <10% on off diagonal of the Cross-Orthogonality Matrices
4. >80% on the diagonal values Pseudo-Orthogonality Matrices (Used to establish upper bound only)

The summary tables for each of the pretest analysis of each FEM is shown Table 3.1. There are two tables shown for each FEM with the Upper Bound being where the Pseudo-Orthogonality criteria is no longer met and the Lower Bound being where the Self-Orthogonality criteria is no longer met. The optimal set of test DOF is between these two bounds and is usually much closer to the Lower Bound.

This study shows that the use of 3D tetrahedral solid elements is not conducive to this type of sensor selection approach. It should be made clear that for the Solid 3D FEM, the only test DOF the computer was allowed to select were on the external surface. This was done due to the fact that accelerometers cannot be placed inside the test article. It is understood that a 2D

Table 3.1 FEM pretest analysis comparisons

		Upper Bound					Lower Bound					
Simple 2D Shell FEM	FEM Freq. (Hz)	TAM Freq. (Hz)	% Freq. Difference	PORTHO Diag.	XORTHO Diag.	Max Self-Otho Off Diag.	FEM Freq. (Hz)	TAM Freq. (Hz)	% Freq. Difference	PORTHO Diag.	XORTHO Diag.	Max Self-Otho Off Diag.
	551	554	0.70	97.26	100.00	2.27	551	557	1.09	95.77	99.99	3.23
	873	887	1.54	94.05	99.99	1.55	873	895	2.45	90.75	99.98	2.81
	1017	1031	1.38	94.67	99.97	2.15	1017	1045	2.69	90.40	99.63	2.53
	1366	1403	2.72	89.74	99.94	3.28	1366	1432	4.83	82.69	99.83	5.12
	1485	1532	3.17	88.12	99.90	2.31	1485	1571	5.85	79.58	99.53	3.23
	1682	1750	4.03	85.19	99.88	1.99	1682	1802	7.12	75.72	99.53	5.74
	1697	1768	4.17	85.59	99.39	2.15	1697	1883	10.95	86.96	83.66	5.21
	1865	1966	5.41	80.34	99.37	2.31	1865	2054	10.17	70.15	93.88	5.21
1899	2005	5.58	80.42	99.42	3.28	1899	2098	10.49	67.37	98.06	5.74	
104 DOF						54 DOF						
Complex 2D Shell FEM	FEM Freq. (Hz)	TAM Freq. (Hz)	% Freq. Difference	PORTHO Diag.	XORTHO Diag.	Max Self-Otho Off Diag.	FEM Freq. (Hz)	TAM Freq. (Hz)	% Freq. Difference	PORTHO Diag.	XORTHO Diag.	Max Self-Otho Off Diag.
	664	668	0.62	97.54	100.00	1.49	664	670	0.82	96.79	100.00	2.66
	1064	1076	1.11	95.69	99.99	0.85	1064	1082	1.73	93.40	99.95	2.46
	1234	1252	1.47	94.32	99.99	1.07	1234	1261	2.23	91.55	99.97	1.80
	1566	1610	2.78	89.59	99.94	1.81	1566	1629	4.02	85.46	99.82	2.68
	1693	1750	3.36	87.53	99.93	1.49	1693	1791	5.77	79.35	99.81	2.66
	1894	1961	3.51	86.98	99.96	3.26	1894	1991	5.13	81.74	99.84	4.88
	2136	2232	4.53	83.80	99.77	0.90	2136	2277	6.61	77.60	99.26	1.17
	2191	2300	4.97	81.46	99.72	1.07	2191	2334	6.56	75.89	99.71	2.50
2375	2505	5.46	80.23	99.51	3.26	2375	2584	8.78	71.03	98.53	4.88	
113 DOF						73 DOF						
Solid 3D FEM	FEM Freq. (Hz)	TAM Freq. (Hz)	% Freq. Difference	PORTHO Diag.	XORTHO Diag.	Max Self-Otho Off Diag.	FEM Freq. (Hz)	TAM Freq. (Hz)	% Freq. Difference	PORTHO Diag.	XORTHO Diag.	Max Self-Otho Off Diag.
	675	678	0.54	97.88	100.00	1.49	675	682	0.98	96.16	100.00	2.84
	1063	1077	1.28	95.02	99.99	2.75	1063	1088	2.36	91.11	99.95	5.11
	1224	1237	1.07	95.81	99.99	1.13	1224	1248	1.98	92.47	99.97	2.16
	1551	1588	2.40	90.91	99.96	3.08	1551	1619	4.35	84.33	99.84	5.85
	1701	1749	2.79	89.46	99.96	1.49	1701	1787	5.06	81.87	99.83	2.84
	1885	1953	3.60	86.77	99.93	3.36	1885	2007	6.48	77.84	99.68	6.91
	2114	2189	3.54	87.25	99.77	1.02	2114	2260	6.91	78.55	98.30	1.90
	2196	2289	4.23	83.69	99.64	1.13	2196	2358	7.35	72.91	99.29	2.16
2384	2518	5.61	80.02	99.55	3.36	2384	2629	10.28	67.01	98.49	6.91	
910 DOF						425 DOF						

Shell elements exhibit similar issues in that the test DOF selected are technically on the center line of each surface and can also not be selected, however, all the mass of the FEM is distributed to those same nodes in a 2D shell element. With a solid 3D element, the mass is distributed in a much finer fashion and much more difficult to capture using limited instrumentation. Both the Simple and complex 2D shell FEMs do a reasonable job of selecting an optimized set of test DOF, with the Simple 2D Shell FEM doing a slightly better job.

After seeing these results, it was questioned about whether the appropriate DOF selection method was being utilized or not. Therefore a simple plan to evaluate other DOF selection processes was created and carried out. The flow chart shown in Fig. 3.9 describes this process.

After finishing this process on all three FEMs, the results clearly showed that the IRKE selection method outperformed the Effective Independence selection method. The other finding was that no matter the method used, the solid 3D FEM always required much higher DOF counts to achieve results within the stated guidelines above. This study served as a good confirmation that the standard way the engineers had been doing pretest sensors selections for past modal test was indeed the most efficient way to do them.

The final step was to utilize the Simple 2D Shell FEM, which in the studies above showed the best ability to predict an optimal sensor set, to finalize the number and location of the sensors. A set of 75 DOF was selected which met the overall majority of the pretest guidelines were met and can be seen in detail in Fig. 3.10.

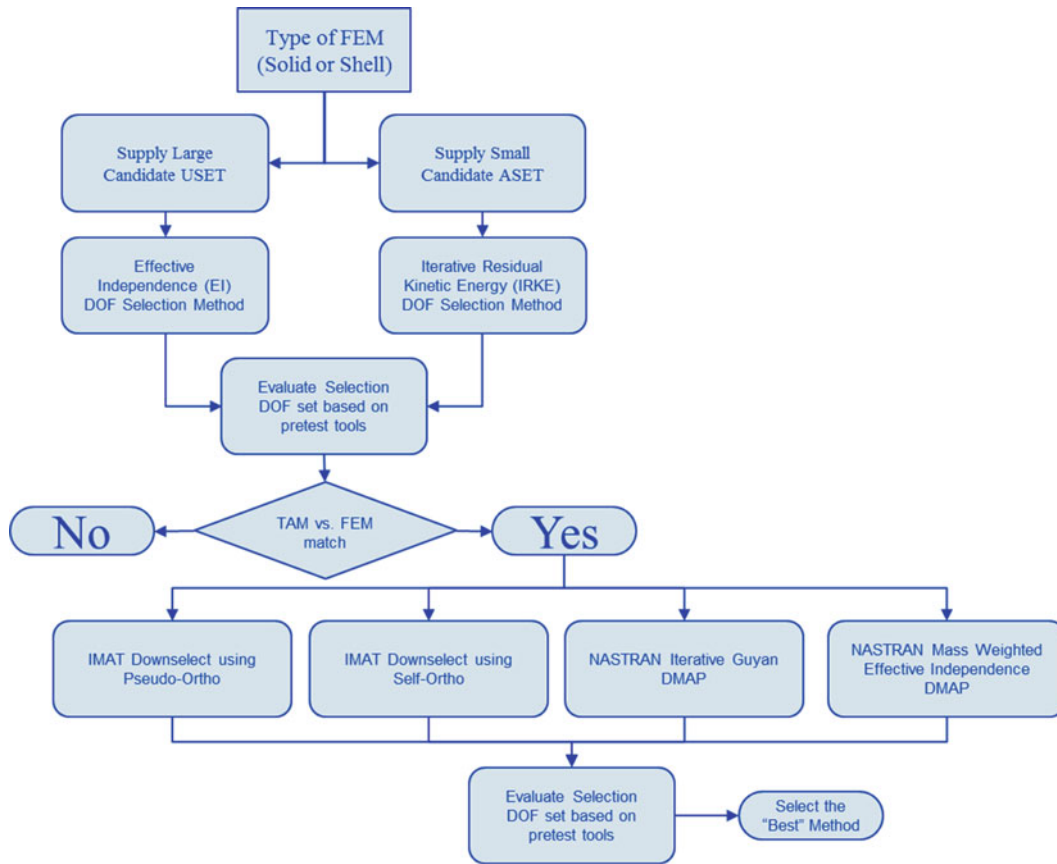


Fig. 3.9 Pretest analysis methodology evaluation flow chart

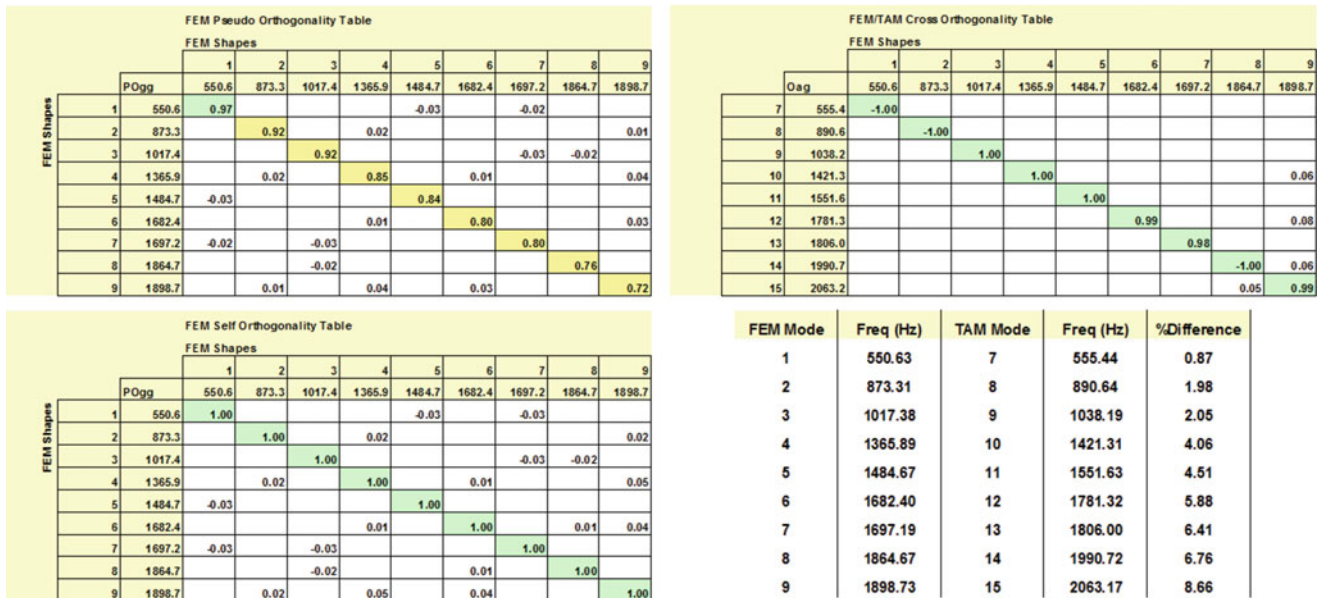


Fig. 3.10 Simple 2D shell FEM final pretest results

3.5 Bookend Free-Free Modal Test and Model Correlation

The test article was suspended from a soft bungee cord displayed in Fig. 3.11 that resulted in a bounce mode at 3 Hz and all of the remaining suspension modes (e.g. first and second pendulum modes) below 3 Hz so that all suspension modes are more than two orders of magnitude below the first flexible body mode.

An impact mallet with a hard black vinyl tip was utilized to excite the structure. This tip was able to produce high quality excitation with good coherence up to 1400 Hz shown in Fig. 3.12. However, the FRFs seem to hold their quality of 2300 Hz. Because this is not an actual test of flight hardware, it was considered acceptable to ignore the guidelines in this specific case and use the modal parameters extracted up to 2300 Hz.

Now that test results had been obtained, it was possible to determine the answers to the new few questions about which FEM construction technique would best predict the actual test results without model updating and the FEM engineers should continue to utilize going forward in the research.

1. Which model is the most accurate correlation without any model updating?
2. Is modeling in so much detail with the Complex 2D Shell FEM required or what subset of modeling features are really necessary?
3. Which model would be the “best” to use? “Best” meaning a good balance of both accuracy of the hardware while also being user friendly.

The Solid 3D FEM was not able to be included fully in this part of the study because the reduced mass and stiffness matrices generated using the chosen set of DOF was so insufficient, it corrupted the cross-orthogonality matrices. However, the frequency comparison for the Solid 3D FEM was generated for reference in Fig. 3.13.

One can see the results in Fig. 3.13 that the Complex 2D Shell FEM does the best job predicting the real test results when considering it can be better utilized in a pretest sensor effort. The Solid 3D FEM, as expected, does a very decent job in predicting the results. It only slightly over predicts the stiffness of the test article. The Simple 2D Shell FEM under predicts the stiffness of the model and thus is simulating a test article that is too flexible.

In a normal modal testing effort, test engineers would probably not see a need to update anything with either the Complex 2D Shell FEM or the Solid 3D FEM. However, in this research effort it was desired to know what features in the Complex 2D Shell FEM were really necessary. By starting with the Complex 2D Shell FEM and slowly removing one complicated feature after another, it was revealed that really only one complex feature, the spider RBE2 elements connecting the plates together, is necessary in making any 2D shell FEM most accurately simulate real test results. In Fig. 3.14, one can observe the comparison between the starting Complex 2D Shell FEM to the much simpler correlated version.

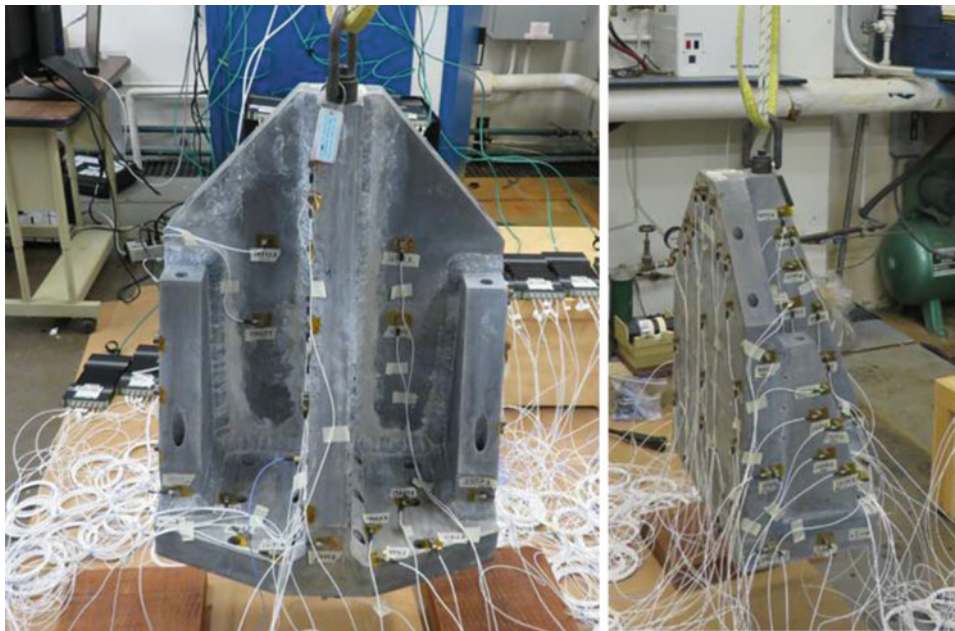


Fig. 3.11 Bookend free-free modal test setup

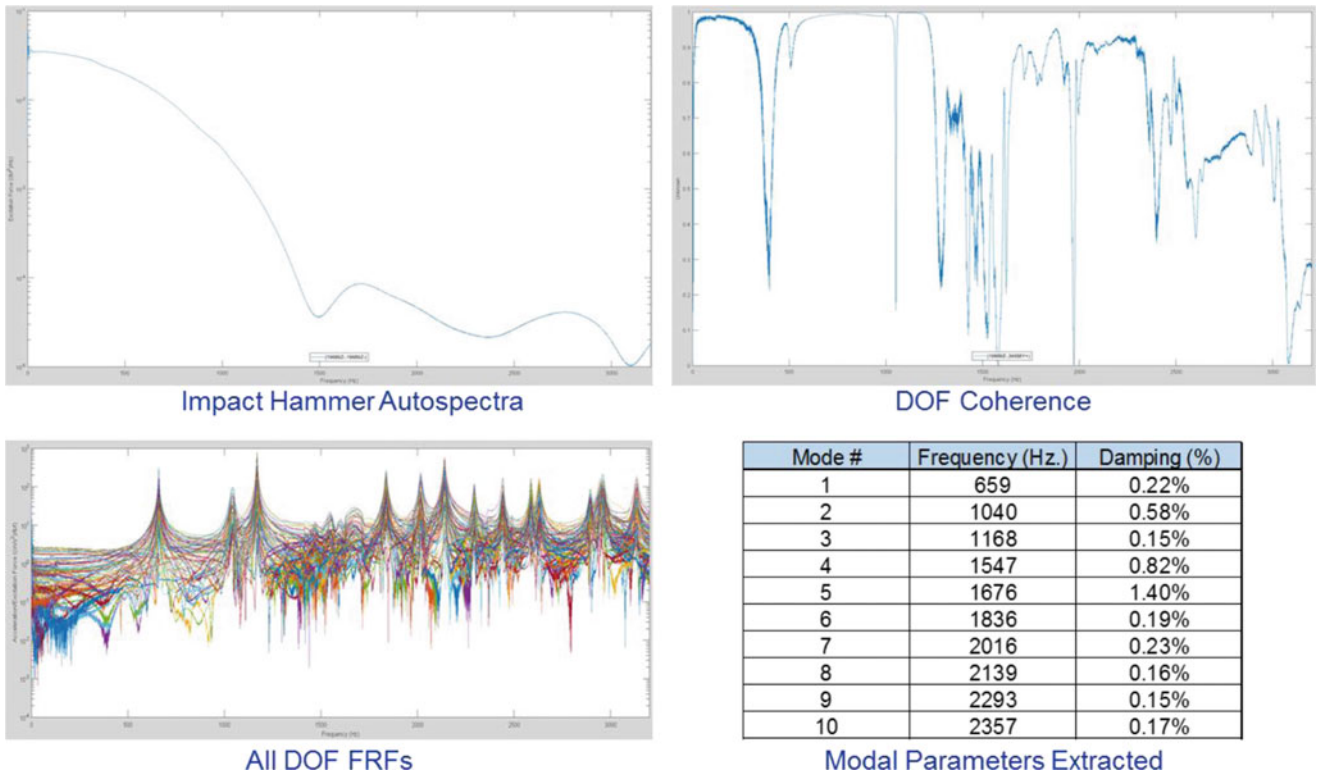


Fig. 3.12 Bookend free-free modal test results

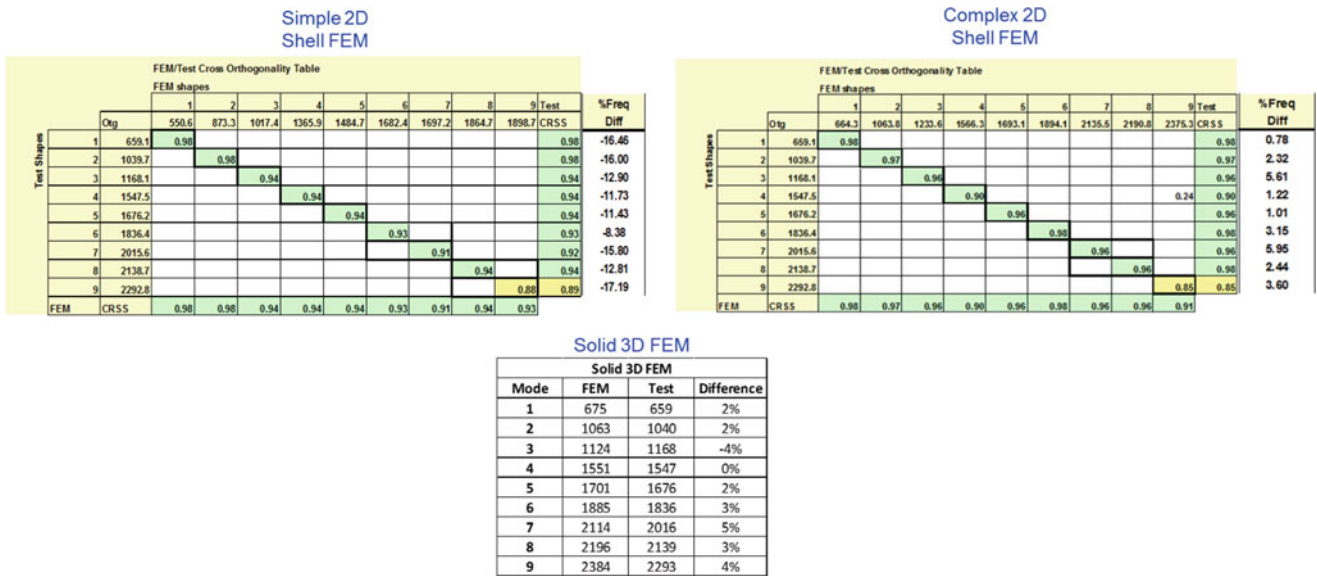


Fig. 3.13 Test vs. FEM correlation results for different FEM modeling techniques

All of the other element offsets and thickness variations that were input to try and capture the true geometry did not seem to make a significant impact, and in some cases, introduced inaccuracies into the FEM. The strain energy plots were a helpful indicator of this inaccuracy which would show discontinuities in the strain energy contour plots at these modeling features. When using this updated much simpler version of the Complex 2D shell model, one can see in Fig. 3.15, that the higher off diagonal value in the cross-orthogonality matrix was actually being generated due to these complicated modeling features.

Based on everything taken into account during these studies, it appears that the best FEM to use throughout the entire process would be the updated 2D complex FEM where the only complexity is the RBE2 spider at each of the joints. This

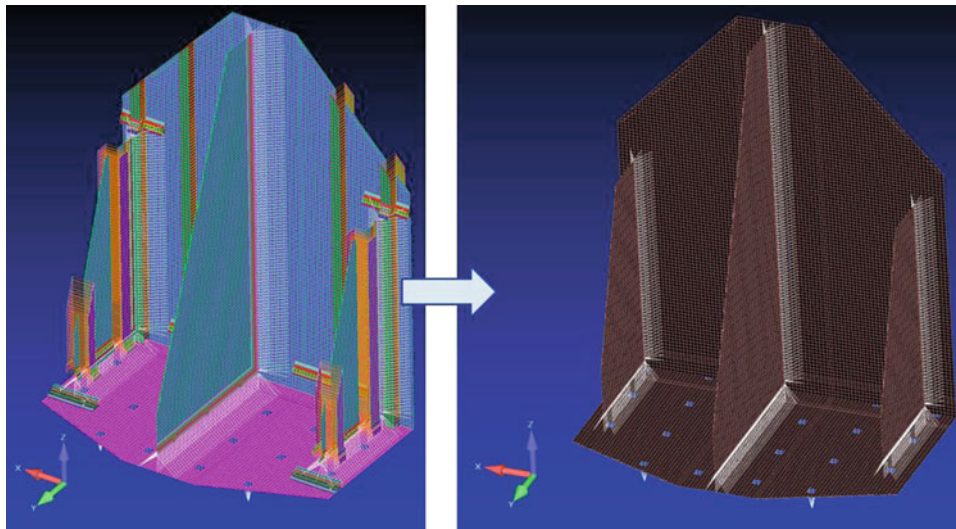


Fig. 3.14 Complex 2D shell FEM transition to simpler 2D shell FEM

Original Complex 2D FEM											Updated Complex 2D FEM														
FEMTest Cross Orthogonality Table											FEMTest Cross Orthogonality Table														
FEM shapes											FEM shapes														
Test Shapes	Orig	1	2	3	4	5	6	7	8	9 Test	%Freq	Test Shapes	Orig	1	2	3	4	5	6	7	8	9 Test	%Freq		
										CR 55	Diff											CR 55	Diff		
1	659.1	0.98									0.78	1	659.1	0.98									0.98	-2.26	
2	1039.7		0.97								2.32	2	1039.7		0.98									0.98	0.62
3	1168.1			0.96							5.61	3	1168.1			0.96								0.96	2.91
4	1547.5				0.90					0.24	1.22	4	1547.5				0.91							0.91	-0.17
5	1676.2					0.96					1.01	5	1676.2					0.97						0.97	-1.06
6	1836.4						0.90				3.15	6	1836.4					0.90						0.98	2.73
7	2015.6							0.96			5.95	7	2015.6						0.96					0.96	1.78
8	2138.7								0.96		2.44	8	2138.7							0.97				0.97	1.18
9	2292.8									0.85	3.60	9	2292.8										0.87	0.87	1.68
FEM	CR 55	0.98	0.97	0.96	0.90	0.96	0.90	0.96	0.96	0.91		FEM	CR 55	0.98	0.98	0.96	0.91	0.97	0.98	0.96	0.97	0.93			

Fig. 3.15 Updated FEM cross-orthogonality comparison

updated complex 2D FEM is actually not much complicated to construct over the simple 2D FEM. It gives the best predictions without any model updating even occurring which means the technique can be trusted more without the presence of test data. Finally, it allows for a very accurate pretest sensor analysis to be performed. From this point on in the research, only the updated 2D complex FEM will be utilized. It will be referred to as the test article FEM from this point on as well.

3.6 Multi-shaker Support Setup

In order to correctly utilize the fixed based correction methods, one basic requirement must always be met. There must be an independent uncorrelated excitation source for every shape that is attempting to be removed. The expectation, based on past studies performed by ATA Engineering [7] on a shaker table, was that the removal of the shaker slip table motion would require at least seven external portable shakers. This meant that engineers would need to come up with structural supports to hold the portable shakers. The main design requirements of these supports were that they needed to allow for easy maneuvering of the shakers, allow for adequate height clearances over the slip table, and be cost effective to fabricate. The lab has relied on catwalks spanning over the large shakers that run on tracks at the edges of the building. It was decided to utilize the same tracks and wheel system for this new test capability. The final product displayed in Fig. 3.16 consists of S6 x 12.5 standard steel I-Beams and manual 1 ton plain trollies attached to 1 ton hand chain hoists which run along the axis of the I-beams. In past experience on fixed based modal testing, engineers have learned that hand chain hoists are the best option to accurately position the shakers due to their ability to pull large lengths of chain and only move the shakers up or down fractions of an inch. They do not jolt up or down like other electronic cable wenchers or chain hoists that have been previously used. Beam clamps were placed on either end of the trolley to hold it stationary once the shakers were located.



Fig. 3.16 Multi-shaker support beams, trolleys, and manual chain hoists

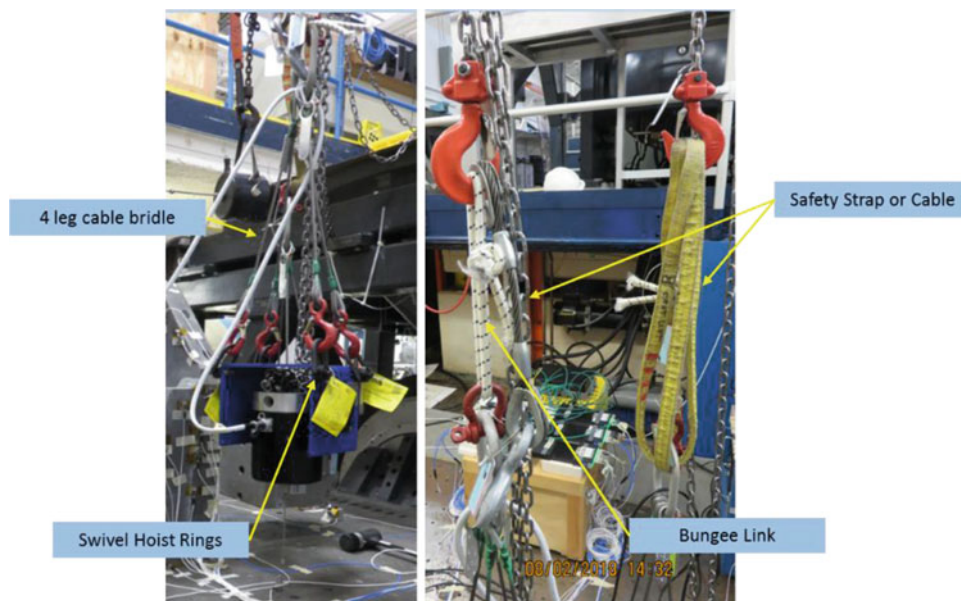


Fig. 3.17 Shaker support attachments

To support attachment of the portable shakers to these hoists, a standard lifting hardware setup was created. This lifting hardware setup, shown in Fig. 3.17, consisted of (order from shaker to hoist): swivel hoist rings fastened to the four corners of the portable shaker trunnions, four-leg cable bridles, and finally a bungee cord link along with a loosely fitted safety strap. The loosely fitted lifting strap was put in place because the bungee cord links were not load tested. Therefore, to ensure safety, the lifting straps would not allow the shakers to fall if the bungees were to break. Normally, turnbuckles would be used between the swivel hoist rings and the four-leg cable bridles so that the shaker orientation could be accurately set, however, the lab did not own enough of these for this research and a decision was made to not utilize them in this first phase. Looking back, they would have been helpful to have and are strongly suggested to be used in the future.

3.7 Traditional Fixed Based Modal Test

The test article FEM that was correlated using the free-free test data documented in previous sections was constrained at all the fastener locations using RBE2 spiders. The modal analysis was performed to identify the target modes that would be extracted in the fixed based testing. Figure 3.18 shows the frequencies, associated modal effective mass, and the deformation shapes of the selected target modes.

#	Frequency (Hz)	T1	T2	T3	R1	R2	R3	Description
1	545	0%	44%	1%	78%	0%	0%	1st Bending Along Y Axis
2	608	34%	0%	0%	0%	57%	27%	1st Bending Along X Axis
3	1014	20%	0%	0%	0%	31%	8%	2nd Bending of Front Plate along with Bending of Central Gusset
4	1311	0%	8%	2%	0%	0%	0%	3rd Bending of the Front Plate along with 1st Bending of Outer Gussets out of phase from each other
5	1392	1%	0%	0%	0%	0%	0%	Central Gusset bending out of phase from outer gussets which are in phase with each other
6	1627	4%	0%	0%	0%	0%	14%	All 3 gussets bending in phase and front plate 2nd bending
7	1642	0%	7%	0%	0%	0%	0%	Oil Canning Mode of Front Face

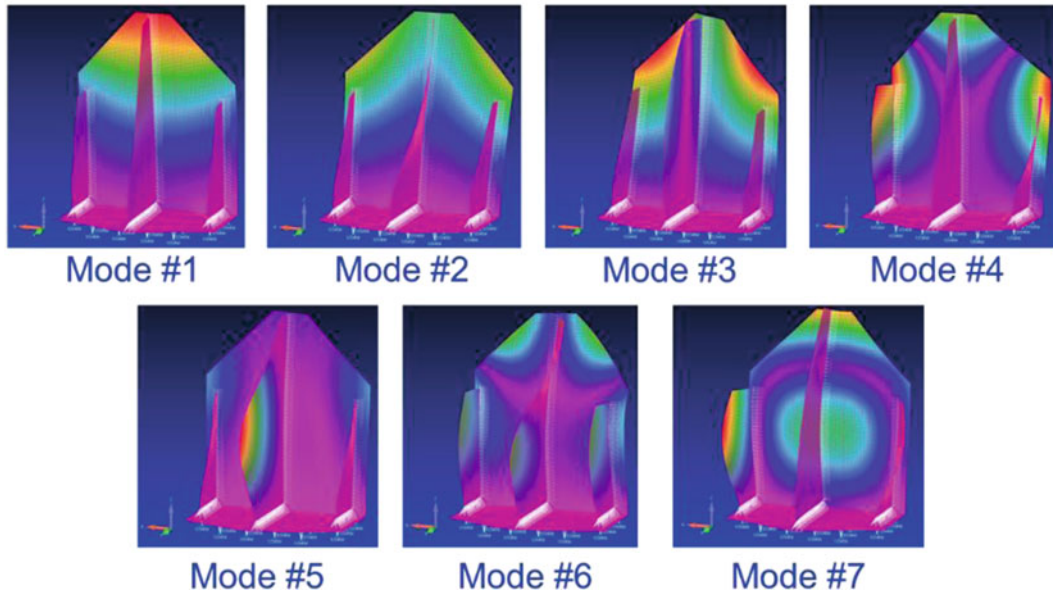
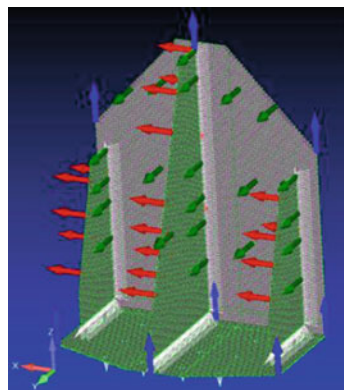


Fig. 3.18 Bookend fixed based target modes



		FEMTAM Cross Orthogonality Table								
		FEM Shapes								
			1	2	3	4	5	6	7	
TAM Shapes	Oag	544.8	607.7	1013.8	1311.0	1391.6	1627.4	1641.9		%Difference
	1	548.7	-1.00							0.72
	2	614.9		1.00						1.18
	3	1046.7			-1.00					3.24
	4	1343.1				-1.00				2.44
	5	1435.2					-1.00			3.13
	6	1697.2						-0.98	0.18	4.29
	7	1712.5						0.17	0.98	4.30

Fig. 3.19 Bookend fixed based modal testing pretest results

It was decided in an attempt to keep things simple to only go after the first seven modes which allowed engineers to reduce the required instrumentation on the test article from 75 to 53. The final sensor locations can be seen in Fig. 3.19 which also includes the pretest Cross-Orthogonality matrix and frequency differences between the reduced TAM and full FEM shapes.

It was important to the engineers performing the research to have a good baseline of fixed based modal parameters using the traditionally accepted fixed based approach of testing on a seismic mass modal floor. The lab has a 10 ft. x 10 ft. square modal floor that has a 4// x 4// square hole pattern. The test article was bolted down to the modal floor using 3/8// diameter fasteners that were all torqued to 20 ft. lb. To be able to accurately capture the modal floor response, accelerometers were installed on the modal floor near the four corners of the test article. Impact hammer testing using a modal mallet with a black vinyl tip was utilized to excite the test article on the modal floor. Impacts were taken on the test article top in all three directions as well as at all four modal floor accelerometer locations. All data was processed using the impact hammer measured force as the reference. The end result of this testing was that the seven target modes were successfully able to be

Table 3.2 Fixed based testing cross-orthogonality matrix and frequency comparison

		FEM Test Cross Orthogonality Table								%Freq Diff	
		FEM shapes									
		1	2	3	4	5	6	7	Test		
		Otg	544.8	607.7	1013.8	1311.0	1391.6	1627.4	1641.9	CRSS	
Test Shapes	1	394.1	0.96	0.24						0.96	38.26
	2	452.3	0.26	0.94						0.94	34.36
	3	698.0	0.23	0.30	0.89					0.89	45.25
	4	1091.6				0.95				0.95	20.11
	5	1271.1					0.93	0.22		0.93	9.48
	6	1433.1				0.31		0.91		0.91	13.55
	7	1498.8				0.38			0.88	0.89	9.55
FEM		CRSS	0.96	0.94	0.89	0.95	0.93	0.91	0.88		

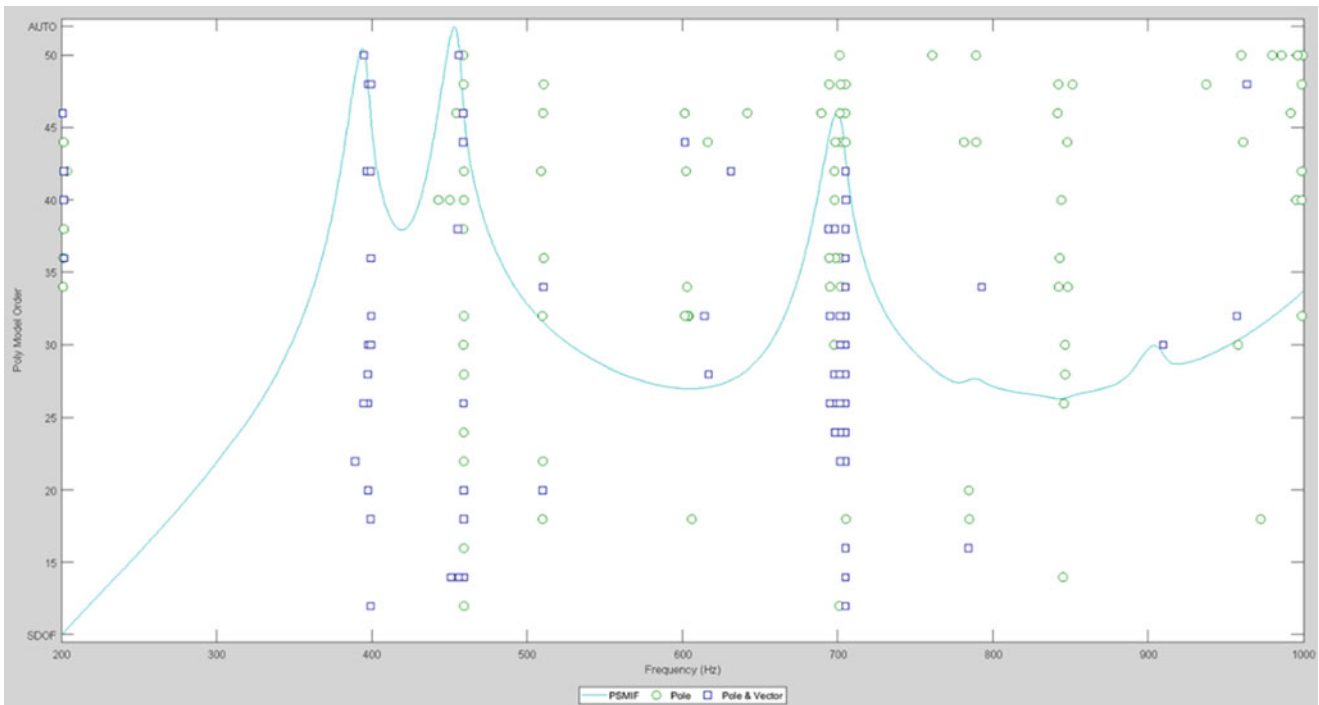


Fig. 3.20 Stability plot from fixed based modal test results

extracted from the testing and it showed that significant model updating to the boundary conditions should be performed. Illustrated in Table 3.2, the RBE2 spider element modeling technique fixing the base of the test article was much too stiff.

The model updating work was chosen to be delayed so that the testing efforts could continue. When looking into the extracted mode shapes, it was discovered that the modal floor was flexing slightly along with the test article. This was completely unexpected as all testing done in the past on the modal floor had never yielded results where the floor appeared to be excited along with the test article. Most aerospace test articles have fundamental resonances well below 400 Hz. However, the fundamental mode of this test article was 400 Hz. The fixed base correction approach would now have to be applied on the modal floor to remove its influence on the test article, an unexpected challenge that would eliminate the ability to use these results as the baseline in the study. The other thing observed was that the frequency response functions appeared to be “bent” over thus the CMIF was also “bent” over as shown in Fig. 3.20. The pole estimates were generating several of the same poles just slightly shifted over in frequency also displayed in Fig. 3.20. This is usually a sign that non-linear behavior exists. The only explanation to explain this behavior was that the bookend coming up off the floor. The interface stiffness in the vertical up direction is much less than in the vertical down direction where the bookend is in contact with the modal floor. The torqued down 3/8” bolts are the only thing creating the stiffness in the up vertical direction.

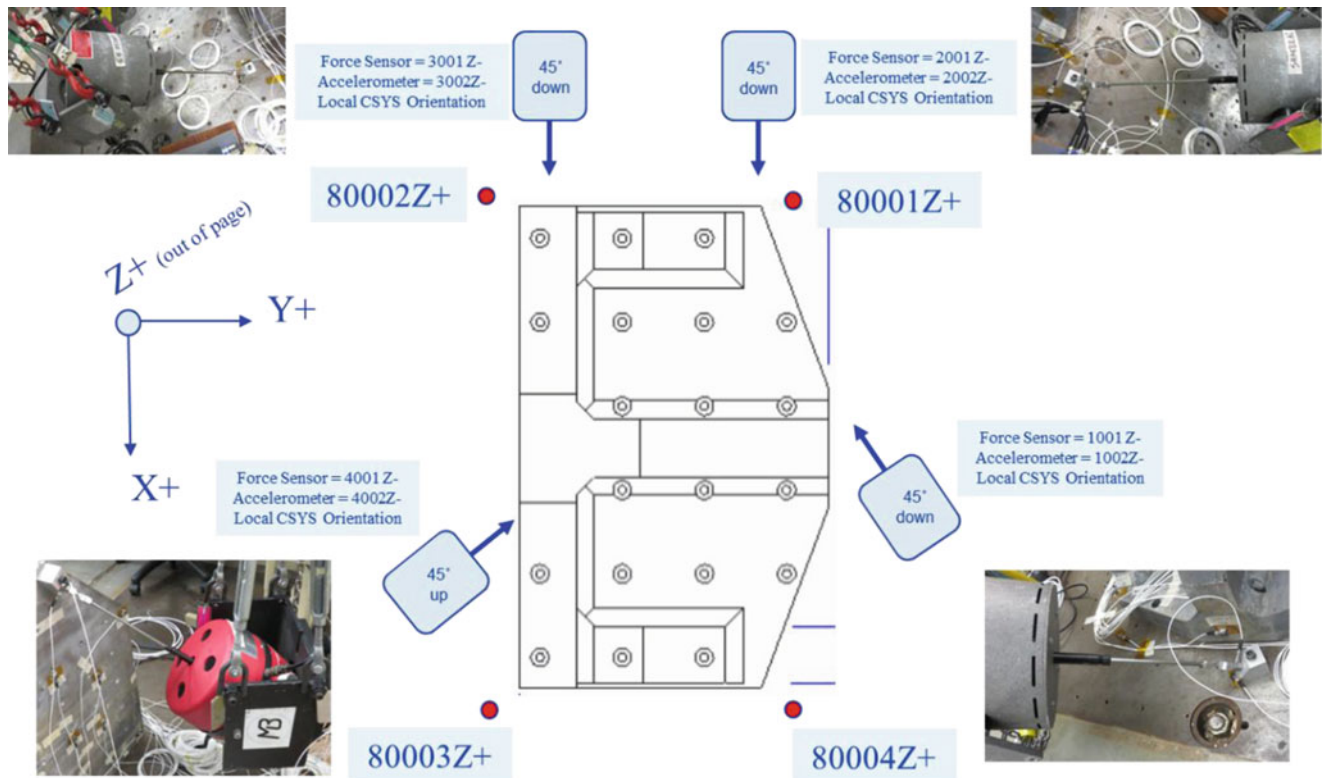


Fig. 3.21 Modal floor multi-shaker layout

At this point, because the modal floor had not reacted as expected and the test article base appeared to be exhibiting non-linear behavior, an adjustment to the test plan was made. In attempting to address the first challenge of the modal floor flexing, multi-shaker testing on the modal floor was planned out where test engineers would utilize the labs four small portable shakers, exciting three on the modal floor and one on the test article. Refer to Fig. 3.21 for more clarification.

The reason for choosing three shakers on the floor was to allow for the best ability to excite the deformation shapes observed in the extracted fixed based test shapes. There appeared to be three main deformations of the modal floor accelerometers. These deformations can be defined as:

1. All four accelerometers deforming in phase along Z axis
2. 80001Z+ and 80002Z+ deforming out of phase relative to 80003Z+ and 80004Z+ along Z axis
3. 80001Z+ and 80004Z+ deforming out of phase relative to 80002Z+ and 80003Z+ along Z axis

Ideally, test engineers would have liked to drive vertically downward along Z-axis with all three floor shakers. However, it was not possible to drive right next to the test articles vertically because the shaker trunnions would be contacting the test article. Thus to create enough space to allow the shakers to stay clear of the test articles, 45° mounting blocks were used to allow the shakers to drive downward at a 45° angle.

The shakers relied on analog filters to bandpass limit the excitation frequency between 200 and 2000 Hz. Through previous testing experience, these analog filters have been utilized to at least limit the lower frequency range as much as possible to minimize shaker bouncing to protect them against over stroking when suspended. The frequency response functions shown in Fig. 3.22 using the three floor shakers as references and the four modal floor accelerometers as references clearly show dynamic response in the floor taking place.

Using the three shaker drive points as references, new FRFs were generated that would remove the motion of the modal floor from the test article. This was completed using two different approaches. First, the FRFs were calculated using the shaker forces as references, then the references were switched out using the Structural Modification Using (Frequency) Response Function (SMURF) approach that was coded into the IMAT software by Kevin Napolitano of ATA Engineering. This technique rearranges the FRF matrix by replacing the current references with new references through a partial inversion of the FRF matrix [11]. The second approach used, referred to as Drive Point (DP in Table 3.3), was simply using the shaker drive point accelerometers as references in the formulation of the FRFs. Modes were extracted from the FRF created from

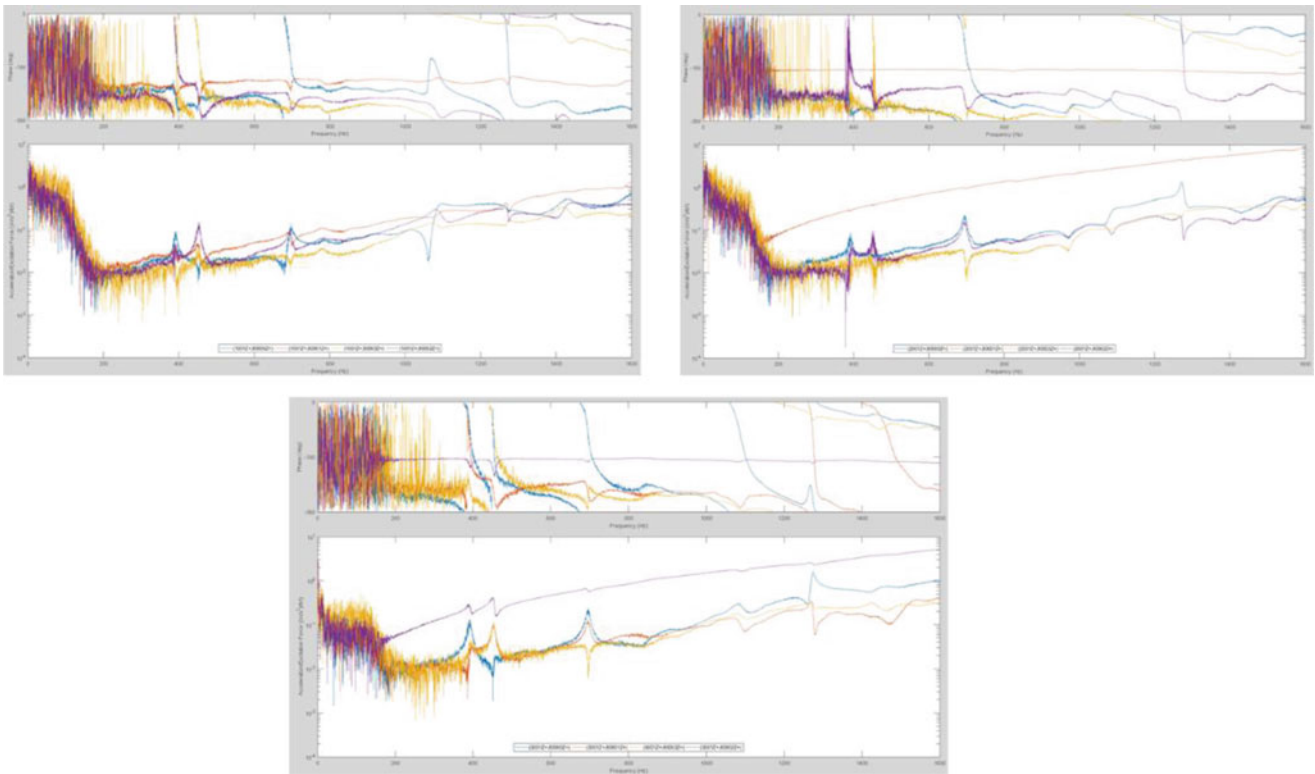


Fig. 3.22 Frequency response functions of modal floor accelerometers (responses)/modal floor shakers (references)

Table 3.3 Fixed based modal frequency comparison table

Uncorrected	SMURF Corrected		DP Accels Corrected	
Freq (Hz)	Freq (Hz)	% Diff	Freq (Hz)	% Diff
394	401	2%	400	1%
452	463	3%	461	2%
698	709	2%	706	1%
1089	1098	1%	1095	1%
1275	1282	1%	1279	0%

both correction techniques and compared back to the uncorrected modal parameters. This showed that the effect of the floor compliance (although minimal) was successfully able to be removed using either technique utilized.

More testing was desired to be performed with the shakers on the modal floor to allow engineers to determine if more torque on the fasteners would help reduce the effect of the non-linear behavior at the base of the bookend, but due to time restraints, it was decided to move onto the shaker slip table testing and if time permitted at the end, the test article could be returned to the modal floor to investigate that further.

3.8 Shaker Slip Table Modal Test

The bookend with its instrumentation installed was transferred as a unit onto the shaker slip table interface next. The shaker support beams and shakers were then positioned into place around the shaker slip table. The lab didn't own the quantities of portable shakers and signal generators required to perform the objectives of this slip table test. The plan was put into place to get a short term rental of the shakers from The Modal Shop and supplement the current signal generators currently owned by the lab by renting the extra LAN-XI 3160 modules from Bruel and Kjaer. The shaker layout was first setup to allow for the removal of the six rigid body modes of the slip table from the test article. The large electrodynamic shaker was disconnected

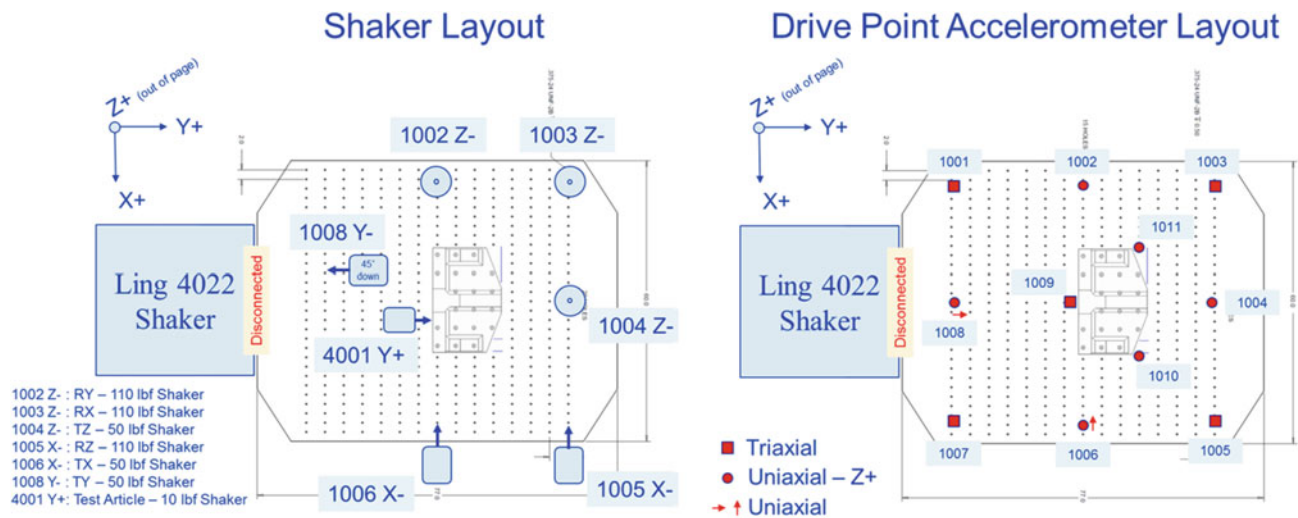


Fig. 3.23 Shaker slip table multi-shaker layout

from the slip table to start off with. It was intended to utilize the large shaker as one of the independent excitation sources in this first stage of the research, but time did not allow for it. It is planned to be utilized in testing going forward in this research investigation. For the first tests, the slip table oil was turned on to allow for free motion. The layout of the shakers and instrumentation can be seen in Fig. 3.23.

The shakers were analog band pass limited from 15 to 800 Hz. They were all run at the same forcing level with the exception of the shaker on the test article which was too small to achieve the same force level. In addition, multi-shaker data was also taken with the slip table oil off. Test engineers made the decision early on to take data on as many different test configurations as they could think of during the rental period of the shakers and extra LAN-XI modules. This put on hold any data processing and review until after all the testing was complete. This was definitely not the ideal way to carry this out, but it was extremely important to test engineers to get data on as many different configurations as they could think of while they had the equipment available.

After all the multi-shaker testing was completed, additional test configurations were collected on the shaker table utilizing impact hammer testing at all the drive point accelerometer locations. This was done to see if in the data processing, all the impacts could be concatenated and then processed as if they were all performed in the same test. It was desired to see if this testing would generate similar results to the multi-shaker testing. Another test configuration that was performed was to move all the accelerometers positioned on the slip table next to the test article as opposed to the edges of the slip table. This was done to see if better results could be obtained by only removing motion close to the test article as opposed to the entire slip table interface. In all 85 different tests, shaker and impact hammer, were carried out during this first phase of the research effort.

3.9 Future Work

It is important that the reader understand that this work was simply the first phase of what potentially could be a three phased research effort. The first goal of the second phase will be to process and analyze all the collected data from the test runs performed in this first phase and be able to determine what test configurations worked best at removing the base motion on the slip table. There is a concern about the test article chosen being too stiff and not really accurately simulating traditional aerospace structures. The stiffer the test article, the more modes the slip table will have influencing the test article base. Very preliminary investigation into the data shows that the final slip table rigid body mode occurs almost 150 Hz below the first test article mode. For every additional mode in the slip table above the last rigid body mode another shaker would need to be added to remove that influence from the test article. This concern might turn out to drive a test article change to one that is more representative of a realistic aerospace structure. Another concern that needs to be sorted out before going much further is if torquing the fasteners down higher than the typical NASA standard would help linearize the base of the bookend. Once these current unknowns are sorted out and the findings of the data documented, then engineers would like to develop a test

approach for utilizing the large electrodynamic shaker as one of the independent uncorrelated inputs into the shaker slip table. The first step would be to try this at low levels of excitation. If this works, then it would be desired to increase the drive level of the large electrodynamic shaker and see if it would be possible to shake at flight random vibration test levels while exciting fixed based modes at the same time. Most of this described testing work would be carried out in the third phase of the research.

3.10 Summary

Based on the limited data that has been reviewed and processed up to the point of writing this paper, there is confidence that several fixed based correction options can be employed on the vast array of test data collected during this initial phase of the research effort. The trade studies performed on the simple beam were invaluable in helping get started in utilizing these methods and developing the basic understanding. More will be done with that test data to further enhance the understanding of the fixed based correction methods and their limitations. The trade studies performed utilizing different techniques of constructing FEMs was extremely helpful to first reassure test engineers that the pretest sensor selection methods they had been utilizing are the most efficient in addition to defining the best modeling technique that will be utilized going forward on this research. Finally, the lessons learned in setting up the infrastructure to support multiple shakers and driving them in a MIMO test effort will translate outside of this research study into all MIMO testing the lab performs in the future. Engineers understand that they have simply started to scratch the surface with this testing of what could be possible going forward and that a lot of work still remains in the process.

Acknowledgements A special thank you to Kevin Napolitano and Elliot Haag of ATA Engineering Inc. for providing engineering support and guidance throughout this initial phase of the research effort.

References

1. Carne, T.G., Martinez, D.R., Nord, A.R.: A comparison of fixed-base and driven base modal testing of an electronics package. In: Proceedings of the 7th International Modal Analysis Conference. pp. 672–679 (1989)
2. Beliveau, J.G., Vigneron, F.R., Soucy, Y., Draisey, S.: Modal parameter estimation from base excitation. *J. Sound Vib.* **107**, 435–449 (1986)
3. Fullekrug, U.: Determination of effective masses and modal masses from base-driven tests. In: Proceedings of the 14th International Modal Analysis Conference. pp. 671–681 (1996)
4. Sinapius, J.M.: Identification of fixed and free interface normal modes by base excitation. In: Proceedings of the 14th International Modal Analysis Conference. pp. 23–31 (1996)
5. Mayes, R.L., Bridgers, L.D.: Extracting fixed base modal models from vibration tests on flexible tables. In: Proceedings of the 27th International Modal Analysis Conference (2009)
6. Napolitano, K., Yoder, N.: Fixed base FRF using boundary measurements as references – analytical derivation. In: Proceedings of the 30th International Modal Analysis Conference (2012)
7. Napolitano, K., Yoder, N., Fladung, W.: Extraction of fixed-base modes of a structure mounted on a shake table. In: Proceedings of the 31st International Modal Analysis Conference (2013)
8. Staab, L., Winkel, J., Suárez, V., Jones, T., Napolitano, K.: Fixed base modal testing using the mechanical vibration facility 3-axis base shake system. In: Proceedings of the 34th International Modal Analysis Conference (2016)
9. Napolitano, K., Winkel, J., Akers, J., Suárez, V., Staab, L.: Fixed base modal survey of the MPCV Orion European Service Module Structural Test Article. In: Proceedings of the 36th International Modal Analysis Conference (2018)
10. Napolitano, K.: Personal interview with James Winkel (2017, Nov 14)
11. Crowley, J.R., Klosteman, A.L., Rockin, G.J., Vold, H.: Direct structural modification using frequency response functions. In: Proceedings of the 2nd International Modal Analysis Conference (1984)



Chapter 4

Pressure Stiffened Modal Correlation of a Cylindrical Pressure Vessel

Emily A. Jewell and Isam Yunis

Abstract Acoustoelastic structures are a complex dynamic system that exhibit modal coupling between a structure and its enclosed acoustic fluid. Common structures that exhibit this phenomenon in the aerospace industry are pressure vessels such as a solid rocket boosters or advanced solid rocket motors. When a structural analyst simulates the structural modes of these pressure vessels with shell finite elements, they often apply an internal pressure force in their model to represent the acoustic fluid. In a model free of boundary conditions, the application of this internal pressure force produces modal results that ground some rigid body modes, often going from six to three zero-frequency modes. Therefore, since the finite element modal simulation inappropriately grounds the structure and thus is unable to accurately predict the rigid body modes, it calls into question whether the elastic or flexible modes predicted by the same modal analysis are accurate. This paper presents an experimental study to address this question by designing, analyzing, fabricating, and testing a simple cylindrical pressure vessel. A free-free steel cylindrical pressure vessel was modeled with finite elements and modal tested with and without pressure. Modal tap testing was used to extract the structural response and compute frequency response functions which were compared to analytical results to discern the accuracy of the predicted elastic modes of the pressure vessel.

Keywords Acoustics · Modal analysis · Acoustoelasticity · Pressure vessel · Fluid-structure interaction

4.1 Introduction

Structural dynamicists rely on modal analysis to accurately characterize and simulate complex elastic systems. Pressure vessels pose a secondary challenge towards these simulations due to acoustoelastic effects generating a coupled response between the structure and the enclosed acoustic fluid [1]. Two common aerospace structures susceptible to these effects are solid rocket boosters and advanced solid rocket motors. During launch, thrust or pogo oscillations can be produced in these boosters and motors as the propellant experiences an acoustic excitation that couples with the booster's structural response. This results in vibrations throughout the structure which pose strong loadings on electronic and avionics systems located on the booster, as well as to the attached rocket, cargo, or crew [2]. In several severe cases, these thrust oscillations have resulted in complete rocket failures [2, 3]. It is therefore critical to design these aerospace structures to efficiently dampen or diminish such oscillations [4, 5]. At the backbone of the solution strategies for oscillation characterization and mitigation is a finite element modal analysis of the flight structure free of fixed boundary conditions, hereafter denoted as free-free.

Modal analysis is typically performed on rocket booster or motor models with an internal pressure force to represent the acoustic effects of the propellant within the structure. In general, a free-free analysis of a structure results in six rigid body modes (mode shapes with frequency of 0 Hz) corresponding to unrestricted motion in the three degrees of translation and three degrees of rotation that govern motion of all 3-D structures. However, when the pressurized structure's free-free modal analysis is performed, the six rigid body modes are raised and no longer occur at zero frequency, suggesting an unrealistic grounding of the system due to pressure-stiffening. Nonetheless, the elastic or flexible modes from these models are still commonly used by analysts for acoustoelastic modal coupling analysis of the structure. Thus, since the rigid body modes

E. A. Jewell (✉)

Langley Research Center, National Aeronautics and Space Administration, Hampton, VA, USA

Department of Aeronautics and Astronautics, Stanford University, Stanford, CA, USA

e-mail: ejewell@stanford.edu

I. Yunis

Langley Research Center, National Aeronautics and Space Administration, Hampton, VA, USA

e-mail: isam.yunis@nasa.gov

cannot be accurately predicted by the finite element modal analysis, it is unknown whether the flexible modes are accurate and should be used for further analysis. To answer this question, an acoustoelastic structure was designed, fabricated, and modal tested with and without pressure to discern the true elastic modes of the structure. These results were then compared to finite element results to determine whether free-free modal analysis models give accurate results for pressure vessels and similar acoustoelastic structures. For this paper, the finite element models were produced in Femap and analyzed with MSC Nastran.

4.2 Design of Pressure Vessel Using Finite Elements

A small pressure vessel was desired so that it could be easily analyzed, fabricated, certified, and tested at NASA's Langley Research Center (LaRC). Design requirements for the vessel were imposed by both the researchers and LaRC safety codes. Requirements created by the former included having the first flex mode in bending, a frequency shift of approximately 10% between the unpressurized and pressurized test cases of the structure, ensuring the structure would not yield at this analytically chosen pressure level, and simulating a reduction in the quantity of rigid body modes from six to three or fewer. For the first requirement, the first flex mode was specified as a bending mode to encourage the designed structure to be similar dynamically to a solid rocket booster or advanced solid rocket motor. For the second requirement, a large frequency shift between the pressurized and unpressurized cases allowed for greater fidelity when experimentally evaluating the mode frequencies of the structure.

Design requirements posed by LaRC were in accordance with LPR 1710.40 M (Internal Langley Research Center Pressure Systems Handbook) and ASME Section VIII—Div 1 & 2 (ASME's Boiler and Pressure Vessel Code). Key requirements included, material certifications for all components, detailed part, assembly, and weld drawings, weld inspections and certifications, finite element stress analysis at Maximum Allowable Working Pressure (MAWP), and a hydrostatic proof test.

4.2.1 Final Acoustoelastic Structure Design

The final pressure vessel geometry is shown in Fig. 4.1 and was a 50.8 mm (2 in.) outer diameter, 315 mm (12.4 in.) long cylinder with flat, 19 mm (0.75 in.) thick end caps. The tube of the vessel was 1.24 mm (0.049 in.) thick. Both the end caps and tube were Low-Alloy Steel and modeled with finite elements properties for AISI 8630 with a yield strength of 310 MPa (45,000 psi). The endcaps were welded to the tube with 4.4 mm (0.175 in.) welds in accordance with ASME Section VIII.

To pressurize the system, both a fill and relief valve were added to the system. They were placed at opposite endcaps to balance the system. The valves were sized to be fail safe when connected to a standard, 20.68 MPa (3000 psi) gaseous N₂ K-bottle (GN2). The total mass of the system unpressurized was approximately 2.0 kg (4.5 lb).

The finite element model (FEM) used for stress analysis of the pressure vessel is shown in Fig. 4.2, with 6.4 mm (0.25 in.) NPT holes in the endcaps at the valve connections. The model was made of NASTRAN CQUAD4 elements with 40 elements circumferentially, and 90 elements axially. The end caps use the same 40 circumferential grids and 9 radial elements.



Fig. 4.1 Final manufactured pressure vessel with pressure system components attached. The fill valve and K-bottle connection are shown on the right, the pressure vessel centered, and the relief valve to the left

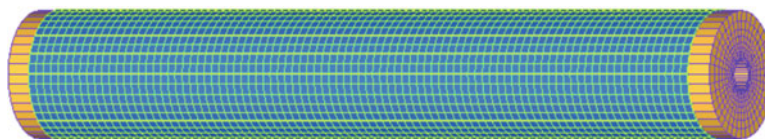


Fig. 4.2 FEM of pressure vessel used for static stress analysis

4.2.2 Finite Element Results for Comparison

To discern the pressure vessel geometry, linear modal analysis was performed on various pressure vessel models. The structure depicted in Figs. 4.1 and 4.2 was selected since it had both the first elastic mode in bending, and an approximate 10% shift in frequency between pressurized and unpressurized mode frequencies that did not yield the structure. The FEM used for this modal analysis differed from Fig. 4.2 by having elements covering both valve holes and by representing the fill and relief valves by point mass elements connected with RBE3 elements to the vessel. This mesh can be seen on mode displacement plots in Fig. 4.3.

Results from modal analysis of the structure are presented in Table 4.1. The table contains the modal frequencies for the first ten modes of the structure for the unpressurized, 2.00 MPa (290 psi), and 1.38 MPa (200 psi) cases, with corresponding percent shift in frequency from the unpressurized case. For all three pressurization levels, the first six modes are the rigid body modes, then Modes 7 and 8 are bending modes, and Modes 9 and 10 are shell modes. There was no discernable difference in the mode shapes with any of the trial pressures. It should be noted that the 2.00 MPa pressurization case was the designed pressurization case for the experiment, since it gave a 9% shift in frequency. Results for the lower 1.38 MPa case are also presented in Table 4.1 for redundancy in comparing error between experimental results and predicted analysis results. Also, after the pressurization levels were determined through modal analysis, a static analysis was performed pressurizing the structure to the desired level to verify that the pressure vessel would not yield.

Table 4.1 also reveals that the bending modes do not shift in frequency between the pressurized and unpressurized cases. This is expected since pressurizing the structure should stress the end caps and ovalize the shell walls. Since the bending motion is independent of the pressure expansion of the system, the bending modal frequencies should remain consistent whether the system is pressurized or unpressurized. Therefore, only the first shell modes, Modes 9 and 10, are deemed significant and were the basis for comparison between the finite element results and experimental results.

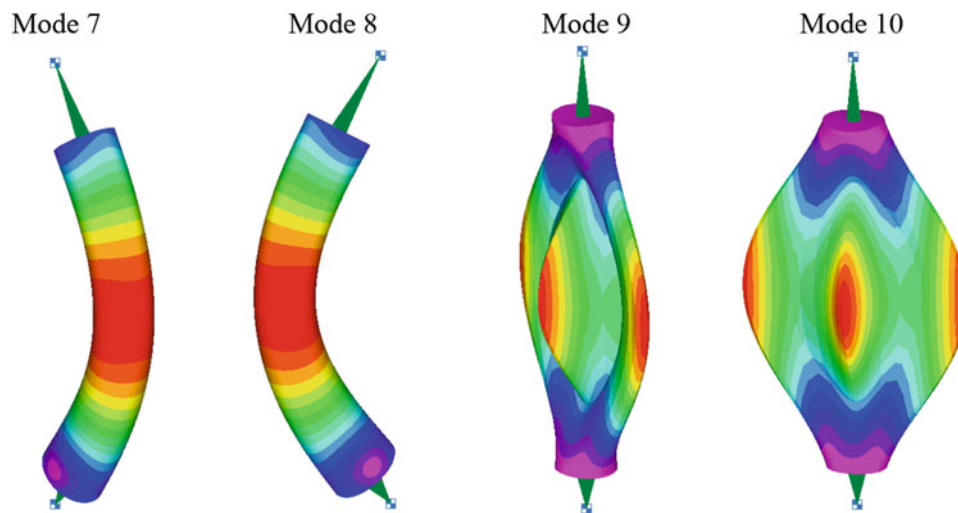


Fig. 4.3 Displacement plots of first four flex mode shapes with no internal pressure

Table 4.1 FEM predictions for modal frequencies of unpressurized and pressurized cases

Mode #	Unpressurized (Hz)	Pressure 1.38 MPa (Hz)	% Shift	Pressure 2.00 MPa (Hz)	% Shift
1	1.78E-03	13.67	10 ⁵	16.46	10 ⁵
2	5.49E-03	1.98	10 ⁴	2.39	10 ⁴
3	6.16E-03	1.98	10 ⁴	2.39	10 ⁴
4	7.41E-03	0.02	10 ²	0.04	10 ²
5	7.83E-03	5.12	10 ⁴	6.16	10 ⁴
6	8.74E-03	5.12	10 ⁴	6.16	10 ⁴
7	1129	1129	0	1129	0
8	1129	1129	0	1129	0
9	1659	1760	6	1804	9
10	1659	1760	6	1804	9

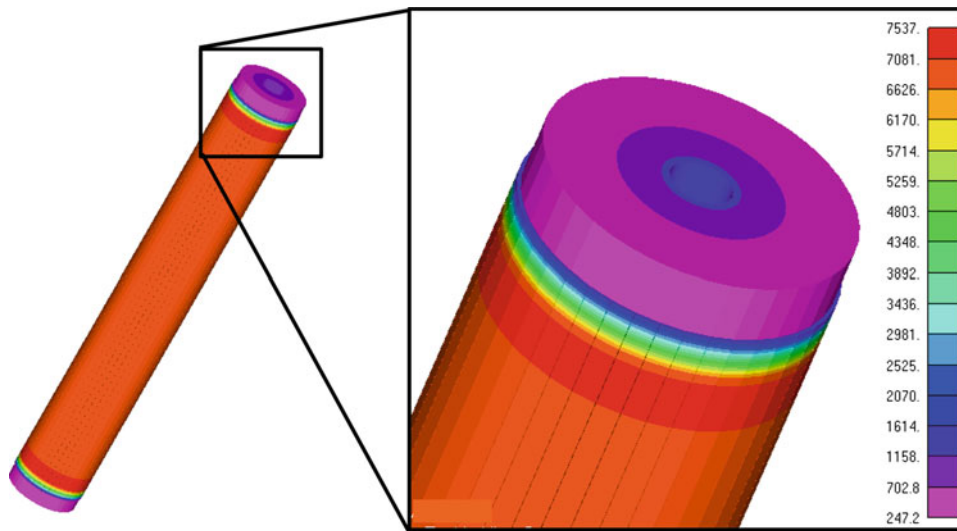


Fig. 4.4 Finite element static stress analysis of pressure vessel at 2.76 MPa (400 psi) internal pressure with element thicknesses depicted. Scaling in psi

4.2.3 Required Pressure System Testing and Results

Before the pressure vessel could be modally tested at LaRC, the vessel needed to pass several system tests in accordance with LPR 1710.4 M. This included a 100% visual weld inspection, finite element stress analysis at MAWP, and a hydrostatic test. The MAWP needed to have a minimum factor of safety (FoS) on the stress of 3.5 per ASME Section VIII. Due to the 100% visual only inspection on the weld, and no radiographic, magnetic particle, liquid penetrant, or ultrasonic inspection, a weld efficiency factor of 0.7 also needed to be applied to FoS calculation. Using the material yield strength of 310 MPa, an internal pressure of 2.76 MPa (400 psi) gave a maximum stress of 52.0 MPa (7540 psi) at the red region depicted in Fig. 4.4, giving a FoS of 4.18, above the required 3.5. Thus 2.76 MPa was safely deemed MAWP, and again it can be noted since the experimental pressure was selected as 2.00 MPa, the structure will not yield during testing.

A hydrostatic proof test was then performed at 1.5 times the MAWP, or 4.14 MPa (600 psi), as required by ASME Section VIII. Images of the test set-up are presented in Fig. 4.5. After passing this test, the vessel was approved for modal testing.

4.3 Modal Test of Acoustoelastic System

To modal test the structure, the pressure vessel was instrumented with 12 uniaxial accelerometers and 2 tri-axial accelerometers as shown in Fig. 4.6. Accelerometers 1, 4, 7, and 10 were mounted 90° from each other and 38 mm (1.5 in.) from the fill valve endcap. Accelerometers 2, 5, 8, and 10 were 90° from each other and at the midplane of the vessel. Accelerometers 3, 6, 9, and 12 were 90° from each other and 38 mm (1.5 in.) from the relief valve endcap. Accelerometers 13 and 14 were tri-axial and mounted on the valves.

The complete modal test set-up is depicted in Fig. 4.7. The free-free boundary condition was simulated by suspending the vessel on two bungees connected near the fill and relief valves, with bungee frequencies all <5 Hz. An instrumented test hammer with a brass tip was used for all tap testing. In total, four modal tap tests were conducted on the system as follows: (1) Unpressurized (2) 2.00 MPa (3) 1.38 MPa (4) Unpressurized.

For Cases 2 and 3, the K-bottle and hose were connected to the structure to maintain pressurization throughout the duration of the test. It is expected that this hose connection may shift the bending mode frequencies of the system but not the shell modes, the modes of interest.



Fig. 4.5 In the top image, complete hydrostatic proof test set-up with pressure gauges to the left and the designed pressure vessel clamped in the background on the right, circled in red. In the bottom image, a close view of the pressure vessel being vented initially during the hydrostatic proof test as the vessel fills with water at a low pressure

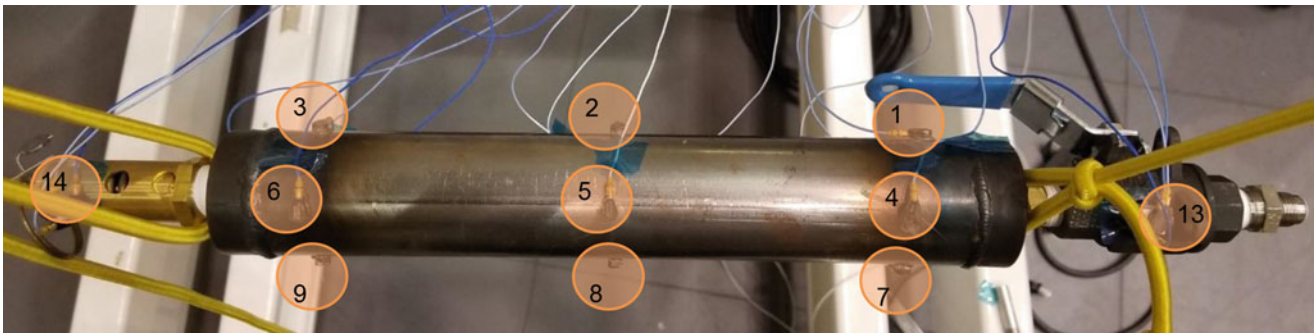


Fig. 4.6 Accelerometer numbers and locations on pressure vessel. Fill valve on the right, relief valve on the left. Accelerometers 10 (radially patterned with 1, 4 and 7), 11 (with 2, 5, and 8), and 12 (with 3, 6, and 9) are not shown

4.3.1 Modal Tap Test Results

For Case 1, drive points were at Accelerometers 4, 5, 8 and 9 to capture both the bending and shell elastic modes. For Cases 2, 3, and 4, the drive point was at Accelerometer 8 since only the shell modes were desired, as discussed in Sect. 2.2. Figure 4.8 presents the Frequency Response Function (FRF) of all four cases. Examining this plot makes it clear that the bending modes are in fact impacted by the additional boundary condition imposed on the system by the hose connection since the bending mode frequency decreased from 1156 Hz for the Unpressurized Case 1 and 4, to approximately 1140 Hz. However, the shell modes are still distinct and dominant peaks between 1600 and 1700 Hz. Table 4.2 presents a summary of the results for all four cases including the estimated frequency and damping as derived by circle-fitting the drive point FRF in the region of resonance. From Table 4.2, it is evident that Cases 1 and 4 gave nearly identical results, confirming that the structure did not change by the pressurization process. Therefore, Case 1 is what is referred to as the unpressurized case going forward.

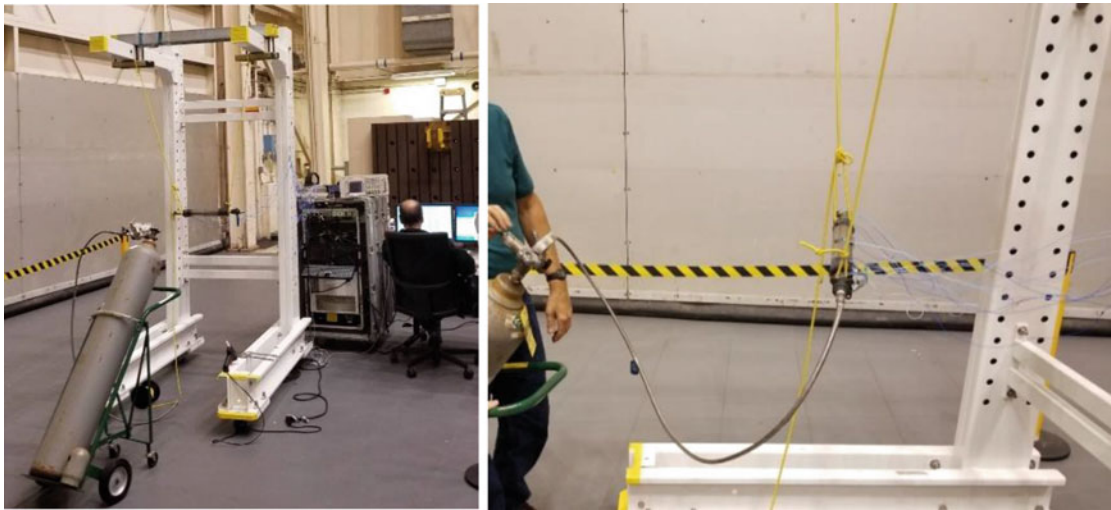


Fig. 4.7 In the left image, complete test set-up with K-bottle, bungee suspended pressure vessel, and data acquisition system. In right image, test article being pressured via the K-bottle connection

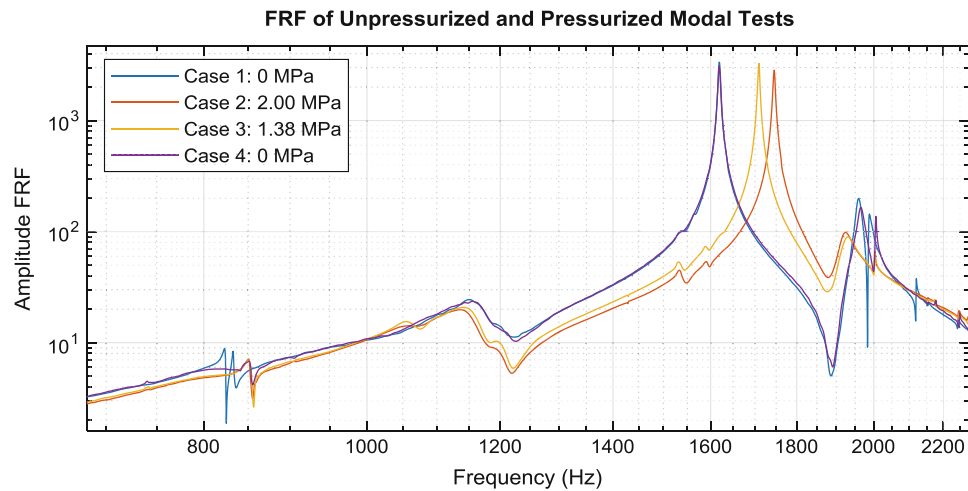


Fig. 4.8 Overlay of modal test FRFs for all four pressurization cases

Table 4.2 Summary of shell bending mode frequencies and estimated damping from circle-fitted results for all four cases

Case	Pressure (MPa)	First shell mode frequency (Hz)	Damping (%)
1	0	1619	0.16
2	2.00	1745	0.38
3	1.38	1710	0.17
4	0	1618	0.16

4.4 Comparison of Experimentally Measured and Simulated Flex Modes

The MSC Nastran modal frequencies (predicted modes) and experimentally measured modal frequencies (measured modes) were first compared for the unpressurized case and are presented in Table 4.3. Initial percent error calculations between both mode shapes and methods are presented in Column 5.

The FEM was then correlated to the unpressurized case by adding the accelerometer mass to the valves, 0.5 g (1e-3 lb) per accelerometer, shifting and correcting the thickness of the endcaps to match the machined pressure vessel, and reducing the cylinder tube thickness from 1.24 mm (0.049 in.) to 1.23 mm (0.0485 in.), accounting for the smallest allowable machined part tolerance. These corrections gave predicted modes identical to measured modes, 1156 Hz and 1619 Hz respectively and a Final Difference Percent Error of 0% as shown in Column 6.

Table 4.3 Finite element analysis predicted and experimentally measured modal frequencies for unpressurized structure

Mode #	Mode description	Predicted frequency (Hz)	Measured frequency (Hz)	Initial difference (%)	Final difference (%)
7	Bending	1129	1156	-2.34	0.0
9	Shell	1659	1619	2.47	0.0

Table 4.4 Correlated FEM predictions for modal frequencies of unpressurized and pressurized cases

Mode #	Unpressurized (Hz)	Pressure 1.38 MPa (Hz)	% Shift	Pressure 2.00 MPa (Hz)	% Shift
1	2.25E-03	14.24	10 ⁵	17.15	10 ⁵
2	5.03E-03	2.09	10 ⁴	2.51	10 ⁴
3	5.92E-03	2.09	10 ⁴	2.51	10 ⁴
4	7.07E-03	0.06	10 ²	0.09	10 ³
5	7.57E-03	5.47	10 ⁴	6.59	10 ⁴
6	8.88E-03	5.47	10 ⁴	6.59	10 ⁴
7	1156	1156	0	1156	0
8	1156	1156	0	1156	0
9	1619	1724	6	1769	9
10	1619	1724	6	1769	9

Table 4.5 Final results comparing correlated FEM predicted and experimentally measured modal frequencies

Case	Pressurization (MPa)	Predicted mode frequency (Hz)	Measured mode frequency (Hz)	% Error
1	0	1619	1619	0.00
2	2.00	1769	1745	1.38
3	1.38	1724	1710	0.82

Modal analysis was then re-performed on the updated FEM and final results for all three pressure cases are given in Table 4.4. Ultimately, the predicted first shell mode frequencies are 1619 Hz for the unpressurized case, 1769 Hz for the 2.00 MPa case, and 1724 Hz for the 1.38 MPa psi case.

4.4.1 Predicted Versus Measured Shell Mode Frequencies

Table 4.5 presents a summary comparing MSC Nastran first shell modes from the correlated model to the experimental results. Percent errors were found to be 1.38% for the 2.00 MPa case, and 0.82% for the 1.38 MPa. An alternative comparison is examining the difference in the frequency shift due to pressure stiffening. This percent error calculation gives the error between the predicted frequency shift (e.g., for 2.00 MPa, 150 Hz) to the measured frequency shift (e.g., for 2.00 MPa, 126 Hz). This yields a frequency difference percent error shift of 16.0% for the 2.00 MPa case, and 13.3% for the 1.38 MPa case. These larger error values in the difference are likely due to small uncertainties in pressurization measurements during test due to the resolution of the pressure gauges. Therefore, even though finite element models for free-free pressure vessels yield unrealistic rigid body modes, Nastran is still able to reasonably predict the structural modes of the pressurized and unpressurized structure.

4.5 Conclusion

By designing, analyzing, fabricating, and testing a cylindrical pressure vessel, it was discerned that MSC Nastran can accurately predict pressurized and unpressurized flex modes of acoustoelastic shell structures, despite the rigid body modes being inaccurately predicted. A simple pressure vessel was designed and certified following ASME Section VIII Boiler and Pressure Vessel Code, and then modal tap tested to determine the structure's frequencies with and without internal pressure. Comparing these test results to a correlated finite element simulation revealed that the predicted and measured modes differed by less than 2% error. Therefore, pressurized flexible modes may be used for dynamic analysis of rockets even though the rigid body modes exhibit grounding.

Acknowledgements The authors would like to thank the various personnel at LaRC who helped ensure the completion of this project. Special appreciations are extended towards Ms. Christy Swartz, Dr. Kenny B. Elliott, Mr. Brian Emmett, Mr. Richard J. Bodkin, Mr. Joe O'Connell, and Mr. Dale LeBlanc.

References

1. Dowell, E.H., Gorman, G.F., Smith, D.A.: Acoustoelasticity: general theory, acoustic natural modes and forced response to sinusoidal excitation, including comparisons with experiment. *J. Sound Vib.* **52**(4), 519–542 (1977)
2. Larsen, C.E.: NASA experience with POGO in human spaceflight vehicles. NATO RTO Symposium (2008)
3. Ryan, R.S., Kiefling, L.A., Buchanan, H.J.: Simulation of Saturn V S-II stage propellant feedline dynamics. *J. Spacecr. Rocket.* **7**(12), 1407–1412 (1970)
4. Dotson, K.W.: Mitigating pogo on liquid-fueled rockets. *Crosslink.* **5**(1), 26–29 (2003)
5. Bastia, D., Zupp, G.: Prevention of Space Shuttle Pogo: Brief History. Space Shuttle Program Pogo Historical Study Data Book. The Boeing Company, Chicago, IL (2007)



Chapter 5

Pretest Analysis for Modal Survey Tests Using Fixed Base Correction Method

Peter Kerrian and Kevin L. Napolitano

Abstract A fixed base correction method that uses acceleration constraint shapes as references to transform flexible or dynamically active boundary conditions into fixed boundaries has been recently implemented for modal tests. The method uses test data directly to generate constraint shapes associated with accelerometer measurements at the test article and test fixture interface that are then used as references when calculating corrected fixed base frequency response functions (FRFs). The main challenge with the method is that at least one disturbance source, such as a modal shaker, must be applied to the boundary structure for each constraint shape used, so it is advantageous to understand how many constraint shapes may be required to fix a boundary for test planning purposes. This paper outlines a procedure that uses multipoint constraint equations in an analysis model of an integrated test article and its test fixture to determine the number of exciters necessary to apply the fixed base correction method. The method is verified by comparing mode shapes of the fixed base test article to the system model with a number of multipoint degrees of freedom constrained.

Keywords Modal testing · Vibrations · Base-shake · Environmental testing · Fixed base · Constraint shapes

Nomenclature

CS	Constraint shape
DOF	Degree of freedom
DP	Drive point
FB	Fixed base
FEA	Finite element analysis
FEM	Finite element model
FRF	Frequency response function
H	CS from SVD of FRF matrix
MAC	Modal assurance criteria
MPC	Multipoint constraint
PSMIF	Power spectral mode indicator function
RV	Residual vectors
SC	CS from SVD of shape coefficients
SMURF	Structural modification using frequency response functions
SVD	Singular value decomposition

5.1 Introduction

Modal tests are performed to validate analysis models of structures, and it is important to support a test article using fixtures that allow an engineer to focus his time and effort on updating the analysis model instead of the supports. Oftentimes, however, inadequate boundary condition fixtures are used in modal surveys because the design and manufacture of a proper boundary condition may be too expensive for a program. Engineers then spend great effort and expense during the model correlation task modeling and correlating the test fixture instead of the analysis model, and errors in modeling of the test fixture propagate to the updated analysis model.

P. Kerrian · K. L. Napolitano (✉)
ATA Engineering, Inc., San Diego, CA, USA
e-mail: kevin.napolitano@ata-e.com

Recently, a fixed base correction method has been implemented that uses acceleration constraint shapes as references when calculating frequency response functions (FRFs) to transform flexible or dynamically active boundary conditions into fixed boundaries [1–4]. In this method, the number of exciters mounted to the boundary must be equal to or greater than the number of constraint shape references. Usually, the number and location of exciters on the boundary are determined in an ad hoc manner. However, as the implementation of the method has progressed, there have been requests to test structures on more complicated boundary conditions such as static test fixtures which, while being very good for their purpose of providing static loads, are not very good at providing a solid interface for modal surveys.

Unfortunately, applying the fixed base correction method directly to FRFs generated from an analysis model does not result in accurate fixed base correction estimates due to modal truncation. Although residual vectors can be used to estimate the response of out-of-band modes, they are still not accurate enough to result in accurate fixed base corrections. This paper outlines a pretest analysis procedure that can be utilized to determine the number of exciters used to generate constraint shapes. To account for the error, an improved method was developed that integrates the constraint shapes into the finite element analysis (FEA) as multipoint constraints (MPC) during the modal eigenvalue solution. The resulting synthesized fixed base FRFs from the full system model reproduce the true fixed base corrected FRFs significantly better than the coordinate transformation method. The efficacy of including more constraint shapes on reducing the error of modal frequencies is also investigated.

5.2 Motivation and Example Structure

Research using accelerations as references to fix degrees of freedom in modal tests has been widely published [5]. Recently, the method has been extended by fixing constraint shapes of structure boundaries instead of individual physical degrees of freedom [6–11]. For either method, a partial inversion of the FRF matrix is performed to utilize the accelerations or constraint shapes as references. Accurately accounting for the residual vectors is essential because shifts in the fixed based modal frequencies result from shifts in the antiresonances of the original FRF set. During testing of the structure, the response transducers measure the entire response of the system, including the modes in frequency range of interest as well as the residual vectors from modes outside of the target mode set. However, when an engineer performs a pretest analysis to identify target and secondary modes, the residual vectors are not included and thus the calculated fixed base FRFs do not match the true fixed base FRFs.

To demonstrate these challenges, a representative rectangular aerospace test article, shown in Fig. 5.1, with eight attached substructures was developed, and an octagonal static test cell with cross I-beam support was underdesigned to provide a sufficient amount of base motion. The test article was attached to the static test cell with 204 stiff spring elements. The fixed base FEA model was solved for the fixed base modes with the degrees of freedom (DOFs) of the spring elements on the static test cell fixed. The primary target modes for the modal survey were identified as all modes below 50 Hz, and secondary target modes were identified as all modes below 100 Hz. Table 5.1 contains the modal frequencies and effective mass fractions for primary and secondary target modes. For the orientation of the test article, the X and Z axis are in plane, and the Y axis is out of plane and follows the length of the test article. Target modes with low effective mass fractions are attributed to primarily substructure modes. The primary bending modes of the overall test article are located at 31.2 and 37.3 Hz. The vertical mode of the test article at 116 Hz was intentionally temporarily excluded from this pretest analysis in order to gauge accuracy of the method when a mode with significant effective mass fraction is excluded.

The FEA model was solved for the modes of the test article attached to the static test cell, which would be representative of the test configuration. Two shaker locations were selected on opposite sides on the top of the test article. An additional 12 shaker locations, 8 vertical and 4 lateral, were selected on the static test cell that would be used for the fixed base correction method. FRFs were synthesized from the mode shapes between all 14 shaker locations. Following the structural modification using frequency response functions method (SMURF), a partial FRF matrix inversion was performed using the 12 shaker DOFs to make the drive point acceleration references. The resulting FRF associated with the two shaker forces on the structure should correspond to fixed base FRF. Power spectral modal indicator functions (PSMIFs) were computed from the test article drive points FRFs for both the true fixed based FRFs (blue curve) and the synthesized fixed base FRFs from the full system model (red curve) and are shown in Fig. 5.2. Performing the FRF matrix inversion on the system modes did not accurately obtain the fixed base FRFs because the residual terms from higher frequency modes were not included, as would be in the measured test FRFs. The FEA model was resolved for the mode shapes and residual vectors for all the shaker locations. New FRFs were synthesized with the residual vectors and the process was repeated to obtain an updated fixed base PSMIF for the system. As shown in Fig. 5.2, the PSMIF calculated with the residual vectors, plotted in green, was a significant improvement in representing the true fixed base PSMIF over the full system model without the residual vectors.

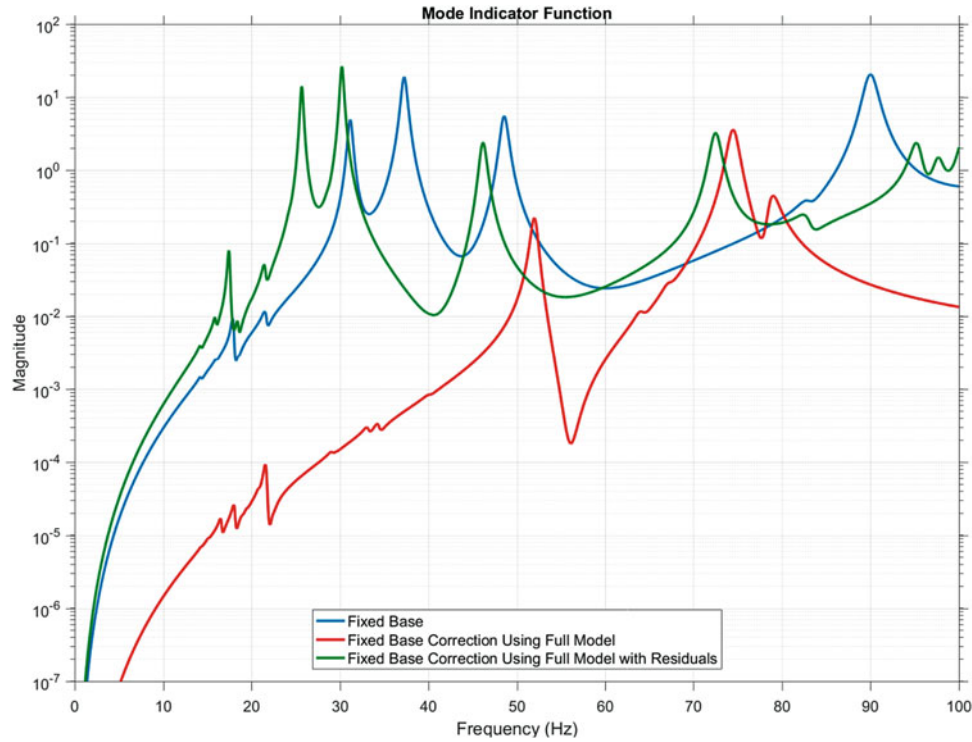


Fig. 5.2 Fixed base PSMIF comparison of true fixed base model (blue), full model (red), and full model with residual vectors (green)

However, the residual vectors calculated from the FEA model are an estimate, and the errors between the true and synthesized FRFs, especially the antiresonances, are accentuated during the partial matrix inversion, which leads to the discrepancies in the PSMIFs.

5.3 Constraint Shape Calculation

The motion of a boundary interface between two structures can be represented by a linear combination of basis vectors, also known as constraint shapes. The first step in calculating constraint shapes for a test article attached to a static test cell is determining the set DOFs at the interface, $\{x_B\}$. The entire static test cell could be included in $\{x_{B_s}\}$ to completely remove the motion of the test cell. However, the complexity of the constraint shapes required to represent this motion would be challenging to capture with a finite number of shakers attached to the static test cell. As a result, the subset of DOFs in $\{x_B\}$ should be sufficiently large to capture the motion at the test article interface with the static test cell. For this pretest analysis example, $\{x_B\}$ included DOFs fixed for the fixed base solution, as well as rings of adjacent nodes inside and outside the original set, for a total of 1911 DOFs.

Figure 5.3 contains images of the FEM showing both the set of DOFs included in the constraint shape calculation and the connection interface between the test article and the static test cell. Nodes in blue correspond to the direct connection points, while nodes in red are adjacent nodes. The test article is attached with stiff springs.

Two potential methods that can be used to calculate the constraint shape of the full system model using singular value decomposition (SVD) are studied here. The first method is to calculate the constraint shapes directly from the shape coefficients at the interface between the test article and the static test cell. The shape coefficient matrix $[\phi]$ is partitioned down to the matrix $[\phi_B]$, which contains the shape coefficients for the DOFs in $\{x_B\}$. The second method is to synthesize the FRFs $[H_B]$ between the shaker locations on the test article and the interface DOFs contained in $\{x_B\}$ and perform the SVD on the matrix $[H_B]$.

$$[\phi_B] = [U][\Sigma][V]^H \text{ or } [H_B] = [U][\Sigma][V]^H \quad (5.1)$$

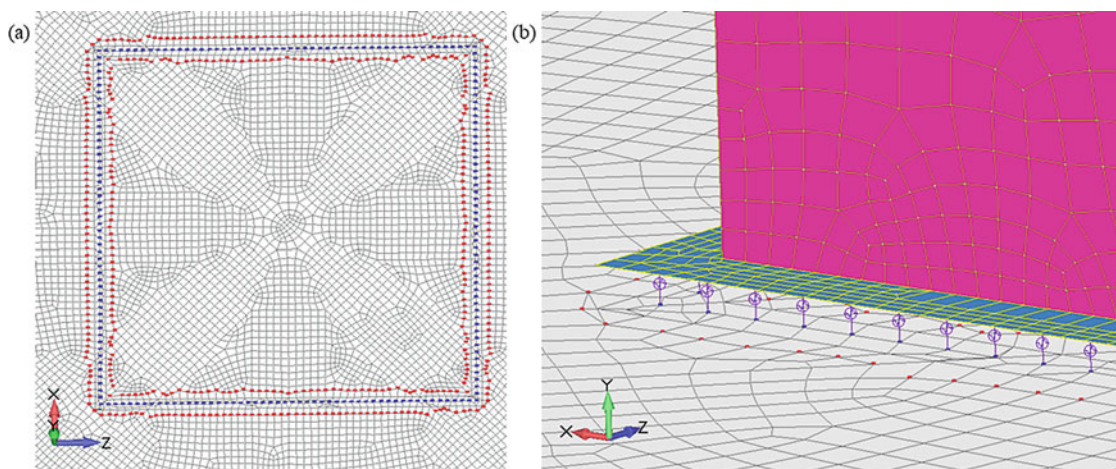


Fig. 5.3 (a) FEM nodes contained in constraint shape DOF set, $\{x_B\}$; the blue nodes correspond to direct attachment to the test article and the red nodes are adjacent nodes; (b) connection between test article and static test cell floor

Table 5.2 Singular values from shape coefficients and FRF matrix methods

N	Shape coefficient		FRF matrix	
	σ_n/σ_1	Sum % of total	σ_n/σ_1	Sum % of total
1	1.00	24.79%	1.00	40.41%
2	1.00	49.47%	0.60	64.86%
3	0.98	73.75%	0.30	76.99%
4	0.48	85.52%	0.21	85.54%
5	0.25	91.76%	0.20	93.82%
6	0.24	97.81%	0.12	98.86%
7	0.01	98.12%	0.01	99.28%
8	0.01	98.43%	0.01	99.62%
9	0.01	98.74%	0.00	99.75%
10	0.01	99.00%	0.00	99.83%
11	0.01	99.20%	0.00	99.89%
12	0.01	99.36%	0.00	99.93%
13	0.01	99.52%	0.00	99.95%
14	0.01	99.68%	0.00	99.96%
15	0.00	99.75%	0.00	99.97%

The constraint shapes for either method are defined by the columns of the left singular vector ($[\psi] = [U]$). The singular values of $[\Sigma]$ can be normalized to the maximum singular value to the relative contribution of each constraint shape to the overall motion of the interface DOFs and assist in determining the number of constraint shapes required to eliminate all of the interface motion. If a limited number of constraint shapes can completely represent the motion of the interface, then the method will be 100% effective. Either method is acceptable to calculate the constraint shapes. The difference between the two is that the shape methods favors the motion of the interface, while the FRF matrix method favors the motion of the base excited by the shakers.

For the pretest analysis example, the full system model produced 31 modes below 100 Hz. Constraint shapes were calculated via both methods. Table 5.2 contains a listing of the ratio of the singular values to the first singular value, and the ratio of the sum of the N singular values to the total sum of singular values. The cumulative sum percent total describes what percentage of the total motion of the interface DOFs is captured by constraint shapes 1 to N. Table 5.2 also demonstrates that with 15 constraint shapes, all but 0.25% of the interface motion is captured by the subset of constraint shapes.

A cross modal assurance criteria (MAC) was calculated to compare the constraint shapes generated from the shape coefficient method and the FRF matrix method. As shown in Table 5.3, the rigid body modes comprise the first six for each method but with a different order. The primary difference is that the Z-lateral shape from the FRF method contains an RX rocking component resulting in the lower MAC Value.

Table 5.3 Cross-MAC table between shape and FRF matrix constraint shapes

		Cross MAC Table																Test	
		FRF Matrix Constraint Shapes																	
Shape Coefficient Constraint Shapes	MACtg	1	2	3	4	5	6	7	8	9	10	11	12	13	14	15	16		
	1	1.000		0.99															1.00
	2	0.996						0.88											0.94
	3	0.980	1.00																1.00
	4	0.475		1.00															1.00
	5	0.252				0.89													0.94
	6	0.244					1.00												1.00
	7	0.013							0.22	0.77									0.88
	8	0.012									0.85								0.92
	9	0.012										0.79							0.89
	10	0.010							0.77	0.23									0.88
	11	0.008																0.63	0.79
	12	0.007												0.83					0.91
	13	0.007											0.76			0.23			0.87
	14	0.006																	0.41
	15	0.003																	
	16	0.002														0.53			0.73
FEM	CRS	1.00	1.00	1.00	0.94	1.00	0.94	0.88	0.88	0.99	0.95	0.87	0.91	0.73	0.48		0.79		

Table 5.4 contains plots of the first 12 constraint shapes calculated via the shape coefficient method. The first 6 correspond to the rigid body modes of the interface. The next 6, and all subsequent constraint shapes not shown, are flexible motion of the static test cell floor plates. The first 6 flexible shapes have two antinodes on each of the four sides and have primarily vertical deformation, which would make them easy to constrain with two vertical shakers on each side. The higher order constraint shapes have significantly more complicated deformation patterns, implying nonphysical motion that is an artifact of the SVD.

5.4 Application of Constraint Shape to Frequency Response Function Calculation

The constraint shapes can be applied to the FRF matrix to remove the interface motion in the following procedure. First, the mode shapes from the full model are used to synthesize the FRF matrix, $[H]$, which includes the interface DOFs, $\{x_B\}$, and the shaker DOFs, $\{x_I\}$.

$$\begin{Bmatrix} x_I \\ x_B \end{Bmatrix} = \begin{bmatrix} H_{II} & H_{IB} \\ H_{BI} & H_{BB} \end{bmatrix} \begin{Bmatrix} f_I \\ f_B \end{Bmatrix} \quad (5.2)$$

The constraint shapes, $[\Psi]$, relate the interface DOFs to a set of DOFs associated with each constraint shape, $\{\epsilon\}$.

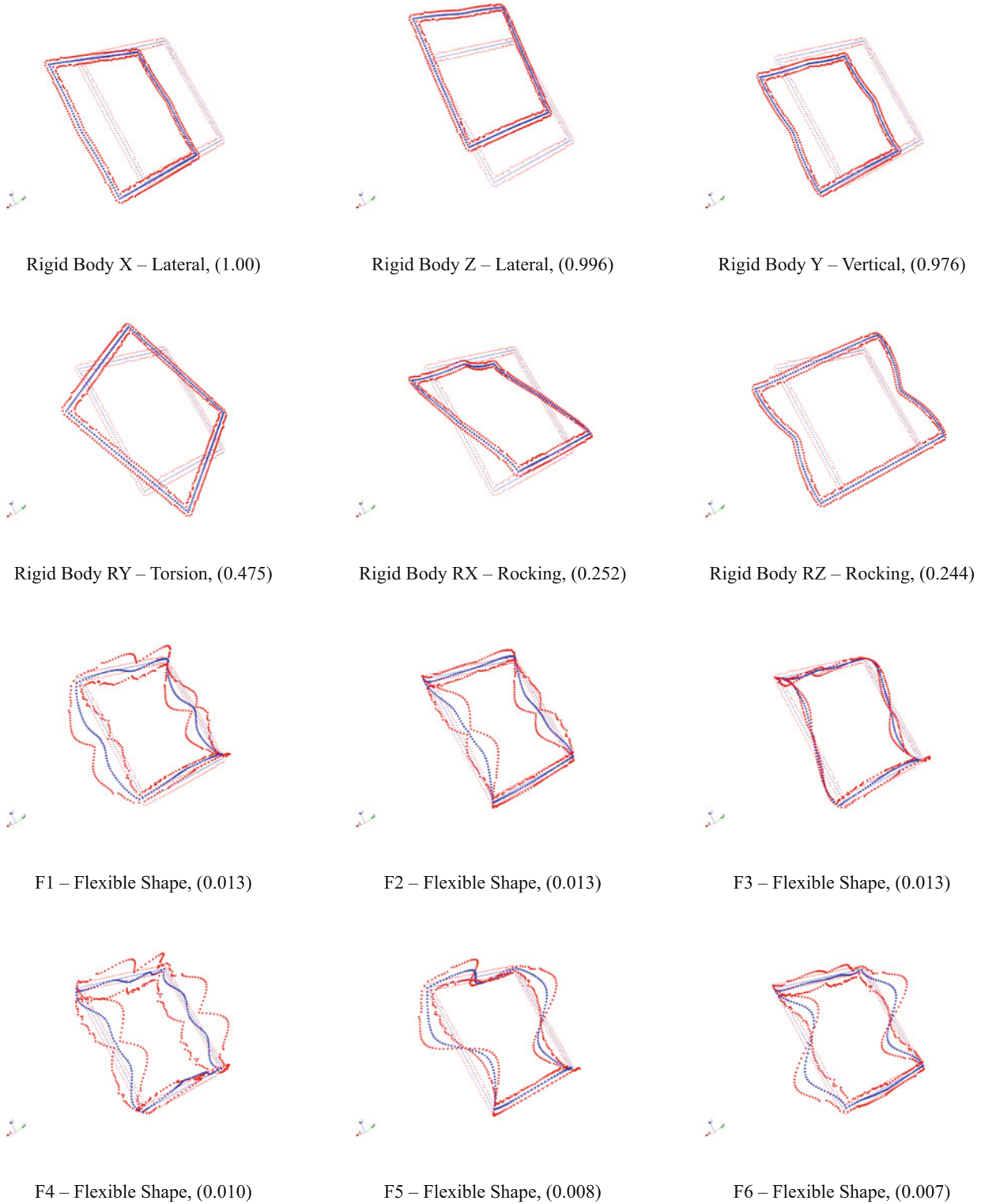
$$\{x_B\} = [\Psi]\{\epsilon\} \quad (5.3)$$

The constraint shapes can be inverted to reduce the interface DOFs to a single DOFs associated with each constraint shape as

$$\{\epsilon\} = [\Psi]^+ \{x_B\} \quad (5.4)$$

The FRF matrix can be back expanded in to include the DOFs associated with each constraint shape.

$$\begin{Bmatrix} x_I \\ \epsilon \end{Bmatrix} = \begin{bmatrix} H_{II} & H_{IB} \\ \Psi^+ H_{BI} & \Psi^+ H_{BB} \end{bmatrix} \begin{Bmatrix} f_I \\ f_B \end{Bmatrix} \quad (5.5)$$

Table 5.4 Constraint shapes calculated from SVD of mode shape coefficients

A partial matrix inversion of the FRF matrix can be performed to utilize the constraint shape DOFs as references to remove the base motion of the interface and obtain the fixed base FRFs.

$$f_B = -(\Psi^+ H_{BB})^T \Psi^+ H_{BI} f_I + (\Psi^+ H_{BB})^T \epsilon \quad (5.6)$$

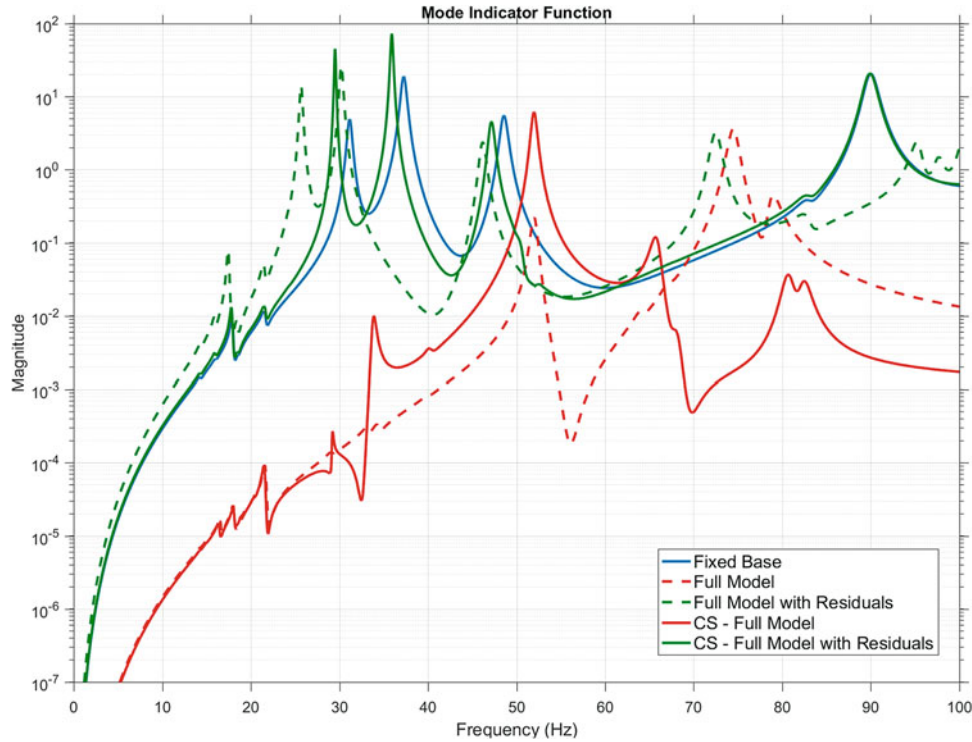


Fig. 5.4 PSMIF comparison of fixed base FRFs for true fixed base model (blue), full model (red), and full model with residual vectors (green); solid lines correspond to FRFs with constraint shapes applied; dashed lines are original curves

The resulting FRF matrix relation is as follows:

$$\begin{Bmatrix} x_I \\ x_B \end{Bmatrix} = \begin{bmatrix} H_{II} - H_{IB}(\Psi^+ H_{BB})^T H_{BI} & H_{IB}(\Psi^+ H_{BB})^T \\ H_{BI} - H_{BB}(\Psi^+ H_{BB})^T \Psi^+ H_{BI} & H_{BB}(\Psi^+ H_{BB})^T \end{bmatrix} \begin{Bmatrix} f_I \\ \epsilon \end{Bmatrix} \quad (5.7)$$

PSMIFs were calculated from the constraint shape corrected fixed base FRFs for the full model solved with and without residual vectors and are shown in Fig. 5.4. The solid lines correspond to the constraint shape corrected PSMIFs and the dashed lines were the original PSMIFs from Fig. 5.2. As expected, the constraint shape corrected model with the residual vectors matches the overall trend of the true fixed base PSMIFs significantly better than the full model without residual vectors. However, the frequencies of the three primary test article modes between 30 and 50 Hz are still underpredicted by 3–5%. Ultimately, an additional procedure is needed to properly constrain the interface motion and accurately predict the fixed base FRFs.

5.5 Multipoint Constraint Method

The method developed to predict the fixed base FRFs of a test article attached to a flexible static test cell involves incorporating the constraint shapes into the eigensolution as MPC equations. The original frequency domain equation motion solved for the system is

$$(s^2 [M] + s [C] + [K]) \{x\} = \{f\} \quad (5.8)$$

The physical base DOFs can be generalized to constraint shape DOFs utilizing the constraint shapes calculated from the SVD of either the shape coefficients or the FRF matrix, and the associated null space.

$$\{x_B\} = \begin{bmatrix} \Psi & N(\Psi^T) \end{bmatrix} \begin{bmatrix} \epsilon \\ \epsilon_N \end{bmatrix} \quad (5.9)$$

A transformation matrix, $[T]$, is defined that relates the internal test article degrees of freedom, $\{x_I\}$, and the boundary degrees of freedom, $\{x_B\}$, to the generalized constraint shape DOFs.

$$x = \begin{Bmatrix} x_I \\ x_B \end{Bmatrix} = \begin{bmatrix} I & 0 & 0 \\ 0 & \Psi & N(\Psi^T) \end{bmatrix} \begin{Bmatrix} x_I \\ \epsilon \\ \epsilon_N \end{Bmatrix} = T\bar{x} \quad (5.10)$$

The transformation matrix can be applied to the mass, damping, and stiffness matrices as well as the force vector.

$$(M_{\Psi\Psi}, C_{\Psi\Psi}, K_{\Psi\Psi}) = T^T (M, C, K) T \quad \text{and} \quad f_{\Psi} = T^T f \quad (5.11)$$

The new equation of motion for the system with the boundary DOFs reduced to a set of generalized constraint shape DOFs is

$$\left(s^2 M_{\Psi\Psi} + s C_{\Psi\Psi} + K_{\Psi\Psi} \right) \{\bar{x}\} = \{f_{\Psi}\}. \quad (5.12)$$

Since the constraint shapes are used as references when calculating FRF, they are moved to the right-hand side of the equation, which results in the same eigenvalue equation as fixing them in an FEA. By fixing the DOFs associated with the generalized constraint shapes, the rows and columns associated with the generalized DOFs are eliminated from the eigensolution and the reduced system model is

$$\left(s^2 M_{\bar{\Psi}\bar{\Psi}} + s C_{\bar{\Psi}\bar{\Psi}} + K_{\bar{\Psi}\bar{\Psi}} \right) \{\bar{x}_{\bar{\Psi}}\} = \{f_{\bar{\Psi}}\} \quad (5.13)$$

where

$$\{\bar{x}_{\bar{\Psi}}\} = \begin{Bmatrix} x_I \\ \epsilon_N \end{Bmatrix} \quad \text{and} \quad \{f_{\bar{\Psi}}\} = \begin{Bmatrix} f_I \\ f_{\epsilon_N} \end{Bmatrix}.$$

In directly applying this equation formalization to the FEA model, MPC equations are calculated that relate the interface DOFs to the generalized constraint shape DOFs, which are defined as scalar points (S-points). One S-point is required for each interface DOF to include the null set of SVD and to ensure a square MPC constraint matrix. A subset of N-S-points are fixed to eliminate the motion of the first N constraint shapes.

5.6 Multipoint Constraint Fixed Base Correction Results

FEA models of the full system with the MPC equations applied were solved for all modes up to 100 Hz with residual vectors for all shaker locations using both the shape coefficient method and the FRF matrix method to calculate the constraint shapes. Individual modal solutions were solved that incorporated N constraint shapes as MPC equations to examine how the fixed base FRFs changed as more constraint shapes were included.

Figures 5.5 and 5.6 contain a PSMIF comparison between the true fixed base FRFs and corrected fixed base FRFs for a different number of constraint shapes for both the shape coefficient method, Fig. 5.5, and the FRF matrix method, Fig. 5.6. For both methods, inclusion of all six rigid body modes sufficiently captures the overall trend of the true fixed base correction method. Including these six rigid body constraint shapes corresponds to removing 97.8% of the interface motion for the shape coefficient method and 98.9% of the interface motion for the FRF matrix method. There are two interesting observations that can be made.

First, for the shape coefficient methods, the true fixed base trend requires six constraint shapes, while the FRF matrix method only requires five constraint shapes. The modal frequency error is still significant, but the overall trend is correct. This artifact can be explained because the sixth constraint shape calculated from the FRF matrix method is the Y-vertical rigid body motion shape. The five previous constraint shapes have already reduced the lateral and rotational interface motion.

Second, the modal frequencies of the MPC models solved with the six rigid body constraint shapes calculated via both methods are equivalent. A slight discrepancy might be expected because of the difference in the percent of the total interface

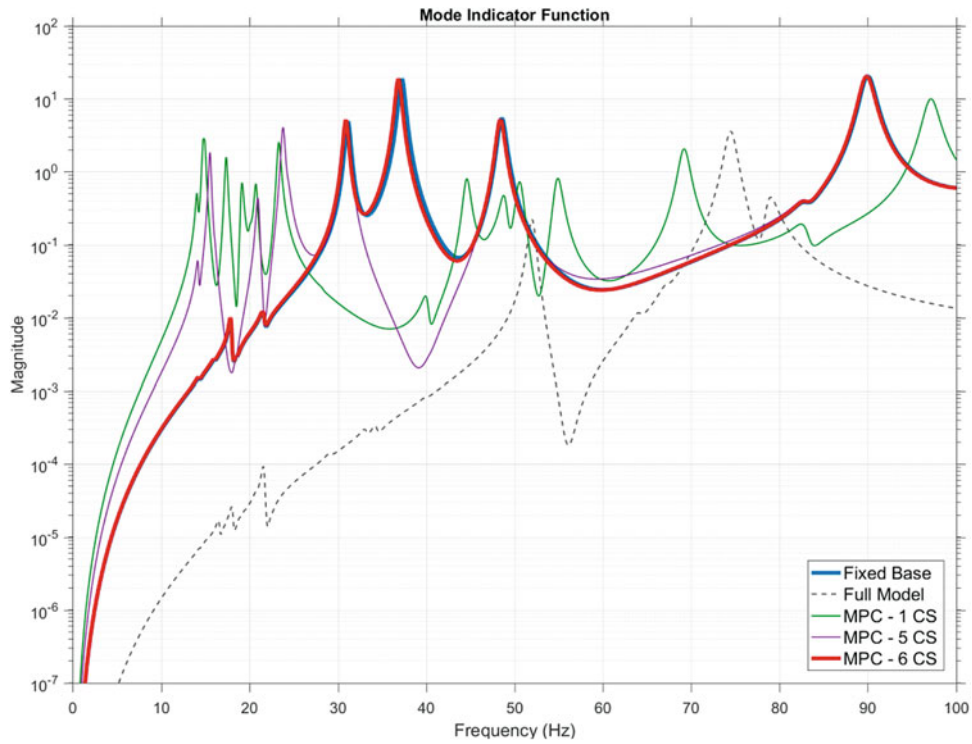


Fig. 5.5 PSMIF comparison for fixed base model, full system model, and MPC models with 1, 5, and 6 constraint shapes derived from the shape coefficients included in the eigensolution

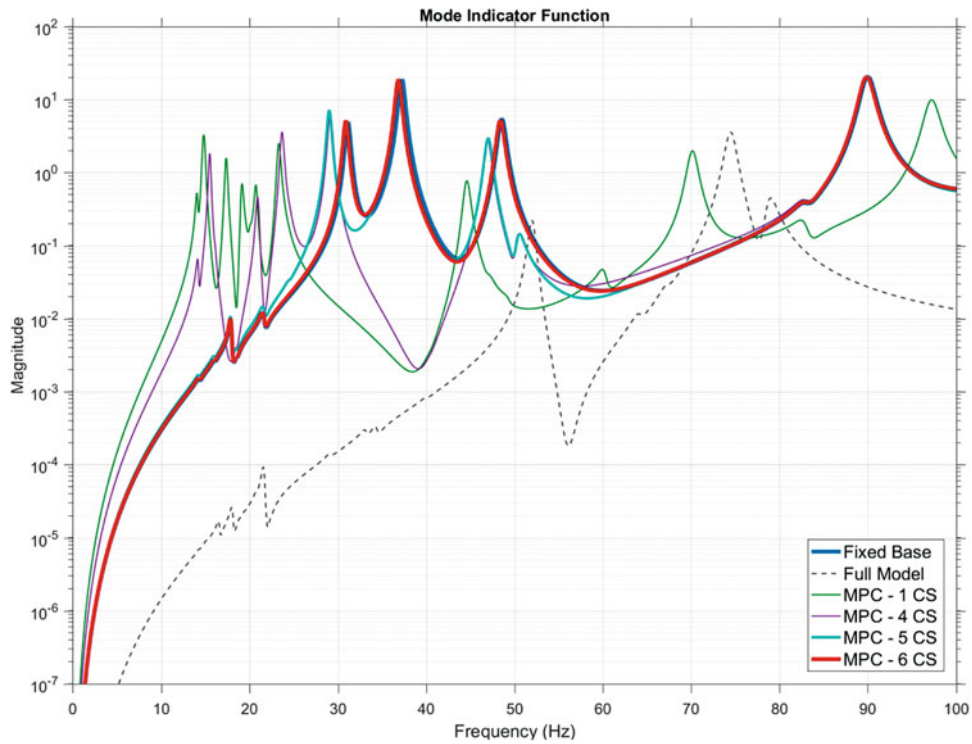


Fig. 5.6 PSMIF comparison for fixed base model, full system model, and MPC models with 1, 4, 5, and 6 constraint shapes derived from the FRF included in the eigensolution

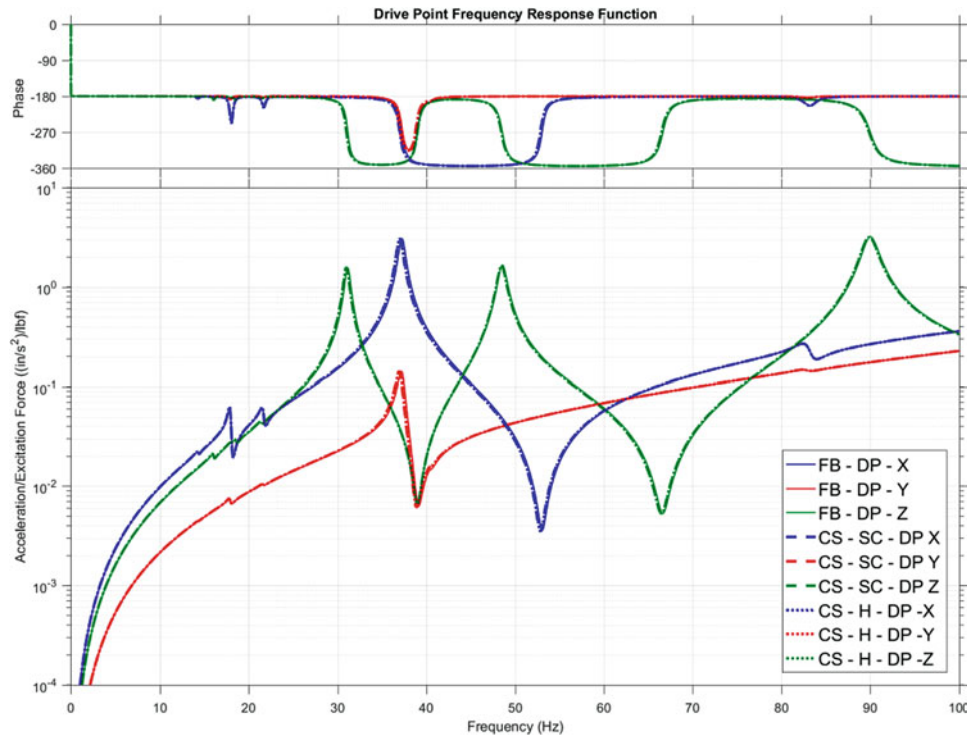


Fig. 5.7 Drive point (DP) FRFs in the X, Y, and Z directions for (1) true fixed base (FB) FRFs, (2) corrected fixed base FRFs calculated from 14 shape coefficient constraint shapes (CS–SC), and (3) corrected fixed base FRFs calculated from 14 FRF matrix constraint shapes (CS–H)

motion encompassed by the six rigid body constraint shapes. However, the frequencies for all models solved with 6–31 constraint shapes for both methods are equivalent, indicating that either constraint shape calculation method is acceptable. For visualization, Fig. 5.7 shows drive point FRFs for all three directions for the true fixed base model (FB–DP) and models solved with 14 constraint shapes for both the shape coefficient method (CS–SC–DP) and the FRF matrix method (CS–H–DP). For all three cases, the curves overlay almost exactly with a minimal frequency shift at the peaks of the FRFs.

With the fixed base FRFs accurately captured, only a minor frequency discrepancy between the true fixed based modes and the corrected fixed base modes remains. The frequency error can be reduced by including more constraint shapes. Figure 5.8 shows the PSMIFs in the region of the first two primary test article modes between 29 and 40 Hz to compare the true fixed base modal frequencies to the modal frequency obtained by including an increasing number of constraint shapes. As expected, the frequency error decreases as more constraint shapes are included. Figure 5.9 shows the percent of true fixed base modal frequency as a function of number of constraint shapes included in the MPC equation eigensolution. Modes with low effective mass fractions, those associated with subsystem components, are accurately predicted within 0.2%. Modes 19, 20, and 22 correspond to the three primary peaks observed in the fixed base PSMIFs between 30 and 50 Hz. Inclusion of only the 6 rigid-body constraint shapes brings all modes to within 1.2%, while inclusion of all 31 constraint shapes reduces the frequency error to within 0.6%. The remaining percent error is most likely associated with only including the translation DOFs at the interface in the constraint shape calculation. If all six interface DOFs were included, the frequency error should be eliminated. The primary reason for only including the translational DOFs in the pretest analysis is the pretest analysis is designed to identify accelerometer locations for the modal survey tests. The constraint shape accelerometer subset cannot capture rotational DOFs.

Figure 5.9 can also aid in determining the number of constraint shapes, and ultimately independent shaker locations, required to apply the pretest analysis. As the trends show, the frequency error does not decrease gradually as more constraint shapes are included in the solution, but rather decreases in discrete steps. A return-on-investment determination can be made to identify the decrease in frequency error by including each additional shaker. For example, mode 20 indicates that going from 12 to 13 constraint shapes reduced the frequency error of that mode 0.27%. Additionally, modes 5 and 25 also decreased their percent error, which suggests the inclusion of the 13th constraint shape is merited. However, above 19 constraint shapes, there is little reduction in frequency error, so there is no reason to include additional constraint shapes because the constraint shapes account for 99.94% of the interface motion.

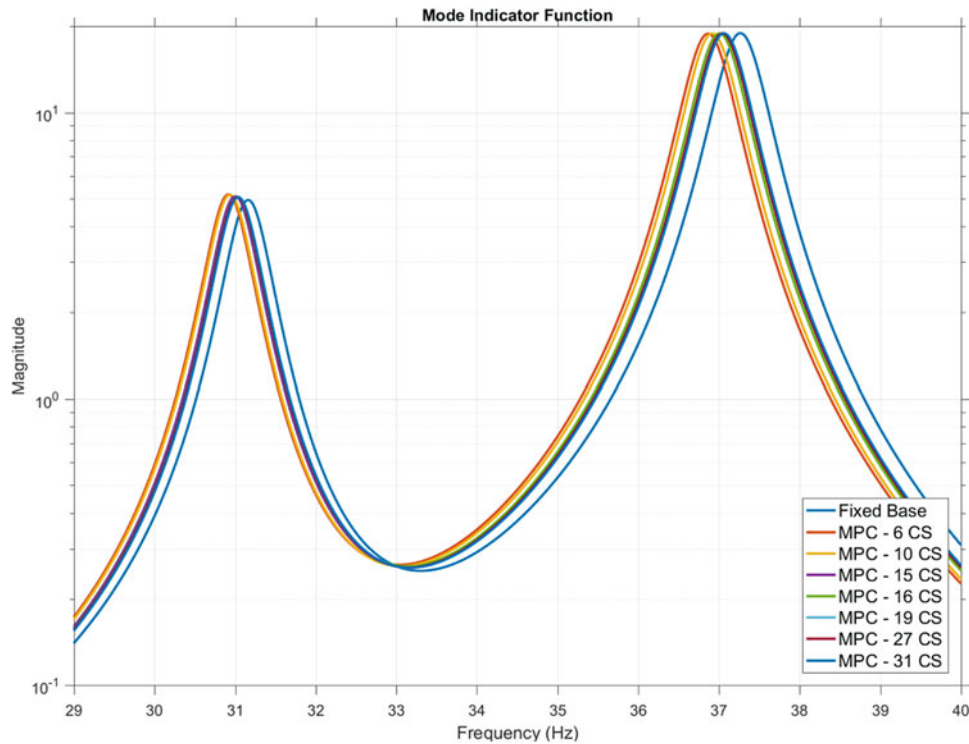


Fig. 5.8 PSMIF comparison of fixed base model with increasing number of constraint shapes calculated from shape coefficients included in the MPC equations of the eigensolution

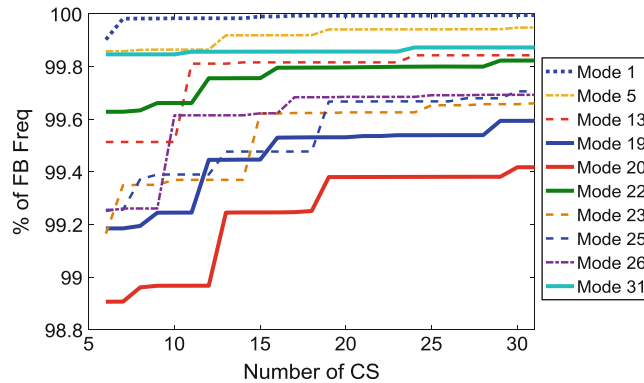


Fig. 5.9 Percent of true fixed base modal frequencies for increasing number of FRF matrix constraint shapes

Finally, to ensure the accuracy of the model, the process was repeated by including all modes up to 250 Hz in the constraint shape calculation. The Y-vertical mode of the test article at 116 Hz is now included in the pretest analysis. Figures 5.10 and 5.11 show a comparison of the drive point FRFs up to 100 Hz in the Y direction for a combination of true fixed base FRFs solved up to 100 and 250 Hz with and without residuals as well as the MPC corrected fixed base FRFs solved with 14 constraint shapes solved and residual vectors. Figure 5.10 shows the imaginary component of the FRFs while Fig. 5.11 shows the magnitude and phase of the FRFs. In Fig. 5.10, both MPC solutions with residual vectors accurately captured the true fixed base FRFs with minor discrepancies. This indicates that the FEA models only need to be solved to the frequency of the highest mode of interest, and including residual vectors sufficiently captures the higher frequency content. Figure 5.11 demonstrates the importance of including the residual vectors in the fixed base solution as well. Ignoring the Y vertical mode at 116 Hz, a comparison of the blue and black solid lines shows the change in the FRF when the residual vectors are included for modes above 100 Hz. The peaks of the imaginary plots are accurately captured, but the antiresonances in the magnitude and phase plot are not. The same comparison can be made for solutions up to 250 Hz by comparing the green and red curves.

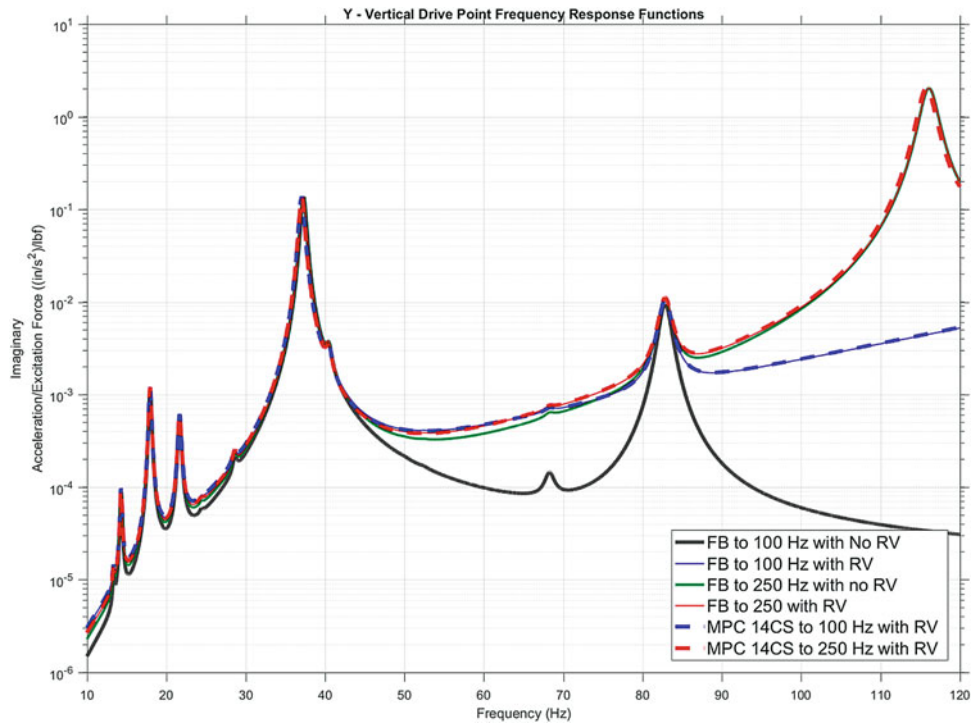


Fig. 5.10 Imaginary part of Y-vertical drive point FRF for fixed base (FB) model solved to 100 or 250 Hz with and without residual vectors (RV) compared to MPC eigensolution with 14 constraint shapes solved to 100 or 250 Hz

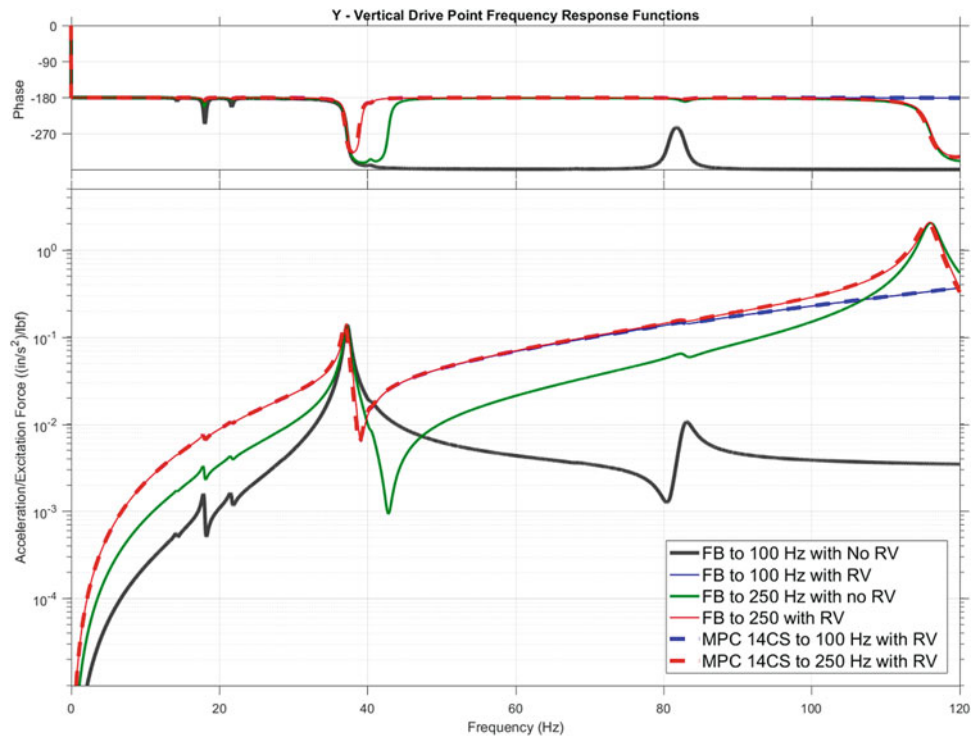


Fig. 5.11 Magnitude and phase of Y-vertical drive point FRF for fixed base (FB) model solved to 100 or 250 Hz with and without residual vectors (RV) compared to MPC eigensolution with 14 constraint shapes solved to 100 or 250 Hz

5.7 Formalized Procedure

The formalized procedure of the pretest analysis for modal surveys using the fixed base correction method is as follow:

1. Calculate the fixed base modes of the test article up to a sufficiently high frequency to capture all of the primary and secondary target modes of the system. Ensure to include residual vectors in the solution.
2. Calculate the mode shapes for the test configuration consisting of the test article attached to static test cell.
3. Identify the interface DOFs between the test article and static test cell that will be used in the constraint shape calculation.
4. Identify potential shaker locations on the test article.
5. Calculate the constraint shapes using either the shape coefficient method or the FRF matrix coefficient method.
6. Generate MPC equations relating the interface DOFs to the S-points.
7. Build and solve the full system model, which includes
 - One S-point per interface DOF and
 - Fixing the first N–S-points based on the singular values.
8. Calculate the frequency difference between fixed base modes and the MPC constrained fixed base modes.
9. Determine whether more or less constraint shapes are needed to bring frequency difference within an acceptable level.
10. Repeat steps 7–9 until enough constraint shapes are included to reduce modal frequency errors to desired level.
11. Synthesize FRFs from the constraint shape corrected mode shapes for all the shaker locations.
12. Apply the fixed base correction method to the synthesized FRFs.
13. Compare the test article drive point FRFs for the true and corrected fixed base model to validate model.

5.8 Summary

This paper has presented a formalized pretest analysis procedure that can be utilized for modal survey tests using the fixed base correction method. The method is based on calculating constraint shapes that capture the relative motion of the interface between the test article and the static test cell. The constraint shapes are applied as MPC equations in the eigensolution of the full system model to reduce the relative motion. When the fixed based correction method is applied to FRFs synthesized from the corrected full system model, the fixed base FRFs are reproduced with only a minor error, less than 1%, in the predicted modal frequencies.

References

1. Carne, T.G., Martinez, D.R., Nord, A.R.: A comparison of fixed-base and driven base modal testing of an electronics package. In: Proceedings of the Seventh International Modal Analysis Conference, Las Vegas, NV, February 1989. pp. 672–679
2. Beliveau, J.G., Vigneron, F.R., Soucy, Y., Draisey, S.: Modal parameter estimation from base excitation. *J. Sound Vib.* **107**, 435–449 (1986)
3. Fullekrug, U.: Determination of effective masses and modal masses from base-driven tests. In: Proceedings of the 14th International Modal Analysis Conference, Dearborn, MI. pp. 671–681 (1996)
4. Sinapius, J.M.: Identification of fixed and free interface normal modes by base excitation. In: Proceedings of the 14th International Modal Analysis Conference, Dearborn, MI, February 1996. pp. 23–31
5. Imregun, M., Robb, D.A., Ewins, D.J.: Structural modification and coupling dynamic analysis using measured FRF data. 5th International Modal Analysis Conference (IMAC V), London, England (1987)
6. Mayes, R.L., Bridgers, L.D.: Extracting fixed base modal models from vibration tests on flexible tables. In: Proceedings of the IMAC-XXVII, Orlando, FL, February 2009
7. Napolitano, K., Yoder, N.: Fixed base FRF using boundary measurements as references – analytical derivation. In: Proceedings of the 30th International Modal Analysis Conference (2012)
8. Mayes, R., Rohe, D., Blecke, J.: Extending the frequency band for fixed base modal analysis on a vibration slip table. In: Proceedings of the 31th International Modal Analysis Conference (2013)
9. Napolitano, K., Yoder, N.: Extraction of fixed-base modes of a structure mounted on a shake table. In: Proceedings of the 31th International Modal Analysis Conference (2013)
10. Staab, L., Winkel, J., Suárez, J., Jones, T., Napolitano, K.: Fixed base modal testing using the mechanical vibration facility 3-axis base shake system. In: Proceedings of the 34th International Modal Analysis Conference (2016)
11. Winke, J., Akers, J., Suarez, V., Staab, L., Napolitano, K.: Modal survey of the MPCV Orion European Service Module Structural Test Article using a multi-axis shake table. In: Proceedings of the 37th International Modal Analysis Conference (2018)



Chapter 6

Fixing Degrees of Freedom of an Aluminum Beam by Using Accelerometers as References

Kevin L. Napolitano

Abstract Modal tests are performed to validate analysis models of structures, and it is important to support a test article use fixtures that allow an engineer to focus his time and effort on updating the analysis model instead of the supports. Oftentimes, however, inadequate boundary condition fixtures are used in modal surveys because the design and manufacture of a proper boundary condition may be too expensive for a program. An alternative approach of creating appropriate boundary conditions by using accelerations as references to fix degrees of freedom is presented in this paper and is demonstrated using test results from a tap test on an aluminum beam. Frequency response functions (FRF) are generated directly and indirectly using a partial inversion of the FRF matrix for several different boundary condition cases using the same set of test data. Modes are extracted from the resulting FRF and are compared to an analysis model.

Keywords Modal testing · Vibrations · Structural modification · Fixed base · Constraint shapes

6.1 Introduction

Modal tests are performed to validate analysis models of structures, and it is important to support a test article use fixtures that allow an engineer to focus his time and effort on updating the analysis model instead of the supports. Oftentimes, however, inadequate boundary condition fixtures are used in modal surveys because the design and manufacture of a proper boundary condition may be too expensive for a program. Great effort and expense is then spent during the model updating task accounting for the test fixture instead of the analysis model. Errors from the test fixture model then propagate to the updated analysis model, degrading the results of the model updating task.

Both modal substructuring and frequency based substructuring methods have been used to help extract fixed base modes from structures mounted on uncertain boundary conditions. An excellent description of both methods are described in the following reference [1].

An approach of creating appropriate boundary conditions by using accelerations as references to fix degrees of freedom is presented in this paper and is demonstrated using test results from a tap test on an aluminum beam. This method is not new and follows frequency base substructuring techniques [2, 3]. Frequency response functions (FRF) are generated directly by using accelerations as references when calculating FRF [4] or indirectly using a partial inversion of the measured acceleration/force FRF matrix for several different boundary condition cases using the same set of test data. In doing so, modes extracted from the resulting FRF are associated with those same acceleration degrees of freedom fixed.

6.2 Theoretical Background

The derivation of the partial inversion of the FRF matrix $[H(\omega)]$ is presented here. It is equivalent to the Structural Modification Using Frequency Response Functions (SMURF) method. An FRF matrix, $[H(\omega)]$ can be partitioned into two sets of degrees of freedom, those associated with internal DOF “i”, and those associated with boundary DOF “b”. A subset of the internal DOF can be further partitioned to DOF where forces are applied, specified by the subscript “f”. In this derivation, the boundary DOF are assumed to be impacted by a force. Thus, the FRF matrix can be partitioned as follows

K. L. Napolitano (✉)
ATA Engineering, Inc., San Diego, CA, USA
e-mail: kevin.napolitano@ata-e.com

$$\{a(\omega)\} = [H(\omega)]\{f(\omega)\} = \begin{Bmatrix} a_i(\omega_k) \\ a_b(\omega_k) \end{Bmatrix} = \begin{bmatrix} H_{if}(\omega_k) & H_{ib}(\omega_k) \\ H_{bf}(\omega_k) & H_{bb}(\omega_k) \end{bmatrix} \begin{Bmatrix} f_f(\omega_k) \\ f_b(\omega_k) \end{Bmatrix}. \quad (6.1)$$

Hereafter, the frequency, (ω) , will be removed to simplify the equations. The responses or outputs, $\{a\}$, are on the left hand side. The references or inputs, $\{f\}$, are on the right hand side, and the FRF matrix, $[H]$, describes their relationship at a given frequency.

A partial inversion of the FRF matrix can be performed to make the boundary accelerations references and the boundary forces responses. This is done by rearranging the second row of Eq. (6.1) such that

$$f_b = -H_{bb}^{-1}H_{bf}f_f + H_{bb}^{-1}a_b \quad (6.2)$$

Plugging Eq. (6.2) into the top row of Eq. (6.1) yields the following equation

$$\begin{Bmatrix} a_i \\ f_b \end{Bmatrix} = \begin{bmatrix} H_{if} - H_{ib}H_{bb}^{-1}H_{bf} & H_{ib}H_{bb}^{-1} \\ -H_{bb}^{-1}H_{bf} & H_{bb}^{-1} \end{bmatrix} \begin{Bmatrix} f_f \\ a_b \end{Bmatrix} = \begin{bmatrix} \overline{H}_{if} & \overline{H}_{ib} \\ \overline{H}_{bf} & \overline{H}_{bb} \end{bmatrix} \begin{Bmatrix} f_f \\ a_b \end{Bmatrix} \quad (6.3)$$

Many derivations yield the same results for \overline{H}_{if} by making the unnecessary assumption that $a_b = 0$. Doing so obscures quite a bit of useful information. For any linear relationship in the form of $\{x\} = [C]\{y\}$, that the matrix element C_{JK} is equal to the value of x_J due to a unit input at y_K , holding all other elements in $\{y\}$ equal to zero. Thus, there is no reason to enforce $a_b = 0$ in the derivation and all four elements of $[\overline{H}]$ can be used. Each element in has physical meaning.

\overline{H}_{if} is the FRF matrix of outputs a_i due to unit input forces in f_f , holding all acceleration DOF in a_b fixed.

\overline{H}_{bf} is the FRF matrix of reaction forces f_b due to unit inputs forces at f_f , holding all acceleration DOF in a_b fixed.

\overline{H}_{ib} is the FRF matrix of outputs a_i due to unit inputs in a_b and not applying forces in f_f .

\overline{H}_{bb} is the FRF matrix of reaction forces f_b due to unit inputs at a_b and not applying forces in f_f .

Note that this partial matrix inversion is equivalent to techniques described in other frequency based substructuring techniques. However, it should be noted that the calculation of the matrix $[\overline{H}]$ can also be calculated directly by using both forces f_f and a_b as references when calculating FRF from time domain data.

6.3 Test Setup

The test setup is shown in Fig. 6.1. A 73.1 in. cylindrical aluminum beam with a diameter of 2 in. was suspended in a free-free boundary condition with two soft rubber bands. A total of 26 accelerometers were bonded to the beam at 13 equally spaced locations. The accelerometers were mounted to measure both out of plane axes of the beam. The beam was impacted at five equally spaced locations along the beam in two axes; 1X+, 1Y+, 4X+, 4Y+, 7X+, 7Y+, 10X+, 10Y+, 13X+ and 13Y+.

6.4 Signal Processing

The test data was appended into a single time history file which was then processed to calculate FRF in one of two ways. The first method used all the force channels as references to calculate baseline FRF matrix $[H]$. Then the partial matrix inversion method was used to fix whichever sets of accelerometers were defined for each boundary condition case. The second method involved using the time histories of different sets of accelerometers directly when calculating FRFs.

Processing the time history data into frequency response functions was complicated by the fact that the aluminum beam had very low levels of damping. These light levels of damping magnified small errors in the test setup and test conduct to produce drive point FRF that are physically unrealizable. The phase of all drive-point FRF should stay within a 180° band. Zeros in all FRF should be associated with a positive phase shift, and poles should be associated with a negative phase shift. Figure 6.2 presents two example FRF with two different exponential windows applied. The red FRF has a conventional 10% exponential window, but it has a negative phase shift associated with the zero near 300 Hz. The blue curve has a very drastic exponential window used in this paper that inputs enough damping into the FRF so that the phase shift is positive. However, there is still a frequency range from 360 to 510 Hz where the phase is slightly outside the 180° band.

Fig. 6.1 Aluminum beam test setup

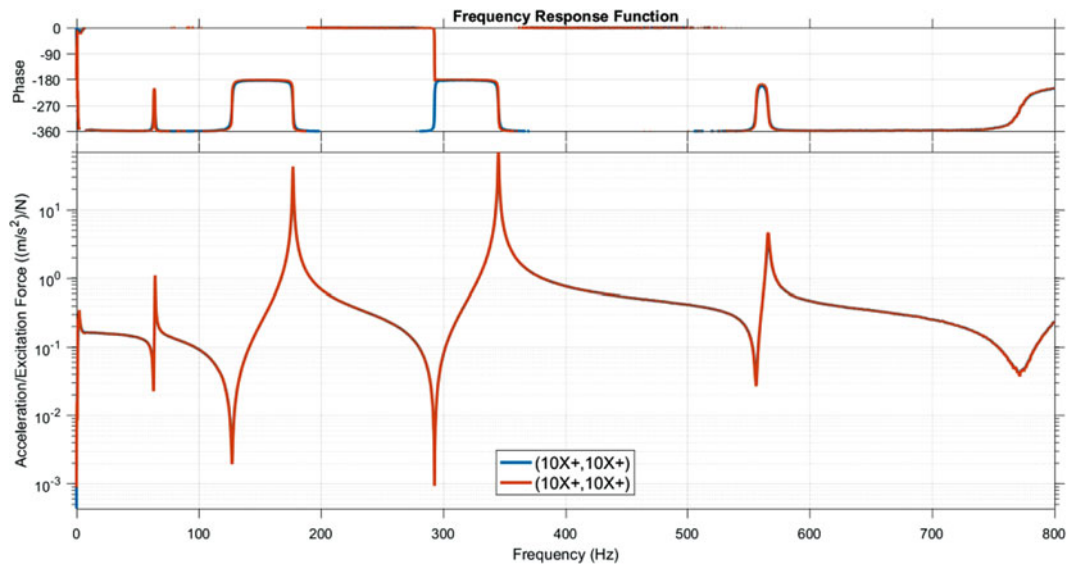
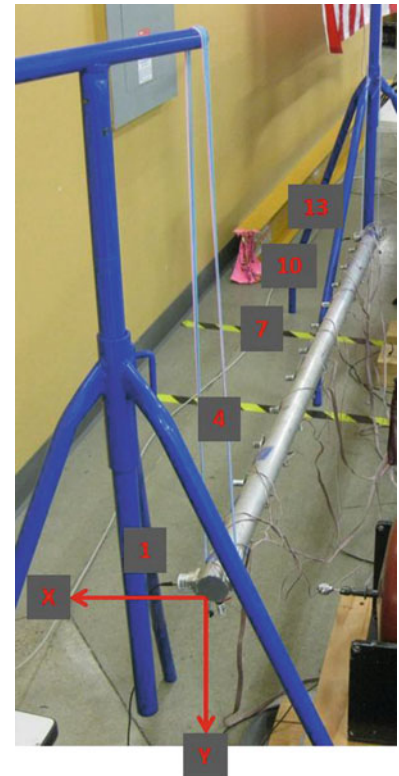


Fig. 6.2 Drive point FRF processed with different exponential windows. Red function was processed with 10% exponential window. Blue function was processed with 0.0001% exponential window

Table 6.1 Signal processing parameters

Method	Welch
Frequency lines	6401
Δf /Frame length	0.125 Hz/8 s
Exponential window	0.0001%
Basis vectors	All force channels

The signal processing parameters used to calculate FRFs are presented in Table 6.1. The parameters were selected to ensure the phase shift of all drive point FRF was negative for all resonant frequencies for the free-free test case.

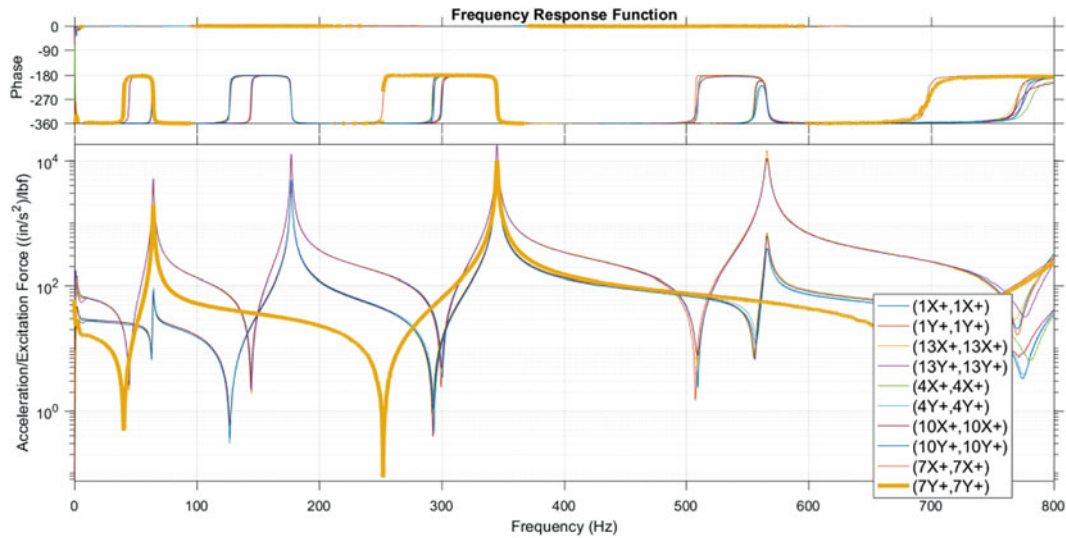


Fig. 6.3 Drive point [A/F] FRF

Since the magnitude of the accelerations is very small at many frequencies, the force channels were used as the basis vectors since their values are relatively smooth over the entire frequency range [5]. Using forces as basis vectors for calculating $[H]$ is equivalent to using the H_1 method. Also, since the basis vectors were the same for both methods, the FRF results were equivalent whether or not $[H]$ was calculated with accelerometer references directly, or if Eq. (6.3) was used.

A plot of the drive point FRF associated with $[H]$ are presented in Fig. 6.3. The phase of the drive point FRF should be between -180° and 360° , but the phase drifts slightly out of the range in some frequency ranges. This would be an indication that there is negative damping in the system, which is physically not possible. The cause of the out of band phase is unknown. It could be the result of the extreme signal processing parameters that were needed process the very lightly damped aluminum beam, or perhaps a test conduct issue such as misalignment of accelerometers or inconsistency in impact hammer excitation.

6.5 Test Results

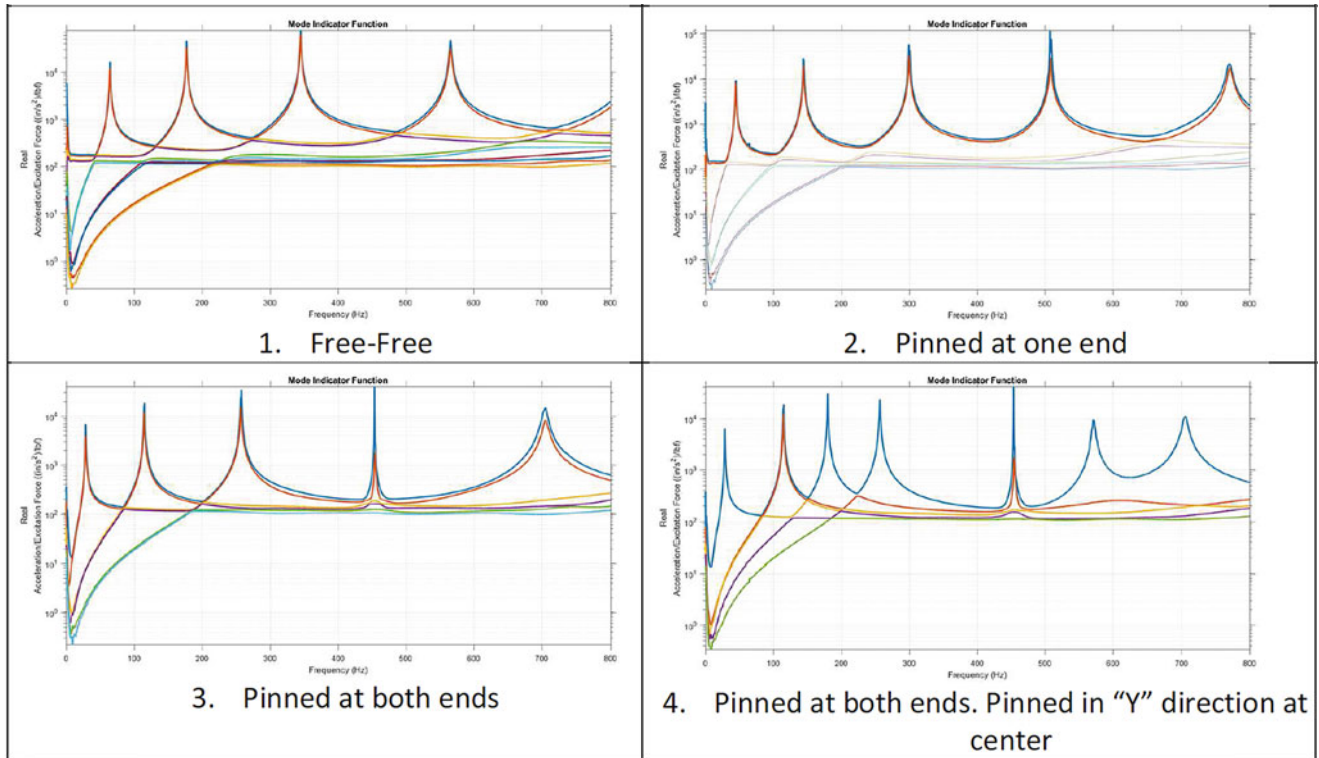
The data was used to generate several different boundary conditions by using different accelerometers as references. The different cases are shown in Table 6.2. When an accelerometer is used as a reference, its corresponding force is treated as a response degree of freedom.

A complex mode indicator function (CMIF) all of the resulting FRF for each boundary condition case is presented in Fig. 6.4. The CMIF functions were generated using all acceleration responses and force references. Note that for the baseline free-free case, there are four curves with constant lines at low frequency. These correspond to the two lateral and two rotation lateral rigid body modes of the beam. For the case where the beam is pinned at one end (Node 1 fixed), there are only two constant lines at low frequency which correspond to the two beam rigid body rotation modes. The first three cases have repeated modes at each frequency because the structure is symmetric about both axes. This is indicated by the primary and secondary CMIF curve peaking at the same frequencies.

Mode shapes for Case 4 are presented in Fig. 6.5. Note that the shapes in the “Y” direction are the same as the simply supported case since the center of the beam is still allowed to move in that direction. However, the modes in the “X” direction are all fixed at the center (Node 7). Note that mode pairs 2/3 and 6/7 appear to be repeated roots because the center of the beam is a zero for the simply supported modes.

Table 6.2 Boundary condition cases

Boundary condition	Acceleration reference	Force reference
1. Free-Free		1X+, 1Y+, 4X+, 4Y+, 7X+, 7Y+, 10X+, 10Y+, 13X+, 13Y+
2. Hinged at one end	1X+, 1Y+	4X+, 4Y+, 7X+, 7Y+, 10X+, 10Y+, 13X+, 13Y+
3. Simply Supported	1X+, 1Y+, 13X+, 13Y+	4X+, 4Y+, 7X+, 7Y+, 10X+, 10Y+
4. Simply Supported plus pinned at center in one direction	1X+, 1Y+, 7X+, 13X+, 13Y+	4X+, 4Y+, 7Y+, 10X+, 10Y+

**Fig. 6.4** Complex Mode Indicator Function for each boundary condition cases

6.6 Acceleration as References

The FRF in the matrix associated with accelerations as both references and responses, \overline{H}_{ib} , can also be used to extract modes with the same boundary conditions FRF associated with \overline{H}_{if} . They are oftentimes useful for extracting modes that are not as well-excited by the applied forces. Note that the mode shape at 454 Hz for Cases 3 and 4 are not as well excited as the other modes. This is because the forces are applied at Nodes 4, 7, and 10 which are at zeros of those modes. The CMIF of the \overline{H}_{ib} matrix is presented in Fig. 6.6. In this case the 454 Hz modes are clearly observable.

6.7 Reaction Forces

Reaction force FRF at the fixed boundary conditions can also be calculated by viewing the FRF associated with $[\overline{H}_{bb}]$ and $[\overline{H}_{bf}]$ FRF. The drive points of $[\overline{H}_{bb}]$ for boundary condition case 4 is presented in Fig. 6.7. Note that the reaction force is increasing at low frequencies for the FRF associated with the “X” direction but are leveling off for FRF associated with the “Y” direction. The reason this occurs is that there are three supporting the “X” direction. If one location moves, the other two will resist motion to create static reaction forces. The reason the function increases is because a unit acceleration is

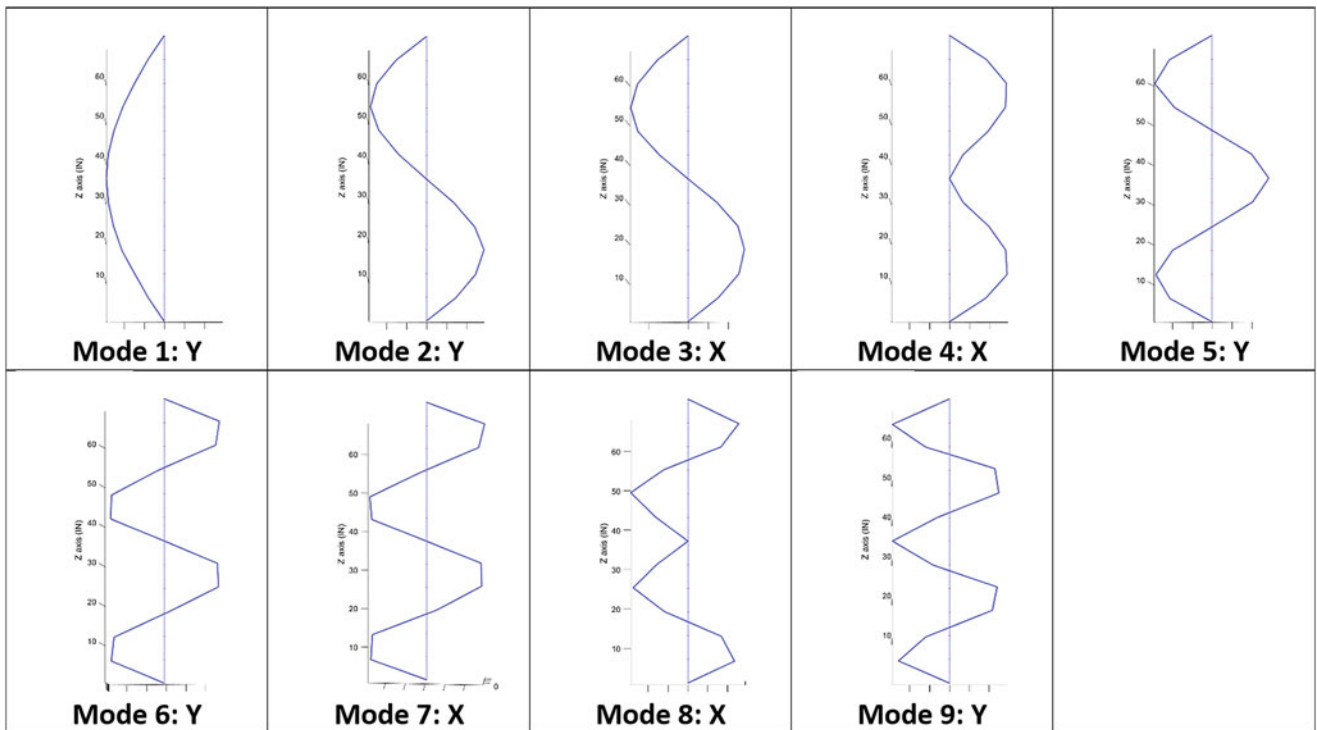


Fig. 6.5 Mode shapes for boundary case 4

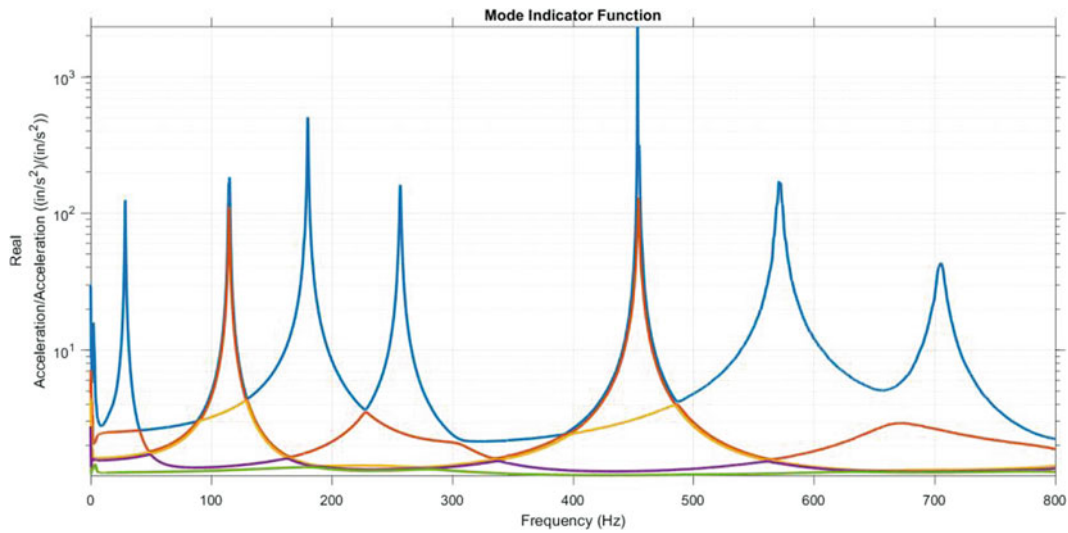


Fig. 6.6 CMIF of [A/A] FRF from boundary case 4

equivalent to an increasing displacement as frequency decreases. The other direction levels off because there are not enough fixed points to statically resist motion, so only the rigid body inertia of the beam is resisting the input acceleration.

6.8 Damping Discussion

A table of modal parameters for boundary condition case 4 is presented in Fig. 6.8. Higher levels of damping at the lower frequencies is due to the effects of the exponential window. There was one anomaly in the test results which was that damping of the modes near 453 Hz (Modes 7 and 8) was slightly negative. This result was confirmed by performing mode enhancement

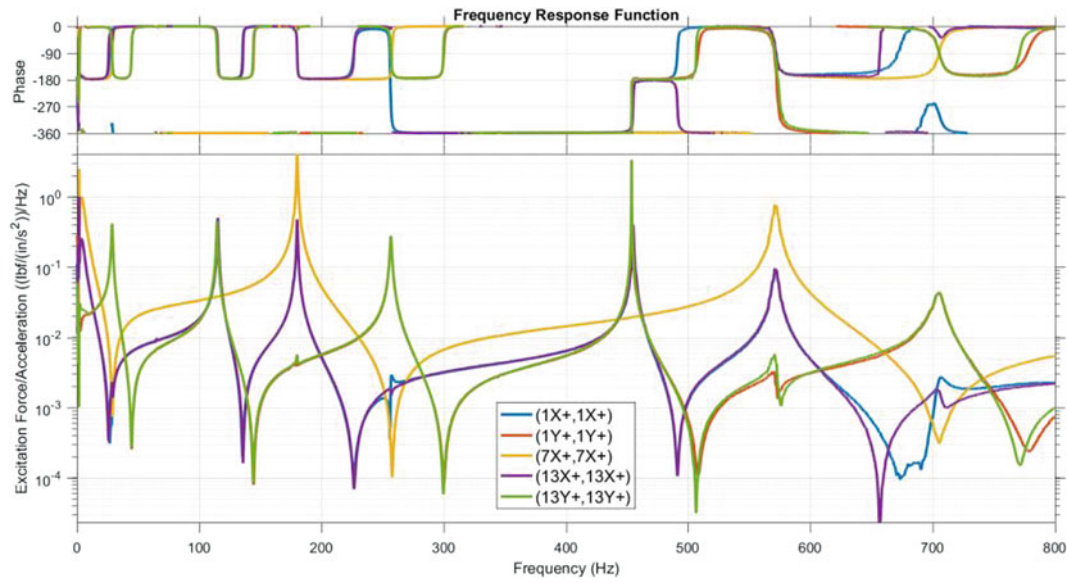


Fig. 6.7 Drive point reaction forces for boundary condition case 4

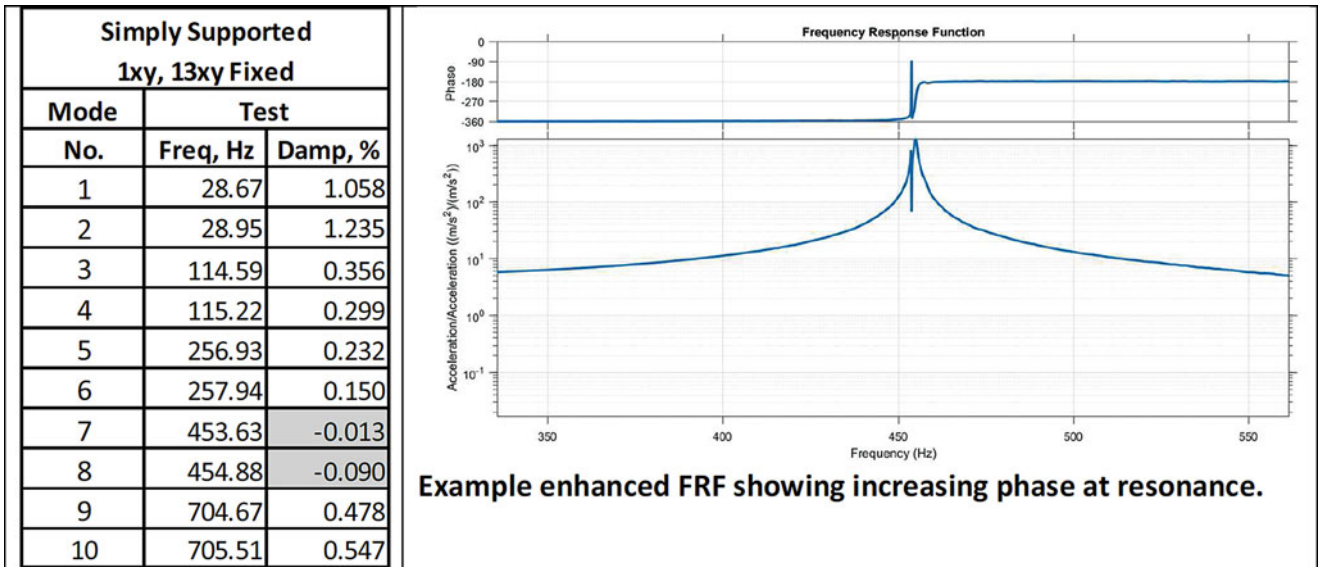


Fig. 6.8 Negative damping example

and spatial filtering to the test data in order to generate an enhanced FRF using the Multivariate Mode Indicator Function [6] on Mode 8. The enhanced FRF clearly shows an increasing phase which confirms the negative damping estimate. Thus, while the signal processing parameters were adjusted to remove negative damping from the drive points, it wasn't enough to remove negative damping results from the all of the test results.

6.9 Comparison to Analysis Model

Results of a comparison between test measured and analysis frequencies are presented in Fig. 6.9. Measured frequencies were within 2% for all four boundary condition cases. Overall, the FEM consistently over-predicted frequency. The excellent correlation between all four cases confirms that using accelerations as references to enforce boundary conditions works.

Free Suspension			
Mode	Test	FEM	
No.	Freq, Hz	Freq, Hz	% Diff
1	64.42	65.52	1.70
2	64.53	65.52	1.54
3	177.14	180.18	1.71
4	177.19	180.18	1.69
5	345.18	351.91	1.95
6	345.32	351.91	1.91
7	565.73	578.81	2.31
8	565.85	578.81	2.29

Simply Supported: 1xy, 13xy Fixed			
Mode	Test	FEM	
No.	Freq, Hz	Freq, Hz	% Diff
1	28.67	29.25	2.00
2	28.95	29.25	1.01
3	114.59	116.74	1.87
4	115.22	116.74	1.32
5	256.93	261.76	1.88
6	257.94	261.76	1.48
7	453.63	463.13	2.10
8	454.88	463.13	1.82
9	704.67	719.27	2.07
10	705.51	719.27	1.95

Hinge: 1xy Fixed			
Mode	Test	FEM	
No.	Freq, Hz	Freq, Hz	% Diff
1	44.63	45.42	1.76
2	44.81	45.42	1.35
3	144.15	146.86	1.87
4	144.75	146.86	1.45
5	299.58	305.31	1.91
6	300.58	305.31	1.57
7	507.45	519.54	2.38
8	509.34	519.54	2.00
9	769.85	787.91	2.35
10	771.39	787.91	2.14

Combined: 1xy, 7x, 13xy Fixed			
Mode	Test	FEM	
No.	Freq, Hz	Freq, Hz	% Diff
1	28.92	29.25	1.12
2	114.63	116.74	1.84
3	115.23	116.74	1.31
4	180.00	181.49	0.83
5	256.86	261.76	1.91
6	453.62	463.13	2.10
7	454.56	463.13	1.89
8	570.10	581.11	1.93
9	704.97	719.27	2.03

Fig. 6.9 Comparison of test versus analysis frequencies

6.10 Summary

This paper presents an alternative method of creating proper boundary conditions through testing rather than expensive fixture hardware. The method exploits the fact that modes extracted from FRF with acceleration DOF as references results in those same DOF being fixed. The FRF can be calculated directly using accelerations as references, or they can be calculated by performing a partial matrix inversion of the FRF matrix. Oftentimes the resulting FRFs associated with accelerations as references can be used to extract modes as well as measure reaction forces of the test derived boundary conditions.

References

- Allen, M.: Recent advances to estimation of fixed-interface modal models using dynamic substructuring. In: Proceedings of the 36th International Modal Analysis Conference (2018)
- Crowley, J.R., Klosterman, A.L., Rocklin, G.T., Vold, H.: Direct structural modification using frequency response functions. In: Proceedings of the Second International Modal Analysis Conference, Orlando, Florida, February 1984. pp. 58–65
- Imregun, M., Robb, D.A., Ewins, D.J.: Structural modification and coupling dynamic analysis using measured FRF data. 5th International Modal Analysis Conference (IMAC V), London, England (1987)
- Napolitano, K., Yoder, N.: Fixed base FRF using boundary measurements as references – analytical derivation. In: Proceedings of the 30th International Modal Analysis Conference (2012)
- Napolitano, K.: Using singular value decomposition to estimate frequency response functions. In: Proceedings of the 34th International Modal Analysis Conference (2016)
- Napolitano, K., Rietz, R.: Using FRF interpolation to help separate closely spaced modes. In: Proceedings of the 24th International Modal Analysis Conference (2006)



Chapter 7

Signal Reconstruction from Mobile Sensors Network Using Matrix Completion Approach

Soheil Sadeghi Eshkevari and Shamim N. Pakzad

Abstract Bridge system identification is recently studied using mobile sensing network data. As one possible solution, the data collected by moving sensors are to be mapped to some predefined virtual stationary locations and then, using estimated stationary data, various system identification methods can be applied. The mapping function, however, has not been studied thoroughly so far. STRIDEX, which is a recently proposed platform for bridge SID using mobile sensing, assume *sinc* function as an estimator for the mapping function. Despite its effectiveness under certain conditions, the function cannot accurately estimate stationary time responses from mobile data in more realistic cases of moving sensors with random presence over the bridge. In this paper, an alternative solution based on low-rank matrix completion problem is proposed and motivations for this choice are discussed. This method attempts to complete the matrix as accurate as possible by convex optimization, given a sparse matrix of acceleration values with various time and space coordinates. A comprehensive comparison between *sinc* and matrix completion approaches is performed and the results are evaluated in terms of the response prediction accuracy in both time and frequency. Results show that the proposed matrix completion signals are a very good match to the actual signals, while the reconstructed signals using *sinc* are sometimes not as accurate.

Keywords Signal reconstruction · Matrix completion · Convex optimization · Discrete signal interpolation · Mobile sensing

7.1 Introduction

Mobile sensing is a relatively new approach for structural health monitoring in which, vibration sensors are attached to single or multiple mobile carriers and collect data as a function of time and space while moving over a structure. The approach has some significant advantages compared to the traditional stationary sensing paradigm, e.g., more spatial information, less maintenance costs, and scalability [1–3]. By advancements of the wireless technologies, wireless sensor networks are gradually complementing wired sensors and enabling mobile sensors usage more comprehensively [4–6]. Current smartphones already have various types of motion sensing chips embedded in them, which allow the possibility of crowdsourcing [3]. Many bridges have thousands or hundreds of thousands of daily commuters, each carrying at least one smartphone that is sensing the vibration of the bridge in real-time. This situation highly motivates researchers to provide mathematical platforms for utilizing these abundant data for understanding the behavior and characteristics of the bridges.

The data collected by mobile sensors contain bridge vibrations in addition to vibrations from other sources as well, i.e., the road surface roughness-caused vibrations and the vehicle suspension dynamical response. This disables system identification (SID) platforms since they are designated to feed in pure structural vibrations. To circumvent this problem, researchers have taken three main approaches to treat this data: to control sensing conditions such as vehicles speed and the road roughness intensity [7, 8], to model vehicle bridge interactions in closed-form [9, 10], and to use blind source separation techniques to extract different components of the original signal [11]. The last approach is able to provide an estimation of the pure bridge response. In this paper, it is assumed the vibrations collected by moving carriers are either pure or can be extracted.

The main approach for using mobile sensors data for bridge SID is to convert them to the corresponding data of some virtual stationary sensors as illustrated in Fig. 7.1. In this figure, eight moving sensors are collecting vibration responses of a beam at different locations and directions. The idea is to estimate stationary responses at virtual fixed sensors from these eight channels of data. By doing so, these stationary signals can be used in conjunction with a variety of available SID methods for partial or comprehensive bridge modal identification.

S. Sadeghi Eshkevari (✉) · S. N. Pakzad
Department of Civil and Environmental Engineering, Lehigh University, Bethlehem, PA, USA
e-mail: ses516@lehigh.edu; pakzad@lehigh.edu

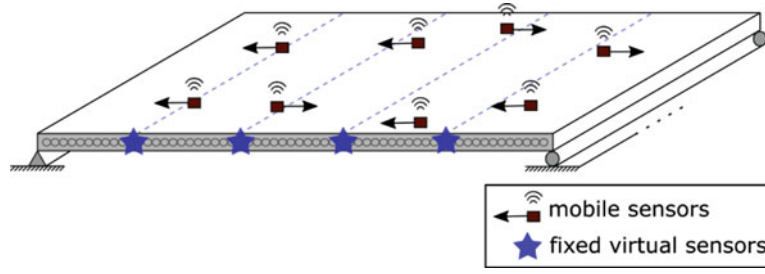


Fig. 7.1 Schematic demonstration of signal reconstruction problem

Qin et al. [12] adopted Eigensystem Realization Algorithm (ERA) method for bridge modal identification, using time signals collected by fixed sensors. In this study, 96 accelerometers are placed on the deck and towers of a bridge and the method was successful to identify 76 modes. Later, Ren et al. [13] estimated the modal parameters of a steel arch bridge analytically and experimentally. In this method, wired accelerometers were located statically at various locations of the bridge and Stochastic Subspace Identification algorithm was deployed to identify parameters. As a significant application of bridge modal identification methods, Weng et al. [14] conducted a comprehensive monitoring procedure for modal identification of a cable-stayed bridge, using wireless sensors that were placed fixed on limited locations. In order to enhance the information collected from the bridge, wireless sensors' layout was reconfigured repeatedly. This study implicitly demonstrated the main disadvantage of the stationary sensor networks which is the limitation of the spatial resolution for a fixed sensor network. These studies mainly were able to estimate low-resolution mode shapes, since the data was limited to certain locations. Kim et al. [4] alternatively investigated the Golden Gate Bridge using a complex wireless sensor network. The sensing network complexity indeed resulted in a denser mode shape estimation, however, this enhancement cost both computationally and financially. More recently, Magalhães et al. [15] developed a software that can process stationary sensing data in real-time and results in modal identification outputs. While successful, the method is still limited to the available data from stationary channels and cannot help higher resolution concern as the other methods. Therefore, a mapping function that interpolates mobile sensing data to multiple virtual stationary sensing locations plays a key role to bridge the gap existed between mobile sensing and conventional stationary sensing paradigms.

The problem of mobile sensing turns into two phases: (a) signal reconstruction for stationary nodes given mobile measurements and (b) further process using available SID methods. Having a reliable transformation from mobile sensors to virtual stationary ones enables to enhance identified mode shapes resolution by assigning many virtual stationary points. However, since the mobile sensing paradigm for bridge SID is a relatively fresh topic, there are not extensive studies in the first phase of the process.

A comprehensive study in this field has been recently done by Matarazzo and Pakzad [16]. Truncated physical model for dynamic sensor networks was proposed for reformulating the standard equation of motion of a bridge into a reduced modal state-space representation as shown in Eq. (7.1):

$$\begin{aligned}
 x_k &= Ax_{k-1} + n_k \\
 y_k &= \Omega_k C x_k + v_k \\
 x_1 &\sim N(\bar{\mu}, \bar{V}) \\
 \eta_k &\sim N(0, Q) \\
 v_k &\sim N(0, R)
 \end{aligned} \tag{7.1}$$

where A is the state matrix, C is the observation matrix, x_k is the state vector which is not observable, and y_k is the observation vector, which is the collected data at the accessible channels as will be called virtual probing locations (VPLs) throughout this paper. η_k and v_k are systemic and sensing noises respectively, which for simplicity are assumed to be uncorrelated Gaussian white noise with covariance matrices as Q and R . Ω_k is the mode shape regression function (MSR). A bridge sensed by stationary sensors has the term Ω_k equal to the identity matrix since the observation location is fixed relative to the modal coordinates. However, if the sensor network is in motion, C matrix has to be time varying. To circumvent this time-variance, the MSR function is introduced to transform mobile sensing data at each time step to the estimated values at the VPLs. In [16], the MSR term Ω_k was approximated using basis functions, specially the *sinc* function [17]. The idea is that given a set of measured data s at a certain time, estimated values at another set s_x are calculated using the following transformation:

$$\begin{aligned}
\mathbf{s} &= [s_1 \ s_2 \ \dots \ s_N]^T \\
\mathbf{s}_x &= [s_{x1} \ s_{x2} \ \dots \ s_{xN}]^T \\
\Omega &= \left[\operatorname{sinc} \left(\frac{1}{\Delta s_x} (\mathbf{s} - s_{x1}) \right) \ \operatorname{sinc} \left(\frac{1}{\Delta s_x} (\mathbf{s} - s_{x2}) \right) \ \dots \ \operatorname{sinc} \left(\frac{1}{\Delta s_x} (\mathbf{s} - s_{x3}) \right) \right]_{N \times N}
\end{aligned} \tag{7.2}$$

where Δs_x is the distance between the locations of the destination set \mathbf{s}_x . The transformation should be performed repeatedly for every time samples. Intuitively, the *sinc* basis function interpolates values of unmeasured locations by superimposing of multiple decaying waves initiated at measured locations and weighted by the magnitude of the measured data. The *sinc* interpolation is an accurate estimator of discrete signals with missing values. In fact, the *sinc* function acts as a window and results in an interpolation with the same frequency contents as of the original data (band limited by the window). The function was comprehensively used for bridge modal identification as the primary mapping transformation [1].

Equation (7.2) is tailored to map N mobile measurements to the same number of VPLs. It means that at each time sample, the number of mobile sensors presented on the bridge should be equal to the number of VPLs. In the case study shown at [1], the sensing network included six equally spaced mobile sensors that did not leave the beam during the sensing time and a VPL set of six was assumed as well. In this case, the assumption of equality between the number of VPLs and mobile sensors is valid; however, this situation may not be always practical since in a real application, the number of moving carriers on the bridge is not precisely controlled. The *sinc* mapping equation can be updated to the following format to be more flexible for more realistic scenarios:

$$\begin{aligned}
\mathbf{s}_i &= [s_{1i} \ s_{2i} \ \dots \ s_{J_i}]^T \text{ at } T = t_i \\
\mathbf{s}_x &= [s_{x1} \ s_{x2} \ \dots \ s_{xN}]^T \\
\Omega &= \left[\operatorname{sinc} \left(\frac{1}{\Delta s_x} (\mathbf{s}_i - s_{x1}) \right) \ \operatorname{sinc} \left(\frac{1}{\Delta s_x} (\mathbf{s}_i - s_{x2}) \right) \ \dots \ \operatorname{sinc} \left(\frac{1}{\Delta s_x} (\mathbf{s}_i - s_{x3}) \right) \right]_{J_i \times N}
\end{aligned} \tag{7.3}$$

In Eq. (7.3), \mathbf{s}_i is a vector of locations for the available measurements at time t_i , which can be different in length for every time step. However, \mathbf{s}_x is constant since the VPL set does not change over time. This new equation enables mapping a random number of measured data to a different number of VPLs (for example, 10 or 5 measured values to 8 VPLs). The approach is able to enhance the resolution of the identified mode shapes by repeatedly changing the location of VPL sets and superimposing identified modes.

In this study, alternatively, a novel approach for signal reconstruction is proposed, using the idea of matrix completion. Bridge responses can be represented as a matrix of time and space in which columns stand for the degrees of freedom (DOFs) and rows correspond to the time steps. Therefore, in a mobile sensing scenario, the matrix is built up sparsely by mobile measurements as shown in Fig. 7.2. Signal reconstruction attempts to complete this sparse matrix given limited available observations. After this matrix completion, stationary sensing signals at every location are estimated as the column vectors of the matrix and can be further used for bridge SID (and other applications that inherently require higher resolution data, such as damage detection). This can ultimately lead to identifying highly dense mode shapes, as wells as other modal properties.

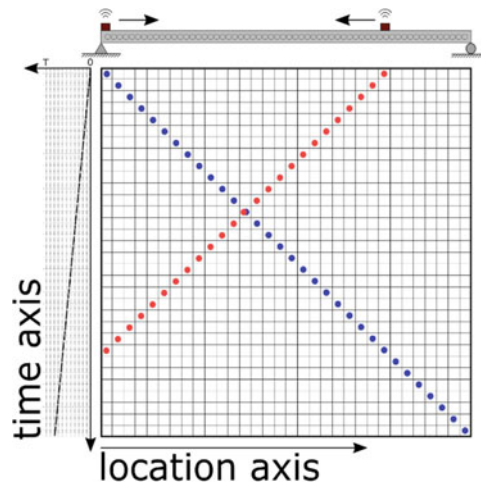


Fig. 7.2 Illustration of sparse response matrix

This approach can handle any randomly collected data over a bridge, e.g., random commuting vehicles and partial length scanning. If the matrix is low-rank, the completion task can be performed using convex optimization [18, 19]. This method has been used in prediction of recommendation systems in the field of data science, however its application in structural health monitoring is novel.

7.2 Matrix Completion

According to the classical matrix completion literature, in order to estimate missing entries of a sparse matrix, the matrix has to be low-rank or can be accurately approximated with a low-rank matrix [18]. If this assumption holds, the completion task is a convex optimization problem and is solvable using linear methods, e.g., Gradient Descent [19]. Bridge response at each physical point (DOF) is a superposition of its modes; however, not all of these modes have the same participation in the response. As a common practice in structural dynamics, a truncated modal model of a structure yields a sufficiently accurate response when compared to a full model [20]. In this truncated model, a limited number of modes that have significant participation factors are included in the analysis. In terms of computational costs, this model is significantly less expensive since the model order is extremely smaller than the number of DOFs or all the natural modes. This fact shows that the response of a bridge at every location is dominated by a few time invariant modes. This concept intuitively shows that the response matrix is a low rank with the rank equal to the number of significant modes.

The problem of matrix completion has been studied and different solutions have been proposed [21–23]. In this study, the low-rank matrix completion using alternating minimization [19] has been utilized. In this method, the response matrix of time and space is decomposed into two rectangular matrices with lower dimensions equal to a predetermined rank. The values of these two matrices are the parameters to be optimized in order to minimize the difference between the actual and estimated observations. The optimization problem is shown in Eq. (7.4):

$$\begin{aligned} \min_{A,B} \frac{1}{2} \|\widehat{M} - \text{dotproduct}(P, AB)\|_2^2 \\ \widehat{M} = \text{dotproduct}(P, M) \end{aligned} \quad (7.4)$$

where $M_{N \times N}$ is the response matrix and N is the number of DOFs. $A_{N \times K}$ and $B_{K \times N}$ are two rectangular matrices, K is the truncation degree which corresponds to the level of desired modal truncation ($K \ll N$). P is a binary matrix that activates observed entries of M . Note that M is a sparse matrix with available entries in space and time coordinates of which moving sensors were present.

Low-rank matrix completion using alternating minimization is a method that gives best decomposing matrices for a given data. The original optimization algorithm alternatively takes a gradient step towards the optimal point of the decomposition matrices, i.e., $A_{N \times K}$ or $B_{K \times N}$ one at a time to reach the optimality. In this paper, however, both matrices take the gradient step simultaneously as shown in Algorithm 7.1. The proof of convergence to the optimality for a low-rank matrix is presented in [19].

Algorithm 7.1: One step minimization for matrix completion

1. Input \widehat{M} , threshold, and α
 2. Initiate A^0 and B^0 randomly
 3. $err = 1.0$, $temp = \|\widehat{M} - \text{dotproduct}(P, A^0 B^0)\|_2^2$
 4. **while** $err > \text{threshold}$ **do**:
 5. $\{A^{t+1}, B^{t+1}\} \leftarrow \{A^t, B^t\} - \alpha \nabla \frac{1}{2} \|\widehat{M} - \text{dotproduct}(P, A^t B^t)\|_2^2$
 6. $err = \|\widehat{M} - \text{dotproduct}(P, A^{t+1} B^{t+1})\|_2^2 - temp$
 7. $temp = \|\widehat{M} - \text{dotproduct}(P, A^{t+1} B^{t+1})\|_2^2$
 8. Return $A^T B^T$
-

In this algorithm, a threshold is selected for the residual between two consecutive objective function values. The rate of gradient is also set as α . P matrix is a matrix of binary values with all zeros except than ones only on at observed coordinates. That implies that by giving \hat{M} as the input, P is achievable (P is the activator of the observed entries of the sparse matrix \hat{M}).

The method has some primary assumptions that guarantee its convergence: (1) the sampled entries of the matrices should be enough to ensure the problem is not underdetermined, and (2) the distribution of the observed entries over the matrix should be uniform and random [18]. The first assumption is physically interpreted that the number of vehicles scanning a bridge should be sufficiently large. The second one is not exactly achievable in a mobile sensing paradigm since vehicle measurements plug in the entries of the matrix in a diagonal manner. However, the presence of the vehicles and their initial locations are reasonably considered as random. Therefore, as a contribution, in this study a semi-random observation distribution is studied.

7.3 Motivations

In this study, the problem of reconstruction of signals at VPLs from mobile sensor network data is investigated. This is an important problem, since it makes conventional system identification techniques applicable for the data coming from a mobile sensing paradigm as well. In particular, this study has the following contributions:

1. A method for accurately reconstructing spatially and temporally varying signal using a limited portion of data available is proposed.
2. The method is scalable regarding data availability. This means that the method works with any portion of the observable data (e.g. 0.2% to 2.0% observed entries in the response matrix—the range that works with this algorithm). This flexibility is achieved by the parameter K which will be discussed later.
3. The method is the first to estimate stationary signals from the data collected by a mobile sensor network that includes randomly moving carriers (the bridge is not sensed by evenly placed sensors; i.e., mobile sensors commute erratically).

In the next section, a finite element model is built and investigated for the signal reconstruction using two methods: (1) the *sinc* function, and (2) the matrix completion. The main advantages of the proposed method are then demonstrated and discussed.

7.4 Problem Statement

A 2D model of a 500 m long bridge with a single span is modeled in OpenSees. The span supports are fixed and the bridge is discretized into 5000 DOFs that are equally spaced. The bridge is under ambient random loads at nine equally distanced points while being monitored. A Rayleigh damping of 2% at the first and eighth modes is included in the model. Modal analysis of the bridge results in the following natural frequencies for the first four modes: 0.265 Hz, 0.732 Hz, 1.436 Hz, and 2.373 Hz. By this linear dynamic analysis, the dynamic response at each DOF is calculated to produce a dense response matrix.

The bridge response is collected in a mobile manner via commuting vehicles within a designated sensing duration. This data produces a sparse matrix of bridge responses with time and space coordinates. Using this, the objective is to reconstruct data collected by 20 virtual probing location (VPLs) equally spaced over the bridge. The process is performed using two methods: (1) the *sinc* interpolation function, and (2) the matrix completion using convex optimization. Ultimately, by using these reconstructed signals, modal identification of the bridge can be performed in multiple ways.

In this study, three sensing scenarios with different number of commuting vehicles is investigated. Particularly, the cases with 50, 100, and 150 (random directions; either left to right or the opposite) scans are considered and both reconstruction methods are compared. These numbers determine the number of vehicles present on a bridge within the monitoring time duration. In other words, these three cases simulate three levels of traffic volume on the bridge: low, medium, and high. The scans mostly contain partial information (a portion of the bridge is scanned by each vehicle). For instance, when the time slot begins, a vehicle has just 10 DOF remained to exit the bridge, however, this is counted as a scan. In contrast, if a vehicle enters the bridge within the time slot, but cannot exit in time, it is also a valid scan. Considering this definition, the number of investigated scans are reasonable. For this bridge, considering its relatively long span, if there are three lanes in each direction, a simple calculation results in 8, 17, and 25 scans from each lane in 100 s (total monitoring duration) respectively for three cases of interest.

In addition, this study assumes that the vehicles flow on the bridge is random. It is the first study that considers this realistic assumption for the bridge modal identification using mobile sensors' data. In terms of comparison between results, both methods are applied for reconstructing stationary signals and the outputs are investigated in both time and frequency. Time signals have a broad application in damage diagnosis and localization [24, 25] while the frequency representation of signals is widely used for system identification purposes. Therefore, signal reconstruction quality is evaluated in both domains.

7.5 Numerical Modeling

The response of the bridge at all DOFs are recorded with the sampling frequency of 50 Hz for 100 s. As a result, the dimension of the response matrix is 5000×5000 , with 5000 columns associated with each DOF and 5000 rows for each time step. This matrix is then sampled according to the time-space coordinates of each vehicle. Computationally, this means that certain number of secondary diagonals and anti-diagonals of the matrix (from FE model) are selected randomly and the remaining entries assumed as missing data. This matrix is called the sparse matrix of observations. Note that some of these random secondary diagonals are very short duration readings, e.g. a vehicle that is leaving the bridge when sensing duration begins. Thus, the number of readings is not the same as the number of vehicles occupying the bridge at each time. The latter is in fact not constant since vehicles are randomly leaving and entering the bridge at different times.

The heatmap of the sparse matrices (upper left 1000×1000 entries) in three cases are plotted in Fig. 7.3. The horizontal and vertical axes in the heatmap show spatial and temporal coordinates, respectively. Each diagonal belongs to one scan. The slopes of diagonals are the same, implying that the velocity of scanning vehicles are the same and equal to 5.0 m/s. This simplifying assumption is held in this study; however, the vehicles' speed can be different for each scan. The spatial responses of the bridge are plotted in two snapshots at times 20 and 30 s and shown in Fig. 7.4. The solid line, which is a train of weighted impulses, corresponds to the sparse observations available for these two times.

As the first approach, the stationary VPL data are estimated from mobile sensors' data using Eq. (7.3). Alternatively, the reconstructed stationary signals for all DOFs including VPLs are achieved using the matrix completion approach. Note that the latter method hands in all responses by one analysis, while the *sinc* method needs repetitive reconfiguration of VPLs to reproduce estimations for all DOFs ($\frac{5000}{20} = 250$ VPL sets needed). This does not necessarily mean that the *sinc* method is computationally more costly, since the computational effort for each VPL set is less than the optimization process for the matrix completion. However, the need for VPL reconfiguration before each analysis results in a two-step process, which is more complex than the single step solution of the matrix completion.

7.6 Comparing Methods

After generating the sparse matrix of responses, both stationary signal reconstruction methods (the *sinc* and the matrix completion) are applied. In order to apply the first method, two parameters should be given, the number of VPLs and the eccentricity. In this study, with no loss of generality, 20 VPLs with no eccentricity (symmetrically located over the bridge) are

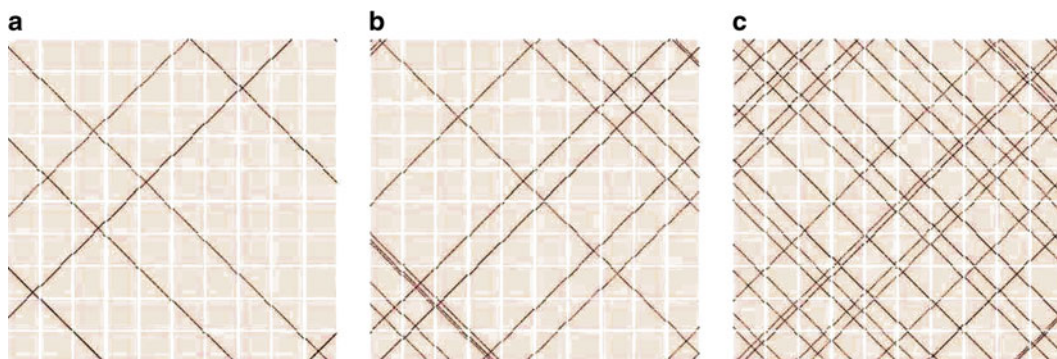


Fig. 7.3 Heatmap of observed data (shaded lines indicate the observed entries). (a) 50 scans, (b) 100 scans, (c) 150 scans

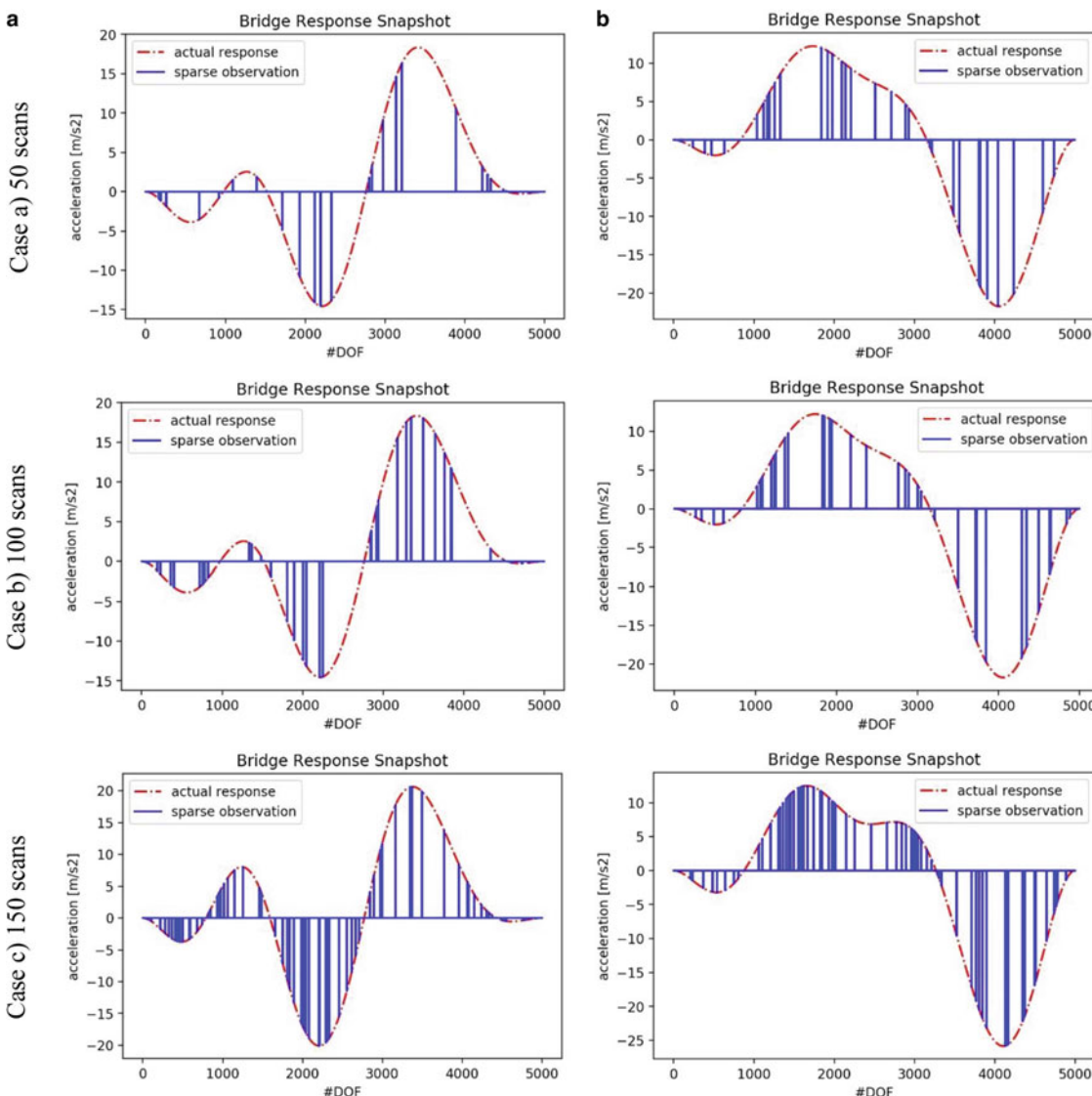


Fig. 7.4 Sparse vs. actual spatial responses

assumed. In the second method however, no such assumptions are needed. In turn, this method needs the rank of estimated decomposing matrices (K) to be guessed in advance. In this study, this parameter for each of three cases is selected by trying different values and choosing the best one in terms of performance.

Reconstructed time signals from both methods on four VPL locations (VPLs 4, 8, 12, and 16 that are located at DOFs 1000, 2000, 3000, and 4000) are compared with the actual stationary signals determined from the FE model and are presented in Figs. 7.5, 7.6, 7.7, 7.8, 7.9 and 7.10. As explained, cases A, B, and C are presenting three level of data availability. To express the level of sparsity of the matrix, observation rate is calculated as the number of observed entries divided by the total number of entries. In cases A, B, and C with 50, 100, 150 available mobile scans, this rate equals 0.565%, 0.904%, and 1.428%, respectively. For these cases, K values are set as 6, 12, 18, which yield the most accurate estimates while keeping the complexity low.

Figures 7.5, 7.7, and 7.9 show that the *sinc* method is not desirably accurate in estimating unobserved signals. In fact, the method is exclusively exact in the neighborhood in which some observed data exist. This is obvious from Eq. (7.2) since a reconstructed signal is mostly affected by the closest observed data. In addition, Eq. (7.2) is originally proposed for cases in which: (a) the number of observed entries per time step is constant, and (b) this number is always equal to the number of VPLs. Both of these conditions are violated in a scenario of random scanning. In contrast, from Figs. 7.6, 7.8, and 7.10, the

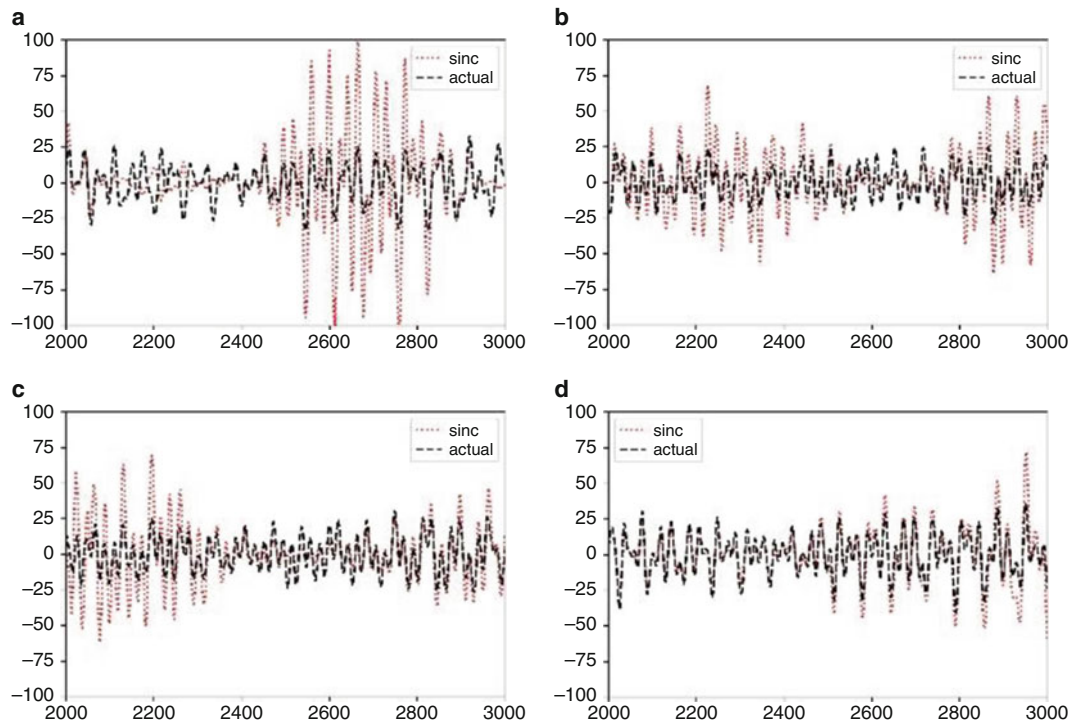


Fig. 7.5 Actual vs. *sinc* function reconstructed signals at different VPLs (case A). (a) VPL 4, (b) VPL 8, (c) VPL 12, (d) VPL 16

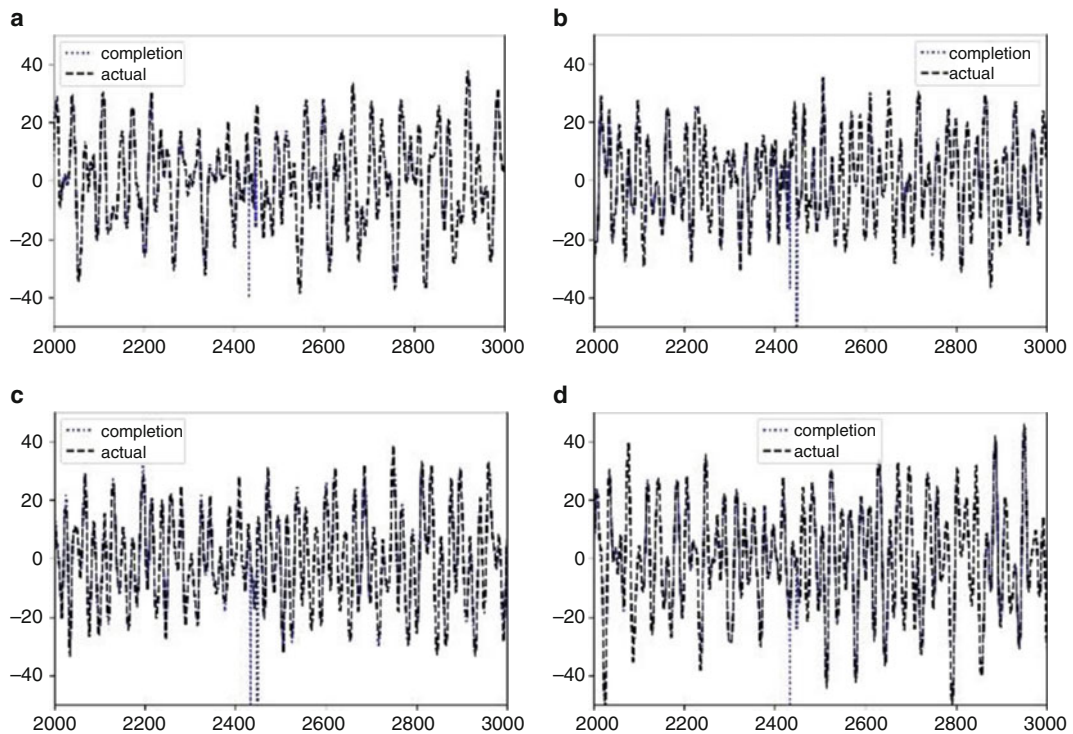


Fig. 7.6 Actual vs. matrix completion reconstructed signals at different VPLs (case A). (a) VPL 4, (b) VPL 8, (c) VPL 12, (d) VPL 16

matrix completion method favorably reconstructs signals, with almost exact solutions. A comparison between approximated time signals from both methods demonstrates that the matrix completion method yields a uniform accuracy over the time, counter to the *sinc* method.

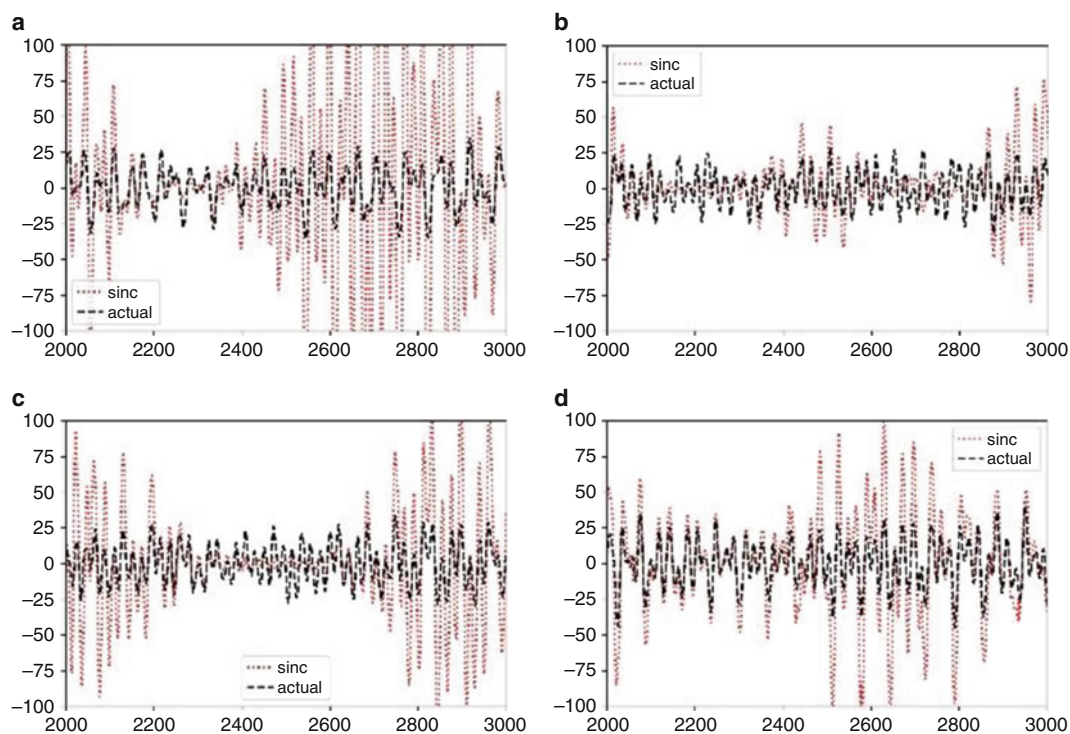


Fig. 7.7 Actual vs. *sinc* function reconstructed signals at different VPLs (case B). (a) VPL 4, (b) VPL 8, (c) VPL 12, (d) VPL 16

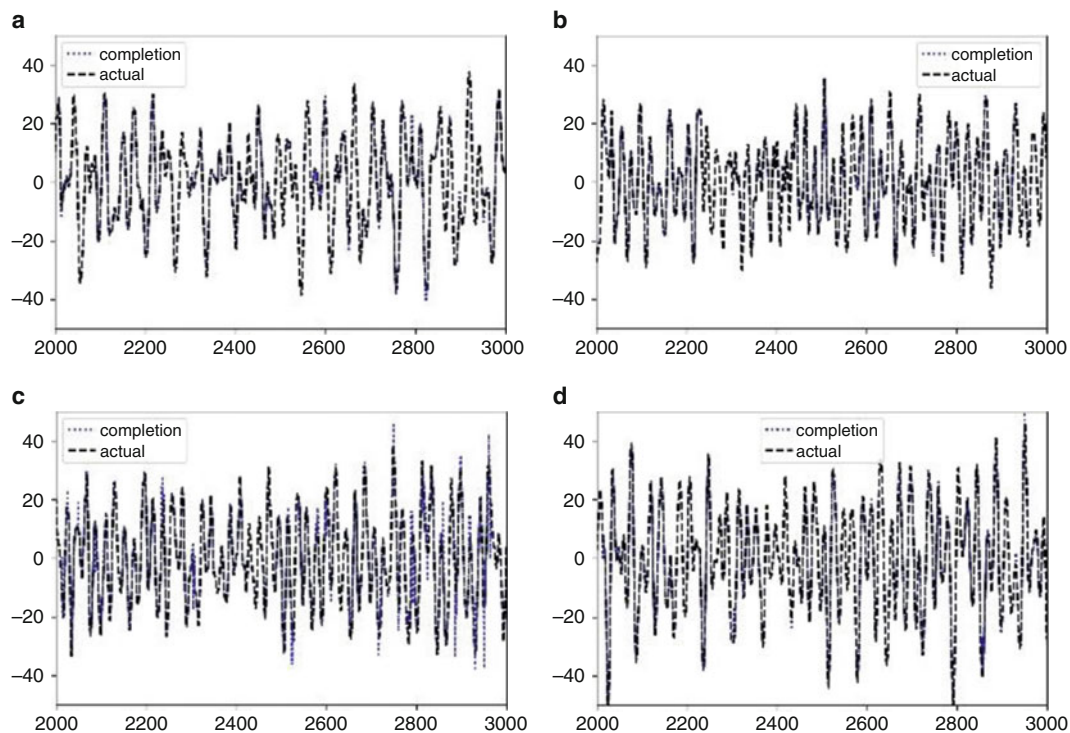


Fig. 7.8 Actual vs. matrix completion reconstructed signals at different VPLs (case B). (a) VPL 4, (b) VPL 8, (c) VPL 12, (d) VPL 16

By comparing results of three cases, it is clear that the stationary signal estimations of the *sinc* method do not improve by adding more observations, while the matrix completion approach leads to results that are more accurate, e.g., comparing Figs. 7.6b and 7.8b. Note that all time signal plots here are presented over one fifth of the monitoring duration for more clarity.

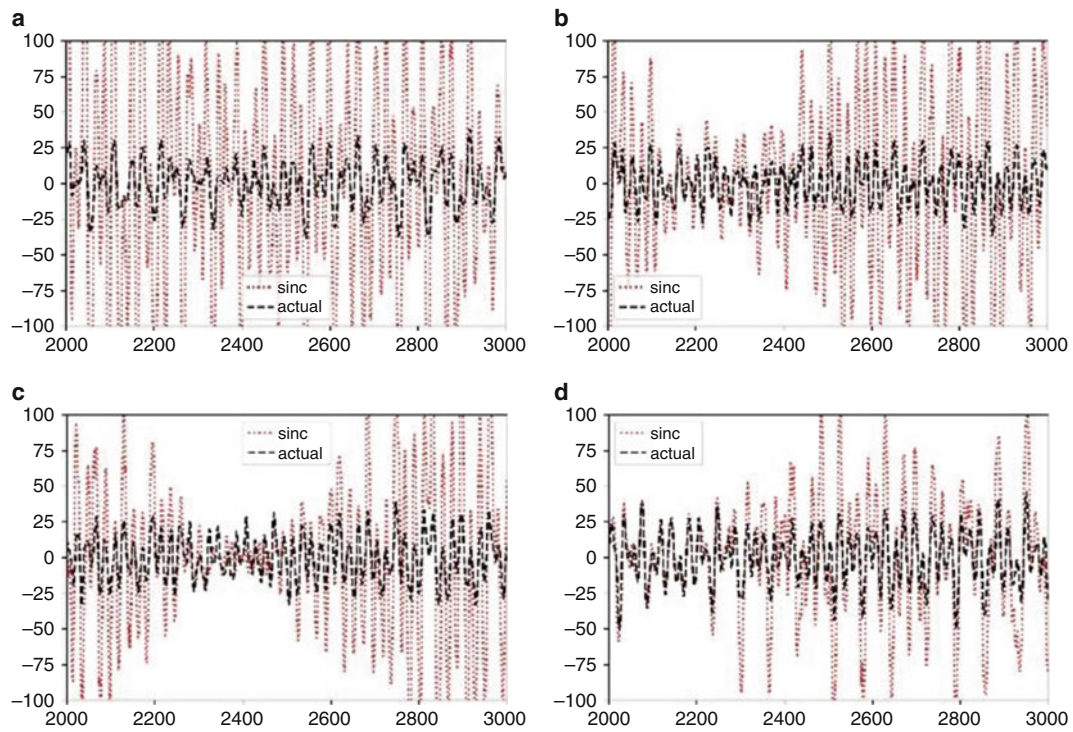


Fig. 7.9 Actual vs. *sinc* function reconstructed signals at different VPLs (case C). (a) VPL 4, (b) VPL 8, (c) VPL 12, (d) VPL 16

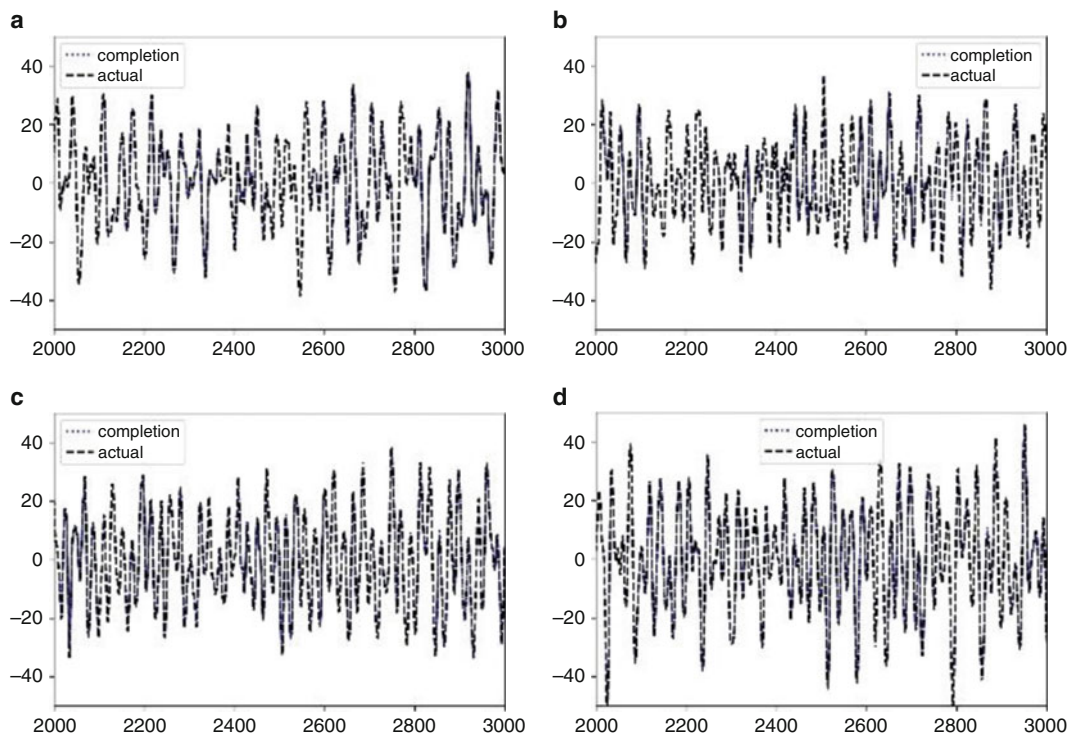


Fig. 7.10 Actual vs. matrix completion reconstructed signals at different VPLs (case C). (a) VPL 4, (b) VPL 8, (c) VPL 12, (d) VPL 16

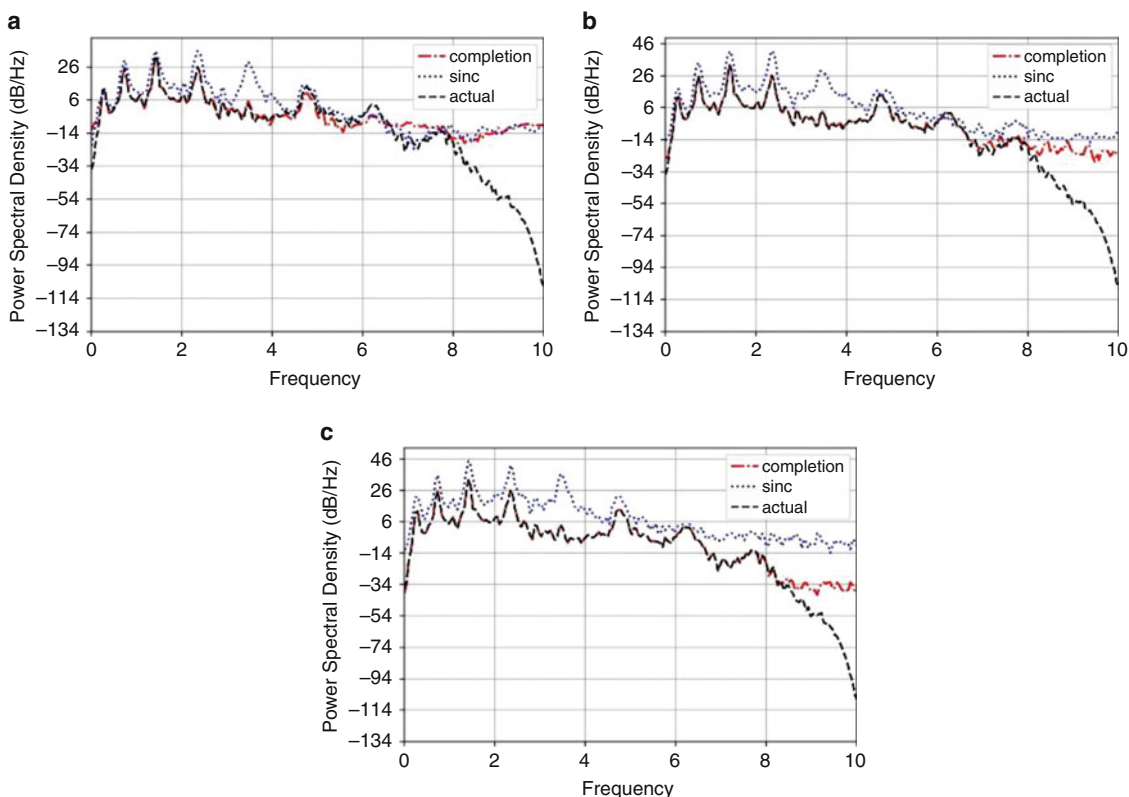


Fig. 7.11 PSD comparison for reconstructed signal at VPL 4. (a) Case A, (b) case B, (c) case C

Figures 7.11, 7.12, 7.13 and 7.14 show the power spectral density (PSD) functions of the reconstructed and actual signals. The frequency range is selected as 0–10 Hz. In Fig. 7.11, all three signals (the *sinc* and the matrix completion estimated signals vs. the actual signal) show peaks at the same frequencies. However, the matrix completion signal fits more exactly over lower frequencies (i.e. 0–6 Hz). In addition, in Fig. 7.11, PSD of the *sinc* method shows a large peak at the fifth natural mode, which is not detectable at the location of VPL 4 (DOF 1000). Despite its relevance to the fifth mode, this additive content is an error in signal reconstruction and does not belong to the actual signal collected at this VPL. In contrast, the matrix completion method is more successful to follow the actual frequency contents.

A comparison between three cases in PSD figures (e.g., Fig. 7.12) yield that the accuracy of the matrix completion method is highly enhanced as the number of observations increases. For instance, the matrix completion result in Fig. 7.12a does not successfully capture frequency contents of the actual signal over 6–10 Hz. Moreover, the first peak is weakly extracted as well. These two issues, however, are addressed when 100 or 150 scans are considered (case B and case C shown in Fig. 7.12b and c, respectively). In fact, by increasing the observations, the *sinc* method is not influenced as much in the frequency domain, while the matrix completion approach is significantly improved. In the matrix completion approach, there is a trade-off between the data availability and the desired accuracy. For example, if the SID purpose is limited to a few first modes, a limited number of observed data is sufficient, e.g., case A.

In the matrix completion method, K (the rank of the response matrix) is correlated to the number of modes included in the approximated signals. For instance, $K = 6$ is assumed for case A, and from Fig. 7.12a one can realize that the first six modes are estimated accurately, while higher modes are not included as much. However, K has to be in a balance with the data availability. For instance, $K > 6$ yields worse results for case A since there is not enough observation to tune the parameters of the decomposing matrices.

It has been shown in [1] that the estimated VPL signals resulted from the *sinc* method under some conditions (constant number of moving nodes and permanent presence of sensors) are suitable for bridge SID purposes. However, in this study, it is shown that if these conditions do not hold, the estimations are not as accurate, particularly for the time signals, while the matrix completion method results in very exact estimations on both time and frequency. These time signals correspond to different locations of the structure and are intensively useful for damage localization purposes.

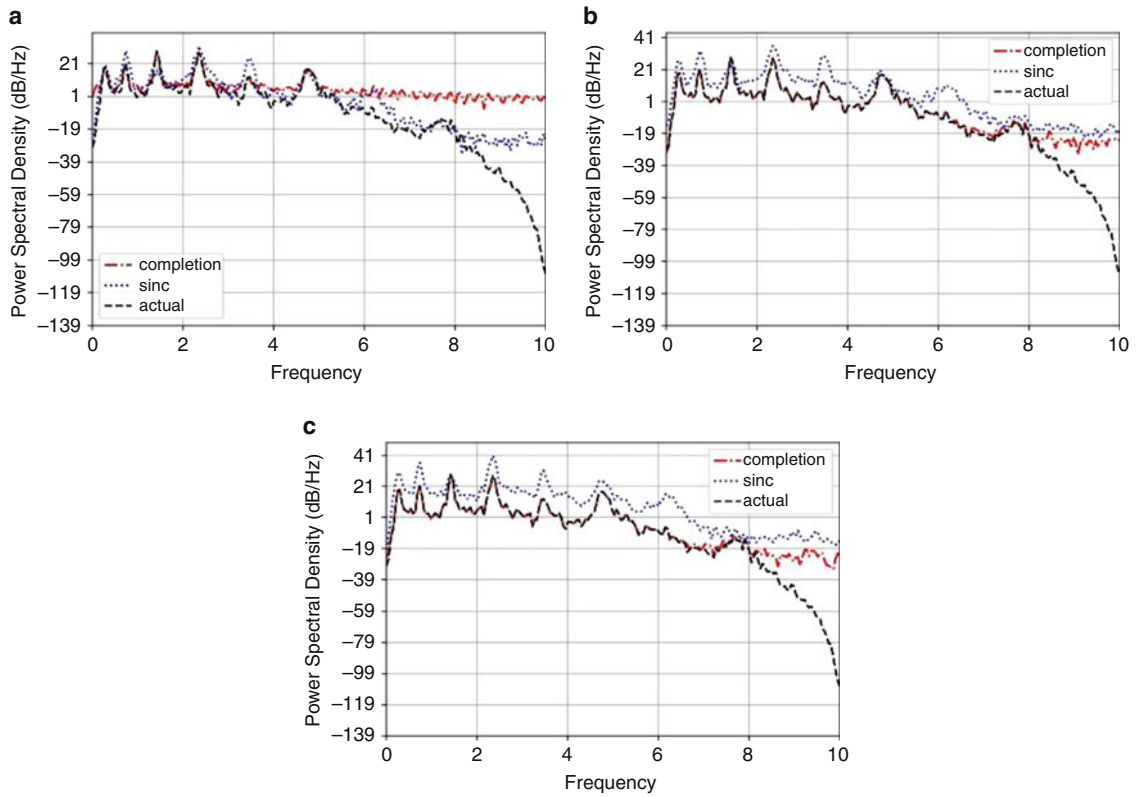


Fig. 7.12 PSD comparison for reconstructed signal at VPL 8. (a) Case A, (b) case B, (c) case C

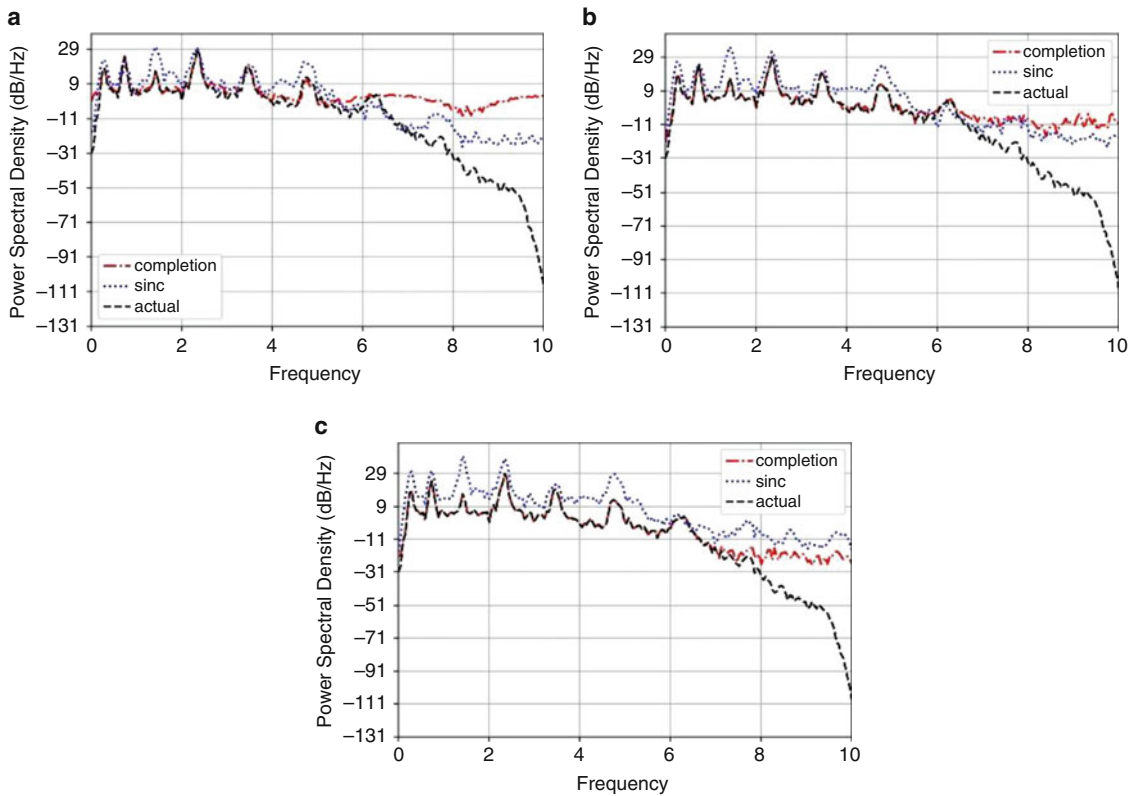


Fig. 7.13 PSD comparison for reconstructed signal at VPL 12. (a) Case A, (b) case B, (c) case C

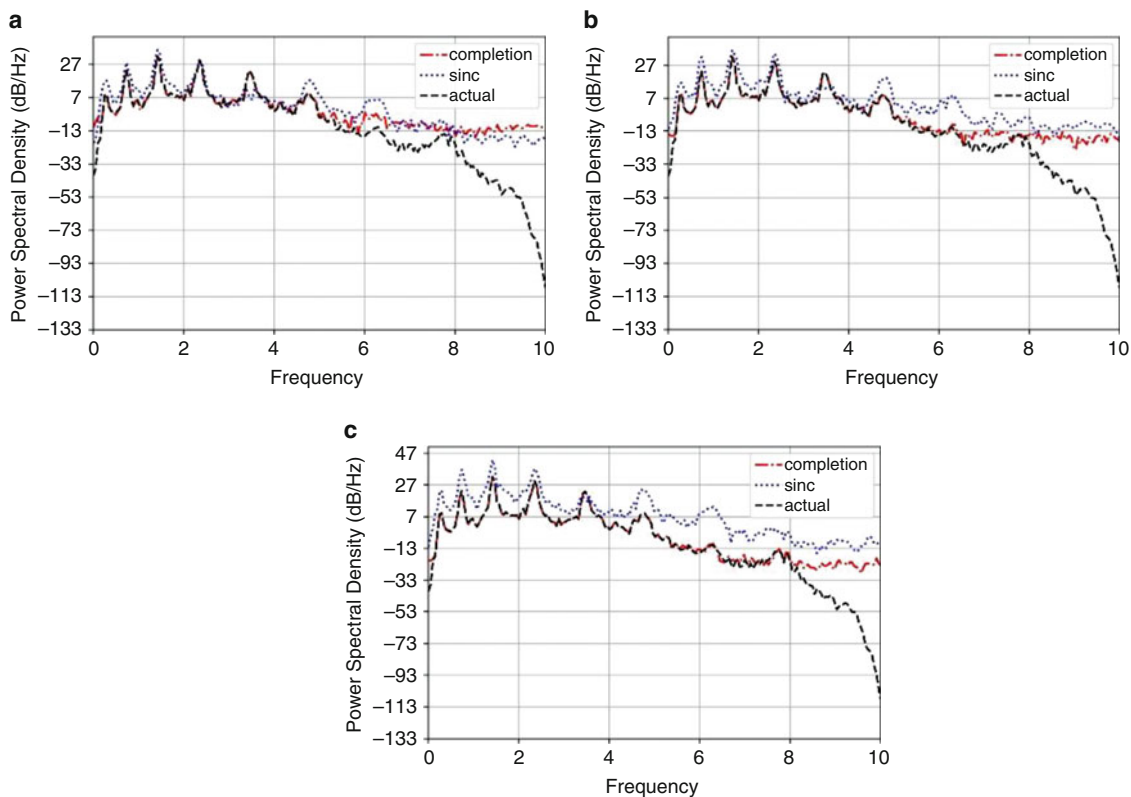


Fig. 7.14 PSD comparison for reconstructed signal at VPL 16. (a) Case A, (b) case B, (c) case C

Table 7.1 Accuracy of reconstructed signals

	VPL	PSD residual		Time signal residual	
		sinc	matrix completion	sinc	matrix completion
case A)	4	5317.1	90.3	1575.1	84.4
	8	1505.5	24.5	1173.9	148.8
	12	1517.6	33.1	1173.8	86.8
	16	3020.7	39.4	1044.7	45.9
case B)	4	22279.3	1.5	3130.9	13.1
	8	4975.0	3.7	1916.4	21.2
	12	4327.8	12.0	1763.8	51.6
	16	4383.9	12.0	1848.6	37.1
case C)	4	37037.9	1.4	3923.1	9.6
	8	14505.0	6.3	2665.0	21.9
	12	12390.0	11.0	2713.7	28.8
	16	20292.0	5.0	2852.4	21.8

Table 7.1 presents the residuals between the actual VPL signals and the estimated ones from either of the investigated methods. The residual is the second norm of the difference between actual and estimated vectors of time or frequency. Table 7.1 shows that as the observation availability grows (case A to case C), the time and frequency residuals reduce in the matrix completion approach. However, this trend is not detectable in the results of the *sinc* approach (in fact, the trend is the opposite). These numerical measures support the conclusion that the matrix completion approach outperforms the *sinc* approach significantly.

7.7 Conclusion

In this study, a novel method for estimating bridge vibration responses at fixed locations from vibrations measured by moving sensors was proposed. The procedure is based on the idea of low-rank matrix completion problem and is solvable by convex optimization algorithms. Previously, the *sinc* interpolation function was introduced for the same purpose; therefore, in this study, the performances of these two were compared. A finite element model of a 500 m (5000 DOF) long single span bridge was build and three levels of data availability (observed responses) were considered. In particular, both time and frequency representations of the reconstructed signals at four virtual probing locations were compared with the actual stationary sensed data from FE model. Two assumptions were held to simulate a more realistic sensing scenario: (1) vehicles randomly enter and exit the bridge with random directions, and (2) at the beginning of the monitoring duration, multiple vehicles are randomly present. The most significant observations are as follows:

- Matrix completion approach estimates significantly better time signal reconstruction at all three levels of data availability considered in this study. This promising ability is highly effective for damage localization methods that mainly rely on responses at certain locations.
- The proposed method is superior in terms of the accuracy of the power density estimation (PSD) of the responses, compared to the *sinc* function. This feature potentially enables more accurate system identification analyses from data reconstructed by the matrix completion method.
- In terms of the scalability, the proposed method is more desired since its performance enhances as the data availability grows. This property was not observed in the *sinc* method.
- Matrix completion approach is a one-step algorithm and yields a complete estimation of response signals at all DOFs included in the model, while the *sinc* method needs to be repeated multiple times to reach the same level of spatial information.

The *sinc* approach was originally proposed for a sensing scenario in which at every time step, the number of available moving sensors on the bridge is equal to the number of preset VPLs. This condition, however, was not held in this study since more general scenarios were of interest (random presence and commute of moving sensors). As a result, it was observed that the *sinc* method lost accuracy when the number of moving observations surpassed the number of VPLs. These imply that the proposed method (matrix completion) is a more robust solution for the problem of stationary signal reconstruction from data collected by a mobile sensor network.

Acknowledgement Research funding is partially provided by the National Science Foundation through Grant No. CMMI-1351537 by Hazard Mitigation and Structural Engineering program and by a grant from the Commonwealth of Pennsylvania, Department of Community and Economic Development, through the Pennsylvania Infrastructure Technology Alliance (PITA).

References

1. Matarazzo, T.J., Pakzad, S.N.: Scalable structural modal identification using dynamic sensor network data with STRIDEX. *Comput. Civ. Infrastruct. Eng.* (2017). <https://doi.org/10.1111/mice.12298>
2. Zhu, D., Yi, X., Wang, Y., Lee, K.-M., Guo, J.: A mobile sensing system for structural health monitoring: design and validation. *Smart. Mater. Struct.* **19**(5), 55011 (2010)
3. Matarazzo, T., Vazifeh, M., Pakzad, S., Santi, P., Ratti, C.: Smartphone data streams for bridge health monitoring. *Procedia Eng.* **199**, 966–971 (2017)
4. Kim, S., et al.: Health monitoring of civil infrastructures using wireless sensor networks. In: *Proceedings of the 6th International Conference on Information Processing in Sensor Networks - IPSN '07*, p. 254 (2007)
5. Lynch, J.P., Loh, K.J.: A summary review of wireless sensors and sensor networks for structural health monitoring. *Shock Vib. Digest.* **38**(2), 91–130 (2006)
6. Asadollahi, P., Li, J.: Statistical analysis of modal properties of a cable-stayed bridge through long-term wireless structural health monitoring. *J. Bridg. Eng.* **22**(9), 4017051 (2017)
7. Malekjafarian, A., O'Brien, E.J.: Identification of bridge mode shapes using Short Time Frequency Domain Decomposition of the responses measured in a passing vehicle. *Eng. Struct.* **81**, 386–397 (2014)
8. Yang, Y.-B., Lin, C.W., Yau, J.D.: Extracting bridge frequencies from the dynamic response of a passing vehicle. *J. Sound Vib.* **272**(3–5), 471–493 (2004)
9. González, A., O'Brien, E.J., Mcgetrick, P.: Identification of damping in a bridge using a moving instrumented vehicle. *J. Sound Vib.* **331**, 4115–4131 (2012)
10. Marulanda, J., Caicedo, J.M., Thomson, P.: Modal identification using mobile sensors under ambient excitation. *J. Comput. Civ. Eng.* **31**(2), 4016051 (2017)

11. Sadeghi Eshkevari, S., Pakzad, S.: Bridge Structural Identification Using Moving Vehicle Acceleration Measurements, pp. 251–261. Springer, Cham (2019)
12. Qin, Q., Li, H.B., Qian, L.Z., Lau, C.-K.: Modal identification of Tsing Ma bridge by using improved eigensystem realization algorithm. *J. Sound Vib.* **247**(2), 325–341 (2001)
13. Ren, W.-X., Zhao, T., Harik, I.E.: Experimental and analytical modal analysis of steel arch bridge. *J. Struct. Eng.* **130**(7), 1022–1031 (2004)
14. Weng, J.-H., Loh, C.-H., Lynch, J.P., Lu, K.-C., Lin, P.-Y., Wang, Y.: Output-only modal identification of a cable-stayed bridge using wireless monitoring systems. *Eng. Struct.* **30**(7), 1820–1830 (2008)
15. Magalhães, F., Cunha, Á., Caetano, E.: Online automatic identification of the modal parameters of a long span arch bridge. *Mech. Syst. Signal Process.* **23**(2), 316–329 (2009)
16. Matarazzo, T.J., Pakzad, S.N.: Truncated physical model for dynamic sensor networks with applications in high-resolution mobile sensing and BIGDATA. *J. Eng. Mech.* **142**(5), 4016019 (2016)
17. Gensun, F.: Whittaker–Kotelnikov–Shannon sampling theorem and aliasing error. *J. Approx. Theory.* **85**(2), 115–131 (1996)
18. Candès, E.J., Recht, B.: Exact matrix completion via convex optimization. *Found. Comput. Math.* **9**(6), 717–772 (2009)
19. Jain, P., Netrapalli, P., Sanghavi, S.: Low-rank matrix completion using alternating minimization. In: Proceedings of the 45th Annual ACM Symposium on Theory of Computing - STOC '13, p. 665 (2013)
20. Chopra, A.K.: Dynamics of Structures. Theory and Applications to Earthquake Engineering. Prentice Hall, Englewood Cliffs, NJ (2017)
21. Candès, E.J., Eldar, Y.C., Strohmer, T., Voroninski, V.: Phase retrieval via matrix completion. *SIAM Rev.* **57**(2), 225–251 (2015)
22. Candès, E.J., Plan, Y.: Matrix completion with noise. *Proc. IEEE.* **98**(6), 925–936 (2010)
23. Cai, J.-F., Candès, E.J., Shen, Z.: A singular value thresholding algorithm for matrix completion. *SIAM J. Optim.* **20**(4), 1956–1982 (2010)
24. Nair, K.K., Kiremidjian, A.S., Law, K.H.: Time series-based damage detection and localization algorithm with application to the ASCE benchmark structure. *J. Sound Vib.* **291**(1–2), 349–368 (2006)
25. Sohn, H., Farrar, C.R.: Damage diagnosis using time series analysis of vibration signals. *Smart Mater. Struct.* **10**(3), 446–451 (2001)

Chapter 8

All Vibration Is a Summation of Mode Shapes



Brian Schwarz, Patrick McHargue, Jason Tyler, and Mark Richardson

Abstract This paper expands on the ideas presented in two previous papers (Schwarz et al., Curve fitting analytical mode shapes to experimental data, IMAC XXXIV, 2014; Schwarz and Richardson, Linear superposition and modal participation, IMAC XXXII, 2014). Here, we again show with examples how all vibration, whether it is represented in the form of time waveforms, frequency spectra, or ODS's, can also be represented as a summation of mode shapes. The title of this paper is actually a universal law which is used for all modal analysis,

Fundamental Law of Modal Analysis (FLMA): All vibration is a *summation* of mode shapes.

The modal parameters of a structure can be obtained in two ways,

1. **Experimental Modal Analysis (EMA):** Extracting EMA mode shapes by curve fitting a set of experimentally derived time waveforms or frequency spectra that characterize the structural dynamics
2. **Finite Element Analysis (FEA):** Solving for the FEA mode shapes from a set of differential equations that characterize the structural dynamics

In this paper, it will be shown how the benefits of analytical FEA mode shapes can be combined with experimental data to yield more robust dynamic models (Richardson and Richardson, Using photo modeling to obtain the modes of a structure, Proceedings of the International Modal Analysis Conference, 2008; Richardson, Sound Vib Mag, 2005). FEA mode shapes will be used to “*decompose*” and then “*expand*” experimental data to include DOFs that cannot or were not determined experimentally (Schwarz et al., Using mode shapes for real time ODS animation, IMAC XXXIII, 2015).

A *unique advantage* of this approach is that *only mode shapes* themselves are required. Modal frequency and damping are not required. Another *unique advantage* is that mode shapes from an FEA model *with free-free boundary conditions* and *no damping* can be used.

It usually requires a great deal of skill and effort to modify an FEA model and its boundary conditions so that its modal frequencies and mode shapes accurately match EMA modal frequencies and mode shapes. In addition, adding accurate damping to an FEA model is usually so difficult that damping is left out of the model altogether. The approach presented here circumvents both of these difficulties.

Keywords Auto power spectrum (APS) · Cross power spectrum (XPS) · Frequency response function (FRF) · Operating deflection shape (ODS) · Experimental modal analysis mode shape (EMA mode shape) · Finite element analysis mode shape (FEA mode shape) · Modal assurance criterion (MAC) · Shape difference indicator (SDI) · Multi-input multi-output (MIMO) modeling and simulation

B. Schwarz · P. McHargue · J. Tyler · M. Richardson (✉)
Vibrant Technology, Inc., Centennial, CO, USA
e-mail: mark.richardson@vibetech.com

8.1 Introduction

A mode of vibration is a mathematical representation of a structural resonance. When forces are applied and therefore energy is trapped within the boundaries of a structure, it will resonate. Any structure which is made out of one or more elastic materials will exhibit resonant vibration.

Resonant vibration can be thought of as a *mechanical amplifier*. That is, when forces are applied to a structure, some of its modes will *readily absorb the energy* causing the structure to resonate with *excessive levels of deformation*. This causes premature failure of bearings and gears, and material fatigue and failure.

Each mode is defined by three distinct parts; a *natural frequency*, a *damping or decay constant*, and a *mode shape*. A mode shape represents the “*standing wave deformation*” of the structure at the natural frequency of a resonance. This standing wave behavior is caused when energy becomes trapped within the material boundaries of the structure, and must be absorbed by the damping mechanisms that are present.

Both EMA and FEA are based upon the FLMA. FLMA is *assumed by all of the curve fitting methods* that are used to extract EMA mode shapes from experimental data.

8.1.1 Modal Testing

All structural dynamic response data is initially acquired as multiple time waveforms. Using the FFT algorithm, each time waveform is transformed into its corresponding Fourier spectrum without loss of information. The Fourier spectra of multiple time waveforms can be further processed into a variety of frequency domain functions, including Auto and Cross spectra, FRFs, Transmissibility's, and ODS FRFs. All of these frequency functions preserve the structural dynamics originally captured in the time waveforms.

All modal testing is based on the FLMA, namely that all vibration data in the form of either time waveforms or frequency spectra is a *summation of resonance curves*, each curve due to a mode of vibration.

8.1.2 Curve Fitting

Multiple time waveforms or frequency spectra defined for different DOFs (motions at different points in different directions) are needed to extract EMA mode shapes from experimental data.

An **Operating Deflection Shape (ODS)** is the data at the same sample from *two or more time* waveforms or frequency spectra that characterize the vibration of a machine or structure.

ODS data over a span of time or frequency samples is then “*curve fit*” to estimate the modal parameters of each resonance [6]. The curve fitting process involves matching an *analytical parametric model* to the experimental data, usually in a “*least-squared-error*” sense. In other words, the unknown modal parameters of the analytical model are estimated in a manner which minimizes the difference between the experimental data and the analytical model over a band of samples.

8.2 Expanding Experimental Data

In this paper, it will be shown with two examples how analytical FEA mode shapes can be used to “*expand*” order-based ODS's and experimental time waveforms to include DOFs that were not determined experimentally [4]. Unlike the “*curve fitting*” used to extract EMA mode shapes, in this process the unknown *participation of each mode shape* in the experimental data is determined by a different “*least-squared-error*” process. The participation of each mode is then used to “*expand*” the data to include the original DOFs plus extra DOFs calculated from the DOFs of the mode shapes.

The following examples are used to illustrate shape decomposition and expansion,

1. Order-based ODS's of a rotating machine are decomposed and expanded from a few experimentally derived DOFs to 1000's of DOFs
2. The sinusoidal response time waveforms of a structure are decomposed and expanded to include twice as many DOFs as the original data

These examples illustrate the combined use of FEA mode shapes and experimental data to create more robust structural dynamic models, which in turn can be used in further structural dynamics applications.

In these examples only FEA mode shapes are used to decompose and expand the experimental data.

8.3 Expanding Order-Based ODS's

In a rotating machine, the dominant forces are applied at multiples of the machine running speed, called orders. An **order-based ODS** is assembled from the **peak values** at one of the orders in a set of output-only frequency spectra. Auto spectra, Cross spectra, or ODS FRFs can be calculated from output-only data that is acquired while the machine is running. When displayed in animation on a 3D model of the machine, an order-based ODS is a convenient way of visualizing distributed vibration levels caused by unmeasured internal forces. These distributed vibration levels can be represented as a summation of resonances and can be used for monitoring the health of the machine.

In this example, it is shown how **modes participate differently** at different operating speeds in an order-based ODS of a rotating machine. The **modal participation** is then used to **expand** the order-based ODS's, and they become a valid representation of the ODS for both the **measured and un-measured** DOFs of the machine.

Experimental ODS data was obtained from the rotating machine shown in Fig. 8.1. In Fig. 8.2 the model shows the eight tri-axial accelerometers used to acquire operating data, one on each bearing block and three on each side of the base plate. When post-processed, the accelerometer data provided ODS's with 24 DOFs, thus defining 3D motion on the machine at eight points.

The machine was supported on **four rubber mounts** (one under each corner), so its **rigid body motion** participated significantly in its ODS's. **Six rigid-body** and **four flexible-body** FEA mode shapes were obtained from an FEA model of the base plate and bearing blocks. These ten mode shapes were used to expand the experimental ODS's.

One of the **rigid-body** mode shapes is shown in Fig. 8.3, and a **flexible-body** mode shape is shown in Fig. 8.4. These FEA mode shapes have 1938 DOFs in them, including the 24 DOFs of the eight accelerometers.

A comparison display of a 1938-DOF expanded ODS versus its original 24-DOF experimental ODS is shown in Figs. 8.5, 8.6 and 8.7. Each of these Figure contains an expanded versus an original ODS at a different machine speed. The expanded ODS is displayed on the left and the 24-DOF ODS is displayed on the right in each Figure. The participation bar charts on

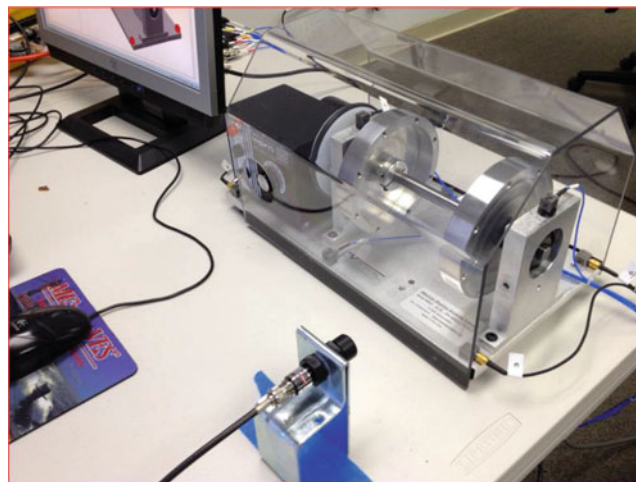


Fig. 8.1 Variable speed rotating machine

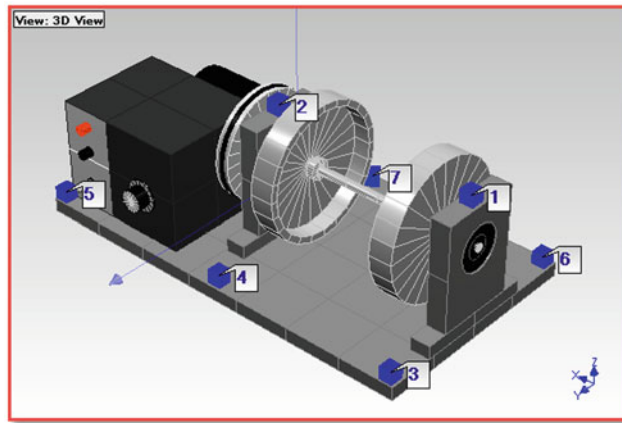


Fig. 8.2 Model of the rotating machine showing accelerometers

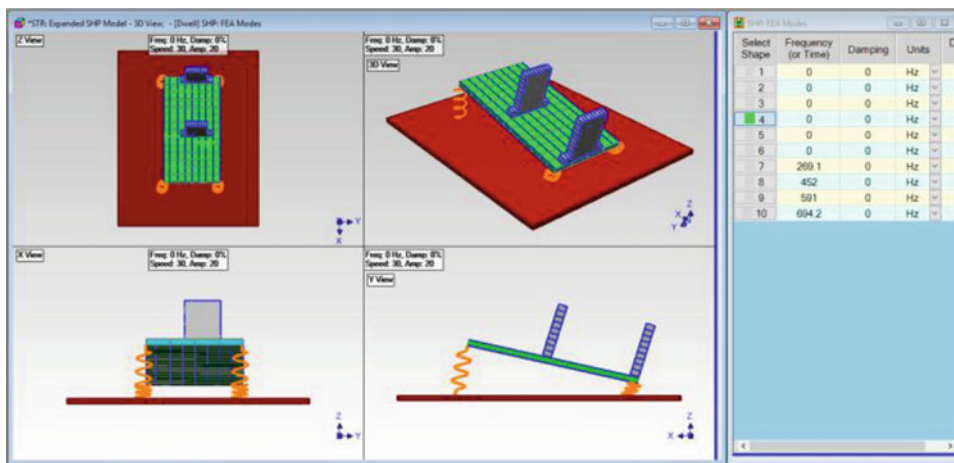


Fig. 8.3 Rigid-body mode of base plate and bearing block

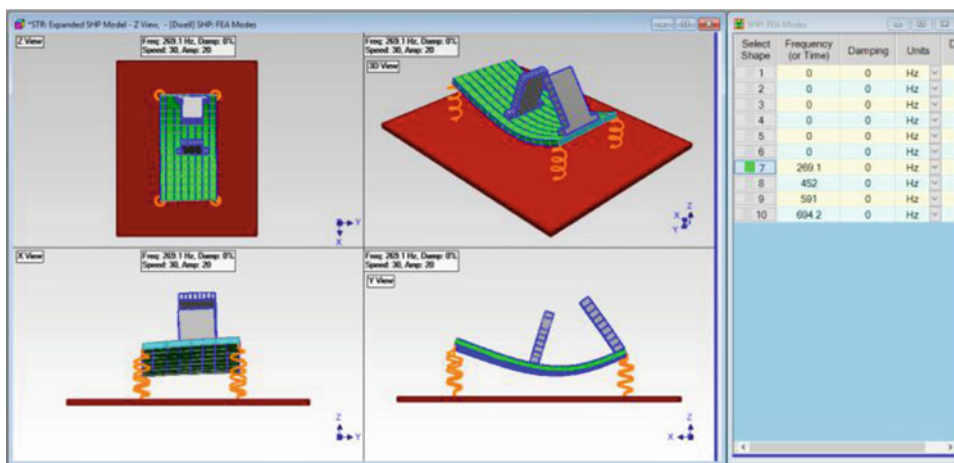


Fig. 8.4 First flexible mode of base plate and bearing block

the right side of each Figure show the participation of each FEA mode shape in each ODS. The bars show that the *rigid-body modes dominate* each ODS, but they participate differently at each speed.

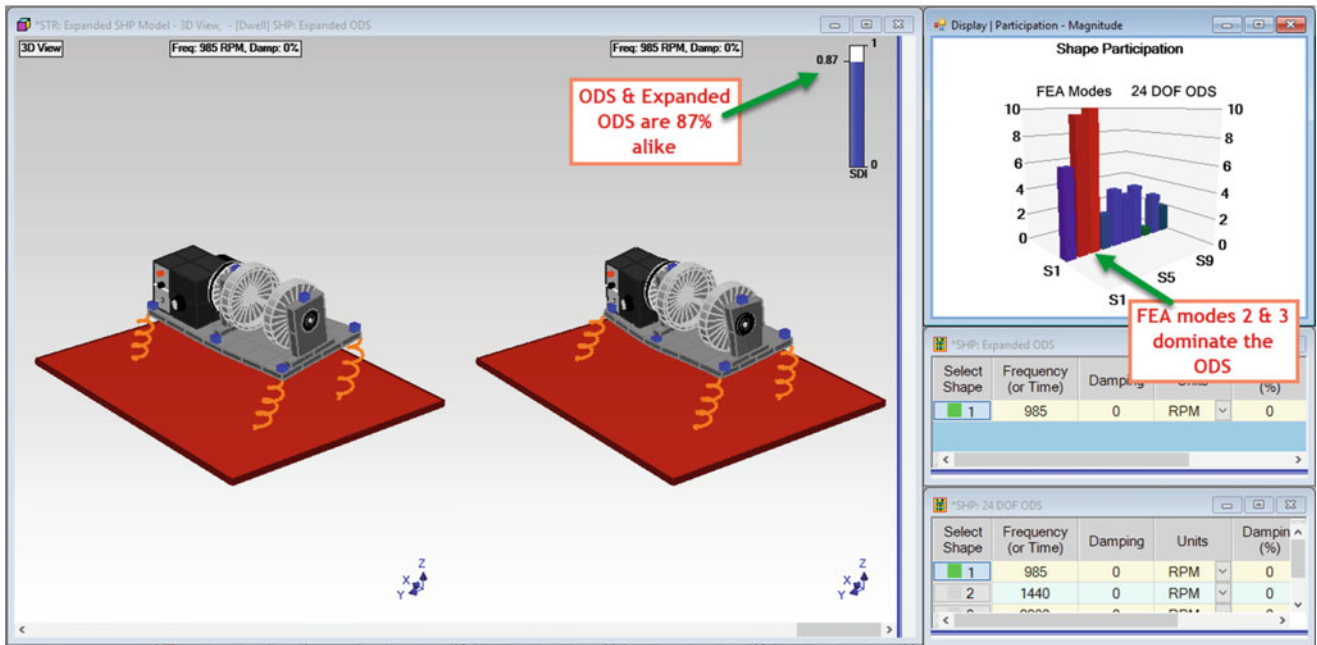


Fig. 8.5 ODS expansion at 985 RPM

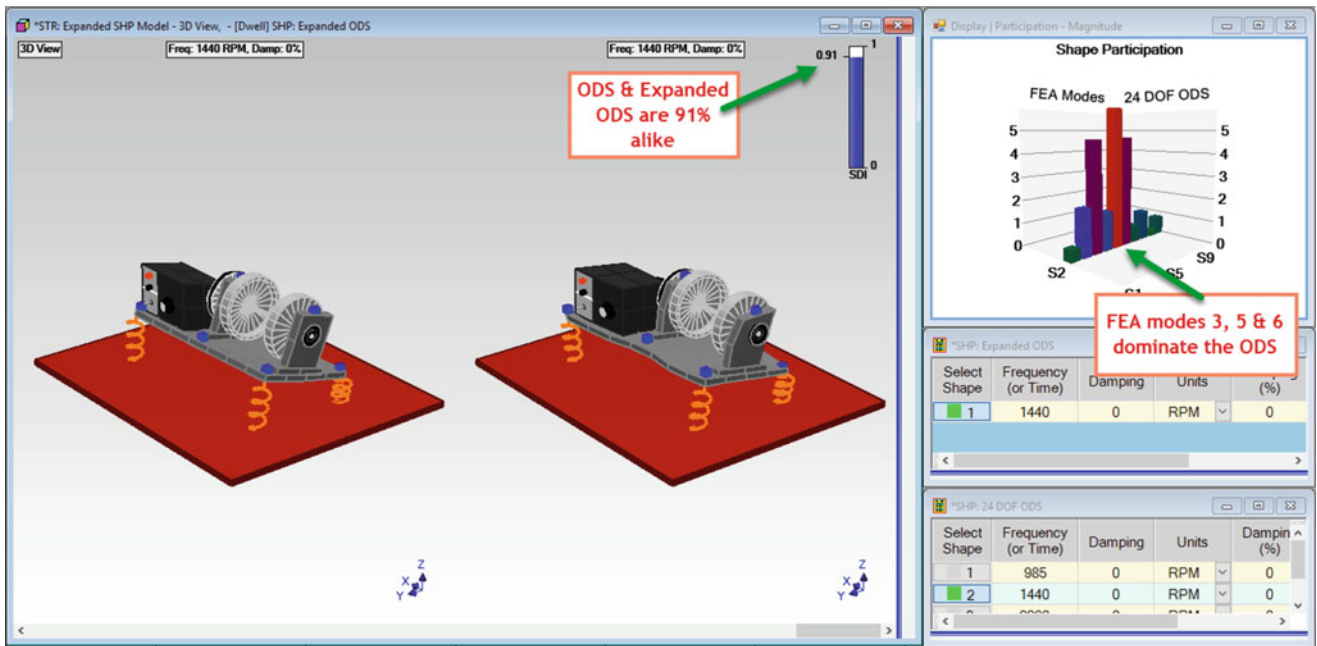


Fig. 8.6 ODS expansion at 1440 RPM

The SDI (shape difference indicator [3]) is also shown in the shape comparison display. SDI values range between 0 and 1. A *value of "1"* means the two shapes are *identical*. The high SDI values in Figs. 8.5, 8.6 and 8.7 indicate that at each speed, the expanded ODS *closely matches* the 24-DOF ODS; (**0.87 at 985 RPM**), (**0.91 at 1440 RPM**), (**0.94 at 2280 RPM**).

Complex valued modal participations were used to curve fit the normal FEA mode shapes to the complex experimental ODS data.

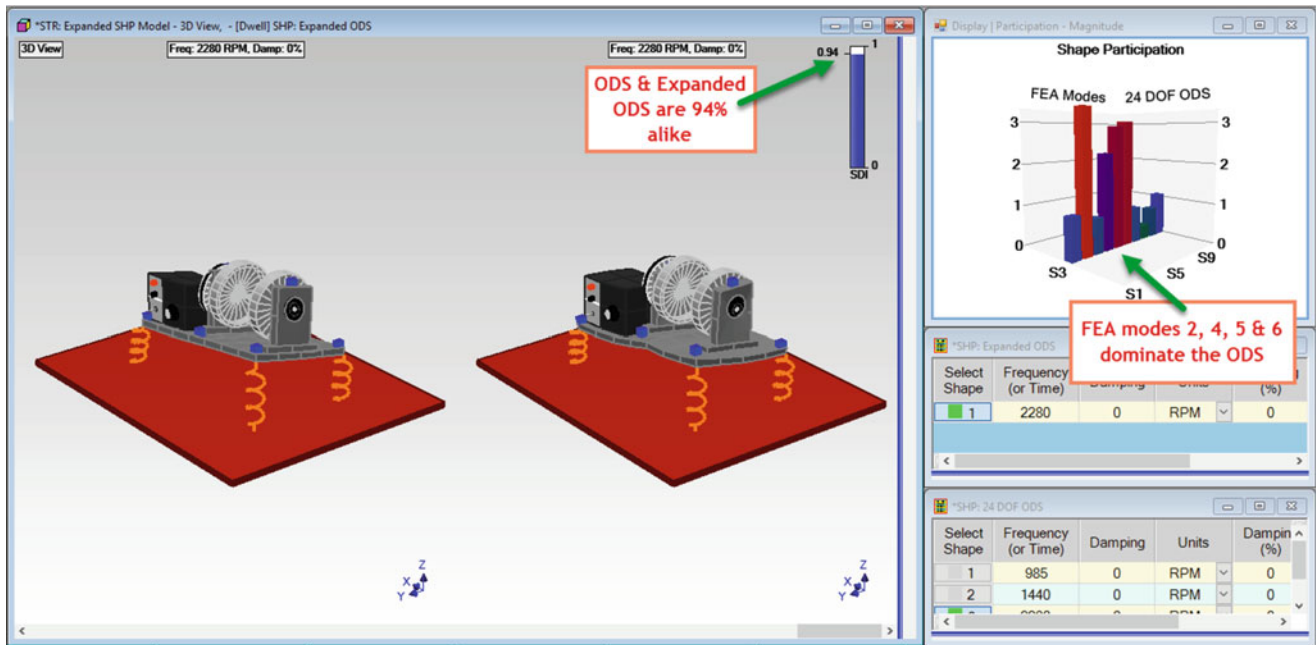


Fig. 8.7 ODS expansion at 2280 RPM

The high SDI values in Figs. 8.5, 8.6 and 8.7 verify that even complex valued ODS data can be *accurately represented as a summation of normal mode shapes*.

8.4 Expanding Sinusoidal Responses

In this second example, MIMO modeling and simulation was used to calculate simulated responses to two sinusoidal excitation forces applied to the Jim Beam structure shown in Fig. 8.8. The forces were applied at points 5 and 15 in the Z-direction on the top plate of the beam, that is at DOFs 5Z and 15Z. Two cases were simulated,

1. Two 500 Hz In-Phase sinusoidal excitation forces
2. Two 500 Hz Out-of-Phase sinusoidal excitation forces

The sinusoidal In-Phase and Out-of-Phase force time waveforms are shown in Figs. 8.9a, b. Each time waveform contains **5000 samples**. The cursor values in Fig. 8.9a show that the two forces are In-Phase with one another. The cursor values in Fig. 8.9b show that the two forces are Out-of-Phase with one another.

Four of the EMA mode shapes with frequencies *surrounding 500 Hz* are displayed in Figs. 8.10a–d. These modes are expected to participate in the response of the Jim Beam at 500 Hz. The 493 Hz mode is nearest to 500 Hz, so it *should dominate* the sinusoidal response. We will see that in fact it does dominate the response, but depending on the phases of the excitation forces, *other modes will also participate* in the response.

The MAC values between 10 of the EMA and FEA mode shapes of the beam are shown in Fig. 8.11. MAC *values above 0.9* indicate that two mode shapes are *co-linear*. That is, two shapes *lie on the same straight line* (have the *same shape*) but they may be scaled differently.

The frequencies of the FEA and EMA modes are listed in Figs. 8.12a, b. Notice that the frequency of each FEA mode shape is *much less* than the frequency of the corresponding EMA mode shape with which it has a high MAC value. The frequency differences will not matter however, because only the FEA mode shapes are used to decompose and expand the time waveforms.

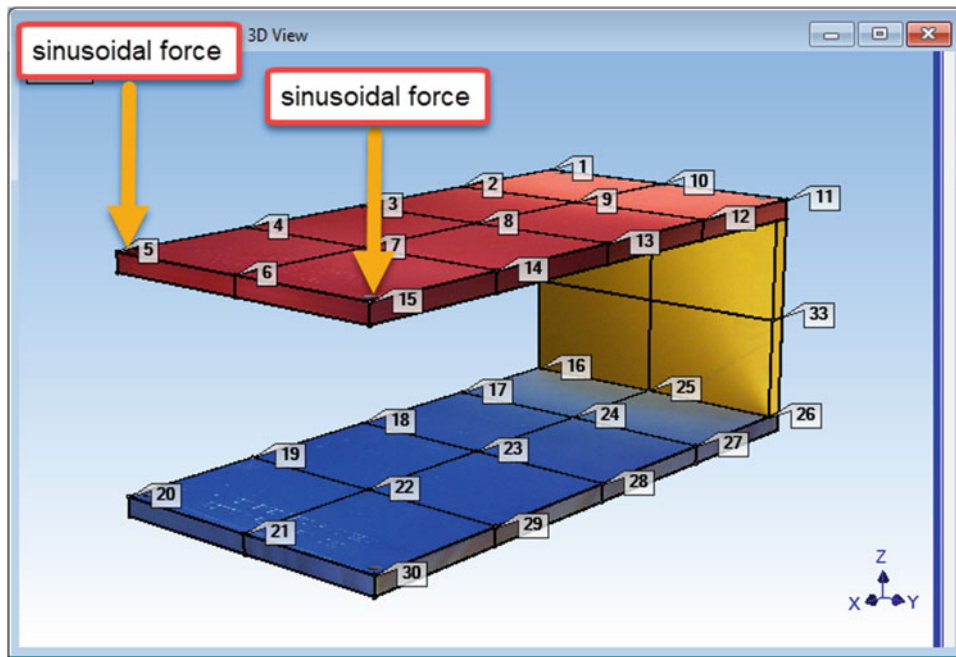


Fig. 8.8 Sine wave excitation at points 5 and 15

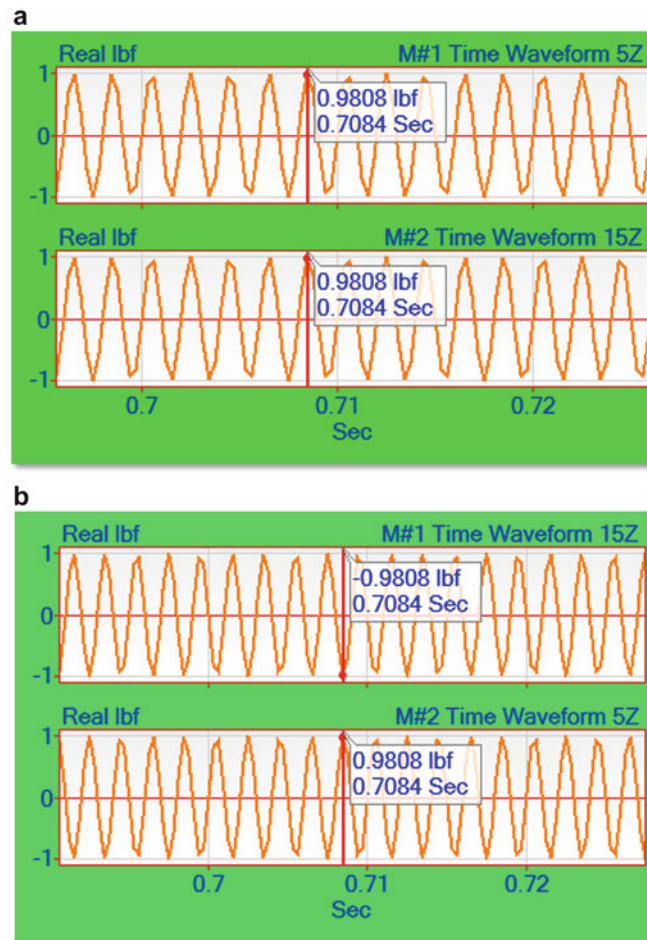


Fig. 8.9 (a) In-phase sine wave excitation at DOFs 5Z and 15Z. (b) Out-of-phase sine wave excitation at DOFs 5Z and 15Z

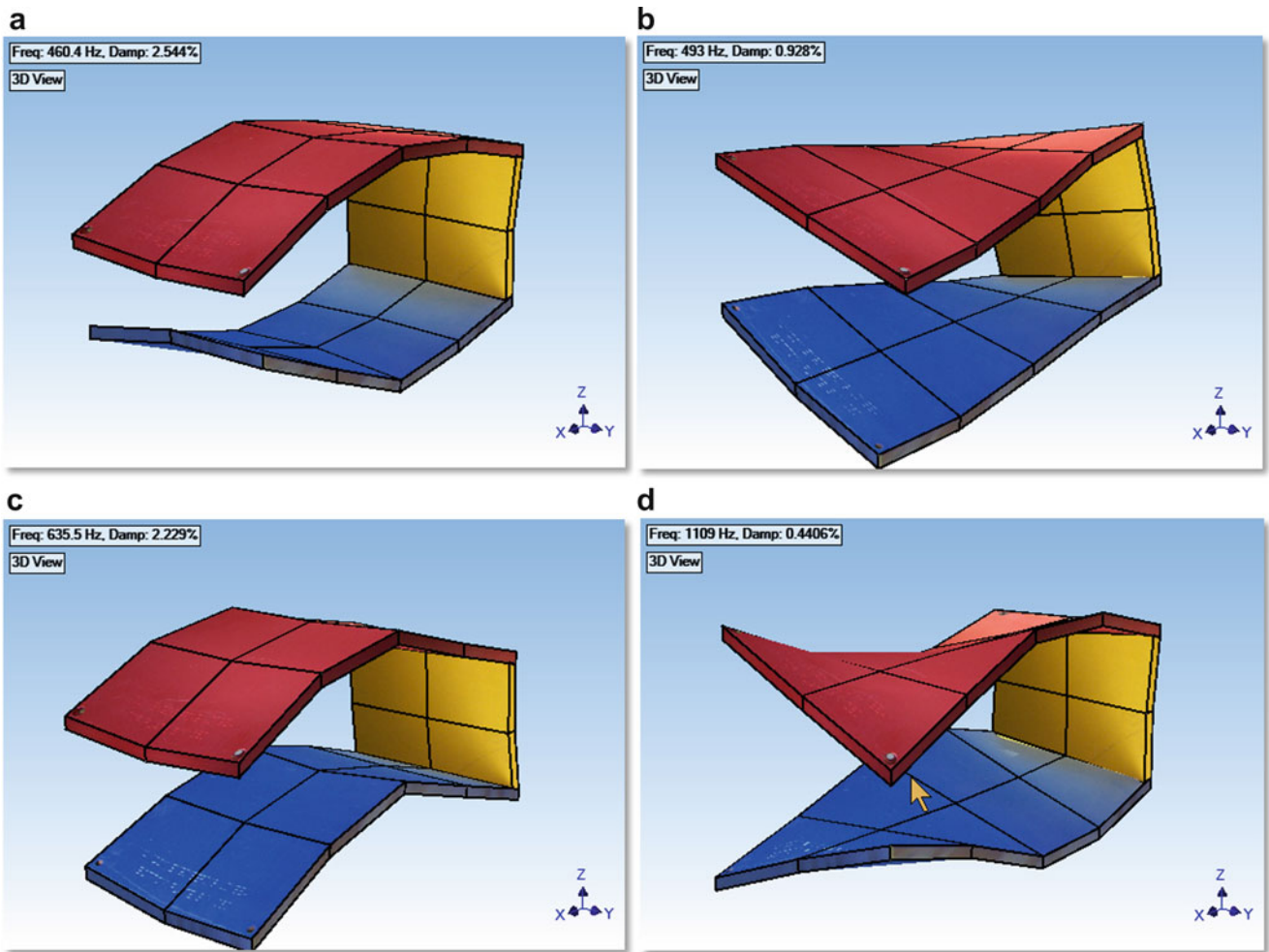


Fig. 8.10 (a) EMA mode shape at 460 Hz. (b) EMA mode shape at 493 Hz. (c) EMA mode shape at 636 Hz. (d) EMA mode shape at 1109 Hz

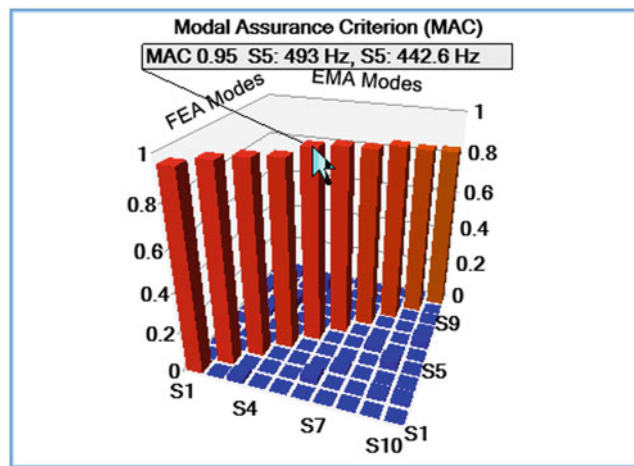


Fig. 8.11 MAC values between EMA and FEA modes

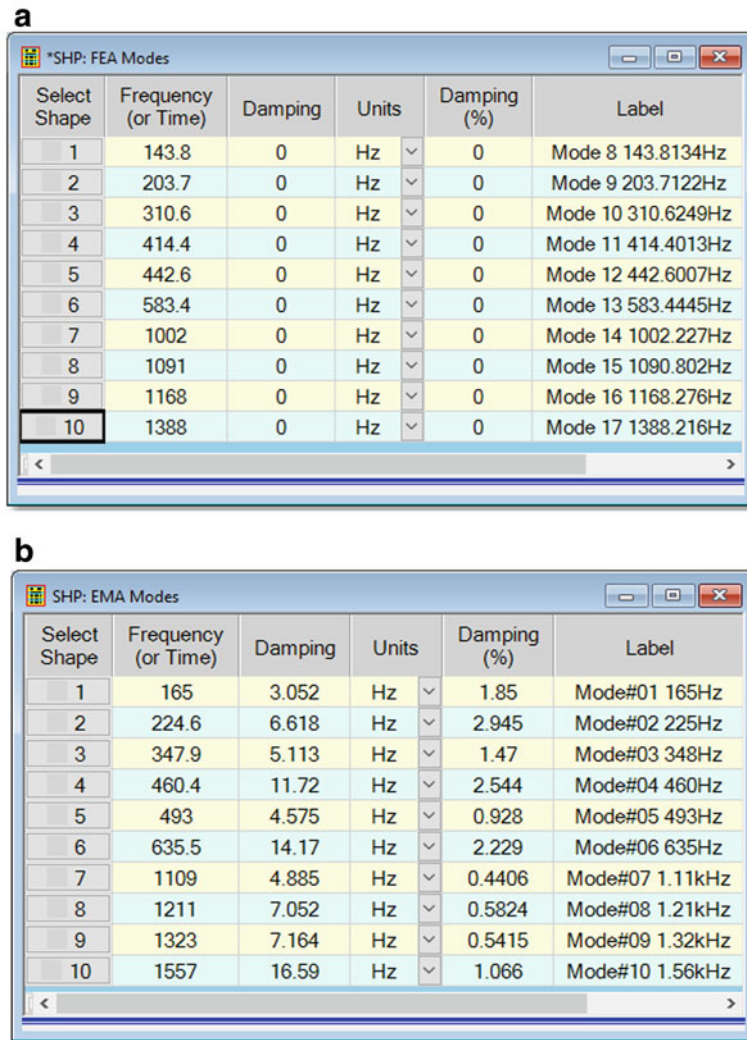


Fig. 8.12 (a) FEA modal frequencies. (b) EMA modal frequencies

8.4.1 Response to In-Phase Forces

In Fig. 8.13, the simulated response of the Jim Beam structure to two In-Phase forces is displayed on the left. These responses were calculated using the EMA mode shapes, which were used to synthesize FRFs, which then were multiplied by the Fourier spectra of the forces to obtain Fourier spectra of the response DOFs of the Jim Beam. The Fourier spectra of the responses were then inverse Fourier transformed to obtain the response time waveforms displayed on the *upper right* of Fig. 8.13. The MIMO modeling and simulation process is depicted in Fig. 8.14.

The FEA mode shapes were then curve fit to the simulated responses and used to expand them from 99 to 315 DOFs. The expanded response time waveforms are displayed on the *lower right* in Fig. 8.13. The time-based ODS at the *current Line cursor position* in the simulated responses is displayed on the *left-hand model*, and the expanded ODS from the *same cursor position* is displayed on the *right-hand FEA model*.

The MAC bar between the two time-based ODS's (simulated and expanded) is also displayed in the *upper right corner* of the ODS display. This *MAC value of 0.95* indicates that the two ODS's are *nearly co-linear*, meaning that they are *essentially the same shape*.

In Fig. 8.15, the two blocks of response time waveforms are correlated using MAC and SDI [3]. The *upper graph is the MAC values* between each sample of the simulated time waveforms versus the same sample of the expanded time waveforms. The *lower graph is the SDI values* between the same samples in each data block of time waveforms. Both MAC and SDI

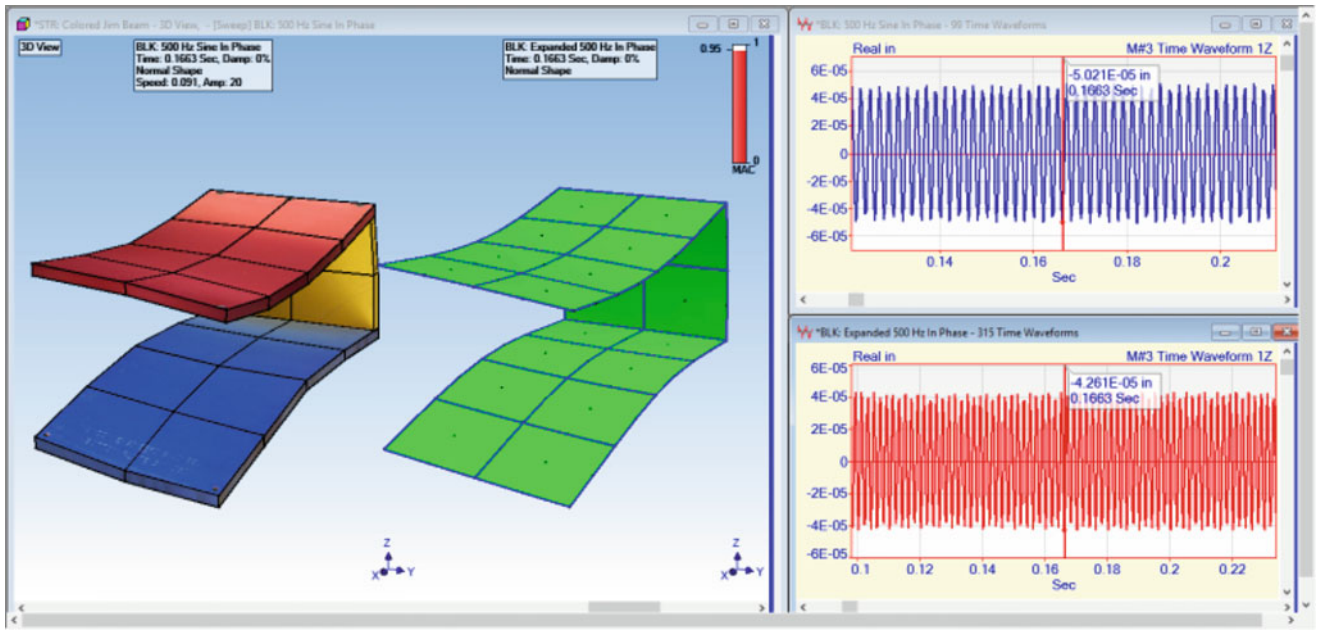


Fig. 8.13 Simulated vs. expanded response to in-phase forces

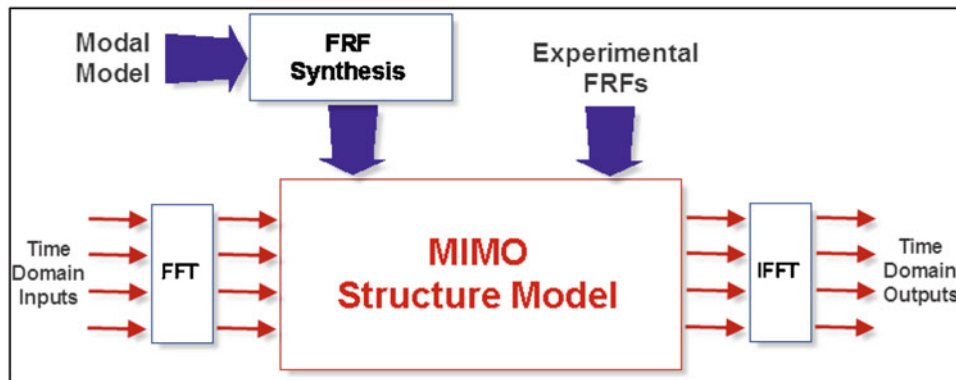


Fig. 8.14 MIMO modeling and simulation

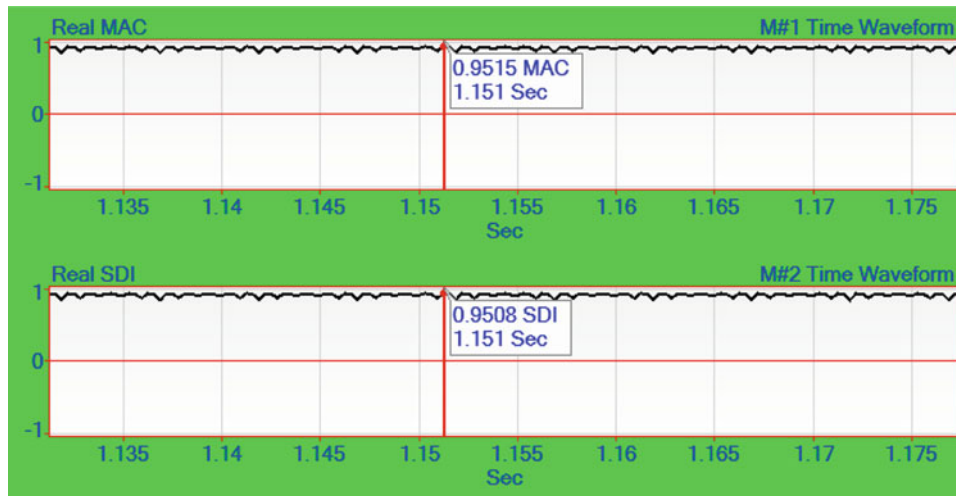


Fig. 8.15 Correlation of simulated and expanded time waveforms

indicate that the data at the same sample was *nearly identical* in both data blocks. Not all samples are shown, but this was true *for all 5000 samples* of both time waveforms.

8.5 Modal Participation in Responses to In-Phase Forces

Figures 8.16a, b show the participation of the EMA and FEA mode shapes in two time-based ODS's taken from the simulated and expanded waveforms shown in Fig. 8.13. The simulated responses were calculated using MIMO simulation and the EMA mode shapes, while the expanded responses were calculated by curve fitting the simulated responses with FEA mode shapes. These results show that both the EMA and FEA mode shapes participate in the simulated and expanded ODS's in a similar way. *Mode #5 dominates* each ODS, but *modes #4, #6 and #7 also participate* in each ODS.

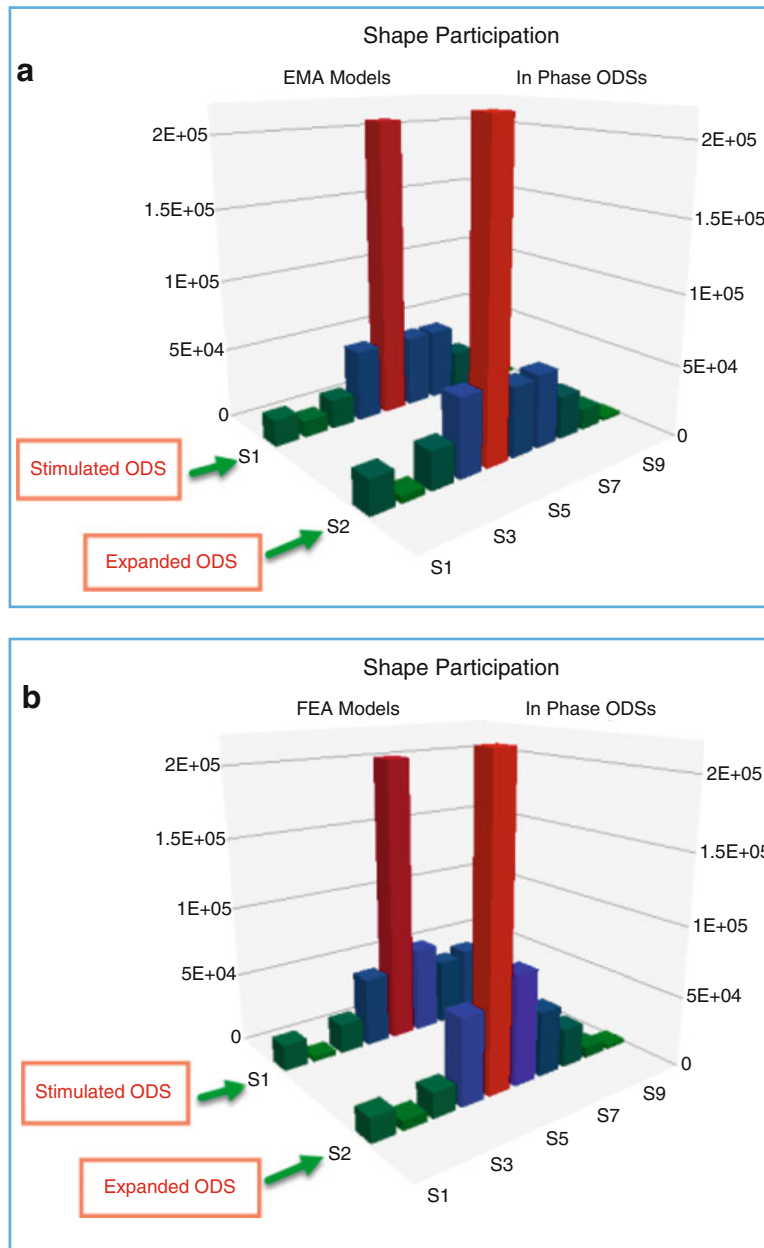


Fig. 8.16 (a) EMA mode shape participation in the ODS's. (b) FEA mode shape participation in the ODS's

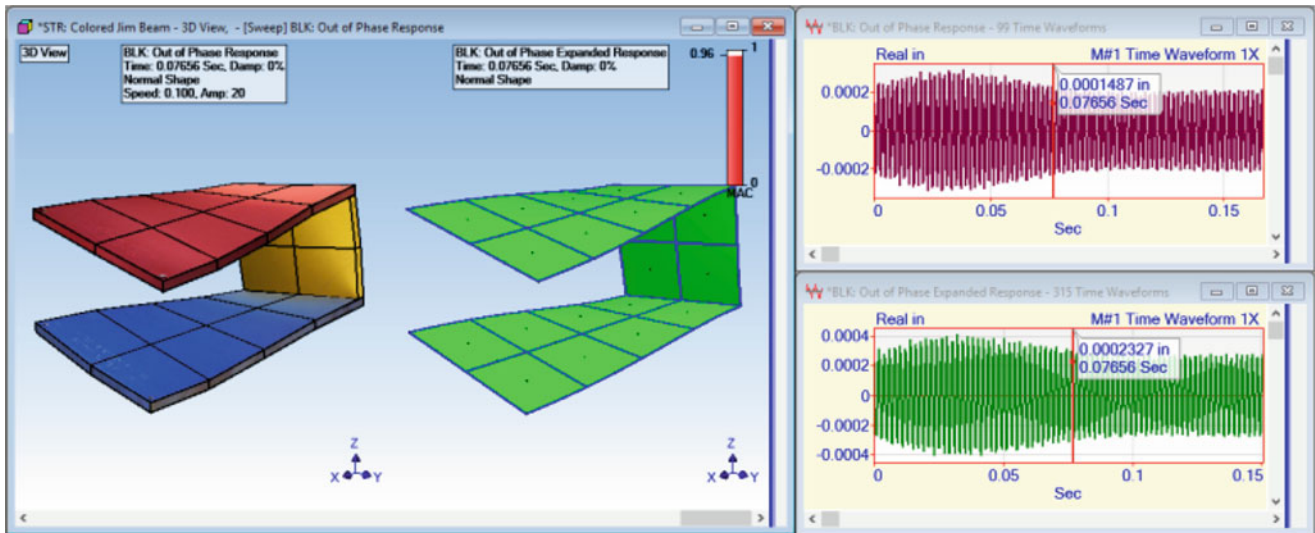


Fig. 8.17 Simulated vs. expanded response to out-of-phase forces

The mode shapes of modes **#4** and **#6** are *in-phase* with the two In-Phase excitation forces at DOFs 5Z and 15Z, so they also participate in the ODS's. However, the mode shapes of modes **#5** and **#7** are *out-of-phase* with the two In-Phase excitation forces at DOFs 5Z and 15Z. Yet both of these mode shapes also participate in the ODS's. How can this be true?

The only explanation for the participations of **modes #5 and #7** shown in Fig. 8.16a, b is that even though these two mode shapes are *out-of-phase* with the two In-Phase excitation forces at DOFs 5Z and 15Z, these mode shapes *sum together* in a manner which contributes to the ODS's, with **mode #5** still dominating both ODS's.

8.5.1 Response to Out-of-Phase Forces

In Fig. 8.17, the simulated response of the Jim Beam structure to two Out-of-Phase forces is displayed on the left. These responses were calculated using the MIMO simulation depicted in Fig. 8.14 and the EMA mode shapes, which were used to synthesize FRFs, which then were multiplied by the Fourier spectra of the forces. The Fourier spectra of the responses were then inverse Fourier transformed to obtain the response time waveforms displayed on the *upper right* of Fig. 8.17.

The FEA mode shapes were then used to expand each sample of the simulated response time waveforms. Those expanded responses are displayed on the *lower right* in Fig. 8.17. The time-based ODS at the *current Line cursor position* in the simulated responses is displayed on the *left-hand model*, and the ODS from the same cursor position in the expanded responses is displayed on the *right-hand FEA model*.

The MAC bar between the two time-based ODS's (simulated and expanded) is also displayed in the *upper right corner* of the ODS display. This *MAC value of 0.96* indicates that the two ODS's are *nearly co-linear*, meaning that they are *essentially the same shape*.

In Fig. 8.18, the two blocks of response time waveforms are correlated using MAC and SDI [3]. The *upper graph is the MAC values* between each sample of the simulated time waveforms versus the same sample of the expanded time waveforms. The *lower graph is the SDI values* between the same samples in each data block of time waveforms. Both MAC and SDI indicate that the data at the same sample was *nearly identical* in both data blocks. Not all samples are shown, but this was true *for all 5000 samples* of both time waveforms.

8.5.2 Modal Participation in Responses to Out-of-Phase Forces

Figure 8.19a, b show the participation of the EMA and FEA mode shapes in two time-based ODS's taken from the simulated and expanded response data blocks shown in Fig. 8.17. The simulated responses were calculated using the EMA mode shapes, and the expanded responses were calculated by curve fitting the ten FEA mode shapes to the simulated responses.

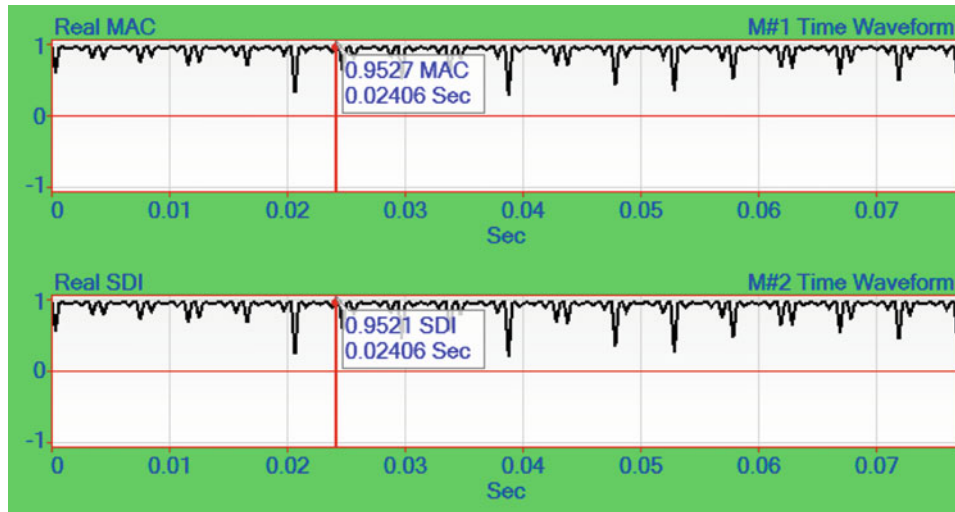


Fig. 8.18 Correlation of simulated and expanded time waveforms

These results clearly show that both the EMA and FEA mode shapes participate in the response ODS's in a similar way. In this case, because *its mode shape is in-phase* with the two Out-of-Phase excitation forces at DOFs 5Z and 15Z, **mode #5 dominates the response**, and there is *very little participation* from the other modes.

8.6 Conclusions

In a previous paper [1] it was also shown how mode shapes can be used to decompose and expand a set of FRFs, Cross spectra, and ODS FRFs. In those cases, it was demonstrated that frequency domain vibration functions can be accurately decomposed into a *summation of resonance curves* by curve fitting them with a set of mode shapes, one frequency at a time. These participations of mode shapes at each frequency were then used to construct an *expanded set of measurements* using all of the DOFs of the mode shapes.

In this paper, the same procedure was used to decompose and then to expand several order-based ODS's, and to expand simulated sinusoidal response time waveforms. Both of these examples illustrated how the free-free FEA mode shapes of a machine or structure can be used to decompose and expand data according to the following law,

Fundamental Law of Modal Analysis (FLMA): All vibration is a *summation* of mode shapes.

This decomposition and expansion using FEA mode shapes offers some important advantages,

- Real-world time or frequency vibration data can be *accurately curve fit* using FEA mode shapes
- Normal mode shapes derived from an FEA model with *free-free boundary conditions* and *no damping* can be curve fit to real-world vibration data that includes *real-world damping and boundary conditions*
- FEA normal mode shapes can be used to curve fit complex valued vibration data

It usually requires a great deal of skill and effort to modify an FEA model and its boundary conditions so that its modal frequencies and mode shapes accurately match EMA modal frequencies and mode shapes. Adding accurate damping to an FEA model is usually so difficult that damping is left out of the model altogether. The approach used here circumvents both of these difficulties.

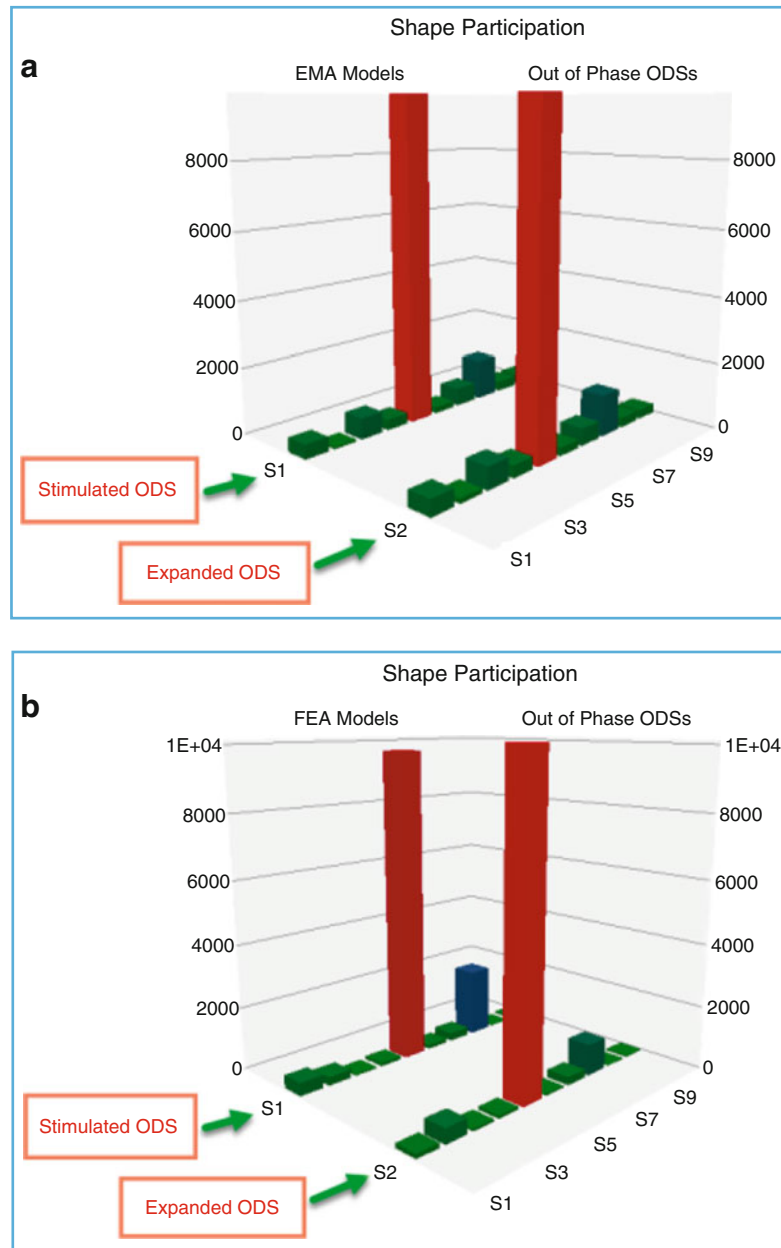


Fig. 8.19 (a) EMA mode shape participation in the ODS's. (b) FEA mode shape participation in the ODS's

Experimental vibration data *always includes* both *real world boundary conditions* and *real-world damping*.

It was shown in the first example that complex ODS data can be accurately decomposed and expanded using the *normal mode shapes* of the bearing blocks and base plate of a rotating machine. These normal mode shapes were derived from a relatively simple FEA model with free-free boundary conditions and no damping.

Normal modes can be used to expand *complex vibration data* because the *modal participation factors* used to decompose and expand the complex data are also complex valued.

In the second example, normal mode shapes were used to decompose and expand real valued time waveforms. Curve fitting FEA mode shapes to this data yielded an unexpected participation of the mode shapes when two In-Phase sine wave forcing functions were applied to the top two corners of the Jim Beam structure.

The intuitive belief that the mode with natural frequency closest to a sinusoidal forcing frequency should dominate the vibration response turned out to be true, but it was found that other modes also participate in a response based on their mode shapes, not their frequencies.

Applying this approach to any vibration data that is acquired directly from a machine or structure can provide the necessary information for continuously monitoring its resonant properties. Furthermore, this decomposition and expansion capability is useful for creating the resonant properties of *un-measured or un-measurable* portions of a machine or structure.

This combined use of a *simplified FEA model* and a *small amount of experimental data* means that less time and expense are required to obtain meaningful data for use in machinery and structural health monitoring, and for more quickly diagnosing and mitigating noise and vibration problems.

References

1. Schwarz, B., Richardson, S., Richardson, M.: Curve Fitting Analytical Mode Shapes to Experimental Data. IMAC XXXIV, 25–28 Jan 2016
2. Schwarz, B., Richardson, M.: Linear Superposition and Modal Participation. IMAC XXXII, 3–6 Feb 2014
3. Richardson, S., Tyler, J., McHargue, P., Richardson, M.: A New Measure of Shape Difference. IMAC XXXII, 3–6 Feb 2014
4. Schwarz, B., Richardson, S., Richardson, M.: Using Mode Shapes for Real Time ODS Animation. IMAC XXXIII, 3–5 Feb 2015
5. Richardson, S.C., Richardson, M.H.: Using photo modeling to obtain the modes of a structure. In: Proceedings of the International Modal Analysis Conference (2008)
6. Richardson, M.: Is it a mode shape or an operating deflection shape? Sound Vib. Mag. (Mar 1997)
7. Richardson, M.: Modal analysis versus finite element analysis. Sound Vib. Mag. (Sept 2005)

Chapter 9

Modal Testing Using the Slinky Method



Brian Schwarz, Patrick McHargue, and Mark Richardson

Abstract Conventional broad-band modal testing is done by acquiring a single-reference or multiple-reference set of FRFs and curve-fitting them to obtain modal parameters. Since a (fixed) reference sensor is required throughout the data acquisition process, testing a large structure requires that a (potentially) long wire be used to connect the reference sensor to the acquisition system.

In a previous paper (McHargue et al., ODS & modal testing using a transmissibility chain, IMAC XXXVI, 2017), a new modal testing method was introduced which does not require the use of a fixed reference sensor. This method is based on the calculation of a series of Transmissibility's, called a TRN chain. This method has several important advantages,

1. Excitation forces need not be acquired
2. Only two response sensors are required for data acquisition
3. The two sensors can be physically close to one another throughout data acquisition

Since the excitation forces need not be measured, data for calculating a TRN chain can be acquired from an operating machine, or during any test where excitation is provided by impacting or by using one or more shakers.

A Slinky test is a unique way of acquiring a TRN chain. In a Slinky test, one sensor is merely “*hopped over*” the other sensor with each new acquisition, as shown in Fig. 9.3. As the two sensors are moved over the surface of the structure in this manner, a “*chain*” of Transmissibility's is calculated from the acquired data.

A TRN chain can be “*seeded*” with an Auto spectrum, Cross spectrum, Fourier spectrum, or FRF to yield a single-reference set of measurements, from which experimental modal parameters can be extracted. A Slinky test is much faster, easier, and less costly than a conventional modal test.

Keywords Transmissibility chain (TRN chain) · Fourier spectrum (DFT) · Auto power spectrum (APS) · Cross power spectrum (XPS) · Frequency response function (FRF) · Operating deflection shape (ODS) · Experimental modal analysis mode shape (EMA mode shape) · Operational modal analysis mode shape (OMA mode shape) · Modal assurance criterion (MAC) · Shape difference indicator (SDI)

9.1 Introduction

To obtain the experimental ODS's or mode shapes of a machine or structure, each degree-of-freedom (DOF) of a shape must contain the *correct magnitude and phase relative to all other DOFs*. If all sensor data is *simultaneously acquired*, each shape will contain the correct relative magnitudes and phases. However, simultaneous acquisition requires that all sensors be connected to a multi-channel acquisition system so that all of the data can be acquired from all channels at once.

Experimental ODS's and mode shapes are obtained from a set of cross-channel measurements where a *fixed reference sensor* is used throughout the test. For large test articles, the wire from the reference sensor to the acquisition system *could be very long*. In a roving impact test, the wire from the instrumented hammer to the acquisition system *could also be long*.

B. Schwarz · P. McHargue · M. Richardson (✉)
Vibrant Technology, Inc., Centennial, CO, USA
e-mail: mark.richardson@vibetech.com

The **Product** of two Transmissibilitys is
another Transmissibility

$$TRN(3:1) = TRN(3:2) \times TRN(2:1)$$

The **Inverse** of $TRN(2:1)$ is $TRN(1:2)$

$$TRN(1:2) = \left(\frac{1}{TRN(2:1)} \right)$$

Fig. 9.1 Transmissibility properties

Operational modal parameters (frequencies damping, and mode shapes) are typically obtained by curve fitting a *single reference set* of output-only Cross spectra or ODS FRFs. An *experimental modal model* (a set of mode shapes containing the mass, stiffness and damping properties of the structure) is typically obtained by curve fitting a *single reference set* of calibrated FRFs.

9.1.1 Cross-channel Measurements

An **output-only Cross spectrum** is a cross-channel frequency-based measurement defined as the Fourier spectrum of one response multiplied by the complex conjugate of the Fourier spectrum of the other response. An **FRF** is a frequency-based cross-channel measurement defined as the Fourier spectrum of a structural response (in displacement, velocity, or acceleration units) divided by the Fourier spectrum of an excitation force that caused the response. An **ODS FRF** is a frequency-based cross-channel measurement defined as the Auto spectrum of a vibration response together with the phase between the response and a reference response.

Transmissibility is a frequency-based cross-channel measurement defined as the Fourier spectrum of a vibration response divided by the Fourier spectrum on another response, as shown in Fig. 9.1.

9.2 Transmissibility Properties

Transmissibility has two unique properties that make it useful for recursive post-processing of response data from a Slinky test.

1. The Transmissibility between DOF 1 and DOF 2 multiplied by the Transmissibility between DOF 2 and DOF 3 equals the Transmissibility between DOF 1 and DOF 3
2. The Inverse of the Transmissibility between DOF 1 and DOF2 is the Transmissibility between DOF 2 and DOF 1

These two Transmissibility properties are shown in Fig. 9.2, and are used to post-process the data in a TRN chain of measurements.

9.3 Slinky TRN Chain Measurement

In a Slinky test, data is acquired in a chain fashion as depicted in Fig. 9.3. The three measurements shown in Fig. 9.3 are made with two sensors (for example accelerometers), and a 2-channel acquisition system.

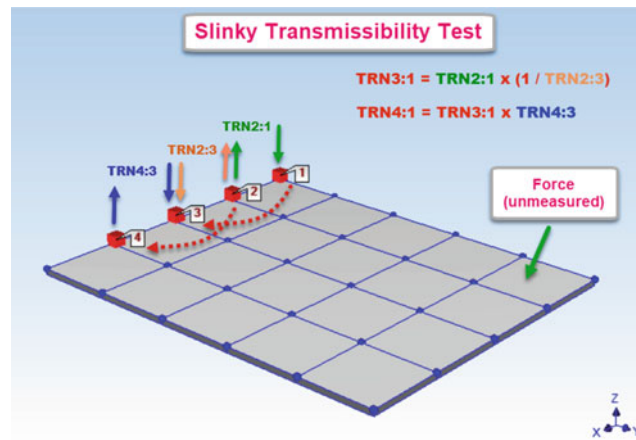


Fig. 9.2 Slinky test

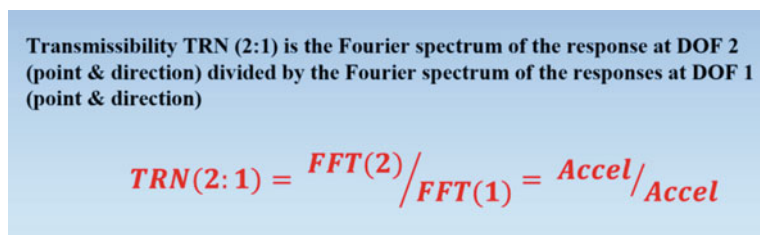


Fig. 9.3 Transmissibility

Not only is the equipment required to do a Slinky test much less costly, but this method can be used to test *any sized test article*, especially large ones.

The sensor data used in the **denominator** of a Transmissibility is called the **Input**, and the sensor data used in the **numerator** is called the **Output**. The test procedure depicted in Fig. 9.3 is as follows;

- Attach sensors to *points 1 and 2*
- Acquire vibration data from points 1 and 2. Designate *point 1 as Input* and *point 2 as Output*
- Calculate **TRN(2:1)**
- Move the sensor from *point 1* to *point 3*
- Acquire vibration data from points 2 and 3. Designate *point 3 as Input* and *point 2 as Output*
- Calculate **TRN(2:3)**
- Move the sensor from *point 2* to *point 4*
- Acquire vibration data from points 3 and 4. Designate *point 3 as Input* and *point 4 as Output*
- Calculate **TRN(4:3)**

In a Slinky test, *only one sensor must be moved* between acquisitions. *Either sensor can be moved* between acquisitions. *Hopping one sensor* over the other is *not necessarily required*.

Regardless of how the TRN chain is acquired and calculated, it can always be post-processed into a single-reference TRN chain using the two unique properties of Transmissibility's shown in Fig. 9.2. It is also shown in Fig. 9.3 how the TRN chain is post-processed to yield a *single-reference TRN chain*.

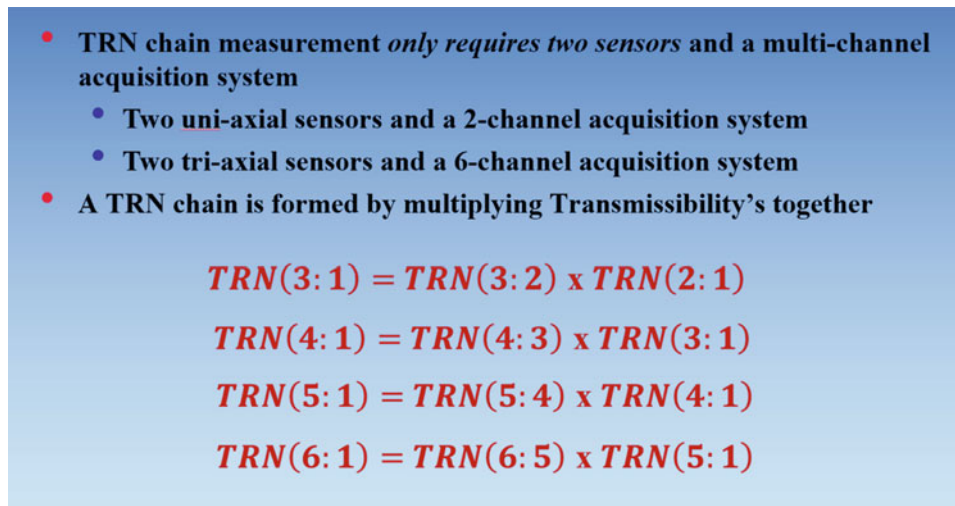


Fig. 9.4 TRN chain from two sensors

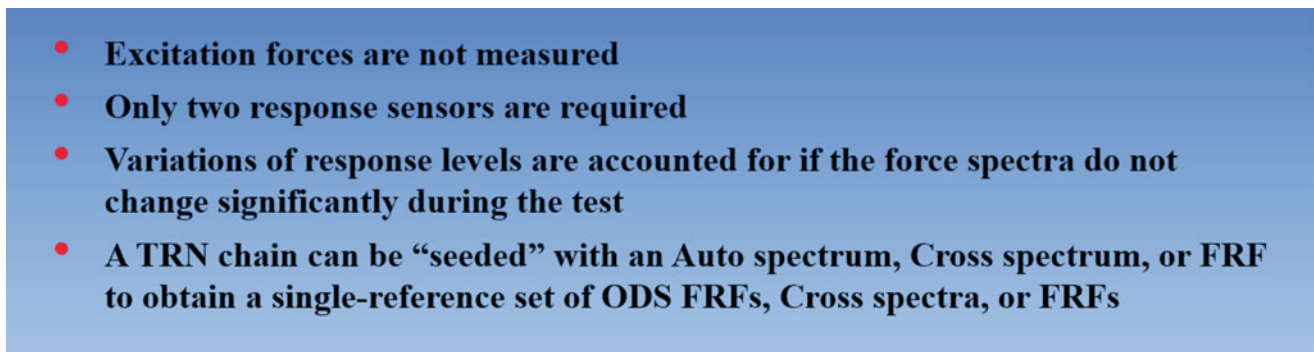


Fig. 9.5 TRN chain benefits

9.4 Benefits of a TRN Chain

A TRN chain can be measured using a *pair of uni-axial sensors* or a *pair of tri-axial sensors* as described in Fig. 9.4. Using *two tri-axial sensors* will capture the *3D motion* of a machine or structure at each test point, thus yielding ODS's and mode shapes that describe its *3D motion*.

The benefits of TRN chain testing are summarized in Fig. 9.5. Its greatest benefit is in acquiring data from operating machines or vehicles where the excitation forces cannot be measured. Also, since acquisition of the excitation force (or forces) is not required, any artificial excitation forces can be provided, either by impacting at a fixed DOF or by providing steady state excitation with one or more shakers.

9.5 Seeding a TRN Chain

Once a TRN Chain has been calculated for all points and directions (DOFs) on the test article, it can be “seeded” using either an Auto spectrum, Cross spectrum, Fourier spectrum, or an FRF to yield a single reference set of measurements from which ODS's and mode shapes can be extracted.

- Seeding with an Auto spectrum yields a *single reference set* of ODS FRFs
- Seeding with a Cross spectrum yields a *single reference set* of Cross spectra
- Seeding with a Fourier spectrum yields a *single reference set* of Fourier spectra
- Seeding with an FRF yields a *single reference set* of FRFs

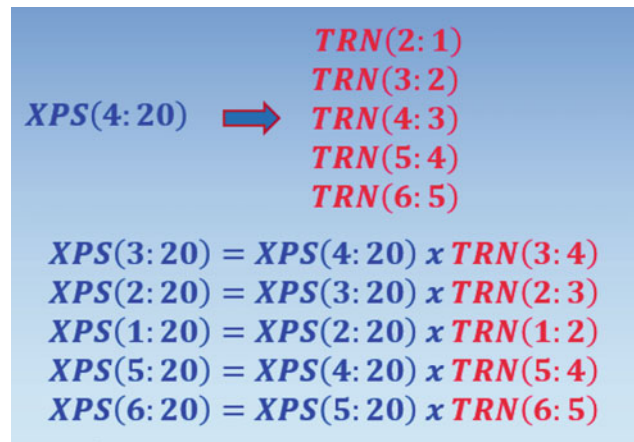


Fig. 9.6 Seeding with a cross spectrum

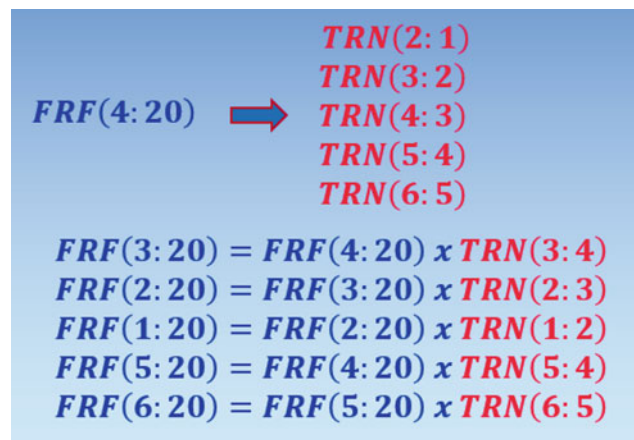


Fig. 9.7 Seeding with an FRF

A TRN chain is seeded with a Cross spectrum in Fig. 9.6, and the same chain is seeded with an FRF in Fig. 9.7. Notice that the *reference DOF* of the Cross spectrum or FRF of the seed can be from *anywhere on the machine or structure*.

The only requirement for seeding a TRN chain is that the *Output DOF of the seed be the same as one of the Output DOFs* of the chain.

9.6 Round Trip Simulations

To demonstrate the Slinky testing method, two *round trip simulations* are used,

- Slinky test of an aluminum plate using *two uni-axial* accelerometers
- Slinky test of the Jim Beam using *two tri-axial* accelerometers

In both simulations, the following steps were carried out,

1. Experimental FRFs are acquired by impact testing the structure
2. The FRFs are used to calculate responses of the structure to random excitation
3. A TRN chain is calculated from the random responses
4. The TRN chain is seeded with an FRF
5. The single-reference FRFs are compared with the original FRFs

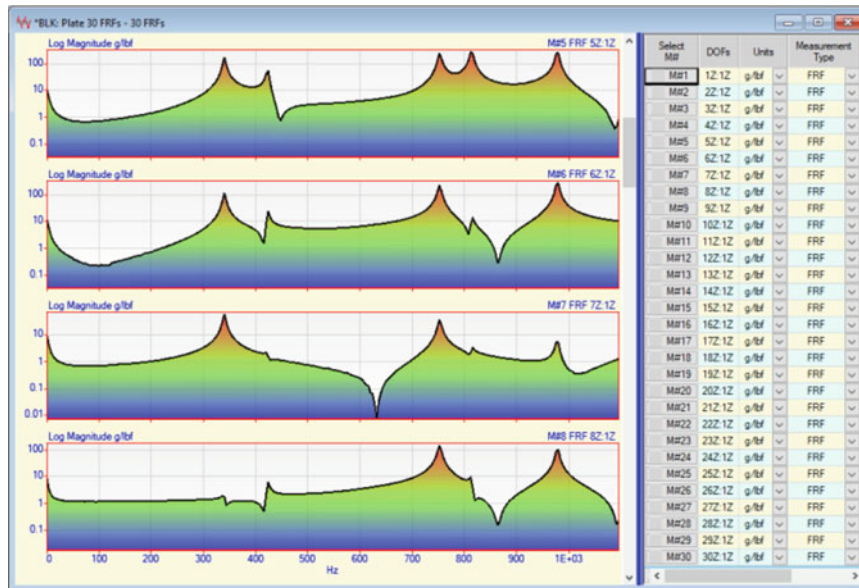


Fig. 9.8 Experimental FRFs from the aluminum plate

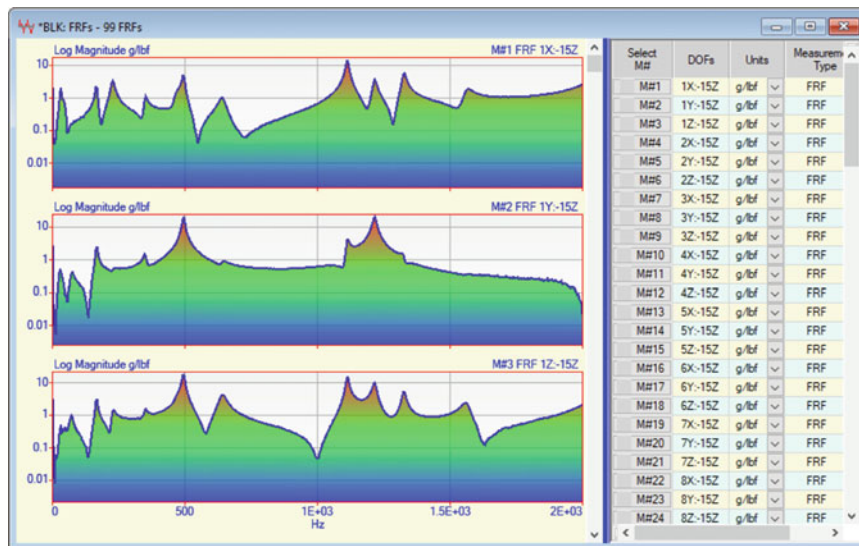


Fig. 9.9 Experimental FRFs from the Jim Beam

9.6.1 Experimental FRFs

To provide the simulated response data, each structure was first impact tested to obtain a single-reference set of FRFs that characterized its dynamic properties. A *roving impact test* was performed on the aluminum plate with an accelerometer attached at one corner (DOF 1Z). The plate was impacted at 30 points (DOFs 1Z to 30Z), and 30 FRFs were calculated between each impact DOF and the fixed reference DOF 1Z. Several FRFs from the aluminum plate are shown in Fig. 9.8.

A *roving accelerometer test* was performed on the Jim Beam. A model of the Jim Beam is shown in Fig. 9.14. It was impacted at one corner of the top plate (DOF 15Z) throughout the test. A tri-axial accelerometer was moved from point 1 to point 33 between acquisitions of data. Ninety-nine FRFs were calculated, each FRF between the impact DOF and the 3D motion at each point on the beam. Several experimental FRFs for the Jim Beam are shown in Fig. 9.9.

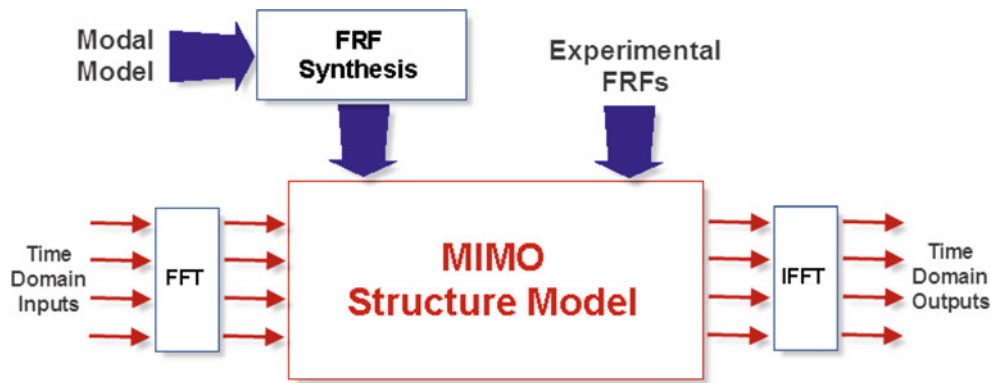


Fig. 9.10 MIMO modeling and simulation

9.7 MIMO Modeling and Simulation

Using its FRFs as its dynamic model, random excitation of each structure was simulated by calculating its responses to a random excitation force. This calculation was done using the FRF matrix-based MIMO modeling and simulation depicted in Fig. 9.10. The MIMO calculations depicted in Fig. 9.10 were used to calculate random responses to random excitation on both the aluminum plate and the Jim Beam. The following steps were used to calculate time domain waveforms due to a random excitation force,

1. A sequence of *ten random time waveforms* was created as *a simulated force input* to each structure
2. The experimental FRFs were multiplied by the Fourier spectrum of the Input force to obtain the Fourier spectrum of each response Output
3. The Fourier spectrum of each Output was Inverse transformed to obtain the time waveform of a random response

This process is referred to as **Multi-Input Multi-Output (MIMO) Modeling and Simulation**. The Fourier spectrum of the random Input and the Fourier spectra of several Outputs are shown in Fig. 9.11. These spectra each have 10,000 samples in them. The original random force signal was created with 20,000 samples, enough samples to calculate Transmissibility's with 1000 samples each, using 10 spectrum averages to remove the random noise from the data. Each time window of 2000 samples also had a *Hanning window* applied to it before transforming it to a Fourier spectrum. A Hanning window must be applied to the time waveforms to minimize the effect of the *non-periodic random signals* on the Fourier spectra.

9.8 Slinky Test of the Aluminum Plate

A Slinky test using a *pair of uni-axial accelerometers* was simulated on the aluminum plate by “*simultaneously acquiring*” its random response from a pair of points at a time. Each pair of responses was used to calculate one Transmissibility. This test is depicted in Fig. 9.12.

The plate has a (5 by 6) grid of 30 numbered test points shown in Fig. 9.12. A TRN chain of 29 Transmissibility's was calculated between each successive pair of grid points on the plate. Some of the Transmissibility's are displayed in Fig. 9.13.

It must be emphasized that the *peaks in a Transmissibility are not resonance peaks*. A Transmissibility is a different complex waveform than an FRF. Transmissibility's *cannot be curve fit using an FRF-based curve fitting method*.

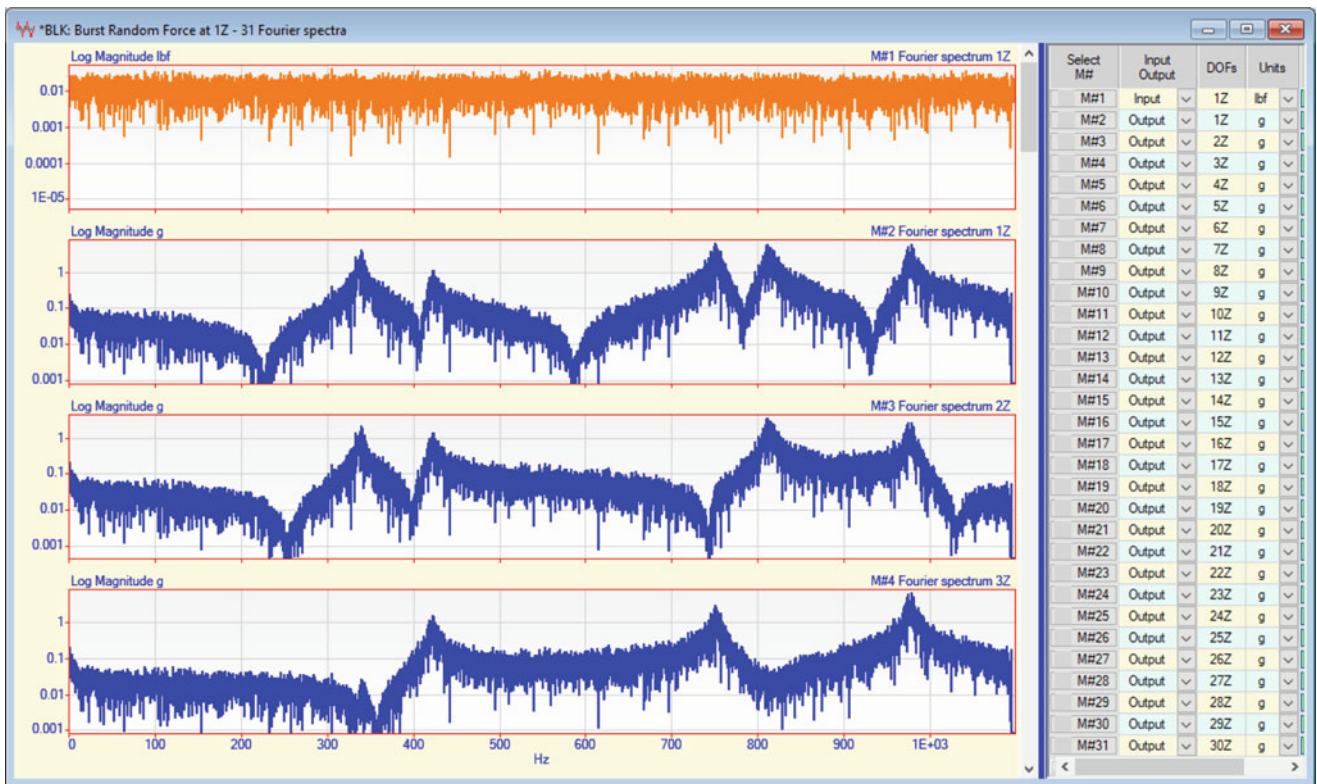


Fig. 9.11 Fourier spectra of excitation force and MIMO responses

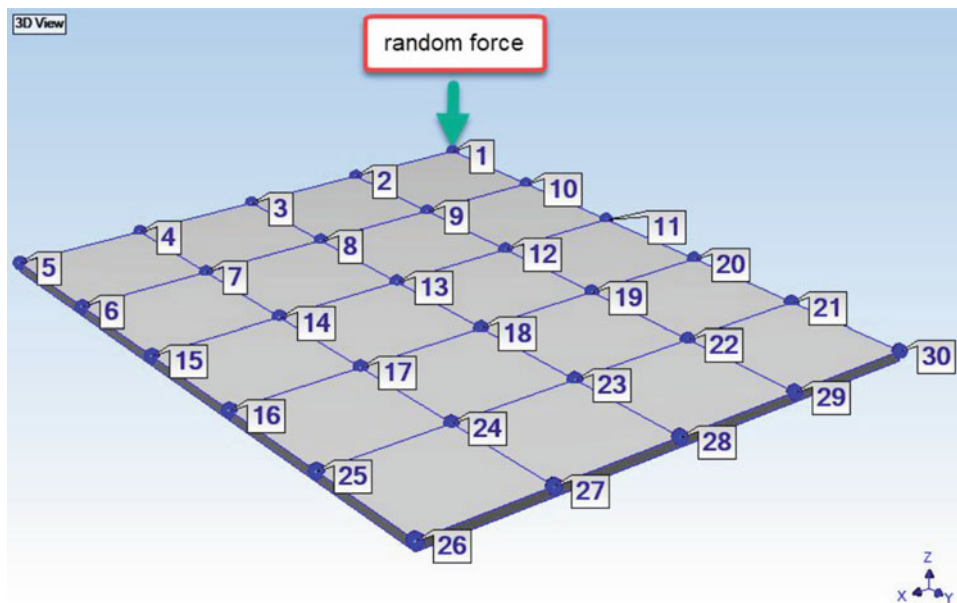


Fig. 9.12 Test points on the plate

9.8.1 Seeding the TRN Chain with an FRF

The TRN chain of 29 Transmissibility's was *seeded* with **FRF 15Z:1Z**. This FRF is between Roving DOF (15Z) and the Reference DOF (1Z). Seeding the TRN chain with **FRF 15Z:1Z** yielded a set of *FRFs with reference DOF (1Z)*, some of which are shown in Fig. 9.14.

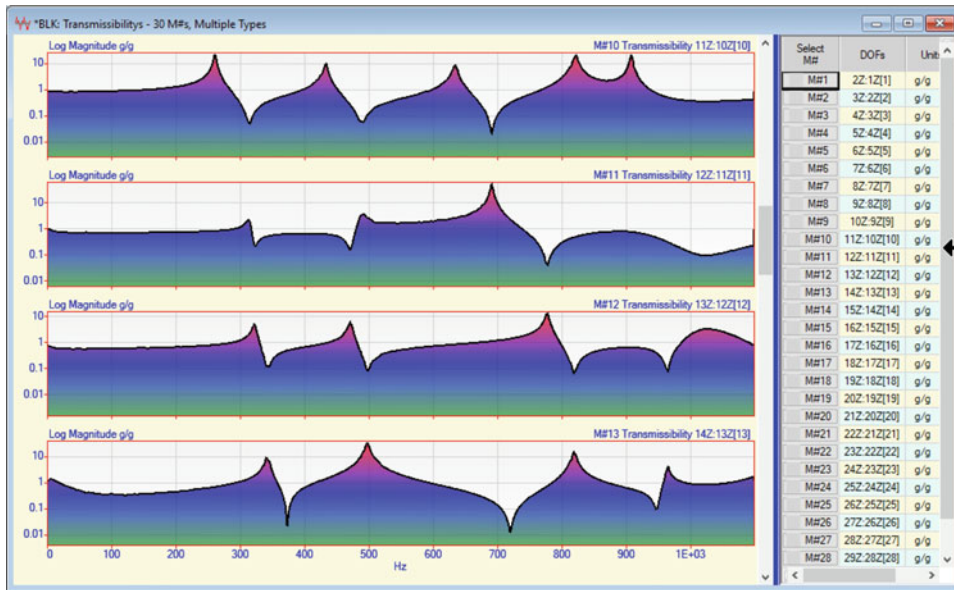


Fig. 9.13 TRN chain from the plate



Fig. 9.14 FRFs from seeding the plate TRN chain

A TRN chain can be seeded with any FRF, provided that the *Roving DOF of the seed matches* one of the DOFs in the TRN chain.

FRF 15Z:1Z was chosen as the seed so that the resulting single-reference set of FRFs would have reference DOF (1Z), hence they could be numerically compared with the original experimental FRFs that were used to calculate the random response of the plate.

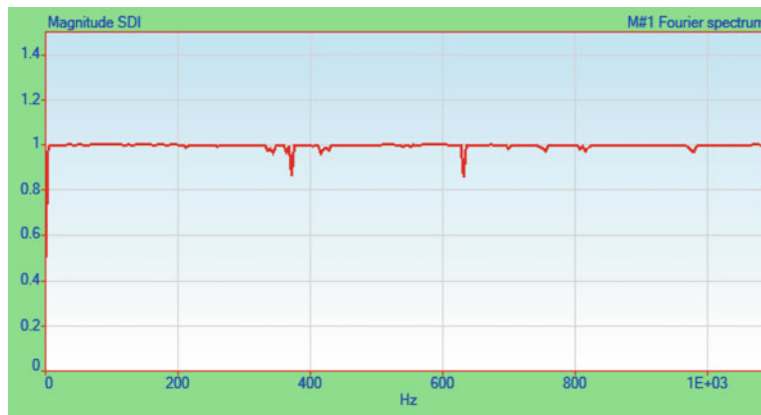


Fig. 9.15 Correlation of experimental and slinky FRFs for the plate

9.8.2 Comparing Experimental and Slinky FRFs of the Plate

To confirm the accuracy of the simulated Slinky test on the aluminum plate, the FRFs calculated by seeding the Slinky TRN chain were numerically compared with the original experimental FRFs. The results are shown in Fig. 9.15. The two sets of FRFs are numerically compared at each frequency sample using the SDI metric [2]. Like the MAC metric [3], SDI has values between 0 and 1. MAC measures the *co-linearity* of two shapes. SDI measures the *difference* between two shapes.

An *SDI value of “1”* for a sample means that the ODS (complex values of the FRFs) in one set of FRFs equals the values of the FRFs for the same sample in the other set. An *SDI value above 0.90* at a sample indicates a *strong correlation* between the two sets of FRFs for that sample. It is clear from Fig. 9.15 that the round-trip simulation yielded FRFs with reference DOF 1Z that *closely correlated at all frequencies* with the original experimental FRFs that were used to create the random responses of the plate.

9.9 Slinky Test of Jim Beam

A Slinky test using a *pair of tri-axial accelerometers* was simulated on the Jim Beam by “*simultaneously acquiring*” its 3D random responses at pairs of points. In this example six channels of data were “*simultaneously acquired*” from each pair of points to simulate a test using *tri-axial accelerometers*. Three responses from each point (in the X, Y, and Z directions) were used to calculate Transmissibility’s. Each Transmissibility was calculated between a pair of response DOFs, therefore, five Transmissibility’s were calculated between each pair of points.

The same random force that was used to excite the aluminum plate was also applied to the Jim Beam, but it was applied at DOF 15Z, as shown Fig. 9.16. Ninety-nine experimental FRFs were used to model the dynamics of the Jim Beam using the MIMO response calculation, depicted in Fig. 9.10.

A TRN chain of *160 Transmissibility’s* was calculated between each successive pair of points on the Jim Beam. Five Transmissibility’s were computed for each of the 32 pairs of points. A portion of the TRN chain is shown in Fig. 9.17.

9.9.1 Seeding the TRN Chain with an FRF

The TRN chain of 160 Transmissibility’s was *seeded* with **FRF 4Z:15Z**. This FRF is between Roving DOF (4Z) and the Reference DOF (15Z). Seeding the TRN chain with **FRF 4Z:15Z** yielded a set of *FRFs with reference DOF (15Z)*, some of which are shown in Fig. 9.18.

A TRN chain can be seeded with any FRF, provided that the *Roving DOF of the seed* matches one of the DOFs in the TRN chain.

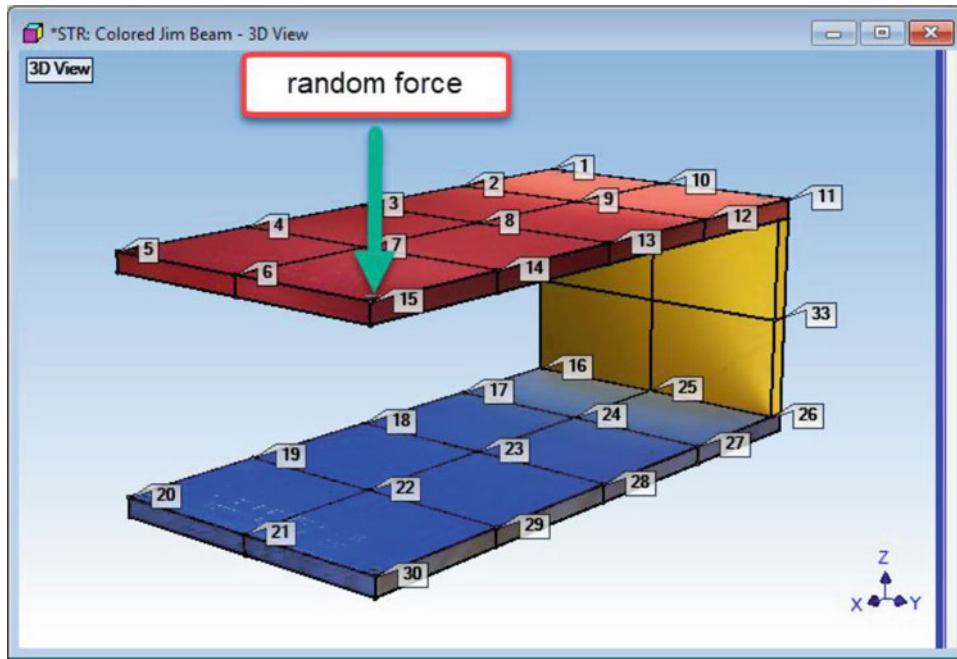


Fig. 9.16 Slinky test points on the Jim Beam

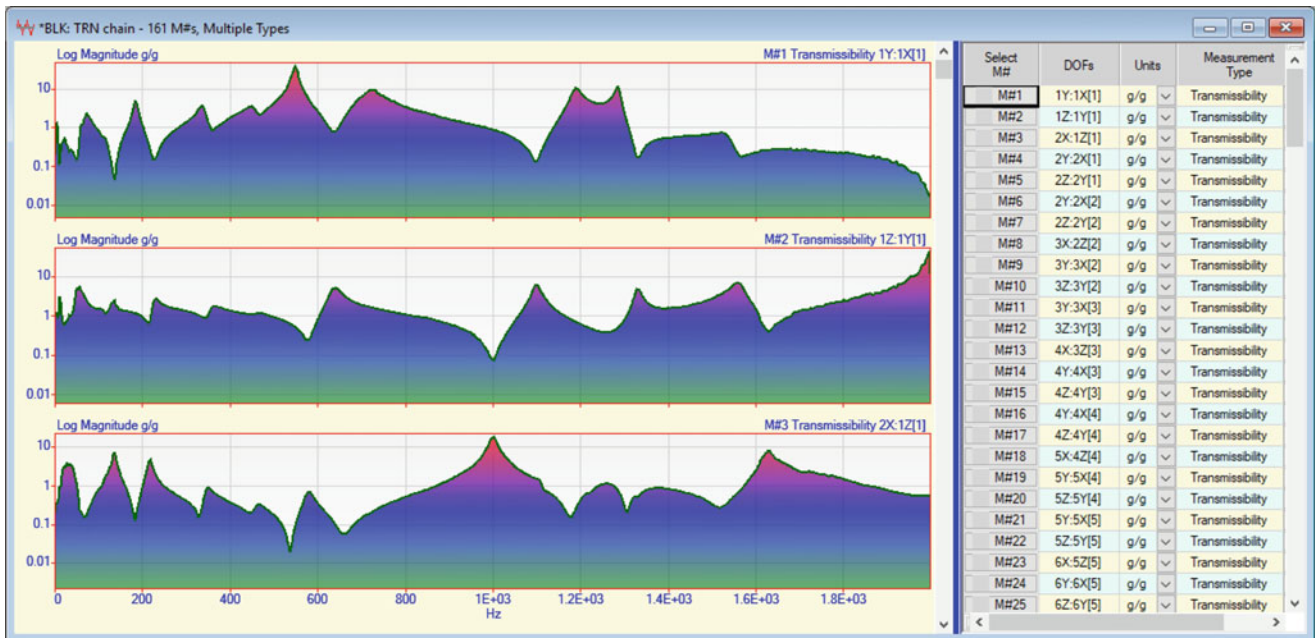


Fig. 9.17 TRN chain for Jim Beam

9.9.2 Comparing Experimental and Slinky FRFs of the Jim Beam

To confirm the accuracy of the simulated Slinky test on the Jim Beam, the FRFs calculated by seeding the Slinky TRN chain were numerically compared with the original experimental FRFs. The results are shown in Fig. 9.19. The two sets of FRFs are numerically compared at each frequency sample using the SDI metric [2]. SDI has values between 0 and 1.

An *SDI value of "1"* for a sample means that the ODS (complex values of 99 FRFs) in one set equals the values of the 99 FRFs for the same sample in the other set. An *SDI value above 0.90* at a sample indicates a **strong correlation** between the

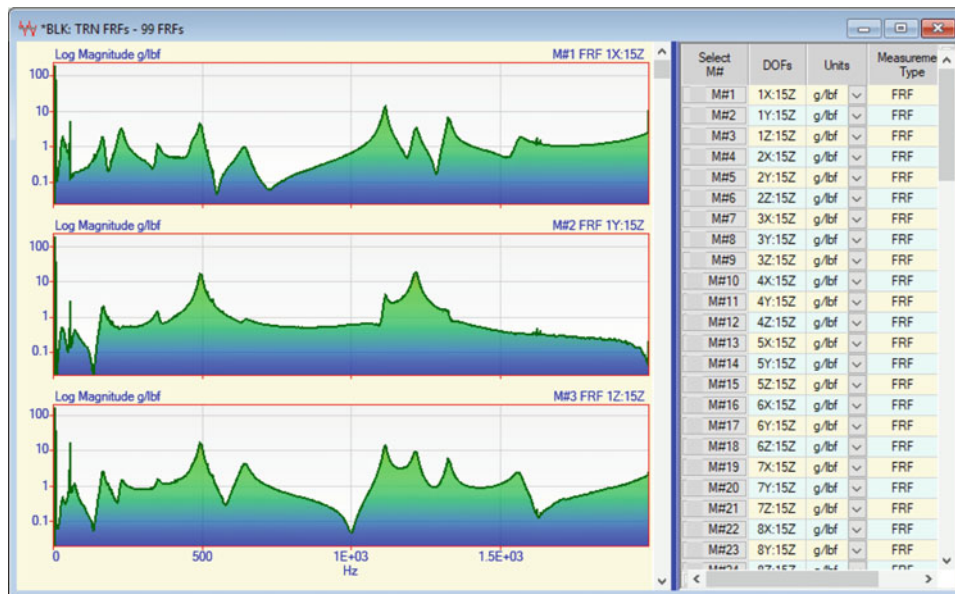


Fig. 9.18 FRFs from seeding the Jim Beam TRN chain

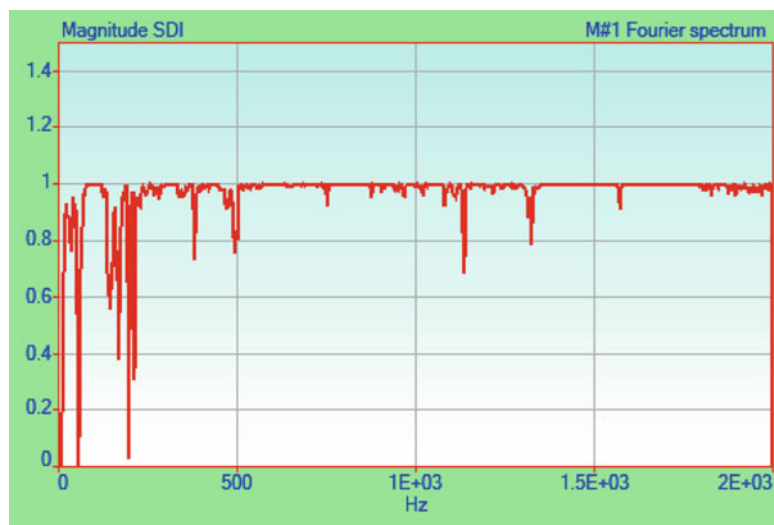


Fig. 9.19 Correlation of experimental and slinky FRFs for the Jim Beam

two sets of FRFs for that sample. Except for a few samples at low frequencies, it is clear from Fig. 9.19 that the round-trip simulation yielded FRFs with reference DOF 15Z that *closely correlated at all frequencies* with the original experimental FRFs.

9.10 Conclusion

In this paper, a new testing method was introduced which is based on the measurement of a chain of Transmissibility's called a TRN chain. Using this new method, *any machine or structure, large or small*, can be tested with as little as *two uni-axial response sensors*, a *2-channel acquisition system*, and *two short wires* from the sensors to the acquisition system.

Moreover, this method can be used to test running machinery or large structures such as bridges and buildings because only the responses are measured. The *excitation forces do not have to be measured*.

Using a conventional broad-band testing method, a *single reference set* of measurements is required to obtain experimental ODS's or mode shapes. This means that *one sensor must remain fixed* throughout the data acquisition process. Consequently, the fixed reference sensor(s) must be connected by wire to the acquisition system, and this wire could be very long.

It was shown with two examples how a TRN chain is calculated from the simulated random responses of the structures. The aluminum plate example illustrated testing with *two uni-axial accelerometers*, and the Jim Beam example illustrated testing with *two tri-axial accelerometers*. In both cases, single-reference sets of FRFs were obtained by seeding each TRN chain with an FRF seed. In both cases, the resulting FRFs *closely correlated at all frequencies* with the set of experimental FRFs that were used to create the responses of the structures to a random force input.

Two unique properties of Transmissibility's make the post-processing of *any* TRN chain a straightforward calculation.

The *Slinky* testing method makes the measurement of a TRN chain even easier. This simple process of *hopping one sensor over the other* means that only one sensor must be moved between acquisitions. In fact, it does not matter which one of the sensors is moved, if each Transmissibility is labeled with the correct Input (denominator) and Output (numerator) DOFs.

A drawback of this testing approach is that experimental noise, either in the seed or in some of the Transmissibility's, will propagate through the post-processing of the TRN chain. Noise propagated through the post-processing could explain the low SDI values at some frequencies in Fig. 9.19. However, using more spectrum averages (only 10 were used) in the TRN chain and seed calculations will reduce the noise in the results.

References

1. McHargue, P., Schwarz, B., Richardson, M.: ODS & modal testing using a transmissibility chain. IMAC XXXVI, Feb 2017
2. Richardson, S., Tyler, J., McHargue, P., Schwarz, B., Richardson, M.: A new measure of shape difference. IMAC XXXII, 3–6 Feb 2014
3. Allemang, R.J.: The modal assurance criterion (MAC): twenty years of use and abuse. In: Proceedings of the International Modal Analysis Conference (2002)



Chapter 10

Numerical and Experimental Modal Analysis of a Cantilever Beam Axially Loaded by a Tendon Which Is Attached in a Single Spanwise Location

Vaclav Ondra and Branislav Titurus

Abstract It has been recently proposed to incorporate a tendon in a rotorcraft blade to introduce a means of controlling its dynamics properties. This has been shown as an effective resonance avoidance mechanism that should allow rotorcraft to operate with shape adaptive blades or with variable rotor speed, thereby increasing their performance and efficiency. In the previous studies, the tendon was attached to the blade's tip, passed freely through its whole body and was fixed at the root of the blade. The tendon was therefore free to vibrate unrestrictedly inside the blade. This, despite delivering the required changes to dynamics, may not be the most optimal and viable design. In this paper, a modification of this concept is investigated. Unlike in the previous studies, the tendon does not pass freely through the blade, but it is connected to it in a single spanwise location using a mechanical attachment. This coupled blade-tendon system is studied both numerically and experimentally. The blade is modelled as the Euler-Bernoulli beam, the tendon as a taut string, and the attachment point as a concentrated mass. The boundary and connectivity conditions are used to ensure the required coupling between the beam and the tendon. Free vibration analysis is conducted using a boundary value problem solver and a bench-top experiment is used for validation of the numerical results. The variation of modal properties with the applied tendon tension and the location of the attachment point is investigated. It is found that many features observed in the previous studies, such as the frequency shift and frequency loci veering, are still exhibited by the modified system, but they are manifested under different loading conditions. In this way, the attachment points may influence the ability to control the beam's dynamic properties. The implications of these phenomena for the application of an active tendon in rotorcraft are discussed.

Keywords Coupled beam-tendon system · Theoretical and experimental modal analysis · Axially loaded beam · Frequency reduction · Frequency loci veering

10.1 Introduction

Recently, it has been proposed to incorporate a tendon in a rotorcraft blade to introduce a means of controlling its dynamics properties [1]. A simplified, non-rotating model of this mechanism was investigated in [2–4] both numerically and experimentally. It was found that the beam-tendon system exhibits reduction in the beam natural frequencies due to a tendon-induced axial force as well as veering between beam-dominated and tendon-dominated modes. These findings were further numerically examined in [5] for rotating pre-twisted beams. It was shown that although the rotation has a significant effect on the tendon, the tendon is still able to influence the modal characteristics of the blade significantly. Moreover, it has been discussed in [6] that the active tendon concept can serve as a resonance avoidance mechanism by allowing the rotorcraft to operate with shape adaptive blades or with variable rotor speed, thereby increasing their performance and efficiency. In all these previous studies, the tendon was attached to the blade's tip, passed freely through its whole body and was fixed at the root of the blade. The tendon was therefore free to vibrate unrestrictedly inside the blade, which, despite delivering the required changes to dynamics, may not be the most optimal and viable design. In this paper, a modification of this concept is investigated whereby the tendon does not pass freely through the blade, but it is connected to it in a single spanwise location using a mechanical fixture instead.

Free vibration of beams and tendons (cables, strings) have been extensively studied, because they are two essential structural elements that are frequently used in many engineering applications. There is an overwhelming number of studies

V. Ondra (✉) · B. Titurus
Department of Engineering, University of Bristol, Bristol, UK
e-mail: vaclav.ondra@bristol.ac.uk

that focus on different aspects of beam and string modelling, application and testing [7–10]. However, very few studies of coupled beam-tendon systems can be found in literature. To the best knowledge of the authors, a similar system has been considered only in a handful of studies. For instance, a string-beam system has been used as a representation of an optic cable coupler in [11] and its bifurcation and chaotic dynamics mathematically investigated in [12]. In these studies, however, the axial tension of the string had no influence on the beam so that the beam dynamics could be considered separately from the string.

The objective of this paper is to study the free vibration of a non-rotating beam-tendon system where the coupling between the beam and the tendon is realised at the tip and a single spanwise location. Due to this coupling, the vibration of the beam and tendon must be considered simultaneously as they influence each other. The paper is organised as follows: in Sect. 10.2 the theoretical model of the system is presented and the numerical procedure used to obtain the modal properties is briefly described. The effect of an attachment point and its location on the modal properties and structural stability are then experimentally and numerically investigated in Sect. 10.3. Finally, in Sect. 10.4, the main findings are summarised, and potential implications to the application of an active tendon concept as a vibration control method in rotorcraft are discussed.

10.2 Theoretical Model

The considered system can be seen in Fig. 10.1. The system consists of a straight hollow cantilever beam with a double sectional symmetry that is axially loaded by a tendon. The rectangular cross-section is used in the present numerical and experimental studies. The tendon is attached at the tip of the beam and fixed (clamped) at the same place as the beam. Unlike in the previous studies, the beam and the tendon are also connected in, generally, several spanwise locations using attachment fixtures such as the one schematically shown in Fig. 10.1b. It is assumed that each attachment point ensures the equality of the beam and tendon displacements while the slope of the tendon is different on each side of the attachment. In addition, the attachment fixture is assumed to be friction-free, i.e. the magnitude of tension P is not changed when passing through the fixture. Each attachment fixture has a mass m_i and is placed at the distance L_i from the clamp. Although there is no limit on the number and locations of the attachments, this paper investigates a beam-tendon system with a single attachment fixture only.

The equations of motion describing the beam-tendon system are

$$EIw'''' + Pw'' + m\ddot{w} = F, \quad (10.1a)$$

$$-Pw_t'' + m_t\ddot{w}_t = 0, \quad (10.1b)$$

where EI is the bending rigidity of the beam, P is the applied force which is transmitted by the tendon so it acts as an axial force at the tip of the beam, m is the mass per meter of the beam, m_t is the mass per meter of the tendon, F is the distributed excitation force that is only applied to the beam, $w(t, x)$ and $w_t(t, x)$ are vertical displacements of the beam and the tendon, respectively, t is time, x is an independent spatial variable measured along the span of the beam, $\dot{(\)} = \partial/\partial t$ and $(\)' = \partial/\partial x$. While these two equations are fully uncoupled, the beam and the tendon interact with each other through the tip mass and attachment fixtures.

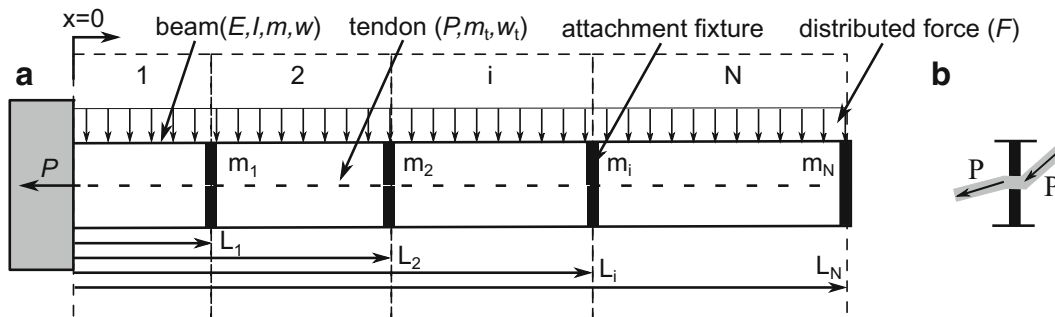


Fig. 10.1 Coupled beam-tendon system: (a) description of the system, and (b) idealisation of the attachment fixture

This interaction is captured by the following boundary and connectivity conditions—the beam-tendon system is fixed at one end ($x = 0$)

$$w = 0, \quad (10.2a)$$

$$w' = 0, \quad (10.2b)$$

$$w_t = 0. \quad (10.2c)$$

and free at the other end (for $x = L_N$)

$$EIw_N'' = 0, \quad (10.3a)$$

$$-EIw_N'' - Pw_N' + m_N\ddot{w}_N + Pw_{tN}' = 0, \quad (10.3b)$$

$$w_{tN} = w_N. \quad (10.3c)$$

where m_N is the tip mass. The origin of these boundary conditions is discussed in detail in [4] where they were also experimentally validated. In addition, for every attachment point (for $x = L_i$ where $i = 1, 2, \dots, N - 1$),

$$w_i^{(R)} = w_{i+1}^{(L)}, \quad (10.4a)$$

$$w_i'^{(R)} = w_{i+1}'^{(L)}, \quad (10.4b)$$

$$EIw_i''^{(R)} = EIw_{i+1}''^{(L)}, \quad (10.4c)$$

$$-EIw_i'''^{(R)} - Pw_i'^{(R)} + Pw_{ti}'^{(R)} = -EIw_{i+1}'''^{(L)} - Pw_{i+1}'^{(L)} + Pw_{t(i+1)}'^{(L)} + m_i\ddot{w}_{i+1}^{(L)}, \quad (10.4d)$$

$$w_{ti}^{(R)} = w_i^{(R)}, \quad (10.4e)$$

$$w_{t(i+1)}^{(L)} = w_{i+1}^{(L)}, \quad (10.4f)$$

where the superscripts $\bullet_i^{(R)}$ and $\bullet_i^{(L)}$ mark the right and left side of the i^{th} interval, respectively. The first four equations ensure the connectivity of beam's displacements, slopes, moments and shear forces, respectively, on each side of the attachment fixture while the last two equations ensure the same displacement of the beam and the tendon.

In order to evaluate the modal properties (natural frequencies and mode shapes) of the beam-tendon system, an assumption of the normal mode is used. A solution of any given dependent variable is expressed as a multiplication of the time-invariant mode shape and the time-varying harmonic function of the constant frequency in the following form

$$w(t, x) = W(x)e^{i\omega t}, \quad w_t(t, x) = W_t(x)e^{i\omega t}. \quad (10.5)$$

Substituting the normal mode forms into the partial differential equations (PDEs) allows one to eliminate time and rewrite the PDEs into a system of first order ordinary differential equations (ODEs) that, together with the boundary conditions (BCs), define a boundary value problem. This boundary value problem can then be solved by a Matlab bvp4c solver [13] for unknown natural frequencies ω and corresponding mode shapes components $W(x)$ and $W_t(x)$. This solver is very versatile since it uses a collocation method but may suffer from a decreased numerical performance if an appropriate starting guess is not provided.

10.3 Numerical and Experimental Results

In this section, numerical and experimental results are presented. The experimental set-up used can be seen in Fig. 10.2. A similar experimental set-up to test the beam-tendon system with no attachment fixtures was already used in [3, 4]. It consists of a cantilever beam-tendon system that is gravity-loaded using the masses placed on the hanging platform, and hardware required for experimental modal analysis. As in the previous studies, one attachment point was required at the clamp to ensure the same total length of the beam and the tendon. Unlike in the previous studies, the attachment fixture ensuring the

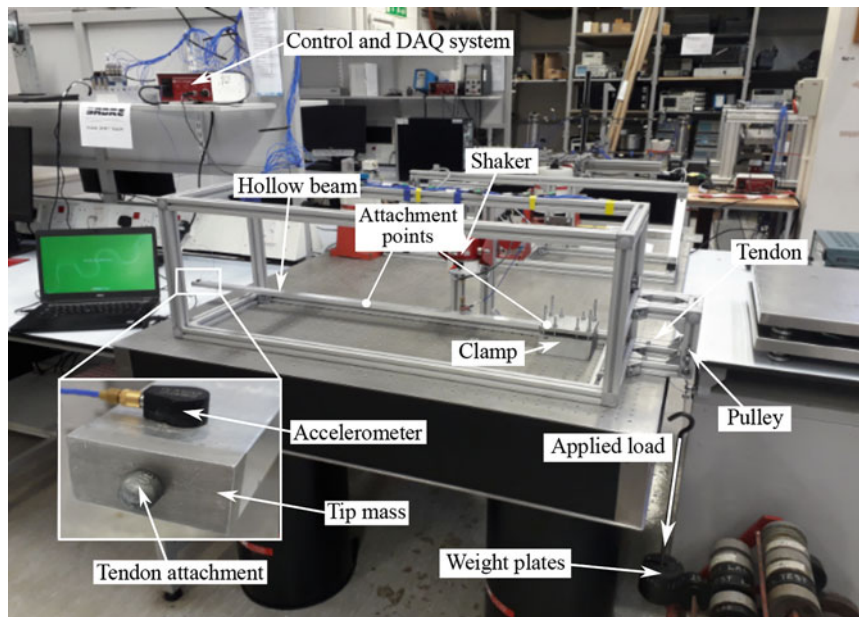


Fig. 10.2 The experimental set-up with the attachment point in $L_1 = 0.5L$

same displacements of the beam and the tendon, was placed either in the middle of the beam, i.e. $L_1 = 0.5L$, or close to the tip in $L_1 = 0.9L$. The intermediate attachment point was cut out from plexiglass while the one in the clamp was realised using magnets.

Experimental modal analysis and the estimation of the modal parameters were conducted in the same way as in [4]. The measurement was repeated twice—by increasing the amount of the weight plates in two-kilogram increments from 2 to 50 kg and subsequently by decreasing the mass back to 2 kg. The natural frequencies extracted from these two measurements were averaged to obtain the frequency-loading diagrams presented.

The computed frequency-loading diagrams are also shown. The parameters used in the theoretical model are not the same as in [4] because both the beam and the tendon were slightly different than in the previous experiments. The parameters used were $EI = 157.79 \text{ N m}^2$, $m = 0.2911 \text{ kg m}^{-1}$, $m_t = 0.011 \text{ kg m}^{-1}$, $m_N = 0.0062 \text{ kg}$, $m_1 = 0.001 \text{ kg}$ and $L = 1 \text{ m}$.

10.3.1 System with the Attachment Point in $0.5L$

The frequency-loading diagram of the system with one intermediate attachment point which is located in $L_1 = 0.5L$ can be seen in Fig. 10.3. The correlation between the numerical and experimental results is comparable to [4]. It can be seen that the first two beam-dominated modes match the experimental results very well, while the third and fourth mode exhibit constant offsets from the experimental results. These offsets can be attributed to the known issue of the Euler-Bernoulli theory which causes increasingly over-predicted natural frequencies of higher modes. The offset of the beam-dominated modes does not seem to have any significant effect on the tendon-dominated modes. The level of the correlation between the experimental and numerical values of natural frequencies of the tendon-dominated modes, which increase rapidly with increasing weight, is very good. It is important to note that for the second tendon-dominated mode, the experimental values hint the presence of the two modes that are very close to each other while the computed results predict two modes with the same frequency. This can be easily explained by an imperfection or slight asymmetry in the experiment set-up which causes one half of the tendon to be slightly longer than the other one, thereby causing a slight shift of its natural frequencies. Alternatively, it is possible that the tension in one part of the tendon, presumably the one closer to the tip, is slightly lower, which can also cause a shift between the natural frequencies. The slight decrease of the tension in the second part of the tendon might be also caused by friction in the attachment fixture. Regardless of this imperfection, the rate of increase of the natural frequencies of the tendon-dominated modes with the applied load match very well to the computed one.

The comparison of the computed results with and without the attachment fixture made in Fig. 10.3 reveals several interesting phenomena. It can be seen that while the two sets of beam-dominated modes almost coincide with each

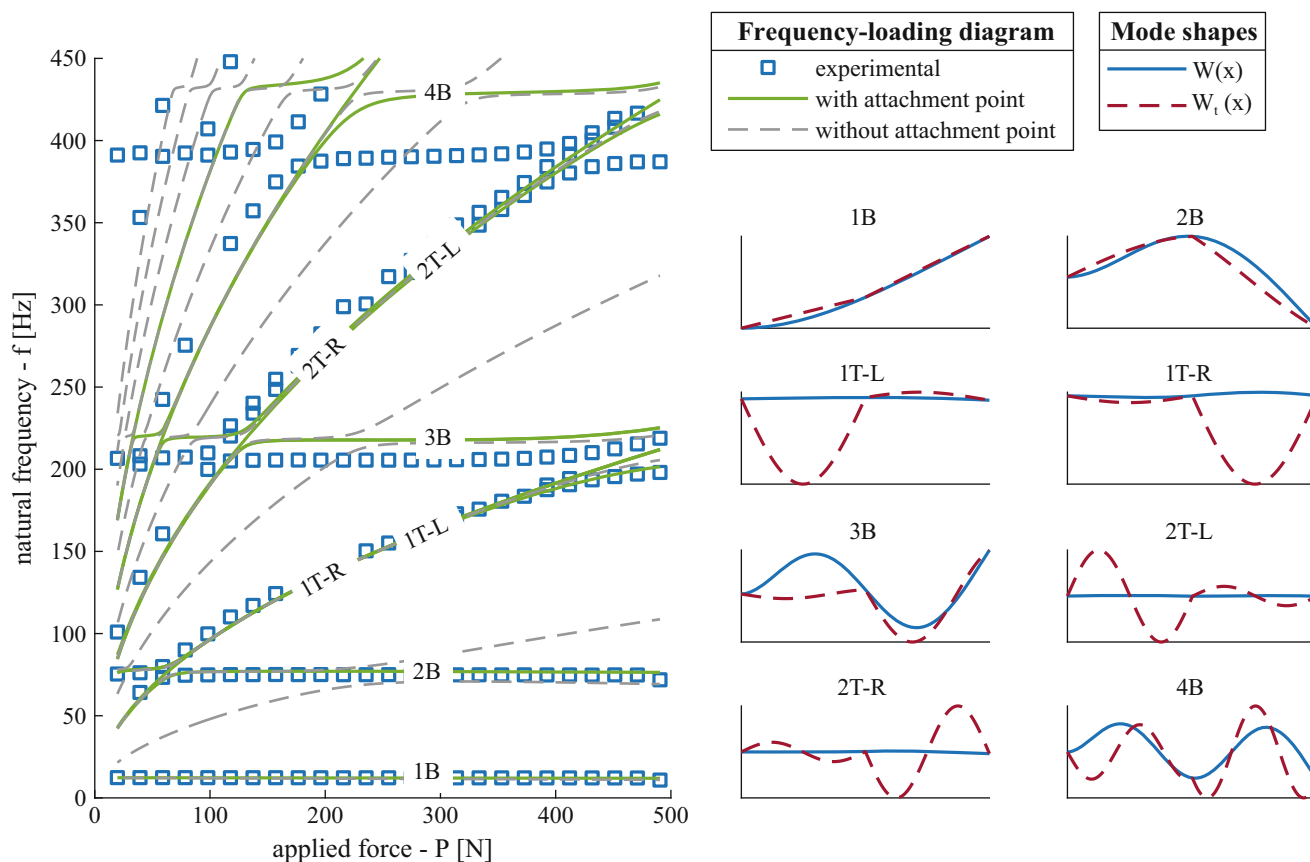


Fig. 10.3 Comparison of the computed and experimentally measured frequency-loading diagrams for the system with a single attachment point in $0.5L$, and the mode shapes for $P = 300$ N. The x^{th} beam-dominated mode is marked by “xB”, while the x^{th} tendon-dominated mode intrinsic to the left and right part of the tendon are marked by “xT-L” and “xT-R”, respectively

other, only every second tendon-dominated frequency locus of the system with the one attachment point coincides with some frequency locus of the system without the attachment. Although some of the natural frequencies coincide, the mode shapes of these modes are different due to the attachment fixture. The natural frequencies coincide because the length of the tendon’s segment in the system with the attachment is exactly halved, leading to twice as high natural frequencies of any given mode compared to the system with no attachment. The rate of increase of the frequency loci is however the same. Due to a larger number of the tendon-dominated modes for the system without the attachment, more veering regions can be seen. In addition, it can be noticed that the veering regions of the two systems are different. For the system with the attachment point, there is always a frequency locus passing through the veering region while there is no such locus for the system with no attachment. The locus, which passes through the veering regions unaffected, belongs to one of the pair of the tendon-dominated modes that share the same natural frequency when away from this veering region. This phenomenon can also be observed in the experimental data between 400 N and 500 N at about 400 Hz. From the numerical results, it is possible to determine which tendon-dominated mode (left or right) veers and which passes through the veering region unaffected. However, since the mechanism is not yet theoretically fully understood, it is not further discussed and should be a subject of further investigation.

The modes shapes of the system can be seen in the right part of Fig. 10.3. Although the attachment point is not displayed, its position can be deduced from these modes shapes. The first fourth bending modes that are dominated by the motion of the beam (marked as xB) are present. Then, the mode shapes that are intrinsic to the left part of the tendon (marked as xT-L) can be seen. In these modes, the deflection of the beam and the right part of the tendon is minimal and the mode shape is localised to the left part of the tendon. On contrary, the modes of the right part of the tendon (marked as xT-R) are only localised in the right part of the tendon. It should be noted that many more vibration modes exist for very low tendon tensions (e.g. $P < 50$ N in the frequently-loading diagram). However, due to the need to provide a reliable starting guess to the numerical solver used and the closeness of the natural frequencies of these modes, it was not possible to map this region comprehensively.

10.3.2 System with the Attachment Point in $0.9L$

The frequency-loading diagram of the system with one intermediate attachment point which is located in $L_1 = 0.9L$ can be seen in Fig. 10.4. The correlation between the numerical and experimental results is very similar to Fig. 10.3. The first two beam-dominated modes match the experimental results very well, while the third and fourth mode exhibit constant offsets, which can be again attributed to a limitation of the Euler-Bernoulli theory. The level of correlation between the experimental and numerical values of the natural frequencies of the tendon-dominated modes, which increase rapidly with increasing applied force, is very good. Unlike in Fig. 10.3, none of the experimentally acquired tendon-dominated frequency loci indicates the presence of two natural frequencies close to each other. This is given by the fact that the two parts of the tendon are very different in their length, and therefore possess very different natural frequencies. It can be seen from the comparison of the computed results with and without the attachment fixture made in Fig. 10.4 that two sets of tendon-dominated natural frequencies do not coincide. The tendon-dominated natural frequencies of the system with the attachment are slightly higher than the natural frequencies of the system without the attachment. This is caused by the fact that they are mainly driven by the left part of tendon, which is only slightly shorter than the full length of the tendon. However, the rate of increase of the frequency loci is again the same.

The modes shapes of the system can be seen in the right part of Fig. 10.4. In this case, no modes dominated by the right part of the tendon are shown, because their natural frequency is outside the investigated frequency region for $P = 300$ N. The location of the attachment point can be again easily deduced from the same displacements of the beam and the tendon.

In order to investigate the veering between the tendon-dominated and beam-dominated modes, two veering regions have been measured in detail. The detailed measurements have been conducted using the stepped-sine excitation procedure [14] with a fine frequency resolution and small weight increments. The measured frequency response functions (FRFs), identified natural frequencies and computed frequency loci can be seen in Fig. 10.5. From Fig. 10.5a and c the presence of veering

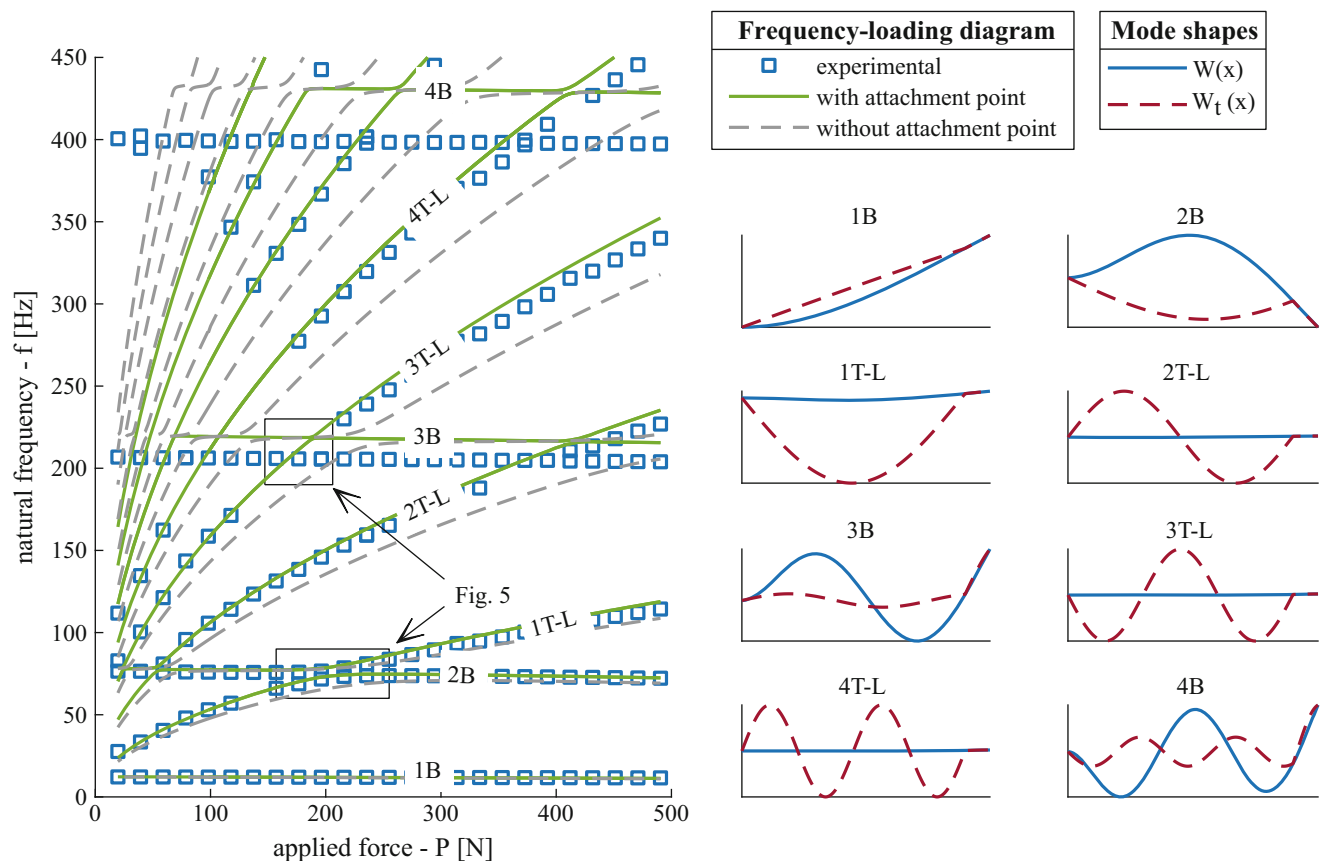


Fig. 10.4 Comparison of the computed and experimentally measured frequency-loading diagrams for the system with a single attachment point in $0.9L$, and the mode shapes for $P = 300$ N. The x^{th} beam-dominated mode is marked by “xB”, while the x^{th} tendon-dominated mode intrinsic to the left part of the tendon are marked by “xT-L”

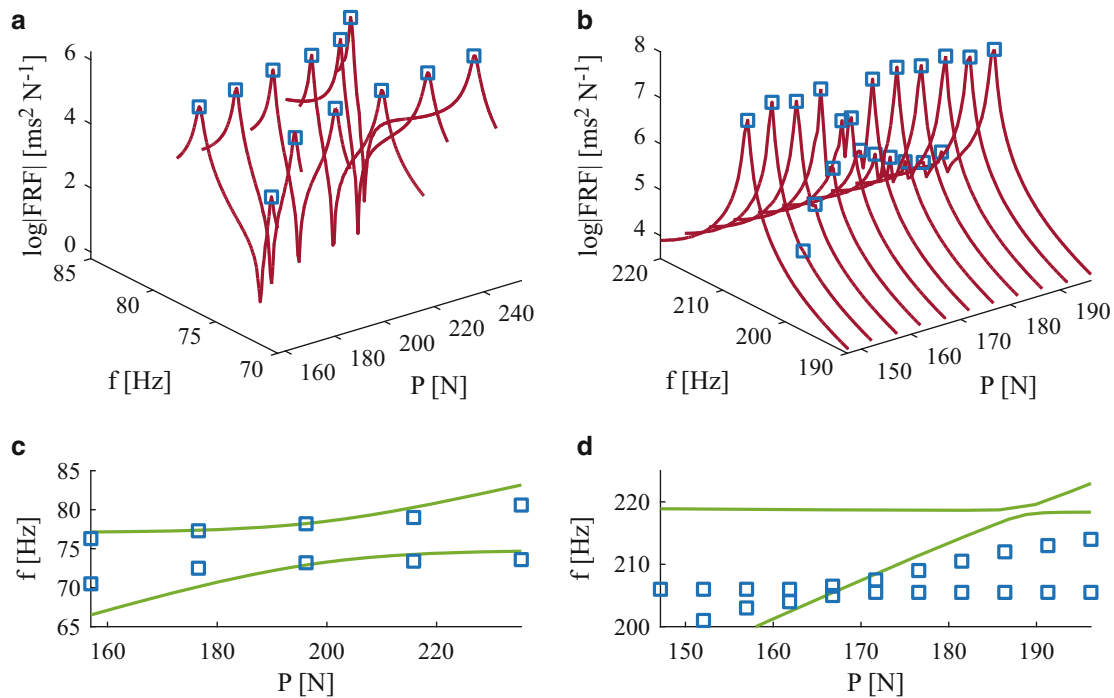


Fig. 10.5 Two veering regions of the beam-tendon system with a single attachment point placed in 0.9L (the measured frequency response functions are shown in red, the identified natural frequencies in blue, and the computed frequency loci in green)

between the second beam-dominated mode (2B) and first tendon-dominated mode (1T-L) is clear. This veering region is very wide (the minimal separation of the natural frequencies is approximately 5 Hz), and the region is spread over approximately 80 N. There is also an anti-resonance between the two peaks. The computed frequency loci match the measured results very well too. In contrast, the presence of the veering between the third tendon-dominated mode (3T-L) and third beam-dominated mode (3B) is not so obvious from the measured data in Fig. 10.5b and d. Although 0.5 kg increments (approximately 5 N) of the applied load have been used, the veering region cannot be identified from the experimental results alone. Only when considered in conjunction with the computed frequency loci, the veering region can be identified in the experimental data as well. This veering region is very narrow (the minimal separation of the natural frequencies is approximately 1 Hz) and the veering takes place over approximately 20 N. Moreover, there is no anti-resonance observed between the peaks. The computed frequency loci in Fig. 10.5d does not match the measured data accurately. However, this is solely caused by the offset of the beam-dominated frequency locus, while the size and shape of the veering region seem to match the experimental data well.

10.3.3 Stability of the System with One Attachment Point

It has been shown that the correlation between the computed and experimentally measured results is very good when considered globally in terms of the frequency-loading diagrams and locally in terms of the veering regions. In this section, the stability of the beam-tendon system with a single attachment point is discussed.

The stability loss due to divergence of the beam occurs when the lowest natural frequency drops to zero due to the applied axial force [15–17]. The frequency locus of the first mode in the region of experimental loading is shown in Fig. 10.6. Three system configurations are considered. These are the configuration without the attachment point as in [4], with the attachment point in 0.5L as in Fig. 10.3 and with the attachment point in 0.9L as in Fig. 10.4. It can be seen that although the match with the experiment data is not perfect, the trends and mutual relations between the three configurations were captured correctly by the computational model. The frequency locus of the system with no attachment point exhibits the steepest decrease with the increasing applied force, while the attachment point located in 0.5L leads to the modest decrease. This indicates that the frequency locus of the former configuration reaches the zero frequency before the latter system. Consequently, these

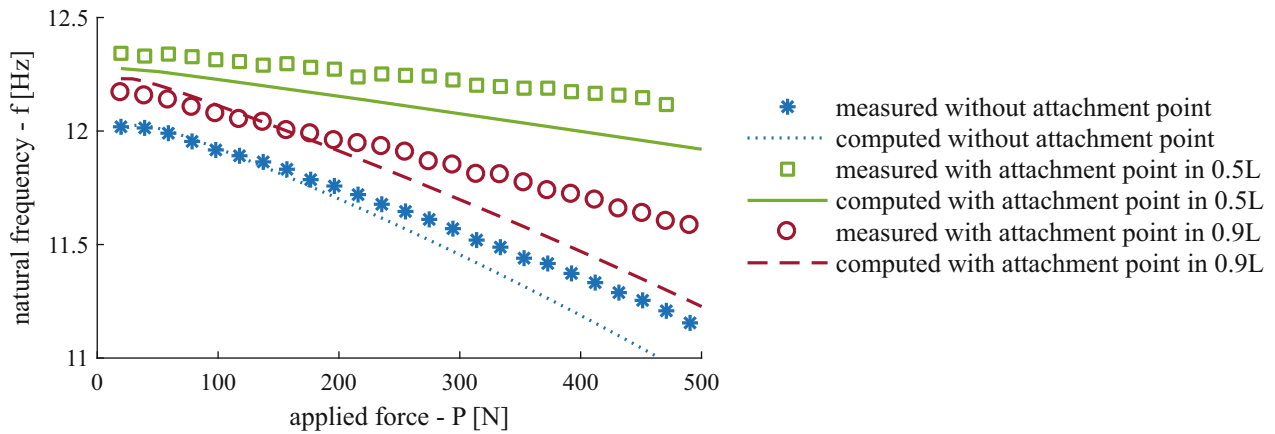


Fig. 10.6 The detail of the frequency-loading diagram in the proximity of the first bending mode for three system configurations

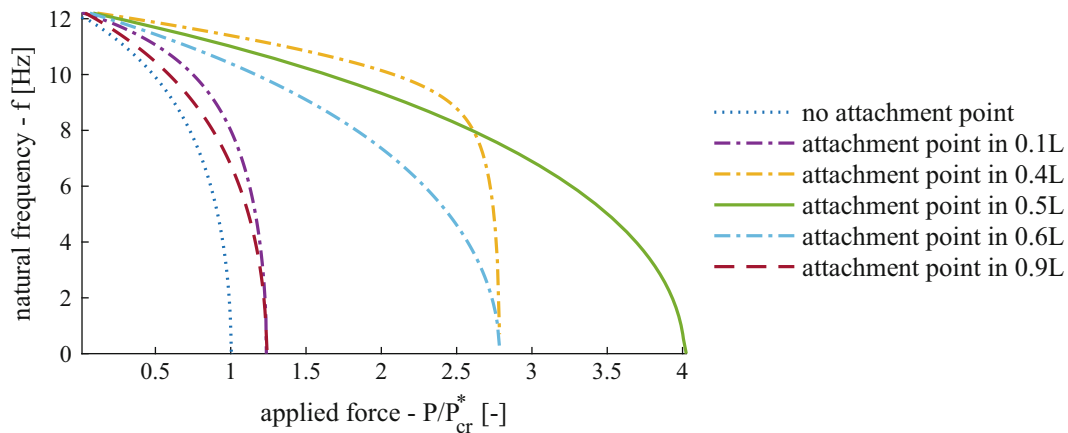


Fig. 10.7 Stability of the beam-tendon system with a single attachment point, normalised by the critical force of the system without an attachment point P_{cr}^*

experimental and computational results suggest that the critical force of the system without an attachment point is lower than the critical force of the system with an attachment point.

This observation is confirmed in Fig. 10.7 using the frequency loci computed up to the critical force. Apart from the configurations investigated so far, three more locations of the attachment points (in 0.1L, 0.4L and 0.6L) are shown. It can be seen that for any placement of the attachment point, the critical force is higher than for the system with no attachment point. It is also clear that the critical force of the system with the attachment point in 0.5L is significantly higher than for any other considered system. Furthermore, although the frequency loci of the systems with the attachment points in 0.4 and 0.6 are different from each other, the critical force of these systems is the same. The same can be said for the systems with the attachment points placed in 0.1L and 0.9L.

It is suggested that the critical force of the systems with the attachment points placed in 0.1L and 0.9L is lower and closer to the critical force of the system with no attachment point, because the length of the longest active part of the tendon (in both cases equal to 0.9L) is almost the same as the full length of the tendon (L) in the system with no attachment points. In contrast, in the systems with the attachment points in 0.4L and 0.6 the longest active part of the tendon is shorter (equal to 0.6L) and hence the critical force is higher. For the shortest length of the tendon achievable using a single attachment point (0.5L) the critical force is at its maximum as seen in Fig. 10.7. Therefore, it appears that the longest active part of the tendon is a major factor influencing the stability of the coupled beam-tendon system with a single attachment fixture. This conclusion is in line with an intuitive interpretation of the limit cases—when the attachment point is either very close to the clamp or very close to the tip, the coupled beam-tendon system is practically the same as the system with no attachment point and therefore the critical forces of these two system should be the same.

10.4 Discussion

In comparison to the beam-tendon system with no attachment fixtures investigated in [3, 4], the main findings can be summarised in the following remarks

- The attachment points divide the tendon into segments with higher natural frequencies whose rate of change is however the same.
- The number of tendon-dominated modes and veering regions in the considered frequency region is lower, and the mode shapes are different.
- The stability of the system depends on the position of the attachment point. However, the critical force is always higher than the critical force of the system with no attachment point.

Although the presence of the attachment fixture(s) may seem to be a minor modification to the beam-tendon system, it might have arguably significant implications with regards to the application of the active tendon concept as a means of resonance avoidance in rotorcraft [6]. For instance

- It should be possible to adjust the natural frequencies of the tendon-dominated modes by specific placement of the attachment fixtures such that these frequencies are out of excitation regions while the beam's natural frequency reduction capability remains.
- Since the critical force is higher, the active tendon concept can operate over a wider range of loading.
- Overall, the attachment points seem to be an important design element which significantly increases the design space, and should therefore be considered for future improvements of the concept.

Overall, the correlation between the experimental and computed results presented in this paper is very good. Therefore, the developed theoretical model with a single attachment point can be considered to be successfully validated. In the future, the numerical and experimental studies for several attachment points should be conducted. In addition, the application of the beam-tendon system with attachment points for resonance avoidance in rotorcraft should be investigated.

10.5 Conclusion

The numerical and experimental model of the coupled beam-tendon system has been presented in this paper. A number of system's configurations, and vibration and stability analyses have been shown. It has been found that all features observed for the system with no attachment points, such as the changes of the natural frequencies of the beam-dominated modes and the frequency loci veering, are still exhibited by the coupled system. However, they are manifested under different loading conditions due to the changes in the natural frequencies of the tendon-dominated modes. In addition, while the stability of the system depends on the position of the attachment point, the critical force is always higher than for the system with no attachment. With regards to the future application of the active tendon concept in rotorcraft, it can be concluded that the attachment fixtures are an important design element which should be further investigated in subsequent studies.

Acknowledgements The authors would like to acknowledge the financial support of the European Community's Horizon 2020 Program provided through the project "Shape Adaptive Blades for Rotorcraft Efficiency (SABRE)", Grant Agreement 723491.

References

1. Rauleder, J., van der Wall, B.G., Abdelmoula, A., Komp, D., Kumar, S., Ondra, V., Titurus, B., Woods, B.K.S.: Aerodynamic performance of morphing blades and rotor systems. In: AHS International 74th Annual Forum & Technology Display, Phoenix, Arizona (2018)
2. Dibble, R.P., Titurus, B.: Helicopter rotor blade modal tuning using internal preloads. In: International Conference on Noise and Vibration Engineering (ISMA2016) (2016)
3. Ondra, V., Dibble, R.P., Titurus, B.: Towards an application of an active tendon in rotorcraft: a numerical and experimental study of coupled bending-torsion vibration of a beam-tendon system. In: International Conference on Noise and Vibration Engineering (ISMA2018) (2018)
4. Ondra, V., Titurus, B.: Theoretical and experimental modal analysis for a beam-tendon system. Mech. Syst. Signal Process. (2019, under review)
5. Ondra, V., Titurus, B.: Free vibration analysis of rotating pre-twisted beams subjected to tendon-induced axial loading. J. Sound Vib. (2019, under review)

6. Ondra, V., Dibble, R.P., Titurus, B.: The use of an active tendon concept in rotorcraft with variable-speed rotors. In: AIAA Science and Technology Forum and Exposition (AIAA SciTech 2019) (2019)
7. Rao, S.S.: *Vibration of Continuous Systems*. Wiley, New York (2007)
8. Rosen, A.: Structural and dynamic behaviour of pretwisted rods and beams. *Appl. Mech. Rev.* **44**(12), 483–515 (1991)
9. Hodges, D.H.: *Nonlinear Composite Beam Theory*. American Institute of Aeronautics and Astronautics, Reston (2006)
10. Nayfeh, A.H., Pai, P.F.: *Linear and Nonlinear Structural Mechanics*. Wiley, New York (2008)
11. Cheng, G., Zu, J.W.: Dynamic analysis of an optical fiber coupler in telecommunications. *J. Sound Vib.* **268**(1), 15–31 (2003)
12. Cao, D.X., Zhang, W.: Global bifurcations and chaotic dynamics for a string-beam coupled system. *Chaos Solitons Fractals* **37**(3), 858–875 (2008)
13. Kierzenka, J., Shampine, L.F.: A BVP solver based on residual control and the Matlab PSE. *ACM Trans. Math. Softw.* **27**(3), 299–316 (2001)
14. Ewins, D.J.: *Modal Testing: Theory, Practice and Application*. Research Studies Press Ltd, Philadelphia (2000)
15. Bazant, Z.P., Cedolin, L.: *Stability of Structures: Elastic, Inelastic, Fracture and Damage Theories*. World Scientific, Singapore (2010)
16. Virgin, L.N.: *Vibration of Axially-Loaded Structures*. Cambridge University Press, Cambridge (2007)
17. Timoshenko, S., Gere, J.M.: *Theory of Elastic Stability*. Engineering Societies Monographs. Dover Publications, New York (1961)



Chapter 11

Designing a Modal Test Plan Based on Finite Element Method Results

Yan Cao and Liu Jinming

Abstract This chapter introduces some principles and methods for designing modal test plans based on finite element method (FEM) results. The number of points in FEM is closed, generally in the thousands. From the FEM results, many orders of modal frequencies and vibration shapes can be obtained. However, in a modal test, only the foremost orders are concerned; thus, the number of measured points is limited, generally in the tens. There are 2–4 exciting points for a multi input multi output (MIMO) test, whereas 1 exciting point is practical for a single input single output (SIMO) test when the modes are not closed. When the number of foremost orders and measured points are fixed, it is not practical to automatically compute the position of the total measured points from the FEM results for several reasons. First, the computing work is very complex and time-consuming. Second, for the best mathematical results, some key points may be lost and some points that cannot be measured are included. Most importantly, none of these point are able to construct a regular plane, so the result is unacceptable aesthetically. The practical approach is to design an initial plan in which the position is measured manually according to common experience and the space is evenly distributed. By computing the maximum value of the un-diagonal elements of the modal assurance criterion (MAC) matrix and observing the modal shape animation of the simplified results, some measured positions can be modified. If some points need to be deleted in the initial base, this task can be completed automatically by dividing all measured positions into two groups: points that are allowed to be deleted and points that cannot be deleted. After the positions of all measurements are fixed, the number of exciting points and their positions can be obtained automatically according to the exciting energy distribution of different orders in each position.

Keywords FEM · Modal test · Exciting points · GVB · MvMIF

11.1 Introduction

In production design, dynamic analysis using the finite element method (FEM) is necessary. The FEM results generally need to be verified by a modal test. If there is an obvious discrepancy between the modal test and the FEM results, then the FEM model will be optimized until the error is acceptable. Furthermore, one important parameter—the damping ratio—cannot be obtained from FEM analysis. It can only be estimated based on previous experience or identified from the modal test.

If FEM results exist, the modal test plan can be constructed based on the FEM results. This chapter describes some principles to simplify the grids to make them suitable for modal tests. In addition, the preferred methods for exciting points and pure normal test designs will be discussed.

11.2 Simplifying Grids

From the FEM results, many orders of modal frequencies and vibration shapes can be obtained. However, in a modal test, only the foremost order modes are considered. The measured points are limited and generally number in the tens or hundreds. Therefore, the FEM grids need to be simplified with a larger size that is suitable for modal tests.

Y. Cao
Department of Mechanical Engineering, Tsinghua University, Beijing, China

L. Jinming (✉)
China Orient Institute of Noise & Vibration, Beijing, China
e-mail: Liujm@coinv.com

The simplified process can be completed manually for the following reasons:

1. To retain the key points: If some key points are lost, then the test object cannot be shown correctly.
2. To ensure that the simplified grids are evenly distributed: The planes of the constructed grids should be acceptable from an aesthetic viewpoint.
3. To avoid the points that cannot be measured.
4. To avoid the time-consuming computation of automatic simplification.

An example is given to illustrate the simplification process. In Fig. 11.1, an FEM grid with 6307 points is shown. In Fig. 11.2, a simplified grid with 426 points for a modal test is shown.

From the FEM result, each mode's vibration shape in the simplified grid can be obtained. Figure 11.3 shows the modal assurance criterion (MAC) matrix and Table 11.1 shows the matrix values for the FEM. Figure 11.4 shows the MAC matrix and Table 11.2 shows the matrix values for the simplified grid.

Fig. 11.1 FEM grid

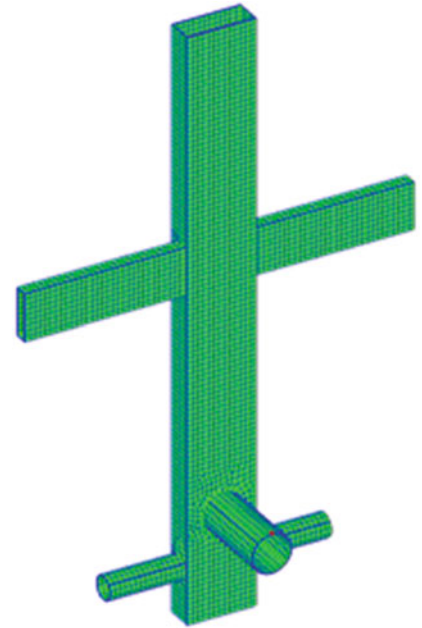
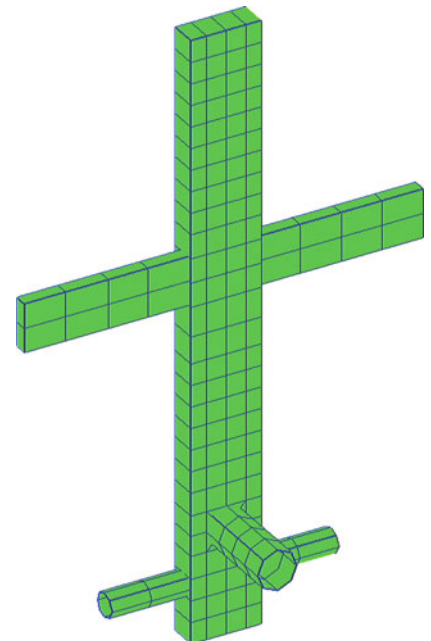


Fig. 11.2 Simplified grid



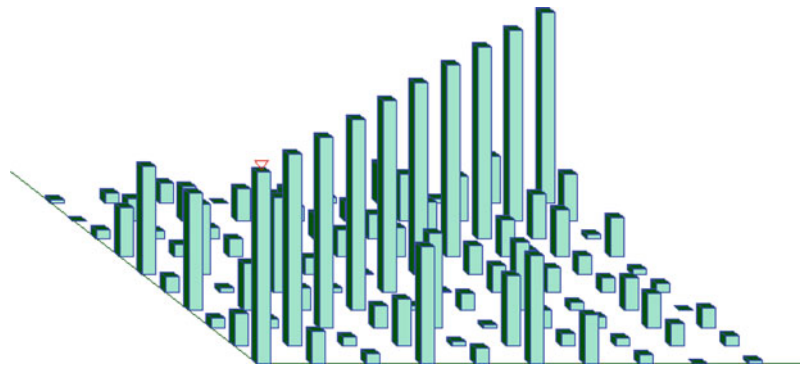


Fig. 11.3 MAC matrix for FEM

Table 11.1 MAC matrix values for FEM

207.33	0.02	0.06	0.11	0.00	0.05	0.03	0.21	0.03	0.25	1.00
183.31	0.00	0.12	0.19	0.17	0.08	0.10	0.25	0.24	1.00	0.25
143.95	0.05	0.04	0.06	0.04	0.13	0.13	0.20	1.00	0.24	0.03
139.09	0.26	0.07	0.10	0.36	0.14	0.16	1.00	0.20	0.25	0.21
132.24	0.57	0.37	0.02	0.09	0.01	1.00	0.16	0.13	0.10	0.03
126.73	0.08	0.03	0.50	0.03	1.00	0.01	0.14	0.13	0.08	0.05
96.94	0.61	0.24	0.12	1.00	0.03	0.09	0.36	0.04	0.17	0.00
75.73	0.05	0.05	1.00	0.12	0.50	0.02	0.10	0.06	0.19	0.11
67.67	0.17	1.00	0.05	0.24	0.03	0.37	0.07	0.04	0.12	0.06
47.40	1.00	0.17	0.05	0.61	0.08	0.57	0.26	0.05	0.00	0.02
	47.40	67.67	75.73	96.94	126.73	132.24	139.09	143.95	183.31	207.33

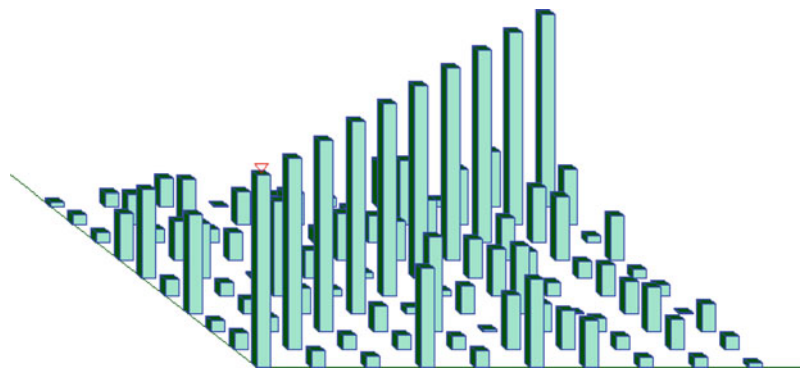
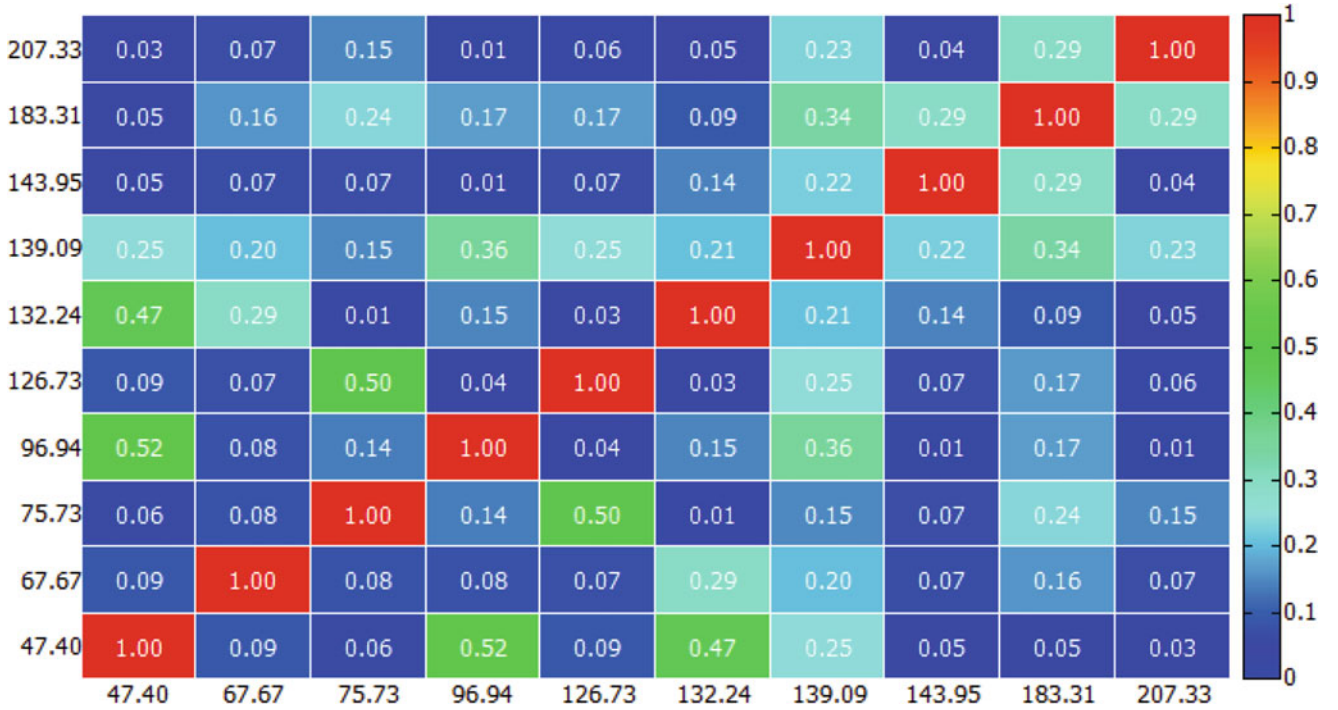


Fig. 11.4 MAC matrix for the simplified grid

Table 11.2 MAC matrix values for the simplified grid

The MAC matrix can be used to verify the simplification effect. If the mode frequency distribution is considered, a pole weighted MAC (pwMAC) matrix [1] can be used to replace the MAC matrix.

By computing the maximum value of un-diagonal elements in the MAC matrix, a different test plan can be evaluated. Smaller maximum values are better. In this way, the further deletion of some points can be completed automatically.

11.3 Exciting Points Selection

After grid simplification, the number of measured points is reduced. For a modal test plan, the exciting positions should be chosen. For a multi input multi output (MIMO) test, between 2 and 4 exciting points is sufficient. When the modes are not closed, 1 exciting point is adequate for a single input single output (SIMO) test. For each grid point, there are three directions to excite. However, only the direction direct to the grid plan is considered.

To select the exciting points automatically, an index of exciting points should be defined. The index will reflect the least exciting energy of one mode among all modes.

The frequency response function (FRF) between the exciting point and response point is as follows [2]:

$$H_{ij}(\omega) = \sum_{r=1}^n \frac{\phi_{ir}\phi_{jr}}{m_r(\omega_r^2 - \omega^2 + j2\xi_r\omega_r\omega)} \quad (11.1)$$

Here, i is the exciting point, j is the response point, r is the mode order, ϕ is the vibration shape, and n is the total mode number. For each mode, the vibration shape is first normalized with the max modulus of vibration shape as 1.

For a SIMO test, the index of i exciting points is the minimum of $|\phi_{ir}|$, $r = 1, 2, \dots, n$. The exciting point with the maximum index should be chosen to avoid a loss of mode.

For a MIMO test, define E_r as the maximum of $|\phi_{ir}|$, $i = 1, 2, \dots, m$. Here, m is the total number of exciting points. The index of the MIMO test is the minimum of E_r , $r = 1, 2, \dots, n$. The exciting points of m with the maximum index should be chosen to avoid a loss of mode.

11.4 Pure Normal Test

One type of ground vibration test of plane is the pure normal mode test. In this test, a number of exciters are used at the same harmonic frequency, which is one mode's frequency. By adjusting each exciter's amplitude and direction, the pure normal mode will be excited out with a precise modal shape.

For a MIMO test, a multivariate mode indicator function (MvMIF) [3] can determine the exciting force vector and construct the pure normal mode FRF.

For the FEM result, the FRF matrix is known as $H_{q \times p}$, where q is the response point number and p is the exciting point number. The exciting position is assumed to be fixed. In the FEM result, the mode damping ratio is zero. The damping ratio can also be given according to experience.

The real exciting force vector is $F_{p \times 1}$, $\|F\| = 1$ and the response function is $(HF)_{q \times 1}$. Thus, the force vector F will satisfy Eq. (11.2):

$$\min \frac{F^T H_{Real}^T H_{Real} F}{F^T (H_{Real}^T H_{Real} + H_{Imag}^T H_{Imag}) F} = \lambda \quad (11.2)$$

In the pure mode frequency, the matrix can be defined as follows:

$$A = H_{Real}^T H_{Real} \quad (11.3)$$

$$B = H_{Imag}^T H_{Imag} \quad (11.4)$$

From Eq. (11.2), there is:

$$AF = (A + B) F \lambda \quad (11.5)$$

Thus:

$$F^T (A + B)^{-1} AF = \lambda \quad (11.6)$$

By singular value decomposition (SVD) method, singular values are obtained:

$$(A + B)^{-1} A = USU^T \quad (11.7)$$

Here, S is a real positive diagonal matrix with elements from large to small and U is the unified real matrix. Furthermore, $UU^T = I$, where I is the unified matrix.

Let vector $F_{p \times 1}$ be the last column of matrix U . Then, λ equals the smallest element of S .

Given the different positions of exciting points, different λ values will be obtained. Lower λ values are better.

11.5 Conclusion

FEM results can be used to design mode tests that verify the FEM model. The grid simplification can be conducted manually. The maximum values of un-diagonal elements of a MAC or pwMAC matrix can evaluate the simplified grids.

Using an index of exciting points, the selection of exciting points for SIMO or MIMO can be completed automatically. The exciting direction should be chosen as direct to the grid plan.

In a pure normal mode test design, the number of shakers and the corresponding locations of shakers can be determined by the λ value of MvMIF. The force vector appropriation can be calculated by SVD with an FRF matrix.

References

1. Phillips, A.W., Allemang, R.J.: Data presentation schemes for selection and identification of modal parameters. In: Proceedings of 23th IMAC (2005)
2. Heylen, W., Lammeans, S., Sas, P.: Modal Analysis Theory and Testing. Katholieke Universiteit, Leuven, Belgium (1998)
3. Nash, M.: Use of the multivariate mode indicator function for normal mode determination. In: Proceeding of the SEM IMAC 6th Conference (1988)



Chapter 12

Maximizing the Quality of Shape Extractions from Base Shake Modal Tests

Kevin L. Napolitano

Abstract The promise of extracting fixed base modes from structures mounted on shake tables is enticing since doing so allows a testing organization to save a considerable amount of schedule and money by reducing two traditionally separate tests into one. Oftentimes, however, the modal analysis results are not of high quality because the test planning and conduct of base shake environmental tests are not conducive to performing a high-quality modal survey.

This paper will discuss test planning and test conduct methods that can be used to maximize chances for successfully extracting high-quality mode shapes from structures mounted on shake tables. These methods are the same for any modal survey test; sensors should be placed to adequately observe and differentiate modes of a structure, and the excitation must be long enough in duration to adequately define high-quality frequency response functions (FRFs). Finally, methods to separate closely spaced modes by using multiple references, either with multiple-degree-of-freedom shake tables or a single-axis base shake test supplemented with modal shakers, will be discussed.

Keywords Modal testing · Vibrations · Base shake · Environmental testing · Fixed base · Constraint shapes

12.1 Introduction

There has been considerable literature discussing how to extract fixed base modes from structures mounted on shake tables [1–9]. Recently, methods have been developed to extract fixed base modes from structures mounted on flexible shake tables. One method applies a constraint equation to measured mass-normalized mode shapes to generate fixed base modes [10]. A second method uses base accelerations as well as constraint shapes as references to calculate frequency response functions (FRFs) associated with a fixed base [11].

However, in many cases these correction techniques are not required. In these cases, poor-quality modal results are often due to a perceived belief by a program that a modal test will take too much time or effort to conduct, and that “good enough” results can be obtained by analyzing frequency domain results from the environmental test itself. The reality, however, is that high-quality modal test results can be obtained with little extra on-site effort if the modal test engineer can advocate for a few small (or in some cases, more significant) changes in the base shake test. The modal test setup effort can also be performed in parallel with the environmental test setup effort to help reduce schedule.

The objective of this paper is to provide the modal test engineer an outline of potential changes that they can advocate for in order to obtain high-quality modal results. Potential pretest analysis and test conduct adjustments to environmental tests will be discussed that can help a program extract high-quality modal information efficiently.

12.2 Pretest Analysis

The objective of aerospace-quality modal tests of structures mounted on shake tables is to extract fixed base modes, and pretest analysis usually involves selecting accelerometer locations and exciter locations. There are several documents that describe how to define target modes of a structure either through identifying high effective mass modes and/or identifying all modes to a given frequency range. NASA-HDBK-7005 [12] is one such document.

K. L. Napolitano (✉)
ATA Engineering, Inc., San Diego, CA, USA
e-mail: kevin.napolitano@ata-e.com

12.3 Accelerometer Selection

With the deployment of high-quality 24-bit data acquisition systems where the dynamic range of a measurement is determined more by the noise floor of the sensor than the acquisition system, accelerometer sensitivity is becoming less important to the point where one accelerometer type, such as accelerometers with 5 or 10 mV/g sensitivity, can be used for both base shake environmental tests and modal tests. Using the same accelerometers for both the environmental test and the modal survey test is therefore an easy way for a program to reduce cost and schedule.

Oftentimes, however, a test article instrumented for environmental testing will not be adequate for a modal test. Ideally, one would want to instrument the test article for a modal test and then select additional accelerometer locations to ensure that a test article is also instrumented for environmental testing.

The reality, however, is that the modal test most often plays a secondary role in the testing effort, and the modal test engineer is given two options: supplement the current set of accelerometers with a minimal number of modal accelerometers or make do with the current set of environmental accelerometers.

The first option is ideal, and the modal test engineer should advocate for supplementing the environmental accelerometers with additional accelerometers to ensure a high-quality modal survey can be conducted. This can be done manually or by using automated sensor selection methods [13] that help the user up-select from a baseline set of sensors to many more sensors than are necessary to ensure all target modes are observable. An automated down-selection method such as a genetic algorithm [14] or an iterative static condensation method can then be used to minimize the number of added sensors needed to achieve pretest analysis goals.

If adding additional sensors is not allowed, then the engineer should still run the pretest analysis with the current set of sensors to understand what to expect during the modal test.

Sometimes, however, the number of sensors in the environmental test is much larger than necessary to achieve good modal results. If this is the case, then a further down-selection analysis can be performed to remove as many environmental accelerometers as practicable while still achieving the pretest analysis goals. Doing this will help the modal test engineer perform a modal analysis with a reasonable set of sensors, which will help obtain modal analysis results in a timely manner.

The last item to consider with accelerometer selection is ensuring that the assumptions associated with a fixed base test, namely that the base is fixed, can be verified by mounting additional sensors to the shaker table to ensure the six-degree-of-freedom rigid body motion of the table can be characterized. It is very important for the modal test engineer to advocate for the addition of these sensors. It is also advantageous to verify that the connection between the test article and the shaker table is fixed by sets of accelerometers near the interface on both the structure side and the table side.

12.4 Exciter Selection

Exciter selection is a key feature for the success of a modal survey test for two reasons. The first reason is that exciters must be able to excite modes of interest. The second reason is that combinations of shakers must be able to differentiate modes that are closely spaced in frequency.

Most base shake tests only use the base shaker itself to excite the structure, and FRFs are calculated using a base accelerometer that is in-line with the shaker as a reference degree of freedom. The advantage of using the base shaker is that it will automatically excite all the high effective mass modes associated with the drive direction of the shaker. The disadvantage is that it will not be able to help the modal analysis engineer differentiate closely spaced modes. One way to help separate closely spaced modes is to measure high-resolution FRF so peaks that are close together can be differentiated. That said, closely spaced modes are best separated by exciting the structure with multiple references. Six-degree-of-freedom shaker tables are excellent in this respect because there are six independent references that are guaranteed mathematically to excite all the high effective mass modes of a test article.

The modal test engineer has a few choices to add multiple excitation sources to a standard single-axis shaker table:

1. Use the base shaker and additional modal shakers mounted to the test article to excite the structure. In this case, one can use the base shaker drive point accelerometer and the modal shaker forces as references when calculating fixed base FRF.
2. Secure the shaker table to the ground and use modal shakers to excite the structures. One can usually secure the shaker table to the ground by simply turning off the oil that allows the table to slide.
3. Perform multiple tap tests while the shake table is secured.

As with any planned modal survey, trial exciter locations can be assessed with the analysis model [15] to determine whether all target modes can be observed and separated in the FRF data.

12.5 Test Conduct

Too often, modal analysis results from base shake tests are poor because FRFs are calculated from environmental test data which is inappropriate for a modal test. Random vibration tests are usually too short in duration and result in either too few frames of data to calculate high-quality FRFs or frequency spacing too wide to adequately define peaks in FRFs. The sweep rate for sine-sweep tests is also usually too fast, leading to the same FRF quality and frequency spacing issues.

12.6 Test Duration

It is therefore important for the modal test engineer to advocate for an excitation duration that is conducive to calculating high-quality FRFs. This can be accomplished easily by persuading the environmental testing technician to run a separate low-level characterization run for an extended period of time. Although each modal test is different, it is usually a good idea to excite the structure with at least 10 min of random data or perform sine sweeps at a rate of at most 3 min per decade.

Although other excitation techniques can be applied to a base shaker, technicians who run shaker tables usually only apply a true random, sine-sweep, or sine-dwell excitation. Therefore, it is most efficient to use these types of excitations for the modal test.

12.7 Signal Processing

The modal test engineer should also advocate for time-history data to be collected for all sensors. If the facility cannot deliver time-history data, serious consideration should be given to supplementing the test facility's shaker control data acquisition system with a separate acquisition system that can export time-history data. The sensors required for shaker control can be then routed into both data acquisition systems.

The time-history data should be used to calculate FRFs. Doing so will enable the modal test engineer to process the test data with different parameters in order to calculate the highest-quality FRFs practicable. Both random and sine-sweep test data can be processed using a Hanning Window with overlap processing. The frame length and overlap processing percentage can be adjusted to find an optimal result. Usually, both are dependent on the level of inherent damping in the structure. Lower modal damping leads to longer frame lengths and higher overlap percentage.

If time-history data cannot be delivered, then the percentage chance for a successful test diminishes greatly. The next best option is to have the test facility deliver complex spectra data. The modal test engineer can then calculate FRFs by dividing the complex spectra of the response channels by the complex spectra data of the drive point accelerometers.

It should be noted that many facilities have unique signal processing algorithms that use nonstandard methods for calculating complex spectra from sine-sweep tests. One example is the widespread use of a Hilbert transform of the sinusoidal sweep time-history data to calculate the complex frequency response. It should be noted that because the Hilbert transform envelopes the response, the complex spectral data will result in artificially high damping calculations whenever a mode does not reach full resonant response.

12.8 Mode Shape Calculation

Standard modal analysis techniques can be used to calculate mode shape parameters from the resulting FRFs. Once the fixed base modes are calculated, they can be compared to analysis modes using conventional mode shape independence and mode shape completeness measures such as test self-orthogonality and test-finite element model cross-orthogonality calculations.

It is also important to view the test-measured mode shapes to verify the assumption that the modes are actually fixed base modes. One can also compare the imaginary part of the FRF-associated accelerometers on the shake table with the imaginary part of the FRFs associated with accelerometers on the structure. Ideally, there are several orders of magnitude difference between them.

12.9 Summary

The promise of extracting fixed base modes from structures mounted on shake tables is enticing since doing so allows a testing organization to save a considerable amount of schedule and money by reducing two traditionally separate tests into one.

This paper has discussed test planning and test conduct methods that can be used to maximize chances for successfully extracting high-quality mode shapes from structures mounted on shake tables. These methods are the same as for any modal survey test; sensors should be placed to adequately observe and differentiate modes of a structure, and the excitation must be long enough in duration to adequately define high-quality frequency response functions. As always, assumptions of base fixity should be verified at the completion of the modal test.

References

1. Crowley, J.R., Klosterman, A.L., Rocklin, G.T., Vold, H.: Direct structural modification using frequency response functions. In: Proceedings of the Second International Modal Analysis Conference, Orlando, FL, February 1984. pp. 58–65
2. Beliveau, J.G., Vigneron, F.R., Soucy, Y., Draisey, S.: Modal parameter estimation from base excitation. *J. Sound Vib.* **107**, 435–449 (1986)
3. Imregun, M., Robb, D.A., Ewins, D.J.: Structural modification and coupling dynamic analysis using measured FRF Data. In: 5th International Modal Analysis Conference (IMAC V), London, England (1987)
4. Carne, T.G., Martinez, D.R., Nord, A.R.: A comparison of fixed-base and driven base modal testing of an electronics package. In: Proceedings of the Seventh International Modal Analysis Conference. pp. 672–679 (1989)
5. Fullekrug, U.: Determination of effective masses and modal masses from base-driven tests. In: Proceedings of the 14th International Modal Analysis Conference. pp. 671–681 (1996)
6. Sinapius, J.M.: Identification of fixed and free interface normal modes by base excitation. In: Proceedings of the 14th International Modal Analysis Conference. pp. 23–31 (1996)
7. Mayes, R.L., Bridgers, L.D.: Extracting fixed base modal models from vibration tests on flexible tables. In: Proceedings of the 27th International Modal Analysis Conference (2009)
8. Allen, M.: Recent advances to estimation of fixed-interface modal models using dynamic substructuring. In: Proceedings of the 36th International Modal Analysis Conference (2018)
9. Napolitano, K., Yoder, N.: Fixed base FRF using boundary measurements as references – analytical derivation. In: Proceedings of the 30th International Modal Analysis Conference (2012)
10. Mayes, R., Rohe, D., Blecke, J.: Extending the frequency band for fixed base modal analysis on a vibration slip table. In: Proceedings of the 31st International Modal Analysis Conference (2013)
11. Napolitano, K., Yoder, N.: Extraction of fixed-base modes of a structure mounted on a shake table. In: Proceedings of the 31st International Modal Analysis Conference (2013)
12. National Aeronautics and Space Administration: Dynamic Environmental Criteria – NASA Technical Handbook. NASA-HDBK-7005 (2001)
13. Tuttle, R., Cole, T., Lollock, J.: An automated method for identification of efficient measurement degrees of freedom for mode survey testing. In: 46th AIAA/ASME/ASCE/AHS/ASC Structures, Structural Dynamics and Materials Conference, Austin, TX (2005)
14. Stabb, M., Blesloch, P.: A genetic algorithm for optimally selecting accelerometer locations. In: 13th International Modal Analysis Conference, Nashville, TN (1995)
15. Napolitano, K.L., Blesloch, P.A.: Automated selection of shaker locations for modal tests. In: 21st International Modal Analysis Conference on Structural Dynamics, Kissimmee, FL, February 2003



Chapter 13

New Approaches to Inverse Structural Modification Theory Using Random Projections

Prasad Cheema, Mehrisadat M. Alamdari, and Gareth A. Vio

Abstract In many contexts the modal properties of a structure change, either due to the impact of a changing environment, fatigue, or due to the presence of structural damage. For example during flight, an aircraft's modal properties are known to change with both altitude and velocity. It is thus important to quantify these changes given only a truncated set of modal data, which is usually the case experimentally. This procedure is formally known as the generalised inverse eigenvalue problem. In this paper we experimentally show that first-order gradient-based methods that optimise objective functions defined over a modal are prohibitive due to the required small step sizes. This in turn leads to the justification of using a non-gradient, black box optimiser in the form of particle swarm optimisation. We further show how it is possible to solve such inverse eigenvalue problems in a lower dimensional space by the use of random projections, which in many cases reduces the total dimensionality of the optimisation problem by 80–99%. Two example problems are explored involving a ten-dimensional mass-stiffness toy problem, and a one-dimensional finite element mass-stiffness approximation for a Boeing 737-300 aircraft.

Keywords Inverse eigenvalue problems · Modal analysis · Random projections · Particle swarm optimisation · Finite element analysis

13.1 Introduction

Eigenvalue problems are common in the engineering context [1, 2]. As such, they have been used in a plethora of applications such as in analysing the state matrix of an electronic power system [3], in studying the aeroelastic instability for wind turbines [4], for determining the spectral radius of Jacobian matrices [5], and in the operational modal analysis of a structures [6]. The most common eigenvalue problem, known as the *direct* or *forward* problem involves determining the impact of a known set of modifications to a group of matrices, either by computing the eigenvalues, eigenvectors, singular values, or singular vectors of the group of matrices. The direct problem is well studied, and is the subject of many elementary courses in linear algebra, but the *inverse* problem is much more complex.

The inverse problem tries to find or infer a particular type of modification which was applied to a set of matrices, from a larger set of possible modifications, using mainly spectral information [7]. It is clear that this problem would be trivial if all the spectral information of the system before and after any modifications were known (that is, we are not dealing with a truncated modal system), or if the desired modifications were completely unstructured (that is, they are allowed to be any value). Thus in order to strive for more physical, and mathematical solutions we often try to restrict the group of possible matrices for the inverse eigenvalue problem. In a recent review article, Chu [8] devised a collection of 39 possible inverse eigenvalue problems. These problems were roughly categorized based on their: parameterisation, underlying structure, and the partiality of the system description (that is, whether or not we have complete modal information). A summary of the most common kinds of inverse eigenvalue problems are given in Fig. 13.1, where the following terminology is used:

- MVIEP: Multivariate inverse eigenvalue problem
- LSIEP: Least square inverse eigenvalue problem
- PIEP: Parameterised inverse eigenvalue problem
- SIEP: Structured inverse eigenvalue problem

P. Cheema (✉) · G. A. Vio
School of AMME, The University of Sydney, Sydney, NSW, Australia
e-mail: prasad.cheema@sydney.edu.au

M. M. Alamdari
School of Civil and Environmental Engineering, University of New South Wales, Sydney, NSW, Australia

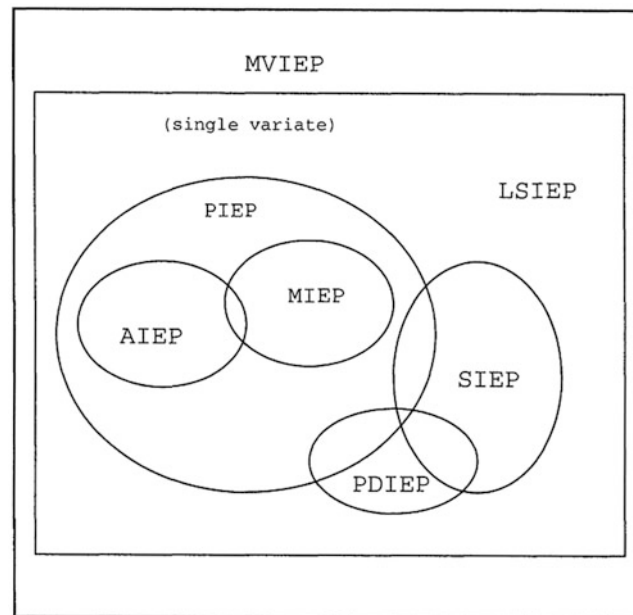


Fig. 13.1 An overview of some of the general classes of inverse eigenvalue problems as defined by Chu [8]

- PDIEP: Partially described inverse eigenvalue problem
- AIEP: Additive inverse eigenvalue problem
- MIEP: Multiplicative inverse eigenvalue problem

In this paper we aim to explore AIEPs which have a highly general parameterisation, in order to demonstrate the potential capabilities of random projections for the inverse eigenvalue problem.

In order to solve for the AIEP we shall define an optimisation problem. Although there are many optimisation procedures available for solving such problems, a particle swarm optimiser (PSO) is used in this paper. PSO is an optimisation procedure first introduced by Eberhart and Kennedy in 1995 [9]. It is a stochastic, population-based optimisation procedure modeled on the observed behaviour of animals which exhibit swarm-like tendencies, such in the social behaviour of birds or insects. Because of this PSO, tries to mimic swarm-like behaviour with each *particle* having access to both: a personal best solution, *and* access to the global optimum, thereby enabling the sharing of information across the swarm. This introduces the idea of the classic *exploration-exploitation* trade-off since the particles are either allowed to *exploit* the current global optimum, or *explore* further if their local optimum is far away from the current global [9, 10].

PSO is used in this paper to perform the optimisation for two main reasons. Firstly, to the knowledge of the authors, it has not previously been used in the context of this problem (AIEP), hence there is novelty in doing so. Secondly, it is a known black-box, gradient-free optimiser which makes it simple to work with since there is no requirement to compute the Jacobian, or calculate analytical gradients [10]. Moreover as we shall demonstrate experimentally, gradient step sizes are required to be very small in the inverse eigenvalue problem, with the issue exacerbating in higher dimensions. PSO as an algorithm has been successfully used in many different areas, including but not limited to reactive power and voltage control problems [11], in the study of material degradation for aeroelastic composites [12], composites structures with robustness [13], and in the optimum design of Proportional-Integral-Derivative (PID) control [14] which additionally helps in justifying its potential to work well in this context.

Regardless, of the choice of optimiser, all optimisation procedures are known to suffer from the *curse of dimensionality*, and since structural problems are generally able to grow without bound in terms of degrees of freedom (for example, a finite element model can keep growing in the number of elements), it is important to devise methods which can help reduce, or at least limit the rate of growth of these dimensions. Random projections have recently emerged as a powerful method to address the problem of dimensionality reduction [15]. This is because theory (in particular the Johnson–Lindenstrauss lemma) suggests that certain classes of random matrices are able to preserve Euclidean distances to within a tolerable error bound in the lower dimensional space [16]. As a result, random projections have been used successfully to reduce the dimensionality of the underlying optimisation problem, consequently allowing for optimisation to be performed in this lower dimensional space [17–19].

Thus, it is ultimately the aim of this paper to explore the impact of random projections and how they may be used in connection with the PSO algorithm for the generalised inverse eigenvalue problem of an additive nature. In the following sections we demonstrate experimentally that gradient-based approaches lose accuracy in even moderate step sizes, and clarify the theory that we shall use from random projections to help in lowering the dimensionality of the underlying optimisation problem. Lastly we showcase a gamut of positive results on a 10 dimensional (meaning a matrix of size 10) toy problem, and 1 dimensional finite element model based on aircraft data for the Boeing 737-300 aircraft.

13.2 Background and Methodology

13.2.1 The Generalised Eigenvalue Problem

Ultimately it is the aim of this paper to use particle swarm optimisation (PSO) in order to try and solve the generalised *inverse* eigenvalue problem, with the use of random projections. We thus commence by formalising the notion of the generalised eigenvalue problem here.

Suppose we have the generalised eigenvalue problem as shown in Eq. (13.1), which represents an undamped mechanical vibration system.

$$\mathbf{M}\ddot{\mathbf{x}} + \mathbf{K}\mathbf{x} = 0 \quad (13.1)$$

where $\mathbf{M}, \mathbf{K} \in \mathbb{R}^{N \times N}$, and $\mathbf{x} \in \mathbb{R}^N$. The eigensystem for Eq. (13.1) defines the following set of eigenvalue, eigenvector pairs: $\mathbb{A} = \{(\lambda_i, \mathbf{v}_i) | i = 1, \dots, N; \mathbf{v}_i \in \mathbb{R}^N, \lambda \in \mathbb{R}\}$. Furthermore we assume that the eigenvalue problem is perturbed via the addition of some arbitrary matrices we denote as $\mathbf{\Delta} \in (\mathbb{R}^{N \times N}, \mathbb{R}^{N \times N})$. That is, from here onwards whenever the $\mathbf{\Delta}$ symbol is written in isolation, in a bold-type font it denotes a 2-tuple of perturbation matrices of the system, that is, $\mathbf{\Delta} := (\Delta\mathbf{M}, \Delta\mathbf{K})$, where $\Delta\mathbf{M} \in \mathbb{R}^{N \times N}$ and $\Delta\mathbf{K} \in \mathbb{R}^{N \times N}$.

$$(\mathbf{M} + \Delta\mathbf{M})\ddot{\mathbf{x}} + (\mathbf{K} + \Delta\mathbf{K})\mathbf{x} = 0 \quad (13.2)$$

The eigenpairs for the modified system shown in Eq. (13.2) may be represented via the following set of eigenpairs: $\mathbb{B} = \{(\sigma_i, \mathbf{w}_i) | i = 1, \dots, N; \mathbf{w}_i \in \mathbb{R}^N, \sigma \in \mathbb{R}\}$. However, if both the initial and modified systems are full rank systems, then it would be trivial to obtain the $\Delta\mathbf{M}$ and $\Delta\mathbf{K}$ matrices. Thus for this paper we assume that we only have access to a truncated eigensystem for the modified system. That is, we only have access to some subset of the pairs: $\mathbb{C} \subset \mathbb{B}$, where $|\mathbb{C}| = n < N$. Thus our objective function in the search for the optimal $\mathbf{\Delta}$ matrices reflects this, in Eq. (13.3).

$$\Delta\mathbf{M}^*, \Delta\mathbf{K}^* = \operatorname{argmin}(\|\sigma_{1:n}^\dagger - \sigma_{1:n}(\mathbf{\Delta})\|_2^2), \quad (13.3)$$

where $\|\cdot\|_2^2$ denotes the square of the standard 2-norm, σ^\dagger denotes the desired eigenvalues, and σ refers to the eigenvalues as calculated from applying the $\mathbf{\Delta}$ matrices (clarified in the prior paragraph in reference to set \mathbb{B}). As is made clear in Eq. (13.3), we only consider the first $n < N$ dimensions, since we are dealing with a reduced set of eigenvalues.

In this paper we propose investigating the solutions for the objective function shown in Eq. (13.3) via PSO. We aim to use a non-gradient based, black-box optimisation since a first order perturbation analysis of the modified eigenvalues seem to suggest that for higher dimensional problems the step-sized used by gradient-based approaches may become prohibitively small. We establish this idea by first developing Lemma 13.2.1 as follows.

Lemma 13.2.1 *Suppose we have the two following generalised eigenvalue problems,*

$$\lambda\mathbf{M}\mathbf{v} = \mathbf{K}\mathbf{v} \quad (13.4)$$

$$(\lambda + \delta\lambda)(\mathbf{M} + \Delta\mathbf{M})(\mathbf{v} + \delta\mathbf{v}) = (\mathbf{K} + \Delta\mathbf{K})(\mathbf{v} + \delta\mathbf{v}), \quad (13.5)$$

where $\mathbf{\Delta}$ perturbations are controlled system inputs, and the δ perturbations are a consequence of applying $\mathbf{\Delta}$. Then,

$$\delta\lambda_i = \frac{\mathbf{v}_i^\top (\Delta\mathbf{K} - \lambda_i \Delta\mathbf{M}) \mathbf{v}_i}{\mathbf{v}_i^\top \Delta\mathbf{M} \mathbf{v}_i}, \quad (13.6)$$

if \mathbf{M} and \mathbf{K} are Hermitian.

Proof By expanding Eq. (13.5), removing higher order terms (that is, keeping only linear terms), and considering the i th eigenvalue-eigenvector pairs we arrive at,

$$\mathbf{K}\delta\mathbf{v}_i + \Delta\mathbf{K}\mathbf{v}_i = \lambda_i\mathbf{M}\delta\mathbf{v}_i + \delta\lambda_i\mathbf{M}\mathbf{v}_i + \lambda_i\Delta\mathbf{M}\mathbf{v}_i. \quad (13.7)$$

Since \mathbf{M} and \mathbf{K} are Hermitian it implies that that the eigenvectors of Eq. (13.4) are mutually \mathbf{M} -orthogonal. Moreover since they are assumed diagonalisable, these eigenvectors form a complete basis. Hence we can express each perturbation vector, $\delta\mathbf{v}_i$ as a sum of the eigenvectors of Eq. (13.4). As an equation this is,

$$\delta\mathbf{v}_i = \sum_{k=1}^N c_k \mathbf{v}_k, \quad (13.8)$$

for some arbitrary constants $c_k \in \mathbb{R}$. Thus, substituting Eq. (13.8) into Eq. (13.7), and using Eq. (13.4):

$$\sum_{k=1}^N c_k \lambda_k \mathbf{M}\mathbf{v}_k + \Delta\mathbf{K}\mathbf{v}_i = \lambda_i \mathbf{M} \sum_{k=1}^N c_k \mathbf{v}_k + \delta\lambda_i \mathbf{M}\mathbf{v}_i + \lambda_i \Delta\mathbf{M}\mathbf{v}_i. \quad (13.9)$$

Finally, left multiplying Eq. (13.9) by \mathbf{v}_i^\top , and re-arranging results in,

$$\delta\lambda_i = \frac{\mathbf{v}_i^\top (\Delta\mathbf{K} - \lambda_i \Delta\mathbf{M}) \mathbf{v}_i}{\mathbf{v}_i^\top \Delta\mathbf{M}\mathbf{v}_i},$$

since the eigenvectors \mathbf{v}_i are \mathbf{M} -orthogonal. \square

Corollary 13.2.1 Suppose we have the two following standard eigenvalue problems,

$$\lambda \mathbf{v} = \mathbf{K} \mathbf{v} \quad (13.10)$$

$$(\lambda + \delta\lambda)(\mathbf{v} + \delta\mathbf{v}) = (\mathbf{K} + \Delta\mathbf{K})(\mathbf{v} + \delta\mathbf{v}). \quad (13.11)$$

Then,

$$\delta\lambda_i = \frac{\mathbf{v}_i^\top \Delta\mathbf{K}\mathbf{v}_i}{\mathbf{v}_i^\top \mathbf{v}_i}, \quad (13.12)$$

if \mathbf{K} is Hermitian.

Proof The proof follows similarly from repeating the steps shown in Lemma 13.2.1, in the absences of the \mathbf{M} and $\Delta\mathbf{M}$ matrices. \square

Note that in Eqs. (13.6) and (13.12), it is not necessarily true that $\mathbf{v}_i^\top \Delta\mathbf{M}\mathbf{v}_i = 1$ since each eigenvector \mathbf{v}_i is only orthogonal with respect to the \mathbf{M} matrix, and not $\Delta\mathbf{M}$. A similar argument may be made with the \mathbf{K} and $\Delta\mathbf{K}$ matrices. In addition, Eqs. (13.6) and (13.12) make clear how the perturbation matrices, Δ , impact the changes in the eigenvalues, $\delta\lambda$, up to a linear approximation (since in the derivation the higher order effects were ignored). As a result this relationship may be used in better understanding gradient-based relationships for eigenvalue problems. That is, we may use these to analyse the potential accuracy and or quality of gradient-based approaches for such problems. An investigation of these ideas is made clear in Fig. 13.2.

Equation (13.13) is used order to calculate the percentage errors for the $|\Delta\delta\lambda_1|$ values in Fig. 13.2, where $\delta\lambda_1^\dagger$ refers to the change in first eigenvalue as obtained from Eq. (13.6), and $\delta\lambda_1$ is obtained using Eqs. (13.1) and (13.2), which refers to the benchmark correct value.

$$\begin{aligned} |\Delta\delta\lambda_1|_\mu &:= \mathbb{E}(|\Delta\delta\lambda_1|) \\ &= \mathbb{E}\left(\frac{|\delta\lambda_1^\dagger - \delta\lambda_1|}{\delta\lambda_1}\right) \end{aligned} \quad (13.13)$$

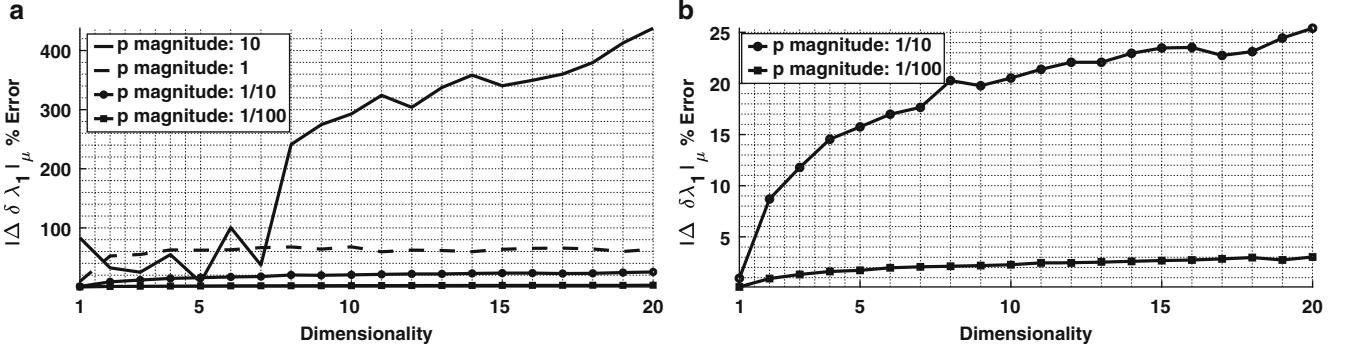


Fig. 13.2 Plots describing how the average magnitudes of the elements (defined by Eq. (13.14)) inside the ΔM and ΔK matrices affect the $\Delta \delta \lambda_1$ term, defined in Eq. (13.13). (a) Different p magnitudes plotted against $|\Delta \delta \lambda_1|_{\mu}$ term as a percentage error. (b) A zoomed-in version of subplot (a) to more clearly show the cases of $p = 1/10$ and $p = 1/100$

In order to calculate the size of terms inside the Δ matrices, Eq. (13.14) is used, where \mathcal{U} refers to the uniform distribution, the $i, j = 1, \dots, d$ indices refer to each term in the matrix, and $d = 1, \dots, 20$ defines the dimensionality (size) of the matrices. Through this definition there are d^2 degrees of freedom inside the matrix at any time.

$$\Delta_{i,j} \sim p \cdot \mathcal{U}[0, 1], \quad (13.14)$$

The value of d changes because we are considering the effect of dimensionality on the quality of the linear step size, $\delta \lambda$. Moreover the scalar $p \in \{1/100, 1/10, 1, 10\}$ defines the magnitude of the terms in the Δ matrices. Thus p in a practical sense (that is, in reference to a gradient-based optimisation algorithm) can be interpreted as the *step size* of the algorithm.

From Fig. 13.2 it can be seen that as the average magnitude of the elements inside the Δ matrices increase, the absolute difference between the theoretical $\delta \lambda_1$ value, and those calculated via Eq. (13.6), that is, $\delta \lambda_1^\dagger$, becomes larger. Even when the average step size takes value $p = 1/100$, there appears to be a bias in the magnitude of the error, which is made clear in the *zoomed in* subplot of Fig. 13.2b. Moreover as the dimensionality of the Δ matrices increase, the $|\Delta \delta \lambda_1|$ errors appear to increase slightly. Hence in summary as this experimental analysis of Eq. (13.6) seems to suggest, gradient based methods are potentially difficult to implement. In particular, it would appear that we would require $p < 1/100$ at a minimum, and that this value would need to continually decrease as dimensionality increases. For this reason, we opt to explore the viability of particle swarm optimisation as a means for optimisation since it is a non-gradient based approach, and gradient-based approaches seem to require very small step sizes for accurate gradients.

13.2.2 Particle Swarm Optimisation

Particle Swarm Optimisation (PSO) is a stochastic, evolutionary optimisation first proposed by Kennedy and Eberhart[9]. The algorithm works by generating an array of candidate particles (the swarm) across an objective space. Within this space each particle searches for the global optimum through the sharing of information within the swarm in a classic exploration-exploitation trade-off. This is clarified in Eqs. (13.15) and (13.16).

$$v_i^{k+1} = \omega v_i^k + c_1 r_1 (p_i - x_i^k) + c_2 r_2 (p_G - x_i^k) \quad (13.15)$$

$$x_i^{k+1} = x_i^k + \alpha v_i^{k+1} \quad (13.16)$$

where α denotes step size, ω controls the particle's inertia, c_1 and c_2 (known as the acceleration coefficients) are constants which control the degree of the *exploration-exploitation* trade-off, p_i and p_G are the local optima, and global optimum, for each, and across all particles respectively (that is each particle stores their own local optimum, but shares knowledge of the current global optimum), and $r_1, r_2 \sim \mathcal{U}(0, 1)$. In this way, every particle is made aware of the current global optimum, and explores the objective space accordingly (as specified through the c_1 and c_2 constants).

Empirical studies in PSO theory have shown that the correct choice of inertia weight is critical in ensuring convergent behaviour of the algorithm [10]. Prior investigations have suggested that the choice of inertia is driven by the acceleration coefficients through: $2\omega > (c_1 + c_2) - 2$. This region describes the set of all c_1 , and c_2 values which guarantee convergent behaviour based on the spectral analysis of the matrix describing the PSO dynamics [20]. However this inequality should be only be taken as a rough guide since it was derived assuming the PSO system has one particle, and one dimension. Empirically however, Eberhart and Shi suggest using values of $\omega = 0.7298$ and $c_1 = c_2 = 1.49618$ for *good* convergent behaviour in general [21].

13.2.3 Random Embedding

An aim of this paper is to explore the capability of random projections to reduce the underlying dimensionality of the generalised eigenvalue problem. In particular, we propose an extremely general parameterisation of the $\Delta\mathbf{M}$, and $\Delta\mathbf{K}$ matrices, and explore whether or not it is possible to solve this problem in a lower dimensional space. The lowest dimensional space in which the problem may be solved completely is known as the *effective dimension*, and is denoted by d_e . In particular the following definition is used to strictly define the notion of d_e , where Definition 13.2.1 is based on Definition 1 of Wang et al. [17].

Definition 13.2.1 (Effective Dimension) Suppose there exists a linear subspace $\mathcal{T} \subset \mathbb{R}^D$, where $\dim(\mathcal{T}) = d_e < D$. A function $f : \mathbb{R}^D \rightarrow \mathbb{R}$ is said to have **effective dimensionality** d_e , if d_e is the smallest integer such that $\forall x \in \mathcal{T}$ and $x^\perp \in \mathcal{T}^\perp \subset \mathbb{R}^D$, where $\mathcal{T} \oplus \mathcal{T}^\perp = \mathbb{R}^D$, we have $f(x + x^\perp) = f(x)$.

A simple example to clarify this definition for the reader may be seen if we define the following function: $f(x_1, x_2) = x_1^2 + x_2^2$, where, $f : \mathbb{R}^{10} \rightarrow \mathbb{R}$, and $x_1, x_2 \in \mathbb{R}$. In this example, although the original space of f is assumed to be 10-dimensional, one may easily observe that it has an *effective dimension* of 2 (that is, $d_e = 2$), since it clearly only makes use of 2 dimensions, of the 10 possible dimensions it has access to. The remaining 8 dimensions are *ineffective dimensions*. Unfortunately, in practice we never really know the actual value of d_e , but we either know or assume from prior knowledge that our problem may have a lower dimensional representation. In other words, in practice we only ever know or use $d \in \mathbb{Z}$ dimensions in total, where $D \geq d \geq d_e$, and thus our random embedding generally occurs via random matrices with dimensionality $D \times d$.

Although the notion of effective dimensionality is developed, it does not explain how such random projections to lower dimensional spaces should occur. Ideally when projecting to a lower dimensional space we desire $\|T(x_i - x_j)\| \approx \|(x_i - x_j)\|$, where $T : \mathbb{R}^n \rightarrow \mathbb{R}^m$ is some linear operator. That is, we aim to reduce the dimensionality of a set of points in some Euclidean space, which approximately retains these pair-wise distances measures in this new, lower-dimensional subspace. A bound on the degree of *distortion* that occurs to the original space when we project to a lower dimensional space is famously shown through the Johnson-Lindenstrauss (JL) Lemma [16], stated in Lemma 13.17.

Lemma 13.2.2 (Johnson-Lindenstrauss Lemma) For any $0 < \varepsilon < 1$, and for any integer n , let k be such that

$$k \geq 4 \frac{1}{\varepsilon^2/2 - \varepsilon^3/3} \log(n)$$

Then for any set X of n points in \mathbb{R}^d , there exists a linear map $f : \mathbb{R}^d \rightarrow \mathbb{R}^k$ such that $\forall x_i \in X$,

$$(1 - \varepsilon)\|x_i - x_j\|^2 \leq \|f(x_i) - f(x_j)\|^2 \leq (1 + \varepsilon)\|x_i - x_j\|^2 \quad (13.17)$$

In effect the JL Lemma tells us that the quality of the projection down to some dimension k , is a function of some allowable error tolerance, ε , and the amount of points involved in the projection n . In particular the relative Euclidean distances will be distorted by a factor of no more than $(1 \pm \varepsilon)$, where $\varepsilon \in (0, 1)$. Note that this makes no reference to the initial dimension of the points existed in before the projection occurred.

Although the JL Lemma is used commonly with large datasets, we are only working with individual, possibly high-dimensional points, which are used as inputs into functions used in an objective function. Thus in the case of random projections of data points into functions we also must consider the effective dimension d_e . Theorem 2 of Wang et al.[17]

implies that no matter the degree of distortion which may occur, there shall always exist a solution in this lower dimensional space. This theorem is restated here in order to self-contain the paper.

Theorem 13.2.1 (Wang’s Existence Theorem) *Assume we are given a function $f : \mathbb{R}^D \rightarrow \mathbb{R}$ with effective dimensionality d_e and a random matrix $A \in \mathbb{R}^{D \times d}$ with independent entries sampled according to $\mathcal{N}(0, 1)$, where $d \geq d_e$. Then with probability 1, for any $x \in \mathbb{R}^D$, there exists a $y \in \mathbb{R}^d$ such that $f(x) = f(Ay)$.*

That is, we should always be able to find some y such that $f(x) = f(Ay)$, where $A \in \mathbb{R}^{D \times d}$ is some random matrix. And thus the distortion of the projection as predicted by the JL Lemma is not as important of a factor if we can ensure $d \geq d_e$, since with a good enough optimisation algorithm, if there exists a $x^* \in \mathbb{R}^D$ which is optimal, then there exists a $y^* \in \mathbb{R}^d$ such that $f(x^*) = f(Ay^*)$. In practice however we may by chance select some $d < d_e$, and so in these cases it may become informative to use JL Lemma as a guide to assist in understanding the degree of distortion which did indeed occur by projecting into this new subspace.

In order to ensure that the point-wise distances in this new subspace abides by the JL Lemma we consider random matrices of the form: $A_{i,j} \sim \mathcal{N}(0, 1/\sqrt{d})$. This is simply a scaled version of the random Gaussian matrices proposed by Wang et al. in Theorem 2, but a Gaussian matrix of this form is known to better preserves distance properties in this new subspace [16].

An issue which may occur when trying to use random embeddings for the purpose of optimisation is that the optimisation bounds which are defined in the larger D -dimensional space may be violated in the lower d -dimensional space. Thus, it is suggested to use a convex projection method to ensure that any variables $y \in \mathbb{R}^d$ fall the into bounding constraints defined by variables $x \in \mathbb{R}^D$. This idea is shown in Fig. 13.3.

Assuming that the feasible set for \mathbf{x} is defined with box constraints, denoted by $\mathcal{X} := [-c, c]^D$ where $c \in \mathbb{R}^+$, a simple way to ensure that $\mathbf{A}\mathbf{y}$ maps to the range defined by \mathcal{X} may be achieved through a least squares method [17]. Mathematically, we define: $p_{\mathcal{X}}(\mathbf{A}\mathbf{y}) = \operatorname{argmin}_{\mathbf{z}} \|\mathbf{z} - \mathbf{A}\mathbf{y}\|_2^2$, where $\mathbf{A}\mathbf{y} \in \mathbb{R}^D$, $\mathbf{z} \in \mathcal{X}$, and $p_{\mathcal{X}} : \mathbb{R}^D \rightarrow \mathcal{X}$ denotes *projection*. This least squares method effectively drops the perpendicular from points outside the bounding box, \mathcal{X} , which can be located arbitrarily in \mathbb{R}^D , towards the nearest point on the boundary of \mathcal{X} . This is made clear in Fig. 13.3.

13.3 Results

13.3.1 Ten-Dimensional Toy Problem

In this section the results of applying the combination of PSO and random embedding for inverse eigenvalue problems in structural engineering are explored. We begin by considering the 10 degree of freedom (DoF) system defined in Eqs. (13.18) and (13.19). The stiffness matrix is based on that of Sivan and Ram [22], with the mass matrix being modified from a diagonal of ones to allow for a more complex scenario.

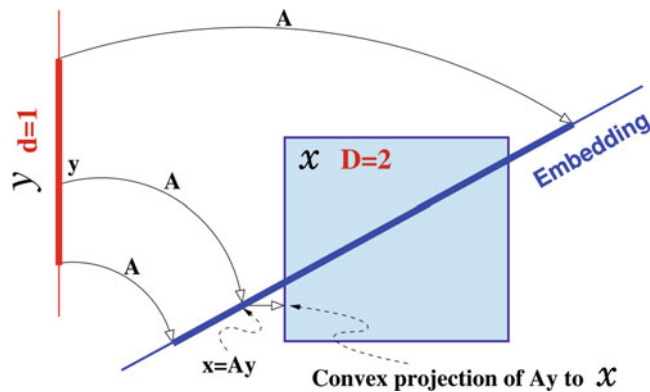


Fig. 13.3 Need to perform a convex projection [17]

$$\mathbf{K} = \begin{pmatrix} 200 & -10 & -20 & -5 & -5 & -10 & 0 & 0 & -50 & -50 \\ -10 & 100 & 0 & 0 & 0 & 0 & -20 & -10 & -20 & -10 \\ -20 & 0 & 300 & -40 & -30 & -60 & -10 & 0 & -20 & -10 \\ -5 & 0 & -40 & 400 & -30 & -40 & -50 & -20 & -10 & -70 \\ -5 & 0 & -30 & -30 & 150 & -10 & -5 & -5 & -20 & 0 \\ -10 & 0 & -60 & -40 & -10 & 250 & 0 & 0 & 0 & -80 \\ 0 & -20 & -10 & -50 & -5 & 0 & 120 & -5 & 0 & -10 \\ 0 & -10 & 0 & -20 & -5 & 0 & -5 & 250 & 0 & -100 \\ -50 & -20 & -20 & -10 & -20 & 0 & 0 & 0 & 350 & -40 \\ -50 & -10 & -10 & -70 & 0 & -80 & -10 & -100 & -40 & 400 \end{pmatrix} \quad (13.18)$$

$$\mathbf{M} = \text{diag}(1, \dots, 10) \quad (13.19)$$

The first two eigenvalues of the generalised eigenvalue problem defined through these particular mass and stiffness matrices are given in Eq. (13.20).

$$\Lambda = (10.99, 19.12) \quad (13.20)$$

Our aim for this problem will be to find some $\Delta\mathbf{M}$ and $\Delta\mathbf{K}$ matrices which will transform the system eigenvalues into those specified by Eq. (13.21).

$$\Lambda^* = (2.00, 5.00) \quad (13.21)$$

In particular we shall work to minimise the objective function defined previously in Eq. (13.3) in order to find the associated the Δ^* matrices. We assume without loss of generality that the Δ matrices are upper triangular, and real valued since the underlying \mathbf{M} and \mathbf{K} matrices are Hermitian and so are by definition symmetric. That is, it suffices to perturb only the upper (or lower) triangular portion of the \mathbf{M} and \mathbf{K} matrices. This means that for each of $\Delta\mathbf{K} \in \mathbb{R}^D$ and $\Delta\mathbf{M} \in \mathbb{R}^D$, there are $D(D+1)/2$ free parameters. In this way the amount of free parameters grows on the order of $\mathcal{O}(D^2)$. We thus use random projections to reduce the effect of this quadratic complexity. One convergence was run for a random projection which reduced the overall dimensional size by an order of magnitude, and another was reducing it by a factor of a half. Convergence results are shown in Fig. 13.4.

From Fig. 13.4a, it would appear that the initial rate of decrease of the random embedding space is slightly faster than the full dimensional space. However, as Fig. 13.4a then further suggests, although a low dimensional space may give a faster initial convergence rate, if the dimensionality reduction is too great, the optimisation routine can become plateau after a certain amount of iterations. This is seen in Fig. 13.4a as the random embedding space remains at approximately 10^0 after iteration 9. Thus it is clear that with this level of dimensionality reduction (for this particular problem), decreasing the

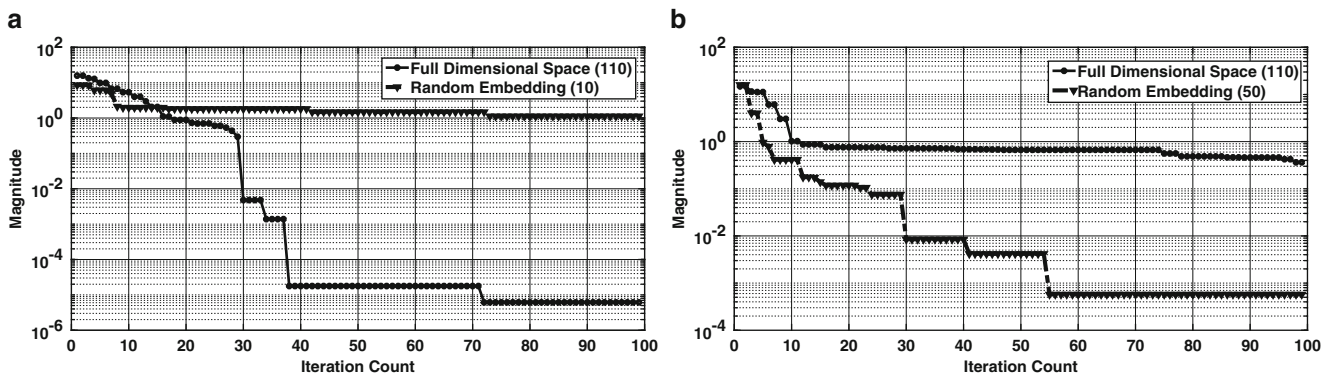


Fig. 13.4 A comparison of the convergence rates between the full-dimensional optimisation problem, and the reduced dimension problem. (a) The average convergence rates of a 110 dimensional space and a 10 dimensional space. (b) The average convergence rates of a 110 dimensional space and a 50 dimensional space

Table 13.1 How the distortion error effects the corresponding dimension of the mapped subspace, for $n = 110$ in accordance with the JL Lemma

Distortion error (%)	10	30	70	100
Dimension	4029	523	143	112

dimensions by an order of magnitude seems to introduce a bias into the optimisation problem. It is conjectured that this is because the value of ‘10’ lies well below the *effective dimension* (the d_e value) for this problem. This hypothesis is supported if we examine the same optimisation problem but instead reduce the exploration space to 50 dimensions as in the case of Fig. 13.4b. We notice that not only do we have the faster initial decrease in optimisation rate, but also we converge to better values, faster.

The reader may additionally notice that in Fig. 13.4a the 110 dimensional space reaches values as low as 10^{-6} , but in Fig. 13.4b it apparently stalls at 10^0 . However this is only due to the truncation of the plotting, since it has been hinted at approximately iteration 98 the full dimensional space starts to decrease its magnitude value again. But this only serves to demonstrate the notion within a 100 iteration limit the random projection has allowed the optimisation to converge better values, significantly faster on average. Indeed, the full dimensional space will *eventually* reach values as low as 10^{-6} , however this toy problem suggests that on average it will not be as fast. Also note that since Fig. 13.4b does not exhibit the same bias problems as in Fig. 13.4a, it would appear that $10 \leq d_e \leq 50$. Hence although we have not been able to determine the *effective dimension*, we can infer a range of existence for it.

Also important to take note of is that for this problem the JL Lemma is not readily applicable since this 110 dimensional space is too low for the Lemma to take practical significance. In particular, if we set $n = 110$ and assume error values of $\varepsilon \in \{0.1, 0.3, 0.7, 1.0\}$ we arrive at Table 13.1.

From Table 13.1 we see that for our toy problem, for an initial dimension of 110, the *sufficient* dimension to guarantee no more than a 10% error in the Euclidean distances between points in the new space is $4029 \gg 110 > 50$. This number seems unreasonable because in lower dimensions the bounds predicted by the JL Lemma are not tight. That is these bounds serve give an idea of *sufficiency*. Consequently by inspecting the mathematical equation of this bound, if the initial number of points is relatively low (as is the case for this toy example) we will not achieve a practically meaningful answer. However an important takeaway from the JL Lemma is that its formulation makes no reference to the initial dimension of projection, only the number of points considered, and so whether or not we began with 110 points, or 110^{110} points, the *sufficient* dimension to guarantee no more than a 10% error between points after a random embedding is $110 < 4029 \ll 110^{110}$. Thus in this case it can be concluded that the initial $n = 110$ value is too small for the JL Lemma to be directly useful.

13.3.2 One-Dimensional Boeing-737 Finite Element Problem

Here we shall explore how the PSO algorithm coupled with random embeddings may be exploited to assist in solving a truncated version of the generalised inverse eigenvalue problem for a 1D Boeing 737-300 (B737) Finite Element (FE) problem. In particular the model used to analyse the B737 plane is outlined in Fig. 13.5. This model is based upon one found in Theory of Matrix Structural Analysis [23].

In Fig. 13.5 it is assumed that the total wing mass is uniformly distributed over the wing span of length $2L$, and its mass is $2M_w$. Moreover the total mass of the fuselage is $2M_F$. The wing elements are approximated as being finite element beam structures and have flexural stiffness given by EI , with the effects of shear deformations and rotary inertia neglected. Assuming only two FE nodes were used in this model, then the one element FE beam matrix for this problem is outlined in Eq. (13.22), where R denotes the mass ratio between the fuselage and the wing, that is, $R = M_F/M_w$, and $\mathbf{q} = [w_1, \frac{\partial_1}{\partial x}, w_2, \frac{\partial_2}{\partial x}]^T$. In order to estimate a value for R the parameters for a B737 were obtained from literature, and summarised in Tables 13.4, 13.5, and 13.6. In order for the FE model to increase its accuracy more nodes must be used, which involves constructing a large block matrix using the elements defined in Eq. (13.22).

$$\left(\begin{array}{c} EI \\ L^3 \end{array} \left[\begin{array}{cccc} 12 & \text{symmetric} & & \\ 6L & 4L^2 & & \\ -12 & -6L & 12 & \\ 6 & 2L^2 & -6L & 4L^2 \end{array} \right] - \lambda M_w \left[\begin{array}{ccc} \frac{13}{35} + R \text{ symmetric} & & \\ \frac{11}{210}L & \frac{L^2}{105} & \\ \frac{9}{70} & \frac{13}{240}L & \frac{13}{35} \\ -\frac{13L}{420} & \frac{-L^2}{140} & -\frac{11L}{210} \frac{L^2}{105} \end{array} \right] \right) \mathbf{q} = \mathbf{0} \quad (13.22)$$

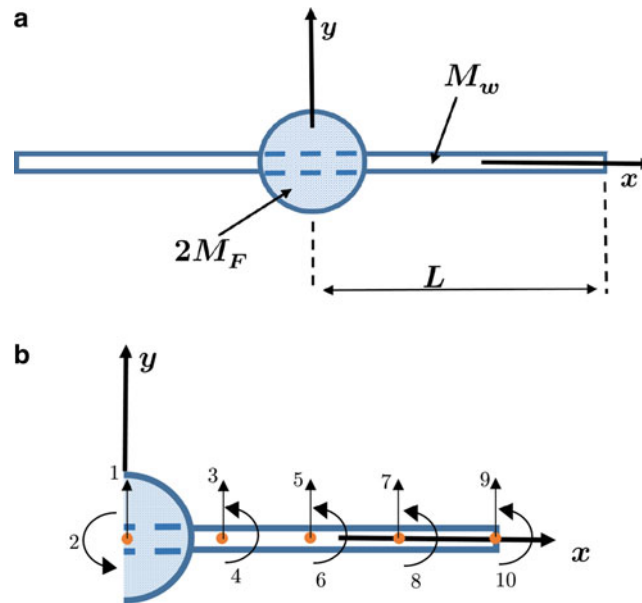


Fig. 13.5 Frontal views of the 1D Boeing 737-300 model which shall be used in the inverse eigenvalue problem. Images based upon Przemieniecki [23]. (a) Frontal view of 1D Boeing 737-300 model showing the fuselage mass, and the wings. (b) Frontal view of the 1D point-mass FE discretisation of the Boeing 737-300 model

As per the recommendation of Przemieniecki [23] the modal analysis of this structure may be separated into its symmetric and asymmetric counterparts, since this wing is symmetric around its fuselage centre. In order to enforce a symmetric condition, the second row and column of Eq. (13.22) needs to be removed since it represents a degree of rotational freedom of the fuselage mass. For symmetry the fuselage mass is only allowed the move in a translational sense (up and down), and as such should not have any gradient (that is, not be able to rotate about some axis). The opposite is true in the case of anti-symmetry where instead the first row and column of the mass and stiffness matrices were removed, since in the case of asymmetry, the fuselage is allowed to rotate about an axis and thus have a defined gradient. Note that although doing this will not dramatically change the eigenvector response of the full system (if they are scaled properly), it can shift the eigenvalues appreciably.

In order to assess the validity of this symmetric–asymmetric separation, Figs. 13.6 and 13.7 representing the modal responses were constructed. Firstly, the mode shapes are consistent with those formulated by Przemieniecki [23], and clearly there exists symmetry and asymmetry for the two shapes. Moreover we notice that the effect of the fuselage mass does have an appreciable albeit small effect on the symmetric modes, and no visible effect on the asymmetric modes, which agrees with Przemieniecki’s analysis, and general intuition. This is because the removal of the first row and columns of the elemental beam matrix results also removes the R variable. Notice also that in both cases (symmetric and asymmetric) there is an unconstrained mode, which mathematically exists due to the FE model having no fixed boundary conditions.

In order to simplify analysis only the symmetric bending mode cases are considered, since as Fig. 13.6a demonstrates, it takes into account the effect of the B737 model through the R variable. As before with the toy example, without loss of generality we aim to formulate the Δ matrices as upper triangular matrices, and perform the random embedding on these upper triangular matrices. However, different to the former case is that due to the reformulation of the problem as an FE model, it is now possible to arbitrarily grow the dimensionality of the problem by increasing the amount of elements of the FE model so that the optimisation problem can grow arbitrarily large, allowing for a more rigorous analysis of the potential usefulness and effects of random projections.

The first three non-dimensional symmetric-mode frequency values of the system under investigation are given in Table 13.2. The frequency values given are non-dimensionalised according to $\lambda^2 \sqrt{M_w L / (ET)}$, and $R = 0$ refers to the base-line reference (if the aircraft purely consisted of beam elements and no fuselage mass), whereas $R = 1.35$ refers to the B737 aircraft parameters, which are the values we will use in the optimisation procedure. As was mentioned earlier, the existence of the fuselage mass does indeed alter the eigenvalues in an appreciable manner. For the optimisation problem, we aim to alter the first three non-dimensional frequencies of the symmetric bending mode to become: $\omega = [2, 7, 22]$. That

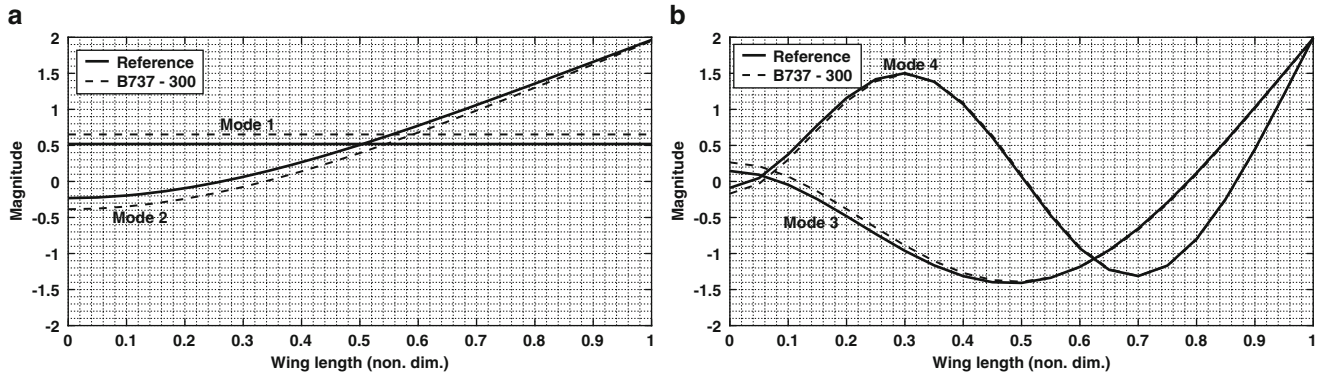


Fig. 13.6 Symmetric bending modes for the 1D B737 FE model. (a) The first two symmetric bending modes (modes 1 and 2). (b) The second two symmetric bending modes (modes 3 and 4)

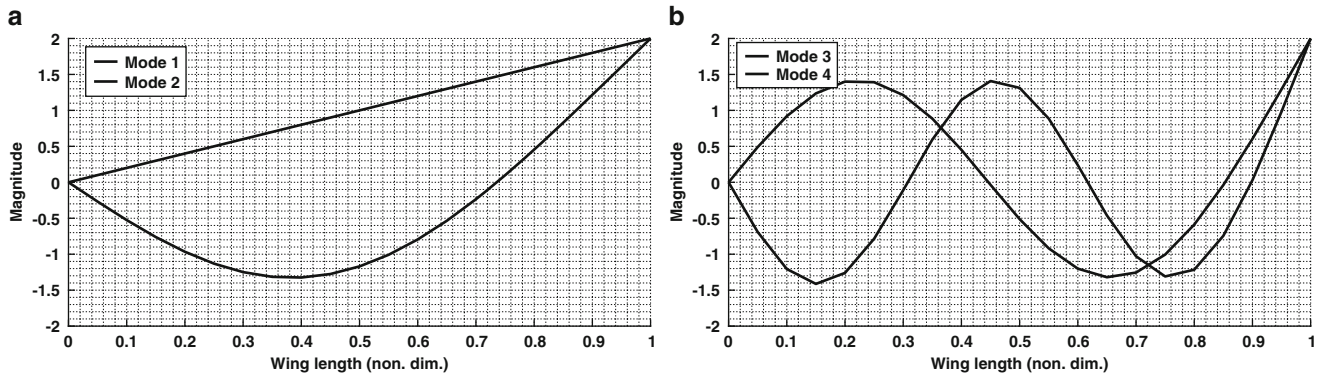


Fig. 13.7 Asymmetric bending modes for the 1D B737 FE model. (a) The first two asymmetric bending modes (modes 1 and 2). (b) The second two asymmetric bending modes (modes 3 and 4)

Table 13.2 First three non-dimensional symmetric-mode frequency values, of the FE model aircraft, non-dimensionalised by $\lambda^2 \sqrt{M_w L / (ET)}$, where $R = M_F / M_w$ is the fuselage-to-wing mass ratio

Frequency number	R = 0	R = 1.35
1	0	0
2	5.59	4.09
3	30.23	23.36

is we would like the following mapping to occur between the eigenvalues, $[0, 4.09, 23.36] \xrightarrow{\Delta} [2, 7, 22]$. This is why only the first three eigenvalues are shown in Table 13.2. Note however any number of eigenvalues may be used, and that from a physical point of view, it does not necessarily make sense to be transforming the first eigenvalue from ‘0’ to ‘2’ since this changes the constraints of the system (as ‘0’ represents rigid body motion). However, the emphasis of this paper is to explore PSO as applied to inverse structural eigenvalue problems in parallel with random projections, and so the objective functions were chosen arbitrarily.

The convergence behaviour for this optimisation problem is shown in Fig. 13.8. In all three cases we note extremely similar behaviour as compared to the toy example. That is, convergent behaviour in the lower dimensional space is initially and consistently much faster in the sense that (faster in the sense that with less iterations, the random embedding method tends to have a much lower objective function magnitude). Eventually however, the full dimensional space does *tend* to approach similar values to the random embedding but this is to be expected, since the full system always perfectly describes the problem, and the problem at hand also does seem to possess a very low effective dimensionality, implying that the optimisation procedure may not need to actively explore all possible dimensions. That is, although the full dimensional space seems high, the particle swarm doesn’t need to explore it fully to obtain a good solution. Regardless of the conjectured advantages of this particular problem, the random projection assists in the notion of *faster* convergence behaviour across all areas.

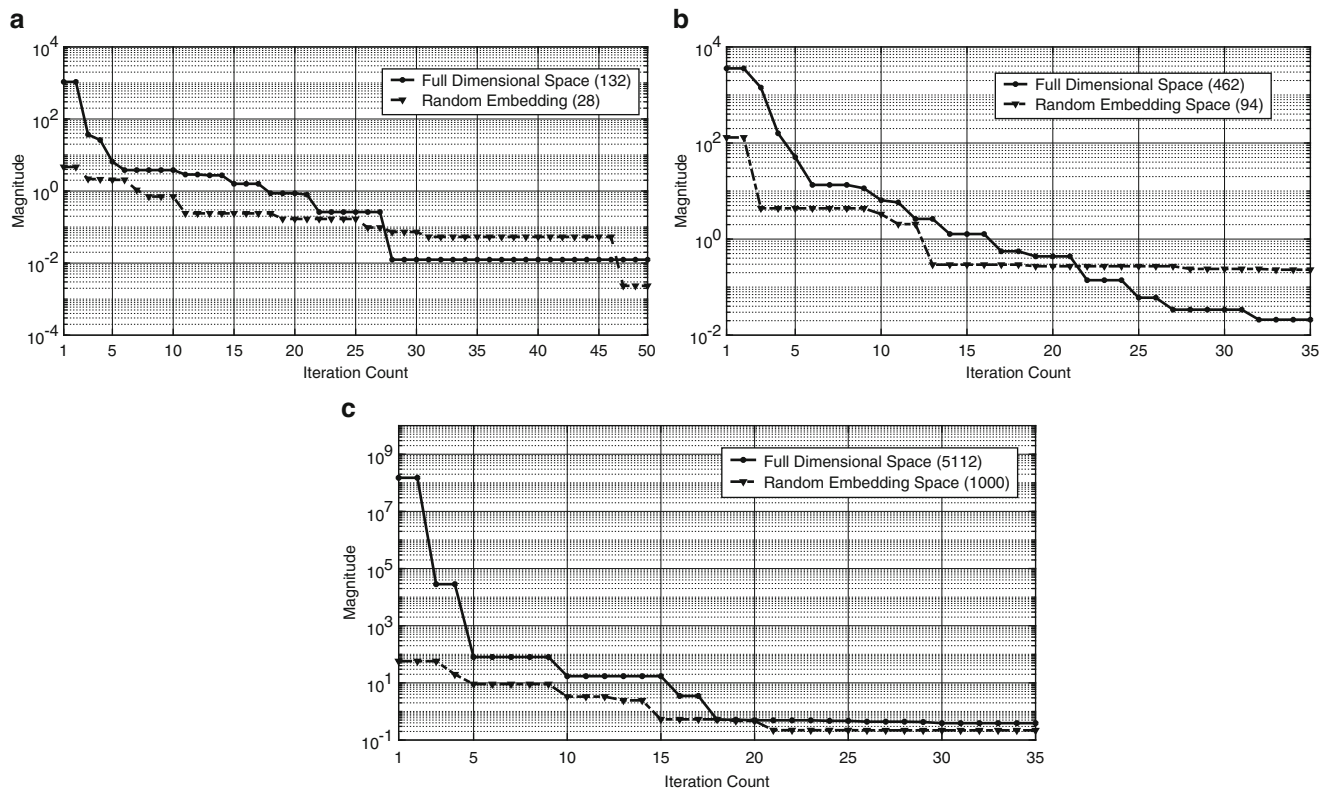


Fig. 13.8 Convergence behaviour of the optimisation problem comparing the full dimensional, and dimensionally reduced spaces. In all cases a population of 500 particles were used, and a standard dimensional reduction of 80% was used for consistency. (a) Convergence of a 5 element discretisation resulting in 132 free parameters. (b) Convergence of a 10 element discretisation resulting in 462 free parameters. (c) Convergence of a 35 element discretisation resulting in 5112 free parameters

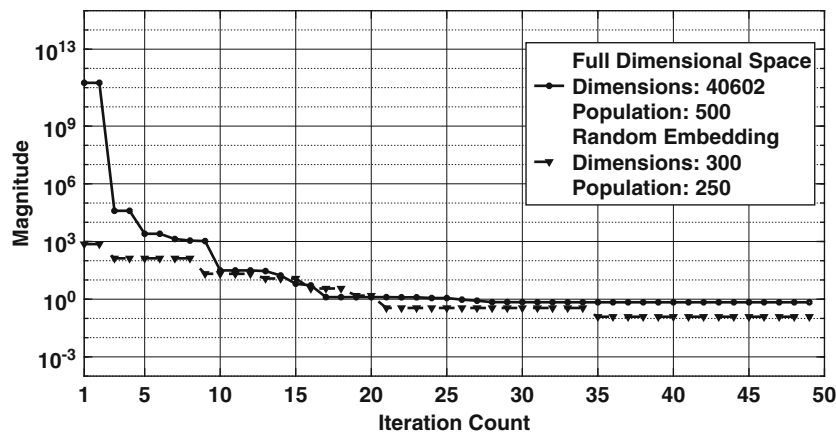


Fig. 13.9 An extreme example showcasing the convergence of a 100 element discretisation resulting in 40,602 free parameters. A dimension reduction of 99.3% was used

In order to explore the capabilities of random embedding even further, it was applied to a case of a 100 element model for the aircraft. This resulted in a large search space of 40,602 free parameters to explore for optimisation. It was proposed to reduce the dimensionality of the problem by 99.3% resulting in a random embedding space of only 300 free parameters. In addition to this, the total amount of particles used in the swarm was reduced by a factor 2 (from 500 to 250). The result of this is shown in Fig. 13.9.

Table 13.3 How the distortion error effects the corresponding dimension of the mapped subspace, for $n = 40,602$ in accordance with the JL Lemma

Distortion error (%)	10	30	50	70	100
Dimension	9096	1180	510	325	255

From Fig. 13.9 once again extremely similar behaviour can be observed as in the previous problems. That is, the lower dimensional space is able to achieve much lower objective function magnitudes, a lot more rapidly. Moreover in this example, it was shown to be able to do this not only in less iterations, but also with less overall particles. In addition, the overall converged solution of this lower dimensional space is much better than the full dimensional solution which simply found it very difficult on average to converge to good values due to the enormous search space. The full dimensional solution could only converge on the order of 10^0 on average, whereas the reduced dimension solution is able to converge to a value on the order of 10^{-2} on average.

Thus as this paper has consistently demonstrated, through the use of random embedding we are able to significantly increase the speed and quality of convergence of a PSO optimiser, in terms of using less overall particles, coupled with less total iterations, ultimately leading to greater overall computational efficiency, in less total time. Note in this case we say ‘a’ solution since the inverse eigenvalue problem with incomplete modal information is in a well known ill-conditioned problem and there does exist many locally optimal solutions. However the main purpose of this paper was not to explore the ability to achieve the global optima (which for the inverse eigenvalue problem, may not necessarily even be the best solution depending on context), but to analyse the applicability of using random projections alongside PSO in order to study the efficiency of an underlying optimisation procedure in the field of structural engineering.

A further point of discussion for the extremely high dimensional problem explored in Fig. 13.9 is to consider the level of distortion that has occurred to the original surface when projecting down to a surface which has 99.3% less overall dimensions. Table 13.3 summarises the relationship for $n = 40,602$ for the JL Lemma. Here we note that for a 70% average discrepancy between the pairwise Euclidean distances of the points in the new lower dimensional space, 325 dimensions are *sufficient*, which is comparable to what was used in Fig. 13.9. Thus the geometry between adjacent points in this new subspace are most likely significantly different to what was in the original high dimensional space. Regardless however, it was nevertheless possible to converge to extremely good values suggesting that even though there may be a large geometric distortion, $d_e \leq 300$. And thus by Theorem 13.2.1 there exists a solution (or several), which we are able to find due to the strength of the black-box PSO algorithm. Note however that if we did not opt to reduce the dimensions by 99.3%, but by a factor of $\approx 80\%$ we could still optimise with 9096 dimensions and achieve no more than 10% error in the pairwise Euclidean distances between points. However the surface distortion issue does not appear to be a huge problem given that the problem has a low underlying effective dimension, and a good optimiser is used (as is the case of PSO).

Lastly it is important for the reader to note that the solutions obtained in this paper will be nonphysical. This is because the Δ matrices are assumed to be full rank, upper-triangular matrices, without physical constraints applied to them (apart from symmetry being enforced via the upper-triangular nature of Δ). In order to enforce complete physicality of the solution it would be necessary to place constraints in the search space (either through equality and or inequality constraints). This idea has been explored partly by previous authors [22, 24], but it remains an open question in the case of truncated modal systems. Nevertheless, although it would be trivial to place constraints on the systems explored in this paper, it remains that the purpose of this paper is to explore the viability of dimensionality reduction for structural vibration problems, of which the results appear to be extremely promising. The placement of constraints would not allow the justified exploration of spaces as high approximately 40,000 in the case of 1D FE model structures.

13.4 Conclusion

Random projection is a popular technique used to reduce the dimensionality of a problem. It has been demonstrated in this paper that by using random projections we were able to successfully perform optimisation in this lower dimensional space which resulted in much faster overall convergence, faster in the sense that on average less iterations were required to achieve much better results. This was demonstrated on an example 10-dimensional toy problem, as well as on a 1-D FE model of a Boeing 737-300 aircraft. Moreover the existence of a moderately small effective dimension was predicted to exist

for generalised inverse eigenvalue problems which have Hermitian matrices. Moreover it was demonstrated experimentally that gradient-based approaches for performing optimisation for eigenvalue problems may necessitate prohibitively small step sizes, which tends to suggest that non-gradient, black-box optimisation methods may be preferred for these types of problems.

Appendix: Boeing 737-300 Data and Formulation

An overview of the data used in modeling the 1D FE model B737 structure is presented in this section, as well as a technical diagram used to extract some of its lengths (Tables 13.4, 13.5, and 13.6).

The equations used for estimating the fuselage and wing masses are available from Roskam [26], in particular the Equations used below refer to Eqs. (15.46), and (15.49) in Roskam. All terms of the below equations are defined in this reference. An overview of the physical dimensions of the aircraft is shown in Fig. 13.10.

$$W_{\text{wing}} = 0.036 S_w^{0.758} W_{fw}^{0.0035} \left(\frac{A}{\cos^2 \Lambda} \right)^{0.6} q^{0.006} \lambda^{0.04} \left(\frac{100t/c}{\cos \Lambda} \right)^{-0.3} (N_z W_{dg})^{0.49} \quad (13.23)$$

$$W_{\text{fuselage}} = 0.052 S_f^{1.086} (N_z W_{dg})^{0.177} L_t^{-0.051} (L/D)^{-0.072} q^{0.241} + W_{press} \quad (13.24)$$

$$W_{press} = 11.9 + (V_{pr} P_\delta) \quad (13.25)$$

Table 13.4 General Flight Parameters, available from *Jane's all the World's Aircraft* [25]

Parameters	Value	Units
Cruise velocity	725.43	ft/s
Cruise altitude	30,000	ft
Air density at cruise	8.91×10^{-4}	slugs/ft ³
Dynamic pressure	234.44	lb/ft ²
Ultimate load factor	5.7	–
Design gross weight	109,269.60	lb

Table 13.5 Fuselage Parameters, available from *Jane's all the World's Aircraft* [25]

Parameters	Value	Units
Length	105.94	ft
Depth	12.33	ft
Wet area	4104.80	ft ²
Tail length	15.89	ft
Cabin Δ pressure	8.00	Pa

Table 13.6 Wing Parameters, available from *Jane's all the World's Aircraft* [25]

Parameters	Value	Units
Wet area	1133.90	ft ²
Weight of fuel in wing	35,640.00	lb
Aspect ratio	9.16	–
Wing sweep at 25% MAC	25.00	Degrees
Thickness-to-chord ratio	8.00	–

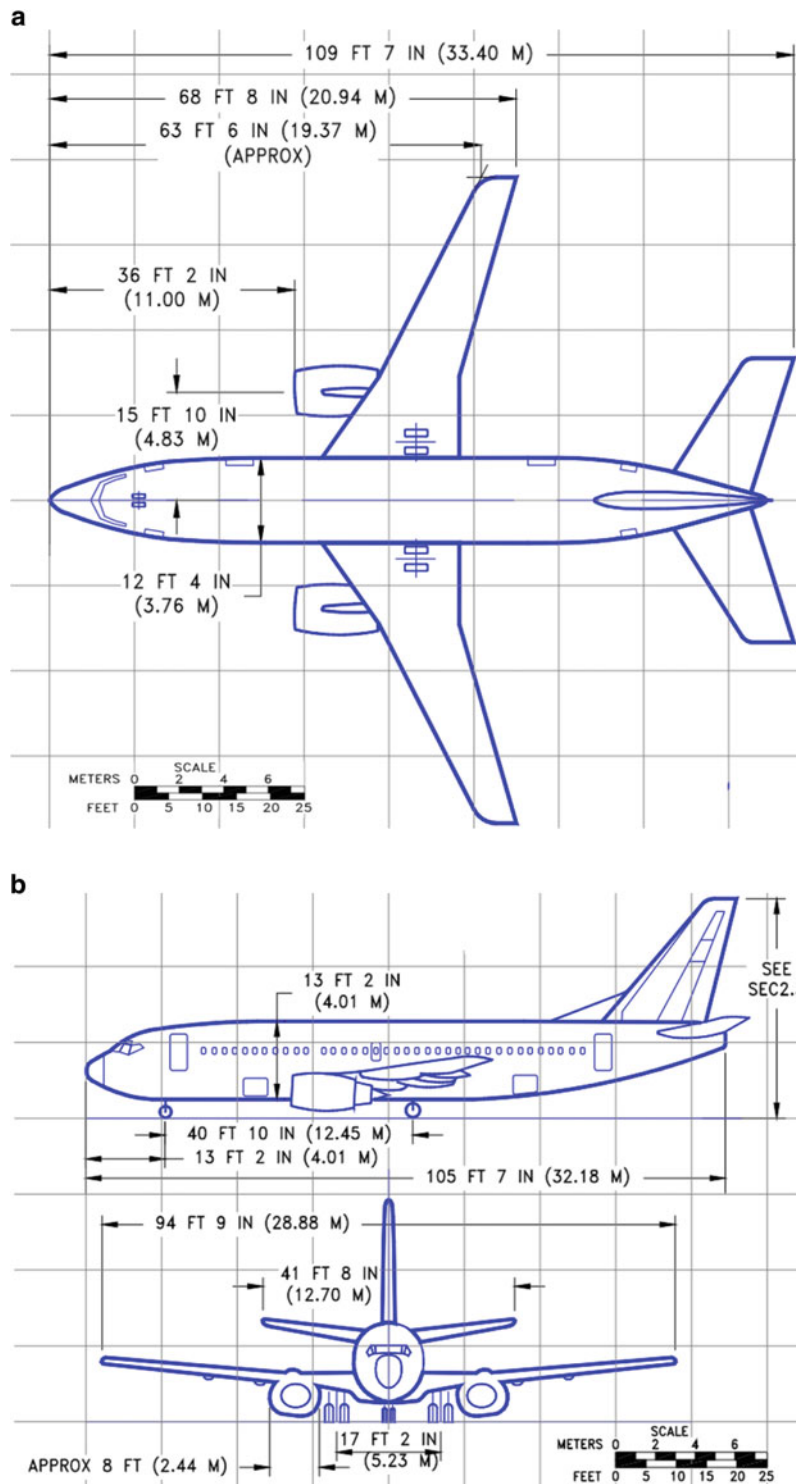


Fig. 13.10 Design views of the Boeing 737 aircraft used to estimate certain lengths in Tables 13.4, 13.5, and 13.6 [27]. (a) Top view of a Boeing 737-300. (b) Side and front views of a Boeing 737-300

References

1. Bathe, K.J., Wilson, E.L.: Solution methods for eigenvalue problems in structural mechanics. *Int. J. Numer. Methods Eng.* **6**(2), 213–226 (1973)
2. Elishakoff, I.: Some questions in eigenvalue problems in engineering. In: *Numerical Treatment of Eigenvalue Problems Vol. 5/Numerische Behandlung von Eigenwertaufgaben Band 5*, pp. 71–107. Springer, Berlin (1991)
3. Lima, E.E.S., Fernandes, L.F.J.: Assessing eigenvalue sensitivities [power system stability]. In: *Power Engineering Society Summer Meeting, 2000. IEEE*, vol. 3, pp. 1958–vol. IEEE, Piscataway (2000)
4. Hansen, M.H.: Aeroelastic instability problems for wind turbines. *Wind Energy Int. J. Prog. Appl. Wind Power Convers. Technol.* **10**(6), 551–577 (2007)
5. Day, J.D.: Run time estimation of the spectral radius of Jacobians. *J. Comput. Appl. Math.* **11**(3), 315–323 (1984)
6. Sun, M., Makki Alamdari, M., Kalhori, H.: Automated operational modal analysis of a cable-stayed bridge. *J. Bridg. Eng.* **22**(12), 05017012 (2017)
7. Chu, M., Golub, G., Golub, G.H.: *Inverse Eigenvalue Problems: Theory, Algorithms, and Applications*, vol. 13. Oxford University Press, Oxford (2005)
8. Chu, M.T.: Inverse eigenvalue problems. *SIAM Rev.* **40**(1), 1–39 (1998)
9. Eberhart, R., Kennedy, J.: A new optimizer using particle swarm theory. In: *Proceedings of the Sixth International Symposium on Micro Machine and Human Science, 1995 (MHS'95)*, pp. 39–43. IEEE, Piscataway (1995)
10. Van den Bergh, F., Engelbrecht, A.P.: A convergence proof for the particle swarm optimiser. *Fund. Inform.* **105**(4), 341–374 (2010)
11. Yoshida, H., Kawata, K., Fukuyama, Y., Takayama, S., Nakanishi, Y.: A particle swarm optimization for reactive power and voltage control considering voltage security assessment. *IEEE Trans. Power Syst.* **15**(4), 1232–1239 (2000)
12. Vishwanathan, A., Cheema, P., Vio, G.: Multi-particle swarm optimization used to study material degradation in aeroelastic composites including probabilistic uncertainties. In: *2017 IEEE Congress on Evolutionary Computation (CEC)*, pp. 2458–2464. IEEE, Piscataway (2017)
13. Vishwanathan, A., Cheema, P., Vio, G.A., et al.: Robust optimisation of time-varying aeroelastic composite structures using multi-particle swarm optimization. In: *17th Australian International Aerospace Congress: AIAC 2017*, p. 599. Engineers Australia, Royal Aeronautical Society, London (2017)
14. Gaing, Z.-L.: A particle swarm optimization approach for optimum design of PID controller in AVR system. *IEEE Trans. Energy Convers.* **19**(2), 384–391 (2004)
15. Bingham, E., Mannila, H.: Random projection in dimensionality reduction: applications to image and text data. In: *Proceedings of the Seventh ACM SIGKDD International Conference on Knowledge Discovery and Data Mining*, pp. 245–250. ACM, New York (2001)
16. Johnson, W.B., Lindenstrauss, J.: Extensions of Lipschitz mappings into a Hilbert space. *Contemp. Math.* **26**(189–206), 1 (1984)
17. Wang, Z., Hutter, F., Zoghi, M., Matheson, D., de Feitas, N.: Bayesian optimization in a billion dimensions via random embeddings. *J. Artif. Intell. Res.* **55**, 361–387 (2016)
18. Gardner, J.R., Kusner, M.J., Xu, Z.E., Weinberger, K.Q., Cunningham, J.P.: Bayesian optimization with inequality constraints. In: *Proceedings of ICML*, pp. 937–945 (2014)
19. Krummenacher, G., McWilliams, B., Kilcher, Y., Buhmann, J.M., Meinshausen, N.: Scalable adaptive stochastic optimization using random projections. In *Advances in Neural Information Processing Systems*, pp. 1750–1758 (2016)
20. Van den Bergh, F., Engelbrecht, A.P.: A study of particle swarm optimization particle trajectories. *Inf. Sci.* **176**(8), 937–971 (2006)
21. Eberhart, R.C., Shi, Y.: Comparing inertia weights and constriction factors in particle swarm optimization. In: *Proceedings of the 2000 Congress on Evolutionary Computation, 2000*, vol. 1, pp. 84–88. IEEE, Piscataway (2000)
22. Sivan, D.D., Ram, Y.M.: Mass and stiffness modifications to achieve desired natural frequencies. *Commun. Numer. Methods Eng.* **12**(9), 531–542 (1996)
23. Przemieniecki, J.S.: *Theory of Matrix Structural Analysis*. Courier Corporation, Chelmsford (1985)
24. Olsson, P., Lidström, P.: Inverse structural modification using constraints. *J. Sound Vib.* **303**(3–5), 767–779 (2007)
25. Taylor, J.W.R.: *Jane's All the World's Aircraft: Founded in 1909 by Fred T. Jane*. Macdonald and Janes's, London (1976)
26. Raymer, D.P.: *Aircraft Design: A Conceptual Approach*. American Institute of Aeronautics and Astronautics, Inc., Reston, 21 (1999)
27. Boeing.: *737 Airplane characteristics for airport planning*. Technical report, 09 (2013)

Chapter 14

Modal Analysis of Wind Turbine Blades with Different Test Setup Configurations



E. Di Lorenzo, S. Manzato, B. Peeters, V. Ruffini, P. Berring, P. U. Haselbach, K. Branner, and M. M. Luczak

Abstract Modal testing of large structures such as wind turbine blades poses several challenges. Applied test setup configuration, test specimen mounting and measurement equipment are known to affect the test results. This paper presents a comparison study of the modal tests of nominally identical 14.3 m long blades. Blade A was supported in free-free boundary conditions and tested with the Experimental Modal Analysis using accelerometers. Blade B was clamped to a concrete block and tested with Operational Modal Analysis and strain gauges. The modes and corresponding natural frequencies obtained from both test cases were compared and correlated with the numerical models of the blades.

Keywords Experimental modal analysis · Operational modal analysis · Strain modal analysis · Wind turbine blade · Structural dynamics identification

14.1 Introduction

Wind turbine blades are tested according to the IEC-61400-23 standard for certification purposes [1]. The test program shall compose mass, centre of gravity and natural frequencies, static tests, fatigue load tests and post fatigue static tests. The static tests are undertaken to verify the blade's ability to resist the ultimate design loads and to relate blade properties, strains and deflections arising from the applied loads. Fatigue tests should ensure that the blade stiffness does not significantly change throughout the test and thus, the blade will be reaching the designed lifetime of 20 (according to IEC-61400-1-ed4) years. Dynamic tests are limited to the identification of the first and second flapwise natural frequencies, and of the first edgewise one. Tests aimed at damping and mode shapes estimation are only optional. However, a deeper understanding of the dynamic behavior of these structures is crucial to better analyze stability problems and failure modes, especially considering the continuing trend to further increase the size, complexity and flexibility of the blades [2].

In addition, the results from a modal test can also be used to validate numerical Finite Element (FE) models to a high degree of accuracy. These models are normally property of the manufacturer of the blade, and for this reason a proper validation is not always possible. In the case discussed in this paper, the FE model is available since it was generated by using DTU's in-house software, which allowed performing a full validation and updating of the model [3].

An extensive measurement campaign was performed at DTU Wind Energy, where a comparison study was carried out on two nominally identical wind turbine blades that were tested in different configurations. For the first test, a blade was supported in free-free boundary condition. Two shakers were used for excitation, and several accelerometers to record the responses at several locations. The data were processed according to the principles of Experimental Modal Analysis (EMA) to identify natural frequencies, modal damping and mode shapes, thus exceeding standard certification requirements.

As a second step, a second blade (nominally identical to the first one) was clamped to a concrete block and a "pull and release test" was performed. Operational Modal Analysis (OMA) was then applied to the strain gauge data used to acquire the structural response at several locations along the blade. Finally, Strain-based Modal Analysis was used to estimate the modal parameters.

E. Di Lorenzo · S. Manzato · B. Peeters
RTD Test Division, Siemens Industry Software NV, Leuven, Belgium

V. Ruffini
Faculty of Engineering, University of Bristol, Clifton, UK

P. Berring · P. U. Haselbach · K. Branner · M. M. Luczak (✉)
Department of Wind Energy, Technical University of Denmark, Roskilde, Denmark
e-mail: mluz@dtu.dk

The structure of the paper is as follows: First, the two test setups will be described in greater detail. Afterwards, the results and the challenges related to both will be analyzed. Finally, the correlation with the FE model will be discussed in both cases.

14.2 Test Setups

The object of the study is a 14.3 m long wind turbine blade made of glass fiber reinforced plastics. Multiple modal tests were carried out to identify the most reliable and time-efficient technique for estimating the modal parameters of the structure under test.

During the first test, the blade was suspended by two elastic chords to reproduce free-free boundary conditions in order to validate the numerical model, as shown in Fig. 14.1. For an optimal excitation of the blade, both edgewise and flapwise directions were excited at two locations: one approximately 4.5 m from the blade root at the suction side (flapwise direction), and one at 8 m from the root on the leading edge (edgewise direction), similarly to the approach adopted in [4].

The structure was excited first with a modal hammer weighing 1 kg with a soft tip to ensure a good excitation between 3 and 150 Hz. In a successive test, a pair of electrodynamic shakers was used in a Multiple-Input Multiple-Output (MIMO) set-up. Both connections between the shakers and the blade were instrumented with load cells in order to get measurements of the applied forces. Finally, a dense grid of 120 measurement points was defined to cover the entire surface of the blade, and the set of 15 available triaxial accelerometers was distributed over 15 equidistant cross sections ranging from the root to the tip of the blade. Afterwards, the 15 accelerometers were moved to a different location along the airfoil, and the measurements were repeated for 8 different locations. The test geometry with the locations of all accelerometers is also shown in Fig. 14.1.

A second test on a nominally identical blade has been performed by instrumenting the structure with 76 strain gauges in order to measure the deformation in several locations during a pull and release test. In this case the blade was clamped to a rigid block through the circular interface plate in a flapwise configuration (Fig. 14.2), and then pulled towards the floor. The applied force and displacements were measured through a reel cable extensometer. Once the blade tip had reached the desired displacement, it was released, and the free vibration response recorded. Afterwards, the measurements from the 76 strain gauges present on the blade were imported into Simcenter Testlab for further processing.

Specifically, Strain-based Modal Analysis [5] was applied, and the results in terms of modal parameters have been compared to numerical results. The strain gauges location is also shown in Fig. 14.2. The gauges used in the experiment



Fig. 14.1 Top view of the wind turbine blade setup (left); test geometry by using accelerometers in free-free conditions (right)

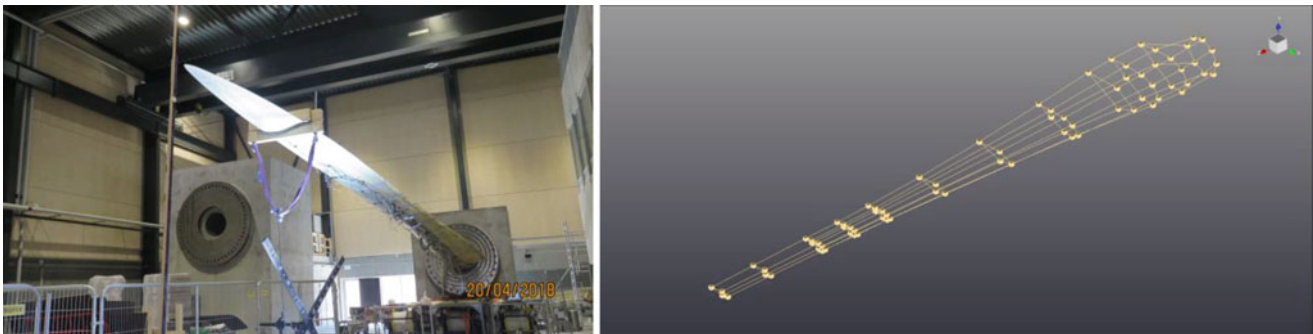


Fig. 14.2 View of the wind turbine blade setup during the pull and release test instrumented with strain gauges (left); test geometry by using strain gauges in clamped conditions (right)

were HBM strain gauges type 10/350 LY 11 with resistance of $350 \Omega \pm 0.35\%$. This type of strain gauges has built in ability to compensate the change of elongation with changing temperatures. Owing to such solution, there was no need of application of dummy strain gauge that would measure the temperature changes in the system, as done in the past. The devices of this type are applicable for strain measurement in one direction—they are denominated as linear strain gauges.

14.3 Hammer vs. Shaker FRF Testing in Free-Free Boundary Conditions

The choice of the excitation when performing a modal test is a crucial step. Several considerations need to be taken into account, especially when testing big structures such as wind turbine blades. In the case of this study, since it was necessary to move the sensors (e.g. accelerometers) from one run to the next, it was fundamental to ensure the repeatability of the excitation source so that all data could be processed together and yield global results. Hammer excitation repeatability depends on the user ability to apply consistently the same impact. Shaker excitation is based on the definition of a reference force profile that can be reproduced with high levels of accuracy, and for this reason should be preferred to the hammer excitation.

During the free-free boundary conditions tests, both excitation modes were applied. Figure 14.3 shows the Driving Point Frequency Response Functions (FRFs) measured during the eight runs with hammer and shaker excitation in both directions. The FRFs in the edgewise direction are very repeatable regardless of the excitation technique. However, the impact testing results show a higher variability, especially at higher frequencies. The noise level was also higher overall than the one obtained by using the shaker excitation. On the other hand, the flapwise results show very poor repeatability with shaker excitation. This is because, during the tests, the shaker was often detaching from the blade because of blade oscillation. The issue could have been solved by using a fixed connection between the shaker and the blade, but it was necessary to use glue to avoid damaging the blade with fixed mechanical connections. In this case, consistently exciting with the hammer was much simpler.

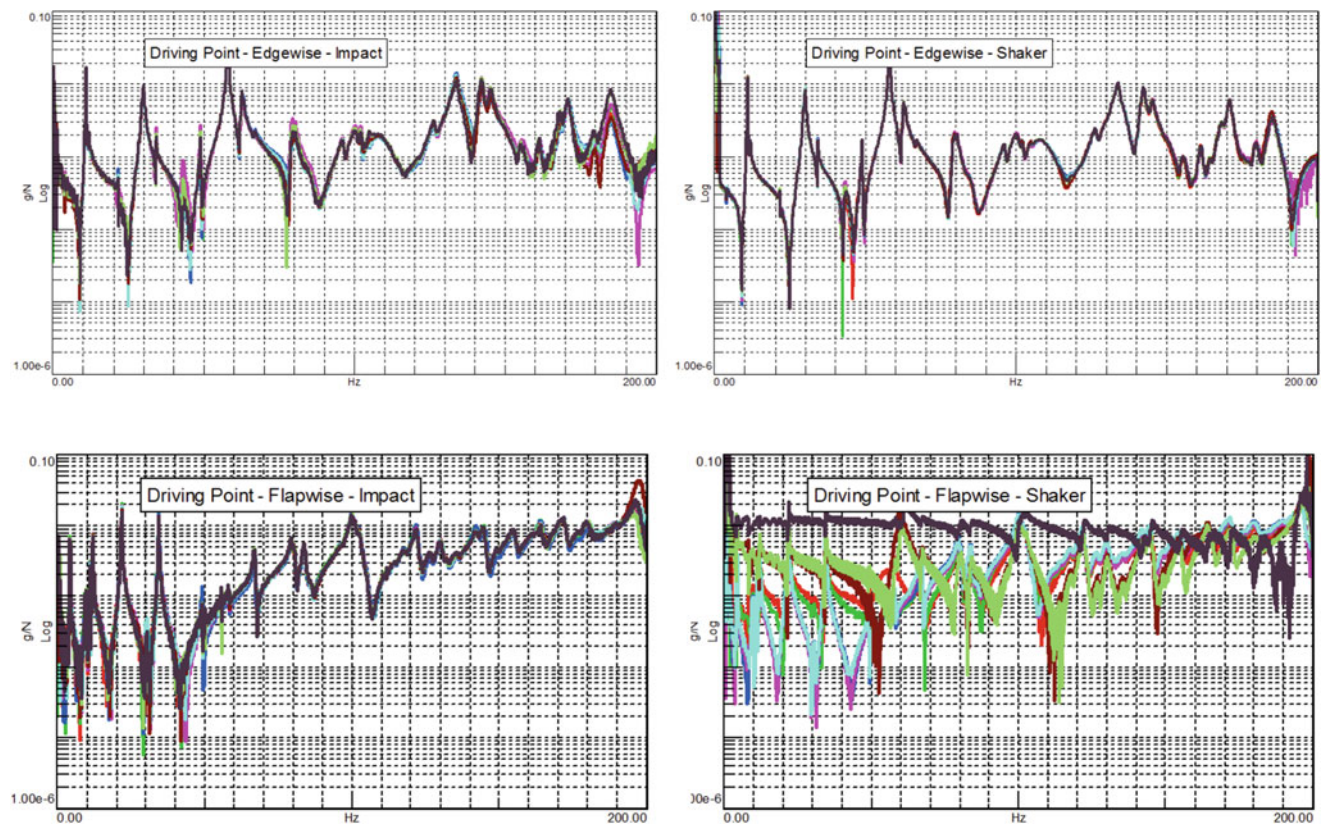


Fig. 14.3 Repeatability analysis: Driving Point FRF over the eight measurement runs for Hammer (left) and Shaker (right) excitation in both Edgewise (Top) and Flapwise (Bottom) direction

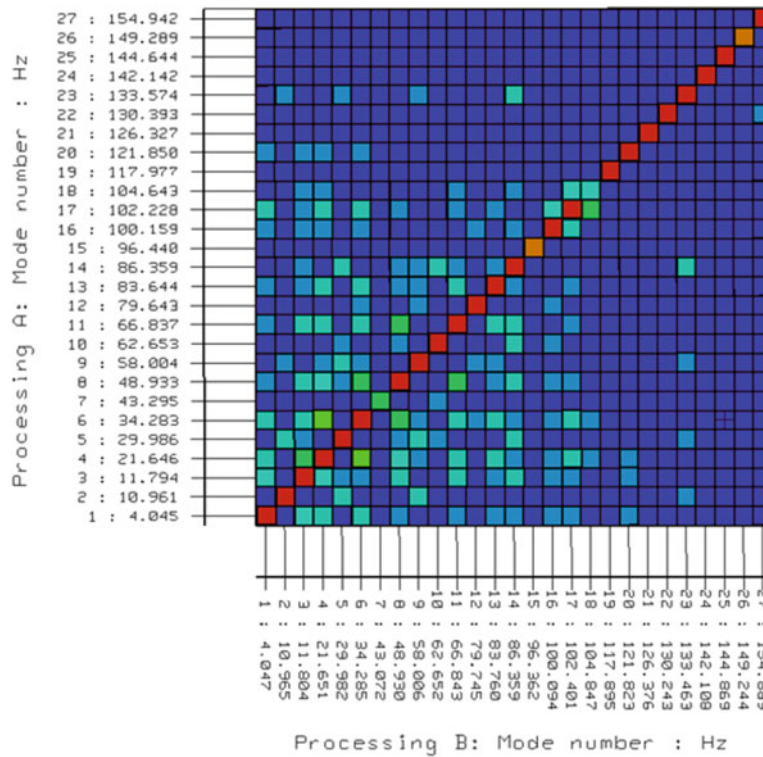


Fig. 14.4 Modal Assurance Criterion matrix for the modal vectors estimated from impact and shaker tests

The FRFs collected in both cases (hammer and shaker testing) were used for estimating the modal parameters of the wind turbine blade by using Simcenter Testlab and the Polymax algorithm [6]. Very low discrepancies are present with respect to the natural frequency identification, whereas more uncertainty characterizes the damping estimates. The differences can be associated to the signal-to-noise ratio, which is lower in the hammer case than in the shaker case.

The mode shapes extracted from the hammer and shaker tests show very good match up to 150–160 Hz, as shown in the Modal Assurance Criterion (MAC) matrix in Fig. 14.4. MAC values close to 100% on the main diagonal confirm that modal vectors from impact and shaker excitation are nearly identical. Low values of the off-main diagonal terms confirm the modes are well discriminated.

14.4 Correlation with FE Model

The numerical Finite Element (FE) model developed in [3] was used for pre-test analysis and for correlation purposes. The model was generated by using the commercial software MSC Patran and DTU Wind Energy in-house software Blade Modeling Tool (BMT). As the experimental grid was derived from the numerical model, no geometric correlation is required as the measurement points were defined to coincide with a node in the FE model. Consequently, the Modal Assurance Criterion between the numerical and experimental could be calculated without further interpolations, and the results are displayed in Fig. 14.5. A good correlation is observed for the first 13 modes, while at higher frequencies, as is generally the case, the model and the experiments start to diverge, as shown in Table 14.1. This is expected observation, as the estimated mode shapes turn from global at lower frequencies towards more local at higher frequency. It is possible to improve the mode shape correlation by increasing the number of measurement locations.

In general, very good agreement was found between all modes with a dominant flapwise direction, with errors between the natural frequencies ranging between 1% and 5%. On the other hand, larger discrepancies (with errors around 10%) were observed for the modes in the edgewise and torsional directions. Before drawing further conclusion, it will be necessary to

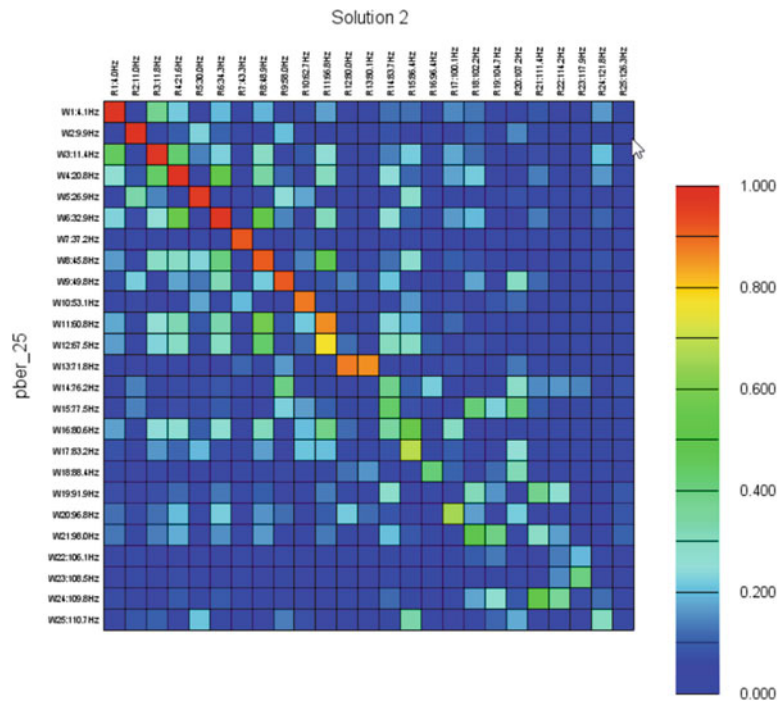


Fig. 14.5 Modal Assurance Criterion between numerical and experimental mode shapes

Table 14.1 Results of correlation analysis between test and simulation results

Mode No.	Test (Hz)	FEM (Hz)	MAC	Freq. error (%)
1	4.05	4.13	0.98	2.14
2	10.96	9.87	0.98	-9.91
3	11.80	11.36	0.97	-3.71
4	21.65	20.81	0.98	-3.86
5	29.98	26.89	0.96	-10.31
6	34.28	32.86	0.97	-4.16
7	43.30	37.25	0.92	-13.98
8	48.93	45.76	0.91	-6.49
9	58.00	49.85	0.92	-14.06
10	62.67	53.14	0.88	-15.20
11	66.84	60.82	0.86	-9.00
12	80.00	71.75	0.87	-10.31
13	86.41	83.19	0.69	-3.73
14	100.10	96.78	0.66	-3.32
15	111.40	109.80	0.53	-1.44
16	133.59	110.73	0.59	-17.11

try to include in the FE model the elastic cords used to suspend the blade. The blade support configuration applied in the test is best available approximation of the free-free boundary conditions. In reality it introduces an observable constraint of the Degree Of Freedom (DOF) by adding stiffness in the edgewise direction. Indeed, the natural frequencies are consistently lower in this direction, so adding the stiffness of the bungees in FE model is expected to bring the numerical and experimental results closer. In general, the good correlation between the global modes at low frequencies gives confidence in the general validity of the model and the general assumption, and an update of the material properties is not deemed necessary at this stage. In Fig. 14.6, a comparison of some of the mode pairs is given. It is important to notice how the correlation is possible not only for the first bending and torsional modes (where the MAC values are very close to 100%), but also for higher order mode shapes.

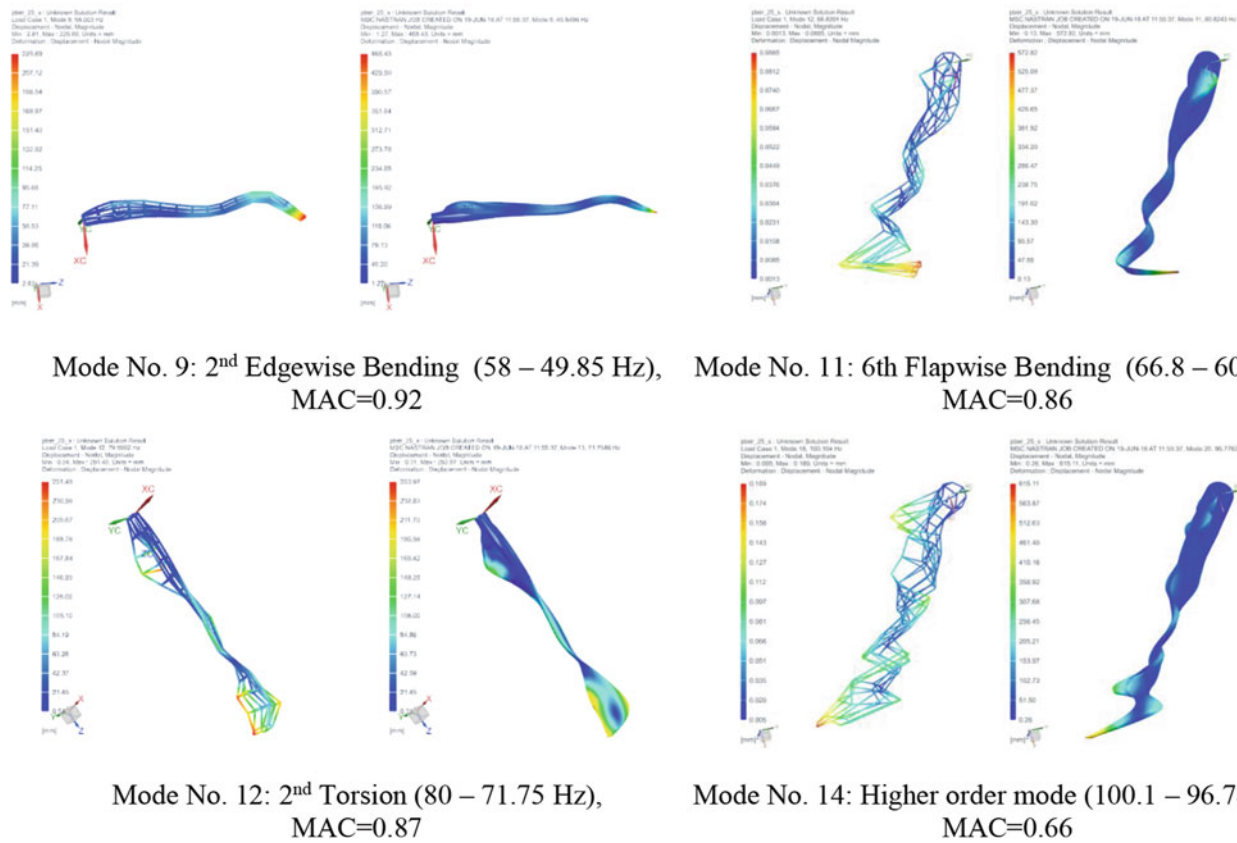


Fig. 14.6 Examples of experimental (left) and numerical (right) identified mode shapes

14.5 Strain-Based Operational Modal Analysis

Modal analysis and testing has traditionally been associated with the use of standard displacement sensors (e.g. accelerometers, laser vibrometers). The use of deformation measurement with strain sensors has gained increased attention in recent years and both academia and industry have started to investigate the advantages which could derive from the use of strain gauges for modal analysis purposes. Strain gauges have been commonly used for static load testing in several application fields, e.g. automotive, aerospace, mechanical. Furthermore, in the wind turbine blade testing they are used for fatigue testing and lifetime prediction and these tests are needed for the certification of the blade. Re-using data from the fatigue test for other objectives, e.g. modal characterization of the structure, would therefore be highly advantageous and cost-effective.

In its first formulation, the Strain-based Modal Analysis [5] was applied in cases in which the input force is well-known and Frequency Response Functions (FRFs) can be calculated. In this work the step further consists in applying the technique to an operational environment in which the input is unknown. This means moving from Experimental Modal Analysis (EMA) to Operational Modal Analysis (OMA) [7].

In order to obtain the strain modal formulation, one can start with the fundamental theory of modal analysis. Modal theory states that the displacement on a given coordinate can be approximated by the summation of a n number of modes, as shown in Eq. (14.1).

$$u(t) = \sum_{i=1}^n \phi_i q_i(t) \tag{14.1}$$

where $u(t)$ is the displacement response in x direction, ϕ_i is the i th displacement vibration mode and q_i is the generalized modal coordinate. For small displacements, given the theory of elasticity, the strain/displacement relationship is given by Eq. (14.2).

$$\varepsilon_x = \frac{\partial}{\partial x} u \quad (14.2)$$

Similarly the same relationship exists between the strain vibration modes and the displacement modes (Eq. 14.3).

$$\psi_i = \frac{\partial}{\partial x} \phi_i \quad (14.3)$$

Taking into account the last two relationships, Eq. (14.1) can be rewritten as Eq. (14.4).

$$\varepsilon(t) = \sum_{i=1}^n \psi_i q_i(t) \quad (14.4)$$

Furthermore, the relationship between the generalized modal coordinate q and the input force F is explicated in Eq. (14.5), where m_i , c_i and k_i are the i th modal mass, modal damping and modal stiffness and ω is the excitation frequency.

Substituting Eq. (14.5) into Eq. (14.4), the relationship between a force input and a strain output in terms of displacement and strain modes is represented in Eq. (14.6).

$$q_i = @Lambda_i^{-1} \phi_i F, \text{ with } @Lambda_i = (-\omega^2 m_i + j\omega c_i + k_i) \quad (14.5)$$

$$\varepsilon_i = \sum_{i=1}^n \psi_i @Lambda_i^{-1} \phi_i F \quad (14.6)$$

Finally, Eq. (14.7) represents the Strain Frequency Response Function (SFRF) in the matrix form.

$$[H^\varepsilon] = \sum_{i=1}^n @Lambda_i^{-1} \{\psi_i\} \{\phi_i\} = [\psi] [@Lambda]^{-1} [\phi]^T \quad (14.7)$$

The matrix $[H^\varepsilon]$ has N_i columns which correspond to the number of excitation points (or the number of inputs) and N_o rows which are the number of strain gauge measurement points (or the number of output measurements).

Few considerations need to be taken into account with respect to the strain modal theory. In fact:

- The SFRF matrix is not symmetric and, as consequence, there is no reciprocity in strain modal analysis;
- Any column of the SFRF matrix contains all information about the strain modes, whereas any row contains information about the displacement mode;
- In order to obtain the strain mode shapes, a fixed excitation points needs to be used and the strain responses should be measured;
- By using roving impact hammer testing the displacement mode shapes can be obtained;
- The similarity of the strain modal formulation and the displacement modal formulation means that the same identification can be used for both techniques.

One of the main advantages with respect to classical accelerometers-based modal analysis is related with the ability to obtain both strain mode shapes and displacement mode shapes with the same type of sensor, which is not achievable with the use of accelerometers. On the other hand several disadvantages needs also to be mentioned. It is, in fact, harder to instrument because the sensors need to be bonded to the structure surface and they are usually not reusable. Furthermore, when compared to accelerometers, a worse signal-to-noise ratio is achieved.

In this work, the input cannot be measured, and the Operational Modal Analysis technique was used to estimate the modal parameters, more specifically, Operational Polymax was employed. The main hypothesis for applying OMA was respected as the data was acquired during the pull-release test in which the blade was free to oscillate.

The recording of the strain gauges was then used to calculate the strain auto- and cross-spectra that serve as input for the Operational Polymax algorithm.

14.6 Pull-Release Test Results

Several tests were performed by varying the load at which the wind turbine blade was subjected. The load was applied through a load clamp attached close to the blade tip. Four different runs at the following force levels were recorded: 1.50, 2.17, 2.65 and 3.17 kN.

In total, 76 strain gauges were attached to the blade. More specifically, 12 sections from the blade root to the blade tip were instrumented with four or eight strain gauges per section. The test geometry is shown in Fig. 14.1.

Time data were acquired with 200 Hz sampling frequency and post-processed in order to be able to derive the strain mode shapes by using Operational Polymax. An exponential window with 10% exponent was applied to the strain gauge time histories to calculate their auto- and cross-spectra, with a frequency resolution of 0.195 Hz. Figure 14.7 shows the acquired time histories for three different points (left) and the calculated cross-power spectra for the same points (right). Figure 14.8 shows the comparison of the calculated auto-power spectra for the same measured point at the four different force levels.

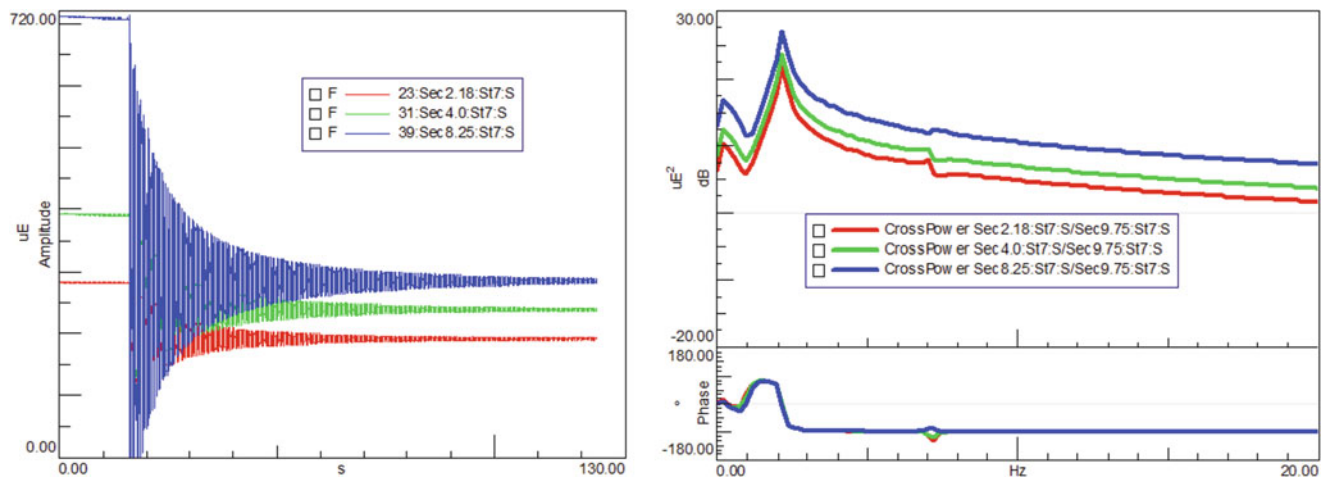


Fig. 14.7 Strain gauges time history for three measured points during pull-release test (left); Calculated cross-powers for the same points (right)

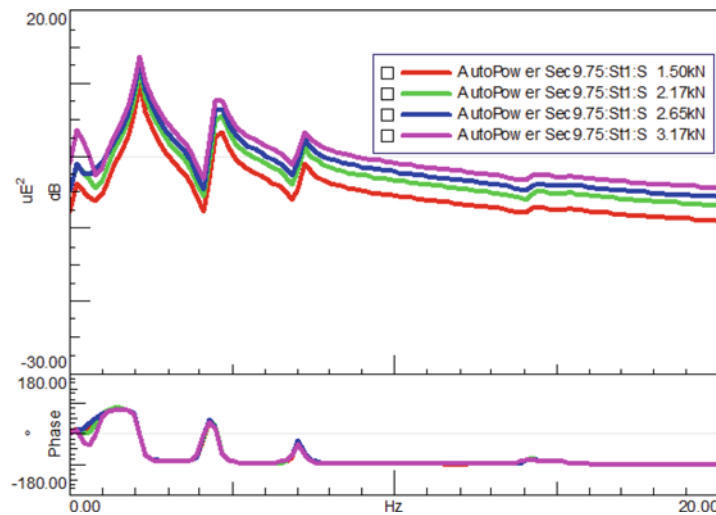
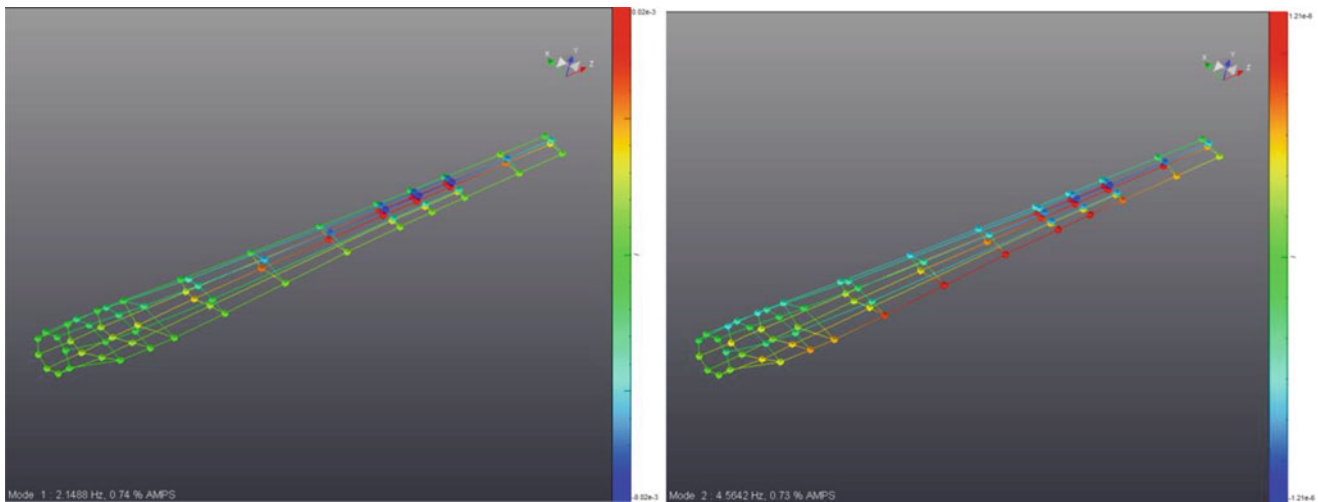


Fig. 14.8 Auto-powers related to the point at 9.75 m from the root section at different force levels (1.50, 2.17, 2.65 and 3.17 kN)

Table 14.2 Results of correlation analysis between test and simulation results in clamped conditions

Pull-release test @1.50 kN	Pull-release test @2.17 kN	Pull-release test @2.65 kN	Pull-release test @3.17 kN	FEM
2.15	2.15	2.15	2.14	2.38
4.56	4.56	4.56	4.55	4.20
7.14	7.14	7.15	7.14	7.35
14.20	14.23	14.20	14.20	12.59

**Fig. 14.9** First flapwise strain mode shape: 2.15 Hz (left); first edgewise strain mode shape: 4.56 Hz (right)

It is clearly visible that the first modes could be easily identified in terms of natural frequencies and damping ratios (listed in Table 14.2 for all four load cases). On the other hand, it is not straightforward to proceed with the direct comparison of strain mode shapes with the FE model results, and requires further work. The first flapwise and the first edgewise strain mode shapes are reported for completeness in Fig. 14.9. Only the natural frequencies are reported in the present study, and compared with each other by applying a clamping condition at the root of the FE model, which was validated by the free-free test results. The match in terms of natural frequencies values is very good, as shown in Table 14.2, where the FE resonance frequencies are listed in the last column.

14.7 Conclusions

The research presented in this paper focuses on the use of different setup configurations to achieve the objective of estimating the modal properties of a wind turbine blade. It has been demonstrated that very good results could be achieved in the two tested configurations: free-free boundary conditions with the use of classical accelerometers-based Experimental Modal Analysis (EMA) and with different input excitations (e.g. hammer, shaker), and strain-based Operational Modal Analysis (OMA) during a pull-release test. The latter is a test which is normally done for fatigue purposes, but the acquired signals could be reused for enriching the available modal properties information and for improving the quality of the numerical models, as both cases yielded a comparably good correlation with the blade Finite Element model. Still, several challenges need to be tackled. Further studies will concern the development of a proper strategy for comparing the strain mode shapes with the FE modes.

Acknowledgements The experimental work described herein has been conducted using mechanical testing and measurement equipment from Villum Center for Advanced Structural and Material Testing (CASMaT). The support from Villum Fonden (Award ref. 00007293) is gratefully acknowledged.

This work was supported by the Danish Centre for Composite Structures and Materials for Wind Turbines (DCCSM), Grant no. 09-067212 from the Danish Strategic Research Council.

The work is supported by the Danish Energy Agency through the Energy Technology Development and Demonstration Program (EUDP), Grant No. 64016-0023. The supported project is named “BLATIGUE: Fast and efficient fatigue test of large wind turbine blades”, and the financial support is greatly appreciated.

This work was funded by the VLAIO Innovation Mandate project number HBC.2016.0235. We are thankful to our colleagues Steen Hjeltn Madsen, Sergei Semenov and Federico Belloni who provided expertise that greatly assisted the measurement campaign.

References

1. International Electrotechnical Commission: International standard IEC 61400-23 Wind turbine generator systems – part 23: full-scale structural testing of rotor blades. In: *Wind Turbines-Part 1: Design Requirements*. International Electrotechnical Commission, Englewood, CO (2014)
2. GE Renewable Energy: GE announces Haliade-X, the world’s most powerful offshore wind turbine (2018)
3. Luczak, M., Peeters, B., Manzato, S., Di Lorenzo, E., Csurcsia, P.Z., Reck-Nielsen, K., Berring, P., Haselbach, P.U., Ruffini, V., Branner, K.: Integrated dynamic testing and analysis approach for model validation of an innovative wind turbine blade design. ISMA 2018 Conference, Leuven
4. Luczak, M., Manzato, S., Peeters, B., Branner, K., Berring, P., Kahsin, M.: Dynamic investigation of twist-bend coupling in wind turbine blade. *J. Theor. Appl. Mech.* **49**, 765–789 (2011)
5. Dos Santos, F.L., Peeters, B.: Strain Modal Analysis – Recent Progress in Flow Control for Practical Flows, pp. 405–428. Springer, New York (2017)
6. Peeters, B., Guillaume, P., Van Der Auweraer, H., Cauberghe, B., Verboven, P., Leuridan, J.: The PolyMAX frequency-domain method: a new standard for modal parameter estimation? *Shock. Vib.* **11**, 395–409 (2004)
7. Peeters, B., Van Der Auweraer, H., Vanhollenbeke, F., Guillaume, P.: Operational Modal Analysis for estimating the dynamic properties of a stadium during a football game. *Shock. Vib.* **14**(4), 283–303 (2007)



Chapter 15

Modal Excitation of Circular Rotating Structures Using an Innovative Electromagnetic Device

Thomas Hoffmann, Martin Jahn, Lars Panning-von Scheidt, and Jörg Wallaschek

Abstract Metallic structures like circular plates or turbine discs feature special mode shapes that can be classified by nodal diameters and nodal circles. It is often desirable to experimentally examine just one mode shape with its distinct nodal diameter and nodal circle. To excite just one mode shape at a certain eigenfrequency the circumferential spectrum of the excitation force must not have other frequency content than the desired frequency and additionally have to resemble the mode shape itself. A device capable of creating such a single mode shape excitation has not existed yet. Here, a patented device is presented which is able to excite a single distinct mode shape of a rotating metallic circular structure. To achieve this the device features a toroidal horseshoe electromagnet with a variable gap geometry. By using the variable gap geometry and variable inductor current any modeshape of a metallic circular rotating structure can be excited. It is also possible to excite a combination of modeshapes by linear superposition of the necessary gap geometries. A brief explanation of the device is given followed by experimental results.

Keywords Harmonic excitation · Cyclic symmetry · Travelling wave · Electromagnetic excitation · Turbine disc

Nomenclature

A	Area
B	Magnetic flux density
I	Current
k	Wavenumber
l, h	Length
N	Coil windings
ND	Nodal diameter
R_m	Magnetic resistance
U_m	Magnetomotive force
μ_0	Magnetic constant
μ_r	Relative permeability
φ	Circumferential angle
τ	Dimensionless time

15.1 Introduction

The blades of turbines or compressors of gas- and steam turbines or aircraft engines vibrate during operation. Inhomogeneities of the flow excite those vibrations. In particular resonance vibrations affect the durability of the blades negatively. This happens through high cycle fatigue or low cycle fatigue during high vibration amplitudes. To avoid this, it is necessary to know the vibrational behaviour of the blades very well. In this paper a patented [1] device for the excitation of rotating

T. Hoffmann (✉) · M. Jahn · L. Panning-von Scheidt · J. Wallaschek
Institute of Dynamics and Vibration Research, Faculty of Mechanical Engineering, Leibniz University Hannover, Hannover, Germany
e-mail: hoffmann@ids.uni-hannover.de

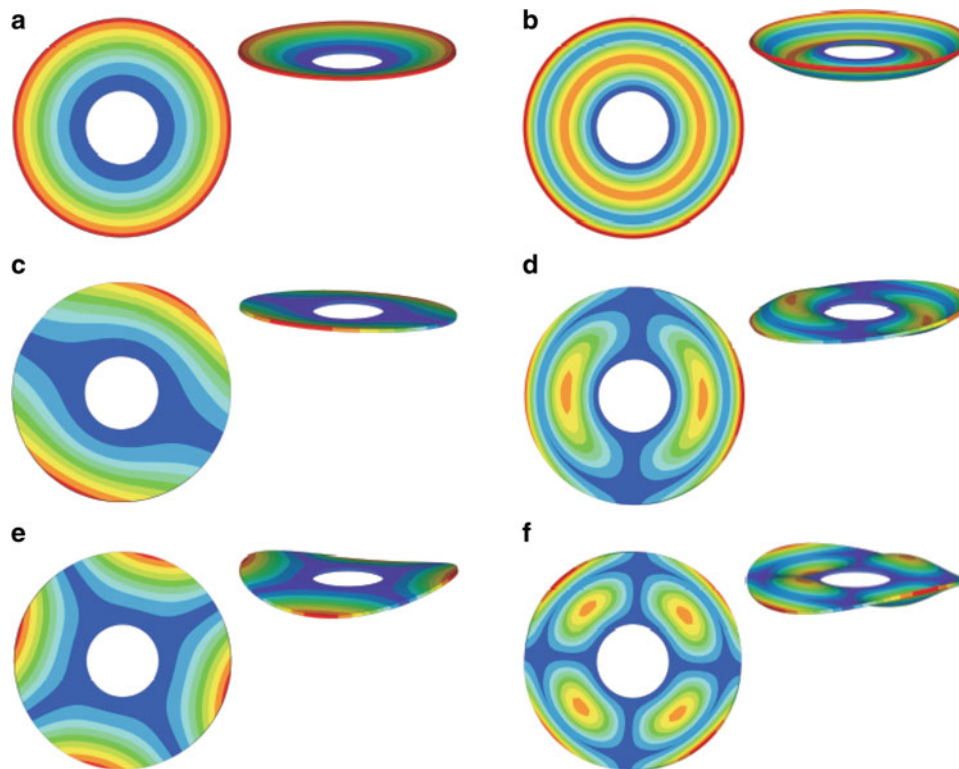


Fig. 15.1 Mode shapes of a plate clamped at the inner ring with different nodal diameters (ND) and nodal circles (NC) [4]. (a) $ND = 0, NC = 0$; (b) $ND = 0, NC = 1$; (c) $ND = 1, NC = 0$; (d) $ND = 1, NC = 1$; (e) $ND = 2, NC = 0$; (f) $ND = 02, NC = 1$

circular structures like turbine discs is presented which solves key issues present in current excitation devices. Although the background of the authors lies clearly in the field of turbine blade dynamics, the device can also be used for other areas where a well defined spatial excitation is needed.

15.1.1 Dynamics of Cyclic Symmetric Structures

The vibration of cyclic symmetric structures like homogeneous circular plates or ideal turbine discs can be described by special characteristics called nodal diameters and nodal circles. Nodal diameters are lines through the center of a circular structure with zero vibration amplitude whereas nodal circles are concentric circles with zero vibration amplitude. In the case of a rotational symmetric plate each mode shape can be described by BESSEL FUNCTIONS [2]. In [3] the mode shapes and eigenfrequencies for different configurations of circular plates are given. Figure 15.1 shows the first six modeshapes of a circular plate fixed at the inner ring. The nodal diameters and nodal circles can be seen clearly by blue diameters or circles. Turbine discs are not rotational symmetric but rather cyclic symmetric. The structure can be divided circumferentially into identical sectors. The smallest possible sector for cyclic symmetry of a turbine disc is equal to the pitch angle between two blades. Besides, a cyclic symmetric structure shows principally the same modeshapes as rotational symmetric structures that can be classified by nodal diameters and nodal circles. Typically, only the nodal diameters are of interest. For a turbine disc each nodal diameter features infinite local blade modes at different eigenfrequencies. Two different blade mode shapes for nodal diameter $ND = 4$ for a generic turbine blading is depicted in Fig. 15.2. Typically, when the turbine disc rotates, the excitation profile that results in a certain nodal diameter vibration is fixed in the inertial system. In the rotating system the blade vibration will form a travelling wave that rotates against the discs direction of rotation.

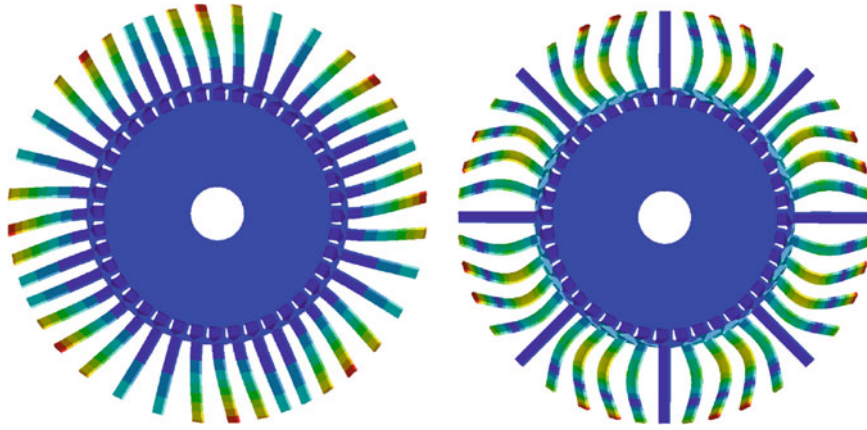


Fig. 15.2 Nodal diameter $ND = 4$ vibrations of the first (left) and second (right) blade bending modes of a turbine disc

15.1.2 Electromagnetic Excitation

The excitation force profile to excite travelling wave modes of rotating circular structures can be described as circumferentially periodic. It can be formulated by the FOURIER series [5]

$$F_E = \sum_{i=0}^{\infty} \hat{F}_{EO_i} \cos(EO_i \varphi + \psi_{EO_i}). \quad (15.1)$$

It describes the spatial force around the circumference with coordinates $\varphi = \Omega t$. It consists of a sum of harmonic terms with frequency $EO_i \Omega$ and phase ψ_{EO_i} . Devices for the excitation of rotating structures are usually designed to excite only certain frequencies EO_i to generate a well defined state of excitation. A widely used method is to use a set of fixed permanent magnets near the structure which act a force on the structure everytime it passes near the magnets. A variable number of magnets can be used. An example of this for the excitation of turbine blades can be found in [6]. The rotating blades are excited by a magnetic force pulse when a blade passes a magnet. If a set of magnets is split up evenly around the circumference the base harmonic of the excitation force is equal the number of magnets. Another example can be found in [7]. But beside the base harmonic many other harmonics get excited which is usually undesirable. This is because of the on-off nature of the excitation force profile when the structure rotates over the magnet. For clarification, the force over time and the corresponding spectrum for such an excitation configuration is shown in Fig. 15.3. By the rule mentioned above the base harmonic should have a period or wavenumber of $k = 1$ which corresponds to $ND = 1$ because the structure passes a single magnet. But caused by the peak-like excitation of the single magnet all other harmonics get also excited as can be seen in the spectrum. There are two main disadvantages caused by this: Firstly, not only the desired nodal diameter $ND = 1$ is excited but also all other nodal diameters which can negatively affect the measurements. Secondly, the energy of the excitation is not only transferred to the desired nodal diameter but rather split between all excited nodal diameters which can result in difficult to measure signal amplitudes. Instead of using permanent magnets electromagnets can also be used to excite the structure. Even non-magnetic materials can be excited by magnets using eddy currents [8]. The underlying problems of exciting unwanted nodal diameters caused by a peak like force signal still persists. In conjunction with electromagnets the described problems can be fully avoided by using a non-rotating structure [9, 10]. In this case a turbine blading is analysed where a single blade always stays on top of one electromagnet. Another example can be found in [11]. But by using a non-rotating structure some effects that only occur under rotation can not be considered like spin softening or stress stiffening. In particular for turbine blading tests the lack of centrifugal force can be problematic for testing damping structures like shrouds or underplatform dampers. For this reasons the excitation of a rotating structure is to be favoured. When using a set of permanent- or electromagnets an unwanted heating of the structure occurs. Eddy currents induced by large spatial gradients of the magnetic fields can lead to the melting of structures rotating in a unsteady magnetic field [8]. The more unsteady the magnetic field is, the lager are the eddy currents and the heating. The electromagnetic excitation device presented in this paper solves all of the mentioned problems. It can be used to excite only the desired nodal diameter and furthermore does not induce strong eddy currents in the structure.

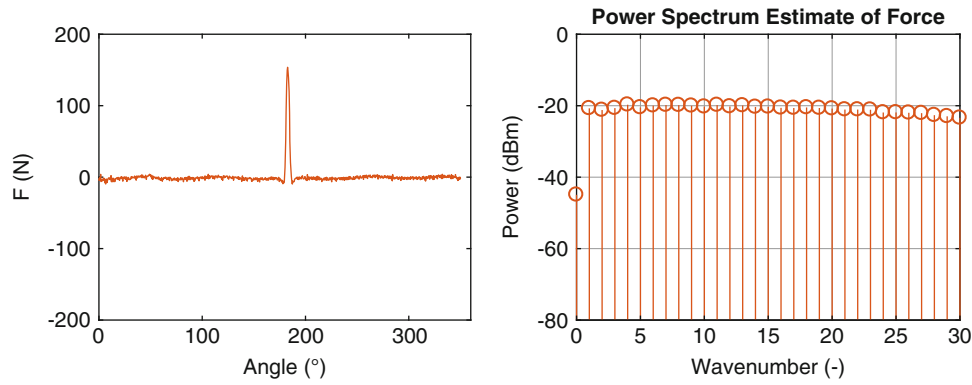
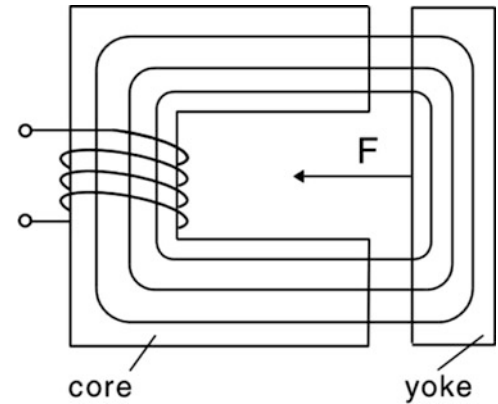


Fig. 15.3 Time series and spectrum of the magnetic flux density for an excitation with a single permanent magnet

Fig. 15.4 Electromagnet [12]



15.2 The Electromagnetic Excitation Device

15.2.1 Electromagnetic Force

The electric energy stored in the field of an electromagnet such as Fig. 15.4 is

$$W = \frac{1}{2}LI^2 = \frac{1}{2} \frac{B^2}{\mu_0\mu_r} Al \quad (15.2)$$

with magnetic flux density B , cross sectional area A of the core, length of the magnetic circuit l and permeability $\mu_0\mu_r$ [12]. Energy is stored in the iron part of the electromagnet (core and yoke) and the air gap. The energy stored in the gap is much higher because $\mu_{\text{Iron}} = \mu_0\mu_{r,\text{Iron}} \gg \mu_{\text{Air}}$. By moving the yoke the energy distribution between the iron part and air part of the magnetic circuit changes and the electromagnetic force can be derived as

$$F = \frac{dW}{dl_{\text{Air}}} = \frac{1}{2} \frac{B^2}{\mu_0} A. \quad (15.3)$$

The magnetic flux density can be expressed as

$$B = \frac{\Phi}{A} = \frac{U_m}{AR_m} \quad (15.4)$$

with the magnetomotive force U_m and the magnetic resistance R_m . For a coil the magnetomotive force is $U_m = NI$ with the number of coil windings N and current I . The magnetic resistance of the air gap is

$$R_{m,\text{Air}} = \frac{l_{\text{Air}}}{\mu_0\mu_{r,\text{Air}} A}. \quad (15.5)$$

The magnetic resistance of the iron core can be neglected because $\mu_{\text{Iron}} \gg \mu_{\text{Air}}$. By inserting Eqs. (15.4) and (15.5) in (15.3) the following relationship for the electromagnetic force is obtained:

$$F = \frac{1}{2} \mu_0 (NI)^2 \frac{A}{l_{\text{Air}}^2} \quad (15.6)$$

The electromagnetic force is inversely dependent on the length of the air gap. This equation can now be used to design the desired force to excite structures. In general either the excitation current I or the air gap l_{Air} can be varied. Because of the need to be able to excite a travelling wave of the rotating structure the air gap has to be varied. By varying solely the excitation current uniformly without any air gap change only a nodal diameter $ND = 0$ excitation could be created. For the electromagnetic force F to be a purely monoharmonic function,¹

$$F = \widehat{F} \sin(\tau) + \bar{F} \quad (15.7)$$

the air gap function can be derived from Eq. (15.6) as

$$l_{\text{Air}}(\tau) = NI \sqrt{\frac{1}{2} \frac{A}{\widehat{F} \sin(\tau) + \bar{F}} \mu_0}. \quad (15.8)$$

The resulting air gap over the dimensionless time variable can be seen in Fig. 15.5 for $k=5$ periods per 2π . Again, an air gap with this function will produce the desired strictly monoharmonic force in the structure. The spectrum of this function has, beside the offset, frequency content on every multiple of the basic harmonic $k = 5$ with descending amplitude. As the force is proportional to the inverse square of the air gap $F \sim l_{\text{Air}}^{-2}$ and proportional to the square of the magnetic flux density $F \sim B^2$, the magnetic flux density is proportional to the inverse of the air gap

$$B \sim \frac{1}{l_{\text{Air}}}. \quad (15.9)$$

As the inverse operation will not change the spectrum qualitatively, the spectrum of Fig. 15.5 is also valid for the to be measured magnetic flux density.

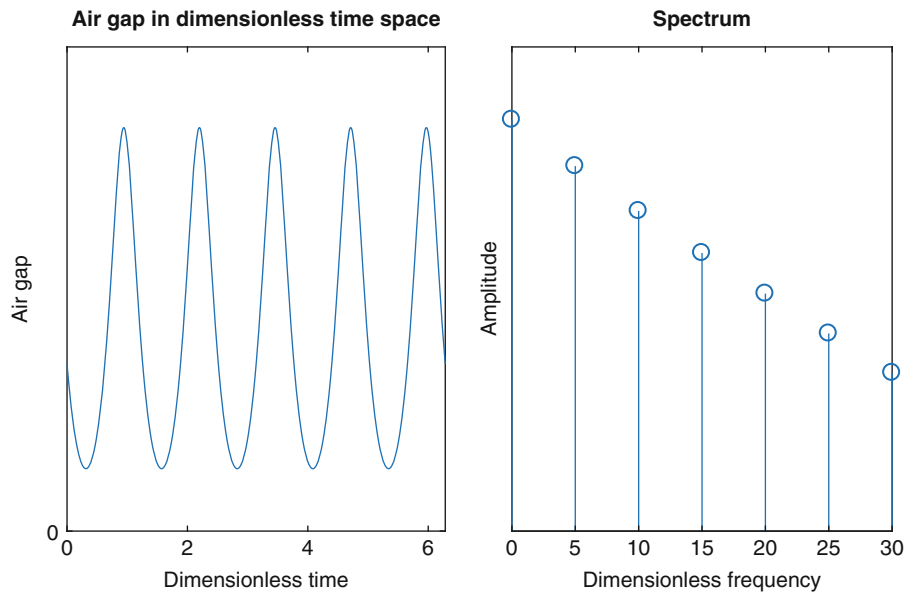


Fig. 15.5 Function of the air gap Eq. (15.8) and its spectrum

¹The offset \bar{F} is necessary as the electromagnetic force must be always positive.

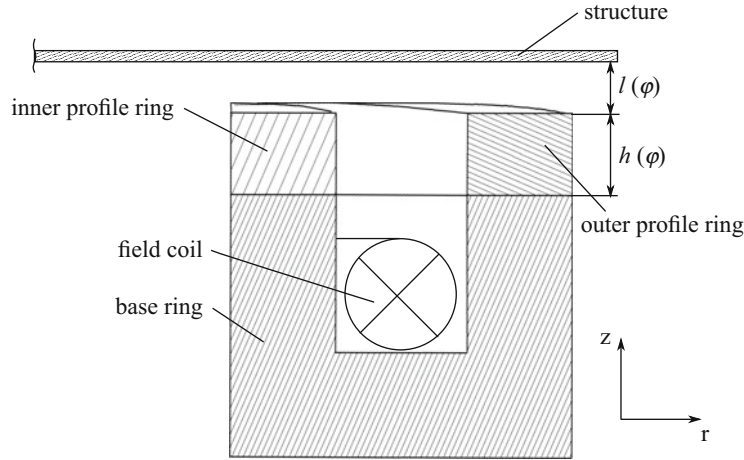


Fig. 15.6 Section view of the excitation device

15.2.2 Design

The device is designed to excite a travelling wave of a rotating circular structure. A sectional view of the device is shown in Fig. 15.6. It consists of a circular base ring with a u-shape section which acts as the core of the electromagnet. It resembles a toroidal horseshoe magnet. Mounted on the base ring are an inner- and an outer profile ring with variable height $h(\varphi)$. The height profile is milled and has to be modified for each desired excitation. The profile ring construction helps to lower manufacturing costs as for new profiles only the rings have to be milled rather than the whole device. Above the device the structure to be excited rotates. The profile ring height and the air gap are related through

$$l_{\text{Air}}(\varphi) = h_0 - h(\varphi) \quad (15.10)$$

with h_0 being the distance between base ring and structure which is shown here for clarity. Here the former nondimensional coordinate τ of Eq. (15.8) is transformed into the circumferential angle by

$$\tau \rightarrow ND\varphi \quad (15.11)$$

with the to be excited nodal diameter ND . The base ring as well as the profile rings are of ferroelectric material of high permeability to guide the magnetic field. The magnetic field is induced by the field coil consisting of N windings of enameled copper wire. The coil is driven by a constant or variable current I . The magnetic flux is guided by the device and closes through the air gap and the structure acting a force on the structure. The profile rings are oriented and fixed on the base ring by dowel pins. It is important that the phase of the milled height function $h(\varphi)$ which is derived from the air gap function by Eq. (15.10) on the profile rings is aligned to ensure proper operation. The device can not only produce a monoharmonic excitation force as shown as an example in Eq. (15.8) but rather any excitation profile by simply calculating the needed air gap from the desired force function as shown above. It is also not limited to excite a nodal diameter denoted by integers. By using a harmonic excitation current in conjunction with the variable gap geometry arbitrary non-integer excitation periods over one revolution can be generated by superposition of a spatial variable gap geometry and a temporal variable excitation current [5]. Photographs of the actual device are shown in Fig. 15.7. The demonstrator has a diameter of 330 mm but can be scaled arbitrarily. On the left the assembled structure can be seen with the explained components. On the top right of the left picture is a port for the coil connection. On the right picture the variable profile height with $k = 5$ periods and the separate base- and profile ring can be seen clearly.

The device is covered by the patent DE102017114153.7 [1].



Fig. 15.7 Photographs of the device

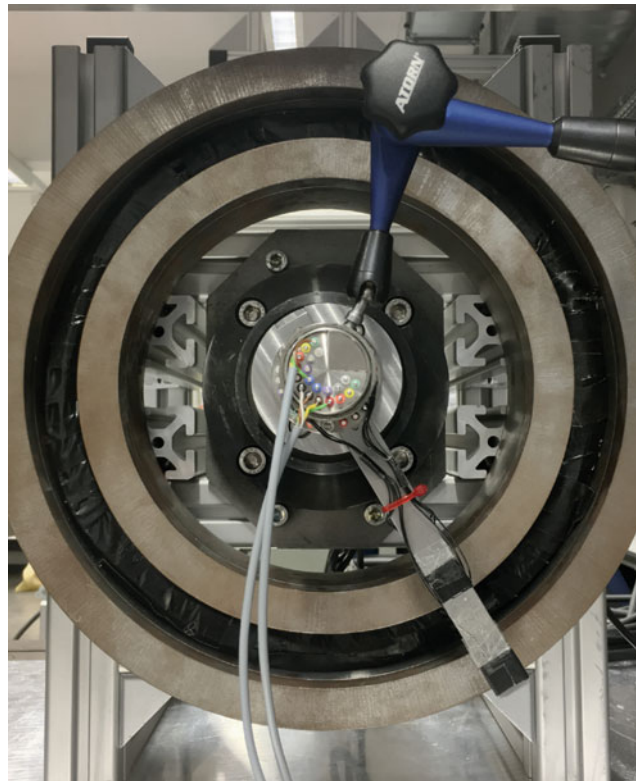


Fig. 15.8 Test setup for measuring the magnetic flux density

15.3 Experimental Results

The goal of this section is to measure the magnetic flux density of the device with profile rings with wavenumber $k = 5$ and variable excitation current and to assess the measured signal spectra. The test setup is shown in Fig. 15.8. The device is mounted on the MORTIMER test rig of the institute. The steel measurement beam is mounted to the shaft of the test rig. Fixed to the beam are two HALL effect sensors, one directly above each profile ring. The signals are transferred by a slip ring to the signal conditioning. The signal conditioning consists of an analog amplifier and an anti aliasing filter of 4th order. The HALL effect sensors are a priori calibrated by a HELMHOLTZ coil pair.

The median free magnetic flux density during one turn is shown in Fig. 15.9a. Note that the constant excitation current causes a large offset which is subtracted here, as it does only cause a static deflection of the structure which is usually not of any interest and eliminated by a high-pass filter. Curves are shown for constant excitation currents of 1 and 10 A. As expected, the magnetic flux density is higher for a higher current. The magnetic flux density on the outer ring is always smaller than on the inner ring. This is because the outer ring has a larger surface than the inner ring, therefore the magnetic

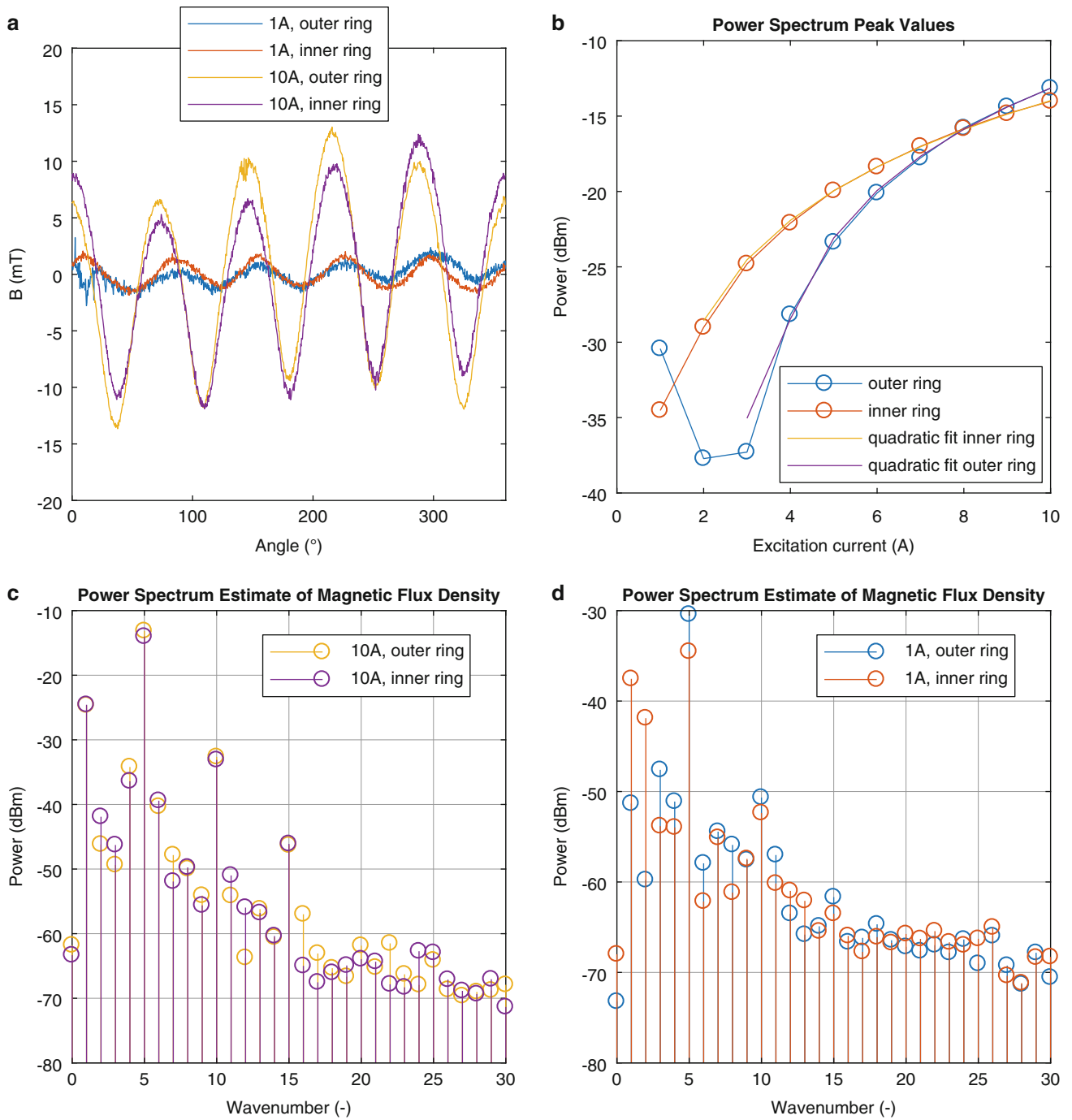


Fig. 15.9 Measurements of the magnetic flux density of the device for different excitation currents. **(a)** Magnetic flux density during one turn for excitation currents of 1 and 10 A. **(b)** Peak amplitudes of the magnetic flux density power spectrum for wavenumber $k=5$. **(c)** Magnetic flux density power spectrum for excitation current of 10 A. **(d)** Magnetic flux density power spectrum for excitation current of 1 A

flux density has to be smaller. The noise on the signals (for example dominant on the first peak of the yellow curve) is mainly introduced by the inverter of the driving motor and can be reduced through averaging. It can already be seen that the shape of the curves are of harmonic nature with $k = 5$ periods per turn. Also, a harmonic content with $k = 1$ period per turn can be seen especially in the larger curve. This is due to alignment imperfections of the measurement beams rotation axis relative to the exciter normal axis. With better alignment this harmonic content vanishes. For this reason, the excited wavenumber of the profile rings has to be chosen as $k = 5$ to not be impacted by the alignment imperfections with $k = 1$. The amplitude of around 10 mT agrees well with conducted magnet field simulations which will be published in future. For further insights, the power spectra are analysed. Figure 15.9c shows WELCHS power spectrum estimate (reference $1 \cdot 10^{-3}$ mT) of the angle-series of the magnetic flux density for 10 A excitation current shown in Fig. 15.9a (yellow and purple plot, plot colours are corresponding). From now on, the spectral lines will be denoted by their wavenumber which, from the point of view of the circular structure to be excited equals to the nodal diameter. For spectrum averaging to reduce noise, 20 revolutions of the beam are measured. The main harmonic content comes with wavenumber $k = 5$, as expected. Also $k = 1$ is notable as it is caused by misalignment of the beam as discussed above. Furthermore, due to the calculated waveform of the magnetic flux density which is proportional to the inverse square root of a sine Eq. (15.9), notable harmonic content with wavenumbers $k = 10$ and $k = 15$ is also present (also compare to the spectrum of Fig. 15.5). It is expected that this spectrum of the magnetic flux density causes a force spectrum which is purely monoharmonic due to Eq. (15.3). The signal peaks ($k = 5$ and $k = 10$) do have a signal to noise ratio of about 20 dBm which equals to $\frac{1}{100}$ and the next signal peak ($k = 15$) has a signal to noise ratio of 15 dBm. This value can be improved by proper shielding of the electronic equipment as it is only caused by interfering electric fields of the test setup. The power spectrum estimate for an excitation current of 1 A is depicted in Fig. 15.9d. As the useful signal decreases, the signal to noise ratio also declines so the higher wavenumber $k = 15$ is not visible any more. For $k = 10$ the signal to noise ratio is 5 dBm and for $k = 10$ it remains 20 dBm. But again, this is due to the electronic equipment and is not a flaw in the concept of the device. For clarity only the spectra for excitation currents of 1 and 10 A are shown. The behaviour of all other excitation levels can be seen in Fig. 15.9b where the peak power levels for each excitation level for wavenumber $k = 5$ is depicted. Except for $I = 1$ A, $I = 9$ A and $I = 10$ A the peak values of the outer ring are always lower than the inner ring. This is the expected behaviour as the magnetic flux density should be higher at the ring with smaller surface. For the lowest excitation current the misbehaviour is due to a low signal to noise ratio, for the higher excitation currents it is most likely caused by a feedback effect of the beams stronger magnetisation. Fitted functions of order 2 are plotted revealing a quadratic behaviour between the power of the magnetic flux density and the excitation current. This equals a linear dependency between the magnetic flux density and the current which is in accordance with Eq. (15.4).

15.4 Conclusions

A electromagnetic device for the excitation of travelling wave modes of rotating structures has been presented. With this device it is for the first time possible to excite a rotating structure like circular blades or turbine discs exactly in the desired modeshapes and nodal diameters without disturbances. The disadvantage of existing excitation concepts explained above, the occurrence of higher harmonic, interfering excitation frequencies, can be completely avoided with the device. It has been shown that the measured magnetic flux density distribution fulfils the predictions. In particular the spectra of the magnetic flux densities promise to achieve the desired properties of the excitation force. It is both possible to create purely monoharmonic excitation forces and any other arbitrary excitation force functions. It is for the first time possible to resemble nodal diameter excitations for rotating structures which are typically used in simulation tools like finite element programs. Therefore, the device can play an important part in validating simulation tools and improve the process of simulation-heavy design chains like for gas turbines.

Acknowledgements The investigations were conducted as part of the joint research programme COOREFlex-turbo in the frame of AG Turbo. The work was supported by the Bundesministerium für Wirtschaft und Technologie (BMWi) as per resolution of the German Federal Parliament under grant number 03ET7041L. The responsibility for the content lies solely with its authors.

References

1. Hoffmann, T., Jahn, M., Panning-von Scheidt, L., Wallaschek, J.: Ein Elektromagnetischer Mechanismus Zur Anregung von Schaufelschwingungen. Patent DE 102017114153.7, vol. 26.07.2017, July 2017
2. Rao, S.S.: Vibration of Continuous Systems. Wiley, Hoboken (2007), oCLC: ocm65301593

3. Leissa, A.W.: Vibration of plates. Tech. Rep. NASA SP-160, Ohio State University, Columbus (1969)
4. Tatzko, S.: Das Dynamische Verhalten von Alternierend Verstimmten Schaufelkränzen Mit Reibelementkopplung. Ph.D. thesis, Leibniz Universität Hannover (2016)
5. Panning, L.: Auslegung von Reibelementen zur Schwingungsdämpfung von Turbinenschaufeln. Ph.D. thesis, VDI-Verlag, Düsseldorf (2005)
6. Sever, I.A., Petrov, E.E., Ewins, D.J.: Experimental and numerical investigation of rotating bladed disk forced response using under-platform friction dampers. In: Proceedings of GT2007 ASME Turbo Expo 2007: Power for Land, Sea and Air, Montreal (2007)
7. Di Maio, D., Ewins, D.: Experimental Measurements of out-of-plane vibrations of a simple blisk design using blade tip timing and scanning LDV measurement methods. *Mech. Syst. Signal Process.* **28**, 517–527 (2012)
8. Provenza, A.J., Duffy, K.P.: Experimental methodology for determining turbomachinery blade damping using magnetic bearing excitation and non-contact optical measurements. In: Proceedings of ASME Turbo Expo 2010 (2010)
9. Berruti, T., Firrone, C.M., Gola, M.M.: A test rig for non-contact travelling wave excitation of a bladed disk with underplatform dampers. In: Proceedings of ASME Turbo Expo 2010 (2010)
10. Firrone, C.M., Berruti, T.: An electromagnetic system for the non-contact excitation of bladed disks. *Exp. Mech.* **52**(5), 447–459 (2012)
11. Jones, K.W., Cross, C.J.: Traveling wave excitation system for bladed disks. *J. Propuls. Power* **19**(1), 135–141 (2003)
12. Kories, R., Schmidt-Walter, H.: *Electrical Engineering*. Springer, Berlin (2003)

Chapter 16

Modal Analysis of a 7 DoF Sweet Pepper Harvesting Robot



Tobias F. C. Berninger, Sebastian Fuderer, and Daniel J. Rixen

Abstract Modal Analysis is a well-established key tool used to analyze the dynamic behavior of a structure. A robot manipulator consists of mechanical structures, like the body links between the joints and gears, and mechatronic components, like motors and their control system. The dynamic behavior of all subcomponents making up the robot arm are individually well understood. However, their respective influence on the dynamic behavior of the entire robot system is still a matter of research. Understanding the dynamics of the manipulator and setting up a validated model of its full dynamics is essential, in order to devise proper control strategies. One specific challenge comes from the fact that the vibration properties (modes, damping and frequencies) depend on the overall pose and thus change during the operation of the robot. Further, non-linearities from the joints and the action of the joint controller can significantly influence the dynamics of the system. In this paper, the influence of these effects on the overall dynamic behavior of a 7 DOF robot manipulator developed for automated sweet pepper harvesting is analyzed, using Modal Analysis.

Keywords Robotics · Dynamics of the TCP · Structural dynamics · Modal analysis · Complex modes

16.1 Introduction

In order to achieve high precision of the tool center point (TCP) of a robot manipulator during rapidly changing and highly dynamic motions, high-fidelity models of the robot system are needed. These models can be used either to predict and improve insufficiencies of a new manipulators design during the development phase or to apply model predictive control techniques to further improve the overall dynamics of the system. Experimental Modal Analysis (EMA) can not only be used to validate and tune already existing models, but can also provide a deeper insight into the manipulators' dynamics to determine which subcomponent contributes to the overall dynamics of the system; and would therefore need a high level of attention in order to achieve an accurate model of the entire system.

Usually the structural dynamics of a robot manipulator are modeled by focusing on its joints. In most cases, the joint dynamics are incorporated by adding spring-damper-systems between the robot links [2–4]. These models are then further refined by having a more detailed look at the transmission system [5], especially by including more accurate friction models [6, 7]. The structural dynamics of the links are usually omitted, or only accounted for by adding a simple spring-damper-system for every link [8].

This work aims to experimentally analyze the dynamic behavior of a typical robot manipulator. While the main goal is to acquire a better understanding of the structural dynamics of a robot arm, we also try to provide a closer look at the general application of an EMA on a robot manipulator. In Sect. 16.2, the overall experimental setup is explained. Section 16.3 goes into detail about preliminary tests to choose the correct hammer tip, measurement bandwidth and time window. Experiments to assess the repeatability of measurements, non-linearities, influence of the joint controller on the measurements and overall dynamics are performed. Finally, a detailed measurement of the dynamics of the TCP during a significant pose change is carried out. An EMA of the CROPS robot for three different poses is performed and discussed in Sect. 16.4.

Similar works can already be found in the literature. Behi and Tesar [9] used EMA for parametric identification of an 4 DOF model of a Cincinnati Miacron T3-776 robot. 2 DOF to model the main joints of the robot and 2 DOF to include the

T. F. C. Berninger (✉) · S. Fuderer · D. J. Rixen
Faculty of Mechanical Engineering, Technical University of Munich, Garching, Germany
e-mail: t.berninger@tum.de; sebastian_fuderer@web.de; rixen@tum.de

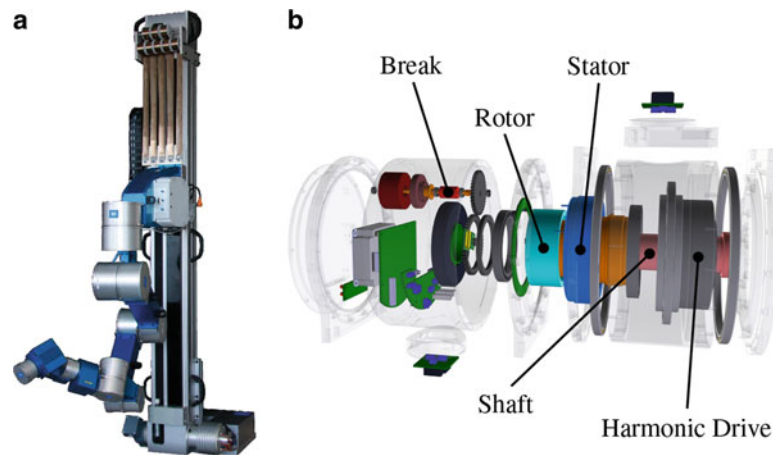


Fig. 16.1 The 2nd generation of the CROPS harvesting robot [1]. (a) CROPS robot in 9 DOF configuration. (b) CROPS drive unit

dynamics of its ground plate. In [10] an EMA was performed on an academic 3 DOF robot arm with two flexible beams as links, which is consequently quite different to a typical industrial manipulator. The analysis is presented for two different poses, which show a significant difference in eigenfrequencies and mode shapes. For this academic robot, the structural dynamics of the links appear to have a much larger influence on the overall dynamics of the robot arm than its joints. Vu et al. [11] did a spectrum analysis of vibration measurements during operation of a grinding robot arm, which also showed a significant change of eigenfrequencies caused by the change of pose during operation. For the same robot, an EMA was performed in [12]. In [13] an EMA was carried out on a Mitsubishi RV-3AL robot, which is mounted on a MetraLabs X3 mobile platform. The analysis was used to tune an existing flexible multi body simulation.

For the work presented here, the second generation of the CROPS robot is used as an example. The robot was developed by the Chair of Applied Mechanics at the TU Munich in 2014 during the European project “*Clever Robots for Crops*” for autonomous sweet pepper harvesting [14]. The manipulator, Fig. 16.1, is carried by one large prismatic joint for vertical movement and consists otherwise of rotary joints [15]. The design of the joints is modular and are otherwise similar to typical robot joints, utilizing a harmonic drive gear and a break on the motor side, Fig. 16.1b [1]. Thanks to the modular design, the robot can be assembled in a 7 or 9 DOF configuration. Here, the 7 DOF assembly is used, Fig. 16.2. The robot has three large rotary joints to position the TCP and three small rotary joints at the end for its rotation, making it quite similar to most industrial robot arms; with the first DOF being the large prismatic joint at the base of the manipulator.

16.2 Experimental Setup

For the dynamic analysis, the CROPS robot changes its pose from a completely stretched out position to a retracted pose, while also rotating around the z -axis of the inertial coordinate system, Fig. 16.2. The vertical position of joint 1 will be kept the same for all tests. The EMA and all other tests is performed on these two poses and a third one half-way through the pose change. The joint angles of the poses are:

$$\begin{aligned} \text{Pose 1: } & \theta_2 = 0^\circ, \quad \theta_3 = 0^\circ, \quad \theta_4 = 0^\circ, \quad \theta_6 = 0^\circ. \\ \text{Pose 2: } & \theta_2 = 45^\circ, \quad \theta_3 = -30^\circ, \quad \theta_4 = -75^\circ, \quad \theta_6 = -45^\circ. \\ \text{Pose 3: } & \theta_2 = 90^\circ, \quad \theta_3 = -60^\circ, \quad \theta_4 = -150^\circ, \quad \theta_6 = -90^\circ. \end{aligned}$$

All tests rely on frequency response measurements performed using a PCB impact hammer and Kistler triax acceleration sensors with 100 mV/g sensitivity and 6 g of weight. Since the first modes are expected to be within the 100 Hz range, it would be possible to use sensors with less bandwidth and higher sensitivity. However, higher sensitivity sensors usually weigh considerably more and will worsen the added mass effect [16], making the chosen sensors a good compromise between weight and sensitivity. Impact locations are near the TCP and on the link between the third and fourth joint, Fig. 16.2a. Since there are a lot of different excitation points and measurement runs, a PCB impact hammer with 0.3 kg mass is preferred to an excitation by a shaker for the sake of convenience. For data acquisition a Siemens LMS system with 24 channels is used, allowing seven triax sensors to be used at the same time per measurement run. One measurement run is performed per link and joint of the CROPS robot, resulting in 11 measurement runs and overall 77 points, each with three measured directions.

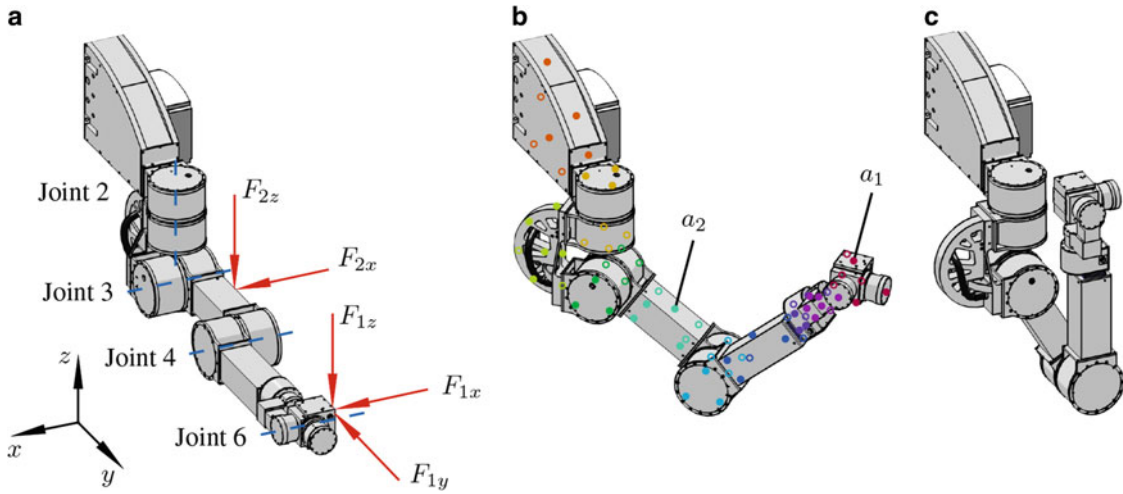


Fig. 16.2 CROPS robot in 7 DOF configuration. (a) First pose with joint numbers and excitation forces. (b) Second pose with measurement points. One color per measurement run. (c) Third pose

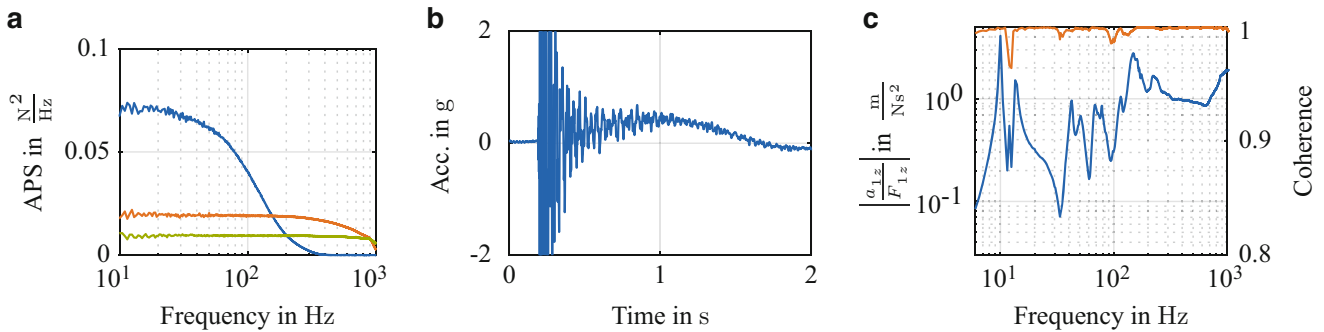


Fig. 16.3 First measurements after an F_{1z} -impact to setup the EMA. (a) Auto power spectrum of the hammer tip force measurement with rubber (blue line), vinyl (orange line), and metal (green line). (b) Time signal of sensor a_1z . (c) Driving point FRF at the TCP (blue line) and coherence (orange line)

The main sensors used to interpret the different tests are located near the TCP (a_1) and between joint three and four (a_2), Fig. 16.2b. The EMA is performed within the LMS Impact Testing software using the PolyMax-Algorithm [17], all further post processing is done using Matlab.

16.3 Preliminary Tests

16.3.1 Hammer Tip, Time Window and Bandwidth

To choose a suitable hammer tip for this application, three different hammer tips made of rubber, vinyl and metal are tested by examining the corresponding auto power spectrum of the hammer force measurement, Fig. 16.3a. The metal tip is able to excite the longest frequency range, but with the least energy below 100 Hz. It will also often cause nearby sensors to reach overload. The rubber tip induces the most energy into the frequency range of interest, but falls under -10 dB right after it. In order to have some margin to also analyze a higher frequency range, the vinyl tip is chosen. The time signal of sensor a_1 in z -direction after an impact on the TCP in the same direction, Fig. 16.3b, shows that a measurement of 2 s provides a good signal-to-noise ratio without having to apply any special windowing and results in an acceptable frequency resolution of 0.5 Hz. A first driving point measurement at the TCP in z -direction after five averages using this setup is shown in Fig. 16.3c. The coherence never drops under 0.95 over the entire frequency range, indicating a very good measurement. The first mode appears to be around 10 Hz, making the frequency resolution just about sufficient. The bandwidth for the measurements is maintained at 1024 Hz, but all following plots will be zoomed in on the 200 Hz range, since all modes of interest are in this area.

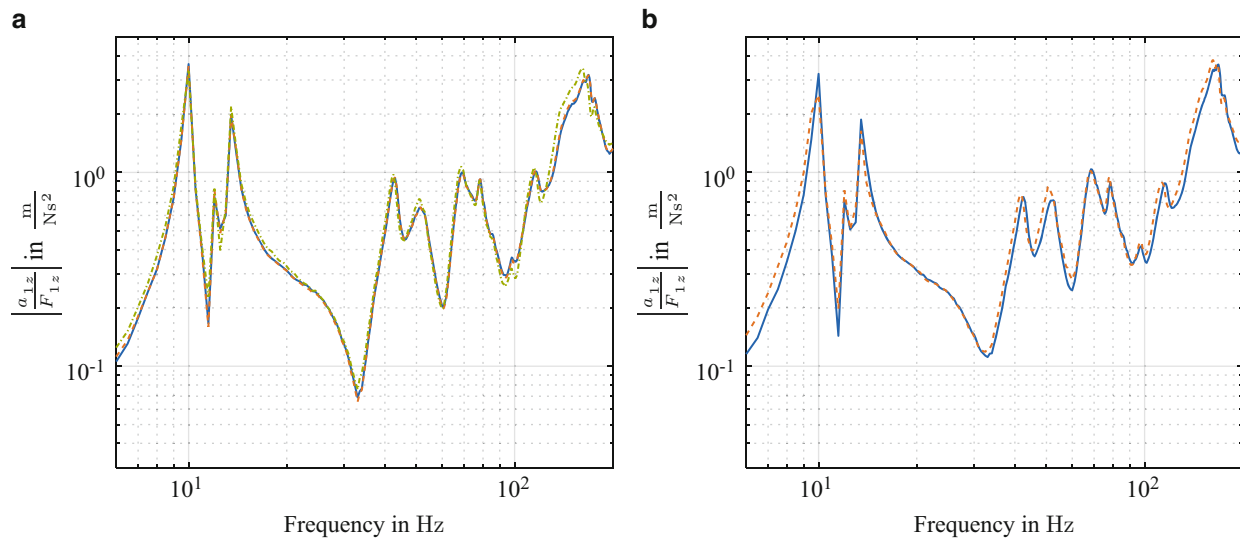


Fig. 16.4 Driving point measurements of the TCP in z -direction to test repeatability and temperature influence. **(a)** Comparison between the reference (blue line), after a significant pose change on the same day (orange line) and after 1 day (green line). **(b)** Comparison between the reference (blue line) and after 30 min of operation (orange line)

16.3.2 Repeatability and Temperature Influence

Considering that a robot arm is a rather complex system, the first area of interest is the repeatability of measurements. To test this, a reference driving point measurement of the TCP is obtained in all three poses. Afterwards, the robot is moved into a different position, back into the initial one of the reference and the measurement is repeated. For a third test, the robot is again moved into a different position and is kept there. After 1 day, the measurements are repeated for all three positions. The breaks are engaged during all measurements. Figure 16.4a depicts the results for the first pose and shows a very good match between the FRF's obtained, which is also true for the other two poses.

Since the joints heat up during operation and might cause a change in the dynamics of the robot arm, a similar test is performed. A reference driving point measurement is again taken in the same way and compared to the same measurement after 30 min of operation, which causes the joints 2–4 to significantly heat up. The results are shown in Fig. 16.4b. A slight displacement of the FRF's in the higher frequency range is noticeable, but overall no significant difference is found.

16.3.3 Non-linearities and Influence of the Joint Controller

A simple way to check for non-linearities in a system is to obtain the same FRF twice, once with a low level of input force and once with a high level. This is done in Fig. 16.5a, in the same way as before and with brakes engaged. A higher amount of damping is clearly visible for the FRF obtained with a high level of force, especially for the higher frequency modes. The same effect can be observed for the FRF's measured in the other two poses. This non-linear behavior is probably caused by the friction present within the joint gears. Since the breaks are engaged on the motor shaft, the harmonic drives are theoretically able to deform and have an impact on the dynamic behavior of the robot arm.

Finally, the influence of the joint controller is tested by comparing driving point FRF's of the TCP taken with engaged breaks, to FRF's taken while the joint controller is holding the respective pose, Fig. 16.5b. The controller seems to only effect the damping of two specific modes around 40 and 100 Hz. This seems to be consistent with observation made during the EMA in Sect. 16.4, since deformation of the motor joint axes only occurs significantly in these modes. This effect can only be observed in pose 1.

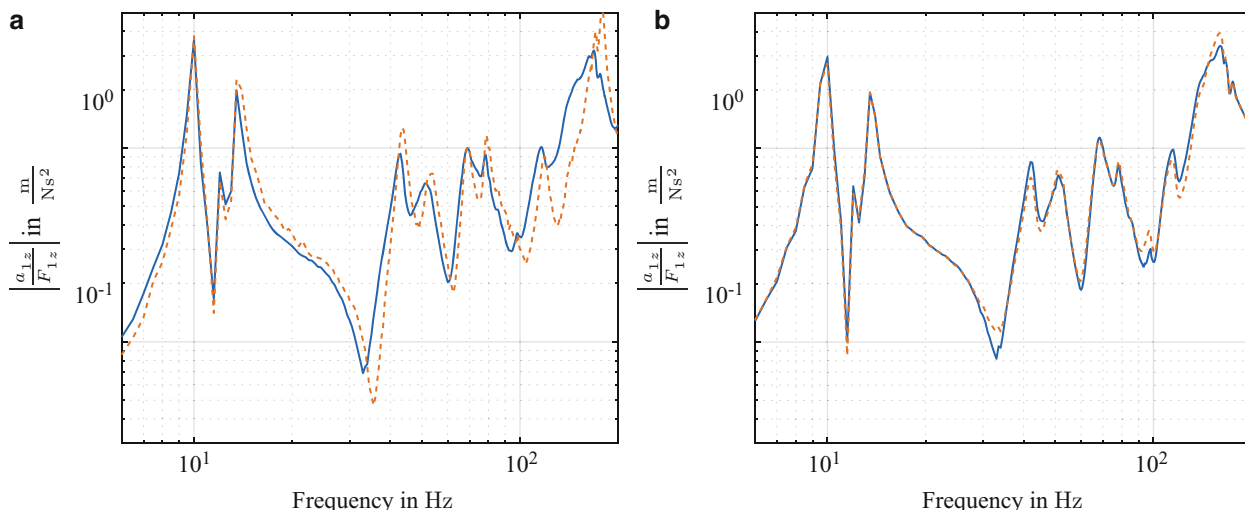


Fig. 16.5 Driving point measurements of the TCP in z -direction to test non-linearities and controller influence. (a) Comparison between a FRF obtained after a hard (blue line) and a soft (orange line) impact. (b) Comparison between a FRF obtained with engaged breaks (blue line) and with activated joint controller (orange line).

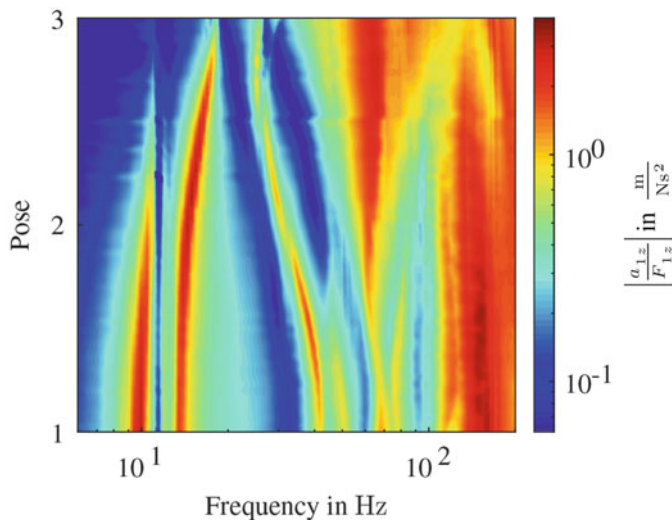


Fig. 16.6 Campbell diagram of the TCP in z -direction for different poses

16.3.4 Influence of the Pose on the TCP Dynamics

To get a first grasp on the influence of the pose on the manipulators overall dynamics, the driving point FRF of the TCP is measured for 60 poses by starting with pose 1 and increasing the joint angles in increments of

$$\Delta\theta_2 = 1.5^\circ, \quad \Delta\theta_3 = -1.0^\circ, \quad \Delta\theta_4 = -2.5^\circ, \quad \Delta\theta_6 = -1.5^\circ,$$

going through pose 2 to 3. The breaks are again engaged for every measurement. The results are plotted in a Campbell-like diagram, which depends on the pose instead of rotational speed, Fig. 16.6. By just looking at the diagram without considering the findings of the EMA in Sect. 16.4, it is already clear that the dynamics depend considerably on the pose of the robot arm. The first mode at 10 Hz barely changes its frequency, but loses almost a decade of amplitude after passing the second pose. The second mode starts at 13 Hz and increases to 20 Hz without loosing amplitude. The third one starts at 40 Hz and changes

the most in frequency, while also loosing and gaining amplitude in between. A new mode appears right below the third one half way between pose 2 and 3, while the third mode loses rapidly in amplitude and makes a right curve.

These measurements underline the importance of high-fidelity models that can accurately depict these changes in dynamics, since the performance of higher level control techniques are usually very dependent on the quality of their underlying models.

16.4 Experimental Modal Analysis

Finally, the EMA is performed. A good way to check the quality of an EMA is, to examine the synthetisation of the measured FRF's. In Fig. 16.7 the FRF's from impact F_{1z} to sensor a_1 are compared to their respective synthetisations in z - and x -direction. Both show a very good match in phase and amplitude, which is also the case for most other measured FRF's.

The resulting mode shapes are depicted in Fig. 16.8. The first mode is a horizontal bending mode in the x - y -plane at 8.6 Hz which is not visible in the Campbell diagram (Fig. 16.6), since it cannot be excited by an impact in z -direction. The main cause for this mode is the bending of the link between joint 1 and 2 and the “C”-shaped link between joint 2 and 3. The rest of the arm behaves almost completely rigidly for this mode and no bending of the joints can be observed. Mode 2 at 10 Hz is the first bending mode in vertical direction, but once again there is no actual bending of the robot arm involved. This mode is caused by the bending of the large beam of the prismatic joint 1, which consequently tilts the entire arm downwards. This also explains why this mode doesn't change its frequency but only loses amplitude in the Campbell diagram (Fig. 16.6): By gradually retracting the robot arm, the leverage of its weight on the large vertical beam of joint 1 decreases as well. Mode 3 at 13.6 Hz looks very similar to mode 2 and yields a very high MAC of 91% in comparison, but is mainly caused by an additional deformation of the “C”-shaped link between joint 2 and 3, while the rest of the robot arm again behaves rigidly. Mode 4 and 5 look like the second horizontal bending mode and both have a vibration node near the small link between joint 5 and 6. The difference between them again being the bending of the “C”-shaped link for mode 5. Mode 6 at 42 Hz is the second bending mode in vertical direction and is actually the first mode which involves the bending of some joints around their motor axis and could actually be observed by the joint controller test in Fig 16.5b. Consequently, this is the first mode that effectively can be influenced by the joint controller, which seems to add some damping to the mode. Mode 7 and 8 are the third bending modes in the horizontal and vertical direction respectively, both having a vibration node at the link between joint 3 and 4 and at the small link between joint 5 and 6. Mode 9 is the first torsional mode around the y -axis. The mode shapes of pose 2 and 3 behave similarly, are difficult to depict on paper and add nothing substantial to the discussion, which is why they are omitted form this paper.

Performing the same analysis using the impact point F_2 generally yields the same mode shapes and eigenfrequencies as impact point F_1 but shows consistently higher phase scatter for the modes of all poses. Complex modes are consistent

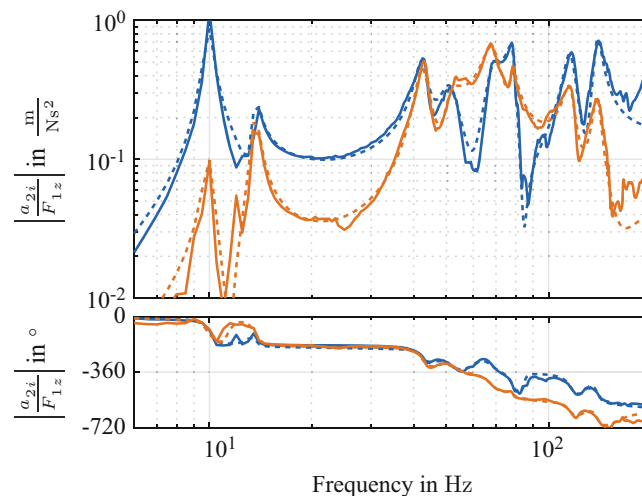


Fig. 16.7 FRF synthetisation using PolyMax. FRF from F_{1z} to a_{2z} (blue line) and a_{2x} (orange line) with their respective synthetisation (dotted lines)

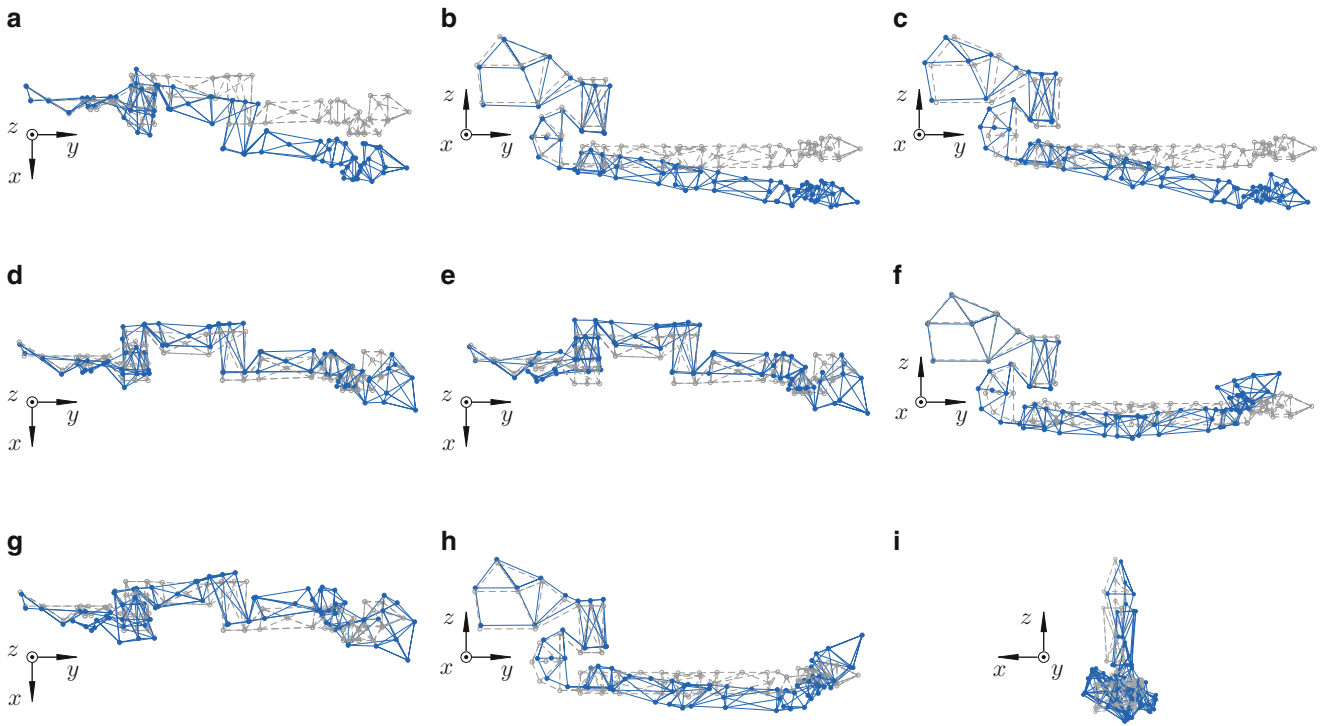


Fig. 16.8 Modeshapes, eigenfrequencies and modal damping for pose 1. (a) Mode 1, 8.6 Hz, 2.4%. (b) Mode 2, 10 Hz, 2.8%. (c) Mode 3, 13.6 Hz, 2.7%. (d) Mode 4, 28.8 Hz, 5.8%. (e) Mode 5, 36.6 Hz, 4.5%. (f) Mode 6, 42.3 Hz, 4.1%. (g) Mode 7, 51 Hz, 6.7%. (h) Mode 8, 68 Hz, 6.4%. (i) Mode 9, 78.2 Hz, 2.7%

with a continuous system with discrete damping points [16], which a robot manipulator ultimately is, since the robot usually consists of lightly damped metal links that are connected by its joints, which concentrate most of the damping within them through their gears and transmission system. One explanation might be that the F_2 hit between the big joints 3 and 4 has less leverage on them than F_1 and therefore activates more damping. This could also explain the non-linear behavior found in Fig. 16.5a.

16.5 Conclusions

This work has shown that a detailed EMA can be performed reliably on a robot manipulator using hammer impacts. Section 16.3 has shown that the repeatability of the measurements, even after large pose changes over multiple days, is very good and that the effect of the temperature due to the heating of the joint motors is insignificant. The results were used to point out structural weaknesses of the CROPS robot, which in this case is mainly the “C”-shaped link between joints 2 and 3. The analysis in Sect. 16.4 showed that the links between the joints have a major effect on the overall dynamics of the robot, namely the eigenfrequencies and mode shapes; while the joints are mainly responsible for the damping of the system and consequently, its non-linear behavior during varying impact forces at the TCP.

While these findings cannot be used to make statements about the dynamic behavior of robot manipulators in general, they at least suggest that the current common practice of only modeling the joints and neglecting the structural dynamics of the links is probably not enough to accurately predict the dynamic behavior of most manipulators over multiple poses, as illustrated by Fig. 16.6. A small correlation could be found between the action of the joint controller and increased damping of the corresponding modes, as well as between impact location and complexity of modes; this might be due to the localized non-linear damping inside of the joints. Since there are only minor indications of these two effects in this rather complex system, it is not possible to draw any decisive conclusions. For this reason, a simple joint test rig will be modified, in order to be able to take a more precise look at the interaction between the structural dynamics of the link, the robot joint and the joint controller.

References

1. Pfaff, J., Baur, J., Schütz, C.: Design of drive units for agricultural robots. In: International Conference of Agricultural Engineering (2014)
2. Abele, E., Bauer, J., Hemker, T., Laurischkat, R., Meier, H., Reese, S., von Strykb, O.: Comparison and validation of implementations of a flexible joint multibody dynamics system model for an industrial robot. *CIRP J. Manuf. Sci. Technol.* **4**(1), 38–43 (2011). <https://doi.org/10.1016/j.cirpj.2011.01.006>
3. Sweet, L.M., Good, M.C.: Redefinition of the robot motion-control problem. *IEEE Control Syst. Mag.* **5**(3), 18–25 (1985)
4. Tomei, P.: A simple PD controller for robots with elastic joints. *IEEE Trans. Autom. Control* **36**(10), 1208–1213 (1991)
5. Schempf, H.: Comparative design, modeling, and control analysis of robotic transmissions. PhD thesis, Massachusetts Institute of technology (1999)
6. Seyffferth, W., Maghzal, A.J., Angeles, J.: Nonlinear modeling and parameter identification of harmonic drive robotic transmissions. In: Proceedings - IEEE International Conference on Robotics and Automation, pp. 3027–3032 (1995). <https://doi.org/10.1109/ROBOT.1995.525714>
7. Baur, J., Dendorfer, S., Pfaff, J., Schütz, C., Buschmann, T., Ulbrich, H.: Experimental friction identification in robot drives. In: IEEE International Conference of Robotics and Automation (2014)
8. Ohr, J., Moberg, S., Wernholt, E., Hanssen, S., Pettersson, J., Persson, S., Sander-tavallaey, S.: Identification of flexibility parameters of 6-axis industrial manipulator models. In: ISMA 2006 (2006)
9. Behi, F., Tesar, D.: Parametric identification for industrial manipulators using experimental modal analysis. *IEEE Trans. Robot. Autom.* **7**(5), 642–652 (1991). <https://doi.org/10.1109/70.97876>
10. Jacobus, R., Serna, M.: Modal analysis of a three dimensional flexible robot. In: Proceedings of the 1994 IEEE International Conference on Robotics and Automation, pp. 2962–2967 (1994). <https://doi.org/10.1109/ROBOT.1994.350889>
11. Vu, V.H., Liu, Z., Thomas, M., Hazel, B.: Modal analysis of a light-weight robot with a rotating tool installed at the end effector. *J. Mech. Eng. Sci.* **231**(9), 1664–1676 (2017). <https://doi.org/10.1177/0954406215619451>
12. Rafeian, F., Liu, Z., Hazel, B.: Dynamic model and modal testing for vibration analysis of robotic grinding process with a 6DOF flexible-joint manipulator. In: 2009 IEEE International Conference on Mechatronics and Automation, ICMA 2009, pp. 2793–2798 (2009). <https://doi.org/10.1109/ICMA.2009.5246491>
13. Fuentes, A.T., Kipfmüller, M., Prieto, M.A.: 6 DOF articulated-arm robot and mobile platform: dynamic modelling as multibody system and its validation via experimental modal analysis. *IOP Conf. Ser. Mater. Sci. Eng.* **257**(1) (2017). <https://doi.org/10.1088/1757-899X/257/1/012008>
14. Bac, C.W., Hemming, J., Barth, R., Wais, E., Henten, E.J.V.: Performance evaluation of a harvesting robot for sweet pepper. *J. Field Rob.* **17**, 1–17 (2017)
15. Ulbrich, H., Baur, J., Pfaff, J., Schuetz, C.: Design and realization of a redundant modular multipurpose agricultural robot. In: Proceedings of the XVII International Symposium on Dynamic Problems of Mechanics (DINAME) (2015)
16. Ewins, D.J.: *Modal Testing: Theory, Practice and Application*, 2nd edn, p. 562. Research Studies Press Ltd., Letchworth (2000)
17. Peeters, B., Van Der Auweraer, H.: PolyMAX: a revolution in operational modal analysis. In: International Operational Modal Analysis Conference (IOMAC), p. 13 (2005)

Chapter 17

Characterizing Dynamics of Additively Manufactured Parts



Gary Adkins, Clayton Little, Peter Meyerhofer, Garrison Flynn, and Kyle Hammond

Abstract Additive manufacturing (AM) presents engineers and manufacturers with unprecedented design freedom compared to conventional manufacturing techniques. This freedom comes with its own challenges. The wide variety of AM techniques, machines, and design geometries introduces difficulties in building consistent parts with known material properties. Of particular interest is the anisotropic nature introduced in the AM process. While AM is being adopted for applications in a variety of industries, the uncertainties introduced in manufacturing are slowing its implementation for critical parts such as structural members and jointed elements. As part of the ongoing effort to alleviate these issues, this paper aims to quantify the dynamic response of AM parts built using a variety of build orientations and internal structures. Multiple parts with theoretically identical external geometries are excited by a shake table while high-speed data are collected using digital image correlation (DIC). A finite element model is developed and calibrated using the DIC data to characterize the material property changes due to selection of build orientation and internal structures.

Keywords Digital image correlation · Finite element model · Fused deposition modeling · Lattice structure · Modal analysis

17.1 Introduction

Additive manufacturing (AM), commonly called 3D printing, has the potential to revolutionize manufacturing, both in terms of design and production. AM is the process of building objects layer by layer, whereas conventional methods involve removing material from a larger bulk piece, or casting an object in a mold. This additive technique greatly expands the design geometries feasible by allowing internal structures that were once prohibitively difficult or expensive to produce. AM emerged in the 1980s and at first developed slowly for several reasons including high cost of equipment, the need for specialized personnel training, and, most critically, the lack of industry standards for process parameters and performance measures. Time has alleviated the first two difficulties, as equipment costs have fallen dramatically with the expiration of fundamental patents and further improvements in technology, while the growth of the maker community, coupled with interest at many universities, has built a community of people experienced in the use of AM [1]. However, defining the performance of AM parts and creating a comprehensive set of manufacturing standards is a more complicated problem. Iterations of the same AM part may look nearly identical on the outside, yet have highly variable and uncertain mechanical properties.

G. Adkins
Mechanical Engineering, College of Engineering, Iowa State University, Ames, IA, USA

C. Little
Mechanical Engineering, College of Engineering, Rice University, Houston, TX, USA

P. Meyerhofer
Department of Mechanical and Aerospace Engineering, Case Western Reserve University, Cleveland, OH, USA

G. Flynn (✉) · K. Hammond
Los Alamos National Laboratory, Los Alamos, NM, USA
e-mail: garrison@lanl.gov

17.1.1 Additive Manufacturing Background

17.1.1.1 Types of Additive Manufacturing

AM techniques have been developed for a diverse array of materials including polymers, ceramics, metals, and composites. Polymer AM techniques include methods such as solidifying a resin using light or heat, melting plastic powder with a laser, binding plastic powders together with an adhesive, and extruding a plastic wire through a heated print head [2]. This last print technique, known as fused deposition modeling, is one of the cheapest and most versatile polymer printing options, making it a popular choice among hobbyists and professionals alike [1]. Metal AM has largely remained the province of industry and academia, primarily due to the far greater equipment and material costs involved. Metallic AM techniques generally work by fusing or melting metal powders, and vary primarily in the means by which the melting is accomplished [2]. Selective laser sintering uses a laser to fuse together selected areas of a bed of heated powdered metal in an inert atmosphere, and repeats the process layer by layer to create the desired part geometry [3]. Selective laser melting and electron beam melting operate similarly, but employ a more powerful laser or an electron beam to completely melt the powder. Laser engineered net shaping eschews a powder bed in favor of firing the metal dust directly into the laser beam using a nozzle. Ballistic particle manufacturing goes a step further, spraying molten metal directly from a nozzle [2].

17.1.1.2 Opportunities of Additive Manufacturing

AM allows designers and engineers to employ novel part geometries that would be costly or impossible to manufacture using conventional methods. Of particular interest are internal lattice structures, which emulate the porosity of natural materials, for example bird beaks. Manufacturing with such lattice structures results in products that are far lighter than bulk materials while maintaining much of their strength [4], which is particularly valuable for applications in aerospace [5]. Furthermore, AM offers manufacturers the opportunity to implement a distributed production environment. Rather than manufacturing all parts at a large central factory and then shipping those parts to their destinations, AM enables adoption of a nodal approach; sending out designs to satellite locations and printing them on-site. This more direct distribution method could dramatically reduce costs by trimming supply chains. For example, the ability to produce parts on demand would be of particular benefit in remote areas, which often face long wait times to receive even simple parts for maintenance and repairs. AM also reduces the consumption of materials by requiring only the amount of material directly used in the part to be consumed. In contrast, conventional bulk manufacturing requires removal of a significant amount of material from the bulk piece to achieve the desired part geometry. While this overrun can be recycled and repurposed, doing so generally requires shipping it off-site, whereas any unused AM material can be reused immediately with little to no reprocessing needed. This efficient material use also leads to greater energy efficiency for AM manufacturing [6].

17.1.1.3 Defining and Refining Additive Manufacturing Material Performance

Since the inception of AM, researchers have endeavored to characterize the mechanical behavior of AM parts. Due to the essentially infinite variety of possible design geometries it is not practical to elucidate every property of every possible combination of build parameters. Instead, researchers seek to identify broad trends as specific variables are altered [7]. Campanelli et al. demonstrated that greater part density yields greater compressive strength [8], while Yan et al. found that smaller lattice unit cells for a given level of porosity also increases compressive strength [9], confirming earlier work by Santorinaios et al. [10]. Multiple studies have shown that mechanical performance varies widely depending on the type of unit cell used to form a lattice [11–15]. Other design factors such as build orientation [16], particle size of the metal powder used [17], power and tracking speed of the laser [18, 19], and post-build processing [16, 20] also have significant impacts on the material qualities of the part produced. The majority of the research performed, to the best of the team's knowledge, to differentiate the mechanical qualities of AM parts has focused on static tensile and compressive tests, leaving something of a void in knowledge about the dynamic behavior of such parts.

Modal analysis, the systematic examination of an object's dynamic behavior within the frequency domain, can effectively evaluate additional mechanical properties of AM parts. West et al. demonstrated the use of modal analysis for determining the yield strength of AM parts [21]. Furthermore, modal analysis is a commonly accepted means of detecting damage in conventionally manufactured materials [22] and can likely be expanded to AM materials [23]. Modal analysis can also be a fast and cost effective method for assessing the quality of mass produced AM parts by comparing an individual part's resonant frequencies to those of an ideal template part [23, 24].

17.1.2 Digital Image Correlation Background

Digital Image Correlation (DIC) employs cameras and unique speckle patterns to quantify slight displacements of specimens during testing, resulting in a highly accurate record of a part's displacement and strain fields [25]. This record is then used to extract mode shapes and relevant frequencies. Extraction of full field strain measurements and modal responses using the DIC algorithm proceeds as follows [26]. A visible, usually planar, surface of the specimen is covered in a speckle pattern, which must be highly contrasting, detailed and aperiodic. After images are taken, the software divides the speckle area into subsets, each of which has a unique intensity signature. A shape function is used as an approximate spatial filter, which is moved over the whole specimen area in search of the best match. That best match provides the displacement estimate. Smaller subsets (requiring more and/or smaller speckles) permit the computation of displacements at higher spatial resolution. Secondary quantities like strain, velocity and acceleration can be calculated from displacement, and time histories from video support the use of Fourier methods.

DIC with one camera allows for 2D imaging and the addition of a second stereo camera allows for 3D imaging. 2D imaging is generally cheaper and easier to set up, but limits analysis to in-plane motion. For more general displacements across multiple degrees of freedom the 3D option is preferable. DIC can be used to perform non-destructive testing of lattice structures in AM parts [20]. This technique has proven to be particularly useful for the early detection of points of failure in AM parts, an important step forward in quality control [27].

17.1.3 Objectives

The wide range of processes included in AM along with a variety of machines for each process, a multitude of parameters that can be varied on each machine when creating nominally identical parts, and a virtually infinite selection of internal part geometries lead to high levels of uncertainty in material properties. While efforts have been made to quantify AM mechanical properties by static testing, much uncertainty remains regarding effects on dynamic response. Full-field measurements from DIC have been proven useful for characterizing mechanical properties from dynamic tests [28] for both isotropic and orthotropic materials [29].

This paper seeks to advance the knowledge of anisotropic build effects on dynamic behavior of AM parts, employing DIC and modal analysis along with systematic comparison to numerical models of part dynamics. Selection of print parameters, including build orientation and internal lattice is first discussed followed by details of the DIC set up and experimental methodology. Development of the accompanying finite element model is presented next. Effective bulk properties of the AM parts are determined through calibration of the model to experimentally measure modal frequencies. Finally, a discussion of the print parameter effects is provided with accompanying recommendations for further investigation.

17.2 Methodology

17.2.1 Design of Test Specimens

Test specimens used for the series of experiments herein are built with ABSplus-P340 polymer using a uPrint SE Plus [30], or with 316L stainless steel using a Concept Laser M2, which is a direct metal laser sintering machine [31]. The parts are designed to be rectangular cantilevers with high aspect ratio cross-sections to obtain relatively large displacements normal to the largest face and provide a wide, flat surface convenient for DIC speckling. Three solid ABS parts are printed with the dimensions shown in Fig. 17.1. Each part is built in a different orientation, as shown in Fig. 17.2. That is, all three parts in this set have the same outer geometry, but have their build layers oriented in different Cartesian directions.

A second set of three ABS parts is printed with internal lattices. Each lattice is a 2D cell pattern printed along the build orientation, as shown in Fig. 17.3. Thus the second set of parts corresponds to the same build orientations as in Fig. 17.2, with lattices oriented vertically with respect to the base plate. The lattices are only built in the cantilever section of each part—the base is left solid. The 2D cell pattern consists of 1.5 mm square holes separated by 1 mm solid walls, and surrounded by a 1 mm thick external wall. Figure 17.4 shows the outer dimensions of the lattice ABS set, which are increased from that of the solid ABS parts to allow for the internal lattice structures.

A third set of parts is built in solid steel. These parts are built with the same geometry as the solid ABS parts (Fig. 17.1), except they are 3 mm thick instead of 4 mm, and have a 5 mm fillet instead of 4 mm. The three steel parts are also built in the same orientations as the three solid ABS parts (Fig. 17.2).

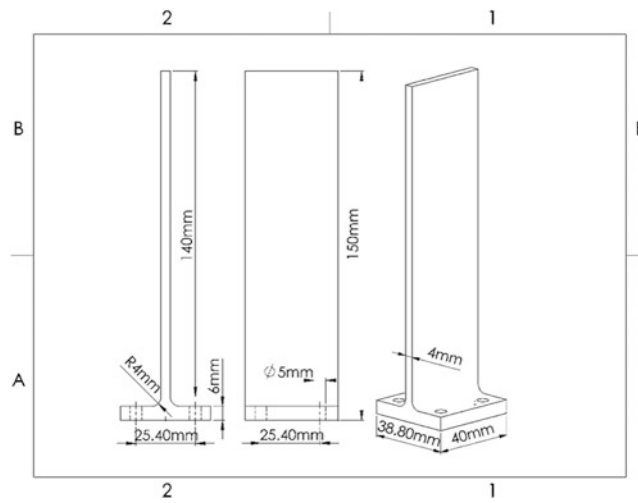


Fig. 17.1 Solid ABS part dimensions

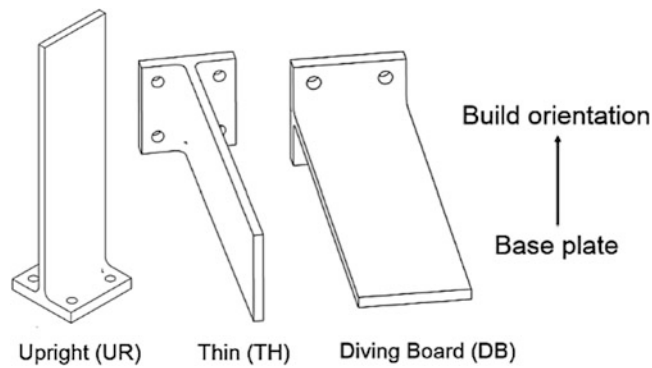


Fig. 17.2 Three unique build orientations

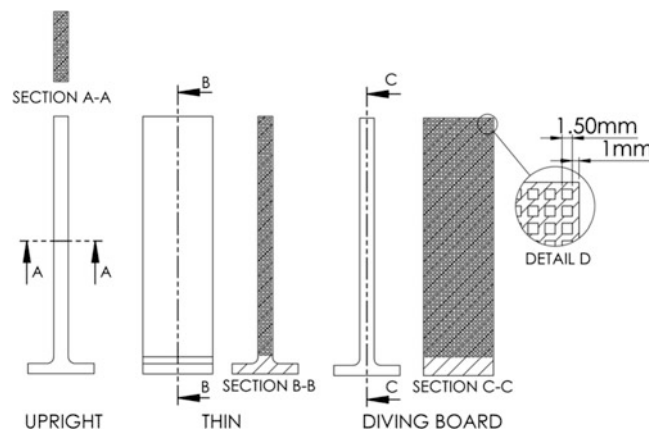


Fig. 17.3 Lattice ABS orientations and geometry

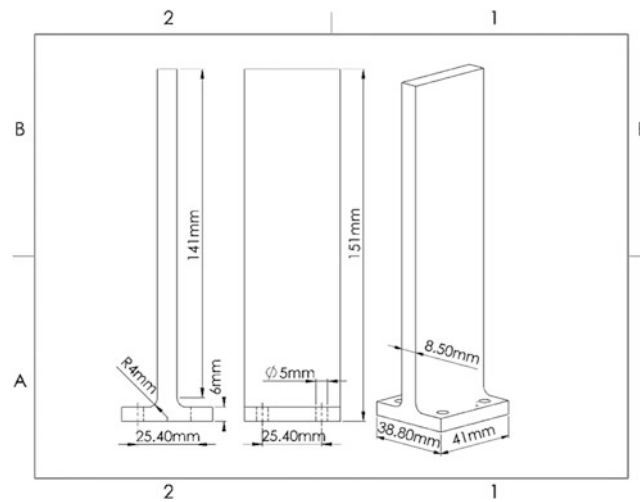


Fig. 17.4 Lattice ABS part dimensions

Fig. 17.5 Part mounted to shake table with speckle pattern applied for DIC



17.2.2 Digital Image Correlation Experimental Setup

The parts were excited by the translational oscillations of a shaker table using the Shaker Control software from Bruel & Kjaer Sound and Vibration Measurement. The shaker table was oriented so that the large face of the part oscillated normal to the imaging plane. Parts are secured to the shaker table with 4 mm bolts, as seen in Fig. 17.5. The bolts are torqued to 1.75 Nm. Parts were tested with a random excitation over select frequency ranges. Measurements for out of plane modes were collected in the following ranges: mode 1 at 20–100 Hz, etc. mode 2 100–500 Hz, mode 3 500–1000 Hz. Measurements for the torsional mode were collected between 20 and 500 Hz. The amplitude of the excitation was $0.5 \text{ g}^2/\text{Hz}$ in the chosen range, with no excitation outside the range.

A speckle pattern is applied to the face of the parts using speckles approximately 1 mm in diameter (Fig. 17.5). Displacement data was collected using two cameras for 3D DIC as shown in Fig. 17.6. The cameras are Photron AX200 Mini models with 35 mm lenses. The image capture software is Vic Snap and the image processing software used is Vic-3D, both produced by Correlated Solutions, Inc. A light source was placed between the cameras and the cameras were positioned about 0.5 m from the part on the shaker table.

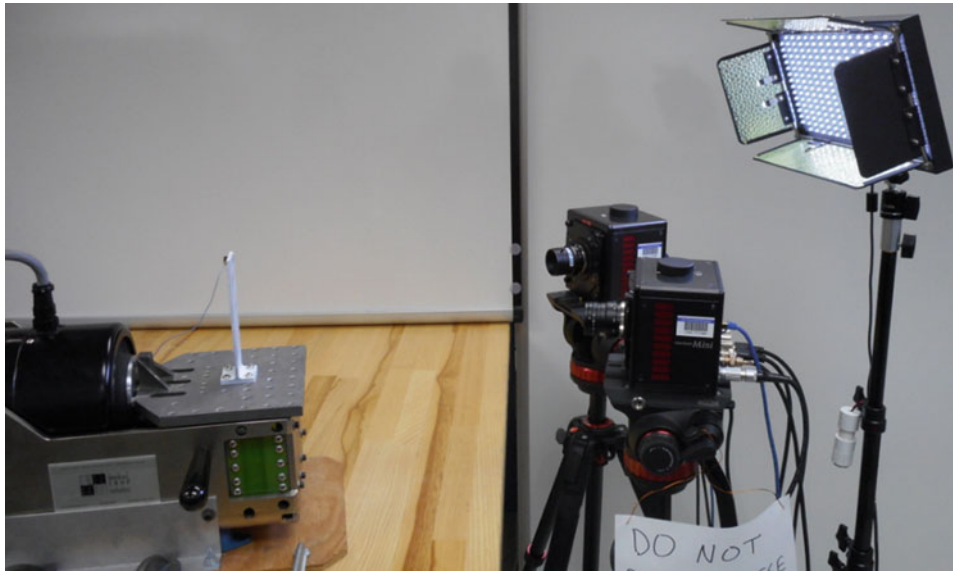


Fig. 17.6 The camera and part setup for DIC measurements. The shake table axis of excitation is towards and away from the cameras

The first step in operating the cameras was to set the focus. The apertures of both cameras were fully opened while live-imaging the part to narrow the depth of field so that the focus was as precise as possible. Next, calibration was performed at 1024×1024 resolution using a target plate associated with the software: holding the plate at different angles allows the software to calculate the location of the cameras in space. To ensure best results the calibration score, a measure of the deviation from a perfect match between the image pairs, was maintained below 0.1.

The part was replaced on the shaker table for data acquisition, and the camera resolution was set to 384×896 . Once the shaker table was turned on and operating at steady state a set of frames was recorded in Vic Snap and sent to Vic 3D for processing. The frame rates selected were dependent on the predicted frequency of the target mode: 750 fps for a target frequency of ~ 100 Hz, 1500 fps for ~ 300 Hz, 3000 fps for ~ 1000 Hz. The software extracts displacement histories of approximately 900 points, in all 3 degrees of freedom.

The 2-dimensional DIC calculation is completed as follows. Each subset of the speckled area of the samples has a unique intensity pattern $F_i(x, y)$ in the reference image (the first image of the series). The intensity pattern in the deformed image is $G_i(x, y, \mathbf{s})$ where \mathbf{s} is the translation vector relative to the reference location of the subset [26]. The translation vector \mathbf{s} is varied and an error metric summed over all pixels in the subset is calculated (Eq. 17.1). The value of \mathbf{s} that minimizes χ^2 is taken to be the best estimate of the subset displacement between the reference and deformed images.

$$\chi^2 = \sum_i (G_i(x, y, \mathbf{s}) - F_i(x, y))^2 \quad (17.1)$$

To calculate the mode shapes and frequencies, the displacement of each point is input to a fast Fourier transform. The displacement magnitudes in the frequency domain are averaged over all points to produce the final power frequency spectrum. The maximum average amplitude was typically about 0.1 mm for the lowest mode, against a noise floor in the frequency domain of 30 nm.

17.3 Finite Element Model

A baseline finite element model is developed using ABAQUS Finite Element software. Mesh fidelity along the cantilever cross section was varied between a shell model, a solid model two elements thick, and a solid model four elements thick. Modes are placed into four distinct classes, out of plane (OOP), torsion (TOR), in plane (IP) and extension (EXT), as shown in Fig. 17.7. The modal frequencies of the first four OOP modes converge at the solid model two elements thick, justifying the selection of this mesh for subsequent simulations (Table 17.1). Quadratic elements (C3D20R) are used with 2×20 elements for the cantilever cross section and 70 elements along the cantilever length. The inner faces of all four bolt holes are assumed to be fixed.

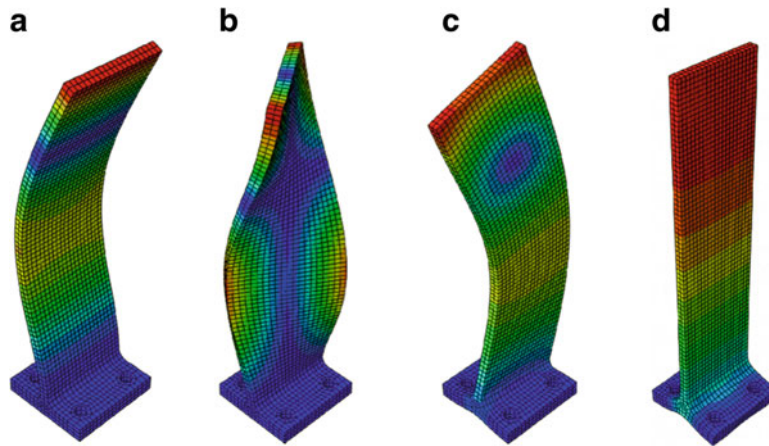
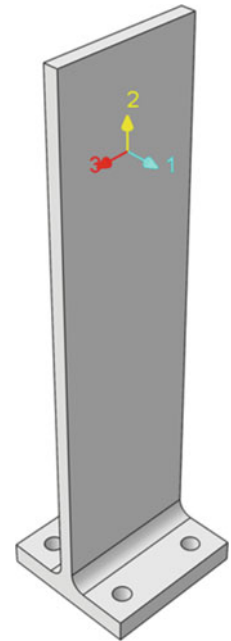


Fig. 17.7 Mode classes found include (a) out of plane (OOP), (b) torsion (TOR), (c) in plane (IP), and (d) extension (EXT)

Table 17.1 Results of mesh convergence study

	Shell	Solid, 2 elements thick	Solid, 4 elements thick
OOP 1 (Hz)	160	162	162
OOP 2 (Hz)	1001	1009	1008
OOP 3 (Hz)	2808	2813	2812
OOP 4 (Hz)	5521	5480	5477

Fig. 17.8 Standard directions assigned to material parameters



Material properties are defined by an elastic orthotropic material model, presented in Eq. (17.2). The ϵ_{12} equation has analogues in the 13 and 23 planes, making the matrix symmetric such that only 3 of the 6 Poisson’s ratios are independent. This model yields a total of 9 independent elastic parameters: $E_1, E_2, E_3, \nu_{12}, \nu_{13}, \nu_{23}, G_{12}, G_{13},$ and G_{23} , corresponding to the global orientation presented in Fig. 17.8.

$$\begin{bmatrix} \epsilon_{11} \\ \epsilon_{22} \\ \epsilon_{33} \end{bmatrix} = \begin{bmatrix} \frac{1}{E_1} & -\frac{\nu_{12}}{E_1} & -\frac{\nu_{13}}{E_1} \\ -\frac{\nu_{21}}{E_2} & \frac{1}{E_2} & -\frac{\nu_{23}}{E_2} \\ -\frac{\nu_{31}}{E_3} & -\frac{\nu_{32}}{E_3} & \frac{1}{E_3} \end{bmatrix} \begin{bmatrix} \sigma_{11} \\ \sigma_{22} \\ \sigma_{33} \end{bmatrix} \quad 2\epsilon_{12} = \frac{\sigma_{12}}{G_{12}} \quad (17.2)$$

17.4 Results and Discussion

17.4.1 Modal Analysis

Uncertainty in the experimentally measured modal frequencies was estimated by running each experiment three times and extracting data from the highest point near the local maximum from the raw data on each run. Figure 17.9 illustrates the extracted modal peaks for three runs. The part for this test is a solid built in a vertical orientation made with ABS plastic, with a 4×40 mm cross-section and a beam length of 140 mm. The shaker table was set to random excitation between 20 and 2000 Hz in the OOP direction. Noise in the measurements is likely caused by ambient vibrations, camera distortion and possible buoyancy waves from the heat of the lights. Despite the background noise the results of interest are not obscured. The precision uncertainty was estimated as half the distance between frequency points on the spectrum and then added to the sample standard deviation to represent the total uncertainty.

The natural frequencies of the first three OOP modes and first torsion mode for the solid ABS parts are given in Table 17.2. The excitation used to obtain the OOP modes was single-axis translational vibration. Such an arrangement minimizes the bending moment of inertia to get the largest possible displacements for easier observation. However, the torsional modes could not be excited with the linear shaker available. Therefore the parts were statically torsion loaded and their transient free responses when released were recorded. Typical DIC images of the first 3 OOP modes are shown in Fig. 17.10. The cameras were able to detect a coherent mode shape on displacement scales below $1 \mu\text{m}$.

The natural frequencies of the first three OOP modes for the lattice ABS parts are given in Table 17.3. Torsion mode frequencies were not calculated for these parts due to their large cross-sectional area, which prevented the torsion modes from being adequately excited and measured.

The natural frequencies for the first three OOP modes, and the first (and, in the DB orientation, second) torsional modes for the steel parts are given in Table 17.4. For these metal parts, torsional data and OOP data were obtained from the same experiments. That is, OOP linear shaker excitation was able to excite the torsion modes enough to be detected, whereas

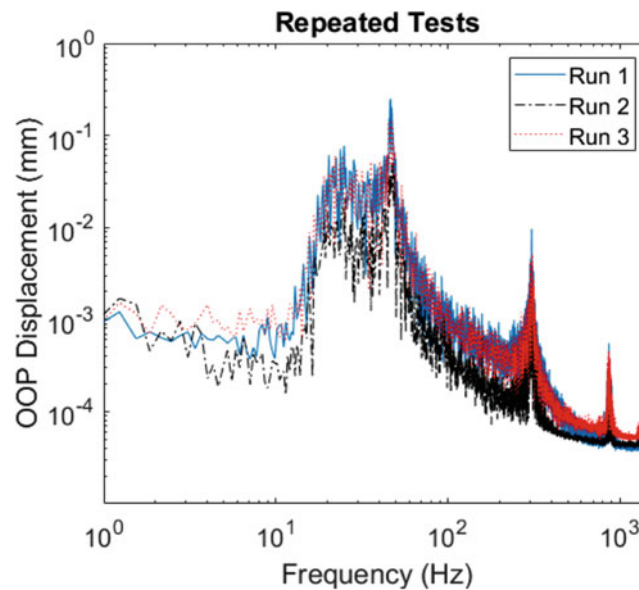


Fig. 17.9 A comparison of displacement spectra between three nominally identical runs for quantifying measurement uncertainty

Table 17.2 Measured natural frequencies of the solid ABS parts built in three distinct orientations

Mode	Orientation		
	UR	TH	DB
OOP 1 (Hz)	47.3 ± 0.9	51.0 ± 0.2	45.5 ± 0.5
OOP 2 (Hz)	308.1 ± 0.6	323.4 ± 0.2	284 ± 3
OOP 3 (Hz)	868 ± 6	909 ± 3	848 ± 8
TOR 1 (Hz)	340 ± 3	350 ± 3	389 ± 2

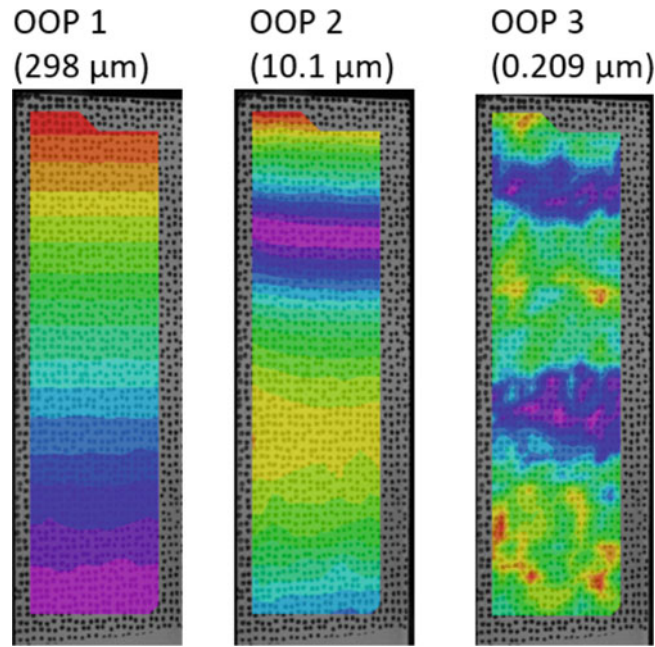


Fig. 17.10 Typical DIC images of the first 3 OOP bending modes, with absolute displacements. Every consecutive peak (yellow/red areas) alternates between into the page and out of the page, while every purple area is a node

Table 17.3 Measured natural frequencies of ABS parts manufactured with three distinct lattice orientations

Mode	Orientation		
	UR	TH	DB
OOP 1 (Hz)	102.5 ± 0.7	99.6 ± 0.7	101.3 ± 0.3
OOP 2 (Hz)	650 ± 3	615 ± 2	629 ± 3
OOP 3 (Hz)	1793 ± 8	1682 ± 5	1759 ± 6

Table 17.4 Measured natural frequencies of the SLM steel parts built in three distinct orientations

Mode	Orientation		
	UR	TH	DB
OOP 1 (Hz)	119 ± 1	120 ± 2	116.7 ± 0.1
OOP 2 (Hz)	716 ± 1	729 ± 3	713 ± 4
OOP 3 (Hz)	899.5 ± 0.3	909 ± 3	780 ± 1
TOR 1 (Hz)	2046 ± 4	2099.8 ± 0.8	2040 ± 3
TOR 2 (Hz)	NA	NA	2439.4 ± 0.4

this was not the case for the plastic parts (thus the need for static torsion loading for the plastic parts). It is believed that the two steel torsion modes are visible even in OOP excitation due to reduced torsional damping compared to the plastic parts.

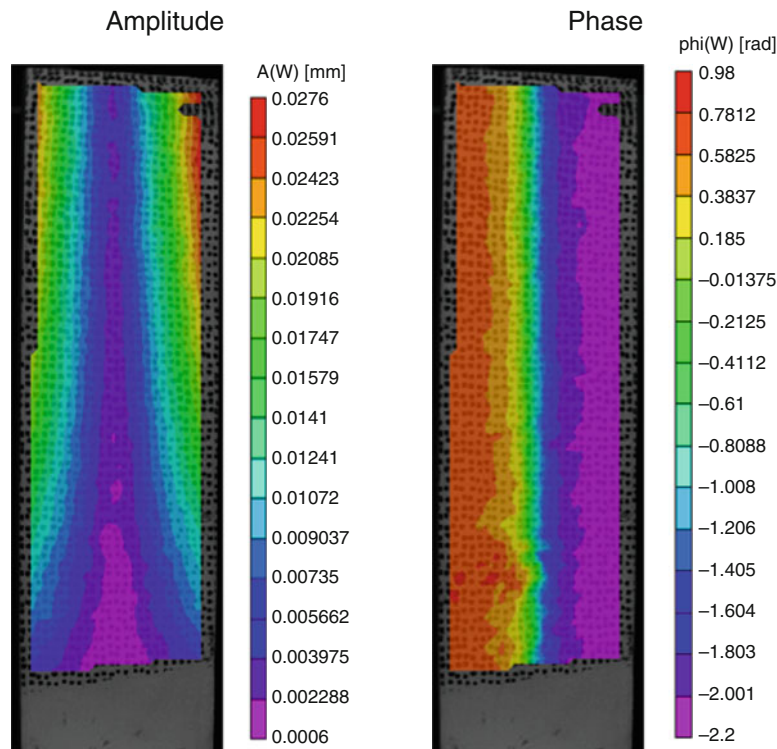
For the solid ABS parts, the thin orientation is the stiffest in bending (implied by high natural frequency), followed by the upright and finally the diving board parts. For the lattice ABS parts, the Upright orientation is the stiffest, followed closely by the Diving Board, and with the Thin orientation least stiff. The solid steel parts had the same pattern of stiffness as the solid ABS parts; the thin orientation was stiffest, followed closely by the upright part, with the DB part having a significantly lower stiffness, as reflected by their natural frequencies.

Damping ratio was determined from the specimen response from torsional loading. A Fourier transform was performed on small windows of the deflection at the two top corners, to capture both the first bending mode (as the corners deflect together) and the first torsion mode (as the corners deflect out of phase). Results are shown in Table 17.5, and a typical DIC image of the first torsion mode (amplitude and phase) is shown in Fig. 17.11.

The diving board orientation appears to be more damped than the thin or upright orientations, though this requires verification. The torsion frequency of the diving board is also significantly higher than the other orientations.

Table 17.5 Estimated damping ratios of the first torsion and OOP modes for all parts

Mode	Orientation		
	UR	DB	TH
ABS Solid TOR 1 Damping Ratio	0.012 ± 0.004	0.015 ± 0.002	0.009 ± 0.004
ABS Solid OOP 1 Damping Ratio	0.010 ± 0.002	0.020 ± 0.004	0.009 ± 0.001
ABS Lattice TOR 1 Damping Ratio	NA	NA	NA
ABS Lattice OOP 1 Damping Ratio	0.012 ± 0.001	0.0078 ± 0.0007	0.0075 ± 0.0006
Steel TOR 1 Damping Ratio	0.0016 ± 0.0003	0.0011 ± 0.0006	0.00025 ± 0.00007
Steel OOP 1 Damping Ratio	0.00025 ± 0.00005	0.0017 ± 0.0001	0.0015 ± 0.0001

**Fig. 17.11** Typical DIC images of the amplitude (left) and phase (right) of the first torsion mode

17.4.2 Simulations

Ten model input parameters present a significant challenge for inverse analysis. In fact, as the following results show, such a problem would be ill-posed and have non-uniqueness of solutions for the specific test structures under consideration. To reduce the model input dimension, a Taguchi orthogonal array subset of the parameter space is simulated in ABAQUS and the relative contribution of each input parameter to the frequencies of each mode class is evaluated. The Taguchi subset consists of 128 parameter sets with each parameter having 2 levels. This yields a factor resolution of 5, so primary factor effects are only confounded with 4-factor interactions or higher. The coefficients of determination for each parameter are presented in Fig. 17.12.

For all mode shape classes, only three of the input parameters are non-negligible: density and two elastic moduli. This creates the previously discussed non-uniqueness issue. Only the two stress moduli are considered in the inverse analyses, since density can be measured empirically (Table 17.6). This reduces the model calibration problem to two dimensions. Broyden's method [32] is used to optimize the simulated modal frequencies to the experimental modal frequencies, with respect to the input elastic and shear moduli. Resulting calibrated values for solid and lattice parts are presented in Table 17.7. Ranges are provided which correspond to the uncertainty of the experimental data. Percent comparisons of the midpoints are also calculated, relative to the Upright orientation.

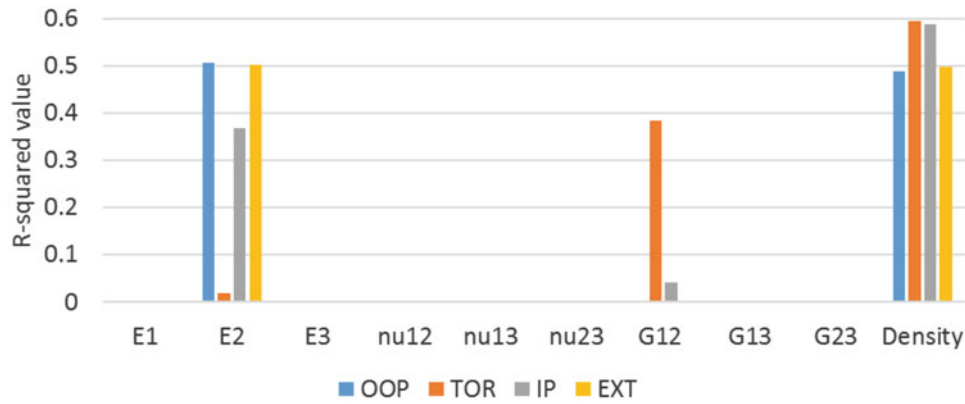


Fig. 17.12 The significance results from the parametric study. Three of ten parameters are found to have high significance, justifying down selection for calibration

Table 17.6 Measured densities of all parts

	UR	TH	DB
ρ (solid ABS) [kg/m ³]	1021.24	992.83	1089.44
ρ (lattice ABS) [kg/m ³]	804.71	747.07	777.19
ρ (solid Steel) [kg/m ³]	7922.42	7712.43	7853.74

Table 17.7 Calibrated elastic parameters for different orientations, internal structure, and material. Percent change is relative to the upright (UR) configuration

		UR	TH	DB
G (solid ABS) [GPa]	Value	0.890–0.921	0.910–0.946	1.282–1.309
	% change	–	+2.48%	+43.07%
E (solid ABS) [GPa]	Value	2.085–2.262	2.458–2.502	2.069–2.139
	% change	–	+14.10%	–3.20%
G (solid Steel) [GPa]	Value	85.5–85.4	81.1–80.8	61.6–61.9
	% change	–	–5.36%	–27.74%
E (solid Steel) [GPa]	Value	187.3–194.0	182.1–195.6	181.5–182.1
	% change	–	–0.95%	–4.64%
E (lattice ABS) [GPa]	Value	1.966–1.977	1.676–1.734	1.849–1.876
	% change	–	–13.52%	–5.53%



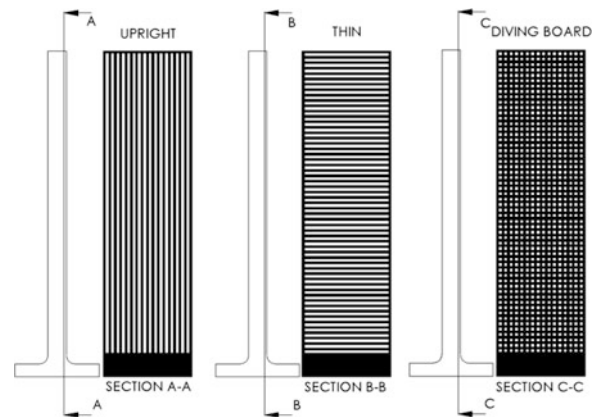
Fig. 17.13 Ink impression of the hatch pattern implemented in the uPrint machine

17.4.3 Discussion

The various stiffnesses of the solid ABS parts in different orientations is potentially explained by the layer build process in the uPrint machine. In general, the print head lays out the boundary of each 2D layer first, then fills the interior with diagonal hatches, as shown in Fig. 17.13. In the thin orientation, these boundaries are aligned axially on the largest face of the part (the imaging face), such that axial loads are borne by continuously extruded filaments. In the DB orientation, however, the build layer boundaries are around the perimeter of this face, and the face is filled with less-stiff diagonal hatches. The upright orientation is distinct in that axial loads are borne by the fused material between build layers. Such a connection is less stiff than the continuous filaments of the thin orientation, but apparently stiffer than the diagonal hatches of the DB orientation.

The printing of lattices, which were aligned with the build direction to avoid using support material, introduces very different anisotropies. It is posited that the anisotropy here is dominated by lattice geometry, not build layer orientation (as is the case for solid parts). The stiffest lattice orientation is upright, since axial loads are resisted with continuous material. The

Fig. 17.14 The geometry of the lattice parts within the outer walls



DB orientation is moderately less stiff than upright, and the thin orientation is the least stiff. Excluding the external walls of the parts (a common element between all three), the DB part has better axial connections than the thin part (Fig. 17.14). If we were to test the in-plane bending modes, we expect the thin and upright parts to be stronger than the DB part for the same reason.

The main result of this work with respect to torsion modes and modal damping ratios is that the DB orientation has the highest torsion frequency, as well as the most damping in both torsion and out of plane modes. If one imagines an oscillating AM part as laminated sheets rubbing against each other, the DB part has by far the largest sheets, and so the highest friction loss. Other damping effects may be less significant. The upright part has a slightly higher torsion frequency than the thin part, and the damping ratios of the two are indistinguishable. The reason for this last observation may be that the thin part has a larger area of contact between adjacent build layers, producing greater stiffness across them.

17.5 Future Work

A primary goal of future research is to apply the same experimental and analytical methods to metal parts that incorporate lattice structures, because those geometries are essential for many promising applications. It would also be interesting to measure the effect of part damage with DIC, either by deliberately introducing flaws into the printed part, or by shaking a resonant mode with sufficient amplitude to induce fatigue cracks or plastic deformation.

This work did not exploit the capability of DIC to calculate full-field strains in the visible face of the parts. Such strain data could be paired with ABAQUS simulations to locally calibrate material properties, such that a spatial distribution could be obtained. This would help model the spatial variation of material properties in metal AM parts, which arise from different thermal cooling and crystallization rates throughout the build process.

Acknowledgements The authors would like to acknowledge the mentors and staff of Los Alamos National Laboratory Engineering Institute for the 19th Dynamics Summer School, which funded this research.

References

1. Gao, W., Zhang, Y., Ramanujan, D., Ramani, K., Chen, Y., Williams, C., Wang, C., Shin, Y., Zhang, S., Zavatiari, P.D.: The status, challenges, and future of additive manufacturing in engineering. *Comput. Aided Des.* **69**, 65–89 (2015)
2. Bikas, H., Stavropoulos, P., Chryssolouris, G.: Additive manufacturing methods and modelling approaches: a critical review. *Int. J. Adv. Manuf. Technol.* 389–405 (2016)
3. Alsalla, H., Liang, H., Smith, C.: Fracture toughness and tensile strength of 316L stainless steel cellular lattice structures manufactured using the selective laser melting technique. *Mater. Sci. Eng. A.* **669**, 1–6 (2016)
4. Seki, Y., Kad, B., Benson, D., Meyers, M.: The toucan beak: structure and mechanical response. *Korean J. Couns. Psychother.* **26**, 1412–1420 (2006)
5. Ferro, C., Varetti, S., De Pasquale, G., Maggiore, P.: Lattice structured impact absorber with embedded anti-icing system for aircraft wings fabricated with additive SLM process. *Mater Today Commun.* **15**, 185–189 (2018)
6. Ford, S., Despeisse, M.: Additive manufacturing and sustainability: an exploratory study of the advantages and challenges. *J. Clean. Prod.* **137**, 1573–1587 (2016)

7. Shamsaei, N., Yadollahi, A., Bian, L., Thompson, S.: An overview of direct laser deposition for additive manufacturing: part II: mechanical behavior, process parameter optimization and control. *Addit. Manuf.* **8**, 12–35 (2015)
8. Campanelli, S., Contuzzi, N., Ludovico, A., Caiazzo, F., Cardaropoli, F., Sergi, V.: Manufacturing and characterization of Ti6Al4V lattice components manufactured by selective laser melting. *Materials*. **7**, 4803–4822 (2014)
9. Yan, C., Hao, L., Hussein, A., Raymond, D.: Evaluations of cellular lattice structures manufactured using selective laser melting. *Int. J. Mach. Tools Manuf.* **62**, 32–38 (2012)
10. Santorinaios, M., Brooks, W., Sutcliffe, C., Mines, R.: Crush behaviour of open cellular lattice structures manufactured using selective laser melting. In: *WIT transactions on the built environment*, vol. 85, no. high performance structures and materials III, pp. 481–490. WIT Press, New Forest (2006)
11. Kohnen, P., Haase, C., Bultmann, J., Ziegler, S., Schleifenbaum, J., Bleck, W.: Mechanical properties and deformation behavior of additively manufactured lattice structures of stainless steel. *Mater. Des.* **145**, 205–217 (2018)
12. Leary, M., Mazur, M., Elambasseril, J., McMillan, M., Chirent, T., Sun, Y., Qian, M., Easton, M., Brandt, M.: Selective laser melting (SLM) of AlSi12Mg lattice structures. *Mater. Des.* **98**, 344–357 (2016)
13. Mazur, M., Leary, M., Sun, S., Vcelka, M., Shidid, D., Brandt, M.: Deformation and failure behavior of Ti-6Al-4V lattice structures manufactured by selective laser melting (SLM). *Int. J. Adv. Manuf. Technol.* **84**, 1391–1411 (2016)
14. Rahman Rashid, R., Mallavarapu, J., Palanisamy, S., Masood, S.: A comparative study of flexural properties of additively manufactured aluminum lattice structures. *Mater. Today Proc.* **4**, 8597–8604 (2017)
15. Xiao, Z., Yang, Y., Xiao, R., Bai, Y., Song, C., Wang, D.: Evaluation of topology-optimized lattice structures manufactured via selective laser melting. *Mater. Des.* **143**, 27–37 (2018)
16. Wauthle, R., Vrancken, B., Beynaerts, B., Jorissen, K., Schrooten, J., Kruth, J., Humbeek, J.: Effects of build orientation and heat treatment on the microstructure and mechanical properties of selective laser melted Ti6Al4V lattice structures. *Addit. Manuf.* **5**, 77–84 (2015)
17. Mullen, L., Stamp, R., Brooks, W., Jones, E., Sutcliffe, C.: Selective laser melting: a regular unit cell approach for the manufacture of porous, titanium, bone in-growth constructs, suitable for orthopedic applications. *J. Biomed. Mater. Res. B Appl. Biomater.* **89**, 325–334 (2009)
18. Qiu, C., Yue, S., Adkins, N., Ward, M., Hassanin, H., Lee, P., Withers, P., Attallah, M.: Influence of processing conditions on strut structure and compressive properties of cellular lattice structures fabricated by selective laser melting. *J. Mater. Sci. Eng. A.* **628**, 188–197 (2015)
19. Topanos, S., Mines, R.A.W., McKown, S., Shen, Y., Cantwell, W., Brooks, W., Sutcliffe, C.: The influence of processing parameters on the mechanical properties of selectively laser melted stainless steel microlattice structures. *J. Manuf. Sci. Eng.* **132**, 041011–041012 (2010)
20. Gorny, B., Niendorf, T., Lackmann, J., Thoene, M., Troester, T., Maier, H.: In situ characterization of the deformation and failure behavior of non-stochastic porous structures processed by selective laser melting. *J. Mater. Sci. Eng. A.* **528**, 7962–7967 (2011)
21. West, B., Capps, N., Urban, J., Pribe, J., Hartwig, T., Lunn, T., Brown, B., Bristow, D., Landers, R., Kinzel, E.: Modal analysis of metal additive manufactured parts. *Manuf. Lett.* **13**, 30–33 (2017)
22. Hearn, G., Testa, R.: Modal analysis for damage detection in structures. *J. Struct. Eng.* **117**(10), 3042–3063 (1991)
23. Pribe, J., West, B., Gegel, M., Hartwig, T., Lunn, T., Brown, B., Bristow, D., Landers, R., Kinzel, E.: Modal Response as a validation technique for metal parts fabricated with selective laser melting. In: *Proceedings of the 27th Annual International Solid Freeform Fabrication Symposium*, Kansas City (2016)
24. Sharratt, B.: Non-destructive techniques and technologies for qualification of additive manufactured parts and processes: a literature review. Sharratt Research and Consulting Inc, Victoria (2015)
25. Reu, P., Miller, T.: The application of high-speed digital imaging correlation. *J. Strain Anal.* **43**, 673–688 (2008)
26. Sutton, M., Orteu, J., Schreier, H.: *Image correlation for shape, motion and deformation measurements: basic concepts, theory and applications*. Springer, New York (2009)
27. Brenne, F., Niendorf, T., Maier, H.: Additively manufactured cellular structures: Impact of microstructure and local strains on the monotonic and cyclic behavior under uniaxial and bending load. *J. Mater. Process. Technol.* **213**, 1558–1564 (2013)
28. Hild, F., Roux, S.: Digital image correlation: from displacement measurement to identification of elastic properties—a review. *Strain*. **42**, 69–80 (2006)
29. Lecompte, D., Smits, A., Sol, H., Vantomme, J., Van Hemelrijck, D.: Mixed numerical–experimental technique for orthotropic parameter identification using biaxial tensile tests on cruciform specimens. *Int. J. Solids Struct.* **44**, 1643–1656 (2007)
30. Stratasy: ABSplus-P430: production-grade thermoplastic for 3D printers (2008)
31. Protolabs: Direct metal laser sintering: stainless steel 316L product specifications (2018)
32. Broyden, C.G.: A class of methods for solving nonlinear simultaneous equations. *Math. Comput.* **19**(92), 577–593 (1965)

Chapter 18

How Linear Is a Linear System?



D. Roettgen, B. Pacini, and B. Moldenhauer

Abstract Often, when testing structures, engineers assume the experimental system only exhibits linear behavior. This linear assumption means that the modal frequency and damping of the structure do not change with response level. In many assembled structures, components are connected through bolted joints. These systems behave in a weakly nonlinear fashion due to frictional contact at these interfaces, but often these structures are still treated linearly at low excitation levels. This work contains a case study where an assumed linear system exhibits nonlinear behavior. Because of this nonlinearity, if the force applied to the structure during *linear* testing is not sufficiently low then the test may capture a nonlinear frequency or damping instead of the true linear parameters. The errors associated with this linearization causes inaccuracy when simulating a system response. In particular, a linear substructuring problem is presented in which true linear frequencies and damping ratios are compared to slightly nonlinear counterparts to observe the error caused in the assembled response. This paper documents lessons learned and heuristics to be considered when capturing true linear parameters from a weakly nonlinear structure.

Keywords Linear modal analysis · Nonlinear systems · Structural dynamics · Heuristics · Best practices

18.1 Introduction

Traditional experimental modal analysis transforms a set of measured responses into single degree-of-freedom (DOF) modal responses. Linear modal analysis is a useful tool for updating finite element models, performing low excitation level system predictions, and obtaining modal information about a mechanical system (i.e., natural frequencies and mode shapes). Many industries manufacture mechanical systems assembled using bolted joints. The frictional interfaces that occur due to these joints often introduce nonlinearity into an otherwise linear system. This type of weakly nonlinear response is often observed experimentally as a small change in frequency and a large change in damping [1–3]. Often this nonlinearity is overlooked when predicting system response which can lead to erroneous results.

This work shows the errors that can arise when one assumes linearity of a weakly nonlinear system. This is shown through an experimental-analytical substructuring when the wrong linear parameters are identified due to a weak nonlinearity. The assembly of interest contains multiple bolted joints which add nonlinearity to the system. This system was previously tested to assess the nonlinear response in [3–5] where in [5] the authors completed nonlinear substructuring on the same structure of interest. In [5] the linear substructuring errors for the system were significantly lower than previous works using similar techniques. This study documents the methods used to minimize these substructuring errors through the use of nonlinear theory and testing, providing heuristics and tools to ensure an experimentalist is obtaining the linear dynamics of a break system.

Sandia National Laboratories is a multisession laboratory managed and operated by National Technology and Engineering Solutions of Sandia, LLC., a wholly owned subsidiary of Honeywell International, Inc., for the U.S. Department of Energy's National Nuclear Security Administration under contract DE-NA-0003525. This paper describes objective technical results and analysis. Any subjective views or opinions that might be expressed in the paper do not necessarily represent the views of the U.S. Department of Energy or the United States Government.

D. Roettgen (✉) · B. Pacini
Department of Structural Dynamics, Sandia National Laboratories, Livermore, CA, USA

B. Moldenhauer
Department of Engineering Physics, University of Wisconsin-Madison, Madison, WI, USA

This paper is organized as follows. Section 18.2 details the substructuring example covered in this work. Section 18.3 provides the theory behind the substructuring method used and the tools suggested to obtain true linear parameters of the system. Section 18.4 steps through a case study on the experimental system. Finally, Section 18.5 contains conclusions from this study.

18.2 Subcomponent Definitions

The structure of interest consists of five main parts: the nose-beam, plate, cylinder, aft-plate, and tail-beam. The beam is bolted to the plate which is attached to the cylinder using eight bolts. The aft plug threads into the cylinder and has a flange that seats on the aft of the cylinder. Finally, the tail is attached to the plug by two bolts. A finite element mesh of the structure is shown in Fig. 18.1 and the physical hardware is shown in Fig. 18.2.

To complete substructuring predictions for this structure, two subcomponent assemblies were tested. The first, subcomponent *A*, consists of the nose-beam, plate, cylinder, and aft-plate, with no tail-beam. The second subcomponent, *B*, consists of the plate, cylinder, aft-plate and tail-beam. Finally, a finite element model of the cylinder with end plates is used to connect the two structures. This work stems from [5] where more details on the experimental set-up and substructuring configurations can be found.

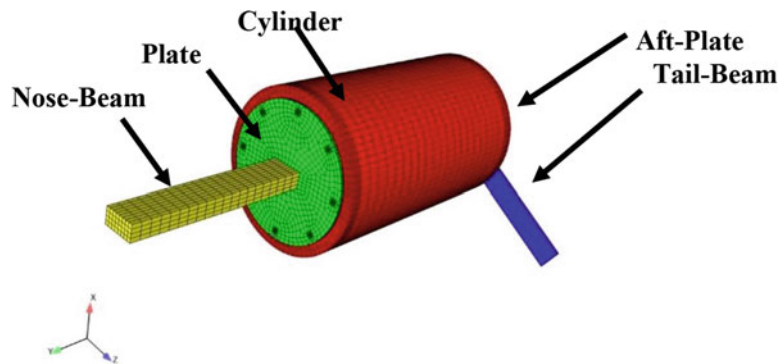


Fig. 18.1 Truth assembly solid model and structure identification

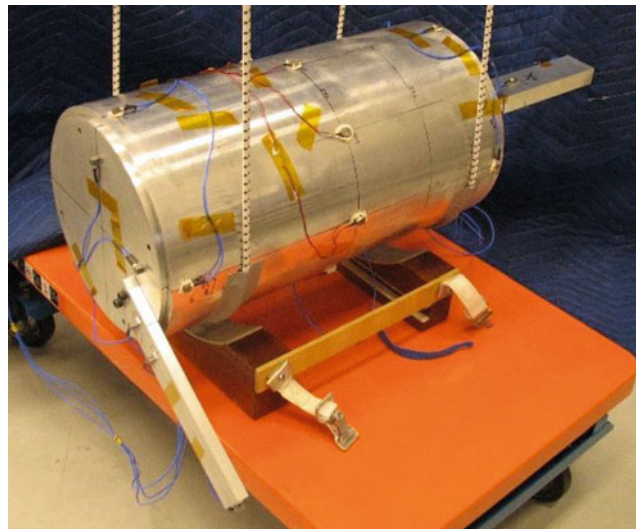


Fig. 18.2 Truth assembly test hardware

18.3 Theory

This section provides an overview for the theory used in this work. First, the dynamic substructuring theory of the transmission simulator (TS) method is presented. Second, a nonlinear analysis tool, the Hilbert Transform, is presented as a means to verify the linear modal parameters extracted from measurements.

18.3.1 Transmission Simulator Method

The Transmission Simulator method was first introduced by Allen and Mayes in [6]. This method provides a quality experimental model and best simulates the boundary conditions between subcomponents by mass-loading the interface between subcomponents. In this study, experimental subcomponent A and B are connected by a central cylinder which acts as a mass-loading of the jointed interface. The theory for the TS method is briefly discussed here for convenience.

First, each subcomponent is written as a set of uncoupled modal equations of motion. Modal parameters ω , ζ , and ϕ are the linear natural frequency, damping ratio, and mode shapes of a subcomponent model. The modal acceleration, velocity and displacement and external force are represented by \ddot{q} , \dot{q} , q , and F , respectively.

$$\begin{aligned}
 \begin{bmatrix} I_A & 0 & 0 \\ 0 & I_B & 0 \\ 0 & 0 & -I_{TS} \end{bmatrix} \begin{Bmatrix} \ddot{q}_A \\ \ddot{q}_B \\ \ddot{q}_{TS} \end{Bmatrix} + \begin{bmatrix} \begin{bmatrix} \ddots & 2\zeta_A\omega_A & \ddots \end{bmatrix} & 0 & 0 \\ 0 & \begin{bmatrix} \ddots & 2\zeta_B\omega_B & \ddots \end{bmatrix} & 0 \\ 0 & 0 & -\begin{bmatrix} \ddots & 2\zeta_{TS}\omega_{TS} & \ddots \end{bmatrix} \end{bmatrix} \begin{Bmatrix} \dot{q}_A \\ \dot{q}_B \\ \dot{q}_{TS} \end{Bmatrix} \\
 + \begin{bmatrix} \begin{bmatrix} \ddots & \omega_A^2 & \ddots \end{bmatrix} & 0 & 0 \\ 0 & \begin{bmatrix} \ddots & \omega_B^2 & \ddots \end{bmatrix} & 0 \\ 0 & 0 & -\begin{bmatrix} \ddots & \omega_{TS}^2 & \ddots \end{bmatrix} \end{bmatrix} \begin{Bmatrix} q_A \\ q_B \\ q_{TS} \end{Bmatrix} = \begin{Bmatrix} \phi_A^T F_A \\ \phi_B^T F_B \\ \phi_{TS}^T F_{TS} \end{Bmatrix}
 \end{aligned} \tag{18.1}$$

To couple the subcomponents, constraints must be enforced on these equations of motion. The constraints are first written in the form of Eq. (18.2). Here, x represents physical displacements of each subcomponent, and \tilde{B} is a Boolean matrix such that the motion of shared DOFs between multiple subcomponents are equal.

$$\tilde{B} \begin{Bmatrix} x_A \\ x_B \\ x_{TS} \end{Bmatrix} = 0 \tag{18.2}$$

Using a modal approximation, this constraint equation can be transformed into modal coordinates as shown in Eq. (18.3). The constraints have been softened using the pseudo-inverse of the TS shapes as it would be difficult to enforce them strictly when using measured data [6].

$$\begin{bmatrix} \phi_{TS}^\dagger & 0 \\ 0 & \phi_{TS}^\dagger \end{bmatrix} \begin{bmatrix} \phi_A & 0 & -\phi_{TS} \\ 0 & \phi_B & -\phi_{TS} \end{bmatrix} \begin{Bmatrix} q_A \\ q_B \\ q_{TS} \end{Bmatrix} = \tilde{B} \begin{Bmatrix} q_A \\ q_B \\ q_{TS} \end{Bmatrix} = 0 \tag{18.3}$$

A coordinate transformation $q = L\eta$ is used to enforce these constraints on the uncoupled equations of motion. Rewriting the constraints in terms of the new generalized coordinate is shown in Eq. (18.4).

$$\tilde{B}L\eta = 0 \tag{18.4}$$

Because \tilde{B} is known and because η is arbitrary, L must reside in the nullspace of \tilde{B} .

$$L = null\left(\tilde{B}\right) \quad (18.5)$$

Using the transformation matrix L , the uncoupled equations of motion can be synthesized into a new set of equations of motion which describe the dynamics of the fully coupled structure. Solving the eigenvalue problem of these equations of motion provides predictions of linear natural frequencies and modes shapes of the assembled structure. Note, the predictions of the assembly involve the linear natural frequencies and damping ratios of the subcomponent system. Therefore, if those are inaccurately measured due to nonlinearity the system level predictions will be inaccurate. This study will explore the magnitude of such errors when the nonlinearity of the system is activated during linear testing.

$$L^T \begin{bmatrix} I_A & 0 & 0 \\ 0 & I_B & 0 \\ 0 & 0 & -I_{TS} \end{bmatrix} L \begin{Bmatrix} \ddot{\eta}_A \\ \ddot{\eta}_B \\ \ddot{\eta}_{TS} \end{Bmatrix} + L^T \begin{bmatrix} \left[\begin{smallmatrix} \dots & 2\zeta_A \omega_A & \dots \end{smallmatrix} \right] & 0 & 0 \\ 0 & \left[\begin{smallmatrix} \dots & 2\zeta_B \omega_B & \dots \end{smallmatrix} \right] & 0 \\ 0 & 0 & - \left[\begin{smallmatrix} \dots & 2\zeta_{TS} \omega_{TS} & \dots \end{smallmatrix} \right] \end{bmatrix} L \begin{Bmatrix} \dot{\eta}_a \\ \dot{\eta}_B \\ \dot{\eta}_{TS} \end{Bmatrix} \\ + L^T \begin{bmatrix} \left[\begin{smallmatrix} \dots & \omega_A^2 & \dots \end{smallmatrix} \right] & 0 & 0 \\ 0 & \left[\begin{smallmatrix} \dots & \omega_B^2 & \dots \end{smallmatrix} \right] & 0 \\ 0 & 0 & - \left[\begin{smallmatrix} \dots & \omega_{TS}^2 & \dots \end{smallmatrix} \right] \end{bmatrix} L \begin{Bmatrix} \eta_A \\ \eta_B \\ \eta_{TS} \end{Bmatrix} = L^T \begin{Bmatrix} \phi_A^T F_A \\ \phi_B^T F_B \\ \phi_{TS}^T F_{TS} \end{Bmatrix} \quad (18.6)$$

18.3.2 The Hilbert Transform

Low-level testing is used to capture the linear modal parameters of each subcomponent. To ensure the linear test is not exhibiting any nonlinear behavior the authors implemented the Hilbert Transform, using the process described below [7]. To use this tool a high-level excitation is performed to obtain ringdown data from the structure. Then, the physical measurements from this excitation are transformed to a modal response using the mode shape matrix as a spatial filter.

The Hilbert Transform assumes the modal response can be rewritten in an exponential form as shown in Eq. (18.7), where $\psi_r(t)$ is the Hilbert envelope and $\psi_i(t)$ is the unwrapped phase.

$$\ddot{q} = e^{\psi_r(t) + i\psi_i(t)} \quad (18.7)$$

This amplitude and phase can be fit and used to calculate a time varying frequency and damping ratio for the measured response.

$$\omega_d(t) = \frac{d\psi_i}{dt} \quad (18.8)$$

$$-\zeta \omega_n(t) = \frac{d\psi_r}{dt} \quad (18.9)$$

These values can then be plotted against response amplitude to obtain amplitude dependent relationships for frequency and dissipation of each mode. At low amplitude levels this relationship will provide the true linear natural frequency and

damping ratio. Comparing these values to those obtained from linear testing can reveal potential errors if the linear test exhibits nonlinear behavior.

18.4 Linear Substructuring Tests and Predictions

In this section the linear substructuring predictions from [5] are investigated. The linear predictions are performed with two sets of data. First, slightly nonlinear modal parameters are used from a low-level modal test. Next, the Hilbert Transform is used to determine a shaker setting which is low enough to extract true linear parameters. The predictions are updated with these new parameters in order to highlight the importance of ensuring a linear test is not exceeding linear response levels.

18.4.1 Original Measurements

Low excitation level impact and shaker tests were performed on subcomponents *A* and *B*. Linear natural frequencies, damping values, and mode shapes were obtained using the Synthesize Modes and Correlate (SMAC) [8] program developed by Mayes and Hensley. The results for substructures *A* and *B* are shown Tables 18.1 and 18.2, respectively. Here, the subscript *o* represents the parameters found from initial testing (which was performed at slightly nonlinear levels).

Linear substructuring predictions were calculated following Eq. (18.6). There are many realizations of substructuring predictions to consider. In this case, the target range for predictions was up to 600 Hz. Thus, following general component mode synthesis heuristics, modes up to 1200 Hz were included in the subcomponent models. This results in 14 modes for both substructures *A* and *B* and only 10 modes for the TS. The predictions from this substructuring exercise are shown in Table 18.3 and compared to the results obtained from an assembled truth test. Here, errors under 5% are marked in green, and errors over 5% are marked in red. Note, the frequency error in these predictions is low (under 2%), but the damping error is high (over 30% on multiple modes). These errors are typical of previous component mode synthesis studies, but in [5] the authors were trying to observe the nonlinearity in the system damping. Thus, a minimization of this damping error was desired.

Table 18.1 Subcomponent *A* original linear parameters

Mode	$f_{n,o}$ [Hz]	ζ_o [%cr]	Shape description
7	128.03	0.38	1st bend of Beam in soft direction
8	170.00	0.28	1st bend of Beam in stiff direction
9	548.36	0.37	Plate axial mode
10	863.75	1.15	(2,0) ovaling of Cylinder
11	878.25	1.11	(2,0) ovaling of Cylinder
12	980.80	0.45	(3,0) ovaling of Cylinder
13	987.70	0.46	(3,0) ovaling of Cylinder
14	1084.20	0.12	2nd bend of Beam in soft direction

Table 18.2 Subcomponent *B* original linear parameters

Mode	$f_{n,o}$ [Hz]	ζ_o [%cr]	Shape description
7	232.23	0.174	1st bend of Tail in soft direction
8	607.00	0.869	1st bend of Tail in stiff direction
9	879.75	0.996	(2,0) ovaling of Cylinder
10	886.06	1.058	(2,0) ovaling of Cylinder
11	981.82	0.437	(3,0) ovaling of Cylinder
12	990.10	0.390	(3,0) ovaling of Cylinder
13	1148.75	1.406	Plate axial Mode
14	1279.50	0.590	2nd bend of Tail in soft direction

Table 18.3 Original linear substructuring predictions

Mode	Predicted $f_{n,o}$ [Hz]	Measured f_n [Hz]	% Diff.	Predicted ζ_o [%cr]	Measured ζ [%cr]	% Diff.	MAC
7	128.50	128.22	0.22%	0.381	0.276	38.22%	1.00
8	170.30	169.46	0.46%	0.282	0.176	60.53%	0.99
9	232.29	233.37	-0.46%	0.168	0.176	-0.70%	1.00
10	548.37	551.39	-0.55%	0.375	0.245	52.97%	0.99
11	606.18	616.25	-1.63%	0.860	0.426	101.57%	1.00

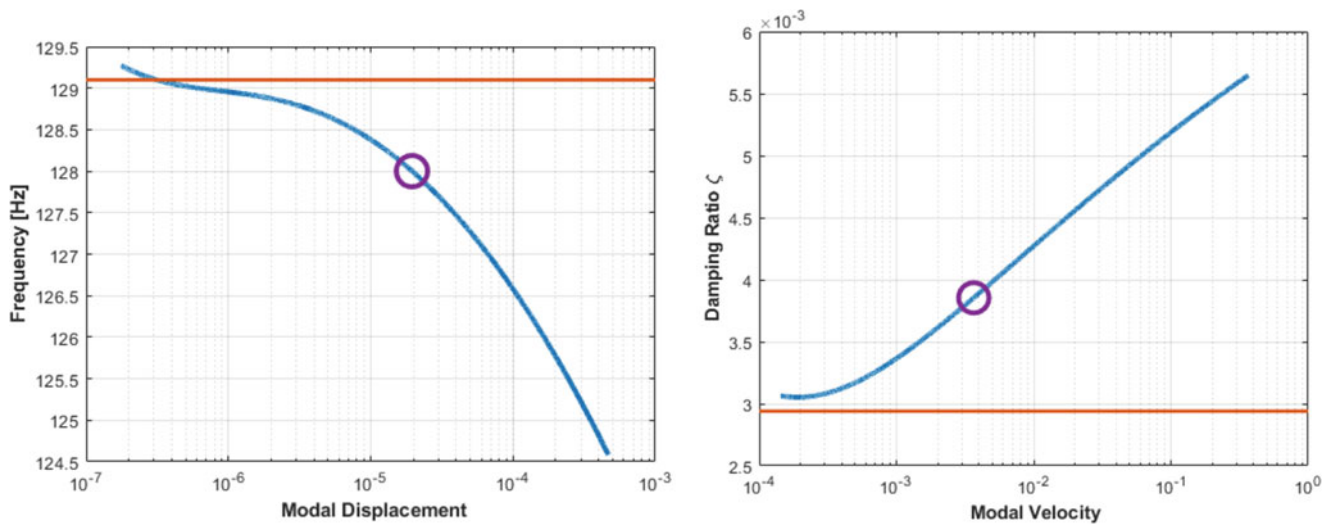


Fig. 18.3 Hilbert Transform derived amplitude dependent relationships for frequency and damping ratio

18.4.2 Example Hilbert Transform Analysis

High-level excitations were performed using a windowed sinusoidal excitation technique discussed in [4], previously know as sine beat excitations [9]. Using the Hilbert Transform as discussed in Sect. 18.3.2 amplitude dependent relations for frequency and damping ratio were obtained for the first mode of the subcomponent *A* and are shown in Fig. 18.3. Here, the blue curve shows the measured amplitude dependent relationship and the purple circular marker shows the assumed linear results from Sect. 18.4.1. The red line shows the true linear parameter as identified from the testing described in Sect. 18.4.3. This analysis was repeated for all modes showing a nonlinear response until linear parameters were identified for all modes used in the substructuring predictions.

18.4.3 Revised Measurements

Updated linear modal parameters were obtained by continually lowering the excitation level until the extracted parameters were not sensitive to such changes. The final updated parameters for Subcomponents *A* and *B* are contained in Tables 18.4 and 18.5. Here, the subscript *o* represents the original measured linear parameters and the subscript *u* denotes the updated parameters. For both subcomponents the frequency error from the original measurements was relatively small (less than 1%) but the damping ratio errors were large (many modes over 50%). This is expected as the amplitude dependence of damping is usually more sensitive than that of frequency in weakly nonlinear structures.

Table 18.4 Subcomponent A updated linear parameters

Mode	$f_{n,o}$ [Hz]	$f_{n,u}$ [Hz]	f_n % Error	ζ_o [%cr]	ζ_u [%cr]	ζ % Error
7	128.03	129.2	-0.91%	0.384	0.294	30.61%
8	170.00	171.1	-0.64%	0.284	0.170	67.06%
9	548.36	552.0	-0.66%	0.373	0.241	54.77%
10	863.75	867.8	-0.47%	1.149	1.122	2.41%
11	878.25	883.3	-0.57%	1.113	0.930	19.68%
12	980.80	980.8	0.00%	0.451	0.447	0.89%
13	987.70	987.7	0.00%	0.456	0.462	-1.30%
14	1084.20	1031.8	-0.10%	0.123	0.090	37.17%

Table 18.5 Subcomponent B updated linear parameters

Mode	$f_{n,o}$ [Hz]	$f_{n,u}$ [Hz]	f_n % Error	ζ_o [%cr]	ζ_u [%cr]	ζ % Error
7	232.23	232.5	-0.12%	0.174	0.168	3.87%
8	607.00	608.9	-0.31%	0.869	0.415	109.25%
9	879.75	882.5	-0.31%	0.996	1.138	-12.47%
10	886.06	892.4	-0.71%	1.058	0.812	30.35%
11	981.82	981.8	0.00%	0.437	0.448	-2.49%
12	990.10	990	0.01%	0.390	0.393	-0.64%
13	1148.75	1171	-1.90%	1.406	1.075	30.79%
14	1279.50	1284.5	-0.39%	0.590	0.480	22.87%

Table 18.6 Updated linear substructuring predictions

Mode	Predicted $f_{n,u}$ [Hz]	Measured f_n [Hz]	% Diff.	Predicted ζ_u [%cr]	Measured ζ [%cr]	% Diff.	MAC
7	129.62	128.22	1.09%	0.295	0.276	6.94%	1.00
8	171.47	169.46	1.19%	0.171	0.176	-2.90%	0.99
9	232.56	233.37	-0.35%	0.168	0.176	-4.47%	1.00
10	552.01	551.39	0.11%	0.241	0.245	-1.43%	0.99
11	608.08	616.25	-1.32%	0.415	0.426	-2.56%	1.00

Table 18.6 contains the substructuring predictions using the updated linear subcomponent parameters. The results showed great improvement in the damping ratio predictions with only one mode having an error higher than 5%. The frequency errors remained mostly constant. The first two elastic modes increased in error, from below 0.5% error to 1% error, while the following three modes all decreased in frequency error. This case study shows that it is prudent to ensure that linear testing is truly linear!

18.5 Conclusions and Remarks

This paper documents lessons learned from a substructuring exercise previously presented in [5]. In this study, the authors completed experimental-analytical dynamic substructuring predictions at linear levels with very low damping ratio errors. To achieve this accuracy, the authors performed multiple tests on each subcomponent to assure that the systems were being tested at low, linear excitation levels. With the original measurements, damping ratio errors as high as 100% were observed. After using a few heuristics to ensure the quality of the extracted linear model, this error was reduced to under 7%, showing a drastic improvement.

It is recommended that, for future test plans, where linear information is desired, test engineers include test points at high-level and use the Hilbert Transform to determine if the low-level set for linear testing is sufficient for capture linear structural dynamic behavior. An alternative recommendation to high-level testing would be to make multiple measurements decreasing the amplitude of excitation in each case until the extracted modal parameters are shown to not change.

Disclaimer This manuscript has been authored by National Technology and Engineering Solutions of Sandia, LLC. under Contract No. DE-NA0003525 with the U.S. Department of Energy/National Nuclear Security Administration. The United States Government retains and the publisher, by accepting the article for publication, acknowledges that the United States Government retains a non-exclusive, paid-up, irrevocable, world-wide license to publish or reproduce the published form of this manuscript, or allow others to do so, for United States Government purposes.

References

1. Segalman, D.: A modal approach to modeling spatially distributed vibration energy dissipation. Sandia National Labs SAND2010-4763, Albuquerque, NM (2010)
2. Deaner, B.J.: Modeling the nonlinear damping of jointed structures using modal models. Masters of Science Thesis, University of Wisconsin, Madison (2013)
3. Mayes, R.L., Pacini, B.R., Roettgen, D.R.: A modal model to simulate typical structural dynamic nonlinearity. In: Proceedings of the International Modal Analysis Conference XXXIV, Orlando, FL (2016)
4. Pacini, B.R., Mayes, R.L., Owens, B.C., Schultz, R.: Nonlinear finite element model updating, Part I: experimental techniques and nonlinear modal model parameter extraction. In: Proceedings of the International Modal Analysis Conference XXXV, Garden Grove, CA (2017)
5. Roettgen, D., Pacini, B., Mayes, R., Schoenherr, T.: Experimental-analytical substructuring of a complicated jointed structure using nonlinear modal models. In: Proceedings of the International Modal Analysis Conference XXXVI, Orlando, FL (2018)
6. Allen, M.S., Mayes, R.L., Bergman, E.L.: Experimental modal substructuring to couple and uncouple substructures with flexible fixtures and multi-point connections. *J. Sound Vib.* **329**(23), 4891–4906 (2010)
7. Feldman, M.: Time-varying vibration decomposition and analysis based on the Hilbert transform. *J. Sound Vib.* **295**(3–5), 518–530 (2006)
8. Hensley, D.P., Mayes, R.L.: Extending SMAC to multiple references. In: Proceedings of the International Modal Analysis Conference XXIV (2006)
9. Fisher, E.G.: Sine beat vibration testing related to earthquake resonance spectra. *Shock. Vib. Bull.* **42**, 1–8 (1972)



Chapter 19

An Interpolation Algorithm to Speed Up Nonlinear Modal Testing Using Force Appropriation

Michael Kwarta, Matthew S. Allen, and Joseph J. Hollkamp

Abstract Force appropriation testing has long been used for ground vibration testing of aircraft, where it is critical to estimate the modal parameters and especially damping accurately. Recently, extensions were presented that allow systematic identification of the nonlinear normal modes (NNMs) of conservative and non-conservative nonlinear structures. While this method provides accurate results with high confidence, it is unfortunately quite slow and so the structure may be subjected to significant damage over the course of a test. This work proposes a new approach in which the test is performed more quickly by simply acquiring measurements near the nonlinear resonance, but without the time consuming tuning required to reach the resonance precisely. Then, the recently proposed single nonlinear resonant mode method is used to interpolate between test points in order to estimate the NNM from each set of forced responses. The method is first evaluated numerically using a reduced model of a curved clamped-clamped beam that exhibits both softening and hardening response due to geometric nonlinearity. Then the method is employed experimentally to measure the first two NNMs of a curved beam that was manufactured from plastic using a 3D printer and the results are compared to the traditional tuning approach.

Keywords Nonlinear normal modes · Force appropriation method · Single nonlinear resonant mode method · Nonlinear modal analysis · Nonlinear frequency response functions

19.1 Single Nonlinear Resonant Mode Method

Frequency response functions of vibrating linear mechanical systems can be expressed as a combination of their linear normal modes. This is possible because the linear modes are orthogonal and can be used to diagonalize the mass and stiffness matrices. This principal of superposition, which is an essential property of linear theory, does not strictly apply to nonlinear systems.

The single nonlinear resonant mode (SNRM) method, which was first proposed in [1], assumes that if (1) most of the vibration energy is restricted to one nonlinear mode and (2) there are no internal resonances between the modes it might be possible to predict the motion by simulating a single nonlinear mode and then superimposing the linear response of the remaining modes, see Eq. (19.1),

$$\mathbf{x}(t) = \text{Re} \left\{ \frac{\tilde{\Phi}_j \tilde{\Phi}_j^T (-\mathbf{F}i) e^{i\Omega t}}{\tilde{\omega}_{0,j}^2 - \Omega^2 + 2i\tilde{\zeta}_j \tilde{\omega}_{0,j} \Omega} + \sum_{\substack{k=1 \\ k \neq j}}^{N_{\text{lin}}} \frac{\Phi_k \Phi_k^T (-\mathbf{F}i) e^{i\Omega t}}{\omega_{0,k}^2 - \Omega^2 + 2i\zeta_k \omega_{0,k} \Omega} \right\}, \quad (19.1)$$

where: Ω is the forcing frequency; Φ_i , $\omega_{0,i}$, ζ_i are the mode shape, natural frequency and modal damping ratio of the i -th mode, respectively; \mathbf{F} is the distribution of a sinusoidal force excitation; j is index of the dominant mode, and N_{lin} denotes the number of relevant linear modes. The quantities marked (\sim) vary with the vibration level. Indeed, the algorithm based

M. Kwarta (✉) · M. S. Allen
UW–Madison, Department of Engineering Mechanics, Madison, WI, USA
e-mail: kwarta@wisc.edu; matt.allen@wisc.edu

J. J. Hollkamp
U.S. Air Force Research Laboratory, Wright-Patterson Air Force Base, Dayton, OH, USA
e-mail: joseph.hollkamp@us.af.mil

on SNRM presented in [2] shows that the prediction of nonlinear frequency response function is possible when the NNM curve is known.

19.2 Nonlinear FRF Interpolation Algorithm Overview

In our work we represented curves in a frequency-velocity plot (v , Ω), where v is the magnitude of velocity complex amplitude at the point of the structure where the maximum displacement occurs and Ω is the aforementioned forcing frequency. Moreover, in the algorithm used here, we assume that the effective NNM frequency $\tilde{\omega}_j$ can vary from the true NNM frequency $\tilde{\omega}_{0,j}$, see Eqs. (19.2) and (19.3). The method discussed here also simplifies the model by assuming that the dominating mode shape $\tilde{\Phi}_j$ does not depend on vibration level. Thus, the proposed algorithm is based on the formulas shown in Eqs. (19.2) and (19.3), where the models for magnitude and phase of the complex amplitude of the velocity are presented.

$$\mathcal{F}(v, \Omega; \tilde{\omega}_j) = v - \left\| \left(\frac{\Phi_j \Phi_j^T \mathbf{F} \Omega e^{i\Omega t} e^{i\tilde{\varphi}_j^{\text{vel}}}}{\sqrt{(\tilde{\omega}_j^2 - \Omega^2)^2 + (2\tilde{\zeta}_j \tilde{\omega}_j \Omega)^2}} + \underbrace{\sum_{\substack{k=1 \\ k \neq j}}^{N_{\text{lin}}} \frac{\Phi_k \Phi_k^T \mathbf{F} \Omega e^{i\Omega t} e^{i\varphi_k^{\text{vel}}}}{\sqrt{(\omega_{0,k}^2 - \Omega^2)^2 + (2\zeta_k \omega_{0,k} \Omega)^2}}}_{\mathbf{B}_{\text{lin}}(\Omega)} \right) \Big|_{\text{pt. of max. deflection}} \right\| = 0 \quad (19.2)$$

$$\mathcal{G}(\Omega; \tilde{\omega}_j) = \tan(\tilde{\varphi}_j^{\text{vel}}) - \frac{-2\tilde{\zeta}_j \tilde{\omega}_j \Omega}{\tilde{\omega}_j^2 - \Omega^2} = 0 \quad (19.3)$$

In the numerical experiments we conducted, the nonlinear mechanical system behavior was caused by the presence of nonlinear restoring force (which was a function of the displacement only) in the equation of motion. Values ζ_j were computed such that the damping matrix is constant, thus $\tilde{\zeta}_j = \zeta_j^{\text{lin}} \omega_{0,j} / \tilde{\omega}_j$.

The algorithm proposed here consists of three stages. In the first stage a $\tilde{\omega}_j$ value is assigned to each (v, Ω) point measured during the simulated experiment or laboratory tests. A value of $\tilde{\omega}_j$ was found for each pair of measured (v, Ω) by using a nonlinear curve fitting routine to minimize Eq. (19.2). Then, various pairs of $(v, \tilde{\omega}_j)$ are used to fit a polynomial to $\tilde{\omega}_j$ as a function of velocity, i.e. $\tilde{\omega}_j = c_0 + c_1 v + \dots$. The objective of the third stage is to find a point (v_*, ω_*) at which FRF intersects the NNM curve. At this particular point Eqs. (19.4) and (19.5) hold (see also Fig. 19.1).

$$\mathcal{F}(v_*, \omega_*; \omega_*) = v_* - \left\| \left(\frac{\Phi_j \Phi_j^T \mathbf{F} e^{i\omega_* t} (-i)}{2\tilde{\zeta}_j \omega_*} + \mathbf{B}_{\text{lin}}(\omega_*) \right) \Big|_{\text{pt. of max. deflection}} \right\| = 0 \quad (19.4)$$

$$\tilde{\varphi}_j^{\text{vel}} \rightarrow -\frac{\pi}{2} \quad \implies \quad \tilde{\omega}_j(v_*) = \tilde{\omega}_{0,j}(v_*) = \omega_* \quad (19.5)$$

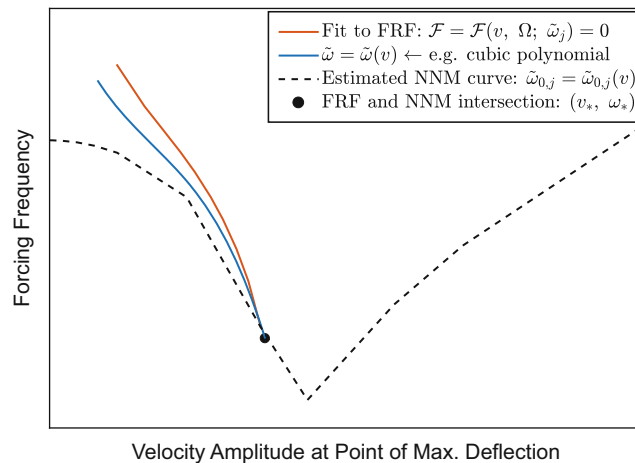


Fig. 19.1 Plot of interpolated frequency response function, effective NNM frequency $\tilde{\omega}_j(v)$ and estimated NNM curve $\tilde{\omega}_{0,j}(v)$. Those three curves would cross one another at point (v_*, ω_*) marked with a filled circle

19.3 Case Study

To test this method, data points (v, Ω) were generated by simulating force appropriation numerically. The test was performed on the one mode ROM of a curved beam with clamped-clamped boundary conditions excited with an uniformly distributed sinusoidal force. The beam was 304.8-mm-long, 12.7-mm-wide, 0.508-mm-thick and had a radius of curvature of 11.43 m. It was constructed of steel with a Young’s modulus of 204 GPa, a mass density of 7860 kg/m³ and Poisson’s ratio of 0.29.

Figure 19.2 shows results obtained in the first two algorithm stages for two regions along the NNM. Using Eq. (19.2) as a model function with $\tilde{\omega}_j$ expressed as a cubic polynomial of v the frequency response functions could be recreated and validated against the true FRF curves measured by carefully tuning the forcing to obtain phase quadrature. As shown in Fig. 19.2 they were successfully reconstructed when the forcing magnitudes were low enough. The NNM of the system was then computed using Multi-Harmonic Balance Method (MHB) and is presented in Fig. 19.3, along with the NNM estimated using the proposed interpolation algorithm and the traditional Force Appropriation Method (FAM).

It is important to note that the only parts of the estimated NNM curve which were successfully found by the algorithm were shown in the chart and that the solution in the vicinity of the turning point was very far from the test data. Moreover,

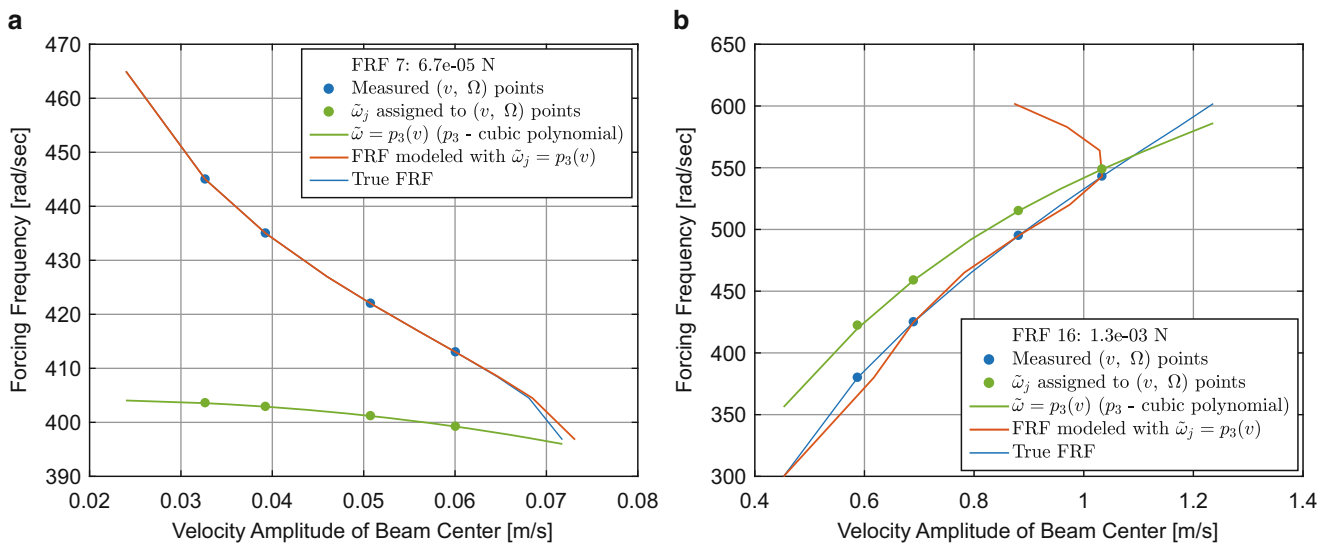


Fig. 19.2 Results of the first two algorithm stages for force magnitudes of (a) 6.7e−5 N (the system exhibits softening at this force level) and (b) 1.3e−3 N (hardening)

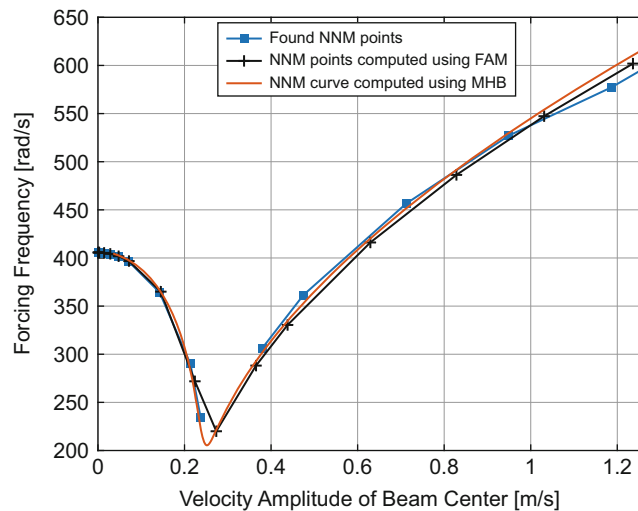


Fig. 19.3 Comparison of the NNM curve computed with the presented algorithm with solutions obtained using the Force Appropriation and Multi-Harmonic Balance Methods

it seems that the algorithm successfully finds the NNM points even if the vibration level is high. Simultaneously, it fails in recreating FRF parts which are close to the nonlinear resonance (see Fig. 19.2b). Further investigation is needed to determine the causes of this behavior.

19.4 Conclusion and Future Work

We proposed an algorithm based on the single nonlinear resonant mode method which interpolates between a few points measured on a nonlinear FRF in order to estimate the NNM curve. Such an algorithm could speed up measurements dramatically.

In the current version of the algorithm we proposed a slight modification to the original SNRM formulation, e.g. we allowed the effective nonlinear natural frequency to vary from the true NNM frequency. The algorithm succeeded in finding the NNM curve for a complicated system that exhibits softening and hardening over most of the range of vibration levels studied. However, it successfully reconstructed the FRFs only for the cases with low forcing magnitudes. Further investigation is needed to determine the causes of this behavior. The algorithm will also be validated against results from other tests, including lab experiments on 3D printed plastic curved beams.

Acknowledgements This work was supported by the Air Force Office of Scientific Research, Award #FA9550-17-1-0009, under the Multi-Scale Structural Mechanics and Prognosis program managed by Dr Jaimie Tiley. The authors would also like to thank Christopher Van Damme for his help during the early stages of this project.

References

1. Szemplińska-Stupnicka, W.: The modified single mode method in the investigations of the resonant vibrations of non-linear systems. *J. Sound Vib.* **63**(4), 475–489 (1979)
2. Peter, S., Scheel, M., Krack, M., Leine, R.I.: Synthesis of nonlinear frequency responses with experimentally extracted nonlinear modes. *Mech. Syst. Signal Process.* **101**, 498–515 (2018)



Chapter 20

Estimating Applied Loads and Response Accelerations on a Dynamic System Using Vibration Data

Eren Koçak, Caner Gençoğlu, Bülent Acar, and Kenan Gürses

Abstract Measured infield accelerometer data is very useful when evaluating the structural dynamics of any mechanical system. Researchers have great difficulty to make measurements from all particular regions where they are interested in due to shortage of measurement channels and difficulty of instrumentation. Thus the vibrations on the rest of the structure should be estimated with limited measured data.

In this study a response acceleration estimation method based on input force estimation is employed. For estimation of applied forces and acceleration data from unmeasured locations of the structure, an accurate model of the system is required. Thus at first stages of the study, FE model is established and updated using experimental modal analysis results. Having the accurate dynamic model, vibration measurements of the structure are done under unknown forces to simulate operational conditions. To estimate applied load location, a state space model (SMM) of the structure is established using updated FE model. By employing augmented Kalman filter (AKF) approach, the location of the applied force is estimated from candidate force input locations, and the force signal is reconstructed.

Knowing the force input location and the transfer function (TF) matrix of the structure, response acceleration power spectral density (PSD) data of the unmeasured locations can be estimated from measured locations. Employing Frequency Response Functions (FRFs) between excitation and measured location, PSD of the input force is obtained. Using input force PSD and FRF between excitation and unmeasured location, the unmeasured PSD data can be predicted.

The methodology presented in this study is applied to the GARTEUR structure which is an internationally accepted de facto model. The FE model of the GARTEUR structure is set up first and subsequently the FE model is verified by modal tests. In the laboratory tests, GARTEUR structure is excited by impact hammer from an arbitrary location. Using the SMM of the GARTEUR and AKF approach, the location of the excitation force is estimated from candidate locations. After this step, PSD for the unmeasured locations are estimated from TF matrix of the structure and measured vibration data. Finally, both estimated and measured acceleration and force data are compared and satisfactory results are obtained.

Keywords Force data estimation · GARTEUR structure · Augmented Kalman filter · Frequency response function

20.1 Introduction

For engineering structures such as bridges, aeroplanes, missiles, satellite launch vehicles, etc., knowing vibration levels on many locations on the structure during operational conditions is not an easy task and even impossible. Due to shortage of measurement channels, difficulties on instrumentation and cost effects drive engineer to find an alternative solution. Thus, operational vibrations of the whole structure should be estimated using measurement from limited locations.

With current technology, vibration characteristics such as natural frequencies and mode shapes of engineering structures could be obtained with experimental modal analysis and/or finite element analysis [1, 2]. Any system model that relates force inputs applied to the structure and obtained response accelerations can be established from the vibration characteristics. Also, response accelerations on any location of the structure could be calculated with FEM by applying known forces to know locations. Thus, one can compute response of the structure as long as locations and amplitudes of operational forces are known. However, for practical cases, measuring the operational loads is very difficult or even impossible. Only available data at hand is the system model and response measurement from limited locations.

At design process of any mechanical system, levels and frequency range of vibration on critical equipment (such as inertial measurement unit, seeker, engine, etc.) should be known. Also modal parameters of system such as natural frequencies, mode

E. Koçak · C. Gençoğlu (✉) · B. Acar · K. Gürses
Department of Dynamic Analysis and Test, Roketsan Inc., Ankara, Turkey
e-mail: cgencoглу@roketsan.com.tr

shapes, and modal damping ratios must be available for system identification. For mechanical systems, ground vibration tests (GVT) can be used to obtain modal parameters of the real accurately. The finite element model of the system can be updated using GVT results. In engineering applications, it is unpractical to make dynamic measurements from all locations of the structure. Due to shortage of measurement channels, difficulty of instrumentation, and cost, accelerations of some important locations cannot be measured directly. Acceleration levels of the unmeasured locations should be estimated using the data of the measured locations and the accurate system model. Force estimation is an intermediate step for acceleration estimation. The force estimation process is an inverse process and it has some difficulties due to ill-conditioned nature of the problem [3]. Other than direct inversion methods for estimation of force, Kalman filter methods can be employed which can be used to estimate the states of a system [4–8]. In augmented Kalman filter (AKF) method, the input of the system is also treated as states of some augmented system, and both system states and inputs are estimated simultaneously [4, 5]. In dual Kalman filter, state estimates and input estimates of the system are computed using two Kalman filters successively [5, 7]. Along with these methods, joint input state (JIS) is also employed in estimation of forces for large engineering structures such as bridges [7–9]. Also usage of Kalman filter together with finite element methods allows engineers to make estimations for unmeasured locations using measured ones [10]. By these estimation methods, operational vibration levels of mechanical structures could be estimated with limited operational measurement data.

In this study a novel approaches based on the finite element (FE) method are proposed for estimation of the acceleration levels for each particular point on the structure that cannot be instrumented. An accurate system modal is obtained by FE and modal test. A steady-space model (SSM) is constructed based on accurate FE data. SMM is used with AKF to specify input location using the test data simulation operation condition. After specify input location, a harmonic unit force was applied as the simulation of impact load from this location. Therefore, FRF of accelerometer locations were obtained with linear SSD FE analysis. These FRFs were used to estimate other accelerometer location responses. Finally, estimated and measured acceleration data are compared, and satisfactory results are obtained.

The methodology presented in this study is proven by test data using the GARTEUR structure which is an internationally accepted de facto model. To obtain TF between two separate locations on GARTEUR, steps which are given below are followed:

1. Creating FE model of GARTEUR.
2. Running linear frequency extraction analysis (modal analysis) of GARTEUR.
3. Updating FE model of GARTEUR with experimental modal analysis.
4. Obtaining response acceleration data at 19 locations on GARTEUR with time domain, step input free vibration test.
5. Specifying input force location by using augmented Kalman filter approach.
6. Running frequency domain dynamic analysis with harmonic unit force of updated FE model of GARTEUR.
7. Obtaining FRF of between force input point and two interested response locations—in application, one of two location acceleration responses will not be known, the other one will be known
8. Obtaining estimated acceleration response of specific location

20.2 State Space Modeling of Vibratory Systems

Considering a linear vibratory mechanical system, the equation of motion can be written as follows:

$$\mathbf{M}\ddot{\mathbf{r}}(\mathbf{t}) + \mathbf{C}_d\dot{\mathbf{r}}(\mathbf{t}) + \mathbf{K}\mathbf{r}(\mathbf{t}) = \mathbf{f}(\mathbf{t}) \quad (20.1)$$

In the equation \mathbf{M} is the mass matrix, \mathbf{C}_d is the damping, and \mathbf{K} is the stiffness matrix. Deformations of the physical locations of the system are denoted in \mathbf{r} vector. Applied forces to the system are given in \mathbf{f} vector.

Equation of motion written in physical domain can be converted to modal domain. By performing modal analysis, natural frequencies and mass normalized mode shapes of the system could be obtained. Transition from modal domain to physical domain could be achieved by the equation below:

$$\mathbf{r}(\mathbf{t}) = \Phi\boldsymbol{\eta}(\mathbf{t}) \quad (20.2)$$

Here Φ is the mass normalized mode shape matrix, and $\boldsymbol{\eta}$ is a vector of modal coordinates.

Mass, damping, and stiffness matrices can be converted to modal domain form as follows [11]:

$$\bar{\mathbf{M}} = \Phi^T \mathbf{M} \Phi \quad (20.3)$$

$$\bar{\mathbf{C}}_d = \Phi^T \mathbf{C}_d \Phi \quad (20.4)$$

$$\bar{\mathbf{K}} = \Phi^T \mathbf{K} \Phi \quad (20.5)$$

$$\bar{\mathbf{f}} = \Phi^T \mathbf{f} \quad (20.6)$$

Thus the equation of motion could be written in modal domain:

$$\bar{\mathbf{M}} \ddot{\boldsymbol{\eta}}(t) + \bar{\mathbf{C}}_d \dot{\boldsymbol{\eta}}(t) + \bar{\mathbf{K}} \boldsymbol{\eta}(t) = \bar{\mathbf{f}}(t) \quad (20.7)$$

Here $\bar{\mathbf{M}} = \mathbf{I}$ since mode shapes are mass normalized.

A dynamic system can be represented in state space form also. For state space representation of the vibratory system, inputs are defined as the applied forces. Outputs of the system are taken as displacements, velocities, and accelerations. States of the system are taken as modal coordinates and derivatives of them. State space equations are given as follows:

$$\begin{aligned} \dot{\mathbf{x}} &= \mathbf{A}\mathbf{x} + \mathbf{B}\mathbf{u} \\ \mathbf{y} &= \mathbf{C}\mathbf{x} + \mathbf{D}\mathbf{u} \end{aligned} \quad (20.8)$$

System states are $\mathbf{x} = \begin{bmatrix} \boldsymbol{\eta} \\ \dot{\boldsymbol{\eta}} \end{bmatrix}$, the input vector is $\mathbf{u} = \mathbf{f}(t)$, and displacements, velocities, and accelerations are system outputs.

For this system the state matrices can be computed as shown [11]:

$$\begin{aligned} \mathbf{A} &= \begin{bmatrix} \mathbf{0} & \mathbf{I} \\ -\bar{\mathbf{M}}^{-1} \bar{\mathbf{K}} & -\bar{\mathbf{M}}^{-1} \bar{\mathbf{C}}_d \end{bmatrix} = \begin{bmatrix} \mathbf{0} & \mathbf{I} \\ -\text{diag}(\omega_i^2) & -\text{diag}(2\zeta_i \omega_i) \end{bmatrix} \\ \mathbf{B} &= \begin{bmatrix} \mathbf{0} \\ \Phi^T \end{bmatrix} \\ \mathbf{C} &= \begin{bmatrix} \Phi \mathbf{0} & \mathbf{0} \\ -\Phi^T \text{diag}(\omega_i^2) & -\Phi^T \text{diag}(2\zeta_i \omega_i) \end{bmatrix} \\ \mathbf{D} &= \begin{bmatrix} \mathbf{0} \\ \mathbf{0} \\ \Phi \Phi^T \end{bmatrix} \end{aligned} \quad (20.9)$$

By modifying \mathbf{B} , \mathbf{C} , and \mathbf{D} matrices, a system model with reduced number of input and outputs can be established.

20.3 Force Estimation Using Kalman Filter

The system model is established in state space. This step enables usage of Kalman filters for input estimation. Considering an engineering system in state space the state equations are:

$$\begin{aligned} \dot{\mathbf{x}}(t) &= \mathbf{A}\mathbf{x}(t) + \mathbf{B}\mathbf{u}(t) + \mathbf{w}(t) \\ \mathbf{y}(t) &= \mathbf{C}\mathbf{x}(t) + \mathbf{D}\mathbf{u}(t) + \mathbf{v}(t) \end{aligned} \quad (20.10)$$

For engineering systems, there will be noise present. In the model the process noise is $\mathbf{w}(t)$ which is assumed to have zero mean with a covariance matrix \mathbf{Q} . Since there will be noise from sensors, the measurement noise is added to the system as $\mathbf{v}(t)$. Similar to the process noise, the measurement noise is also assumed to have zero mean. The covariance matrix of the measurement noise is taken as \mathbf{R} .

A Kalman filter can be used to estimate the states of the above system using the input data and the system outputs. However the problem at hand is to reconstruct the unknown input signal by using measurements from the system. To accomplish this task, there are some Kalman filter algorithms such as dual Kalman filter and augmented Kalman filter [4, 5]. For dual Kalman filter, two successive Kalman filters are applied to estimate the inputs and states in an iterative manner [5]. For augmented Kalman filter approach, the inputs are also treated as states of an augmented system, and one Kalman filter is applied to the augmented system to estimate the states and the inputs at the same time. [4, 5]

To construct the augmented Kalman filter input is assumed fit the model shown [4]:

$$\dot{\mathbf{u}}(t) = \mathbf{0} + \mathbf{p}(t) \quad (20.11)$$

where $\mathbf{p}(t)$ is assumed to be a stochastic process with zero mean and covariance matrix \mathbf{S} . The augmented states are given as $\mathbf{x}_{\text{aug}} = \begin{bmatrix} \mathbf{x} \\ \mathbf{u} \end{bmatrix}$. According to the augmentation of states, the new matrices can be established as follows [4]:

$$\begin{aligned} \begin{bmatrix} \dot{\mathbf{x}} \\ \dot{\mathbf{u}} \end{bmatrix} &= \begin{bmatrix} \mathbf{A} & \mathbf{B} \\ \mathbf{0} & \mathbf{0} \end{bmatrix} \begin{bmatrix} \mathbf{x} \\ \mathbf{u} \end{bmatrix} + \begin{bmatrix} \mathbf{w} \\ \mathbf{p} \end{bmatrix} \\ \mathbf{y} &= \begin{bmatrix} \mathbf{C} & \mathbf{D} \end{bmatrix} \begin{bmatrix} \mathbf{x} \\ \mathbf{u} \end{bmatrix} + \mathbf{v} \end{aligned} \quad (20.12)$$

In this scheme the augmented system matrix is $\mathbf{A}_{\text{aug}} = \begin{bmatrix} \mathbf{A} & \mathbf{B} \\ \mathbf{0} & \mathbf{0} \end{bmatrix}$, the augmented output matrix is $\mathbf{C}_{\text{aug}} = \begin{bmatrix} \mathbf{C} & \mathbf{D} \end{bmatrix}$, the process covariance matrix is $\begin{bmatrix} \mathbf{Q} & \mathbf{0} \\ \mathbf{0} & \mathbf{S} \end{bmatrix}$, and the measurement covariance matrix is \mathbf{R} . In order to have a stable working augmented Kalman filter, the augmented system matrix must be observable through the augmented output matrix. This means enough number of measurements should be taken to estimate given number of input forces.

If there are n number of modes of the vibratory system that are considered when establishing the state space model and there are m number of inputs and q number of outputs of the system, then the number of states of the augmented system will be $2n+m$. The observability matrix which is $(2n+m) \times q$ by $2n+m$ of the augmented system can be computed as follows:

$$\mathbf{O} = \begin{bmatrix} \mathbf{C}_{\text{aug}} \\ \mathbf{C}_{\text{aug}}\mathbf{A}_{\text{aug}} \\ \mathbf{C}_{\text{aug}}\mathbf{A}_{\text{aug}}^2 \\ \vdots \\ \mathbf{C}_{\text{aug}}\mathbf{A}_{\text{aug}}^{2n+m} \end{bmatrix}$$

If the rank of the observability matrix is equal to the number of states of the augmented system, which means $\text{rank}(\mathbf{O}) = 2n+m$, then the system is observable [12].

20.4 Accelerometer Response Estimation Using Transfer Function of System

The relationship between the unknown inputs $\mathbf{x}(t)$ and the measured responses $\mathbf{y}(t)$ can be expressed as [13]:

$$\mathbf{G}_{\mathbf{yy}}(j\omega) = \overline{\mathbf{H}}(j\omega) \mathbf{G}_{\mathbf{xx}}(j\omega) \mathbf{H}(j\omega)^T \quad (20.13)$$

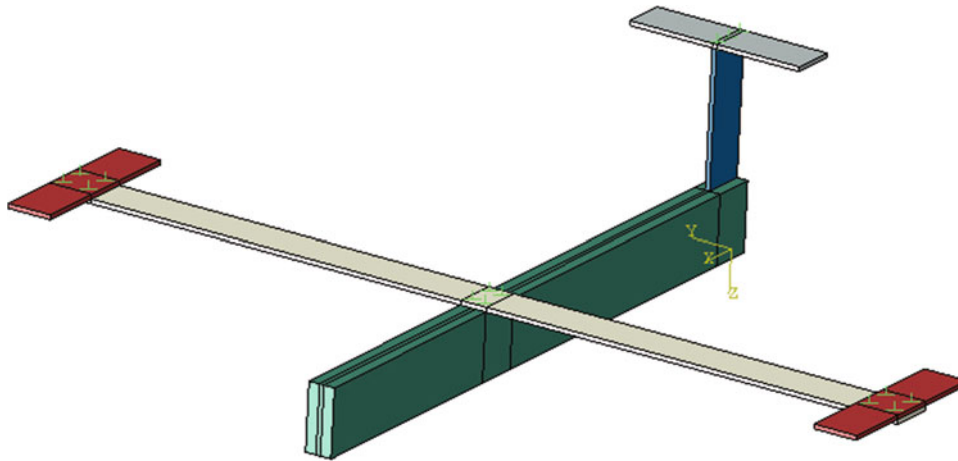


Fig. 20.1 FE model of the GARTEUR structure

where $G_{xx}(j\omega)$ is the $r \times r$ PSD matrix of the input, r is the number of inputs, $G_{yy}(j\omega)$ is the $m \times m$ PSD matrix of the responses, m is the number of responses, $H(j\omega)$ is the $m \times r$ FRF matrix, and “—” and superscript T denote complex conjugate and transpose, respectively.

Within this study, Eq. (20.13) was expressed according to amplitude and without phase information as below:

$$\mathbf{PSD}_j(\text{response}) = \mathbf{FRF}_{ij}^2 \times \mathbf{PSD}_i(\text{input}) \quad (20.14)$$

where \mathbf{PSD}_j is the PSD of response, \mathbf{PSD}_i is the PSD of input, \mathbf{FRF}_{ij} is the FRF between input and output, i is the input point number, and j is the response point number.

20.5 Analysis

The presented response acceleration estimation method was applied to the GARTEUR structure as shown in Fig. 20.1. The GARTEUR structure is modeled with FE model in ABAQUS FE program. The FE model of the GARTEUR consists of 50,000 elements and 60,000 nodes approximately. It is made from aluminum material with Young's modulus of 70 Gpa and poisson ratio of 0.3.

20.6 Experimental Modal Analysis (EMA)

As the experimental modal analysis data was used to create the reference model for the GARTEUR FE model would be compared, it was crucial that these data were as accurate as possible. The discretized geometry of the GARTEUR was defined with small box markers and wire frame placed on the GARTEUR. The box markers and five of them were directly used as the measurement and excitation points, respectively. Thus, 19 ICP type, 3-axis accelerometers were placed on these small box marker coordinates around the GARTEUR as shown in Fig. 20.2.

The GARTEUR structure was hung to portable hoist by using elastic ropes during tests to obtain free vibration condition. Rigidity of the elastic ropes was selected so as no affecting elastic modes from rigid body modes. Additionally, modal electrodynamic hammer with plastic tip was used to excite the GARTEUR structure at experimental modal analysis. Figures 20.3 and 20.4 illustrate experimental modal analysis test setup and accelerometer placements, respectively.

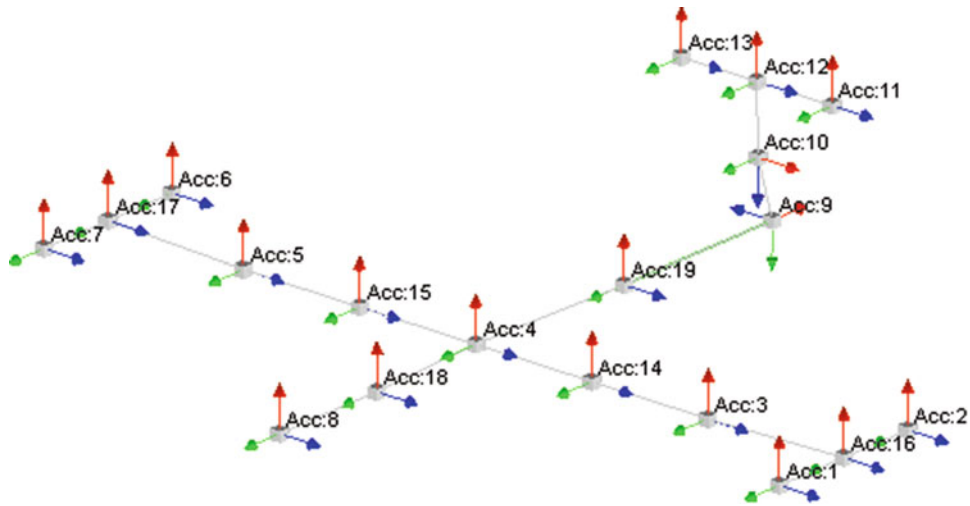


Fig. 20.2 Experimental modal analysis model of the GARTEUR structure

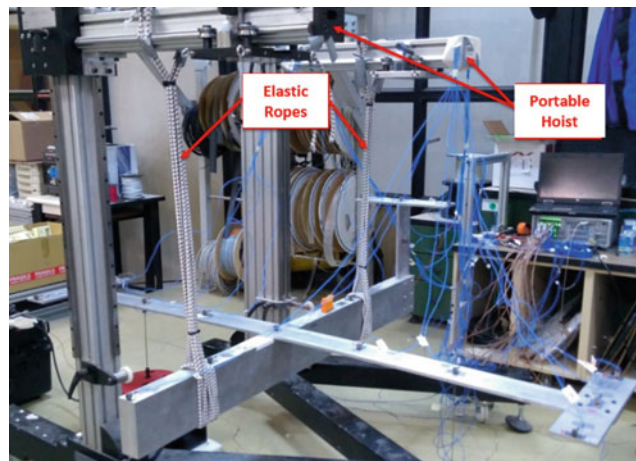


Fig. 20.3 Experimental modal analysis test setup

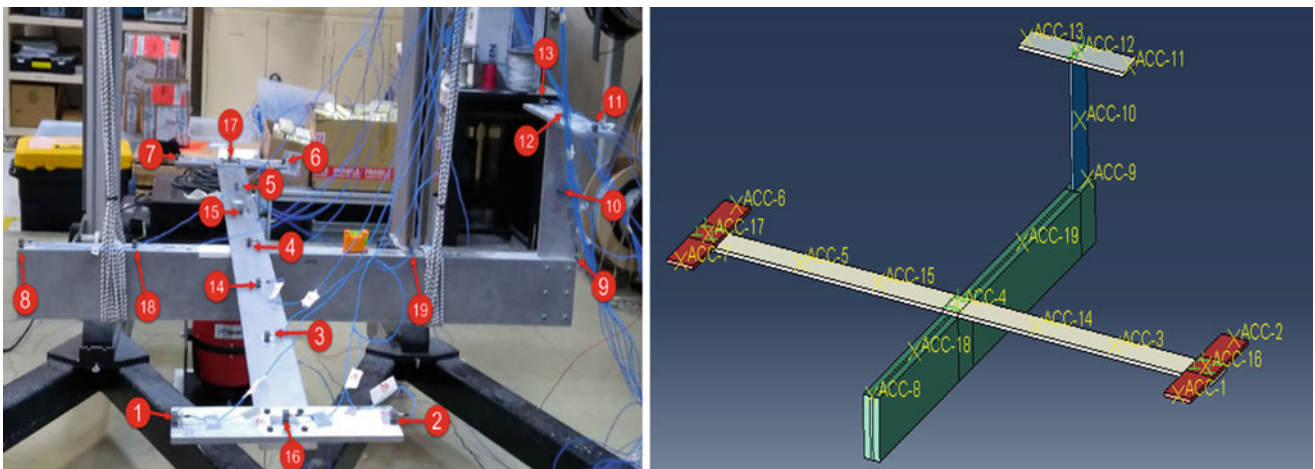


Fig. 20.4 Accelerometer placements on the GARTEUR

20.7 Comparison and Validation of the FE Model

Firstly, experimental modal analysis data was collected by using LMS Test. Lab. Polymax Plus tool. Then, auto-modal assurance criterion (MAC) matrix of the modes which are until 50 Hz was obtained (Fig. 20.5) to calculate the degree of relationship between the vectors of the modes within the experimental. A full set of mode shapes that are until 50 Hz were then exported from the FE model to be compared with the reference data. Young’s modulus of GARTEUR structure material was altered until the frequency of the first elastic mode matched that of the experimental data. Table 20.1 shows that the comparison of the modes in terms of their frequencies with the difference displayed as a percentage. Figure 20.6 illustrates the first elastic mode shapes of finite element model and experimental modal analysis, respectively.

Fig. 20.5 Auto MAC matrix of experimental data

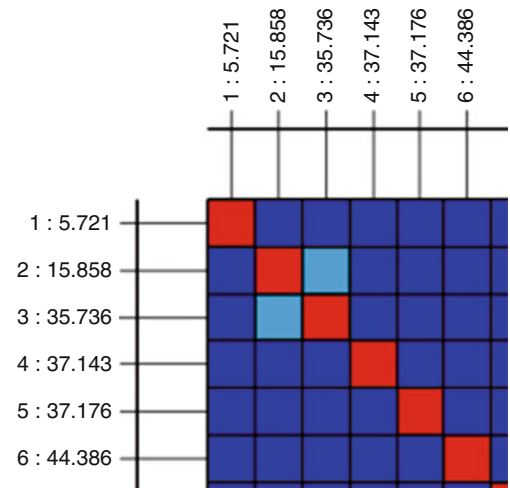


Table 20.1 Comparison between natural frequencies of mode shapes measured from EMA and calculated from FE model

Mode shape	EMA (Hz)	FE (Hz)	Difference (%)
1	5.72	5.73	0.998
2	15.86	15.89	0.998
3	35.74	36.17	0.988
4	37.14	37.77	0.983
5	37.18	37.80	0.984
6	44.39	44.50	0.998

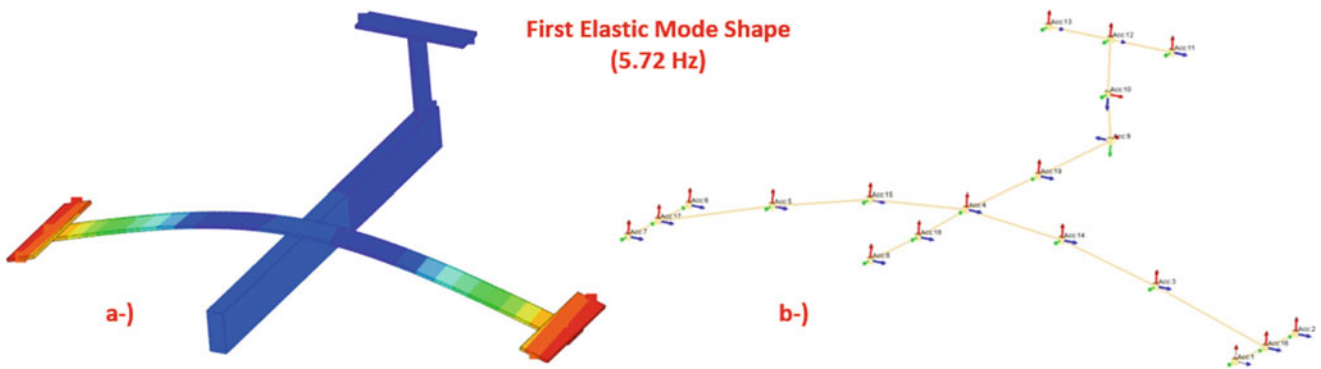


Fig. 20.6 First elastic mode shape of the GARTEUR structure: (a) FE, (b) EMA

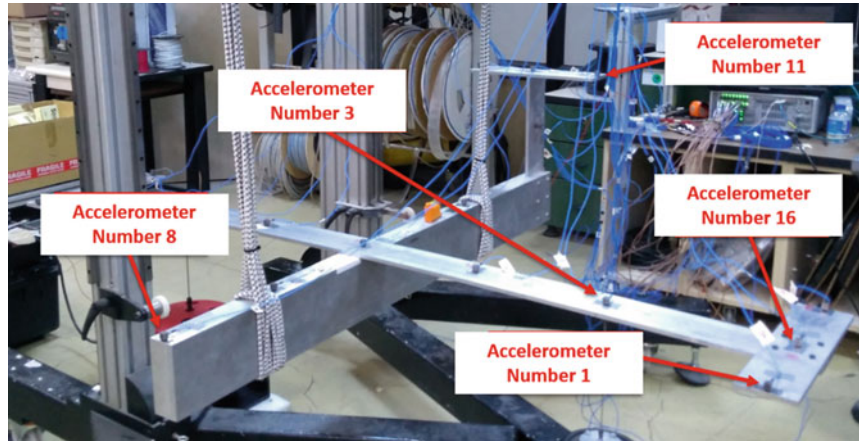


Fig. 20.7 Excitation points of the GARTEUR structure at free vibration test

Table 20.2 SSM input/output location data

Data input	GARTEUR locations	Accelerometer locations	Displacement locations
1	11 Z	10 Y	2 Z
2	1 Z	3 Z	7 Z
3	3 Z	2 Z	
4	8 Z	7 Z	
5	16 Z		

20.8 Time Domain, Step Input Free Vibration Test of the GARTEUR Structure

After validating FE model with experimental data, time domain, step input, free vibration test was performed to simulate operational condition using same test setup with experimental modal analysis. The structure was excited from different accelerometer locations as shown in Fig. 20.7, and time domain vibration data was collected. These collected data was then used for estimation and comparison of response accelerometers data. Additionally, modal electrodynamic hammer was used to give step input to the structure with plastic tip.

20.9 Specifying Force Input Location by Using Augmented Kalman Filter

For the GARTEUR model in this study, location of an impact load out of five possible candidate locations is estimated using only six outputs from the system. Possible candidate locations were selected as given in Table 20.2.

Using MATLAB SMM was established based on force input, accelerometer, and displacement locations given in Table 20.2. Using AKF scheme with the SSM, input forces were reconstructed as shown in Fig. 20.8. Therefore, acceleration location 11 was predicted as step force input location.

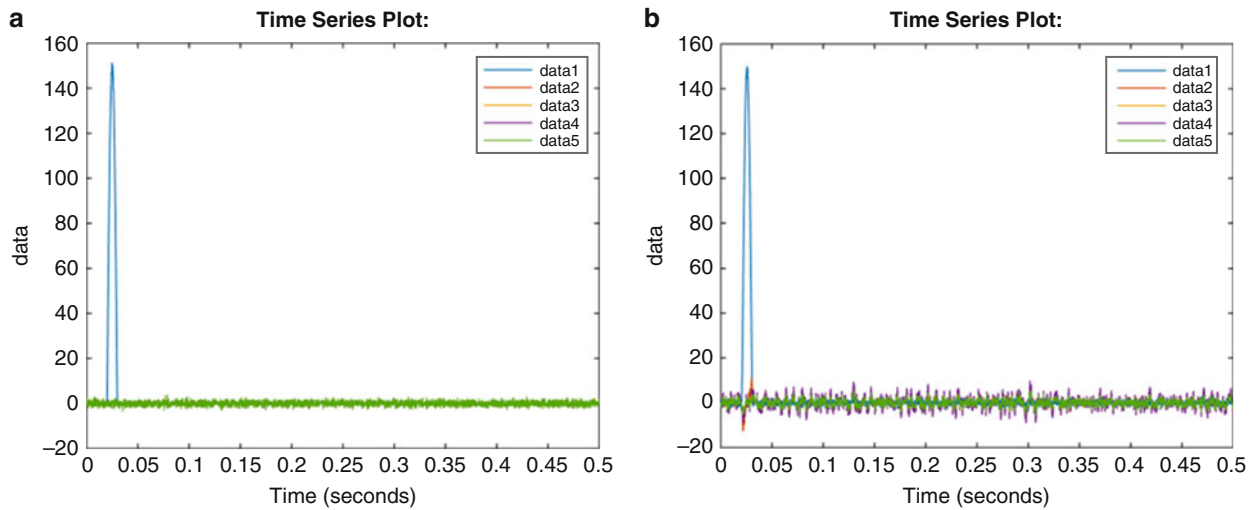


Fig. 20.8 Applied forces to the system (a) and estimated force inputs of the system (b)

20.10 Mode-Based Steady-State Dynamics (SSD) Analysis

After specifying input point as accelerometer number 11 location, a harmonic unit force which has 1–50 Hz frequency range was applied from this location at ABAQUS mode-based, steady-state dynamic analysis. Then, frequency response functions (FRFs) were obtained from all accelerometer locations to use at frequency domain accelerometer response estimation method.

20.11 Frequency Domain Accelerometer Response Estimation Method

At frequency domain accelerometer response estimation method, relationship between power spectral density and FRF was used as described in accelerometer response estimation using transfer function of system section. To estimate an accelerometer response, given below steps are followed:

- (a) Obtained PSD of accelerometer response data
- (b) Obtained PSD of input by using

$$\left(\text{FRF}_{ij}^{-2}\right)^2 \times \text{PSD}_j (\text{Measured response}) = \text{PSD}_i (\text{Input Force}) \text{ formula, where } i = \text{input location, } j = \text{response location,}$$

- (c) Used input force PSD from “b” to estimate accelerometer response by using

$$\text{PSD}_j (\text{Estimated response}) = \left(\text{FRF}_{ij}^{-1}\right)^2 \times \text{PSD}_i (\text{Input Force}) \text{ formula, where } i = \text{input location, } j = \text{response location,}$$

- (d) Comparison of estimated and measured accelerometer response

After steps which were given above were applied to all candidate accelerometer locations, degree of relationship between estimated and measured accelerometer responses were obtained when step input was applied at acceleration location 11 (Fig. 20.9).

Input Point	Estimated Responses	Measured Responses							
		2	3	7	11	13	15	16	17
11	2	Good	Good	Good	Good	Good	Good	Good	Good
	3	Moderate	Good	Good	Good	Good	Good	Good	Good
	7	Moderate	Moderate	Good	Good	Good	Good	Good	Good
	11	Moderate	Good	Good	Good	Good	Good	Good	Good
	13	Moderate	Good	Good	Good	Good	Good	Good	Good
	15	Moderate	Good	Good	Good	Good	Good	Good	Good
	16	Good	Good	Good	Good	Good	Good	Good	Good
	17	Good	Good	Good	Good	Good	Good	Good	Good
		Good Correlation Medium Correlation Moderate Correlation							

Fig. 20.9 Degree of relationship between estimated and measured accelerometer responses

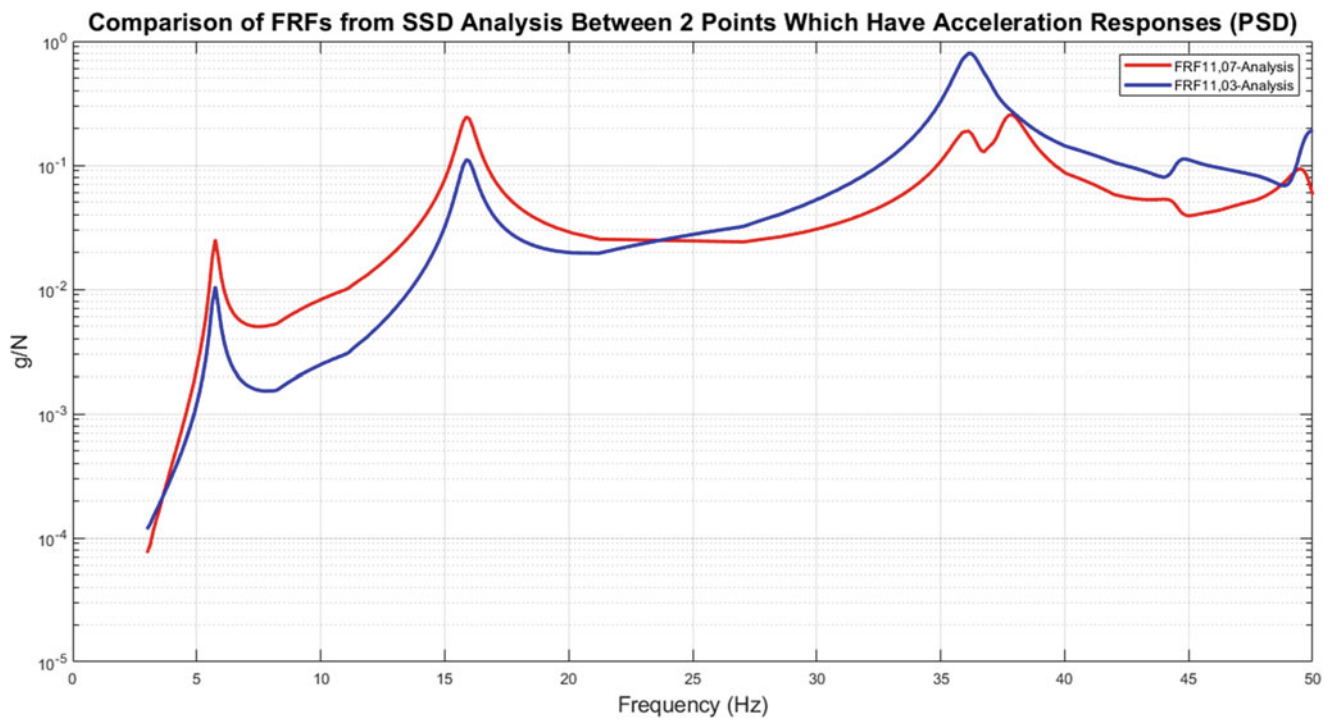


Fig. 20.10 FRFs of two accelerometer locations from linear SSD analysis with input from accelerometer location 11

When input force was applied from location 11, for location 3, vibration data was estimated by using location 7 vibration data. Obtained FRFs, vibration data PSDs, and measured and estimated vibration data PSDs for location 3 were given in Figs. 20.10, 20.11, and 20.12, respectively.

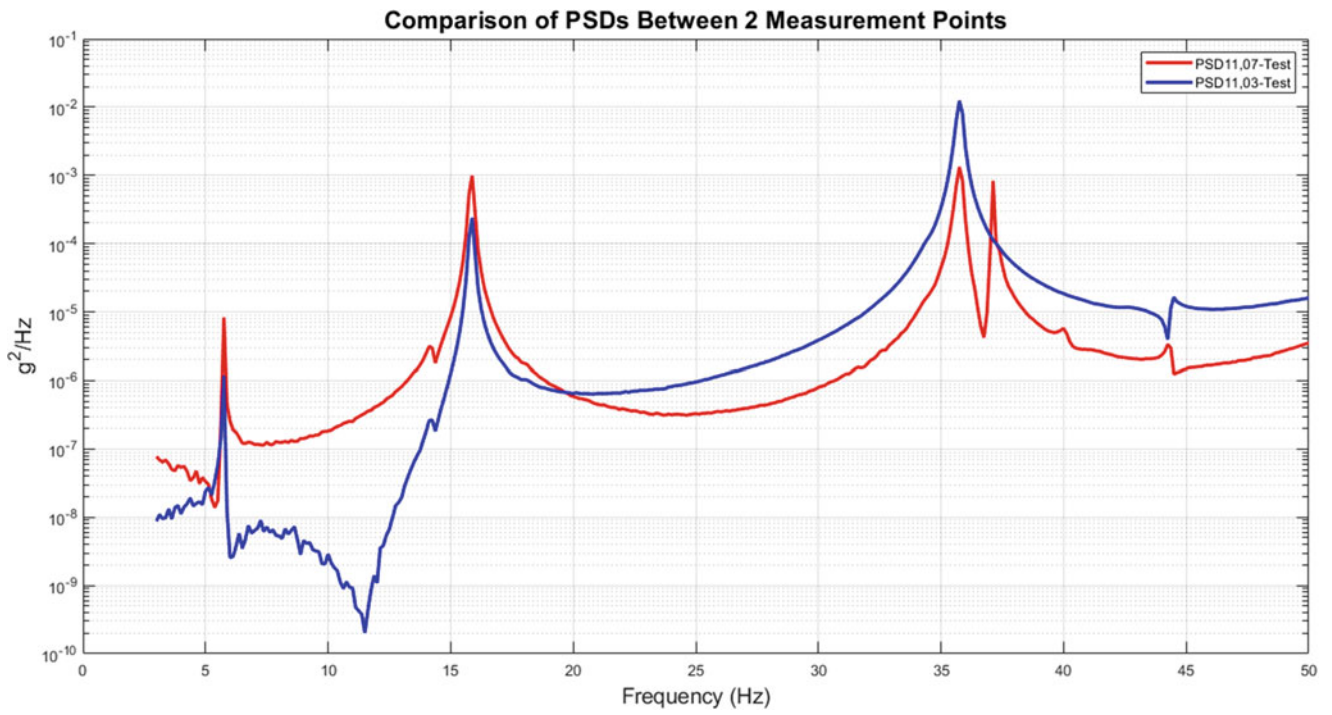


Fig. 20.11 PSDs of two accelerometer locations from free vibration test

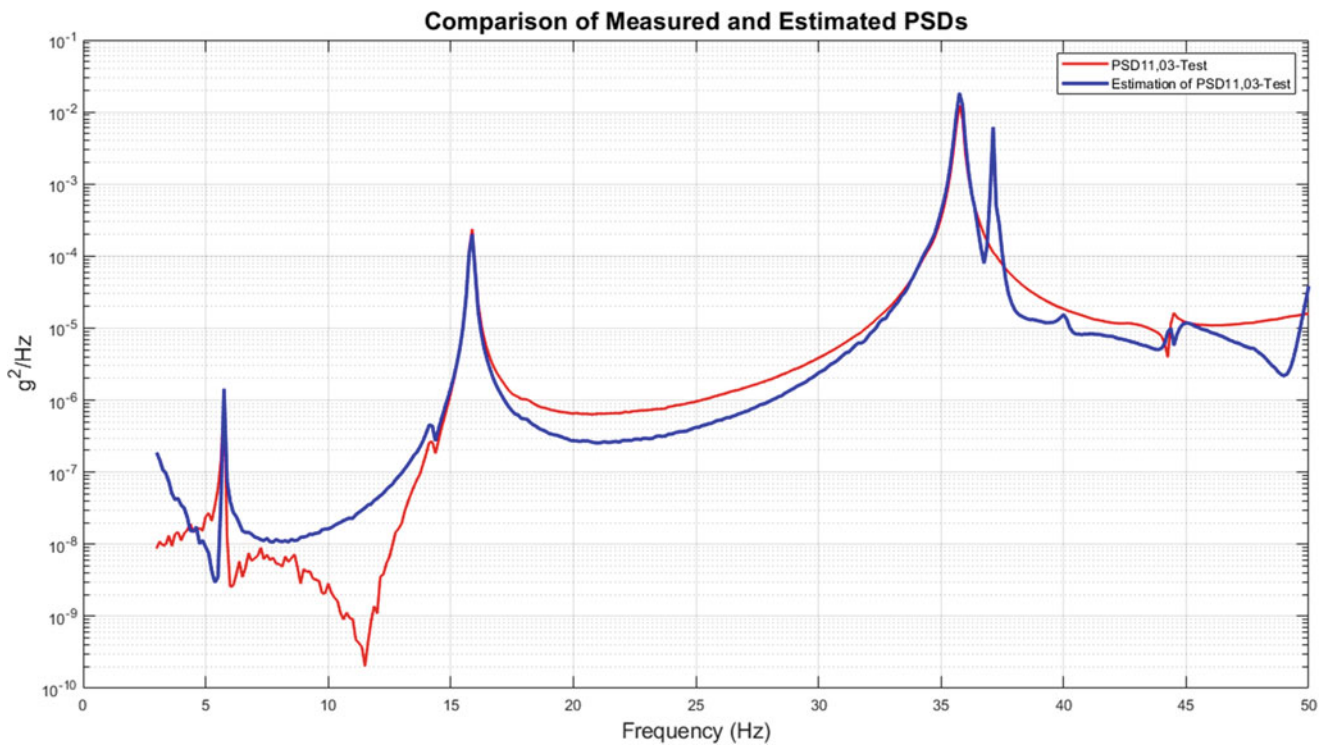


Fig. 20.12 PSDs of measured and estimated data for accelerometer location 3

20.12 Conclusion

In engineering applications, acceleration measurements can not be done from any location of the structure due to shortage of measurement channels, difficulties of instrumentation and cost. Thus, these data must be estimated. In this study, system response estimation method which is based on frequency domain was presented. Firstly, a FE model of the GARTEUR structure was created at ABAQUS FE program. Then, FE modal analysis and experimental modal analysis which was used to update FE model were performed. Consequently, time domain, step input free vibration test was performed to measure system response. This vibration test was carried out to simulate operational condition of the structure. In the test, the GARTEUR structure was excited from one of the five possible candidate locations, and six measurements were done. SSM of the system with five inputs and six outputs was established based on updated accurate FE model. Using augmented Kalman filter approach, the locations of the force were estimated, and force signal was reconstructed. After specify input location, a harmonic unit force was applied as the simulation of impact load from this location. Therefore, FRF of accelerometer locations were obtained with linear SSD FE analysis. These FRFs were used to estimate other accelerometer location responses. Finally, estimated and measured acceleration data are compared, and satisfactory results are obtained.

References

1. Ewins, D.J.: *Modal Testing: Theory, Practice and Application*. Research Studies Press LTD, Baldock, Hertfordshire, England; Philadelphia, PA (2000)
2. Gupta, D.K.: *Inverse methods for load identification augmented by optimal sensor placement and model order reduction*. Theses and Dissertations. Paper 357 (2013)
3. Uslu, A.A., Şanlıtürk, K.Y., Gül, M.: Force estimation using vibration data. In: *Inter-Noise (2017)*
4. Risaliti, E., Cornelis, B., Tamarozzi, T., Desmet, W.: A state-input estimation approach for force identification on an automotive suspension component. In: *International Modal Analysis Conference (Jan. 2016)*
5. Azam, S.E., Chatzi, E., Papadimitrou, C.: A dual Kalman filter approach for state estimation via output-only acceleration measurements. *Mech. Syst. Signal Process.* **60–61**, 866–886 (2015)
6. Kalman, R.E.: A new approach to linear filtering and prediction problems. *J. Basic Eng.* **82**(1), 35–45 (1960)
7. Petersen, Ø.W., Øiseth, O., Lourens, E.M.: Estimation of the dynamic response of a slender suspension bridge using measured acceleration data, X. In: *International Conference on Structural Dynamics, EURODYN (2017)*
8. Kato, Y., Kawahara, M., Koizumi, N.: Kalman filter finite element method applied to dynamic motion of ground, numerical and analytical methods in geomechanics (2008)
9. Maes, K., Smyth, A.W., De Roeck, G., Lombaert, G.: Joint input-state estimation in structural dynamics. *Mech. Syst. Signal Process.* **70–71**, 445–466 (2016)
10. Maes, K., Van Nimmen, K., Lourens, E., Rezayat, A., Guillaume, P., De Roeck, G., Lombaert, G.: Verification of joint input-state estimation for force identification by means of in situ measurements on a footbridge. *Mech. Syst. Signal Process.* **75**, 245–260 (2016)
11. Gencoglu, C., Ozguven, H.N.: Optimal placement of piezoelectric patches on a cylindrical shell for active vibration control. In: *International Modal Analysis Conference (Feb. 2013)*
12. Ogata, K.: *Modern Control Engineering*, 5th edn. Prentice Hall, New Jersey (2010)
13. Bendat, J.S., Piersol, A.G.: *Random Data, Analysis and Measurement Procedures*. John Wiley & Sons, New York (1986)



Chapter 21

Analysis of Coupling Relationship Between Car-Body and Flexible Hanging Equipment

Xiaoning Cao, Xiugang Wang, Qin tao Guo, Ai qin Tian, Shaoqing Liu, Wei Xue, and Jiancai Zou

Abstract Railway vehicle is a complexity dynamic system, vibration characteristics of flexible hanging equipment directly affects the dynamics of vehicle, especially coupled vibration between car-body and equipment. This paper was based on test bench f which supported excitation for the car. Solving method for the dynamic parameters were put forward. Meanwhile, modal parameters identification and coupling relationship analysis between car-body and flexible hanging equipment were carried out, which played an important role to the design of car.

Keywords Coupling relationship · Flexible · Excitation · Mode

21.1 Introduction

Study on the dynamic characteristic under the preparation condition was developed. Under the condition of single-ended bogie excitation, vertical linear sine sweep load were exerted to the vehicle, and taking the top of the vehicle body side wall, side wall beams as research object, the end of vertical was explored. And taking transfer characteristics as the main object, coupling vibration rule among traction converter and body, was analyzed, which provided technical support for the design of high-speed train.

21.2 Analysis Model of Equipment and Car-BODY

Rely on characteristics of vehicle vibration test bench, vertical coupled dynamic model of car-body and flexible hanging equipment was established [1–3], as shown in Fig. 21.1. During the mode, the car-body was taken as Euler beam with the modal information, and the hanging equipment under the car-body was taken as rigid, the vibration characteristics analysis of the elastic beam under the multiple concentrated loads was studied, coupling relationship between the car-body and equipment was analyzed. And F_{dx} was force created by the deformation, M_{dx} is the torque created by deformation; also it could be known that $F_{dx2} = F_{dx} + \frac{\partial F_{dx}}{\partial x} dx$, $M_{dx2} = M_{dx} + \frac{\partial M_{dx}}{\partial x} dx$.

Ignore the influence of car body hysteresis damping; the car body vibration differential equation was obtained as follows:

$$\rho A \frac{\partial^2 z(x_c, t)}{\partial t^2} + EI \frac{\partial^4 z(x_c, t)}{\partial x^4} = \sum_{i=1}^2 F_{pi} \delta(x_c - l_{ci}) + \sum_{j=1}^3 F_{ej1} \delta(x_c - l_{ej} + d_j) + \sum_{j=1}^3 F_{ej2} \delta(x_c - l_{ej} - d_j) \quad (21.1)$$

In the formula: δ is Dirac function; $z(x_c, t)$ is vertical elastic displacement; $F_{pi}(i = 1, 2)$ is the force exerted by the second suspension on the car-body; $F_{ej}(j = 1, 2, 3)$ is the force exerted by the hoisting Set on the car-body.

Solve the formula (21.1) by the separation variable method, assuming that solutions to the equation is the superposition of regularization modal Z_i , which is $z(x_c, t) = \sum_{i=1}^n Z_i(x) \tau_i(t)$; $Z_i(x)$ is Modal Shape function, $\tau_i(t)$ is Canonical coordinates

X. Cao · X. Wang (✉) · A. q. Tian · S. Liu · W. Xue · J. Zou
CRRC Qingdao Sifang Co. Ltd., Qingdao City, China
e-mail: wangxiugang@cqsf.com

Q. t. Guo
Nanjing University of Aeronautics and Astronautics, Nanjing, China

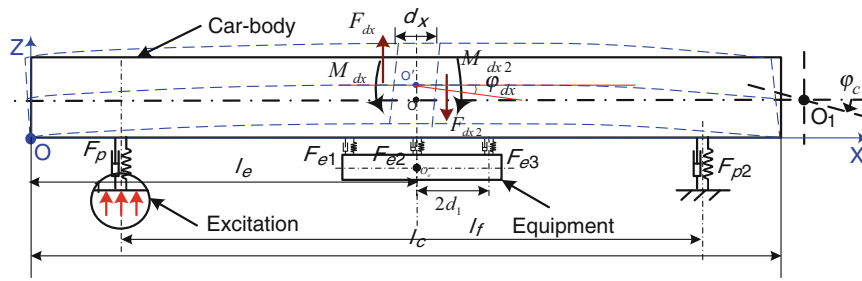


Fig. 21.1 Analysis model of equipment & body

substitute $z(x_c, t)$ into the formula (21.1), and you will find out, multiply both sides of the equation by Z_j , and integrated moving through the car-body length l_c , in combination with orthogonally of vibration mode function.

$$\sum_{k=1}^n \left(EIZ_i^{(2)} \right)^2 \tau_i + \rho A \sum_{k=1}^n Z_i \ddot{\tau}_i = \sum_{i=1}^2 F_{pi} \delta(x_c - l_{ci}) + \sum_{j=1}^3 F_{ej1} \delta(x_c - l_{ej} + d_j) + \sum_{j=1}^3 F_{ej2} \delta(x_c - l_{ej} - d_j) \quad (21.2)$$

$$\ddot{\tau}_j + \omega^2 \tau_j = \int_0^{l_c} Z_j \left(\sum_{i=1}^2 F_{pi} \delta(x_c - l_{ci}) + \sum_{j=1}^3 F_{ej1} \delta(x_c - l_{ej} + d_j) + \sum_{j=1}^3 F_{ej2} \delta(x_c - l_{ej} - d_j) \right) dx \quad (21.3)$$

21.3 Excitation and Measure Points

21.3.1 Excitation of the Test

Excitation was of linear scanning method, which was sine wave with fixed frequency. Taking t_0 as initial time, f_0 as initial frequency, and t was taken as the end time, f_1 was taken as the end frequency, the excited function could be taken as follows [4–6].

$$f(t) = k(t - t_0) + f_0 \quad (21.4)$$

In formula (21.4), k is of sweep velocity, which can be shown as $k = (f_1 - f_0)/(t - t_0)$.

During the test, t_0 is of 0 and f_0 is of 0.1 Hz, f_1 is of 30 Hz, frequency step was 0.05 Hz/s, so the excitation function was $f = 0.05t + 0.1$.

21.3.2 Measure Points

Figure 21.2 was arrangement of testing points for the car-body and traction transfer. It could be known that the car-body was separated to seven parts, and each part contained four acceleration sensors, so the modal parameters could be identified. Meanwhile, measure points were also installed on equipment, numbers of which were BY_1~ BY_8, Then vibration characteristics between equipment and body can be obtained.

According to the structure of traction transfer, it was composed of two parts, which were ontology of the transfer and fans. The transfer was hung up via flexible rubber node, as the weight of transfer measured was about 6 tons. So eight acceleration sensors were installed on transfer, to measure the vibration and transmission characteristics of ontology and fans. The details were showed in Fig. 21.3.

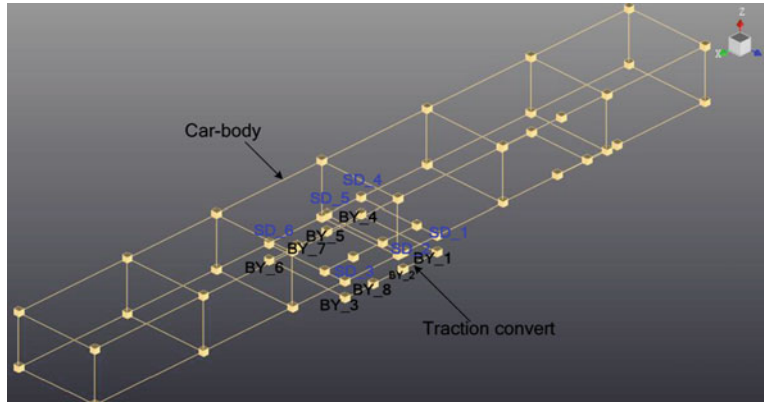


Fig. 21.2 Measure points of car-body and traction transfer numbers SD_1–SD_6 were of corresponding points of BY_1–BY_6

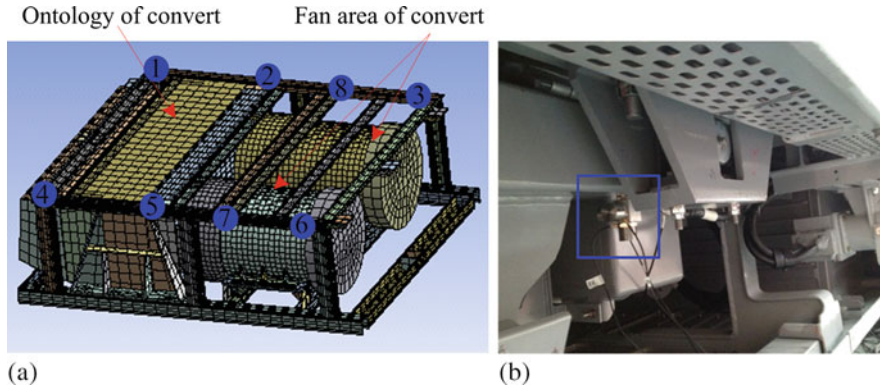


Fig. 21.3 Measure points of traction transfer (a) numbers of 1–8 were test points, (b) was of the acceleration sensor

21.4 Test Analysis

21.4.1 Modal Parameters Identification

PolyMAX method was taken for the modal analysis, which is a new frequency-domain analysis method. Arithmetic of PolyMAX is taken as follows [7, 8].

$$[H(\omega)] = [B(\omega)][A(\omega)]^{-1} \tag{21.5}$$

Make the value assignment for $[B(\omega)]$, $[A(\omega)]$ and Z .

$$[B(\omega)] = \sum_{r=0}^p z^r [\beta_r], [A(\omega)] = \sum_{r=0}^p z^r [\alpha_r], Z = e^{-j\omega\Delta t}$$

In the formula, $[\beta_r]$ is of molecular matrix polynomial coefficients, $[\alpha_r]$ is of molecular matrix polynomial is order of Mathematical model, Z is of polynomial basis function.

Modal parameters of the car-body and transfer were archived via PolyMAX method, which were shown in Figs. 21.4 and 21.5. According to the amplitude-frequency characteristic of car-body and equipment, resonance frequencies of body and equipment were 8.2 Hz and 13.5 Hz. Meanwhile, it can be known that phase of car-body and equipment was same in mode of 8.2 Hz, and phase of car-body and equipment was opposite in mode of 13.5Hz .

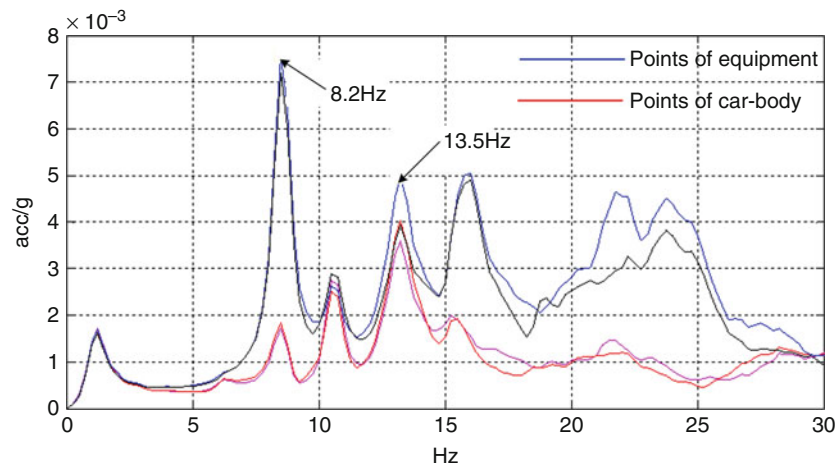


Fig. 21.4 Amplitude-frequency characteristic of car-body and equipment

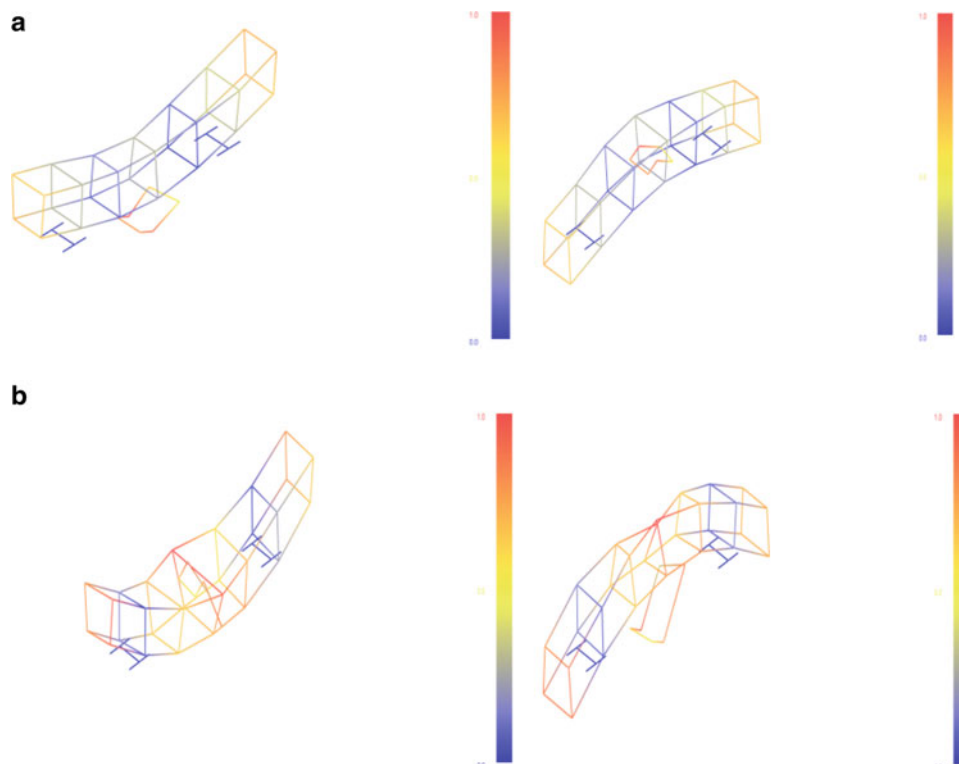


Fig. 21.5 Time domain signals of deformation and load. (a) mode of 8.2 Hz. (b) mode of 13.5 Hz

21.4.2 Vibration Transfer Characteristics

RMS (root-mean-square value) Value is the parameter to evaluate power of signal, which can be used to analyze the transfer characteristics of physical construction. The formula is shown as follows, and N is of sample points.

$$RMS = \sqrt{\frac{1}{N} \sum_{j=0}^{N-1} x_j^2} \quad (21.6)$$

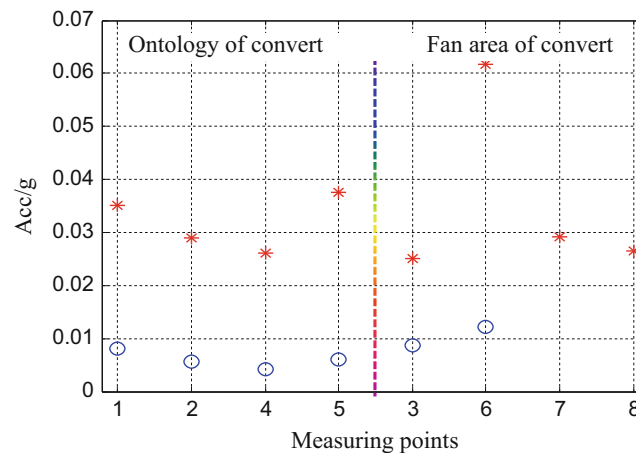


Fig. 21.6 Transfer characteristics of body & equipment (RMS)

In order to analyze the vibration isolation effectiveness of flexible rubber node, this paper separated the traction convert into two parts (ontology & fan area) to evaluate the transfer characteristics, details were shown in Fig. 21.5. In Fig. 21.6, “*” was of RMS value of traction convert, and “o” RMS value of car-body.

It could be known that vibration response of car-body Less than 0.01 g; and vibration response of car-body Less than 0.04 g. So vibration isolation effectiveness of flexible rubber node was about 75%, which proved excellent properties of flexible rubber node.

21.5 Conclusion

This paper made a deep research on the coupling relationship between car-body and flexible hanging equipment could be summarized as follows.

1. Car-body and equipment was considered to resonate in mode of 8.2 Hz with same phase, and was considered to resonate in mode of 13.5 Hz with opposite phase.
2. Vibration response of car-body Less than 0.01 g; and vibration response of transfer convert was less than 0.04 g.
3. Vibration isolation effectiveness of flexible rubber node was about 75%, which proved excellent properties of flexible rubber node.

References

1. Zhang, W.-H., Chen, L.-Q., Huang, L.-X.: Research on measurement method for vehicle parameters. *Rolling Stock*. **38**(12), 1–4 (2000)
2. Murase, S.: Dynamic characteristics of railway vehicles subjected to multiple excitations with phase differences. *JSME Int. J.* **32**(2), 194–199 (1989)
3. Wang, X.-G., Ji, Z.: Research of test method for the natural vibration frequency of bogie[D]. 2012 2nd International Conference on Frontiers of Manufacturing Science and Measuring Technology, IEEE. 7(503–504), 1050–1054 (2012)
4. Yagi, T., Stensson, A., Hardell, C.: Simulation and visualization of the dynamic behavior of an overhead power system with contact breaking. *Veh. Syst. Dyn.* **25**(1), 31–49 (1996)
5. Wang, X., Su, J., Liu, Y., Zhou, D.: Research on dynamic measuring system and model of novel high speed railway vehicle bogie. Ninth International Conference of Chinese Transportation Professionals (ICCTP), Harbin, China (2009)
6. Toyofuku, K.: Study on dynamic characteristic analysis of air spring with auxiliary chamber. *JSAE Rev.* **20**(3), 350–355 (1999)
7. Rade, D.-A.: Optimization of dynamic vibration absorbers over a frequency band [J]. *Mech. Syst. Signal Process.* **14**(5), 679–690 (2000)
8. Huang, S.-J.: Dynamic absorber with active vibration control [J]. *J. Sound Vib.* **178**(3), 323–335 (1994)



Chapter 22

Imager-Based Characterization of Viscoelastic Material Properties

Howard Brand, Tia Kauppila, Kayla Wielgus, Bridget Martinez, Nathan Miller, Trevor Tippetts, Yongchao Yang, and David Mascareñas

Abstract In this work we explore the use of emerging full-field, high-resolution, modal identification techniques from video to characterize the viscoelastic properties of a material. Currently, there are no cost-effective methods to directly measure viscoelastic material properties at intermediate strain rates. These properties can be measured at low strain rates using quasi-static loading techniques, while Split-Hopkinson's bar tests are used at high strain rates. Determining material properties at the intermediate strain rate regime is challenging as it requires large, expensive testing apparatuses and involves complex experimental protocols. An imager-based technique would provide a simpler, more affordable method for measuring viscoelastic material properties at these strain rates. To obtain measurements for intermediate strain rates of viscoelastic materials, we develop a testing protocol that involves creating a simple structure from the material-under-test and measuring its vibrational response using an imager. A finite-element model of the viscoelastic testing structure is also constructed. We extract full-field, high resolution mode shapes and modal coordinates from the video measurements of the structure as it vibrates in the desired strain regime. The frequencies of oscillation and the damping ratios are then identified. This information is intended to be used to perform model updating on the viscoelastic material properties of the finite-element model, resulting in an improved estimate of the material properties. Imager-based techniques are particularly attractive for explosive testing applications because the optics can be adapted to address the small sample sizes necessary for explosive testing. In addition to advancing viscoelastic material modeling, this work points toward the development of an imager-based modal analysis technique for identifying the structural dynamics of micro-scale structures. At this small scale, conventional contact-based sensors would result in mass-loading effects, yielding inaccurate measurements. As a solution, our full-field, high-resolution imager-based technique provides a method to characterize viscoelastic material properties while also demonstrating potential for future work in identifying structural dynamics of micro-scale structures.

Keywords Imager · Modal analysis · Viscoelastic · Intermediate strain rate · PBX

22.1 Introduction

Currently, there is ongoing research focused on being able to characterize properties of materials with the intermediate strain rate regime. Usually solutions consist of relatively large Hopkinson bars around 20–30 m long [1, 2]. This is especially true for viscoelastic materials such as PBX where material properties within a strain rate range 1–1000 1/s haven't been observed. At low strain rates (<1/s), quasi-static load tests are utilized to determine these properties. Likewise, at high strain rates, Split-Hopkinson's bar tests are used. Intermediate strain rate testing yields great challenge and alternative test methods must be employed. Prior and current research utilizes a serpentine transmitted bar which applies pressure to a sample to analyze material properties at intermediate strain rates using strain gauges [3]. However, the abovementioned reference tested elastic materials. Additional attempts such as a time-temperature superposition have been employed to observed material properties

H. Brand · T. Kauppila · K. Wielgus
Los Alamos Dynamic Summer School, Los Alamos, NM, USA

B. Martinez · N. Miller · T. Tippetts · D. Mascareñas (✉)
Los Alamos National Laboratory, Los Alamos, NM, USA
e-mail: dmascarenas@lanl.gov

Y. Yang
Argonne National Laboratory, Lemont, IL, USA

of PBX within areas of the intermediate regime, albeit with limited success [4]. An attractive alternative to measuring material properties are output-only modal analysis methods [5].

Modal analysis is a valuable technique for evaluating the structural health of various structures, ultimately benefiting the civil, mechanical, and aerospace fields. Modal properties of structures are influenced by material properties composing the structure. Traditional modal analysis techniques involve attaching an array of sensors such as strain gauges or accelerometers. Sensors can only be applied to discrete locations on a structure's surface, resulting in low spatial resolution of measurements [6]. The use of sensors also causes mass loading effects which undoubtedly have significant effects on the response of viscoelastic material. A recently emerging imager-based modal analysis method provides a non-destructive mean of extracting material modal properties [6]. These modal properties are extracted at a much higher resolution than traditional contact based methods. Additionally, imager-based modal analysis is more cost-effective in comparison to traditional bar system methods.

The development of an imager-based method for characterizing material properties provides another option for measuring viscoelastic material properties, which is valuable to explosive testing researchers. Recent experimental studies relate to imager-based modal analysis methods, where structural behaviors have effectively been modeled using traditional bench-scale aluminum structures which are excited to extract their responses using image processing techniques [7]. However, imager-based structural health monitoring (SHM) methods have not been thoroughly studied to implement this technique to other applications. The goal of this study is to explore the use of imager-based modal analysis techniques to characterize the material properties of viscoelastic materials. To the authors knowledge, there exists no simple, complete method to directly measure viscoelastic material properties over all strain rates of engineering interest.

Conventionally, explosive materials such as polymer-based explosives (PBX) are tested at small sample sizes. Therefore, this research will involve small-scale material testing, distinguishing it as one of the first studies which uses an imager-based modal analysis for small-scale applications. With future development, this technique may be applied to characterizing the structural dynamics of viscoelastic micro-structures, including modeling cancer cells which also demonstrate viscoelastic behaviors [8].

An application of this study is to model PBX explosives in the intermediate strain rate regime; therefore, additional challenges exist. An exacerbating factor in this research arises from the fact that PBX materials are extremely brittle and cannot undergo large displacements without fracturing. Thus, in order to achieve the intermediate strain rate regime without damaging the PBX, the specimen must be excited in the kHz frequency range. At such high frequencies, the displacements of the specimen are undetectable by the human eye, and these minute displacements add difficulty for the imager-based method to detect motion using a video camera. These challenges are addressed here.

Significant work on phase-based video motion magnification [9] was previously modified to develop a full-field, output-only modal analysis technique for estimating structural vibration responses [6] at high spatial resolution. The displacements are estimated using the phase-based optical flow method. Additionally, the spatial dimension of the video camera is reduced using principal component analysis (PCA). Complexity pursuit then separates the mixed signal into individual mode shapes and modal responses used to characterize the material properties.

This imager-based method was validated through an experimental setup where a specimen was constructed and horizontally excited with a shaker. The vibrational response of the structure was recorded with a camera and analyzed using video processing techniques within MATLAB. The results of this experiment are intended to be compared with a finite-element model, which can then be updated based on the material properties found by the imager-based method.

22.2 Methodology

This study was developed to analyze the potential of emerging, non-destructive, modal analysis techniques being used to characterize the response of polymers in the intermediate strain rate regime. This study was motivated by the use of this technique to study the material properties of PBX. Therefore, the mode of interest and deflection limitations were stipulated by those of PBX and were considered in the experimental setup and parameter design of the imager-based modal analysis method. The limitations stipulated by PBX and their relation to the modal analysis method are discussed in Sects. 2.1 and 2.2 below, respectively.

22.2.1 Modeling PBX in Intermediate Strain Rate

A significant motivation for this project is to extract material properties in the intermediate strain rate regime. This technique will be applicable to the testing of polymer-based mock explosives to better model material properties of these viscoelastic materials. Two limitations in the testing of mock explosives is that the material is extremely brittle and the specimen must be relatively small to prevent fracturing during testing. Therefore, the material cannot undergo more than 0.02% strain. Since motion is periodic, the max strain rate can be used to determine the frequency needed to be in intermediate strain regime.

$$\text{Strain} = 0.0002 \sin(2\pi ft) \quad \text{Strain rate} = 0.0004\pi f \approx 0.0012f \geq 1 \text{ kHz}$$

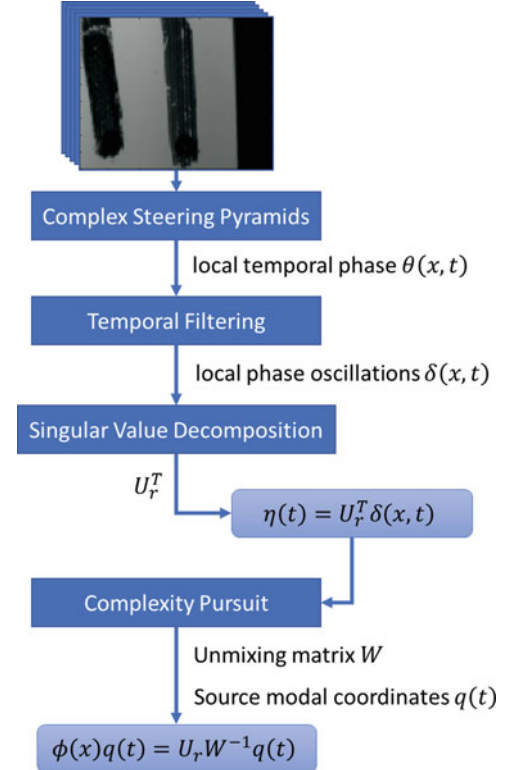
In order to introduce intermediate strain rates for the given specimen without causing fracturing, an excitation frequency of approximately 1 kHz is needed.

At this rate, the specimen will undergo minuscule displacements which are not visible to the human eye. Thus, a magnifying lens is necessary to detect this small motion with the slow-motion camera. A relatively high frame rate is needed in order to avoid aliasing in the extracted video data due to the high frequency excitations. To prevent aliasing, the frame rate for this experiment was set to 6500 fps, reaching beyond the Nyquist frequency associated with our excitation.

22.2.2 Imager-Based Modal Analysis Method

Imager based structural analysis techniques have been shown to provide a non-destructive means of extracting modal properties of materials. The imager-based technique developed in [1], using the techniques developed in [9–11], accomplishes output only modal analysis by means of tracking in plane motion using only an imager. This technique exploits the large number of pixels which can be used to describe to the materials response in order to develop high resolution reconstructions of the material's modal characteristics. Details of the technique are illustrated in a flow chart in Fig. 22.1 below.

Fig. 22.1 Imager-based modal analysis method



In the method, local phase oscillations are extracted according to the method discussed in [9]. Complex steerable pyramid filters are applied to a time series of images [11]. Each level of the pyramid filter are Gaussian windowed sinusoids (at certain spatial frequencies) which allow local amplitude and phase to be characterized at a finite spatial extent. Utilizing this filter over a time series of image data allows for local amplitude and phase over time to be characterized. The object will likely exist as a relatively constant contours in phase space [10]. Showed that the motion field can be estimated by tracking contours in phase space and that phase is more robust to illumination conditions and object distance than intensity-based tracking. This allows individual changes in phase corresponding to complex in-plane motion to be characterized on a local pixel basis. For oscillating responses, a temporal filter is employed to extract pixel level periodic oscillations in phase while removing the DC component. Assuming the dominant direction of the deflection of the material is horizontal the filters are oriented to describe phase changes in the horizontal direction. The extracted phase oscillations therefore, describe the materials response to perturbations. Assuming the physical load of the material remains in the linear elastic regime, the overall response of the material can be well described according to a linear combination of modes excited by the load. In practice there are more pixels capturing the in-plane motion then there are active modes. PCA is used to for dimension reduction of the response. Additionally, PCA is able to retain the frame's high spatial-resolution. The principle components of the system are related to the modal components by linear mixing transformation due to non-uniformities is the system's mass distribution. Complexity pursuit is used to estimate the mixing transform and modal coordinates by exploiting that predictability of statistical independent source signals should be greater than that of their linear mixtures. The complexity pursuit algorithm is an efficient method of separating modes from superposed signals for close, highly damped signals. For a linear system the highest predictable fundamental components should be single sinusoids at natural frequencies corresponding to mode shapes. After modal coordinates are found, a simple Hilbert transform is used to calculate the damping ratios for the video data. This method utilizes an envelope to estimate the damping of the system as the specimen oscillates. Additionally, the displacements of the pixels are found using the superposition of the mode shape multiplied by the time series. The actual metric deformation of the specimen is calculated by multiplying the pixel displacement by the spatial resolution of the lens. The spatial resolution is found by using the pinhole camera model and by using the focal length of the lens, along with the sensor size and the number of pixels in the image.

In exploring the use of this technique for analyzing modal properties of polymers at intermediate strain rates, there were a set of challenges that needed to addressed by the experimental setup:

1. Excitation: The excitation strategy needs to be capable of exciting high frequency modes which can be challenging for stiff polymers. Additionally, the imager method needs to observe a decaying response within these modes. Dynamics must be maintained in the linear regime.
2. Imaging: the viscous properties of the material create highly damped responses. This provides challenges to imaging in the following ways:
 - (a) Rapidly decaying responses require high frame rates.
 - (b) The material undergoes a very low-amplitude response requiring high spatial resolution.
3. Illumination: the extremely high time resolution of the imaging process requires a really high energy and stable light source.

22.3 Experimental Setup

A 10 mm × 10 mm × 85 mm rectangular prism, Teflon specimen was used for the experiment. Markings were applied to the specimen to assist in the phased-based optical flow motion detection technique. The specimen was clamped down using a small vice which was then connected to an aluminum block mounted on a linear guide. A Labworks ET-132-2 shaker was attached to the aluminum mount and used to excite the specimen in the kHz range. The shaker was suspended from a frame by bungee cords to allow for adjustment during testing. This experimental setup is portrayed in Fig. 22.2.

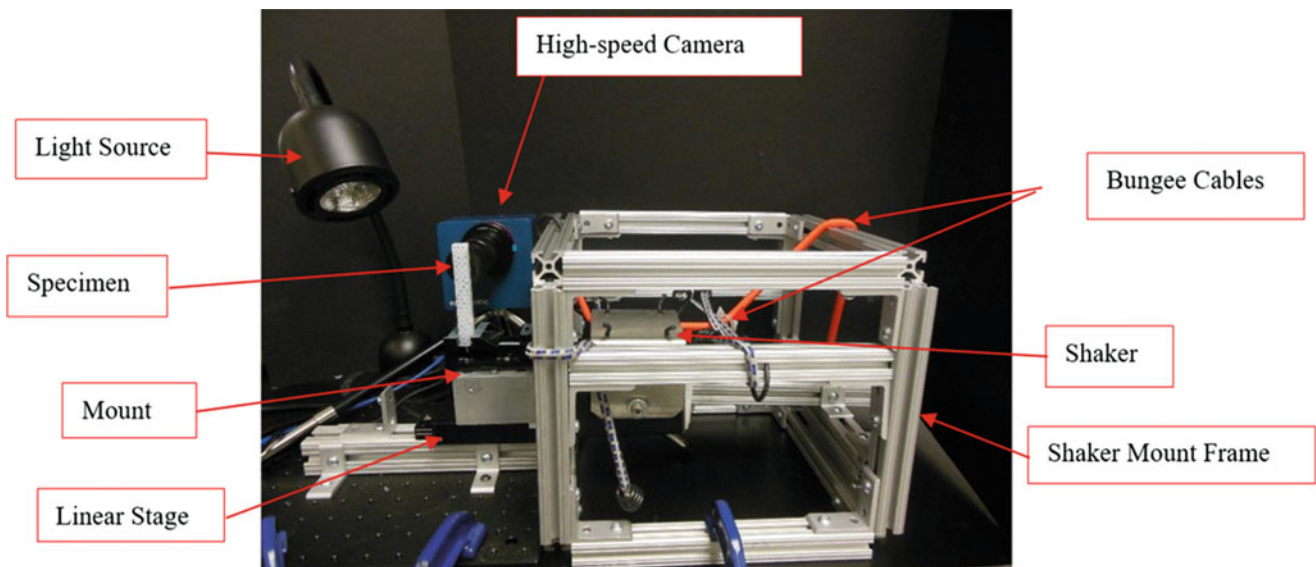


Fig. 22.2 Experimental setup

A resonant frequency of the specimen was found to be 1.47 kHz using an accelerometer. The wave generator was set to a frequency of 1.47 kHz, and the specimen was excited. At the time of recording, the output on the wave generator was turned off, to terminate the shaker excitation into the system. This allowed the specimen to dissipate its kinetic energy, returning to a resting state. This is necessary to identify the damping ratio based on the decay related to the specimen's response.

Videos were taken at two second durations, sampling at 6500 frames per second while the specimen was oscillating at 1.47 kHz. This video was recorded using the Edgetronic SC2+ high-speed camera with a Monocular lab microscope lens. Additional LED lighting was utilized to enhance the lighting projected onto the specimen and back into the camera to aid in the video processing.

After recording, the videos were evaluated using the signal processing technique, which detected motion in the videos and extracted modal properties. From this, the resonant frequencies were identified by the power spectral density figures. Using the Hilbert transform, the damping ratios were calculated from the estimated mode shapes output by the program which depicted the oscillations of the specimen. Additionally, the deformation of the specimen was determined.

22.3.1 Challenges Addressed in the Experimental Setup

The overall challenge in using the imager-based method [6] is capturing the deflection signal with the image sensor. The method uses PCA to perform dimension reduction. PCA forms a basis of the signal along the directions of maximum variance. Solutions to the blind source separation problem are used to find the mode shapes and modal coordinates. This approach was well suited for elastic materials which had relatively high deflections compared to signal noise within their respective linear regimes of response. For previous elastic materials studied, this ensured that the modes of vibration would have more influence on the change in local phase than any other artifacts. Therefore, the first principal components would contain only mode shape information. For stiff polymers (such as the mock representing PBX) there are high speed and high spatial resolution imaging requirements. These high speed and high spatial resolution imaging requirements posed challenges related to the level of influence of the materials response on the temporal phase. These obstacles needed to be met by the experimental setup through the strategies related to excitation, imaging, and illumination.

22.3.1.1 Excitation

The strategy for exciting the material was motivated by a need to excite high frequency modes while remaining within the linear regime of the material response. An additional challenge met by the excitation strategy was preserving the integrity of the (low amplitude) deflection signal as a contributor to the temporal phase. Because of the material's viscous properties, the modal hammer, used in past materials studies with this method, was not a viable option for exciting high frequency modes. A shaker provided a suitable alternative because the input loading could be controlled at a desired frequency. The input signal could then be removed and the decaying response of the specimen observed. Still, an additional obstacle remained, the response was on a micrometer scale and any slight system vibrations of a shaker apparatus could provide input signals comparable to the materials response. Therefore, a suspended shaker was use constructed with a linear stage in order to minimize other possible vibration sources.

22.3.1.2 Imaging

Image resolution is traditionally a trade-off between frame rate, in most imaging systems. The challenge with using an imager-based technique to observe the response of stiff polymers is that it requires both high resolution and high sampling rate, and therefore limits our ability to compromise either one for the other. For this reason, a high-speed camera with a high-magnification lens was used. However, this posed an additional challenge, in that the boundary of specimen was relatively smaller than the surface of the specimen in the field of view of the imager. The imager-based technique observes local changes in phase, in which phase changes at the boundary or edge of the specimen encodes the motion response. The challenge in this application of the technique was that the moving surface of the object was more prevalent then the edge of the specimen in the imager field of view. The temporal phase observed on the surface of the specimen as it is moving does not necessarily relate to the specimen motion response. This means that the surface could potentially contribute more unrelated motion effects to the temporal phase which would exacerbate modal extraction as a principal component. The specimen was marked in order to increase the significance of the motion response on the temporal phase from the point of view of the imager.

22.3.1.3 Illumination

The relatively close proximity of the lens to the specimen required for high frequency response observation provide a challenge to illuminating the specimen. Other challenges arose from the relative high frame rate of the imager. This required the light source to deliver a significant amount of energy back to the image sensor. This also meant that any oscillations in illumination due to oscillations in the illumination power circuit would be observed over the time series image data and contribute to changes in phase comparable to the contributions of the motion of the specimen. It was found that if the oscillations remained consistent, the contributions to temporal phase were statistically independent to that of the specimen motion response.

22.4 Analysis

Additional challenges within this study arose from the fact that specimen displacements are quite small, resulting in difficulty detecting motion and modal properties with video. After testing the specimen at a 1.47 kHz frequency, it was found that imager-based modal analysis techniques are able to detect vibrational responses in this range.

Four modes were extracted using the modal analysis algorithm. As shown by Fig. 22.3, the program extracted the resonant frequency of the specimen at 1.47 kHz indicated by the strong single peak from the power spectral density in component 1. For this same component, the estimated mode corresponding to this excitation clearly depicts the damping of the specimen as the input to the shaker was turned off. Using this modal information, the damping ratio was calculated with the Hilbert transform method, which will be discussed later.

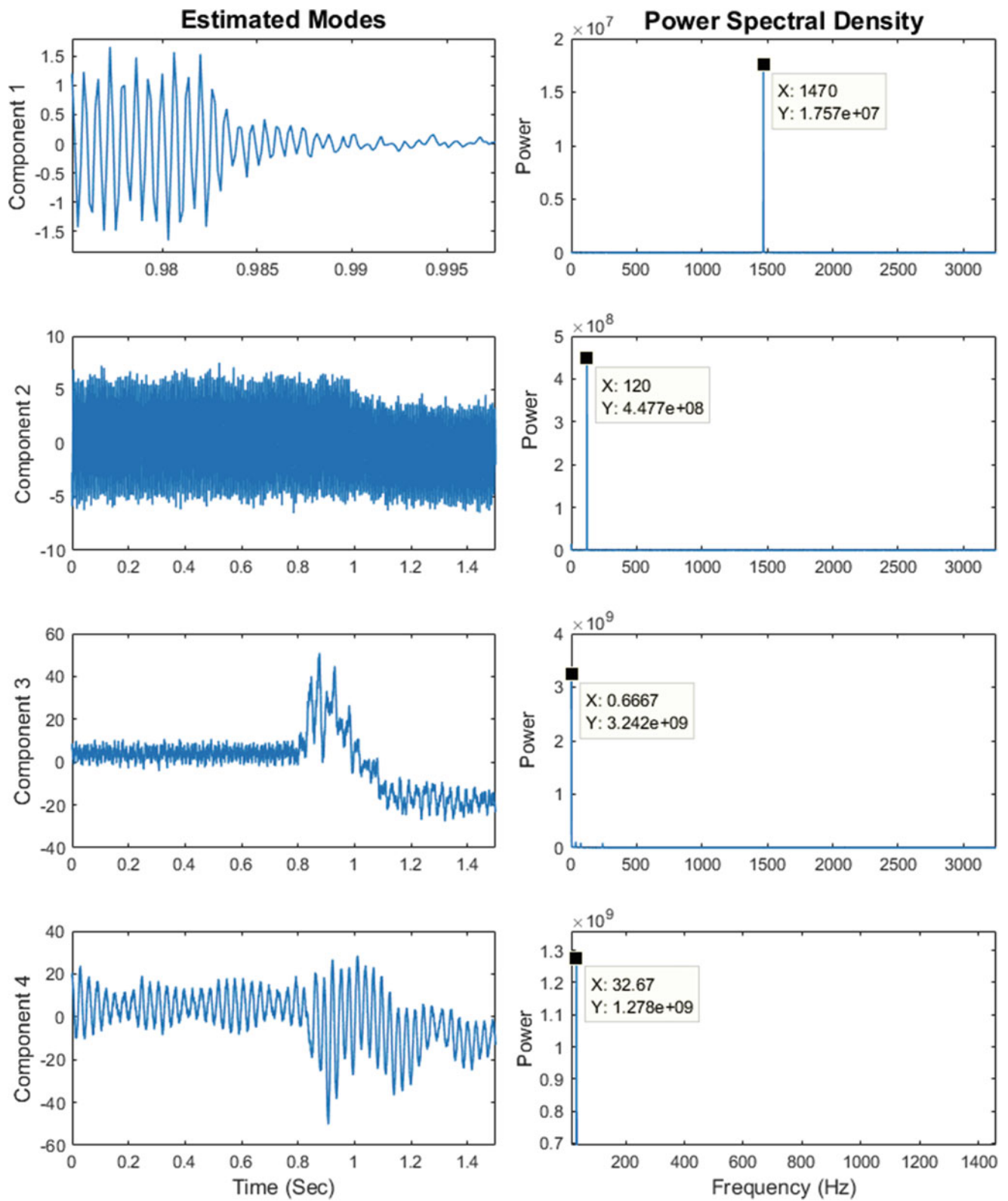


Fig. 22.3 Estimated mode shapes and associated power spectral frequencies

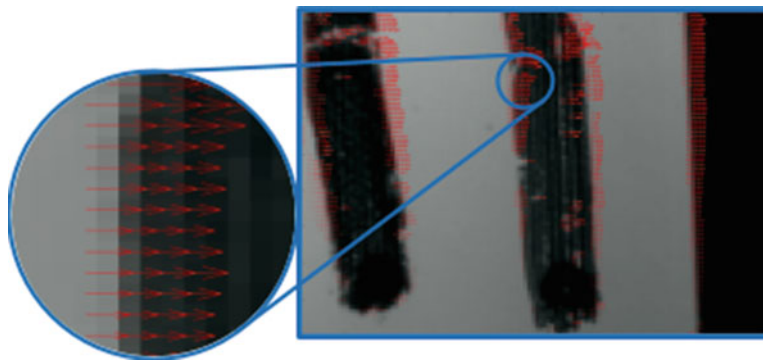


Fig. 22.4 Flow vectors diagram

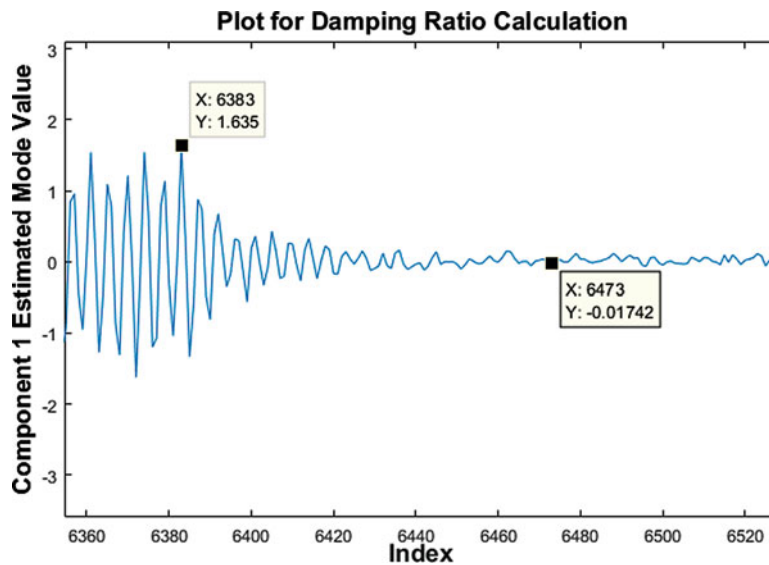


Fig. 22.5 Region for damping ratio calculation using Hilbert transform

From component 2 in Fig. 22.3, strong frequencies components were detected at 120 Hz. These signals are a result of the periodic variations of the light intensity from the LED point light source. Because the light energy is so intense compared to the slight motion of the specimen at 1.47 kHz, this frequency is output by the algorithm as a possible modal property. Due to this known frequency, this signal can be eliminated as a property of the specimen itself, rather we can assert that it is a property of the environment.

Components 3 and 4 found in Fig. 22.3 are identified as computational modes. These are outputs from the algorithm that are not attributed to modal properties of the specimen and may relate to noise within the video data or other possible unknown phenomena. Figure 22.4 shows the direction of the motion associated with the pixels that detected movement. This allows us to analyze each component, indicating whether the component contains modal information or simply noise. Component 1 is identified as a viable mode, as Fig. 22.4 shows the red flow vector arrows all pointing in coherent directions. When the algorithm outputs a computational mode, these components will yield flow vectors which point in all different directions incoherently.

Following the compilation of the estimated modes and power spectral densities, a Hilbert transform is used to calculate the damping ratios of the specimen. This method utilizes an envelope to determine the decay of the signal.

Figure 22.5 shows an example of how the damping ratio is calculated. The original component 1 data is cut down to the regions where the system damps out. This is where the input to the shaker is shut off, allowing the specimen to dissipate its oscillating motion. The cropped region of the data is then input into MATLAB, where a Hilbert transform extracted the damping ratio. The damping ratio relating to this figure is 0.0255% or 2.55% damping. After analyzing 11 tests, the average damping ratio output using this method was 0.023% or 2.3% damping. These damping ratios were compared to damping ratios extracted from accelerometer data with the same method of excitation. The accelerometer data yielded an average damping ratio of 0.026% or 2.6%. This validates the imager-based method for extracting damping ratios.

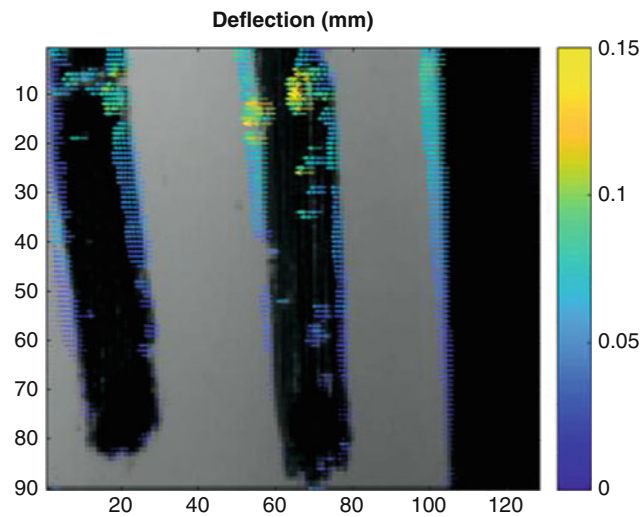


Fig. 22.6 Deflection vector diagram

An advantage of the imager-based method is that deformations of the specimen can be calculated as well. These displacements are found from the superposition of the mode shape vectors multiplied with the time series. Then, these values are converted into metric displacements using spatial resolution calculations. Due to the high spatial resolution, displacements at each pixel which has detected motion, is calculated. With this approach, displacements along different areas on the specimen can be determined, which is not possible using traditional contact-based methods. Figure 22.6 shows an example plot of the deflection vectors for a single frame of time within a single test. The average displacement calculated from the active pixels for this test was 0.01 mm or 0.00043 in.

22.5 Conclusion

Phase-based, full-field imager-based modal identification techniques are able to extract modal parameters of viscoelastic materials at intermediate strain rates. Imager techniques offer valuable capabilities for identifying modal properties, as they possess high spatial resolution. Due to this, displacements and damping ratios of the object can be calculated from the video data, providing further information on a material's response. This work involved oscillating a specimen at a known resonant frequency and then turning off the shaker input to allow the specimen to damp out while recording it. Through a signal processing technique, modal properties were extracted from the video. Successfully extracting the damping ratio and specimen deformations in the intermediate strain rate was accomplished through this study.

Future studies may focus on using averaging across several tests to reduce noise. Further work may address exploring the use of imager-based modal analysis at a smaller scale. This study has shown that cameras are able to detect extremely small displacements, and it is possible that this sort of technology could be applied to micro-scale structures as well. Reduction of the specimen size is another improvement to be explored in order to more accurately represent the PBX explosive. Modeling specimen in a finite element software will aid in verifying the results.

Acknowledgements Los Alamos National Laboratory (LANL) is operated by Los Alamos National Security LLC, for the National Nuclear Security Administration of the U.S. Department of Energy, under DOE Contract DE-AC52-06NA25396. This project was supported by LANL under the Engineering Institute Dynamics Summer School (LADSS) fellowship program. This project was mentored by Bridget Martinez, Nathan Miller, Trevor Tippetts, and David Mascarenas. A special thanks to Gregory Taylor for his previous work and contributions.

References

1. Shim, J., Mohr, D.: Using split Hopkinson pressure bars to perform large strain compression tests on polyurea at low, intermediate and high strain rates. *Int. J. Impact. Eng.* **36**(9), 1116–1127 (2009)

2. Song, B., Syn, C., Grupido, C., Chen, W., Lu, W.: A long split Hopkinson pressure bar (LSHPB) for intermediate-rate characterization of soft materials. *Exp. Mech.* **48**(6), 809–815 (2007)
3. Oppedal, A., Whittington, W., Francis, D., Horstemeyer, F.: A novel intermediate strain rate testing device: The serpentine transmitted bar. *Int. J. Impact. Eng.* **81**, 1–7 (2015)
4. Thompson, D., DeLuca, R., Wright, W.J.: Time-temperature superposition applied to PBX mechanical properties. *AIP. Conf. Proc.* **1426**, 657 (2012)
5. Fan, P.Q.W.: Vibration-based damage identification methods: a review and comparative study. *Struct. Health Monit.* **10**(1), 83–111 (2011)
6. Yang, Y., Dorn, C., Mancini, T., Talken, Z., Kenyon, G., Farrar, C., Mascarenas, D.: Blind identification of full-field vibration modes from video measurements with phase-based video motion magnification. *Mech. Syst. Signal Process.* **85**(15), 567–590 (2017)
7. Yang, Y., Dorn, T., Mancini, Z., Talken, S., Nagarajaiah, G., Farrar, C., Mascarenas, D.: Blind identification of full-field vibration modes of output-only structures from uniformly-sampled, possibly temporally-aliased (sub-Nyquist), video measurements. *J. Sound Vib.* **390**, 232–256 (2017)
8. Corbin, E., Adeniba, O., Ewoldt, R., Bashir, R.: Dynamic mechanical measurement of the viscoelasticity of single adherent cells. *Appl. Phys. Lett.* **108**, 093701 (2016)
9. Wadhwa, N., Rubinstein, M., Durand, F. and Freeman, W.: Phase-based video motion processing. In: *ACM Trans. Graph. Proceedings SIGGRAPH 2013*, Anaheim, CA (2013)
10. Fleet, D.J., Jepson, A.D.: Computation of component image velocity from local phase information. *Int. J. Comput. Vis.* **5**(1), 77–104 (1990)
11. Simoncelli, E.P.: *matlabPyrTools*. [Online] Available: <http://www.cns.nyu.edu/~lcv/software.php> (2009)



Chapter 23

Development and Validation of Data Processing Techniques for Aircraft Ground Vibration Testing

Silvia Vettori, Emilio Di Lorenzo, Bart Peeters, and Antonio Carcaterra

Abstract The modal identification of large and dynamically complex structures (e.g. aircrafts) often requires a multiple-input excitation. Sine sweep excitation runs are applied in order to concentrate more energy on each line of the frequency spectrum. The work is aimed at developing a new data processing technique for aircrafts Ground Vibration Testing when a multi-point sine sweep excitation is used. The Virtual Driving Point method cancels out the necessity of performing as many sweeps as shakers in order to compute the system's FRFs. Each single sweep can be individually performed and the measured data can be independently analyzed. As a result, modal analysis is more easily carried out and each single sweep leads to different modes, whose symmetric or antisymmetric nature depends on the relative phase between inputs that has been adopted during that run (mainly 0° and 180°). This procedure allows to obtain more defined mode shapes and, more generally, reliable results in terms of modal parameters. New data processing techniques, as the ones object of this work, always require to be validated through their application to different data sets. It is indeed important, in order to assess the reliability of the method, to analyze and compare its outcome when applied to different data and to find a constant improvement with respect to results provided by conventional methods. For this reasons, different GVT measurements were performed and post-processed to validate the proposed approach. Before applying the method to a physically acquired data set, it has been tested on a numerically simulated three DOFs system in order to identify the possible results to which it could lead and the advantages that it could bring. Then, three GVT data sets, during which a two points excitation has been used, have been analyzed: a data set acquired during a measurement campaign on an airplane mockup; a data set related to a scaled airplane model, the Garter model, which is bigger than the previous one and is characterized, like large aircrafts, by close modes; a data set acquired during a measurement campaign on a real aircraft, the eFusion Magnus electric aircraft developed in cooperation with Siemens.

Keywords Ground Vibration Testing · Virtual Driving Point · Electric aircraft · Structural dynamics · Non-linearities

23.1 Introduction

Ground Vibration Tests (GVTs) are conducted to determine aircrafts dynamic behavior. They consist in testing the aircraft on the ground, measuring the response that it gives to a multiple-input excitation, provided through either multi-reference random signals or sine sweeps. This procedure allows to define the system's Frequency Response Functions (FRFs), which are then used as starting point for the modal analysis. The extracted data, in terms of natural frequencies, mode shapes, modal masses and damping ratios, are then either directly used to predict the aircraft dynamic behavior when it is flying at a certain speed or they are used to validate and update the Finite Element model, from which flutter prediction can be made [1].

S. Vettori
Siemens Industry Software NV, Leuven, Belgium

University of Rome "La Sapienza", Faculty of Civil and Industrial Engineering, Department of Mechanical and Aerospace Engineering, Rome, Italy
e-mail: silvia.vettori@siemens.com

E. Di Lorenzo (✉) · B. Peeters
Siemens Industry Software NV, Leuven, Belgium
e-mail: emilio.dilorenzo@siemens.com

A. Carcaterra
University of Rome "La Sapienza", Faculty of Civil and Industrial Engineering, Department of Mechanical and Aerospace Engineering, Rome, Italy

Because of the time pressure period during which these tests are performed, usually before the maiden flight of the aircraft, and because of their high development costs, one of the main industrial requests is to reduce test duration. On the other hand there is the need to get more informations from the structure. To guarantee the trade off between test duration reduction and better results achievement, more powerful and advanced techniques are continuously investigated [2].

This work will focus on sine sweep excitation methods, which ensure higher RMS input loads and a better signal-to-noise ratio with respect to the random ones. They also allow to control frequency, amplitude and phase, so that it is possible to characterize non-linearities of the system [3]. Moreover, performing sine sweeps it is possible to provide symmetric and antisymmetric excitations to the structure in order to respectively emphasize symmetric and antisymmetric modes, that are of most concern with respect to others [4]. In the simplest case of two shakers placed on the wings, symmetric excitation is realized applying two sweeps in phase, while an antisymmetric excitation is obtained creating a 180° relative phase between the two inputs. The main drawback of using a sinusoidal sweep method is that different sine sweeps must be performed in series in order to compute the system's FRFs. The number of performed sine sweeps must be at least equal to the number of inputs on the system, so at least equal to the number of shakers. The modal identification process, therefore, cannot be started until all the needed sweeps are performed since all the data are used together to calculate the FRF matrix [5]. Despite this and although sine sweep methods require a longer time duration than the one needed when applying random excitations, swept sine excitation is always preferred to random one, which is usually adopted to have reference FRFs of the system.

The data processing technique for aircrafts Ground Vibration Testing that is going to be described in this paper is able to obtain the system's FRFs in a single run, canceling out the necessity of performing as many runs as shakers, and to lead to improved results in terms of modal parameters, also in presence of non-linearities. Moreover, when a specific relative phase between inputs is used, the method is able to reduce the needed number of sweeps to be performed in order to obtain the complete mode set of the system. This technique has been at first tested on a three DOFs numerically simulated discrete system, afterwards it has been developed and validated on GVT data acquired when a two points excitation configuration is used. The analyzed data sets concern a real airplane, the eFusion Magnus electric aircraft, tested by Siemens Industry Software in 2017, and two different airplane models: the Garteur model, which has been tested by Siemens Industry Software during a measurement campaign at the SOPEMEA laboratories in 2007, and a smaller airplane model that has been tested at Siemens Industry Software laboratories in 2017.

23.2 Conventional FRFs Computation

The H_1 estimator is a commonly adopted tool used to compute averaged FRFs from measurements data with the purpose of reducing the uncorrelated noise present on the measured responses, assuming its absence on the inputs. It can be computed as in Eq. (23.1) if expressions (23.2) and (23.3) are respectively introduced for the autopower spectrum of the inputs and the crosspower spectrum between the inputs and the outputs [6].

$$[H_1(\omega)]_{N_o \times N_i} = [G_{YF}(\omega)]_{N_o \times N_i} [G_{FF}(\omega)]_{N_i \times N_i}^{-1} \quad (23.1)$$

$$[G_{FF}(\omega)]_{N_i \times N_i} = [F(\omega)]_{N_i \times N_{sweeps}} [F(\omega)]_{N_{sweeps} \times N_i}^{*t} \quad (23.2)$$

$$[G_{YF}(\omega)]_{N_o \times N_i} = [Y(\omega)]_{N_o \times N_{sweeps}} [F(\omega)]_{N_{sweeps} \times N_i}^{*t} \quad (23.3)$$

Here N_o is the number of outputs, i.e. the number of responses DOF measured by the accelerometers, N_i is the number of inputs, i.e. the number of forces injected into the system, and N_{sweeps} stands for the number of runs, i.e. different sine sweep excitations and consequent forces and responses collection, that have to be performed in series and then used together for the H_1 computation.

Equation (23.1) shows that matrix $[G_{FF}(\omega)]$ must be inverted to compute the H_1 estimator, which means that it must be a non-singular matrix. To guarantee the autopower spectrum matrix to be non-singular, two main conditions must be satisfied:

- $N_{sweeps} \geq N_i$, i.e. the number of performed sweeps in series must be at least equal to the number of inputs that are given to the system, which corresponds to the number of shakers;
- forces belonging to the different performed sweeps must not be correlated, i.e. the excitation configuration must change from a sweep to another.

In the case of a GVT with two shakers for example, at least two sweeps for each test aimed at computing the system's FRFs must be performed. The two applied forces during the different runs are usually chosen to have the same amplitude in the

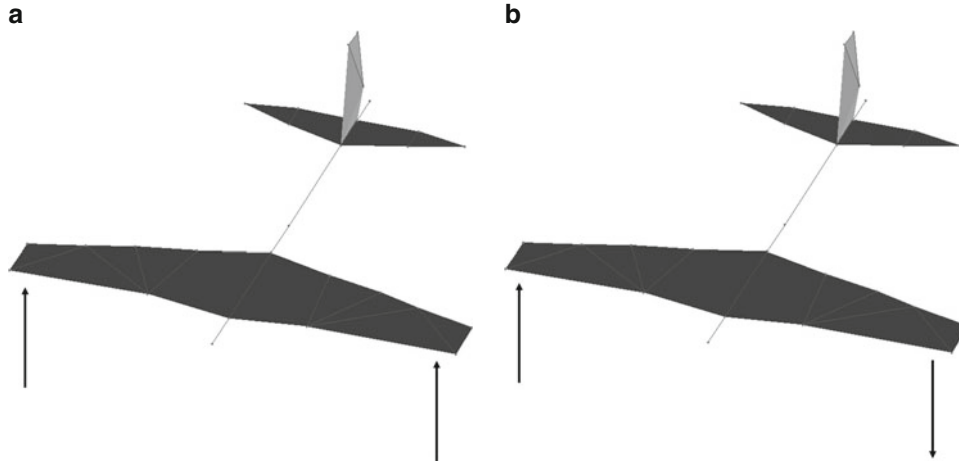


Fig. 23.1 Conventional performed sweeps during a two points excitation sweep test. (a) Sweep 1: symmetric sweep. (b) Sweep 2: antisymmetric sweep

frequency band and for all the sweeps that are executed, while their relative phase changes from a sweep to another in order to satisfy the second condition. Figure 23.1 shows the conventional relative phase scheme that is adopted for a two points excitation configuration: the first sweep is symmetric because the forces are equal both in amplitude and phase, while the second sweep is antisymmetric because the right wing force, i.e. the reference input, maintains a 0° phase while the left wing force switches its phase to 180° , which means that it has an opposite direction with respect to the one of the reference input. This resulting configuration matches also the necessity of an excitation able to emphasize symmetric and antisymmetric modes of the aircraft. Indeed, tail and wings modes, that are mainly symmetric or antisymmetric with respect to the fuselage position if a structural symmetry can be recognized, are considered to be the most interesting modes to be investigated.

23.3 Virtual Driving Point Method for a Two Points Excitation Configuration

The Virtual Driving Point (VDP) method is based on the identification, for each sweep that is performed with multi-point excitation, of a virtual force and a virtual response. Both of them are computed starting from the measured forces and responses of the two actual driving points of the system, i.e. the two physical points where the excitation is applied through the two shakers. Thanks to this procedure, each single sweep can be individually analyzed and a set of system's FRFs, that are then used as starting point for the modal analysis, can be extracted. Therefore, each sweep identifies a specific mode set that, in most of the cases, has to be combined with the others in order to obtain the final mode set of the system.

23.3.1 Adopted Procedure for the VDP Method Application

The VDP mathematical formulation involves inputs and outputs frequency spectra, which can be respectively expressed as in Eqs. (23.4) and (23.5).

$$\{F(\omega)\} = \begin{Bmatrix} F_1(\omega) \\ F_2(\omega) \end{Bmatrix} = \begin{Bmatrix} |F_1(\omega)|e^{j\varphi_1} \\ |F_2(\omega)|e^{j\varphi_2} \end{Bmatrix} \quad (23.4)$$

$$\{Y(\omega)\} = \begin{Bmatrix} Y_1(\omega) \\ \vdots \\ Y_{N_o}(\omega) \end{Bmatrix} \quad (23.5)$$

Here Y_1 and Y_2 are assumed to be the driving points measured accelerations, F_1 is the reference input and F_2 is the delayed input, where the delay is $\varphi = \varphi_2 - \varphi_1$. The computational steps for the VDP method application start from calculating the

amplitude of the virtual force by the vector norm of the actual excitation force vector, as shown in Eq. (23.6).

$$|F_v(\omega)| = \sqrt{|F_1(\omega)|^2 + |F_2(\omega)|^2} \quad (23.6)$$

The virtual acceleration is then computed as in Eq. (23.8) taking into account that Eq. (23.7), which is obtained stating the equivalence between the complex power of the virtual input F_v and the one of the actual inputs F_1 and F_2 , can be also written substituting acceleration to velocity in case of harmonic vibrations.

$$|F_v(\omega)|V_v(\omega) = |F_1(\omega)|V_1(\omega) + |F_2(\omega)|V_2(\omega) \quad (23.7)$$

$$Y_v(\omega) = \frac{|F_1(\omega)|Y_1(\omega) + |F_2(\omega)|Y_2(\omega)}{|F_v(\omega)|} \quad (23.8)$$

For what concerns the virtual force computation, in terms of both amplitude and phase, it is possible to state that, in case of symmetric excitation, the virtual force weighted by its own amplitude is equal to the sum of the two applied forces, each of them weighted by their respective amplitudes. The resulting formula for the virtual force in case of symmetric excitation is described by Eq. (23.9).

$$F_v(\omega) = \frac{|F_1(\omega)|F_1(\omega) + |F_2(\omega)|F_2(\omega)}{|F_v(\omega)|} \quad (23.9)$$

When the excitation is not symmetric and a generic phase lag φ between the inputs is used, a phase correction, whose mathematical proof is not reported here, must be introduced to bring the delayed input F_2 to have the same phase of the reference one in order to be able to sum them up in the F_v computation. Therefore, Eqs. (23.10) and (23.11) are the generic expressions for the virtual force and acceleration that can be applied when any φ between the inputs is used. The introduced phase correction turns into a summation when the excitation is symmetric and a subtraction when it is antisymmetric.

$$F_v(\omega) = \frac{|F_1(\omega)|F_1(\omega) + e^{-j\varphi}|F_2(\omega)|F_2(\omega)}{|F_v(\omega)|} \quad (23.10)$$

$$Y_v(\omega) = \frac{|F_1(\omega)|Y_1(\omega) + e^{-j\varphi}|F_2(\omega)|Y_2(\omega)}{|F_v(\omega)|} \quad (23.11)$$

After its computation, the virtual acceleration $Y_v(\omega)$ is appended to the vector of the measured responses $\{Y(\omega)\}$, and a new response vector of N_o+1 elements, expressed in Eq. (23.12), is obtained.

$$\{Y(\omega)\}_{new} = \begin{Bmatrix} Y_1(\omega) \\ \vdots \\ Y_{N_o}(\omega) \\ Y_v(\omega) \end{Bmatrix} \quad (23.12)$$

For the single sweep a new data set can be considered: the applied force is only one and it is represented by $F_v(\omega)$, while the response vector is $\{Y(\omega)\}_{new}$. From this data set, a column matrix of virtual FRFs can be computed simply using Eq. (23.13).

$$\{H(\omega)\}_v = \{Y(\omega)\}_{new} \frac{1}{F_v(\omega)} \quad (23.13)$$

The virtual driving point FRF is the last element of the column matrix $\{H(\omega)\}_v$.

Once the virtual FRFs matrices are computed for each single sweep, the modal analysis process can start. From the two FRFs sets, $\{H(\omega)\}_{v_{sym}}$ from the symmetric sweep and $\{H(\omega)\}_{v_{ant}}$ from the antisymmetric sweep, two Polymax stabilization diagrams [7] are defined and two groups of system poles, and therefore two different mode sets, are extracted. The system poles, and so the mode shapes, are identified correctly according to their symmetric or antisymmetric nature: symmetric

mode shapes of the system are well detected only by the symmetric sweep, while the antisymmetric mode shapes are well identified only by the antisymmetric sweep. In order to reconstruct a single and complete mode set for the system, symmetric and antisymmetric modes, respectively extracted from $\{H(\omega)\}_{v_{sym}}$ and $\{H(\omega)\}_{v_{ant}}$, must be grouped together. Mode shapes that are part of the final mode set are vectors, as the one expressed by Eq. (23.14), of N_o+1 components, since in the response vector that has been used to compute the FRFs, the additional component $Y_v(\omega)$ related to the virtual response is present.

$$\{\Psi\}_r = \begin{Bmatrix} \Psi_{1r} \\ \vdots \\ \Psi_{N_o r} \\ \Psi_{vr} \end{Bmatrix} \tag{23.14}$$

The Ψ_{vr} component of the mode shapes, i.e. their last element, must be deleted because it represents a non physical DOF which, depending on the scaling scheme that is used, can also have influence on the values of the modal displacements related to the other DOFs. After the last element of the mode shapes has been deleted, the resulting mode shapes are scaled again and all the modal parameters are correctly defined.

23.4 Validation Cases

The VDP method has been at first applied to a three DOFs discrete system in order to investigate the possible results it could lead to and to compare them to the theoretical ones computable through a simple eigenvalue problem. Afterwards, several GVT data sets have been post-processed with the purpose of validating the proposed approach. Each application allowed to identify different specific advantages of the method. The main achieved results are described in the following sections.

23.4.1 Three DOFs Discrete System

The three DOFs discrete system depicted in Fig. 23.2a, symmetric in terms of masses, stiffness and damping ($m_1 = m_2 = m_3 = 0.05$ kg, $k_1 = k_2 = k_3 = k_4 = 10,000$ N/m, $c_1 = c_2 = c_3 = c_4 = 0.2$ kg/s), has been numerically simulated applying two forces F_1 and F_3 to masses 1 and 3, with the intention of simulating the symmetric position that the shakers usually have during GVT. The two forces have been simulated as two linear sine sweeps at 1 Hz/s, symmetric during a first run and antisymmetric during the second.

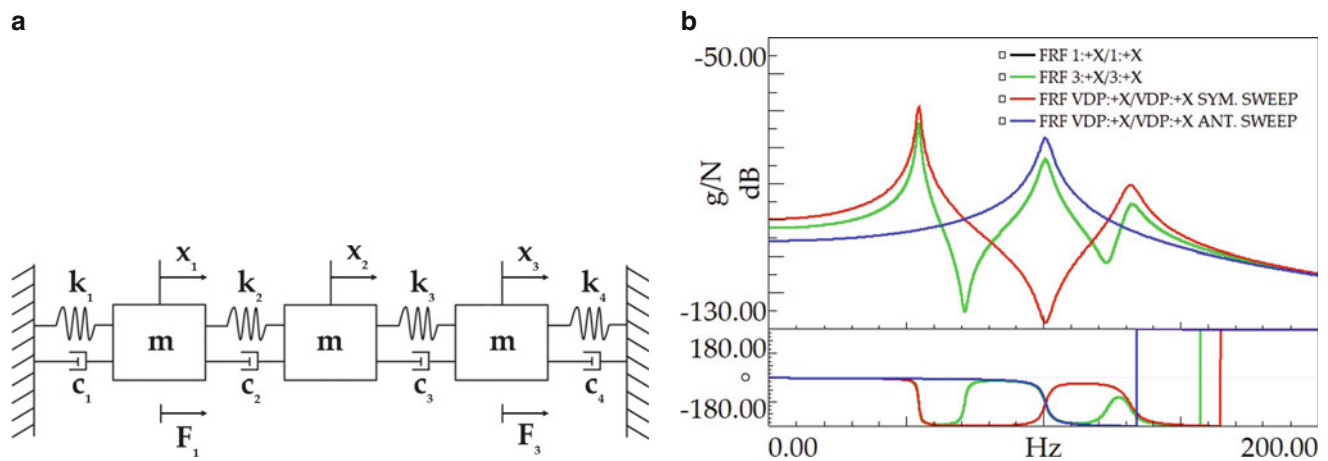


Fig. 23.2 Three DOFs system. (a) Three DOFs system scheme. (b) Actual and virtual driving points FRFs

Table 23.1 Three DOFs system mode sets

	Mode type	Theoretical frequency (Hz)	MIMO set		VDP reconstructed set	
			Undamped frequency (Hz)	Damping (%)	Undamped frequency (Hz)	Damping (%)
1	S	54,476	54,476	1.03	54,481	1.12
2	A	100,658	100,658	1.90	100,651	1.91
3	S	131,517	131,517	2.48	131,514	2.49

S symmetric, A antisymmetric

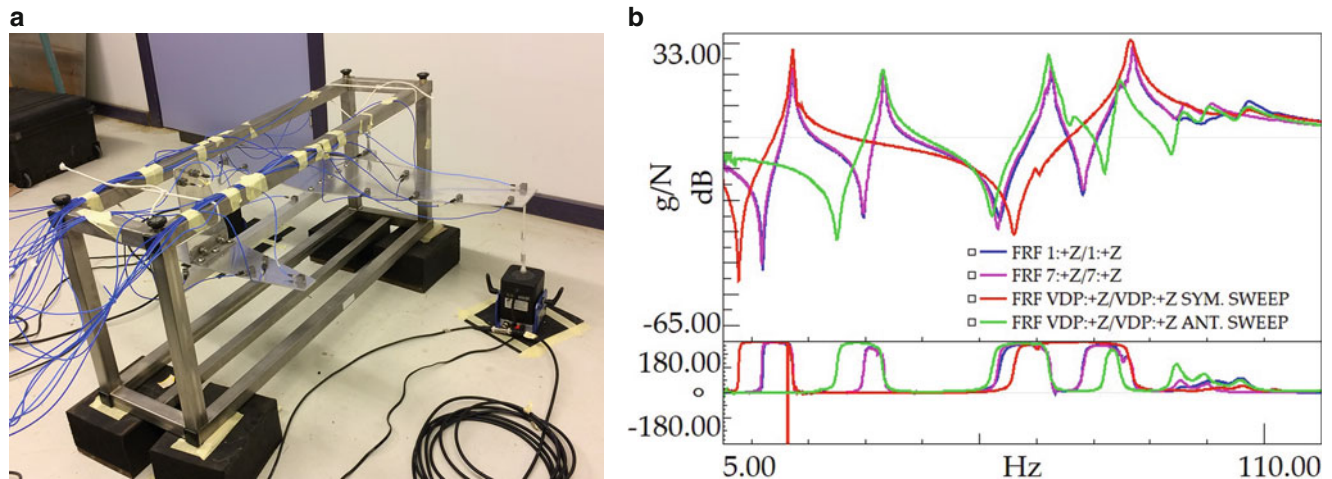


Fig. 23.3 Airplane mockup. (a) Airplane mockup experimental setup. (b) Actual and virtual driving points FRFs

Figure 23.2b compares the actual driving point FRFs, i.e. obtained by using the conventional method, and the virtual driving points FRFs obtained by applying the new technique.

The black and the green curve are the actual driving points FRFs: they are perfectly overlapped thanks to the symmetry of the system. These two curves both show the three peaks correspondent to the three mode shapes of the three DOFs system. The red curve is the virtual driving point FRF obtained when applying the VDP method using data belonging to the symmetric sweep: the peaks in the FRF are only two and they are expected to be related to symmetric mode shapes. The blue curve instead, is the virtual driving point FRF obtained when the method is applied to the antisymmetric sweep data: the peak is only one and it is expected to be related to an antisymmetric mode shape.

The mode sets extracted from the FRFs shown in Fig. 23.2b are compared in Table 23.1 in terms of natural frequencies and damping ratios. Moreover, the identified symmetric or antisymmetric nature of each mode is reported. It is possible to notice that the VDP method correctly identifies the mode set of the system and that the symmetric and antisymmetric nature of the modes actually corresponds to the expected one: the first and third modes are symmetric, while the second one is antisymmetric.

23.4.2 Airplane Mockup: Polymax Stabilization Diagrams and Mode Shapes

The airplane mockup shown in Fig. 23.3a has been tested at Siemens Industry Software laboratories exciting it through two shakers placed at the wings tips and measuring its responses through 18 mono-axial and 6 tri-axial accelerometers. The data have been acquired exciting the system with a logarithmic sine sweep at 1 oct/min, symmetric during a first run and antisymmetric during the second, in a frequency band between 5 and 110 Hz.

Figure 23.3b illustrates the actual and the virtual driving points FRFs on the same plot. The virtual driving point FRF obtained from the symmetric sweep (red curve) shows only some peaks, which are related to the symmetric modes of the system. Indeed, the red curve detects the first peak of the actual driving points FRFs, which is associated to the first wings bending of the mockup. The virtual driving point FRF obtained from the antisymmetric sweep (green curve) instead, does not show the mentioned first peak, because it only identifies peaks associated to antisymmetric modes.

An interesting advantage of the VDP method lies in the clearness of the Polymax stabilization diagrams, as shown in Fig. 23.4, if compared with the ones obtained by using the conventional method.

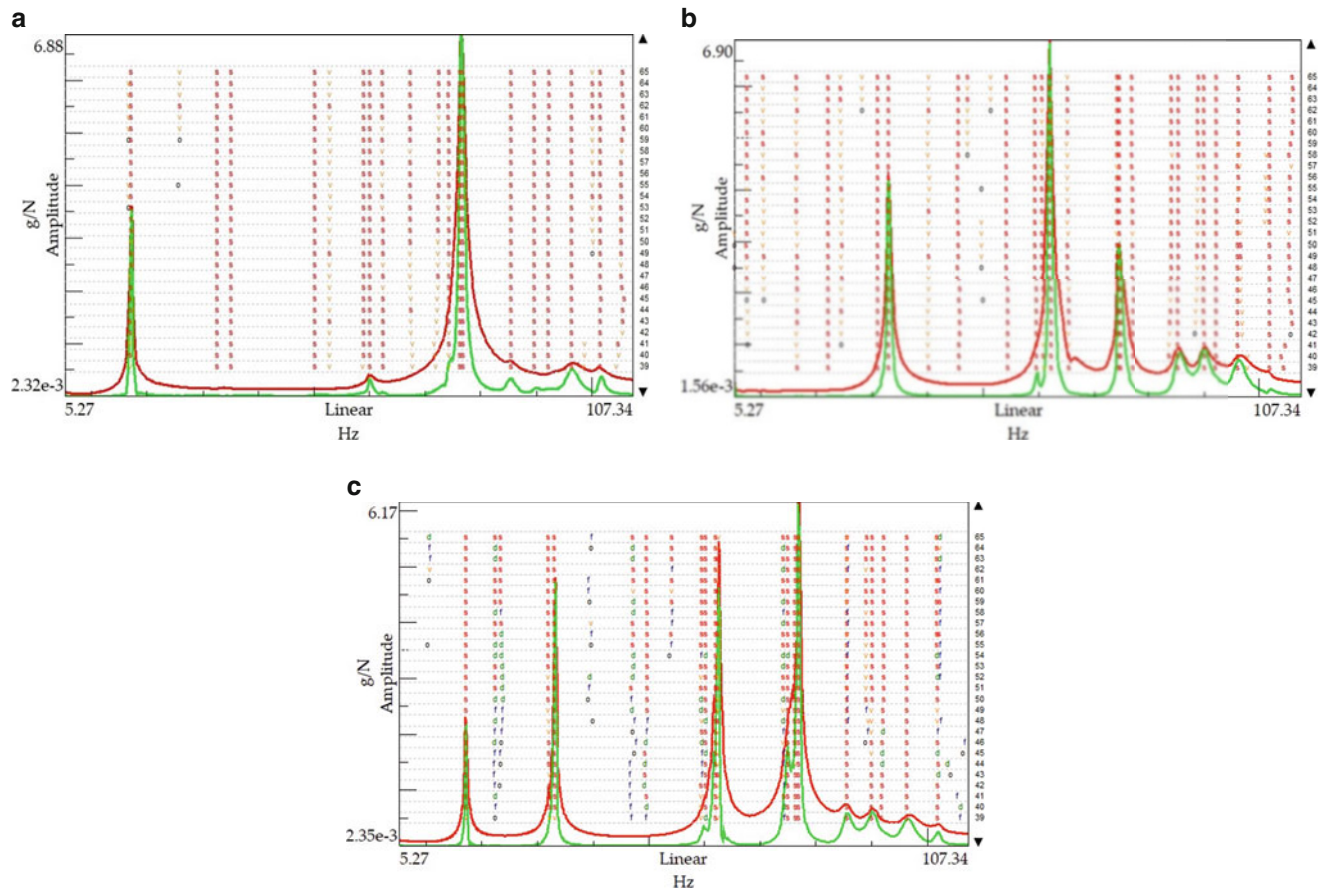


Fig. 23.4 Airplane mockup Polymax diagrams. (a) VDP method: symmetric sweep. (b) VDP method: antisymmetric sweep. (c) MIMO conventional method

Table 23.2 Airplane mockup mode sets

	Mode type	MIMO set		VDP reconstructed set	
		Frequency (Hz)	Damping (%)	Frequency (Hz)	Damping (%)
1	S	17,137	1.05	17,129	1.10
2	A	33,189	0.62	33,024	1.08
3	S	60,299	0.74	60,060	0.70
4	A	62,056	0.82	62,172	0.68
5	A	74,954	0.62	74,760	0.92
6	S	76,938	0.36	76,802	0.86
7	A	85,651	1.36	85,269	1.45
8	A	90,241	0.99	89,942	1.26
9	A	96,459	1.56	96,303	1.49

S symmetric, A antisymmetric

Figure 23.4 illustrates the Polymax diagrams achieved through the VDP method (a and b) and the one obtained by the conventional procedure (c). Comparing the diagrams, it is possible to notice that the VDP method generates stabilization diagrams with poles that are more stable with respect to the ones achieved by the conventional method. Therefore, picking the system’s poles, and so performing the modal analysis, turns out to be easier when using the VDP method. Usually, stable poles related to symmetric modes are found in the symmetric Polymax diagram and stable poles related to antisymmetric modes are found in the antisymmetric Polymax diagram.

Basing on the reasoning mentioned before, the system’s poles have been chosen from a Polymax diagram or from another and the final mode set, reported in Table 23.2, has been reconstructed. The second column of Table 23.2 points out the symmetric (S) or antisymmetric (A) nature of the modes, so it is an indication of the run from which the mode has been selected. In Table 23.2 also the mode set extracted from the modal analysis on the conventional MIMO FRFs, which is

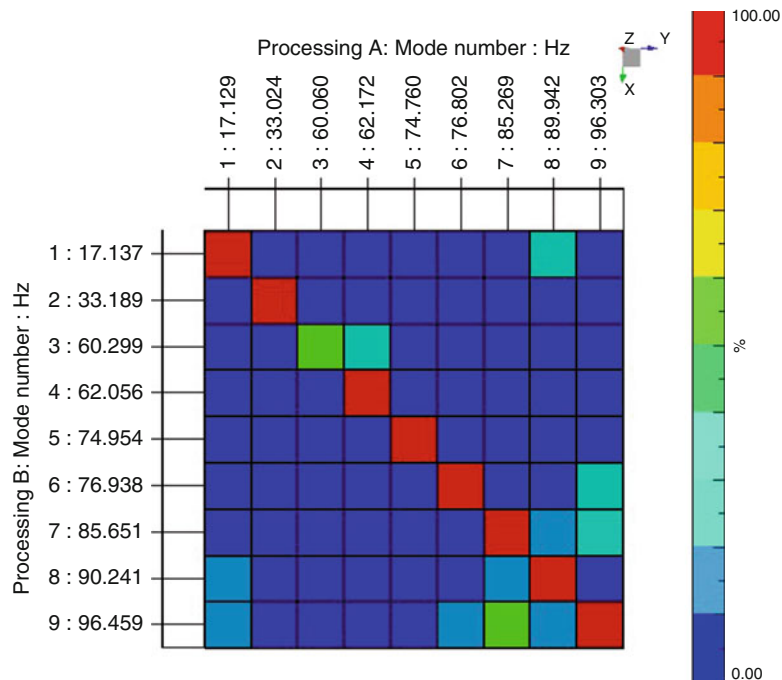


Fig. 23.5 MAC diagram between MIMO and VDP reconstructed sets

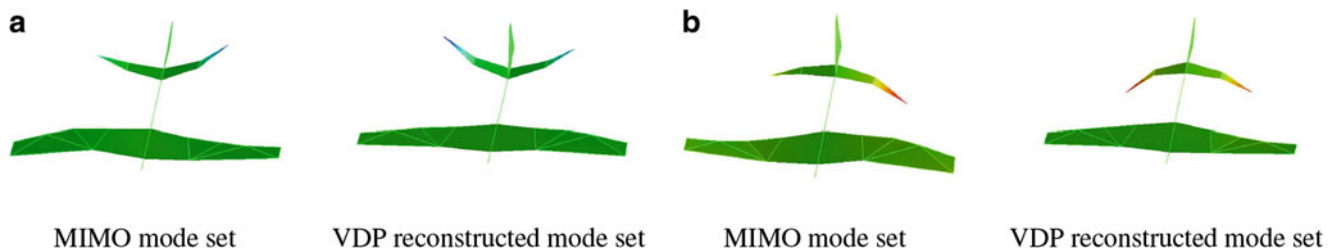


Fig. 23.6 Mode 3 at about 60 Hz. (a) First horizontal tail bending: compression. (b) First horizontal tail bending: traction

considered to be the reference mode set, is reported in order to give a visible comparison. Analyzing both Table 23.2 and the MAC diagram in Fig. 23.5, which shows a high correlation between the MIMO mode set (Processing B) and the VDP reconstructed mode set (Processing A), it is possible to state that the VDP method gives correct results in terms of natural frequencies, damping ratios and mode shapes.

The only exception to the diagonal behavior in the MAC diagram is represented by the low correlation of mode 3. Indeed, Fig. 23.6 clearly shows that mode 3, which corresponds to the first bending of the horizontal tail, is characterized by a clearer mode shape, i.e. a lower complexity, if the VDP method is used. A precise symmetry in the tail displacement is indeed present in the VDP mode shape, while the left and the right halves of the horizontal tail do not move in phase in the MIMO mode shape. Moreover, the MIMO mode shape also shows a small antisymmetric bending of the wings, which is not present in the VDP one. This very low bending is due to the influence of mode 4, which cannot be canceled out when using the MIMO conventional method, but that is completely absent if using the VDP method.

23.4.3 Garteur Airplane Model: VDP Method Application to Data Measured During a Sine Sweep Test with a 90° Relative Phase Between Inputs

The Garteur model, depicted in Fig. 23.7a, is an aircraft scaled model, characterized, like large aircrafts, by closed modes and a weak non-linear behavior. During the measurements carried out by Siemens Industry Software in 2007 at SOPEMEA laboratories, the system has been excited through two shakers placed at intermediate wing points and its responses have been

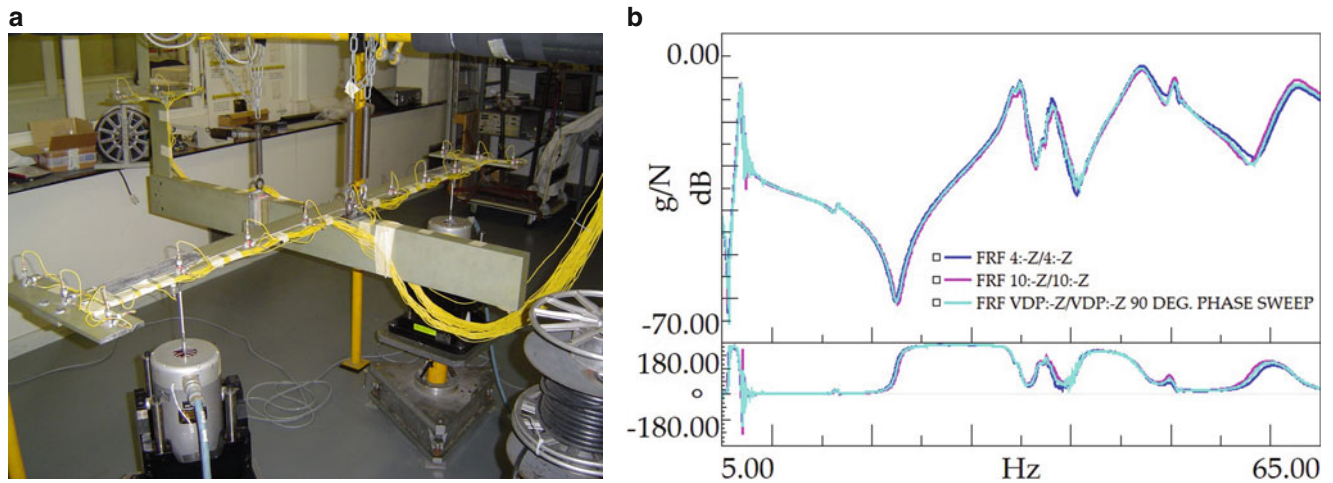


Fig. 23.7 Garteur airplane model. (a) Garteur model experimental setup. (b) Actual and virtual driving points FRFs

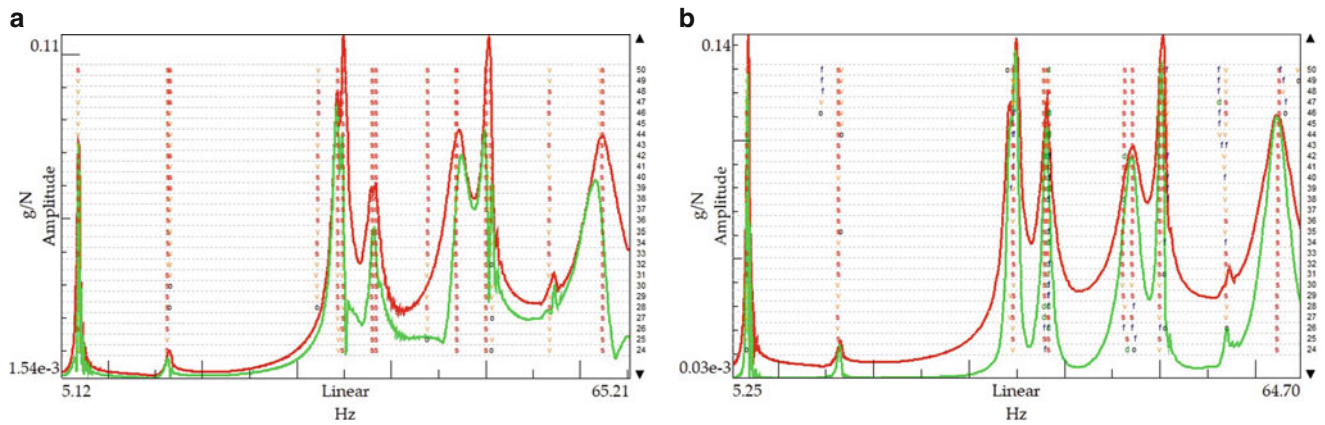


Fig. 23.8 Garteur airplane model Polymax diagrams. (a) VDP method: 90° phase lag sweep. (b) MIMO conventional method measured through 21 tri-axial accelerometers distributed all over the structure. The measurements data here analyzed have been acquired performing a logarithmic sine sweep at 1 oct/min from 5 to 65 Hz. Three sweeps have been applied for each test: a symmetric sweep, an antisymmetric one and a third sweep during which the relative phase between the inputs has been set equal to 90°. The application of the VDP method to data acquired during this third run allowed to achieve a final complete mode set, leading to very important considerations for what concerns the usefulness of the new technique.

Figure 23.7b illustrates the virtual driving point FRF obtained from the 90° phase lag sweep compared to the actual driving points FRFs: the VDP FRF coincides to the actual driving points FRFs detecting all the peaks, related to both symmetric and antisymmetric modes. This behavior introduces a very important advantage brought by the VDP method: the application of the method to a sweep with a 90° relative phase between the inputs allows to obtain, from a single run, all the natural frequencies and modes of the system, canceling out the need of performing as many runs as shakers to determine the complete mode set of the aircraft.

From Fig. 23.8 it is then clear that all the columns of the MIMO stabilization diagram can be also found in the VDP stabilization diagram when the VDP method is applied to a 90° phase lag sweep, which is what was expected looking at the FRFs shapes. Therefore, the complete mode set is directly extracted from the 90° phase lag sweep. Table 23.3 compares the mentioned mode set and the conventional MIMO mode set, pointing out the high correlation between the two results.

Table 23.3 Garteur airplane model mode sets

	Mode type	MIMO set		90° Phase lag set	
		Frequency (Hz)	Damping (%)	Frequency (Hz)	Damping (%)
1	S	6,830	1.70	6,824	0.54
2	A	16,388	1.18	16,366	1.64
3	A	34,623	1.28	34,342	1.13
4	S	37,896	1.26	38,013	1.27
5	A	38,297	1.50	38,468	0.96
6	S	47,117	2.23	46,842	2.49
7	A	49,995	0.77	50,029	0.83
8	S	56,827	0.37	56,766	0.45
9	A	62,168	3.22	62,330	3.11

S symmetric, A antisymmetric



Fig. 23.9 eFusion Magnus electric aircraft

23.4.4 eFusion Magnus Aircraft: Non-linearities

The eFusion aircraft, shown in Fig. 23.9, is an electric airplane designed and built in Hungary by Magnus aircraft and which electric motor is provided by Siemens. During the experimental campaign aimed at characterizing its performance and structural dynamics, the system has been excited through two shakers placed at intermediate wing points and its responses have been measured through 58 mono-axial and 11 tri-axial accelerometers placed all over the structure. Data have been acquired applying a logarithmic sine sweep excitation at 0.6 oct/min in the frequency band between 7 and 50 Hz. This validation case has been useful in order to investigate how the VDP method behaves with respect to non-linearities.

Table 23.4 illustrates the identified VDP mode set and compares it to the one obtained by the MIMO conventional method. It is clear that the two mode sets are strongly comparable.

The eFusion aircraft is characterized by a strong non-linearity around 20 Hz (approximately in between 19 and 22 Hz). Indeed, analyzing how both the actual driving points FRFs shapes change when changing the force level, it is possible to notice, as Fig. 23.10a shows, a visible shift in frequency of the peak around 20 Hz. In particular, when the forces level increases, the natural frequency decreases.

Table 23.4 eFusion aircraft mode sets

	Mode type	MIMO set		VDP reconstructed set	
		Frequency (Hz)	Damping (%)	Frequency (Hz)	Damping (%)
1	S	10,734	1.94	10,694	2.05
2	A	15,430	1.63	15,443	2.28
3	S	16,290	3.52	16,346	3.68
4	A	18,333	2.14	18,159	2.29
5	A	20,236	2.04	20,252	2.09
6	A	23,678	1.43	23,583	2.17
7	A	27,408	2.93	27,757	4.07
8	A	30,918	2.82	30,455	2.32
9	A	36,036	2.65	35,874	2.52
10	S	38,505	0.47	38,459	1.25

S symmetric, A antisymmetric

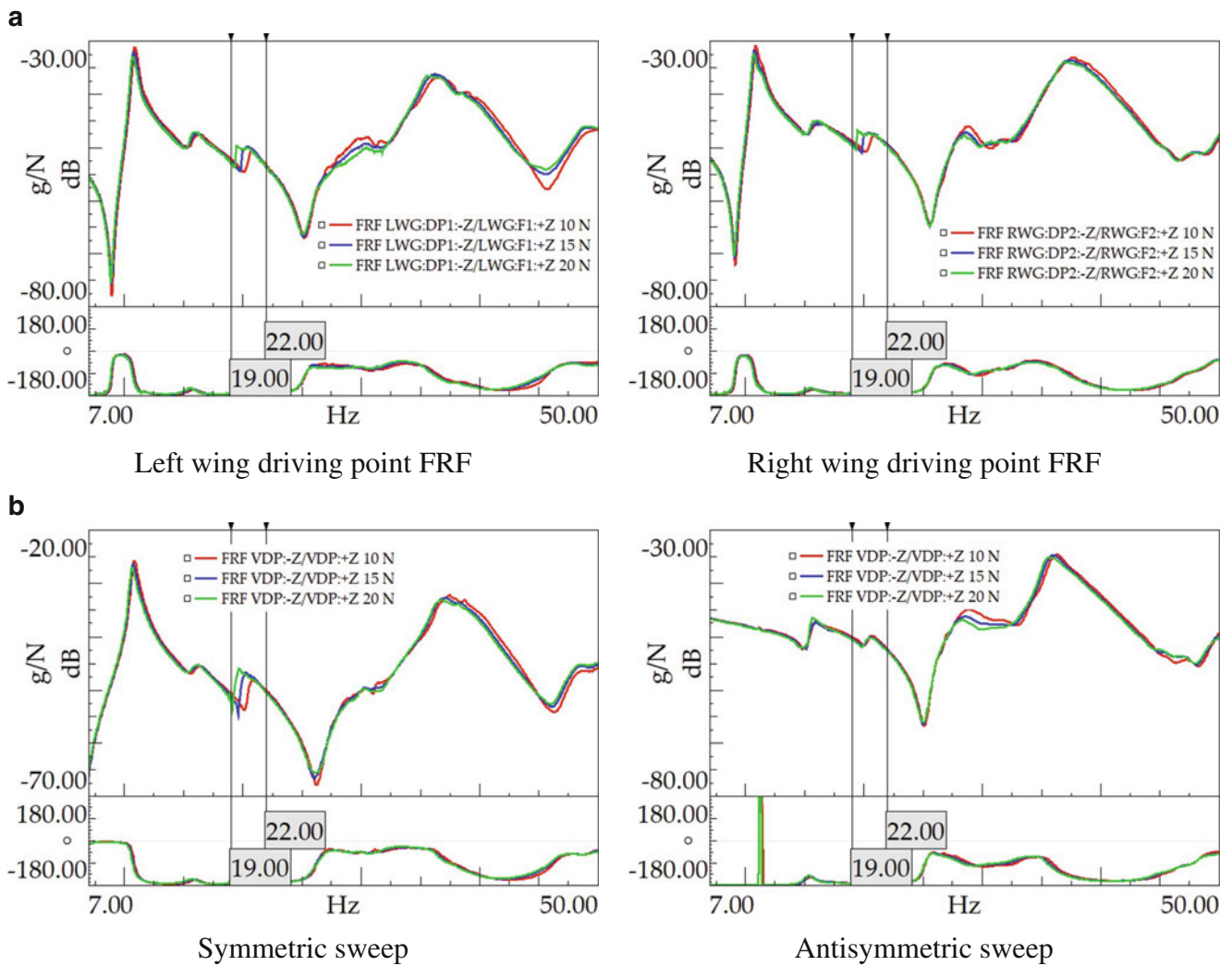


Fig. 23.10 Driving points FRFs at different force levels. (a) Actual driving points FRFs. (b) Virtual driving points FRFs

Figure 23.10b shows instead, the virtual driving points FRFs obtained by the application of the VDP method to the symmetric and antisymmetric performed sweeps. Here it is possible to recognize the presence of the non-linearity only in the symmetric VDP FRF, since the one extracted by the antisymmetric sweep does not show any difference around 20 Hz when the forces level varies. The mode detected around 20 Hz (mode 5 of both the VDP and MIMO mode sets) has a clear antisymmetric nature, as pointed out in Table 23.4, so it is possible to state that, while mode 5 of the MIMO set is influenced by the symmetric non-linearity since both the driving points FRFs show it, mode 5 belonging to the VDP set is not affected by it since it is extracted from the VDP mode set obtained by applying the method to the antisymmetric sweep, whose VDP FRF does not show any non-linear effect around 20 Hz. In conclusion, the VDP method allows to isolate the effect of the non-linearities that belong to one run, so they do not disperse and influence the overall result.

23.5 Conclusions

The work addresses the development and validation of the Virtual Driving Point method, a new data processing technique for aircrafts Ground Vibration Testing. The proposed approach has been derived by a mathematical formulation which demonstrates that the new method is able to compute the system's FRFs separating data measured during the single runs, i.e. the single sweeps during which data are acquired to be then used together in the H1 computation when adopting the conventional method.

The method has been applied to several systems in order to validate it and each data set has led to different interesting results. Its first application to a three DOFs discrete system allowed to understand its working principle and to define the procedure to adopt in order to obtain the desired results in terms of modal parameters. The Virtual Driving Point method detects symmetric and antisymmetric modes of the system depending on the relative phase between the inputs adopted during the analyzed sweep. The final mode set of the system in the frequency band of interest can be reconstructed putting together the modes obtained from the analysis of the different runs. Applying the new method to a data set concerning an airplane mockup, it has been possible to point out the advantages that it gives in terms of clearness of the stabilization diagrams, which makes experimental modal analysis easier and allows to get clearer mode shapes. Afterwards, the Garteur data set allowed to prove that the Virtual Driving Point method is also able to reduce the needed number of sweeps to perform in order to obtain the complete mode set of the system: if a two points excitation is adopted, a single sweep with a 90° relative phase between the two inputs is able to detect all the modes if processed through the VDP method. The method has been also applied to a data set concerning a real aircraft, the eFusion electric aircraft, which has been useful to study the behavior of the VDP method with respect to non-linearities: since it separates the peaks in the FRFs, the non-linear effects belonging to one run do not influence the overall result.

In conclusion, the Virtual Driving Point method cancels out the necessity of performing as many sweeps as shakers in order to compute the system's FRFs. Each single sweep is independently analyzed, leading to different modes, whose symmetric or antisymmetric nature depends on the relative phase between inputs that has been adopted during that run (mainly 0° and 180°). This procedure allows to perform an easier modal analysis, obtaining reliable results in terms of modal parameters and, in particular, clearer mode shapes. This working principle also leads to advantages related to the system's non-linearities and gives, in some cases, the possibility to reduce tests time duration.

References

1. Giclais, S., Lubrina, P., Stéphan, C., Böswald, M., Govers, Y., Ufer, J., Botargues, N.: New excitation signals for aircraft ground vibration testing. In: Proceedings "IFASD 2011" (2011)
2. Govers, Y., Böswald, M., Lubrina, P., Giclais, S., Stephan, C., Botargues, N.: AIRBUS A350XWB ground vibration testing: efficient techniques for customer oriented on-site modal identification. In: Proceedings of the International Conference on Noise and Vibration Engineering ISMA2014, pp. 2495–2507 (2014)
3. Orlando, S., Peeters, B., Coppotelli, G.: Improved FRF estimators for MIMO sine sweep data. In: Proceedings of the ISMA 2008 International Conference on Noise and Vibration Engineering, pp. 229–241 (2008)
4. Füllekrug, U., Böswald, M., Göge, D., Govers, Y.: Measurement of FRFs and modal identification in case of correlated multi-point excitation. *Shock Vib.* **15**(3, 4), 435–445 (2008)
5. Napolitano, K., Linehan, D.: Multiple sine sweep excitation for ground vibration tests. In: IMAC XXVII, Orlando, FL (2009)
6. Heylen, W., Sas, P.: Modal analysis theory and testing. Katholieke Universteit Leuven, Departement Werktuigkunde (2006)
7. Peeters, B., Van der Auweraer, H., Guillaume, P., Leuridan, J.: The polymax frequency-domain method: a new standard for modal parameter estimation? *Shock Vib.* **11**(3, 4), 395–409 (2004)



Chapter 24

Structural Health Monitoring with Self-Organizing Maps and Artificial Neural Networks

Onur Avci, Osama Abdeljaber, Serkan Kiranyaz, and Daniel Inman

Abstract The use of self-organizing maps and artificial neural networks for structural health monitoring is presented in this paper. The authors recently developed a nonparametric structural damage detection algorithm for extracting damage indices from the ambient vibration response of a structure. The algorithm is based on self-organizing maps with a multilayer feedforward pattern recognition neural network. After the training of the self-organizing maps, the algorithm was tested analytically under various damage scenarios based on stiffness reduction of beam members and boundary condition changes of a grid structure. The results indicated that proposed algorithm can successfully locate and quantify damage on the structure.

Keywords Structural health monitoring · Self-organizing maps · Artificial neural networks · Structural damage detection · Damage localization

Notations

C	The scale factor used to scale the damage indices
DI^i	The damage index corresponding to the location of i^{th} accelerometer
k	The total number of accelerometers
$l \times l$	Dimension of a square self-organizing map
M^i	Matrix to store the normalized vectors corresponding to the i^{th} accelerometer
n	The number of time steps recorded
S^i	The acceleration signal measured by the i^{th} accelerometer
SOM^i	Self-organizing map trained to cluster the vectors in the matrix M^i
T_m^i	The measured topology map at the i^{th} accelerometer
T_u^i	The topology map for the undamaged structure corresponding to i^{th} accelerometer
TN_m^i	The normalized measured topology map at the i^{th} accelerometer
TN_u^i	The normalized topology map for the undamaged structure corresponding to i^{th} accelerometer
V_t^i	A vector that stores the acceleration measured by the i^{th} accelerometer at the current time step t along with measurements at d time steps behind
VN_t^i	The resulting vector after normalizing V_t^i
w_i	The random weight vector assigned to the i^{th} neuron in a self-organizing map

O. Avci (✉) · O. Abdeljaber
Department of Civil Engineering, Qatar University, Doha, Qatar
e-mail: oavci@vt.edu

S. Kiranyaz
Department of Electrical Engineering, Qatar University, Doha, Qatar

D. Inman
Department of Aerospace Engineering, University of Michigan, Ann Arbor, MI, USA

24.1 Introduction

Monitoring of engineering structures has always been an interest to facility owners, engineers and researchers. Automated monitoring of response of structures evolved into Structural Health Monitoring (SHM) in time and condition evaluation has become more systematic utilizing different methods [1, 2]. Structural health monitoring (SHM) is being used for different types of structures in various engineering disciplines [3–5] all over the world. Detecting and locating structural damage has been an interdisciplinary area of research in SHM applications [6–8]. While vibration response of structures is predominantly used in modal testing to gain information on the dynamic characteristics of structures [9–17], it is also used for detecting and localizing structural damage in SHM applications. In vibration-based damage detection, parametric methods use sensor measurements to capture changes in dynamic characteristics of a structure [18–20]; while non-parametric techniques utilize statistical means for structural damage evaluation [21–23]. Artificial neural networks (ANNs) are extensively used in structural damage detection studies [24]. Self-organizing maps (SOMs) are a type of unsupervised neural networks utilized for forming a 2D representation of high dimensional data. Work by Tibaduiza et al. [25] is an example study using SOMs for structural damage detection. The study presented in this paper is one of the very few examples on the use of SOMs and ANNs for global structural damage detection. A non-parametric vibration-based damage detection algorithm is developed and SOMs and ANNs are used to generate useful damage indices from ambient vibration response of the structure. The efficacy of the algorithm is validated analytically with FE simulations of a grid structure under two damage scenarios (modification of beams stiffness and changes on boundary conditions).

SOMs are a type of ANNs which can be trained in an unsupervised way. SOM training is simply based on internal properties between the inputs and does not require input-output samples [26]. This training characteristic is an advantage of SOMs over multilayer feedforward neural networks. In SOMs, a network of neurons is typically arranged in a two dimensional rectangular, hexagonal, or irregular grid form. In the grid, each neuron n_i is assigned by a random weight vector $\mathbf{w}_i = [w_{i1} \ w_{i2} \ \dots \ w_{ik}]$, where k is the number of inputs in each data sample. The \mathbf{w}_i 's are adjusted using learning algorithms. For SOM training, batch learning algorithm is predominantly utilized. Further information on SOM operation details can be found in [21, 22, 24].

24.2 The Damage Detection Algorithm

In this work, the structural damage detection algorithm runs based on SOMs processing the ambient condition acceleration data in the time domain to form a topology map for each joint. The structural damage introduced to the structure results in a variation in the structural signature of the system, which is utilized for damage assessment.

24.2.1 SOM Training

- The vibration response of the undamaged structure is recorded under the ambient conditions for n time ($S^{i=1}, S^{i=2}, \dots, S^{i=k}$).
- At each time step t , for each signal S^i , the acceleration value at this time step as well as the values at d time steps behind ($S_{t-d}^i, S_{t-d+1}^i, \dots, S_{t-1}^i$) are stored in a vector $\mathbf{V}_t^i = [S_{t-d}^i \ S_{t-d+1}^i \ \dots \ S_{t-1}^i \ S_t^i]$. A total of n vectors are stored for each acceleration signal.
- The vectors generated in step b are normalized:

$$\mathbf{VN}_t^i = \frac{\mathbf{V}_t^i}{\max |\mathbf{V}_t^i|} \quad (24.1)$$

- The normalized vectors corresponding to each accelerometer signal S^i are arranged in a matrix $\mathbf{M}^i = [\mathbf{VN}_{t=1}^i \ \mathbf{VN}_{t=2}^i \ \dots \ \mathbf{VN}_{t=n}^i]^t$. The total number of matrices created in this step is the total number of accelerometers k .
- \mathbf{SOM}^i is trained to cluster the normalized vectors in each matrix \mathbf{M}^i corresponding to the acceleration signal S^i into a two dimensional topology map \mathbf{T}_u^i with a dimension of $(l \times l)$. As a result, k number of SOMs are trained corresponding to the total number of accelerometers, and a total of k topology maps are generated.

- (f) The trained SOMs are saved to be utilized for damage assessment. The topology maps for the undamaged condition created by each SOM ($T_u^{i=1}, T_u^{i=2}, \dots, T_u^{i=k}$) are normalized.

$$TN_u^i = \frac{T_u^i}{n} \quad (24.2)$$

- (g) The normalized topology maps (NTMs) for the undamaged case ($TN_u^{i=1}, TN_u^{i=2}, \dots, TN_u^{i=k}$) are saved to be utilized for damage assessment.

24.2.2 Structural Damage Assessment

For structural damage detection, SOMs and the NTMs for the undamaged case are used to evaluate the condition of the monitored structure based on the structural signature. In other words, the comparison between the measured topology maps and the generated topology maps for the undamaged case will reveal the damage status.

- (a) The ambient acceleration response of the structure is measured for n time steps ($S^i=1, S^i=2, \dots, S^i=k$).
 (b) The steps b, c, and d described above are repeated to form the matrices ($M^i=1, M^i=2, \dots, M^i=k$)
 (c) For each signal S^i , the corresponding SOM^i trained according to the undamaged response is utilized to create a topology map T_m^i .
 (d) The measured topology maps for the current case ($T_m^{i=1}, T_m^{i=2}, \dots, T_m^{i=k}$) are normalized

$$TN_m^i = \frac{T_m^i}{n} \quad (24.3)$$

- (e) Each measured normalized topology map TN_m^i is compared to the corresponding undamaged normalized topology map TN_u^i . The damage indices at each node are computed ($DI_{i=1}, DI_{i=2}, \dots, DI_{i=k}$) and scaled by a constant C .

$$DI^i = C \times \text{rms} (TN_u^i - TN_m^i) \quad (24.4)$$

- (f) The damage index magnitudes provide information on the difference between the undamaged and damaged structural condition. The distribution of the damage index magnitudes helps to determine the location and severity of damage.

24.3 The Grid Structure

The structure focused in this work is the FE model of a grid structure studied by Gul and Catbas [27]. The structure is made up of six columns and two girders and seven cross beams (Fig. 24.1) modeled in Abaqus 6.12-1 software [28]. For the simulations of this study, 21 accelerometers were assumed to be present at the corresponding nodes of the FE model structure (Fig. 24.1). In the FE model, the vibrations environment for the ambient condition was modeled as an independent stationary white noise signal applied on the grid structure in the gravity direction, as suggested in a similar study [29]. For

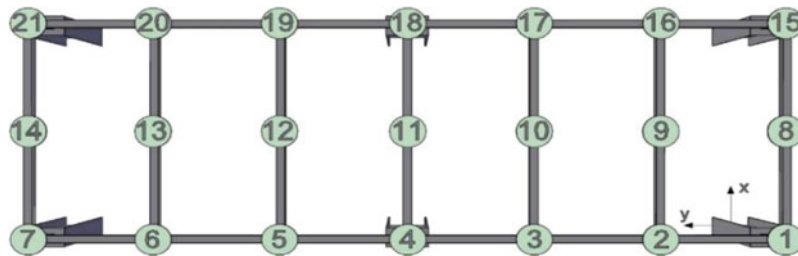


Fig. 24.1 Node numbers on the FE model

the ambient vibrations response simulations, a linear static analysis is run to achieve the deflected shape under self-weight of the structure. Then, a frequency analysis is run to determine the natural frequencies and the mode shapes. Following this, a dynamic analysis is run to predict the acceleration response of the structure at all nodes at 0.001 s time increments. For each node, SOMs were trained and resulting NTMs of the undamaged condition were recorded for damage assessment stage. Data processing and training were conducted in Matlab [30].

24.4 Damage Scenario 1: 50% Local Stiffness Reduction on Cross Beams

The performance of the algorithm is analytically tested with two sets of structural damage scenarios through a FE model. For the first scenario, the stiffness reduction of cross-beams is studied. The FE model of the grid structure along with the SOMs and NTMs for the undamaged state (formed in the training step) is used. The efficacy of the algorithm due to 50% local stiffness reduction is studied for five different cases (Fig. 24.2).

For each damage case, the FE model is modified by reducing the stiffness per Fig. 24.2 and the measured topology maps are compared to the undamaged maps per Eq. (24.4) to generate the damage indices. In the FE model, a random white noise signal (per Matlab function “randn”) is used for ambient load excitations. The average of the damage indices are shown in Table 24.1; and the distribution of damage indices are shown in Fig. 24.3. Based on Table 24.1 and Fig. 24.3, it is observed that the damage index magnitudes are clearly more pronounced at the damaged member locations. This means the nonparametric damage detection algorithm with trained SOMs is very efficient for locating and quantifying structural damage for 50% local stiffness reduction.

24.5 Damage Scenario 2: Rigidity Changes in Boundary Conditions

For the second damage scenario, four cases of boundary condition rigidity changes are considered at the structural connections shown in Fig. 24.4. The average of the damage indices are shown in Table 24.2; and the distribution of damage indices are shown in Fig. 24.5.

It is observed that neither the damage index values of Table 24.2 nor the distributions in Fig. 24.5 are consistent with the corresponding damaged node. Unlike the 50% local stiffness reduction damage scenario, the algorithm is not successful for detecting rigidity changes on boundary conditions. For that purpose, the authors improved the damage detection algorithm with a pattern recognition neural network.

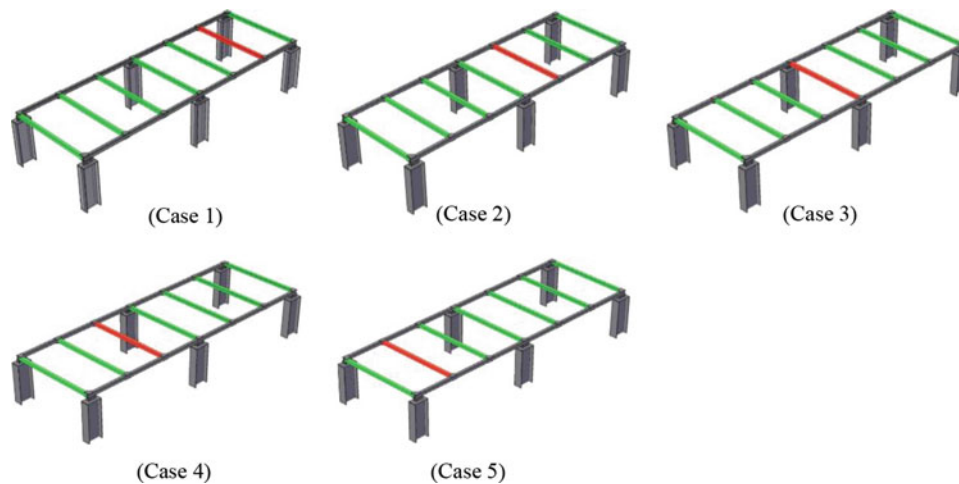


Fig. 24.2 50% local stiffness reduction on red members

Table 24.1 Damage index values per 50% local stiffness reduction

Structural damage case	Damage index (DI)																				
	1	2	3	4	5	6	7	8	9	10	11	12	13	14	15	16	17	18	19	20	21
1	0.96	0.85	0.68	0.56	0.65	0.66	0.84	1.61	3.88	1.00	0.74	0.95	0.68	1.23	0.97	0.79	0.74	0.60	0.72	0.65	0.84
2	0.80	0.56	0.82	0.64	0.81	0.73	0.54	1.50	1.03	4.03	0.83	0.84	0.78	0.59	0.77	0.50	0.88	0.66	0.87	0.71	0.58
3	0.59	0.57	0.57	0.61	0.58	0.59	0.61	0.63	0.78	0.72	2.19	0.71	0.79	0.63	0.61	0.63	0.58	0.60	0.65	0.58	0.60
4	0.58	0.65	0.83	0.65	0.88	0.56	0.78	0.62	0.75	0.81	0.83	4.08	1.03	1.46	0.57	0.72	0.78	0.65	0.89	0.62	0.85
5	0.86	0.59	0.68	0.56	0.70	0.86	0.98	1.21	0.71	0.95	0.74	0.99	3.81	1.56	0.81	0.66	0.67	0.59	0.68	0.91	0.93

Bold values indicate that the DI value successfully corresponds to the damaged member location

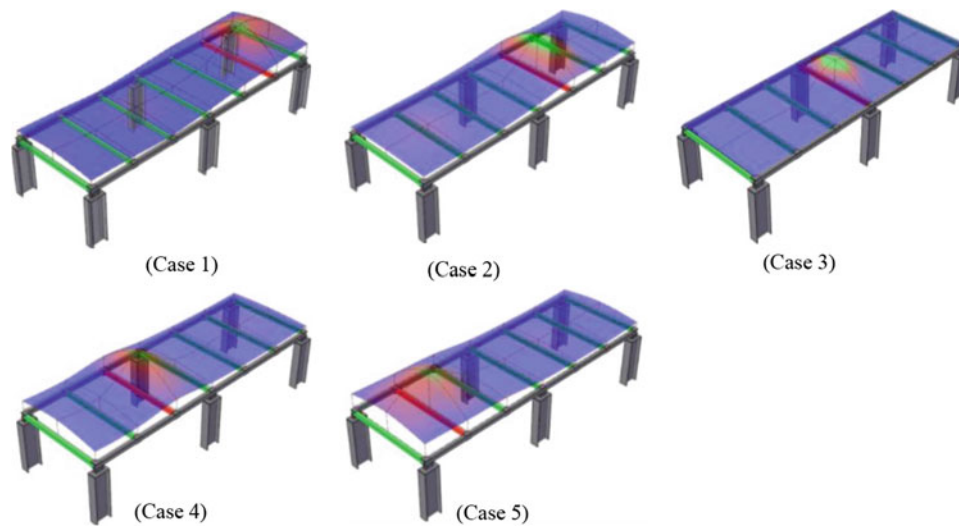


Fig. 24.3 Damage index distributions per 50% local stiffness reduction

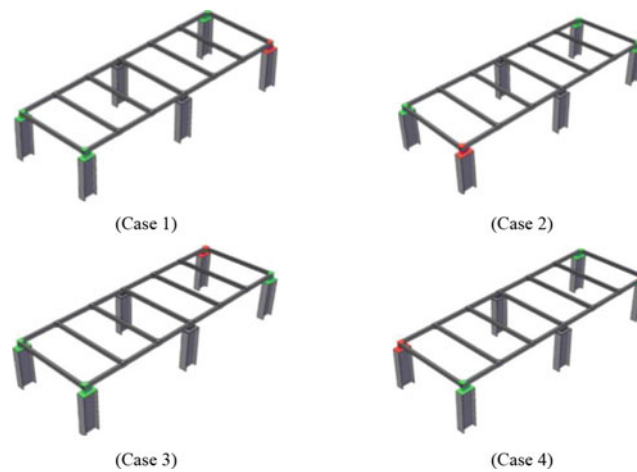


Fig. 24.4 Rigidity changes in boundary conditions (red connection represents the restrained support)

24.5.1 *Introducing a Pattern Recognition Neural Network*

Based on Fig. 24.4, the measured damage index pattern is for five classes (one undamaged and four damaged cases) and the neural network needs to be trained to classify the classes. For that purpose a multi-layer feedforward neural network is used with sigmoid hidden and output neurons. Scaled conjugate gradient backpropagation algorithm was used to train the neural network. The output layer is made up of five neurons for the five structural classes; and the number of neurons in the hidden layer was chosen as 10 using trial and error. The pattern recognition neural network is shown in Fig. 24.6.

After the training, the pattern recognition neural network was tested with the data patterns to demonstrate its capability to recognize damage cases according to the measured damage indices. Table 24.3 presents a comparison between the actual structural cases and the neural network outputs. It is observed that the pattern recognition neural network successfully recognized the structural condition for the entire test samples which means that the improvement have enabled the damage detection algorithm to successfully detect and locate the damage due to rigidity changes in boundary conditions.

Table 24.2 Damage index values per rigidity changes on boundary conditions

Damage case	Damage index (DI)																					
	1	2	3	4	5	6	7	8	9	10	11	12	13	14	15	16	17	18	19	20	21	Total
1	2.47	2.70	4.35	2.26	3.30	1.09	1.74	2.60	4.42	1.90	0.87	3.16	3.92	1.52	5.71	4.35	4.77	4.23	4.93	5.19	7.09	72.54
2	1.81	1.08	3.29	2.27	4.41	2.66	2.44	1.48	3.94	3.15	0.87	1.93	4.37	2.59	6.99	5.16	4.86	4.22	4.83	4.32	5.80	72.48
3	6.15	4.36	4.88	4.05	5.19	5.09	7.50	2.60	4.41	1.90	0.87	3.17	3.91	1.51	2.42	2.77	4.30	2.29	3.23	1.10	1.83	73.54
4	7.54	5.20	5.00	4.04	5.09	4.31	6.09	1.49	3.94	3.15	0.87	1.92	4.37	2.59	1.72	1.13	3.22	2.28	4.28	2.67	2.45	73.35

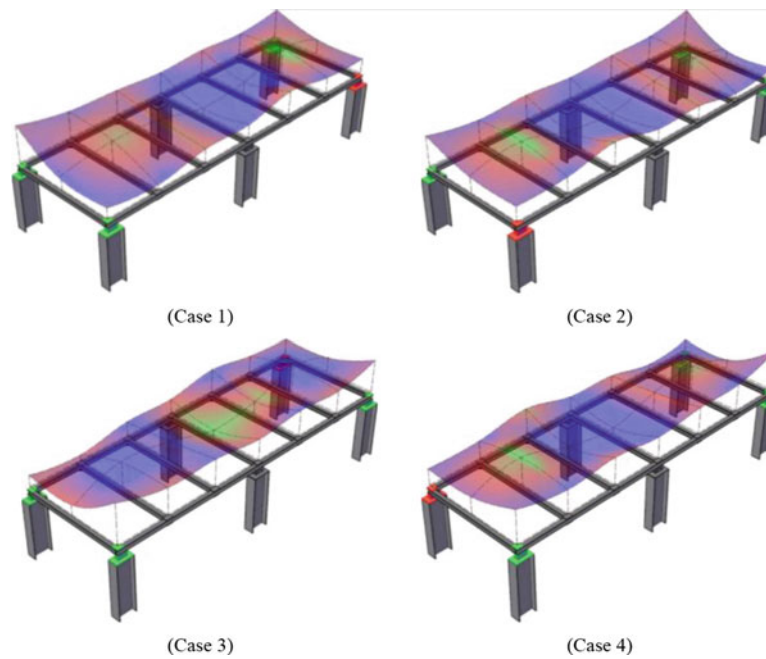


Fig. 24.5 Damage index distributions per rigidity changes on boundary conditions

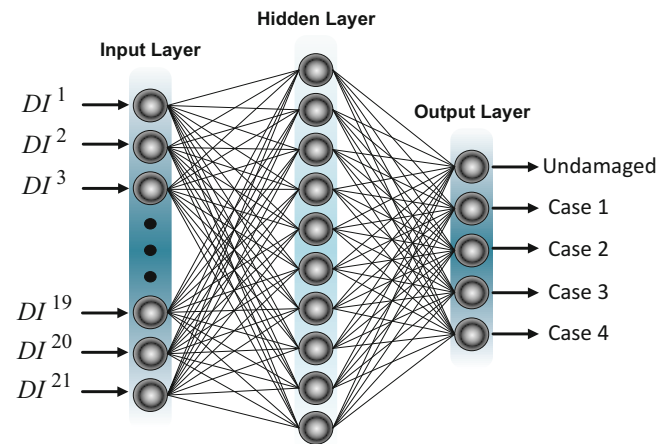


Fig. 24.6 The pattern recognition neural network

24.6 Conclusions

The algorithm presented in this paper is a nonparametric damage detection algorithm deploying self-organizing maps to detect and locate structural damage by analyzing ambient condition accelerations of a grid structure. The algorithm is analytically tested with two sets of structural damage scenarios through a FE model. For member stiffness reduction damage scenario, the damage index magnitudes are clearly more pronounced at the damaged member locations, meaning that the nonparametric damage detection algorithm with trained SOMs is successful at locating and quantifying structural damage. For boundary condition damage scenario at the structural connections, the damage index magnitudes show that the structural damage is detected; however, the distribution of the index values throughout the laboratory structure indicates that the algorithm with trained SOMs is unable to localize the damage. For that purpose, a pattern recognition neural network is trained to identify the pattern of the damage index magnitudes. The ANN improvement on the SOM algorithm was successful at identifying the location of the damaged connection for all cases of the damage scenario.

Table 24.3 Pattern recognition of damage cases due to rigidity changes in boundary conditions using neural network

Structural damage case	Damage index (DI)																				Actual case				Neural network output			
	1	2	3	4	5	6	7	8	9	10	11	12	13	14	15	16	17	18	19	20	21	Undamaged	Case 1	Case 2	Case 3	Case 4		
	1	7.37	5.11	4.89	3.90	4.98	4.20	5.97	1.54	3.98	3.22	0.89	1.98	4.42	2.64	1.77	1.13	3.23	2.29	4.27	2.64	2.43	Case 4	0.00	0.00	0.00	1.00	1.00
2	1.86	1.10	3.22	2.29	4.51	2.75	2.53	1.46	3.87	3.04	0.90	1.85	4.30	2.57	7.10	5.20	4.92	4.37	4.97	4.49	5.98	Case 2	0.00	0.00	1.00	0.00	0.00	
3	1.85	1.10	3.35	2.30	4.44	2.64	2.46	1.49	3.93	3.21	0.90	1.92	4.34	2.56	6.98	5.20	4.91	4.22	4.82	4.34	5.76	Case 2	0.00	0.00	1.00	0.00	0.00	
4	7.50	5.13	4.92	3.99	5.08	4.27	6.06	1.50	3.99	3.17	0.87	1.97	4.43	2.65	1.65	1.11	3.19	2.28	4.21	2.59	2.38	Case 4	0.00	0.00	0.00	0.00	1.00	
5	1.86	1.09	3.29	2.25	4.41	2.67	2.45	1.54	3.98	3.22	0.89	1.98	4.42	2.64	6.86	5.05	4.77	4.11	4.73	4.20	5.66	Case 2	0.00	0.00	1.00	0.00	0.00	
6	1.73	1.08	3.25	2.24	4.36	2.64	2.39	1.50	3.99	3.17	0.88	1.97	4.43	2.66	6.94	5.09	4.80	4.19	4.80	4.29	5.80	Case 2	0.00	0.00	1.00	0.00	0.00	
7	0.28	0.26	0.23	0.26	0.23	0.27	0.28	0.30	0.46	0.36	0.26	0.39	0.46	0.30	0.25	0.28	0.23	0.29	0.30	0.25	0.30	Undamaged	1.00	0.00	0.00	0.00	0.01	
8	6.12	4.32	4.84	3.99	5.11	5.05	7.46	2.67	4.46	1.95	0.88	3.19	3.97	1.53	2.37	2.71	4.26	2.28	3.22	1.08	1.75	Case 3	0.00	0.00	0.00	0.00	0.00	
9	7.68	5.23	5.12	4.23	5.25	4.46	6.24	1.46	3.87	3.04	0.90	1.85	4.30	2.57	1.76	1.15	3.10	2.32	4.40	2.81	2.55	Case 4	0.00	0.00	0.00	0.00	1.00	
10	6.27	4.44	4.97	4.16	5.23	5.17	7.60	2.60	4.40	1.89	0.87	3.11	3.91	1.46	2.42	2.77	4.27	2.28	3.30	1.13	1.81	Case 3	0.00	0.00	0.00	0.00	0.00	
11	2.46	2.68	4.31	2.25	3.30	1.11	1.81	2.64	4.47	1.97	0.89	3.24	3.95	1.58	5.57	4.24	4.66	4.11	4.84	5.09	6.96	Case 1	0.00	1.00	0.00	0.00	0.00	
12	1.77	1.10	3.30	2.25	4.31	2.60	2.37	1.51	4.05	3.22	0.89	1.99	4.46	2.68	6.84	5.04	4.75	4.09	4.65	4.12	5.63	Case 2	0.00	0.00	1.00	0.00	0.00	
13	6.15	4.38	4.85	4.05	5.24	5.11	7.52	2.55	4.39	1.89	0.90	3.17	3.87	1.53	2.51	2.88	4.35	2.36	3.18	1.05	1.85	Case 3	0.00	0.00	0.00	0.00	0.00	
14	6.06	4.34	4.85	3.97	5.20	5.05	7.47	2.60	4.48	1.97	0.89	3.24	3.94	1.51	2.38	2.74	4.24	2.30	3.20	1.07	1.80	Case 3	0.00	0.00	0.00	0.00	0.00	
15	1.81	1.11	3.21	2.28	4.47	2.75	2.50	1.48	3.92	3.09	0.91	1.89	4.39	2.62	6.98	5.11	4.82	4.27	4.91	4.42	5.92	Case 2	0.00	0.00	1.00	0.00	0.00	
16	0.27	0.26	0.24	0.25	0.21	0.25	0.29	0.31	0.47	0.37	0.24	0.42	0.47	0.28	0.24	0.28	0.23	0.29	0.30	0.26	0.30	Undamaged	1.00	0.00	0.00	0.00	0.01	
17	7.48	5.15	5.01	3.97	5.01	4.26	6.06	1.50	3.95	3.25	0.89	1.97	4.41	2.62	1.68	1.12	3.17	2.30	4.20	2.64	2.45	Case 4	0.00	0.00	0.00	0.00	1.00	
18	6.18	4.41	4.94	4.11	5.37	5.21	7.62	2.52	4.35	1.88	0.88	3.17	3.88	1.50	2.42	2.77	4.37	2.29	3.33	1.16	1.90	Case 3	0.00	0.00	0.00	0.00	0.00	
19	2.40	2.71	4.26	2.31	3.27	1.06	1.74	2.60	4.48	1.97	0.89	3.24	3.94	1.52	5.61	4.36	4.70	4.14	4.92	5.16	7.02	Case 1	0.00	1.00	0.00	0.00	0.00	
20	0.10	0.06	0.04	0.11	0.05	0.07	0.09	0.10	0.22	0.18	0.08	0.20	0.23	0.10	0.08	0.12	0.07	0.10	0.12	0.07	0.11	Undamaged	1.00	0.00	0.00	0.00	0.03	

Bold values indicate that the neural network output successfully corresponds to the structural damage case

References

1. Beskhyroun, S., Wegner, L.D., Sparling, B.F.: New methodology for the application of vibration-based damage detection techniques. *Struct. Control. Health Monit.* (2011). <https://doi.org/10.1002/stc>
2. Raghavan, A., Cesnik, C.E.S.: Review of guided-wave structural health monitoring. *Shock Vib. Dig.* (2007). <https://doi.org/10.1177/0583102406075428>
3. Farrar, C., Sohn, H.: Pattern recognition for structural health monitoring. *Struct. Heal. Monit.* (2000)
4. Friswell, M.I., Adhikari, S.: Structural health monitoring using shaped sensors. *Mech. Syst. Signal Process.* (2010). <https://doi.org/10.1016/j.ymssp.2009.10.009>
5. Mansouri, M., Avci, O., Nounou, H., Nounou, M.: A comparative assessment of nonlinear state estimation methods for structural health monitoring. In: *Conf. Proc. Soc. Exp. Mech. Ser.* (2015). https://doi.org/10.1007/978-3-319-15224-0_5
6. Abdeljaber, O., Avci, O., Kiranyaz, S., Gabbouj, M., Inman, D.J.: Real-time vibration-based structural damage detection using one-dimensional convolutional neural networks. *J. Sound Vib.* **388**, 154–170 (2017). <https://doi.org/10.1016/j.jsv.2016.10.043>
7. Abdeljaber, O., Avci, O., Kiranyaz, M.S., Boashash, B., Sodano, H., Inman, D.J.: 1-D CNNs for structural damage detection: verification on a structural health monitoring benchmark data. *Neurocomputing.* (2017). <https://doi.org/10.1016/j.neucom.2017.09.069>
8. Do, N.T., Gul, M., Abdeljaber, O., Avci, O.: Novel framework for vibration serviceability assessment of stadium grandstands considering durations of vibrations. *J. Struct. Eng. (United States)*. **144**, (2018). [https://doi.org/10.1061/\(ASCE\)ST.1943-541X.0001941](https://doi.org/10.1061/(ASCE)ST.1943-541X.0001941)
9. Davis, B., Avci, O.: Simplified vibration response prediction for slender monumental stairs. In: *Struct. Congr. 2014—Proc. 2014 Struct. Congr.* (2014). <https://doi.org/10.1061/9780784413357.223>
10. Barrett, A.R., Avci, O., Setareh, M., Murray, T.M. Observations from vibration testing of in-situ structures. In: *Proc. Struct. Congr. Expo.* (2006). [https://doi.org/10.1061/40889\(201\)65](https://doi.org/10.1061/40889(201)65)
11. Bhargava, A., Isenberg, J., Feenstra, P.H., Al-Smadi, Y., Avci, O.: Vibrations assessment of a hospital floor for a magnetic resonance imaging unit (MRI) replacement. In: *Struct. Congr. 2013 Bridg. Your Passion with Your Prof.—Proc. 2013 Struct. Congr.* (2013)
12. Celik, O., Do, N.T., Abdeljaber, O., Gul, M., Avci, O., Catbas, F.N.: Recent issues on stadium monitoring and serviceability: a review. In: *Conf. Proc. Soc. Exp. Mech. Ser.* (2016). https://doi.org/10.1007/978-3-319-29763-7_41
13. Abdeljaber, O., Younis, A., Avci, O., Catbas, N., Gul, M., Celik, O., Zhang, H.: Dynamic testing of a laboratory stadium structure. In: *Geotech. Struct. Eng. Congr. 2016—Proc. Jt. Geotech. Struct. Eng. Congr. 2016.* (2016)
14. Avci, O.: Nonlinear damping in floor vibrations serviceability: Verification on a laboratory structure. In: *Conf. Proc. Soc. Exp. Mech. Ser.* (2017). https://doi.org/10.1007/978-3-319-54777-0_18
15. Younis, A., Avci, O., Hussein, M., Davis, B., Reynolds, P.: Dynamic forces induced by a single pedestrian: a literature review. *Appl. Mech. Rev.* **69**, (2017). <https://doi.org/10.1115/1.4036327>
16. Catbas, F.N., Celik, O., Avci, O., Abdeljaber, O., Gul, M., Do, N.T.: Sensing and monitoring for stadium structures: a review of recent advances and a forward look. *Front. Built Environ.* **3**, 38 (2017). <https://doi.org/10.3389/fbuil.2017.00038>
17. Avci, O.: Amplitude-dependent damping in vibration serviceability: Case of a laboratory footbridge. *J. Archit. Eng.* **22**, (2016). [https://doi.org/10.1061/\(ASCE\)AE.1943-5568.0000211](https://doi.org/10.1061/(ASCE)AE.1943-5568.0000211)
18. Mansouri, M., Avci, O., Nounou, H., Nounou, M.: Iterated square root unscented Kalman filter for nonlinear states and parameters estimation: three DOF damped system. *J. Civ. Struct. Heal. Monit.* **5**, (2015). <https://doi.org/10.1007/s13349-015-0134-7>
19. Chaabane, M., Ben Hamida, A., Mansouri, M., Nounou, H.N., Avci, O.: Damage detection using enhanced multivariate statistical process control technique. In: *2016 17th Int. Conf. Sci. Tech. Autom. Control Comput. Eng. STA 2016—Proc.* (2017). <https://doi.org/10.1109/STA.2016.7952052>
20. Avci, O., Abdeljaber, O., Kiranyaz, S., Hussein, M., Inman, D.J.: Wireless and real-time structural damage detection: a novel decentralized method for wireless sensor networks. *J. Sound Vib.* **424**, (2018). <https://doi.org/10.1016/j.jsv.2018.03.008>
21. Abdeljaber, O., Avci, O.: Nonparametric structural damage detection algorithm for ambient vibration response: Utilizing artificial neural networks and self-organizing maps. *J. Archit. Eng.* **22**, (2016). [https://doi.org/10.1061/\(ASCE\)AE.1943-5568.0000205](https://doi.org/10.1061/(ASCE)AE.1943-5568.0000205)
22. Avci, O., Abdeljaber, O.: Self-organizing maps for structural damage detection: a novel unsupervised vibration-based algorithm. *J. Perform. Constr. Facil.* **30**, (2016). [https://doi.org/10.1061/\(ASCE\)CF.1943-5509.0000801](https://doi.org/10.1061/(ASCE)CF.1943-5509.0000801)
23. Avci, O., Abdeljaber, O., Kiranyaz, S., Inman, D.: Structural damage detection in real time: implementation of 1D convolutional neural networks for SHM applications. In: Niezrecki, C. (ed.) *Struct. Heal. Monit. Damage Detect. Vol. 7 Proc. 35th IMAC, A Conf. Expo. Struct. Dyn. 2017*, pp. 49–54. Springer International Publishing, Cham (2017). https://doi.org/10.1007/978-3-319-54109-9_6.
24. Abdeljaber, O., Avci, O., Do, N.T., Gul, M., Celik, O., Necati Catbas, F.: Quantification of structural damage with self-organizing maps. In: *Conf. Proc. Soc. Exp. Mech. Ser.* (2016). https://doi.org/10.1007/978-3-319-29956-3_5.
25. Tibaduiza, D.A., Mujica, L.E., Rodellar, J.: Damage classification in structural health monitoring using principal component analysis and self-organizing maps. *Struct. Control. Health Monit.* (2012). <https://doi.org/10.1002/stc.1540>
26. Kohonen, T.: *Self-Organizing Maps*. Springer, New York (2001). <https://doi.org/10.1007/978-3-642-56927-2>
27. Gul, M., Catbas, F.N.: Ambient vibration data analysis for structural identification and global condition assessment. *J. Eng. Mech.* (2008). [https://doi.org/10.1061/\(ASCE\)0733-9399\(2008\)134:8\(650\)](https://doi.org/10.1061/(ASCE)0733-9399(2008)134:8(650)).
28. Dassault Systèmes Simulia, Fallis, A., Techniques, D.: ABAQUS documentation, Abaqus 6.12. (2013). <https://doi.org/10.1017/CBO9781107415324.004>
29. Dyke, S.J., Bernal, D., Beck, J., Ventura, C.: Experimental phase II of the structural health monitoring benchmark problem. In: *Proc. 16th ASCE Eng. Mech. Conf.* (2003)
30. The Mathworks Inc.: MATLAB—mathworks. (2016). Accessed 26-Oct-2016



Chapter 25

A Novel Technique to Extract the Modal Damping Properties of a Thin Blade

T. Mace, J. Taylor, and C. W. Schwingshackl

Abstract Extracting accurate material modal damping from a specimen can be very challenging due to the potential influence of the excitation and measurement system, and the required support of the specimen. This becomes particularly challenging if large amplitudes are required to determine nonlinear behavior, or large damping is present due to the material under investigation. An improved approach is proposed here to enable large amplitude, single harmonic, free decay damping extraction of a flat test specimen. It is based on a setup that uses the inertia of two large, free hanging end masses to enforce a pinned-pinned boundary condition with predetermined nodal locations, ensuring minimum effect of the support structure on the damping behavior. Excitation is achieved with the help of a removable electromagnetic shaker system that enables large amplitude single harmonic excitation, and smooth transition to a free, single harmonic decay. A Laser Doppler Vibrometer is used to measure the free decay, from which amplitude dependent damping can be obtained for individual modes via logarithmic decrement. Initial results of the approach show its great potential to provide reliable, amplitude dependent parameters with minimum impact of the test setup.

Keywords Material damping · Experimental dynamics · Flexural damping · Free-free beam · Mechanical properties · Tip-mass

25.1 Introduction

Damping is a collective term used to describe the various phenomena responsible for energy dissipation in a dynamic system, resulting in the decay of the amplitude of oscillation. Damping can be categorised into four main sources, namely: material damping, joint damping, component damping and transmission damping [1]. On a micromechanical level, material damping is caused by the relative motion of the material's constituent particles, which converts mechanical energy into heat via friction. Material damping, whilst often a relatively minor contributor to the overall damping of a system, can be of particular interest in lightly damped systems where energy dissipation in the material significantly drives the vibrational properties, or in composites, where material damping can increase to much higher levels. Measuring the material damping of a specimen is a challenging task due to 'extraneous' damping introduced externally, commonly from the excitation source and boundary conditions. Or the measurement system. For lightly damped specimens, air damping can also significantly increase the damping of the system. Cantilevered boundary conditions [2] inevitably introduce some degree of frictional damping at the clamping position of the specimen because any relative motion between the rigid clamp and moving specimen will experience frictional resistance. As such, 'free-free' boundary conditions are considered superior and can be achieved by suspending a test specimen through its nodal lines from a thin inextensible string. It is difficult, however, to accurately determine the location of the nodes and, in practice, suspend a specimen from these locations, resulting in some extraneous energy dissipation through the strings. Additionally, alterations to the setup are required if different modes are to be analyzed. Excitation techniques can also introduce damping into the system. Whilst transient hammer testing techniques provide a simple method of exciting a structure via a single impact, the results are not easily repeatable and obtaining an accurate damping estimation from the multimodal response can be difficult for lightly damped specimens with sharp FRF peaks [3]. Instead, it is advantageous to excite a single mode of interest individually with shaker, but this currently limits the damping extraction to frequency based techniques, which can be very tedious for nonlinear dynamic systems. In addition

T. Mace (✉) · C. W. Schwingshackl
Department of Mechanical Engineering, Imperial College London, London, UK
e-mail: tgm18@ic.ac.uk

J. Taylor
Composites and R&T, Rolls-Royce plc., Derby, UK

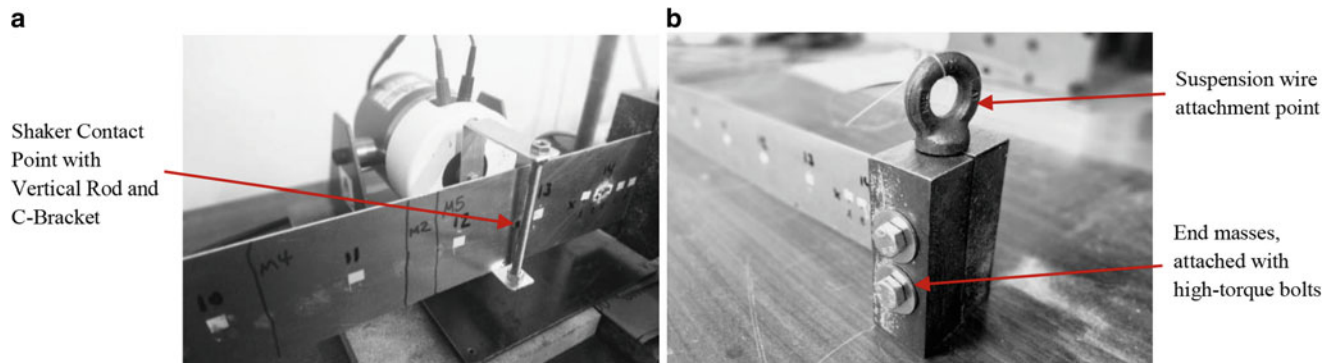


Fig. 25.1 Novel setup, utilizing (a) contacting surface for the excitation and (b) tip masses to enforce a quasi-pinned boundary condition

the nonlinearity in the system can lead to an interaction with the shaker, thereby altering the observed damping behaviour. This study proposes an improved damping extraction technique, with the goal of measuring small levels of damping whilst minimizing the damping introduced from extraneous sources.

25.2 A Novel Method to Extract Damping

The specimen support technique adopted for this study was originally proposed by Bishop et al. [4], and involves the attachment of a mass at both ends of a beam-like specimen. This alters the modeshape of the specimen in the ‘free-free’ configuration, moving the nodes of every mode towards the tips of the specimen. This improves the predictability of the node location, allowing the suspension of the specimen from locations where the damping contribution from the string suspension can be minimized.

An analytical beam model was developed to determine the minimum tip-mass to beam-mass ratio, ‘ m_r ’, considering an Euler-Bernoulli beam with both one-dimensional lumped masses and inertias at both ends. This revealed that a m_r of 10 was required in order to enforce an approximate ‘quasi-pinned’ condition. The specimen used in this study was an aluminium plate (764 mm × 58 mm × 1 mm) requiring tip masses of 1.22 kg at either end. The location of the clamp at the nodal line of the system, the coupled rotation with the beam mode shape, and large bolt torques at the clamps thereby ensured minimal impact of the added frictional interface.

In order to enable a single harmonic, free decay measurement from initial large amplitudes, a new excitation approach was needed that allowed large amplitude levels via a rigid connection, but also enabled free decay for the damping extraction. The final system, that represents a significant improvement over the one presented in [2] consisted of an electromagnetic shaker, but, in lieu of a permanent connection via a stinger, the specimen was connected to the shaker via a c-shaped bracket and vertical rod, which maintained contact with the beam (Fig. 25.1). A small rubber wedge was attached to localize the contact point and reduce chatter. A small preload was introduced between the shaker and the beam to ensure adequate contact. Due to the shaker attachment, only a half-sine forcing function could be introduced to the system, but the resonance excitation frequency ensured that force and response stayed accurately aligned. Once the desired displacement amplitude was reached, decoupling of the exciter and specimen was achieved by introducing a voltage offset into the shaker’s input signal, resulting in a displacement offset of the drive rod that was larger than the initial preloading displacement. Timing of the detachment was thereby crucial in order to ensure a gentle release of the system without introducing an appreciable transient.

In a first instant, time domain data was captured with an accelerometer due to its simplicity. Future measurements will use non-contact measurements to minimize the impact of the accelerometer cabling on the damping. The damping of the system was then subsequently be extracted at different response levels using the logarithmic decrement method.

25.3 Results

An initial roving hammer test was conducted using 22 points across the length of the beam in order to validate the modeshape prediction of the analytical model and to experimentally obtain the resonant frequencies. Figure 25.2 indicates the excellent correlation between the predicted and experimentally obtained modeshapes, verifying the functionality of the analytical

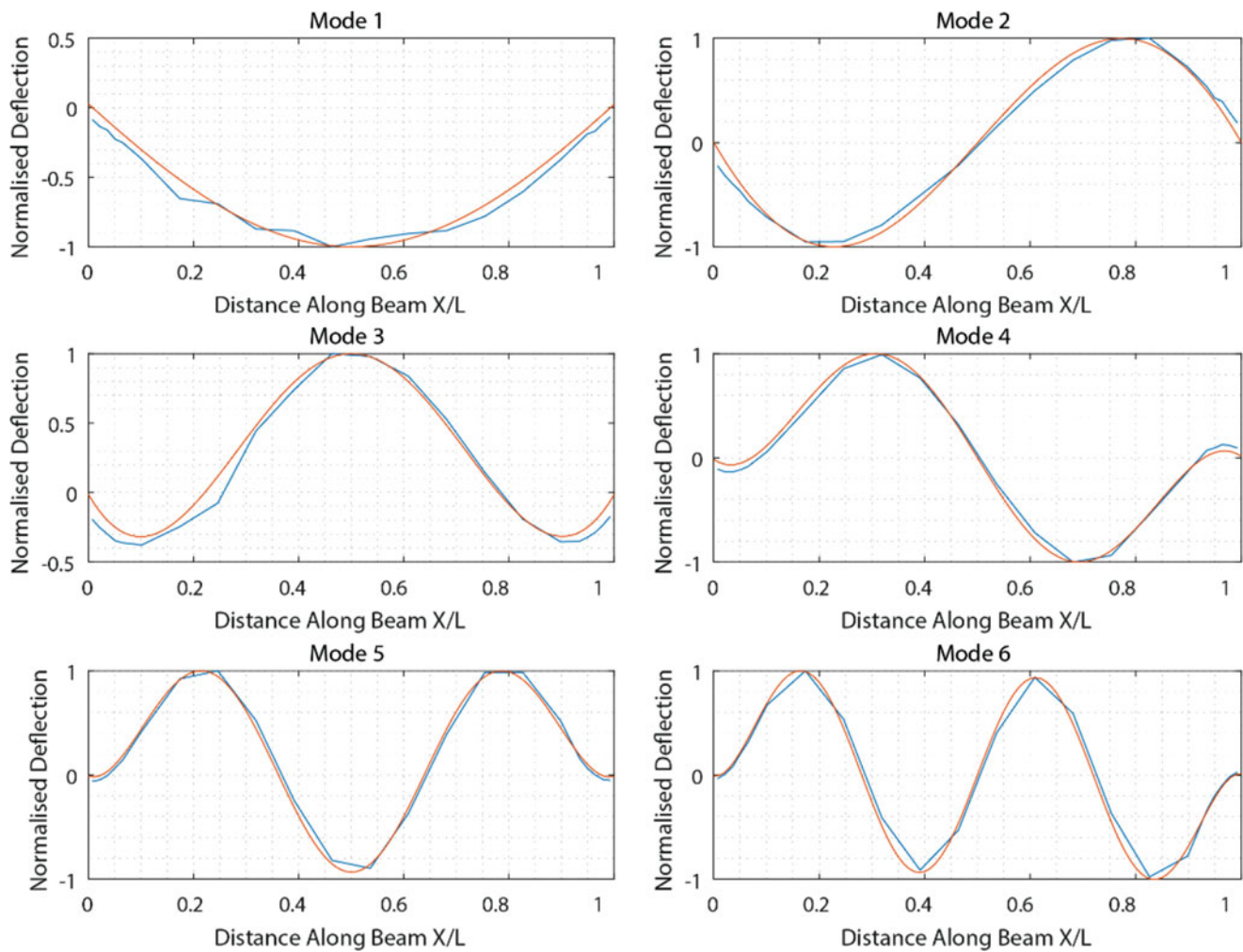


Fig. 25.2 Experimentally obtained modeshapes compared to the analytically predicted modeshapes for the first six flexural modes

model in predicting the node locations as m_r is adjusted. It was observed, that the inertia masses only acted as pinned joints for the first two modes, after which they tended towards fully clamped boundary conditions. Tests on a single harmonic using the free-decay exciter system were conducted, with the results displayed by Fig. 25.3. A high quality single harmonic sine wave excitation can be obtained from the proposed excitation system, with minimal noticeable transient during the release as highlighted by Fig. 25.3b. Following the displacement offset of the shaker contact surface, only a slight distortion of the waveform can be observed to occur for the first few cycles, which rapidly disappears as the waveform returns to that of a decaying sine wave. The decay observed is exponential and only slightly distorted by the rigid body motion of the specimen. The distortion is small enough for an exponential function to be fitted to the decay with confidence. The free decay signal allows the evaluation of the amplitude dependent damping from a single time domain series. Consistent damping ratios of 0.55% were found for the sixth flexural mode using the data displayed in Fig. 25.3, demonstrating the repeatability of the novel setup.

25.4 Conclusion

A promising, novel damping extraction method has been presented, capable of extracting small material damping values from lightly damped specimens whilst minimizing parasitic damping from external sources such as supporting structures and the excitation system. Modelling and validation shows the presence of tip masses to move the nodes to the tips of the specimen, providing the potential to reduce extraneous losses through the specimen's suspension. Testing of the shaker release mechanism demonstrates successful decoupling and a smooth release into a free decay, for accurate logarithmic damping extractions.

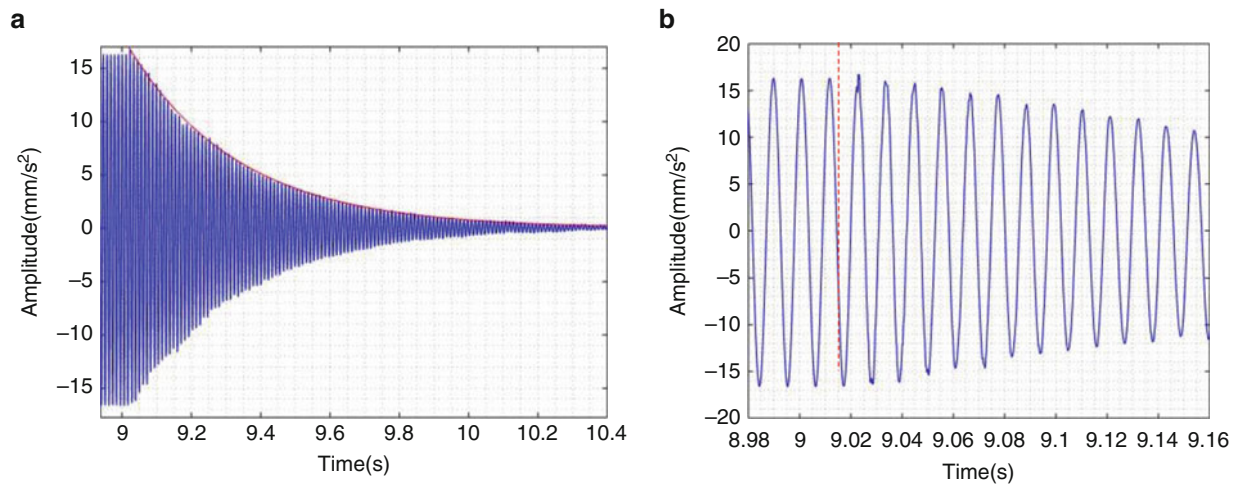


Fig. 25.3 (a) Decay achieved for the sixth flexural mode with a curve fitted for the damping estimation and (b) a close-up of the release zone

Acknowledgements The authors are grateful to Rolls-Royce plc for providing financial support for this project and for giving permission to publish this work.

References

1. Brake, M.R.W.: *The Mechanics of Jointed Structures*, 1st edn. Springer International Publishing, New York (2018)
2. Schwingshackl, C.W., Joannin, C., Pesaresi, L., Green, J.S., Hoffmann, N.: Test method development for nonlinear damping extraction of dovetail joints. In: *Conference Proceedings of the Society for Experimental Mechanics Series*. Springer, New York (2014)
3. Vanwalleghem, J., De Baere, I., Locufier, M., Van Paeppegem, W.: External damping losses in measuring the vibration damping properties in lightly damped specimens using transient time-domain methods. *J. Sound Vib.* **333**(6), 1596–1611 (Mar. 2014)
4. Bishop, J.E., Kinra, V.K.: Some improvements in the flexural damping measurement technique. In: *Mechanics and Mechanisms of Material Damping*, pp. 457–470. ASTM, West Conshohocken (1992)



Chapter 26

Finite Element Model Updating of the UCF Grid Benchmark Connections Using Experimental Modal Data

Milad Mehrkash and Erin Santini-Bell

Abstract Structural connections are a crucial component of any structural system. The connection stiffness can impact the static and especially the dynamic behavior of a structure. Therefore, reliable finite element modeling of the structural systems involves accurate estimation of their connections stiffness parameters. Accurate representation of connection stiffness parameter is one of the most challenging steps in model verification as connections are physically small parts of a structure and some parameter estimation procedures may lack the sensitivity to change in connection behavior to capture the stiffness parameter of connection elements. One of the most well-known experimental structures which has been extensively used in the model updating research field in recent years is a structural frame set up in the University of Central Florida which is known as the UCF Grid. This experimental structure is an instrumented planar grid comprised of several steel members interconnected by gusset plates. The grid is instrumented by eight uniaxial accelerometers to capture the accelerations of the specific nodes of the structure when the grid vibrates due to an excitation. In this paper, the modal data of the grid obtained experimentally by an impact test are used for estimation of the stiffness parameters of the grid joints. A modal based error function method is employed to update the finite element model of the grid built in SAP2000[®] environment. For the model updating computations, an optimization MATLAB[®] code is linked to the SAP2000[®] Open Application Programming Interface to facilitate the parameter estimation procedure. The updated finite element model of the grid based on new estimations for its joints' stiffness parameters could represent the structural behavior of the grid in a more reliable scheme.

Keywords Model updating · Parameter estimation · Joint stiffness · Modal data · UCF Grid

26.1 Introduction

The interface of mechanical and structural members rely on structural connections transmit demands throughout the structure. There are various types of connections that can provide appropriate rigidity for structural joints. The stiffness of connections plays a critical role, particularly in the mechanical behavior and vibration characteristics of complicated systems. Therefore, it is essential to evaluate the rigidity of mechanical systems connections and estimate their stiffness parameters. While most of the connections in the mechanical or structural systems are semi-rigid, they are usually considered as pinned or fixed in the design calculations. From the stiffness viewpoint, a pinned joint assumes no rotational rigidity while a fixed joint assumes an infinite rotational rigidity. This simplification is mainly due to the complexities of modeling semi-rigid connections in analytical models or lack of knowledge about the stiffness parameters of the semi-rigid joints. The former case is no longer common due to computational enhancements; however, the latter is still valid and complicated. Introducing numerous stiffness parameters for modeling of sophisticated connections may mitigate the challenges of finding a stiffness protocol which can represent the realistic mechanical behavior of the joint. However, although simulation of such detailed connections is applicable it may not be practical. Hence, for modeling of complex joints, a trade-off between simplicity and accuracy is required.

The effect of the rigidity of connections on the behavior of mechanical or structural systems has been investigated by many researchers [1]. Li presented a model updating method with emphasis on identification of joint stiffnesses [2]. He defined a reduced-order characteristic polynomial in terms of the measured natural frequency, the partial modal properties predicted from a flawed FEM model. Bayo et al. proposed an approach to model internal and external semi-rigid connections

M. Mehrkash (✉) · E. Santini-Bell
Department of Civil and Environmental Engineering, College of Engineering and Applied Sciences,
University of New Hampshire, Durham, NH, USA
e-mail: mm1193@wildcats.unh.edu

for the global analysis of steel and composite frames [3]. This method is based on a finite dimensioned elastic-plastic four-node joint element that considers the panel zone deformations and all the internal forces that concur at the joint. Cunha et al. applied a model updating technique with static and dynamic data to identify the stiffness of bolted joints for pultruded frame structural systems used in civil construction [4]. In the automotive industry, finite element models which are used for estimation of the body structure performance are classified into two groups. In the first group, a shell model is developed in which the details of each individual part of a structure, including connections are simulated. The second group includes concept models in which all major load-carrying members are simulated with beam elements, while shear panels are simulated with coarse shell elements. In these models, joints are simulated with different parametric representations. There are various techniques for concept modeling of joints, however, two of them are more common. The first method uses an elastic finite element superelement representation with element coefficients determined through optimization routines correlating analysis response with the actual performance of the local joint or overall body. The second method considers a tri-spring representation with parameters simulating certain joint behavior. Shahhosseini et al. discussed these two primary methods for modeling major compliance joints in concept models [5]. Also, structural optimization techniques have been employed for improving the design of complex mechanical systems in which the size, shape and other geometrical properties of the joints are modified to yield an efficient sketch for connections configuration. Kiani et al. presented an approach for evaluating the structural performance of a vehicle model in terms of the joint stiffness. Also, they utilized a material-based technique for joint stiffness modeling by considering changes in the elastic modulus of the material at the designated joint regions. In their research, it was shown that the evaluation of a car body structure based on the optimum joint stiffness could have a superior performance relative to the baseline model without a weight penalty [6].

In this paper, the finite element model of an instrumented experimental frame is developed in SAP2000[®] software [7]. In the preliminary model, all connections are modeled as either simple or fixed. The measured frequency response functions of the frame are used for modal extraction. Then the modal parameters are employed to update the joints stiffness values. It is assumed that the connections of the structure are semi-rigid. Their semi-rigidity is modeled by incorporating partial fixities at the connection zones. The rotational stiffness values of the connections are estimated through an optimization algorithm by an in-house parameter estimation MATLAB[®]-based program [8], developed at University of New Hampshire which takes advantage of SAP2000[®] OAPI. It is shown how the rigidity of connections can affect the modal behavior of the structure. Moreover, the robustness and limitations of the modal stiffness parameter estimation technique are discussed.

26.2 Model Updating

Inherent uncertainty existing in structural modeling, demands an effort to make the mathematical models more representative of the reality by model updating techniques. In general, for updating the finite element models, particularly estimating the joints structural parameters, there are a couple of classes. In the first category which is called direct methods, a set of characteristic equations are solved to determine the joint parameters. These equations include analytical mass and stiffness matrices and experimentally measured modal or FRF data. The other class contains penalty techniques in which some kind of error norms are minimized to reduce the differences between the finite element model and the measurements. Various error functions have been introduced for structural parameter estimation purposes [9]. One of the most robust and common penalty methods of model updating is based on using modal parameters of the structure. In this technique, modal parameters of the structural or mechanical system, including natural frequencies and mode shapes are obtained experimentally and used as the input to the optimization procedure. On the other hand, the mass and stiffness matrices of the system are constructed by the analytical model based on as-built drawings of the structure. The equation of modal stiffness-based error function which is utilized in this research is given by Eq. (26.1) [10],

$$\{E(p)\}_i = [K(p)]\{\Phi\}_i - \omega_j^2 [M(p)]\{\Phi\}_i \quad (26.1)$$

where $\{E(p)\}$ is the modal stiffness-based error function vector, $[K(p)]$ and $[M(p)]$ are analytical stiffness and mass matrices, respectively, $\{\Phi\}$ and ω are the mode shape vector and natural frequency extracted from a non-destructive test, p is the structural parameter to be estimated and i is the vibration mode number. If only some of the degrees of freedom of the structural system are measured in a non-destructive test, which is a common case, the experimental modal data are incomplete. In such conditions, the modal data incompleteness needs to be resolved in some way. One of the suitable methods for removing this issue is partitioning the mass and stiffness matrices and using only the measured DOFs by Guyan reduction technique [11]. Therefore, the mentioned error function can be expressed as [10],

$$\{E(p)\}_i = \left(\left([K_{aa}] - \omega_i^2 [M_{aa}] \right) - \left([K_{ab}] - \omega_i^2 [M_{ab}] \right) \cdot \left([K_{bb}] - \omega_i^2 [M_{bb}] \right)^{-1} \left([K_{ba}] - \omega_i^2 [M_{ba}] \right) \right) \{\Phi_a\}_i \quad (26.2)$$

where the subscripts a and b indicate measured and unmeasured degrees of freedom, respectively and the partitioned mass and stiffness matrices and mode shape vector are shown as

$$[M] = \begin{bmatrix} M_{aa} & \vdots & M_{ab} \\ \dots & \vdots & \dots \\ M_{ba} & \vdots & M_{bb} \end{bmatrix}, \quad [K] = \begin{bmatrix} K_{aa} & \vdots & K_{ab} \\ \dots & \vdots & \dots \\ K_{ba} & \vdots & K_{bb} \end{bmatrix}, \quad \{\Phi\} = \begin{Bmatrix} \Phi_a \\ \dots \\ \Phi_b \end{Bmatrix} \quad (26.3)$$

If it is assumed that the uncertainties are limited to the stiffness parameters of the structure, only the stiffness matrix is updated in each iteration of the optimization procedure. The parameter estimation is implemented by minimizing the error function through the following objective function,

$$J(p) = \sum_i \sum_j E(p)_{ij}^2 \quad (26.4)$$

where J is the objective function and j denotes the parameter number. The iterative updating continues until a defined convergence criterion is satisfied.

26.3 Modal Extraction and System Identification

As mentioned previously, for the modal parameter estimation method, experimental natural frequencies and mode shapes are required. However, the accelerometers can measure the acceleration of structural nodes. Therefore, the experimentally obtained time histories of accelerations need to be processed to provide information about the modal properties of the structure. When the excitation source is known, such as an impact test in a lab, the peak picking method could be a practical technique for extraction of modal parameters of the structure [12]. This method employs signal processing techniques, in which initially using discrete Fourier transform (or power spectral density functions), the frequency spectra of input (impact) and output (acceleration) signals are obtained and then the FRF plots are drawn. The frequencies corresponding to the peaks of the FRF plots give the natural frequencies of the structure and the imaginary parts of the peaks yield the mode shape components of each mode. This technique is based on the fact that in the vicinity of a resonance, contribution of the vibrating mode dominates the FRF, while the effect of other modes is limited.

26.4 UCF Grid and Impact Test

The University of Central Florida (UCF) Grid is an experimental frame at the UCF which is used for model updating tests. This experimental structure was designed and fabricated to simulate the behavior of the deck-on-beam bridges [13]. The UCF Grid has two longitudinal girders, 5.48 long, covering two spans. It also has seven transverse beams connecting the two girders which are 1.83 long with transverse bracing at 0.91 m intervals. All longitudinal and transverse beams are S3 × 5.7 profiles, while the columns of the frame are W12 × 26 profiles. All Girders, beams and columns are made of A36 steel with Young's modulus $E = 200 \text{ GPa}$ and mass density $\rho = 7850 \text{ kg/m}^3$. The length of the columns is 1.07 m and their connection to the base is fixed but to the girders can be considered as pinned. This is because the column-girder connection is made of a cylinder located between two curved bearing plates. The connection of the transverse beams to the girders is comprised of two angle clips and two cover plates so that can transfer shear and moments. Therefore, these joints may behave as semi-rigid connections. Figure 26.1 shows the UCF Grid and its connections. The UCF Grid was instrumented by eight unidirectional PCB 393C accelerometers placed vertically and excited by an IPC 086D20 impact hammer at four locations. The location of accelerometers and impacts are shown in Fig. 26.2 [14].

Nondestructive impact tests were conducted on the UCF Grid by Gul and Catbas to determine its modal parameters [13]. In this paper, the response of the system to impact at node 10 is considered, i.e., the vertical acceleration time histories of



Fig. 26.1 Laboratory setup of the UCF Grid (left) and beam to girder connections (right) [15]

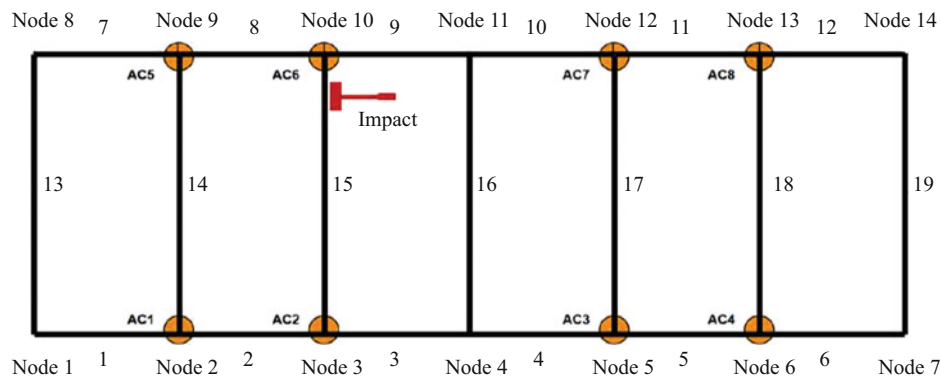


Fig. 26.2 Accelerometer and impact locations [14]

the eight accelerometers are recorded upon the impact hammer excites the frame at the location of the sixth acceleration. Frequency response function of the first accelerometer (AC1) is shown in Fig. 26.3.

26.5 Finite Element Modeling of the UCF Grid

A beam model of the UCF Grid is developed by SAP2000[®] version 19.1.1. All beam and girder connections are modeled as fixed joints and columns are connected to girders by pinned joints. Also, the connection of columns to the base is fixed. Each of the girder or beam members of the grid need to be divided into some smaller members to ensure that there is not any mode mismatch between the analytical and experimental vibrations. The SAP2000[®] model of the UCF Grid is depicted in Fig. 26.4. Considering the first 12 modes, a modal analysis is performed. The analytical and experimental natural frequencies of the UCF Grid are given in Table 26.1. In addition, the corresponding mode shapes are shown in Fig. 26.5. In the mode shapes figure, the columns were replaced by pinned supports to save space as this replacement does not affect the mode shapes. Further, it should be noted that the 7th, 8th and 9th analytical modes cannot be captured by the instrumentation layout used because the mentioned modes relate to the local vibration of beams 13, 16 and 19 as denoted in Fig. 26.2.

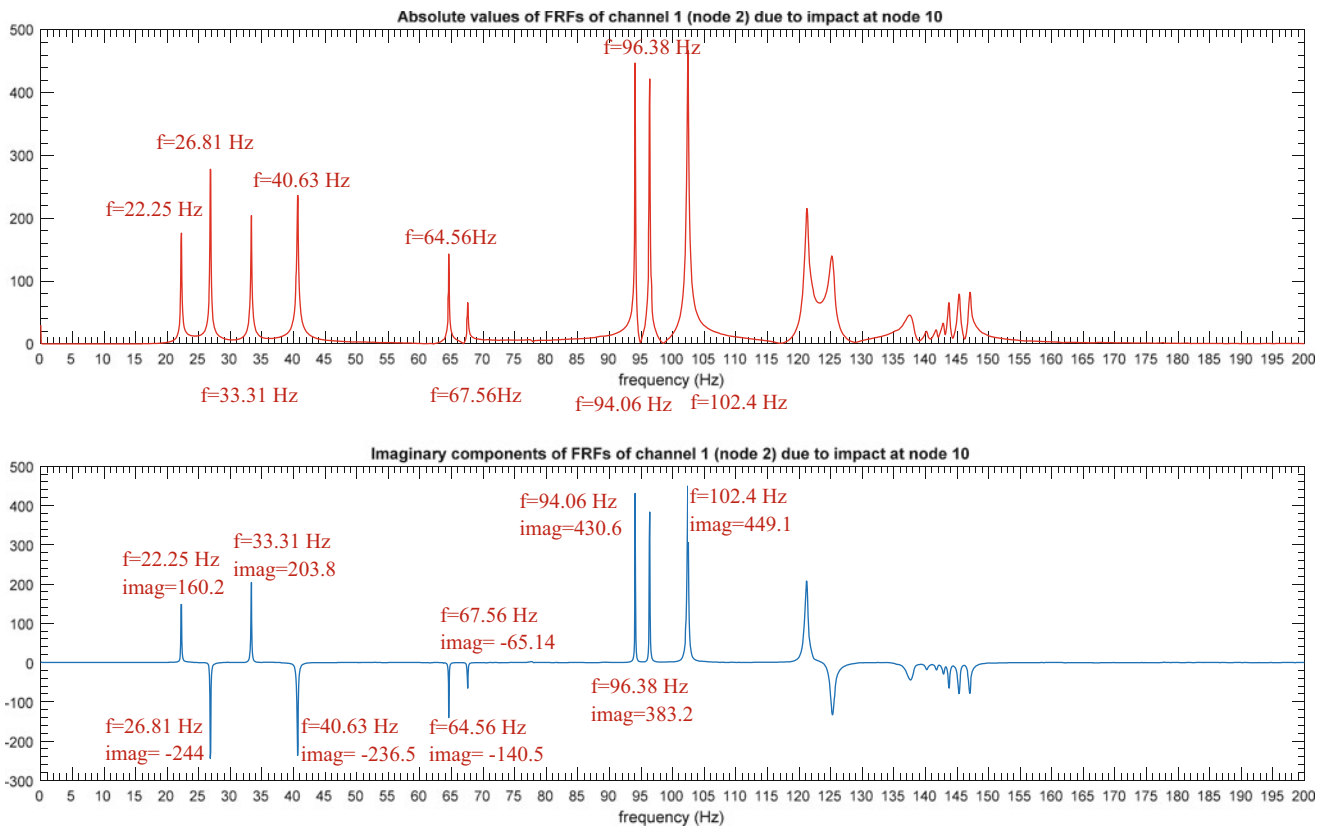


Fig. 26.3 FRF of the first accelerometer due to impact at node 10; absolute values (top), imaginary values (down)

Fig. 26.4 SAP2000® model of the UCF Grid

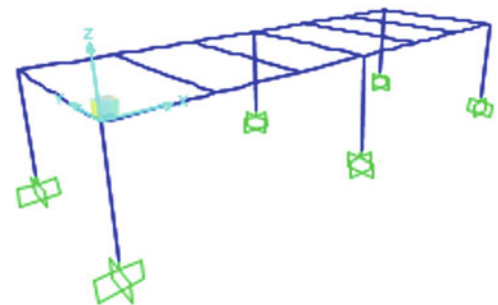


Table 26.1 Analytical and experimental natural frequencies of the UCF Grid

Mode number	Analytical natural frequencies (Hz)	Experimental natural frequencies (Hz)
1	22.63	22.25
2	28.44	26.81
3	33.87	33.31
4	43.76	40.63
5	62.38	64.56
6	65.63	67.56
7	73.20	–
8	73.20	–
9	73.38	–
10	96.33	94.06
11	99.50	96.38
12	109.62	102.40

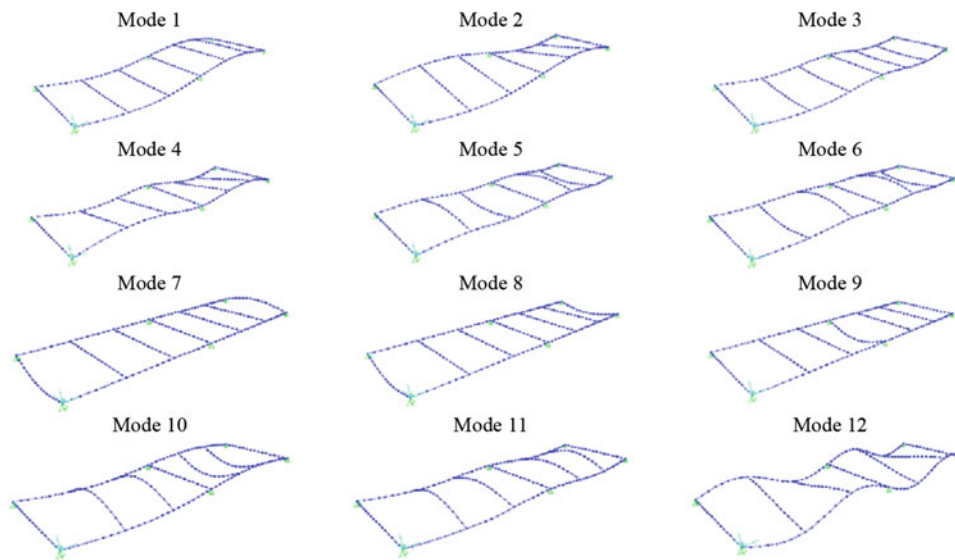


Fig. 26.5 The first 12 analytical mode shapes of the UCF Grid

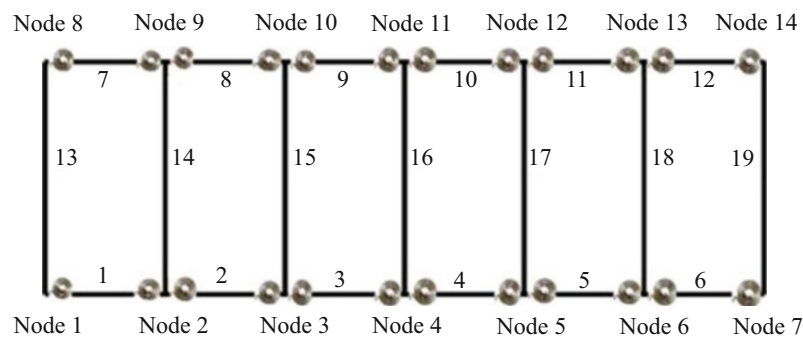


Fig. 26.6 The UCF Grid with partial fixity springs

26.6 Parameter Estimation Analysis

The finite element model of the UCF Grid has been updated by several researchers. Sanayei et al. updated the stiffness and mass of the UCF Grid at the element level, simultaneously using three static and dynamic error functions [14]. Also, Garcia-Palencia and Santini-Bell applied their two-step model updating algorithm for updating mass, stiffness and damping matrices of the UCF Grid using FRF method [16]. They also compared modal and FRF methods for updating the UCF Grid [17].

In this research, it is assumed that the uncertainties are limited to only the rigidity of connections. Therefore, multiple cases are investigated in which the rotational stiffness of the connections are estimated by updating the partial fixities at the ends of members. For the model updating, an in-house MATLAB[®]-based parameter estimation program linked to the finite element model of the UCF Grid through SAP2000[®] Open Application Programming Interface (OAPI) is used. For the minimization of the objective function, *fmincon* from the MATLAB[®] Optimization Toolbox[™] is employed. First, we need to know the initial values which should be assigned to the partial fixity springs at the end of members. Since in a fixed connection, the two connected members do not have any relative rotation, theoretically the stiffness of a partial fixity spring is infinite. However, practically if the magnitude of the stiffness of partial fixities is large enough, the connections behave as fixed joints. In Fig. 26.6, the partial fixity springs have been considered at the connections of beams to girders to simulate the semi-rigid joints. Although the two girders of the UCF Grid are continuous in the longitudinal direction of the grid, the holes of the bolts at the connection zones may have weakened those regions, so semi-rigidity for those joints could be likely. The variations of the UCF Grid natural frequencies with the rotational stiffness of the partial fixity springs are shown in Fig. 26.7. Therefore, this plot could be helpful for selecting the initial values for the partial fixity springs from a reasonable range.

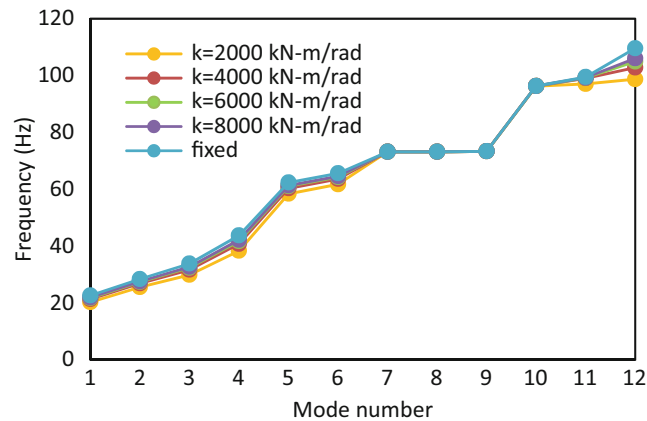


Fig. 26.7 Variations of the natural frequencies of the UCF Grid with the rotational rigidity of beam to girder connections

Table 26.2 Mode selection for parameter estimation and the corresponding estimated partial fixities

Case no.	Considered modes	Estimated k (kN m/rad)
1	1, 2, 3, 4, 5, 6, 10, 11, 12	10,277
2	1, 2, 3, 4, 10, 11, 12	3573
3	1, 2, 3, 4, 5, 6, 12	11,307
4	1, 2, 3, 4, 12	3741

Table 26.3 Analytical, experimental and updated natural frequencies of the UCF Grid

Mode no.	Anal. freq. (Hz)	Case 1 freq. (Hz)	Case 2 freq. (Hz)	Case 3 freq. (Hz)	Case 4 freq. (Hz)	Exper. freq. (Hz)
1	22.63	22.12	21.25	22.17	21.31	22.25
2	28.44	27.81	26.73	27.86	26.80	26.81
3	33.87	32.97	31.46	33.05	31.56	33.31
4	43.76	42.54	40.49	42.64	40.62	40.63
5	62.38	61.57	60.11	61.65	60.21	64.56
6	65.63	64.84	63.41	64.92	63.51	67.56
7	73.20	73.20	73.20	73.20	73.20	–
8	73.20	73.20	73.20	73.20	73.20	–
9	73.38	73.38	73.38	73.38	73.38	–
10	96.33	96.33	96.32	96.33	96.32	94.06
11	99.50	99.32	99.03	99.34	99.05	96.38
12	109.62	106.82	102.07	107.07	102.38	102.40

26.6.1 One-Parameter Estimation Analysis

For the first stiffness parameter estimation procedure, the semi-rigid connections layout of Fig. 26.6 is considered. In this analysis, it is assumed that there is only one parameter to be estimated. Hence, all the partial fixity springs shown in Fig. 26.6 are put in a group, i.e., at the end of model updating, all the springs would have the same updated value. Based on the selection of modes which contribute to the optimization algorithm, four cases are investigated as given in Table 26.2. In none of the four cases, local modes 7, 8 and 9 are considered. The estimated stiffness values of the partial fixity springs are provided in this table as well, while the updated natural frequencies of these four cases are given in Table 26.3. Modal Assurance Criterion (MAC) analysis is done for mode tracking to ensure that the frequencies are correctly assigned to the specific vibration modes. The objective function plots and MAC value graphs of the four cases are shown in Figs. 26.8 and 26.9, respectively. MAC plots ensure that there would be no mode switch due to the change in parameters.

It is observed that the estimated stiffness value highly depends on the selection of modes. In all four cases, the program could find a local minimum for the objective function, however the difference between estimated value of cases 1 and 3 and cases 2 and 4 is significant. The reason for such a considerable difference is the contribution of modes 5 and 6, as in cases 1

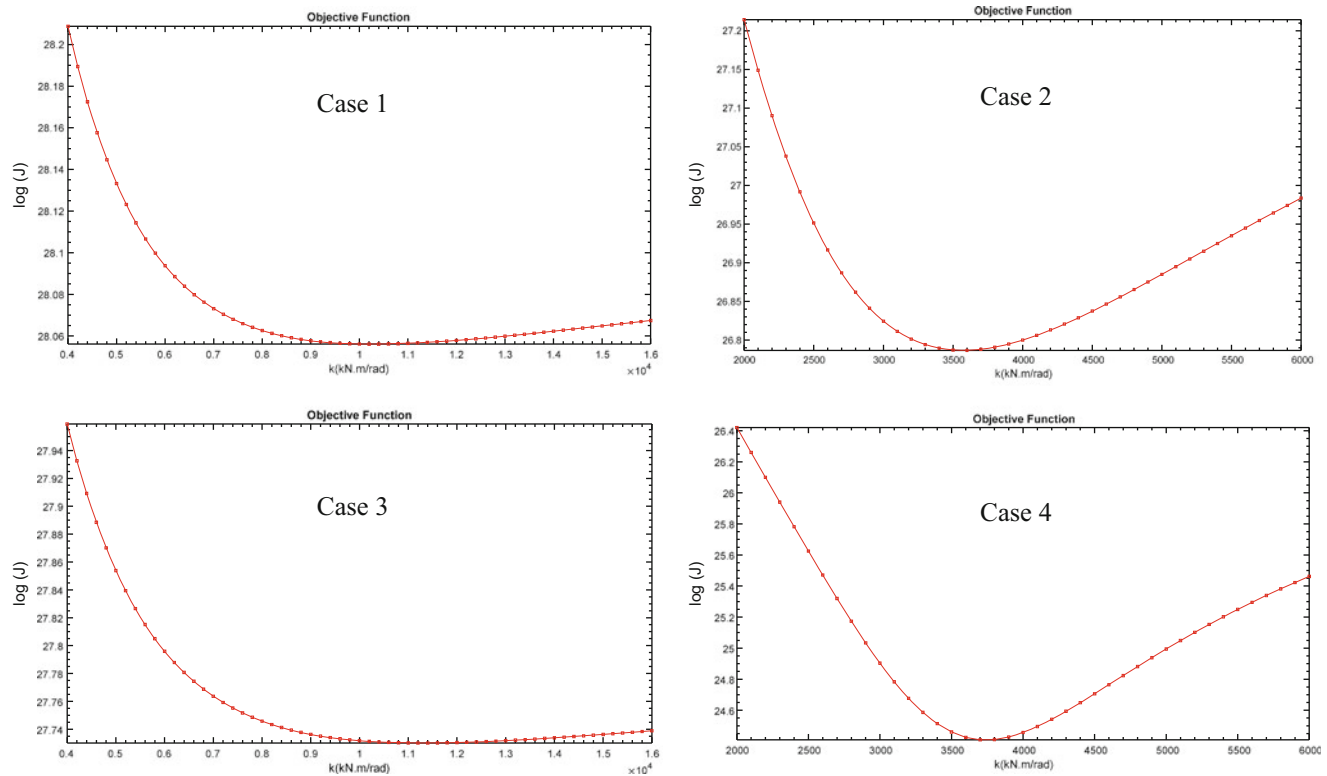


Fig. 26.8 Objective functions of the four cases defined in Table 26.2

and 3, modes 5 and 6 are contributed while in cases 2 and 4, the two mentioned modes are ignored. Comparing MAC plots of cases 3 and 4 with cases 1 and 2 demonstrates that the instrumentation used for this test, is not sufficient for capturing modes 10 and 11. This can be verified as in the MAC plots of cases 1 and 2 (which includes modes 10 and 11), large non-diagonal bars can be seen for modes 10 and 11. An interesting point is the role of modes 5 and 6 in the estimation of stiffness parameter. In these two modes, the vibration of beams 14, 15, 17 and 18 (see Fig. 26.6) is considerable. Therefore, it might be required to update the rotational rigidity of these four members too. Therefore, in the next section, the model updating is performed by considering this additional group of stiffness parameters.

26.6.2 Two-Parameter Estimation Analysis

In this section, as shown in Fig. 26.10, the connections of beams 14, 15, 17 and 18 to the girders are modeled as semi-rigid joints in addition to the previously introduced partial fixities. The previously defined rotational fixities are considered as group 1 and the new spring constants are put in group 2. Hence, in this analysis there are two unknown stiffness parameters. In Fig. 26.10, the group 1 is shown by red boxes and the group 2 is specified by blue boxes. The contributed modes are the same as the ones in case 3 of the previous section, i.e., modes 1 to 6 and mode 12 are contributed. The analytical, experimental and updated natural frequencies for this analysis are given in Table 26.4. Also, the corresponding MAC plot is shown in Fig. 26.11. Further, the updated values for the two partial fixities are given in Table 26.5.

The results of the two-parameter estimation analysis show that considering partial fixities for beam to girder connections does not improve the estimation procedure. In this case, the partial fixity of the parameter 1 converges to the same value of case 3 in one-parameter estimation, while the stiffness of group 2 parameters reaches the upper defined bound. Considering the graphs of Fig. 26.7, this boundary value represents a fixed connection, which was the condition in the one-parameter estimation. Therefore, introducing partial fixities for the beam to girder connections does not provide any information about the semi-rigidity of these joints. Hence, the two-parameter estimation procedure does not show much advantage over the one-parameter estimation.

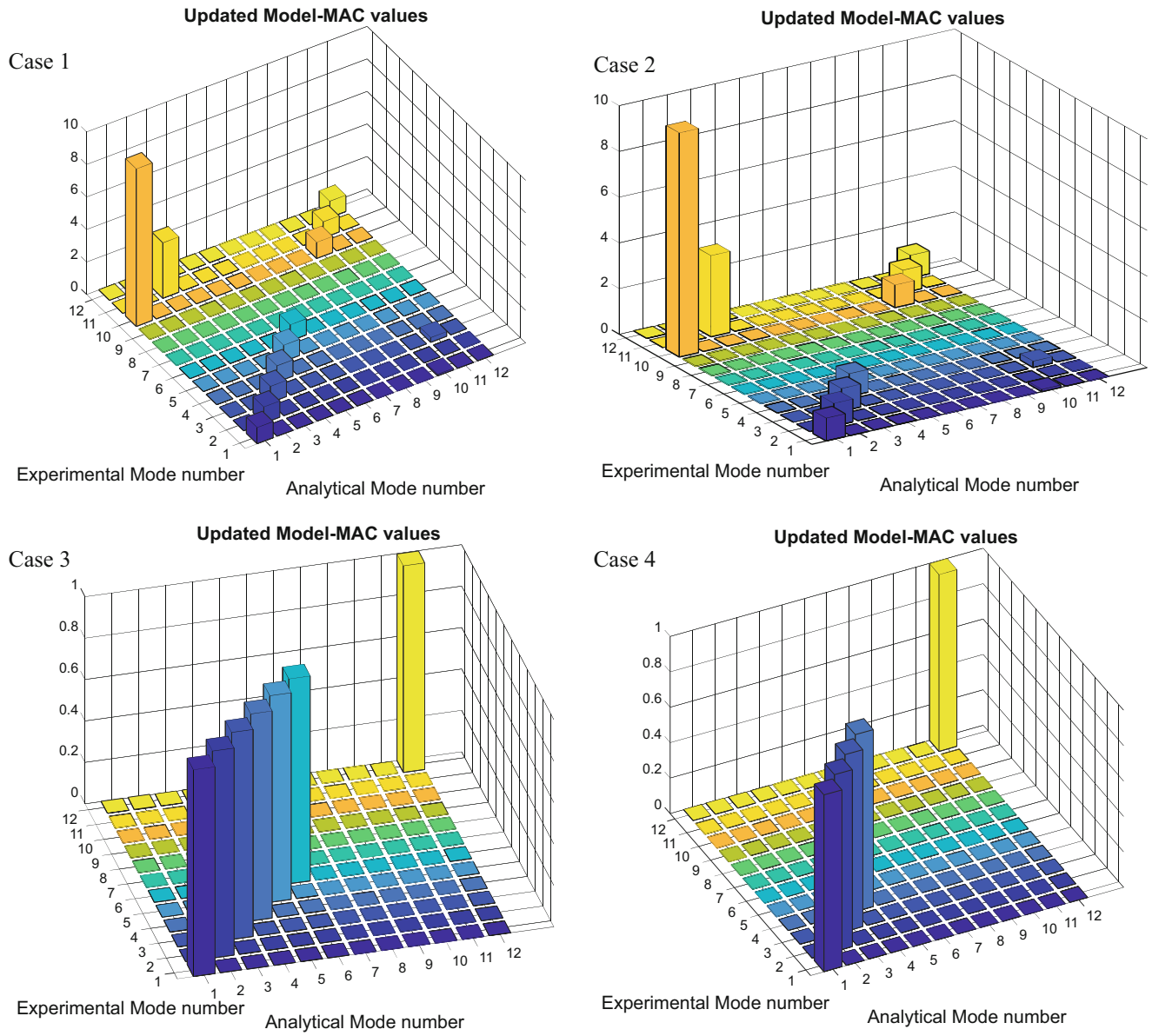


Fig. 26.9 MAC value plots of the four cases defined in Table 26.2

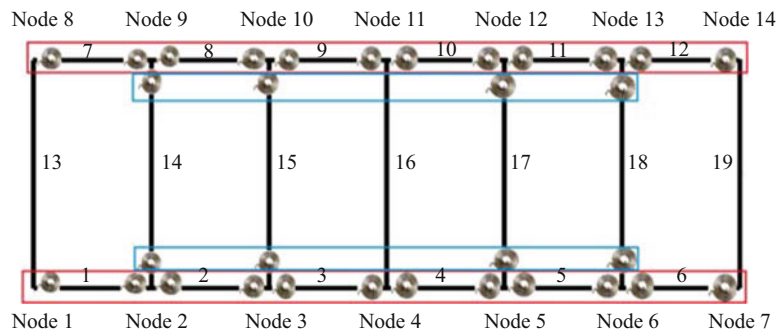


Fig. 26.10 The UCF Grid with partial fixity springs for two groups of connections

Table 26.4 Analytical, experimental and updated frequencies obtained by two-parameter estimation

Mode no.	Anal. freq. (Hz)	Updated freq. (Hz)	Exper. freq. (Hz)
1	22.63	22.17	22.25
2	28.44	27.86	26.81
3	33.87	33.05	33.31
4	43.76	42.64	40.63
5	62.38	61.65	64.56
6	65.63	64.92	67.56
7	73.20	73.20	–
8	73.20	73.20	–
9	73.38	73.38	–
10	96.33	96.33	94.06
11	99.50	99.34	96.38
12	109.62	107.07	102.40

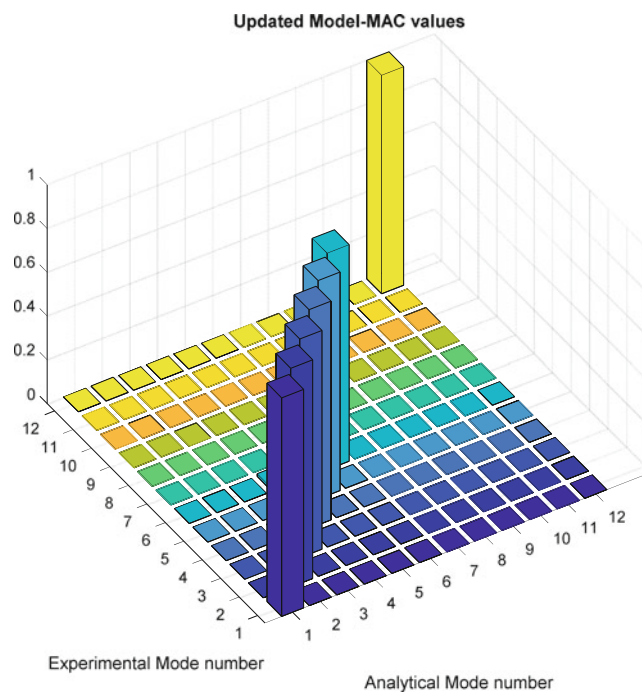


Fig. 26.11 MAC value plot of the two-parameter estimation analysis

Table 26.5 Initial and updated values of two-parameter estimation

Stiffness parameter	Initial stiffness value (kN m/rad)	Updated value (kN m/rad)	Lower bound (kN m/rad)	Upper bound (kN m/rad)
Group 1	8000	11,307	4000	16,000
Group 2	8000	16,000	4000	16,000

26.7 Conclusion

In this paper, the stiffness parameters of the joints of an experimental structure were verified with respect to laboratory collected model response data. The capability of SAP2000[®] software package for incorporating partial fixities at the connection regions as well as the OAPI was employed. It was shown how the joints stiffness of the experimental structure could affect its modal behavior. The parameter estimation operation presented in this paper was limited to updating the rigidity of the joints. Obviously, there are some uncertainties in terms of stiffness, mass and damping of the structure members. In a more comprehensive model updating procedure, those uncertain structural parameters need to be incorporated in the parameter estimation and model updating protocol. Also, it was demonstrated that updating the partial fixity springs

through an automated parameter estimation program which takes advantage of the OAPI algorithms and MATLAB[®] Optimization Toolbox™ options could facilitate the structural model updating procedure. Using this protocol can play an important role in model-based condition assessment and improvement of analytical representation of the modal and dynamic behavior of structural and dynamic systems.

Acknowledgments This material is based upon work partially supported by the National Science Foundation under Grant No. 1430260, FHWA AID: DEMO Program and funding from the NHDOT Research Advisory Council. The authors would like to thank Ted Zoli and Christopher Engel of HNTB for their support in the development of this work and acknowledge Professor F. Necati Catbas and his research group at the University of Central Florida for access of the UCF Grid experimental response data. Any opinions, findings, and conclusions or recommendations expressed in this material are those of the author(s) and do not necessarily reflect the views of the National Science Foundation.

References

1. Mehrkash, M., Santini-Bell, E.: Modeling and characterization of complicated connections in structural and mechanical systems as applied to a gusset-less truss connection. In: 97th Annual Meeting of Transportation Research Board (TRB 2018), Washington D.C. (2018)
2. Li, W.L.: A new method for structural model updating and joint stiffness identification. *Mech. Syst. Signal Process.* **16**(1), 155–167 (2002)
3. Bayo, E., Cabrero, J.M., Gil, B.: An effective component-based method to model semi-rigid connections for the global analysis of steel and composite structures. *Eng. Struct.* **28**(1), 97–108 (2006)
4. Cunha, J., Foltete, E., Bouhaddi, N.: Evaluation of stiffness of semi-rigid joints in pultruded profiles from dynamic and static data by using model updating technique. *Eng. Struct.* **30**(4), 1024–1036 (2008)
5. Shahhosseini, A.M., Prater, G., Osborne, G.M., Kuo, E.Y., Mehta, R.: Major compliance joint modelling survey for automotive body structures. *Int. J. Veh. Syst. Model. Test.* **5**(1), 1–17 (2010)
6. Kiani, M., Motoyama, K., Rais-Rohani, M., Shiozaki, H.: Joint stiffness analysis and optimization as a mechanism for improving the structural design and performance of a vehicle. *J. Automob. Eng.* **228**(6), 689–700 (2014)
7. SAP2000 V. 19.1.1: Computers and Structures, Inc. (2017)
8. MATLAB R2018a: MathWorks, Inc. (2018)
9. Santini-Bell, E., Sanayei, M., Javdekar, C.N., Slavsky, E.: Multiresponse parameter estimation for finite-element model updating using nondestructive test data. *J. Struct. Eng.* **133**(8), 1067–1079 (2007)
10. Sanayei, M., McClain, J.A.S., Wadia-Fascetti, S., Santini, E.M.: Parameter estimation incorporating modal data and boundary conditions. *J. Struct. Eng.* **125**(9), 1048–1055 (1999)
11. Guyan, R.J.: Reduction of stiffness and mass matrices. *AIAA J.* **3**(2), 380 (1965)
12. Ewins, D.J.: *Modal Testing: Theory, Practice and Application*, 2nd edn. Research Studies Press LTD, Massachusetts (2000)
13. Gul, M., Catbas, N.: Test details for the preliminary data for international bridge health monitoring benchmark study, 2nd edn. Structures and Systems Research Group, University of Central Florida, Florida (2008)
14. Sanayei, M., Khaloo, A., Gul, M., Catbas, F.N.: Automated finite element model updating of a scale bridge model using measured static and modal test data. *Eng. Struct.* **102**(1), 66–79 (2015)
15. <http://www.cece.ucf.edu/CITRS/>
16. Garcia-Palencia, A.J., Santini-Bell, E.: A two-step model updating algorithm for parameter identification of linear elastic damped structures. *Comput.-Aided Civ. Inf. Eng.* **28**(7), 509–521 (2013)
17. Garcia-Palencia, A.J., Santini-Bell, E.: Structural model updating using dynamic data. *J. Civ. Struct. Health Monit.* **4**(3), 177–194 (2014)



Chapter 27

Structural Health Monitoring on Industrial Structures Using a Combined Numerical and Experimental Approach

Fabian Keilpflug, Robert Kamenzky, Daniel J. Alarcón, Tarun Teja Mallareddy, and Peter Blaschke

Abstract The Brandenburg industrial landscape is characterized by heavy industry sectors such as metallurgy and mining. Most of these industrial plants (ironworks, refineries, mines, etc.) have their origin in the state-planned rapid industrialization the German Democratic Republic underwent during the 1950s. Therefore, many critical constructive parts of these industrial plants have already surpassed their life expectancy or its remaining life expectancy can no longer be clearly determined due to poor documentation.

Heavy duty bridge cranes are an essential part of heavy industries or warehouses. During the course of their lives, these cranes and their rails are exposed to many different loads, damages and material fatigue processes during operation. Runway beams, those where the bridge crane runs on, are especially prone to the generation of cracks due to material fatigue. Condition monitoring and early damage detection can ensure the long-term load capacity and serviceability of bridge cranes, and contribute to a more cost-effective maintenance.

This paper presents the results of a feasibility study for a vibroacoustic damage detection procedure on bridge crane runway beams. A segment of a railway beam has been studied with experimental modal analysis and the results used to correlate and validate a FE model, generated by means of optical scanning. The modal analysis was performed by means of automatic impact excitation and Scanning Laser Doppler Vibrometry. Several damage cases were later simulated in the FE model, evaluating this way the development potential for a vibroacoustic method for damage detection in bridge crane railway beams.

Keywords Structural health monitoring · Overhead crane · Beam · Scanning Laser Doppler Vibrometry · Damage detection

27.1 Historical Introduction

Brandenburg, a federal state in Germany's northeast region, has traditionally been an agricultural powerhouse. The nineteenth century brought a rapid industrialization to the region, mainly due to its proximity with the German capital Berlin and its efficient waterways. The World War II and its aftermath deeply damaged the region's industrial panorama, which needed to be rebuilt almost from scratch. During the second part of the twentieth century, the German Democratic Republic was founded, being in practice a puppet state from the Soviet Union. The Soviet industrial policy gave an important focus on heavy industry sectors such as mining, metallurgy and oil refining. This heavy and rapid re-industrialization took place in a matter of 20–25 during the decades of 1950s and 1960s [1, 2]. This has severe implications nowadays:

1. These industrial complexes and their largest components and structures are about 50–70 years old and therefore, are very close to the end of their planned service lives.
2. Accurately determining the service life from these structures is a challenging task. Such a rapid industrialization driven by foreign officials implied very poor project documentation. In the worst cases this documentation was lost after the political changes that East Germany and the Soviet Union underwent during the 1980s and 1990s.

F. Keilpflug · R. Kamenzky · D. J. Alarcón (✉) · T. T. Mallareddy
Laboratory for Machine Dynamics and NVH, Technical University of Applied Sciences Wildau, Wildau, Germany
e-mail: daniel.alarcon@th-wildau.de

P. Blaschke
Laboratory for Machine Dynamics and NVH, Technical University of Applied Sciences Wildau, Wildau, Germany
NV Tech Design GmbH, Steinheim, Germany

3. The end of the service life of these vital industrial structures is a region-wide phenomenon that, if not promptly addressed, could affect the entire regional economy.

27.2 Introduction to the Project

Heavy duty overhead cranes are an essential part of the heavy industry complexes described in the previous chapter. These cranes are designed to transport heavy loads along industrial facilities or warehouses. In the experience of the cooperation partner in this project, during decades, these cranes and their rails have been exposed to many different loads, damages and material fatigue processes during operation. Runway beams, those holding the rails where the crane runs on (Fig. 27.1), are especially prone to the generation of cracks due to material fatigue. Replacing these runway beams is an expensive operation: besides the pure replacement costs, the crane simply cannot be operated during the time the runway beams are being replaced. This has in consequence large negative impacts in revenue and plant productivity.

Increased damage incidence in recent years has raised awareness in the Brandenburg heavy industrial sector for a need for continuous condition monitoring [2]. Techniques such as structural health monitoring (SHM) can ensure the long-term load capacity and serviceability of overhead crane runway beams. In addition, the early detection of damages favors planning crane downtimes far in advance, minimizing their economic impact on the plant's economic output.

Common methods of runway rail/beam monitoring include visual inspections, which detect visible local damage. Deformation tests can provide information on the global wear and tear and thus, on the global structural degradation. Implementing SHM techniques has the advantage, for instance, that the damage locations do not have to be known a priori. A SHM system is based on modal system properties, which are acquired in a non-destructive way. The advantages of condition monitoring based on system properties are manifold; e.g., the locations and nature of the damages do not need to be known, or visible. Furthermore, it is not necessary for the measurement sensors to be located near damage points.

A particular case is studied for this paper. In these cases, cracks occur frequently in the upper flange of an I-shaped runway beam during operation. I-shaped beams are an efficient form for carrying bending and shear loads in the plane of the web, but their cross-sections have a reduced capacity in their transverse direction, inefficient in carrying torsion.

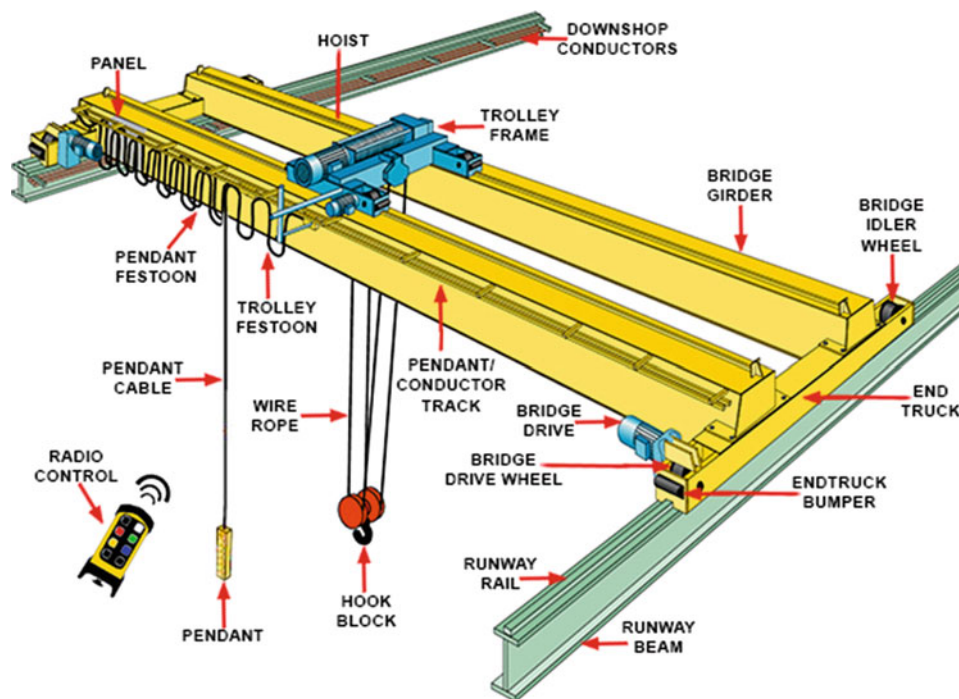


Fig. 27.1 Parts of a bridge crane. This study is centered on runway beams, named at the bottom of the figure (Source: [3])

This paper presents the results of a feasibility study for a vibroacoustic damage detection procedure on bridge crane runway beams. A 2-m beam segment has been dynamically studied and the results used to correlate and validate a Finite Element (FE) model, generated by means of optical scanning. Several damage cases were later simulated in the FE model, evaluating this way the development potential for a vibroacoustic method for damage detection in crane runway beams.

27.3 Materials and Methods

One structure was measured in this project, which is a 2 m long section of a real runway beams supplied by a cooperation partner (Fig. 27.2). In order not to damage the laboratory floor, the runway beam section was supported on wooden blocks and L-profiles as shown at the right side of Fig. 27.2. The influence of the L-profiles was taken in account in the FE model. Both L-profiles contact with the runway beam section at about 300 mm from the runway beam edges. A wooden pallet is visible in the figure below the beam section. It does not contact the beam in the experimental setup and is there mainly for safety purposes.

The dynamic properties of the beam were obtained with two different measurement methods and results were subsequently correlated. One measurement was carried out with a 3D Scanning Laser Doppler Vibrometer mod. PSV-500-3D (Polytec GmbH, Waldbronn, Germany) and the other one with a roving 3-axis accelerometer mod. 356A01 (PCB Piezotronics, Depew, NY, USA).

Given the poor laser reflectivity the railway beam offers, each degree of freedom (DOF) was marked with a small adhesive reflective paper piece. Figure 27.3 shows several measurement setup pictures for clarity. 363 Frequency Response Functions (FRF) were measured, three for each DOF in X, Y and Z direction in both accelerometer and 3D SLDV cases. All DOFs are separated about 200 mm from each other in the Y and Z directions. The 3D SLDV laser heads were positioned at a distance of 3.5 m away from the beam. The roving accelerometer was affixed with paraffin wax on each point. The 3-axis accelerometer was always mounted with the same orientation for data consistency. In both measurements, the beam section was excited by means of the Scalable Automatic Modal hammer SAM2 (NV Tech Design GmbH), applied at the driving point (DOF 55) on the back side of the web with a force of about 300 N. Three averages were needed with an interval of 9 s between impacts to allow the beam vibration to fully decay. For the SLDV tests, data was acquired with the software package PSV 9.3 (Polytec GmbH, Waldbronn), while the accelerometer tests were acquired with a vMeas data acquisition card and software vModal (Maul-Theet GmbH, Berlin). The extraction of modal parameters was carried out with vModal, by manually curve-fitting the obtained FRFs with a generally damped SDOF algorithm.

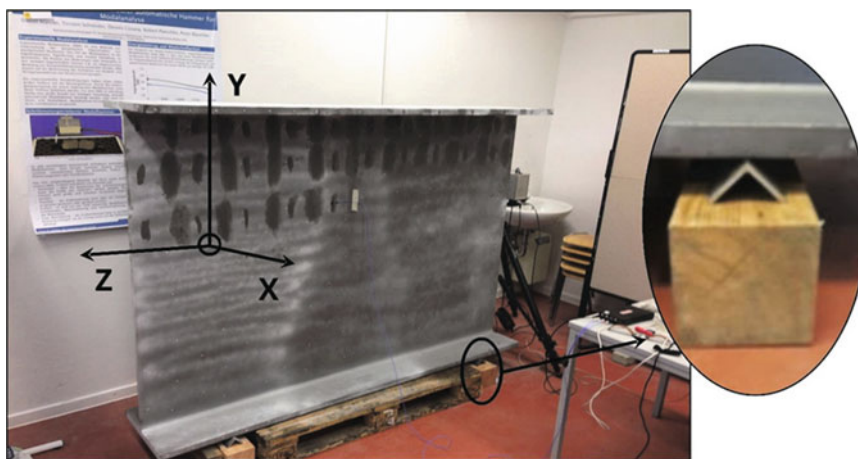


Fig. 27.2 (Left) Accelerometer modal test setup on runway beam section. (Right) Zoomed view of the runway beam section supports

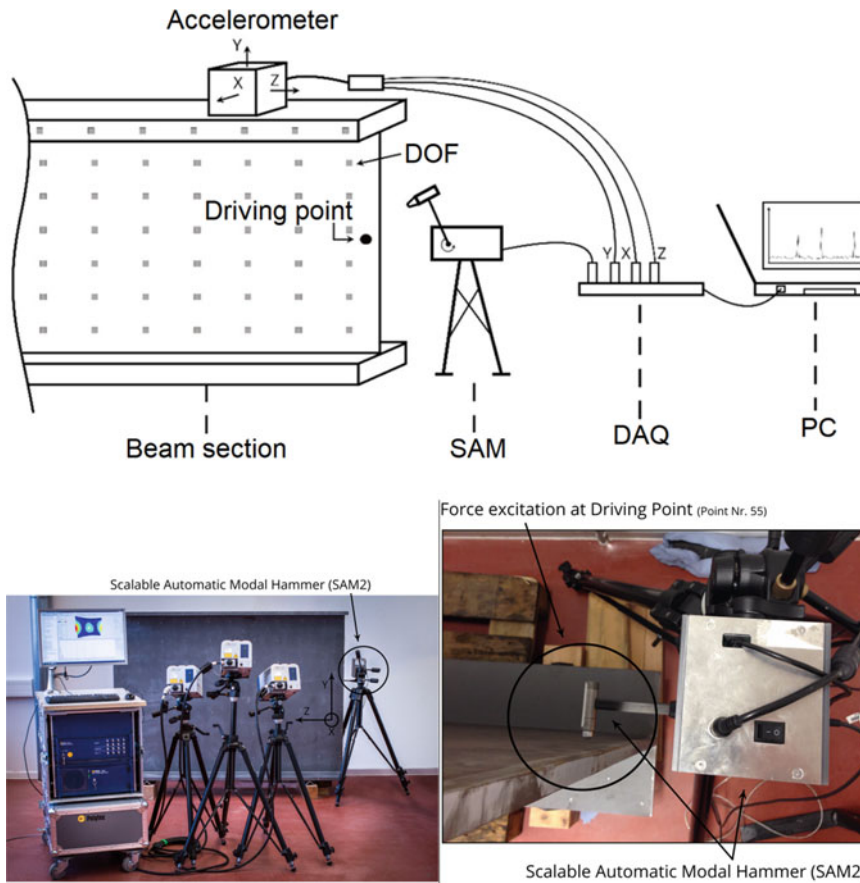


Fig. 27.3 (Top) Experimental setup for the roving accelerometer test. The web and both upper and lower flanges were measured. (Bottom left) Experimental setup for the 3D SLDV test. (Bottom right) Detailed view of the excitation, provided by the Scalable Automatic Modal hammer on the back side of DOF 55

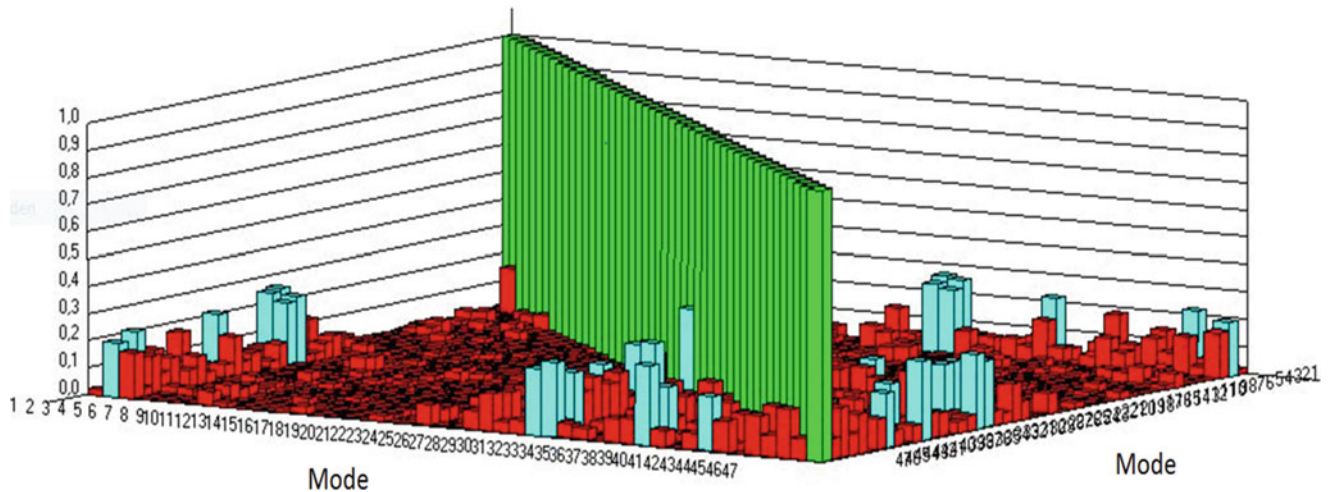


Fig. 27.4 AutoMAC matrix of the measurement using 3D SLDV as output sensor

27.4 Test Results and Discussion

Figure 27.4 shows the AutoMAC matrix for the SLDV test. The AutoMAC for the accelerometer test is similar. It is observed how lower and higher order modes are influenced by spatial aliasing, with very good autocorrelated modes in the middle range.

Table 27.1 Extracted modes from both modal analyses. It is observed how the 3D SLDV procedure offers larger mode sensitivity in lower and higher ranges

Accelerometer		3D SLDV	
Modes	58	Modes	70
Frequency range	11.88–1142.33 Hz	Frequency range	2.99–1578.70 Hz

FRFs obtained by means of 3D SLDV needed re-indexing before they could be correlated with those from the accelerometer measurement, as the data acquisition system assigned different DOF values. A different amount of modes was determined by each study. The evaluation of the two measurement methods covered the following range (Table 27.1).

The comparison of the evaluated data of both measurements extends only over the modes up to 1200 Hz in order to avoid spatial aliasing at higher mode orders, as shown by the AutoMAC. The curve fit procedure is expected to have an influence in the results, as this is a procedure prone to human-influence, especially when highly couple modes are encountered. The lower accelerometer sensitivity to low frequency vibrations, and very prominent 3 Hz rigid body mode, are also clearly observed in the results. The results shown in Fig. 27.5 do not include the first mode in the accelerometer study.

A direct comparison with both modal datasets was carried out as described below, relying on the natural frequency difference (NFD):

$$NFD (EMAR_{r,A}, EMA_{i,B}) = \frac{(\omega_{r,A} - \omega_{i,B})}{\min(\omega_{r,A}; \omega_{i,B})} * 100\%$$

Figure 27.6 shows significantly higher deviations of up to 4.3%. For higher order modes, the other eigenfrequencies of the two measurements correlate very well with each other. In total there is an average percentage deviation of $\approx 0.4\%$ across all 46 modes.

The differences between the modes of the two measurement methods could be partly based on slightly different measurement parameters, e.g., the force excitation varied between the two measurements, because the settings were made individually in both cases. Furthermore, there were slight differences at the excitation place.

Figure 27.7 shows the deviations of the respective modes of both measurements in terms of modal damping ratios. The diagram shows that certain mode pairs are very different and present higher deviations. A look at the mode shapes makes it clear why such a deviation and high values occur. For example, the second mode from the accelerometer measurement is very noisy (Fig. 27.5). The 3D SLDV results show some low-quality measurement DOFs in modes 1 and 3 due to bad signal reflectivity, which also contribute to these deviations.

A cross-correlation MAC matrix (XMAC) was generated to compare between both measurements (Fig. 27.8). Several low frequency modes appear poorly correlated due to the reasons stated above. From about 630 Hz the modes of the 3D SLDV measurement are additionally superimposed with a kind of rigid body motion. This vertical motion adds to the concerned mode shape of the beam and dominates these, so the results of the XMAC presents poor correlation at these modes.

27.5 Model Correlation and Fe Model Updating

A Finite Element (FE) was created based on a geometry scan (Fig. 27.9). The aim is to use a validated FE model to simulate different scenarios of damage and to investigate the sensitivity of the runway beam. Generally, the creation of an accurate dynamic FE model is a continuous process and involves various recurring adjustment steps until a certain degree of approximation to reality is achieved. The method requires a fine adjustment of the parameters in each process section. It should be noted that a model is a simplified reflection of reality and it generally does not capture all the attributes of the original, but only those that are relevant.

Due to the continuous optimization in terms of material parameters, boundary conditions and mesh quality, the result is a numerical model with an average natural frequency deviation of about 2.8% for 40 evaluated modes. Figure 27.9 shows the natural frequency difference matrix for the first 10 natural frequencies between the numerical model 3 and the acquired modes of the accelerometer measurements. It can be seen that modes 1 to 3 have the again highest relative deviation.


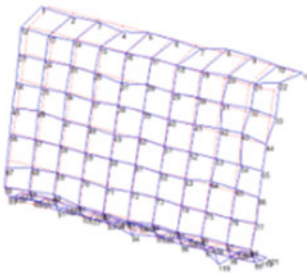
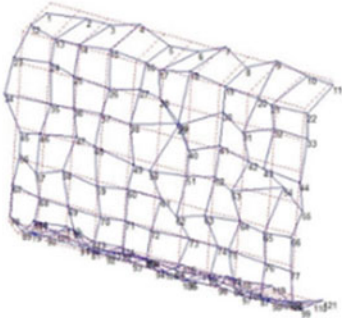
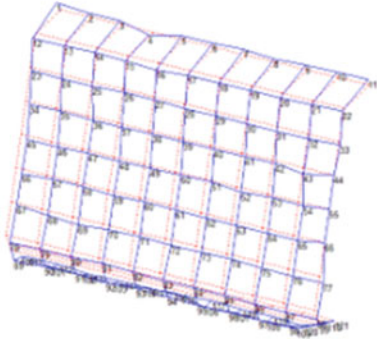
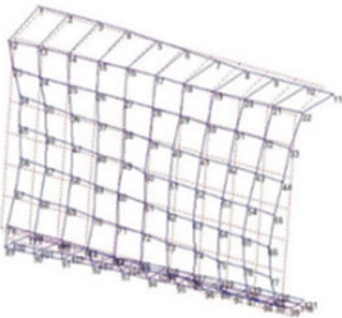
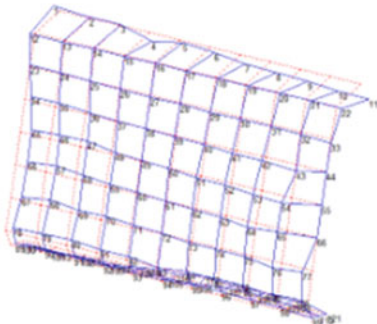
Mode	Piezo	Laser
1. Mode	 $f = 11,88 \text{ Hz} / D = 0,233\% / 1. \text{ Mode}$	 $f = 11,52 \text{ Hz} / D = 0,34\% / 1. \text{ Mode}$
2. Mode	 $f = 26,36 \text{ Hz} / D = 0,10\% / 2. \text{ Mode}$	 $f = 25,24 \text{ Hz} / D = 0,941\% / 3. \text{ Mode}$
3. Mode	 $f = 50,61 \text{ Hz} / D = 0,83\% / 3. \text{ Mode}$	 $f = 48,29 \text{ Hz} / D = 0,775\% / 3. \text{ Mode}$

Fig. 27.5 Direct comparison between eigenfrequencies, damping ratios and mode shapes for both accelerometer and 3D SLDV tests. Note the very noisy mode shape obtained for mode 2 in the accelerometer test. This accelerometer model is rated to work down to 2 Hz, therefore the source of the noise remains unknown

Numerical modal data from ANSYS was exported to FEMTools (DDS, Leuven, Belgium) for a cross-correlation between analytical and experimental data from both accelerometer and 3D SLDV tests. A detailed comparison of the first 10 modes shapes and a classification (clustering) of frequency sectors from all modes were established. Figure 27.10 shows an example of this comparison.

It can be seen that the first three modes of the FEM (Figs. 27.11 and 27.12) show significant deviations in the eigenfrequencies. Besides the reasons stated earlier, spatial resolution has also an impact in this analysis. The assignment of the mode shapes between the EMA and the FE model was visually adjusted because many more modes were extracted by the FE solver. This numerical model with a deviation of less than 5% of the natural frequencies after mode 4, forms a very good basis for the simulation of certain damage situation in the railway beam.

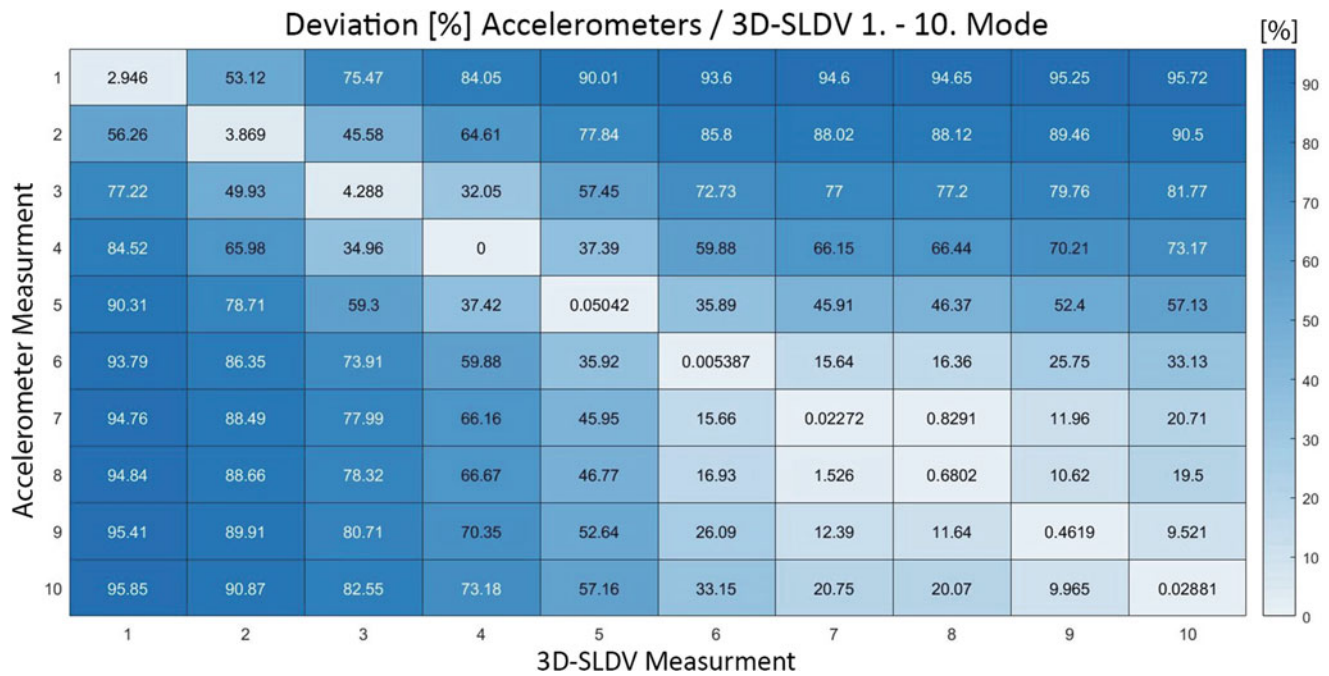


Fig. 27.6 NFD matrix between accelerometer and 3D SLDV tests. Large deviations are observed in modes 1 to 3

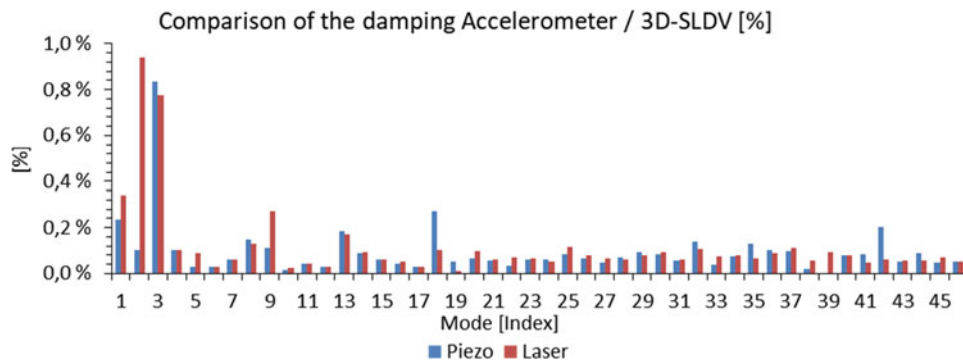


Fig. 27.7 Modal damping ratios comparison between accelerometer and 3D SLDV tests

27.6 Damages Sensitivity Study

According to the experience of the cooperation partner in this project, most of cracks take place in the beam’s upper flanges. One of the aims of this project is to determine whether such damages can be dynamically detected. Due to practical reasons, it is not possible to cause physical damages to the railway beam sections in laboratory scale.

Damages can be described as changes in a healthy system. This can be simulated by applying an external masses and measuring the changes in selected sensitive areas. Numerical and experimental data from this “new” system is to be collected and correlated. Mode shapes are observed and sensitive points are determined in the upper flange. The damages simulation focuses exclusively on the upper flange in this study Fig. 27.13 shows the relationship between DOF sensitivity and mode shape.

To verify the selected sensitive points on the beam, damages were simulated with an added 40 kg mass placed at the top of the upper flange of the beam, on top of DOF 6. Changes in the dynamic parameters are expected (Fig. 27.14).

The investigation of the measuring points follows the cluster of Table 27.2 and the spatial directions X and Y seen in Fig. 27.2. As an example of this analysis, Fig. 27.15 shows the measured FRFs for DOFs 2Y, 4Y and 6Y, with and without mass loading for a Y axis orientation. DOF 6X was set as reference for all FRFs. DOF 2Y presents a higher sensitivity than DOFs 4Y and 6Y.

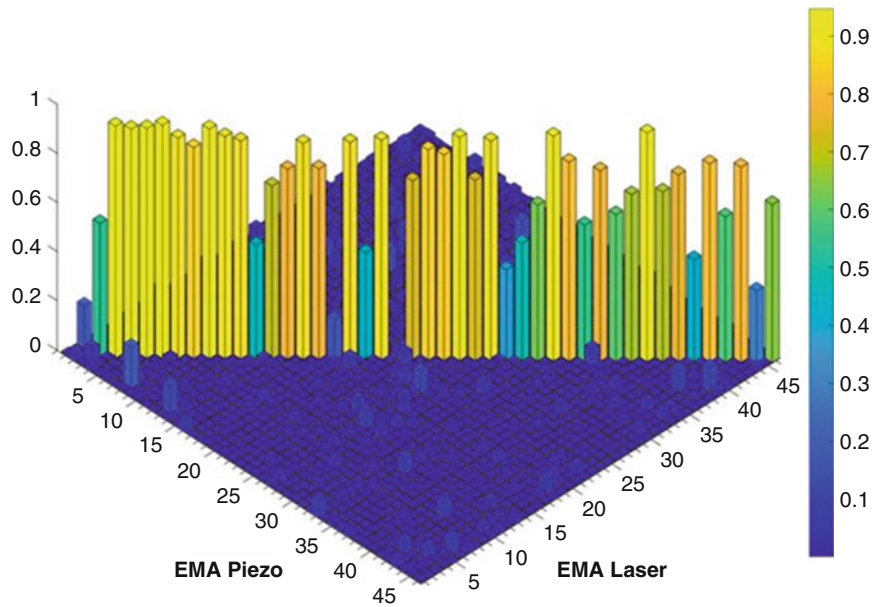


Fig. 27.8 Cross-correlation MAC matrix between accelerometer and 3D SLDV measurements. Low frequency mode pairs 1 and 2 appear poorly correlated

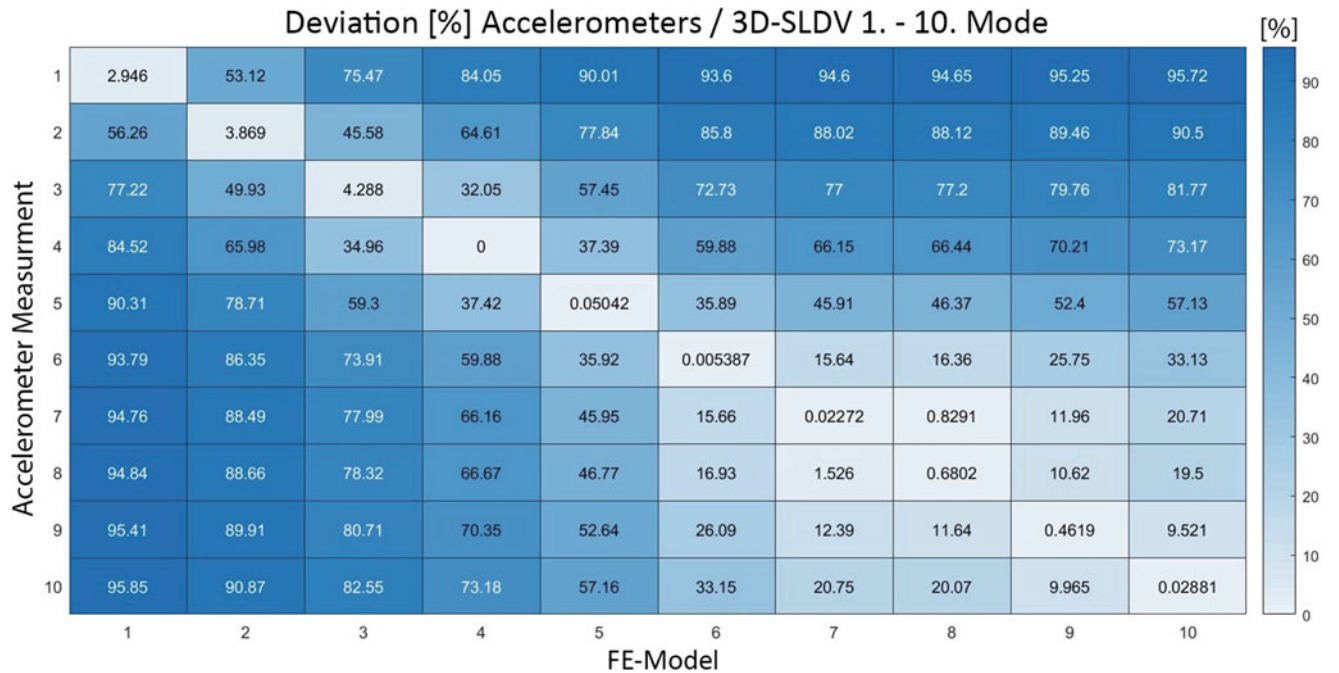


Fig. 27.9 NFD matrix accelerometer and the FE model

In another example, FRFs for DOFs 2X, 4X and 6X present noise all over the spectrum. Mode 5 is increases its amplitude in the loaded case for DOFs 2X and 4X (Fig. 27.16).

The effect of the mass application for the respective displacement, damping or the increase of eigenfrequency amplitudes depends on the associated mode shape and in which region of the upper flange the damage occurs. It is impossible to obtain a uniform statement for all natural frequencies and their peculiarities, because the reaction of each mode is independent of the mode shape.

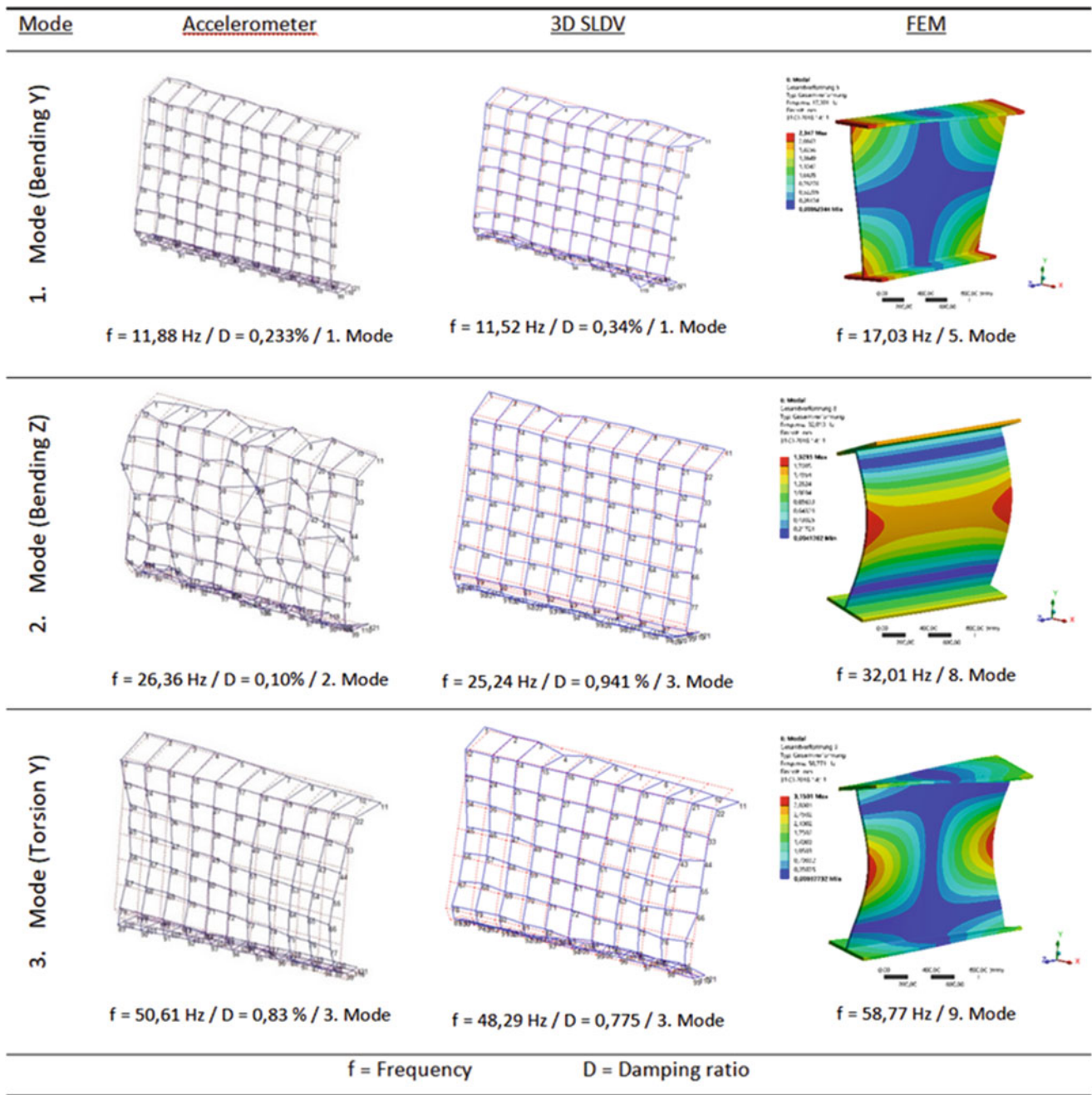


Fig. 27.10 Example of the visual correlation between experimental and numerical mode shapes. Only the three first modes are shown here as an example

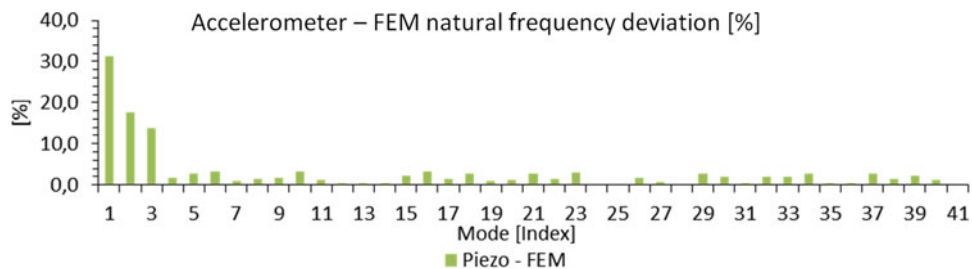


Fig. 27.11 Plot of the relative deviation in eigenfrequencies between accelerometer test and FE model. Note how the highest deviation percentages take place in the first three modes, shown in Table 27.3

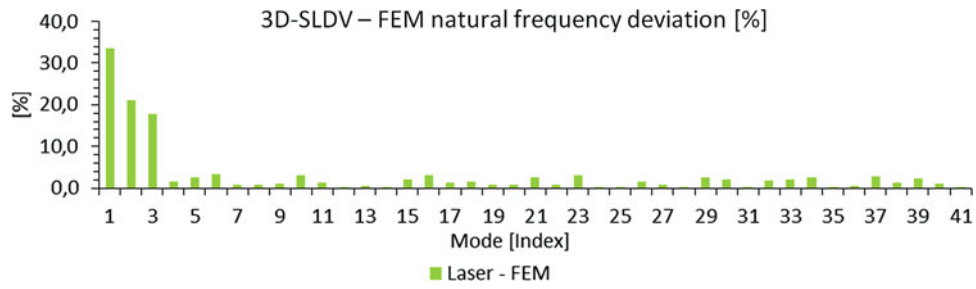


Fig. 27.12 Plot of the relative deviation in eigenfrequencies between 3D SLDV test and FE model. Note how the highest deviation percentages take place in the first three modes, shown in Table 27.3

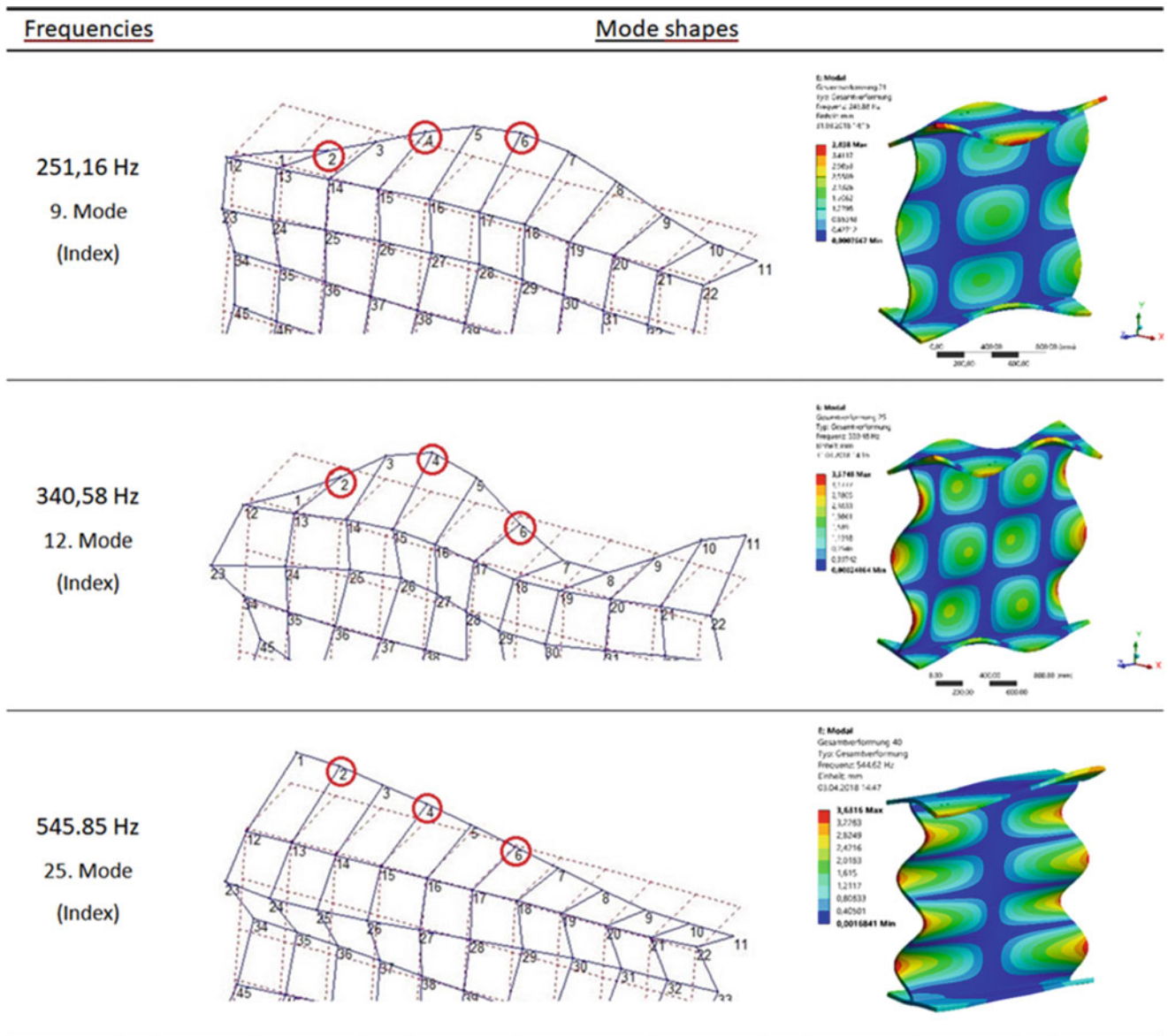


Fig. 27.13 DOF sensitivity for modes 9, 12 and 25. For example, DOF 4Y falls in a node line at mode 9 and thus, is insensitive to this frequency

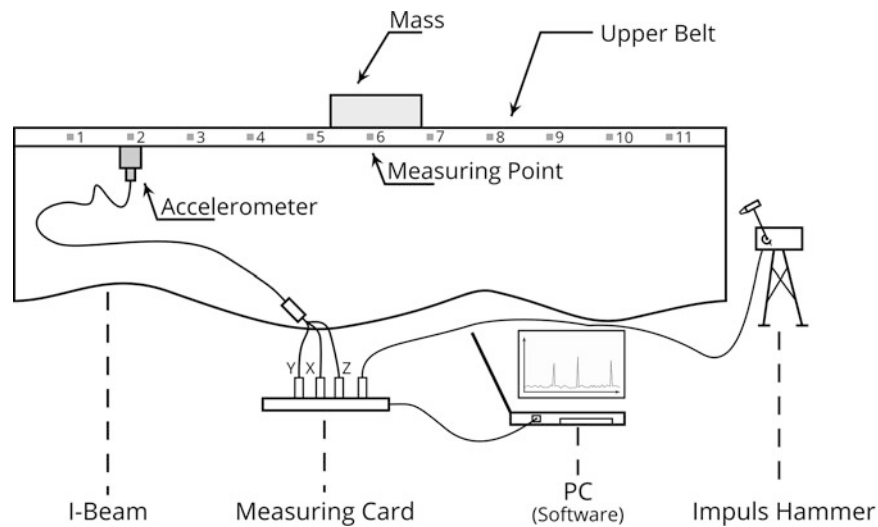


Fig. 27.14 Scheme for the damage detection test setup. Note the addition of the 40 kg mass on top of DOF 6 in this case

Table 27.2 Classification of the modes according to the previously defined frequency ranges (clusters)

Cluster	Bereich	Description
Low frequency modes	10–185 Hz	Vibration area on the web (6 modes)
Medium frequency modes	251–380 Hz	Vibration range on the web and upper flange (6 modes)
High frequency modes	591–733 Hz	Local modes in the web and upper flange (6 modes)

Different damage scenarios can be simulated with a validated FE model of the railway beam section. The aim of the following examination is to determine whether it is possible to detect a crack based by observing eigenfrequency shifts. Four crack dimensional parameters (length, depth, position and width), shown in Table 27.3 and drawn on Fig. 27.17, were correlated with frequency shifts. The obtained eigenfrequencies extracted from the damage simulation were then compared with the natural frequencies of the original FE model. A positive frequency deviation means a reduction in the system stiffness. Several observations can be found in this study.

In the examination of the crack width (ΔW), it can be seen that a width of 5 mm causes the highest frequency deviation (2.04 Hz). The highest natural frequency difference between the three differently simulated crack widths are between the widths of 1 mm and 5 mm and is 0.15 Hz. These results suggest that it is also possible to detect frequency shifts for cracks of less than 1 mm width.

Crack depth (ΔY) seems to be an insensitive parameter in the study if the crack is not fully developed along the flange. A fully developed crack shows significant deviations, of up to 17 Hz, but nevertheless deviations are much lower for a 15 mm crack (2 Hz). No clear shifts are detected for less than 15 mm deep cracks.

The investigations of the crack position (ΔZ) in this railway beam section show this parameter's sensitiveness. Eigenfrequencies are clearly dependent on the position of the crack, and shapes are accordingly influenced. A crack positioned at 230 mm shows only minimal differences because this position is a node line, therefore, there is no significant motion at the cracked area. A crack in the middle of the upper flange at DOF 6 (1050 mm) shows a noticeable shift of the eigenfrequencies at mode 28 (about 360 Hz). The third position at 630 mm (DOF 4) has almost no effect on the lower eigenfrequencies, but higher frequency peaks appear altered. The maximum eigenfrequency deviation at this position is of 20.68 Hz (mode 59). Generally, for all three positions it can be seen that the shifts of the natural frequencies are dependent on the mode shape. At higher frequency ranges, local longitudinal modes appear in the upper Flange, so that it is possible to recognize damages more easily in these ranges.

The longer a crack propagates transversally in the upper flange (ΔX), the larger the shift of natural frequencies is. All simulation variants show how modes 32 (422.89 Hz) and 35 (469.34 Hz) have the highest sensitivity to this parameter (Fig. 27.18). Considering the shapes of both modes 32 and 35, it can be seen that the web vibration dominates with its oscillating shape, but the local motion shape of the upper flange counteracts the elastic deformation. A defect in the upper flange counteracts the web motion and the entire system stiffness is altered. Out of this insight it can be seen why there is an increased sensitivity of the two modes 32 and 35 and the natural frequencies of both shifts.

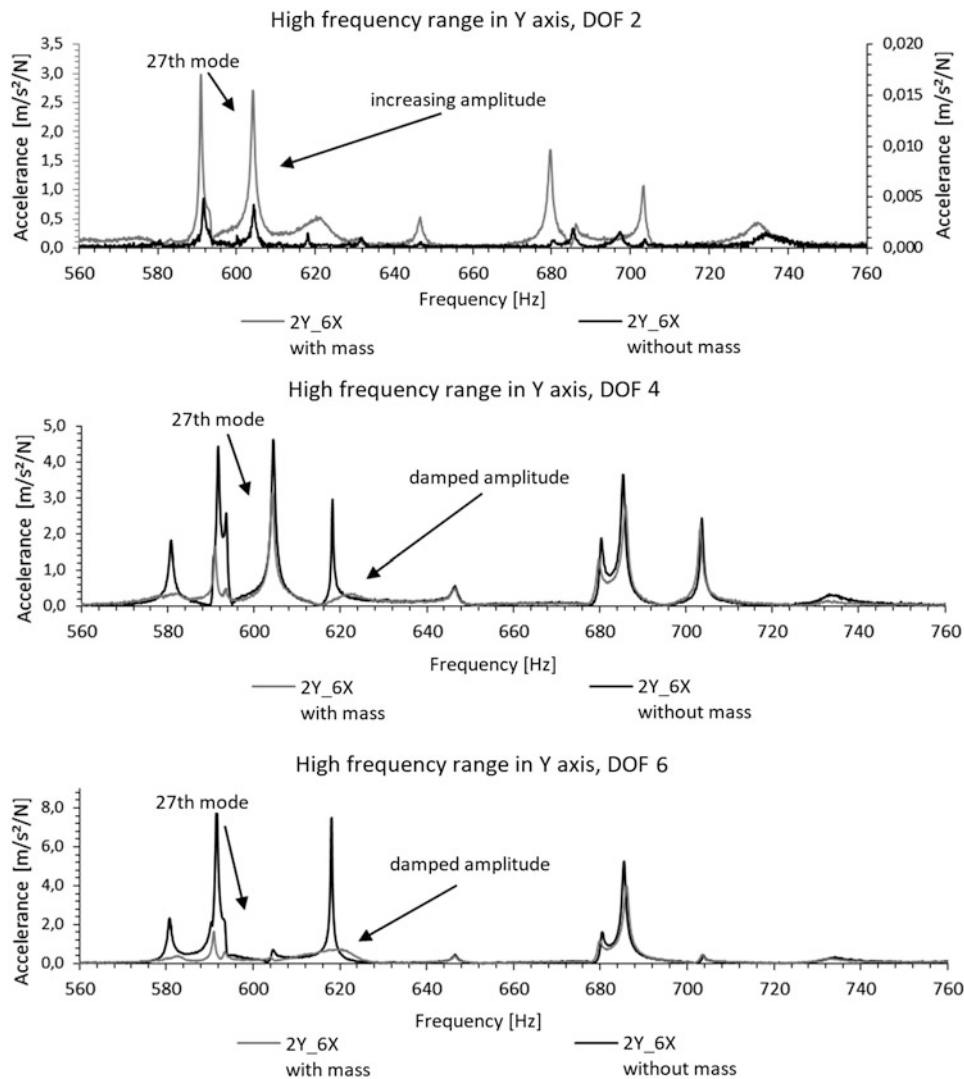


Fig. 27.15 FRFs for loaded and unloaded cases between DOFs 2Y and 6X (top), 4Y and 6X (middle) and 6Y and 6X (bottom), respectively. Large changes are observed in frequency ranges below 660 Hz

27.7 Conclusion

In conclusion, this research project sets the first steps in a larger and longer cooperation project. The present feasibility study includes the vibroacoustic detection of damages to the railway beam section in a laboratory scale and sets the starting point for the ongoing development of a measurement system. The pitfalls of these procedures have been identified in the measurement and cross-correlation phases. A general idea to the damage sensitivities of the studied system has been laid out, and will provide a good insight when dealing with real, 12 m long runway beams.

A working hypothesis is that the mass loading in the middle of the upper flange shows brings significant changes in the system. Figure 27.19 describes how local modes are modified by the mass loading.

Furthermore, some natural frequencies and their damping are shifted and these changes are dependent on the mode shape of the respective mode. Therefore, a sweeping statement is difficult to derive from this investigation because there is a clear dependency between damaged area, frequency shifts and mode shapes.

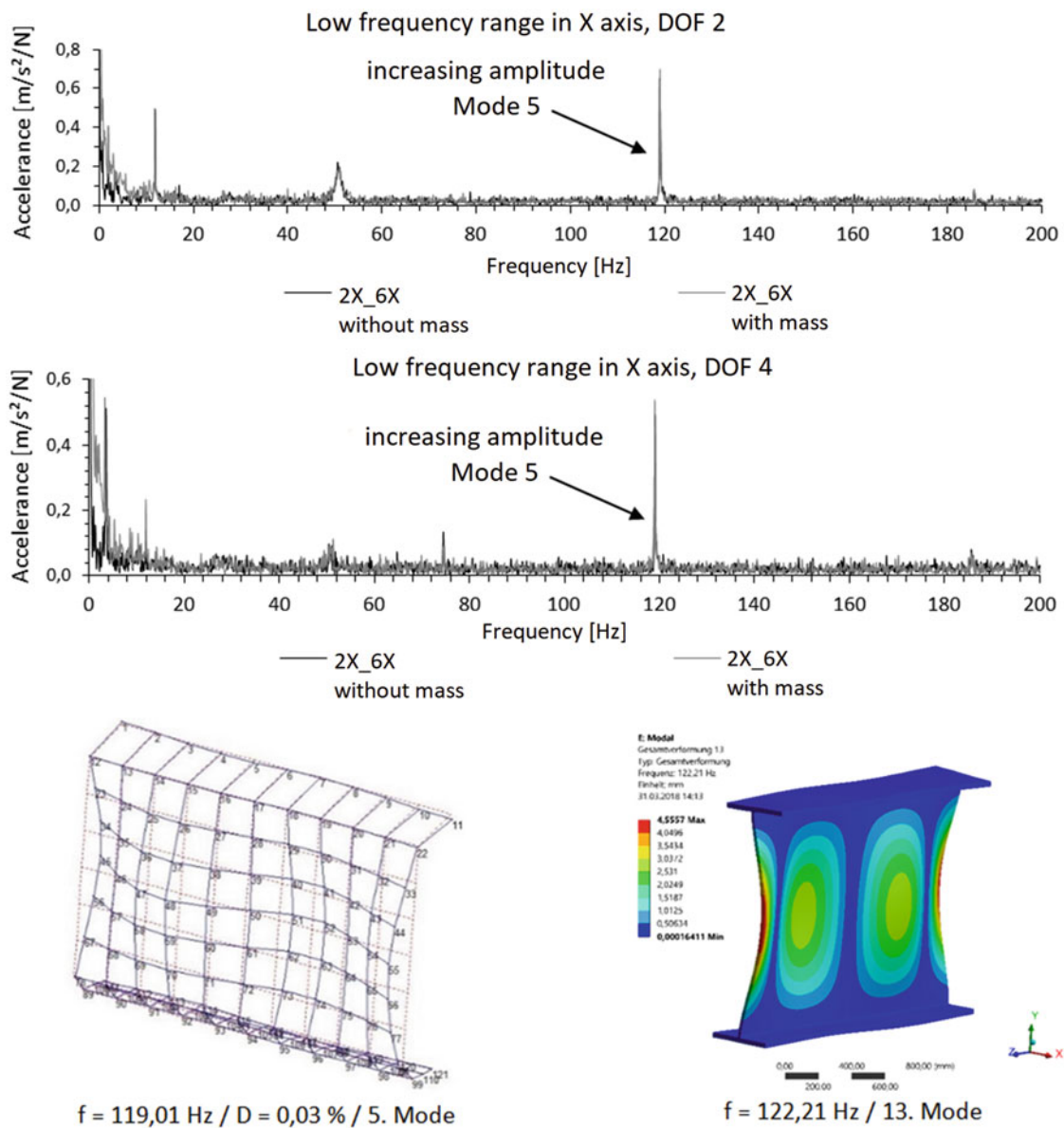


Fig. 27.16 FRFs between DOFs 2X and 6X (top), 4X and 6X (middle) for loaded and unloaded cases. A large increase in amplitude is observed for both cases for mode 5. This mode shape is represented at the bottom of the figure

Table 27.3 Starting parameter values for the damages simulation

Crack length (X)	Crack depth (Y)	Crack position (Z)	Crack width (W)
100 mm	15 mm	1050 mm (measured from the left side)	1 mm

27.8 Further Work

This feasibility study shows that it is possible to detect crack damages on a railway beam laboratory model by studying its dynamic structural behavior. In order to develop a robust structural health monitoring system is necessary to gain further insight in the following areas:

- Expanding this study to installed railway beams, with the corresponding challenges this implies. These beams are originally 12 m long and techniques such as roving accelerometer can be challenging to apply.
- Extension of the FE model to determine sensitive measurement points
- To document in-situ detection of existing cracks and their location and dimensions

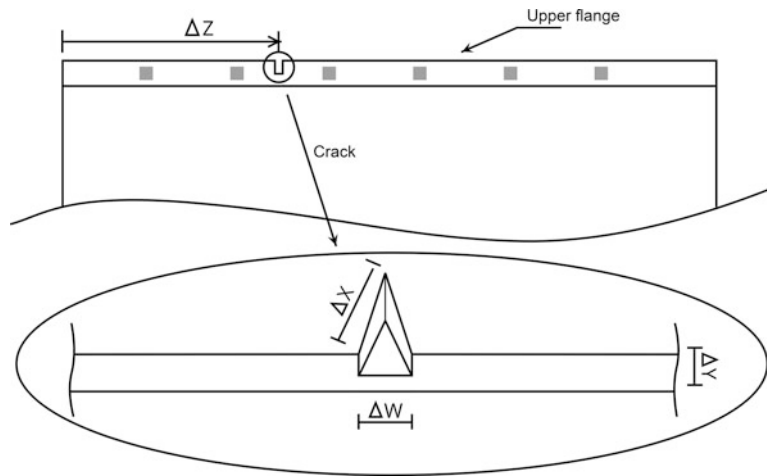


Fig. 27.17 Scheme of the crack parameter variables for the sensitivity study

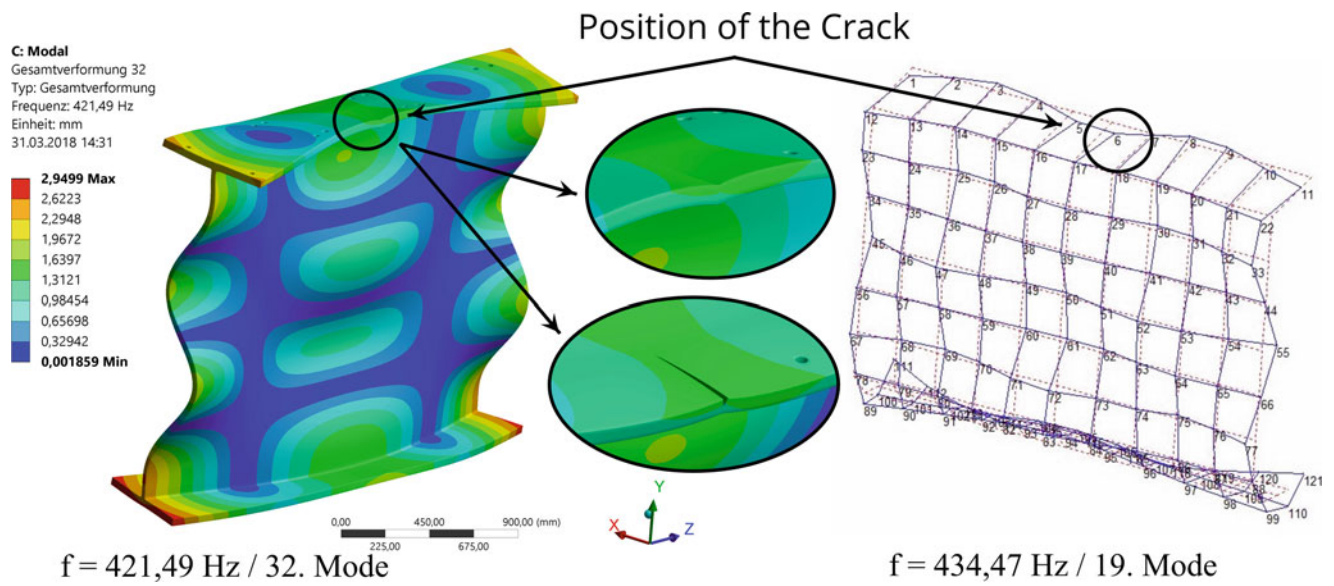


Fig. 27.18 The graphic shows the numerical damaged mode shape (crack at DOF 6) and the unloaded beam for the significant mode 32

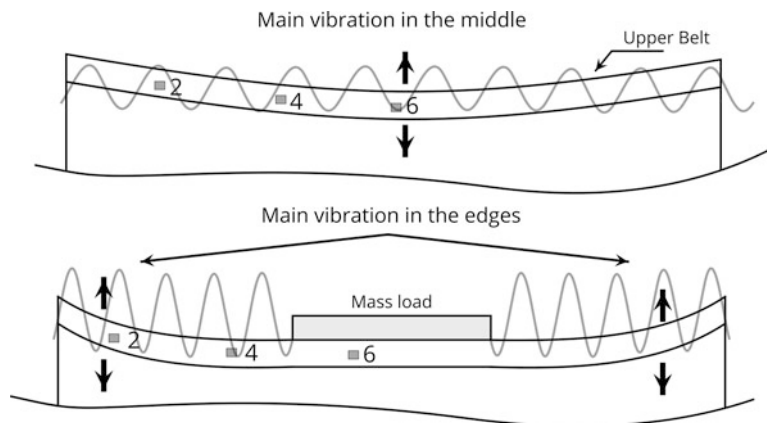


Fig. 27.19 Hypothetical diagram of how local modes in the upper flange are modified by the mass loading

A concept of a crane beam catalog is considered. Each railway beam has its own “identity” in terms of geometry, material parameters and boundary conditions (attachment, support, etc.). Thus, it is not sufficient to verify a beam and to extrapolate the acquired dynamic structural behavior to all other beams. It is necessary to create a feature recognition method on individual parameters and at the same time to compare them with a knowledge database in order to verify the condition of a particular beam.

Acknowledgements The authors would like to express their gratitude to Mr. Torsten Pohlen and Mr. Lars Koczius from ArcelorMittal Eisenhüttenstadt GmbH for their support in the logistics of this project.

References

1. Schlütter, B.: Studieren in Wildau—Ein Hochschul-Porträt in Bildern, MediaService Verlag Bernd Schlütter (2013)
2. Zukunftsagentur Brandenburg: Brandenburgs Schwergewicht—Masterplan für das Cluster Metall Brandenburg, Clustermanagement Cluster Metall Brandenburg (2014)
3. Munck Cranes Inc.: Overhead crane components, online resource. <http://www.munckcranes.com/overheadcranecomponents.asp>. Accessed 20th Oct 2018



Chapter 28

Validation of Automatic Modal Parameter Estimator on a Car Body-in-White

N. Gioia, Pieter-Jan Daems, and J. Helsen

Abstract Noise, vibration and harshness (NVH) problems are critical issues to be tackled by automotive industry to ensure comfort of people. The key role of this problem is played by the susceptibility of the structure to vibrations. Therefore, design values such as the modal parameters (i.e. eigenfrequencies, damping ratios, mode shapes and modal scaling factors) are essential and their experimental validation is of high interest. At this purpose, both Experimental and Operational Modal analysis (EMA and OMA) represent a powerful approach. Previous works have investigated and implemented a completely automated OMA technique for continuously tracking the modes of machines under normal operating conditions. In this work the automatic modal parameter estimator is used to perform automated experimental modal analysis on data acquired from a car body-in-white excited by means of multiple shakers. Fully automated modal analysis is performed with special focus on damping value and mode shape validation. The results obtained with the manual and automatic modal parameter estimators are compared in order to show the validity and performance of the implemented method. Modal parameters estimation is based on the state-of-the-art pLSCF algorithm. To make it suitable for continuous analysis, the algorithm is improved by eliminating all the required human interactions.

Keywords Automatic operational modal analysis · Car body-in-white · Automatic experimental modal analysis · Mode shapes validation · Damping values validation

28.1 Introduction

In machine industry, noise, vibration and harshness (NVH) problems are critical design issues. The key role of this problem is played by the susceptibility of the structure to vibrations. Therefore, design values such as the modal parameters (i.e. eigenfrequencies, damping ratios, mode shapes and modal scaling factors) are fundamental. In initial design stages, the vibration response of the structure is simulated using simplified models. The further the design process evolves, the more complex these models become, e.g. finite element and multibody simulations. Although industry utilize sophisticated modeling tools that already allow an optimized configuration at this stage, the experimental verification of the design values is fundamental for model validation and for guaranteeing safety and reliability of the structure[1]. Since damping and boundary conditions depend on the vibrations amplitude and the modal parameters depend on the (rotating) speed of the structure or the parts, it is important to experimentally verify the design values in normal operating conditions, i.e. around the operating point. The needed validation can be performed both in laboratory conditions or real operating conditions. Experimental and Operational Modal Analysis (EMA and OMA) represent powerful approaches to identify systems with few inputs and hundreds of outputs. EMA is used in case of laboratory tests, when both the vibration response of the structure and the excitation source are measurable. On the other hand OMA is used for identifying a structure excited by (unmeasured) natural and operational forces. The interest in having an automatic operational modal analysis algorithm is due to the possibility of extracting modal parameters from operating machines. The advantage of considering operating machines is the fact that the system is loaded in a representative way. Preferably long-term measurements are used that encompass the different loading conditions the system is subjected to during its lifetime. This requires the use of automatic algorithms able to process the data continuously and autonomously. Not only for these operational modal analysis cases the use of automated modal analysis tools is interesting. Also for experimental modal analysis automation has the advantages of increasing repetitiveness of the analysis. In previous researches [2, 3], we implemented a completely automatic modal parameter estimator coupled with autonomous pre- and post-processing methodologies (signal validation/classification, harmonics removal and modal parameter tracking). The

N. Gioia (✉) · P.-J. Daems · J. Helsen
Vrije Universiteit Brussel (VUB), Brussel, Belgium
e-mail: ngioia@vub.be

complete chain has been used to process data acquired on a wind turbine drivetrain. In this work the automatic modal parameter estimator is used to perform automated experimental modal analysis on data acquired from a car body-in-white excited by means of multiple shakers. The choice of the scope of the analysis is linked to several reasons. First of all, experimental modal analysis is of high interest in automotive industry to solve NVH problems and ensure safe and comfortable cars. The availability of an automatic tool to process experimental data, represents a significant advantage to increase the repeatability of the tests. Secondly, the processed data, have been already analyzed with a commercial manual algorithm (*TestLab*). The knowledge of the modal parameters of the system, allows to focus on damping values and mode shapes validation. In this research indeed, the results obtained with the manual and automatic modal parameter estimators are compared in order to show the validity and performance of the implemented automatic modal analysis method. For this research, the so called *polyreference least-squares complex frequency-domain* estimator has been used as starting algorithm [4].

28.2 Theoretical Background

The Poly-reference Least-Square Complex Frequency-Domain (p-LSCF) method consists in a frequency-domain modal analysis method that requires as primary data the Frequency Response Functions (FRFs) and identifies a right matrix-fraction model:

$$[H(\omega)] = [B(\omega)][A(\omega)]^{-1} \quad (28.1)$$

where $H(\omega) \in \mathbb{C}^{1 \times m}$ is the FRF matrix containing the FRFs between the m inputs and the l outputs; $B(\omega) \in \mathbb{C}^{1 \times m}$ is the numerator matrix polynomial and $A(\omega) \in \mathbb{C}^{m \times m}$ is the denominator matrix polynomial. Each row of the matrix-fraction model can be written as:

$$\forall o = 1, 2, \dots, l \quad \langle H_o(\omega) \rangle = \langle B_o(\omega) \rangle [A(\omega)]^{-1} \quad (28.2)$$

The numerator row-vector polynomial of output O and the denominator matrix polynomial are defined as:

$$\langle B_o(\omega) \rangle = \sum_{r=0}^p \Omega_r(\omega) \langle \beta_{or} \rangle \quad (28.3)$$

$$[A(\omega)] = \sum_{r=0}^p \Omega_r(\omega) [\alpha_r] \quad (28.4)$$

where $\Omega_r(\omega)$ are the polynomial basis functions and p is the polynomial order. In the LSCF method, a z-domain model is used (i.e. a frequency domain model that is derived from a discrete-time model) and, by consequence, the basis functions are:

$$\Omega_r = e^{j\omega \Delta t r} \quad (28.5)$$

with Δt the sampling time.

The polynomial coefficients $\beta_{or} \in \mathbb{R}^{1 \times m}$ and $\alpha_{or} \in \mathbb{R}^{m \times m}$ can be grouped in matrices. The FRF model of Eq. (28.1) can be then written as a function of the coefficients $H(\omega_k, \Theta)$ [4]. In order to find all the unknown model coefficients based on the measured FRFs a non-linear least-squares (NLS) equation error must be minimized. To do so, the equation errors of all the outputs and all frequency lines are combined in a scalar cost function that is minimized by putting its derivatives with respect to the unknown model coefficients equal to zero. Theoretically a complete right-matrix model can be obtained by computing the numerator coefficients solving all the equation deriving from the minimization of the cost function. However, a more practical approach is available. Generally, in modal analysis, one is not only interested in a good model as such, but more important in the accuracy of the estimated modal parameters. When trying to estimate from real data, is then a good approach to over-specify the model order, trying to fit high-order models that contain more modes that the one present in the data. Afterwards, the use of the stabilization diagram can help in separating the physical poles from the spurious ones.

On the stabilization diagram, the poles are shown for increasing model order, and their stability is labeled comparing the poles at one model order with one at a one-order-lower. The use of the stabilization diagram, solves the problem of the a-priori definition of the model order of the system that has to be identified. Once the stable poles and the corresponding

participation factors are selected on the stabilization diagram by the analyst, their value are used in the so-called pole-residue model (Eq. (28.6)) to find the mode shapes:

$$[H(\omega)] = \sum_{i=1}^n \frac{\{v_i\}\langle l_i^T \rangle}{j\omega - \lambda_i} + \frac{\{v_i^*\}\langle l_i^H \rangle}{j\omega - \lambda_i^*} - \frac{LR}{\omega^2} + UR \quad (28.6)$$

where n is the number of modes; \bullet^* is the complex conjugate of a matrix; $v_i \in \mathbb{C}^l$ are the mode shapes; $\langle l_i^T \rangle \in \mathbb{C}^m$ are the modal participation factors and λ_i are the poles, which occur in complex-conjugate pairs and are related to the eigenfrequencies ω_i and damping ratios ξ_i as follows:

$$\lambda_i, \lambda_i^* = -\xi_i \omega_i \pm j \sqrt{1 - \xi_i^2} \omega_i \quad (28.7)$$

$LR, UR \in \mathbb{R}^{l \times m}$, introduced in Eq. (28.6) are respectively the lower residuals and upper residuals modelling the influence of the out-of-bands modes in the considered frequency band. In Eq. (28.6), the only unknown are then the mode shapes, the lower and upper residuals. They can be obtained by solving it in a linear least-square sense. This step is commonly called *least-squares frequency-domain* method.

28.3 Methodology

As stated in the previous section, the stabilization diagram is a powerful approach for avoiding the need of pre-defining the model order of the system. However, it requires the intervention of the analyst, that have to distinguish the stable poles from the spurious ones. To make the Poly-Reference Least-Square Frequency-Domain (p-LSFD) estimator automatic, the main algorithm-analyst interaction has been eliminated. Starting from the ideas investigated from other authors [5–7], the classical stabilization diagram [8] has been substituted with a clustering method that autonomously interprets the information collected in the stabilization diagram. In this work a clustering analysis has been used in order to group the poles showing stable characteristics (i.e. representative of the same mode). The physical modes have been then selected automatically exploiting statistical characteristics of the generated clusters. The advantage of the implemented methodology with respect to previous works [6–8] is the complete automation of the algorithm that selects the parameters required by clustering algorithm autonomously, based on some physical and statistical properties of the signal.

For the validation of the modal parameters estimator, FRFs generated during laboratory tests on a car body-in-white are used as input data. A shaker test was performed on the body-in-white with 2 fixed uniaxial excitation points and 52 triaxial measurement points. A schematic representation of the studied car body is shown in Fig. 28.1.

28.4 Results

The results obtained with *AutoMax*, are compared with the ones obtained with *TestLab*, in order to validate the implemented method. The analysis is performed in the frequency band of interest for the torsional mode of the car. Frequency and damping values have been normalized for confidentiality reasons. For both the frequency and damping values, a relative difference between the estimates obtained with *TestLab* and *AutoMax* is calculated as:

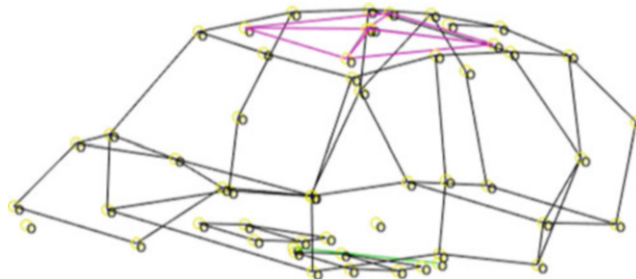


Fig. 28.1 Schematic view of the car and the sensors location

Table 28.1 Comparison of the results obtained with the two different approaches in terms of frequency and damping estimates

Mode number	Normalized frequency			Normalized damping		
	TestLab	AutoMax	Difference [%]	TestLab	AutoMax	Difference [%]
1	0.63	0.63	0.006	0.64	0.62	3.125
2	0.80	0.80	0.024	0.98	1.00	2.04
3	0.85	0.86	0.064	0.45	0.44	2.22
4	0.98	0.98	0.03	0.55	0.52	5.45
5	0.99	1.0	0.09	0.57	0.54	5.26

The values of both the quantities are normalized

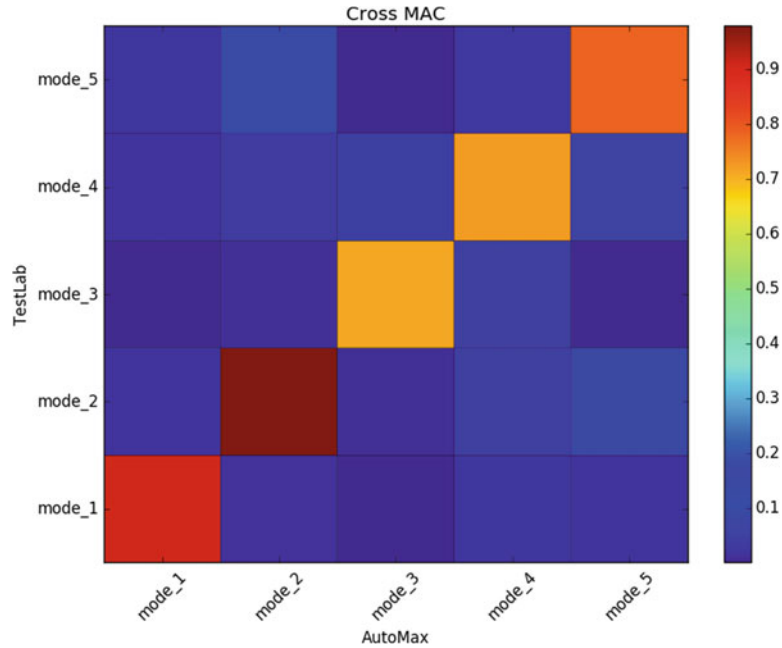


Fig. 28.2 Cross MAC between the mode shapes obtained with TestLab and the one obtained with the new AutoMax. Data values are normalized to be between 0 and 1 for confidentiality reasons

$$Diff_{rel}(x, x_{ref}) = \frac{|x - x_{ref}|}{x_{ref}} \quad (28.8)$$

where x is the frequency or damping estimates obtained with *AutoMax* and x_{ref} the frequency or damping estimates obtained with *TestLab*, used as reference values.

The comparison between frequency and damping (normalized) values is shown in Table 28.1. To validate also the mode shapes, the Cross Modal Assurance Criterion is used [9]:

$$MAC(\{\psi\}_r, \{\psi\}_s) = \frac{|\{\psi\}_r^H \{\psi\}_s|^2}{(\{\psi\}_r^H \{\psi\}_r)(\{\psi\}_s^H \{\psi\}_s)} \quad (28.9)$$

where $\{\psi\}_r$ with $r = 1, \dots, n_{modes_1}$ is the mode shape vector of the set of modes obtained with *AutoMax*, $\{\psi\}_s$ with $s = 1, \dots, n_{modes_2}$ is the mode shape vector of the set of modes obtained with *TestLab*, H is the Hermitian transpose. The MAC matrix is based on the orthogonality conditions of the mode shapes, thus if $\{\psi\}_r$ and $\{\psi\}_r$ are estimates of the same physical mode shape, the modal assurance criterion should approach unity. If $\{\psi\}_r$ and $\{\psi\}_r$ are estimates of the different physical mode shape, the modal assurance criterion should be low or approaching zero. The results of the comparison of the mode shapes is shown in Fig. 28.2. The obtained mode shapes are shown in Figs. 28.3, 28.4, 28.5, 28.6, and 28.7.

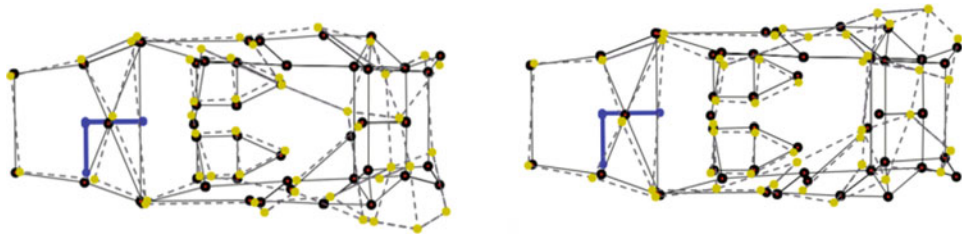


Fig. 28.3 Mode 1: freq = 0.63, damp = 0.62

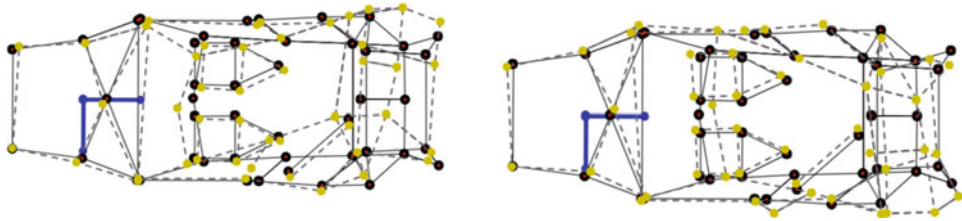


Fig. 28.4 Mode 2: freq = 0.80, damp = 1.00

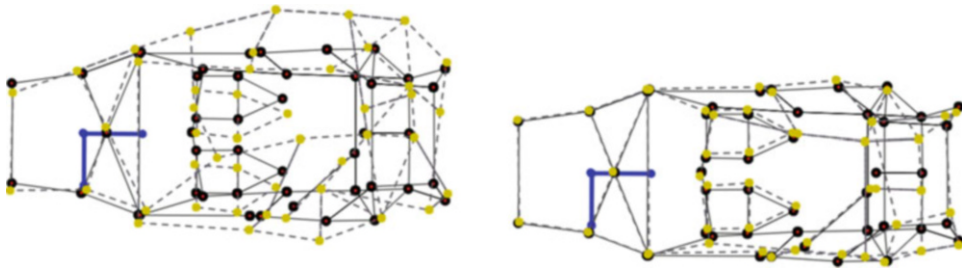


Fig. 28.5 Mode 3: freq = 0.86, damp = 0.44

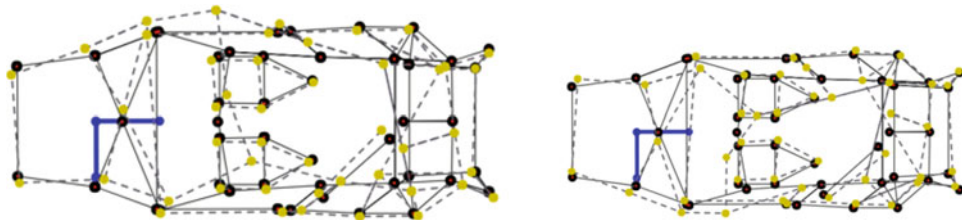


Fig. 28.6 Mode 4: freq = 0.98, damp = 0.52

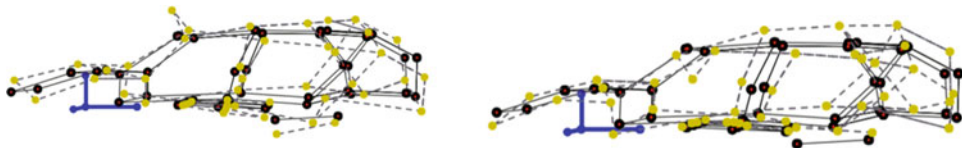


Fig. 28.7 Mode 5: freq = 1.00, damp = 0.54

28.5 Conclusions

During this research the experimental validation of the modal parameters of a car body-in-white has been repeated with a new approach (*AutoMax*). The latter is an algorithm that performs experimental and operational modal analysis autonomously, i.e. without requiring the action of the analyst. The need of this tool is justified by several reasons, such as the elimination of the analyst expertise as aleatory variable, reduction of data processing time, increase of repeatability of the analysis and analysis of machines in real operating conditions. The automatic modal parameters estimator has already been presented in previous work, with the scope of automatically processing data coming from an operating wind turbine drivetrain.

During this work, the method implemented has been validated by means of a comparison of the estimates obtained with *AutoMax* and the ones obtained with *TestLab*, used as solid validated benchmark. The obtained results show the match of the estimates obtained with the two different modal analysis tool. In case of resonance frequencies, the maximum error is 0.09%, while in case of damping ratios the maximum error increases, reaching the 5.45%. A difference in the estimate values was expected, since the analysis performed is not exactly the same, due to some variable that has to be chosen, e.g. the maximum model order for the analysis, the model order at which the poles have been selected on the stabilization diagram from the analyst or algorithm. However, the error is limited, and it is not higher than the error that could have been obtained by manually repeating the analysis twice. Concerning the mode shapes, the cross MAC has been used to compare them in a quantitative way. Also in this case results show a good match of the estimates, having MAC values that are above 0.7 for the same modes and lower than 0.2 for different ones. The conclusions addressed for the damping estimates still hold true for the mode shapes. Moreover the visualization of the mode shapes obtained with *AutoMax* confirm that the mode shapes are the torsional modes that were expected.

Acknowledgements SB PhD fellow at FWO.

This research was performed in the framework of the ongoing research project HYMOP funded by VLAIO Vlaanderen, furthermore we want to acknowledge our partners in acquiring the data.

References

1. Reynders, E.: System identification methods for (operational) modal analysis: review and comparison. *Arch. Comput. Methods Eng.* **19**(1), 51–124 (2012)
2. Gioia, N., Daems, P.J., Peeters, C., El-Kafafy, M., Guillaume, P., Helsen, J.: Influence of the harmonics on the modal behavior of wind turbine drivetrains. In: 2018 International Modal Analysis Conference (IMAC), Orlando, February (2018)
3. Gioia, N., Peeters, C., Daems, P.J., Guillaume, P., Helsen, J.: Dealing with harmonics in continuous modal analysis. In: Proceedings ISMA (2018)
4. Peeters, B., Van der Auweraer, H., Guillaume, P., Leuridan, J.: The PolyMAX frequency-domain method: a new standard for modal parameter estimation? *Shock Vib.* **11**(3, 4), 395–409 (2004)
5. Magalhaes, F., Cunha, A.: Explaining operational modal analysis with the data from an arch bridge. *Mech. Syst. Signal Process.* **25**(5), 1431–1450 (2011)
6. Devriendt, C., El-kafafy, M., Sitter, G.D., Guillaume, P.: Continuous dynamic monitoring of an offshore wind turbine on a monopile foundation. In: International Conference on Noise and Vibration Engineering (ISMA), September 2012, Leuven (2012)
7. Reynders, E., Houbrechts, J., Roeck, G.D.: Fully automated (operational) modal analysis. *Mech. Syst. Signal Process.* **29**, 228–250 (2012)
8. Van der Auweraer, H., Peeters, B.: Discriminating physical poles from mathematical poles in high order systems: use and automation of the stabilization diagram. In: Proceedings of IMTC, 2004 the IEEE Instrumentation and Measurements Technology Conference, Como (2014)
9. Heylen, W., Lammens, S., Sas, P.: Modal Analysis Theory and Testing. Katholieke Universiteit Leuven, Departement Werktuigkunde, Leuven (1997)



Chapter 29

Modal Analysis of Rotating Tires in Stationary and Rotating Frames of Reference

Mohammad Albakri and Pablo Tarazaga

Abstract Design and development of tires require accurate characterization of their dynamic response. For this purpose, Experimental Modal Analysis (EMA) techniques have been heavily utilized. However, as the focus shifts from stationary to rotating tires, testing solutions become limited and more challenging. Conventionally, cleat excitation with force measurements on the fixed spindle has been the standard approach for testing tires in rotation. However, the limited control on the input excitation has hindered the characterization of rotating tires, especially at high frequency.

In this work, EMA of rotating tires mounted on a free-spindle rotating modal rig is investigated. Testing is conducted in stationary and rotating frames-of-reference. In the former configuration, electrodynamic shakers attached to the free-spindle are used to excite the tire and a Scanning Laser Doppler Vibrometer (SLDV) is used to measure the response at the sidewall. For the later frame-of-reference, piezoelectric actuators mounted inside the rotating tire are utilized for excitation, whereas accelerometers mounted on the sidewall are used for response measurement. The capabilities and limitations of both testing configurations are investigated at several rotational speeds. The effects of contact patch excitation and the frequency range of interest on EMA of rotating tires are also addressed.

Keywords Modal analysis · Rotating tire · Piezoelectric excitation · Contact patch excitation

29.1 Introduction

Driven by ride comfort, noise reduction, and performance enhancement requirements, the characterization of a tire's dynamic response has been an essential component in tire development. The complex nature of tires, in terms of its construction, material characteristics, and the interaction between different components, adds to the complexity of the problem. While high-fidelity numerical models are widely adopted to predict a tires' dynamic response, experimental validation of such models remains necessary. For this purpose, Experimental Modal Analysis (EMA) along with Operational Modal Analysis (OMA) techniques have been heavily utilized to characterize tires at different operating conditions, including tire pressure, loading, and rotational speed.

The effects of tires on ride quality have been the focus of several tire manufacturers and research groups. Scavuzzo et al. investigated the effects of tires' material, inflation pressure, rolling speed, and size on tires' performance [1]. They concluded that tire modes of vibrations, excited by tire-road interaction, strongly participate in vehicle vibration and affect ride quality. To investigate tire's modes of vibration, several modal testing techniques have been developed over the last few decades. Wheeler et al. studied the dynamic behavior of a non-rotating tire in the frequency range of 0–300 Hz [2]. They applied EMA with several excitation signals and used the Finite Element Method (FEM) to demonstrate and classify mode shapes. A similar study has been conducted by Kao et al. where EMA and FEM were utilized to study the dynamic response of loaded tires [3]. In these studies, shaker and hammer excitation were the only techniques used to excite the non-rotating tires. More recently, Ferhat and Tarazaga investigated the use of Macro Fiber Composite (MFC) piezoelectric actuators for tire excitation [4]. Although MFC actuators were found to provide a non-intrusive solution for tire excitation, multiple actuators were required to fully excite the tire due to its high material damping.

While the aforementioned efforts have been successful in testing non-rotating tires, the shift to a rotating configuration poses new challenges. Dorfi et al. presented one of the earliest studies in this field where they reported that tire rolling

M. Albakri (✉) · P. Tarazaga

Vibration, Adaptive Structures and Testing (VAST) Laboratory, Department of Mechanical Engineering, Virginia Tech, Blacksburg, VA, USA
e-mail: malbakri@vt.edu

strongly affects the forces measured at the spindle [5]. They also reported rolling-induced material softening, which leads to a reduction in the identified natural frequencies of the rotating tire. Cleat excitation with force measurements on the fixed spindle has been the standard approach for testing tires in rotation [6–8]. This technique provides a limited control on the input excitation. Furthermore, with this excitation technique the input force acting on the tire is unknown, and thus, OMA techniques are commonly adopted to analyze the measured response.

In this work, EMA techniques for rotating tires are investigated. A free-spindle rotating modal rig is used for this study. Unlike fixed-spindle rigs, the free spindle allows input excitation to be directly applied at the spindle itself, which provides more control on the excitation force. The first testing configuration investigated in this work is carried out in a stationary frame-of-reference. An electrodynamic shaker attached to the free-spindle is used to excite the tire, whereas Scanning Laser Doppler Vibrometer (SLDV) is used to measure the response at the sidewall. The second configuration addressed in this work is carried out in a rotating frame-of-reference. MFC piezoelectric actuators mounted inside the rotating tire are used for excitation, whereas accelerometers mounted on the sidewall are used for response measurement. Several factors affecting EMA of rotating tires in these frames-of-reference, such as contact patch excitation and the frequency range of interest, are also investigated.

29.2 Experimental Setup

In this section, the two testing configurations corresponding to the two different frames-of-reference are introduced. Excitation and measurement solutions for each configuration are discussed in detail. All tests are carried out using a free spindle rotating modal rig provided by Hankook tires. Unlike fixed-spindle modal rigs, the rig used in this study allows the input excitation to be applied directly at the spindle itself using electrodynamic shakers. This, in turn, provides more control over the excitation force and its frequency content compared to conventional cleat excitation. While the details of the rotating modal rig used in this study cannot be included due to its proprietary nature, a schematic of its design is shown in Fig. 29.1. The spindle is attached to the structure using spring-like elements, which also provide the loading force to the tire.

29.2.1 Stationary Frame-of-Reference Experimental Setup

The first testing configuration investigated in this work is carried out in a stationary frame-of-reference. For this purpose, an electrodynamic shaker attached to the free-spindle, along the x -direction, is used to excite the tire, whereas a PSV400 SLDV is used to measure the velocity of the sidewall in all three directions. The shaker is driven with a chirp signal over the frequency range of 10–500 Hz and a load cell is used to measure the excitation force acting on the spindle. The tire being tested is an experimental slick tire, 225/45R17 size, provided by Hankook tire.

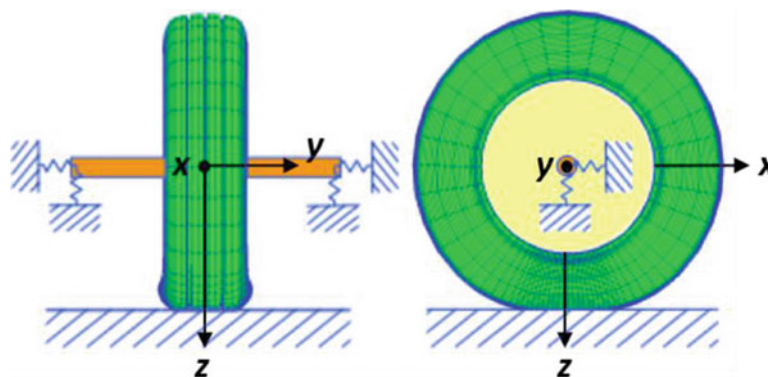


Fig. 29.1 Schematic of the rotating modal rig used in this study [9]

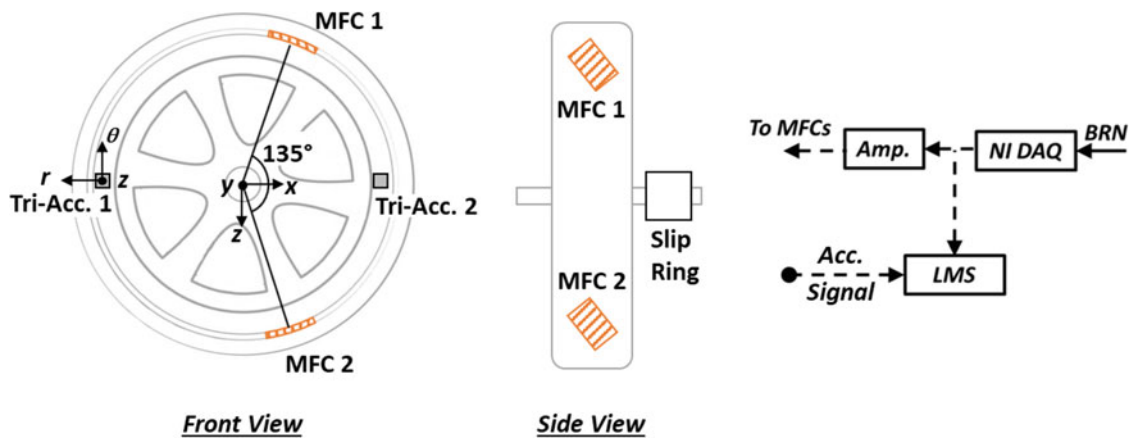


Fig. 29.2 Schematic of the experimental setup in a rotating frame-of-reference

29.2.2 Rotating Frame-of-Reference Experimental Setup

The second testing configuration considered in this study is carried out in a rotating frame-of reference. Figure 29.2 shows a schematic of the experimental setup used in this testing configuration. MFC piezoelectric actuators mounted inside the rotating tire are used for excitation. MFCs are accessed through a connector installed on the wheel. The response of the tire is measured using tri-axial accelerometers mounted on the tire's sidewall. All connections go through a slip ring that is mounted on the spindle, as shown in the figure. The MFC actuators are excited with a Binary Random Noise (BRN). This excitation signal is selected over pure random noise in order to fully utilize the actuation range of the MFC actuators [10]. Two uncorrelated BRN signals are generated using Matlab with an NI-9263 voltage output module. The signals are amplified to an amplitude of 450 V and sent to the MFC actuators through the slip ring. This signal is also used to trigger the LMS system used for data acquisition and post-processing. The same tire tested in the stationary frame-of-reference is used in this set of tests. Since two MFCs are used to excite the tire, uncorrelated BRN is adopted as the excitation signal, which allows defining transfer functions between the measured response and the excitation voltage applied to each of the two MFC actuators.

29.3 Results and Discussion

Experimental results for a rotating tire obtained in stationary and rotating frames-of-reference are presented in this section. The capabilities and limitations of both testing configurations are discussed. The effects of contact patch excitation and frequency range of interest are also addressed.

29.3.1 Rotating Frame-of-Reference

In a rotating frame-of-reference, excitation is provided by two MFC actuators that are mounted inside the tire and rotate with it. As a result, for an axisymmetric structure like the tire, structural modes are expected to follow the rotation of the excitation source. Using accelerometers mounted on the tire's sidewall, the response at a given material point is measured during rotation. With this excitation/measurement combination, EMA can be used, in theory, to define the transfer functions of the rotating tire. However, for a loaded tire mounted on the rotating modal rig, contact patch excitation poses a challenge to the application of EMA in the rotating frame-of-reference.

When the tire is rotating, contact patch excitation, due to the interaction between the tire and the drum, takes place. For the slick tire under consideration, this type of excitation is induced by material deformation at the contact patch. Figure 29.3 shows the effects of contact patch excitation on the out-of-plane acceleration measured at a given point on the sidewall as a function of rotational speed. For comparison purposes, the figure also depicts the acceleration measured at that point when the MFC actuators are active and the tire is not rotating. As noticed in the figure, the impact of contact patch excitation is

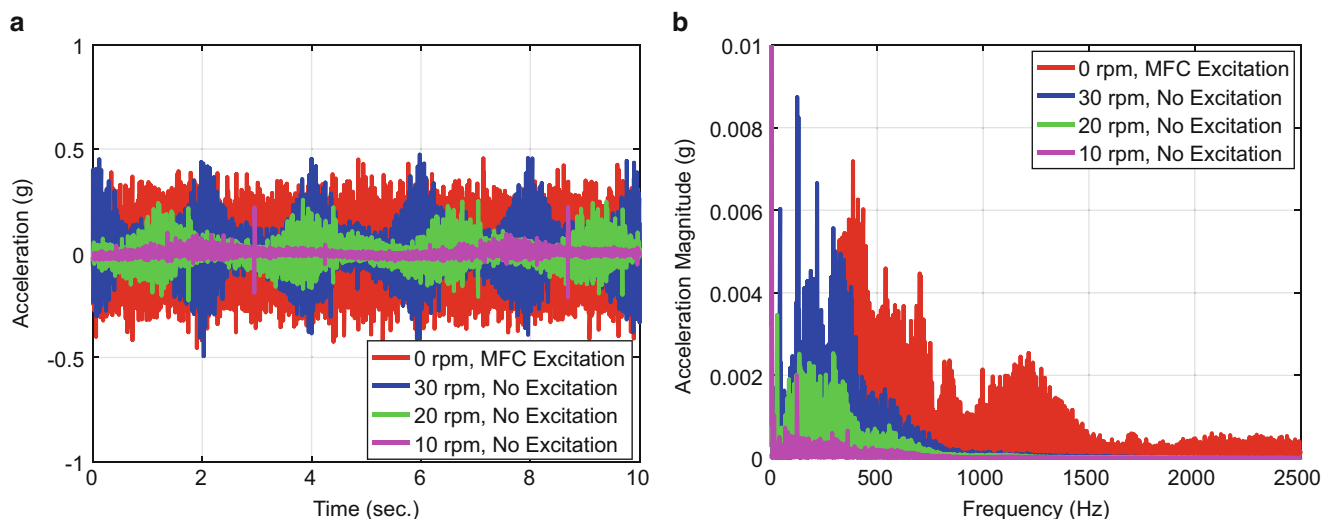


Fig. 29.3 Sidewall out-of-plane acceleration due to MFC excitation as compared to contact patch excitation for a slick rotating tire loaded with 300 lb. (a) Time domain signal and (b) power spectral density

directly proportional to the rotational speed. The instances where the accelerometer approaches the contact area are clear in the figure. For this moderately loaded tire, 300 lb, the acceleration response induced by the contact patch excitation is comparable to that induced by the MFC actuators. Therefore, contact patch excitation needs to be compensated for prior the application of EMA techniques.

Figure 29.3b shows the power spectral density (PSD) of the contact patch and MFC excitations for the frequency range of 0–2500 Hz. The frequency range over which the contact patch excitation is active depends on the rotational speed. For the range of rotational speeds considered in this study, contact patch excitation is found to be dominant over lower frequencies, <400 Hz. The level of contact patch excitation is also found to be directly proportional to loading level. When treaded tires are of concern, additional excitation mechanisms such as local impacts between tread features and the drum are present. This affects the level and frequency content of contact patch excitation, which will be addressed in future studies.

Standard EMA of the rotating tire, with 150 lb load, is applied while ignoring contact patch excitation. The results are shown in Fig. 29.4. The point FRFs measured at Point 1, next to MFC 1, are shown in Fig. 29.4a, whereas the averaged FRFs over 19 points uniformly distributed along the sidewall are shown in Fig. 29.4b. It can be noticed that at the frequency range where the contact patch excitation is active, shown by the PSD plot in Fig. 29.3b, the results of EMA are invalid. This highlights the need for taking contact patch excitation into consideration by implementing appropriate compensation techniques. For the non-rotating tire, the low frequency portion of the measured FRF is also missing. This is due to the fact that at such low frequencies, MFC actuators are not capable of providing adequate excitation force. This is a direct result of the large electrical impedance of MFC actuators at low frequency, which is a common limitation of piezoelectric actuators in general.

At higher frequencies, >400 Hz, contact patch excitation fades and EMA is applicable, as shown in the figure. As the frequency range of interest increases, the effect of rotational speed on the measured FRFs becomes negligible. The high material damping of the rubber results in a strong attenuation of propagating waves, which in turn, prevents the excitation of global structural mode. Thus, what is measured at such frequencies is the local response of tire components at that particular point. When all point FRFs are averaged, shown in Fig. 29.4b, the high frequency response approaches a flat line, indicating the lack of fully developed structural modes.

29.3.2 Stationary Frame-of-Reference

Figure 29.5 shows the mobility FRFs of the rotating tire as measured in the stationary frame-of-reference. For this case, the tire is loaded with 300 lb and the rotational speed is varied from 0 to 30 rpm in 10 rpm increments. Although contact patch excitation is present, as discussed in the previous section, EMA has been successfully applied without compensating for this unknown excitation. This is due to the fact that the excitation force provided by the electrodynamic shaker far exceeds that

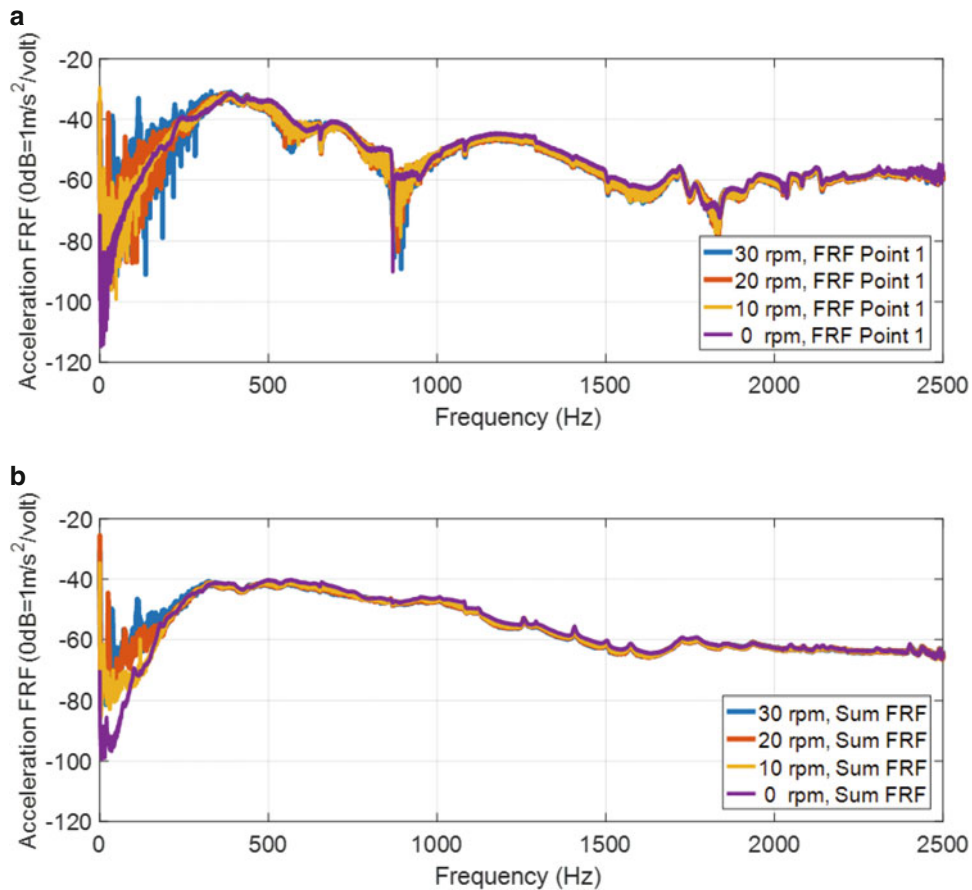


Fig. 29.4 Sidewall acceleration FRFs, in m/s²/V, measured in a rotating frame-of-reference (a) point FRFs measured right next to MFC 1, and (b) averaged FRFs of 19 points uniformly distributed along the sidewall

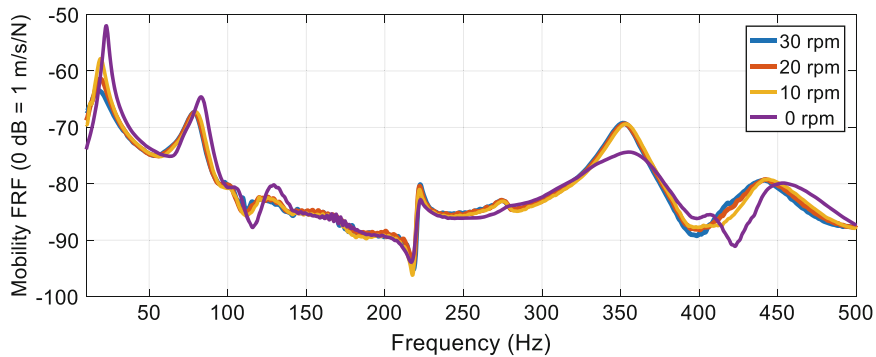


Fig. 29.5 Mobility FRFs measured at the sidewall in a stationary frame-of-reference at different rotational speeds

induced by the tire-drum interaction at the speed and load levels considered in this study. Furthermore, both contact patch and shaker forces are stationary in space, which makes them compatible with this frame of reference.

Measurements in the stationary frame-of-reference reveal the effect of rotational speed on the modal characteristics of the tire. The results are summarized in Table 29.1. For these modes, natural frequencies are found to shift to the left as rotational speed increases. The largest change takes place at the onset of rotation, as a comparison between 0 rpm and 10 rpm FRFs suggests. This is due to rubber softening that takes place upon the application of cyclic loading. Certain modes are found to be marginally affected by tire rotation, such as the one at 221 Hz, which is the first tire cavity mode. Modal damping has also found to be affected by rotational speed, however, a consistent trend has not been observed. Rotation-induced splitting of modes has not been observed in this study since all rotational speeds considered here are relatively low.

Table 29.1 Effects of rotational speed on modal characteristics

0 rpm		10 rpm		20 rpm		30 rpm	
f_n (Hz)	ζ_n (%)	f_n (Hz)	ζ_n (%)	f_n (Hz)	ζ_n (%)	f_n (Hz)	ζ_n (%)
83.7	4.24	81.2	4.29	79.9	2.91	79.4	4.56
106.7	4.34	101.7	5.42	100	4.96	99.8	5.07
220.9	0.92	221.1	0.71	221.3	0.57	221.7	0.60
357.4	3.23	352.9	1.74	352.9	2.17	352	1.89
450.3	2.28	445.5	2.92	440.6	3.06	437.8	3.14

In the table f_n is natural frequency in Hz, and ζ_n is the damping ratio

Future research will address the problem of harmonics and contact patch excitation compensation. Although this was not necessary in the stationary frame-of-reference at the load and speed combinations studied in this work, they are expected to have a greater impact as the applied load and rotational speed increase. OMA in a stationary and rotating frames-of-reference will also be addressed.

29.4 Conclusions

In this paper, EMA of a rotating tire is carried out in stationary and rotating frames-of-reference. The tire is mounted on a free-spindle rotating modal rig and is loaded vertically. Two techniques have been used in this study to excite the tire, an electrodynamic shaker attached to the free-spindle and MFC actuators mounted inside the tire, depending on the selected frame-of-reference. The response is measured at the tire's sidewall using SLDV or tri-axial accelerometers. Slow rolling condition has been investigated with rotational speeds ranging from 0 to 30 rpm.

In a rotating frame-of-reference, contact patch excitation is found to have a significant impact on the system at low frequencies, which renders EMA invalid. This is due to the fact that the magnitude of the unaccounted for contact patch excitation is comparable to that provided by the MFC actuators at that frequency range. For the slick tire considered in this study, the frequency range affected by the contact patch excitation is found to be directly proportional to the rotational speed. At higher frequencies, >1000 Hz, fully developed structural modes have not been observed and only local responses are measured.

EMA of the rotating tire has been successfully carried out in the stationary frame-of-reference. The effects of rotational speed on the tire's modal parameters have been identified. Rotation-induced material softening effects have been observed. This affects the dynamic response of the tire causing natural frequencies of structural modes to shift to the left as rotational speed increases, with the largest impact taking place at the onset of rotation.

Future research will address the problem of contact patch excitation compensation. OMA techniques in stationary and rotating frames-of-reference will also be investigated.

Acknowledgement The authors would like to acknowledge the support provided by the Centre for Tire Research (CenTiRe) at Virginia Tech. The authors are also thankful to Hankook Tire for providing the rotating modal rig and the tires used in this study. Dr. Tarazaga would also like to acknowledge the support provided by the John R. Jones III Faculty Fellowship.

References

1. Scavuzzo, R.W., Richards, T.R., Charek, L.T.: Tire vibration modes and effects on vehicle ride quality. *Tire Sci. Technol.* **21**(1), 23–39 (1993)
2. Wheeler, R.L., Dorfi, H.R., Keum, B.B.: Vibration modes of radial tires: measurement, prediction, and categorization under different boundary and operating conditions. *SAE Trans.* **114**(6), 2823–2837 (2005)
3. Kao, B., Riesner, M., Surulinarayanasami, P.: Modal analysis of a tire and wheel and its application for vehicle ride evaluation. SAE Technical Paper No. 860826, pp. 243–249 (1986)
4. Ferhat, I., Tarazaga, P. A.: Modal Analysis of a Loaded Tire with Non-Contact Measurements and Piezoelectric Excitation. SPIE, Smart Structures NDE Conference, Portland, OR, 25–29 Mar 2017
5. Dorfi, H.R., Wheeler, R.L., Keum, B. B.: Vibration modes of radial tires: application to non-rolling and rolling events. SAE Technical Paper No. 2005-01-2526, pp. 1–8 (2005)
6. Lee, J., Wang, S., Kindt, P., Pluymers, B., Desmet, W.: Identification of the direction and value of the wave length of each mode for a rotating tire using the phase difference method. *Mech. Syst. Signal Process.* **69**, 292–301 (2016)

7. Kindt, P., delli Carri, A., Peeters, B., Van der Auweraer, H., Sas, P., Desmet, W.: Operational modal analysis of a rotating tyre subject to cleat excitation. *Struct Dyn.* **3**, 1501–1512 (2011)
8. Kindt, P., Sas, P., Desmet, W.: Measurement and analysis of rolling tire vibrations. *Opt. Lasers Eng.* **47**(3), 443–453 (2009)
9. Wheeler, R.L., Dorfi, H.R., Griffiths, G.H., Cotton, J.D.: Tire vibration transmission. Part II: test and modal model quality assessment. *Proc. SPIE.* 256–1262 (2000)
10. Ferhat, I., Sarlo, R., Tarazaga, P. A.: 3-D modal analysis of a loaded tire with binary random noise excitation. The Thirty-Sixth Annual Meeting of the Tire Society, Akron, OH, 12–13 Sept 2017



Chapter 30

Combining Machine Learning and Operational Modal Analysis Approaches to Gain Insights in Wind Turbine Drivetrain Dynamics

N. Gioia, P. J. Daems, T. Verstraeten, P. Guillaume, and J. Helsen

Abstract Operational Modal Analysis (OMA) is one of the branches of experimental modal analysis which allows extracting modal parameters based on measuring only the responses of a structure under ambient or operational excitation which is not needed to be measured. This makes OMA extremely attractive to modal analysis of big structures such as wind turbines where providing measured excitation force is an extremely difficult task. One of the main OMA assumption concerning the excitation is that it is distributed randomly both temporally and spatially. Obviously, closer the real excitation is to the assumed one, better modal parameter estimation one can expect. Traditionally, wind excitation is considered as a perfect excitation obeying the OMA assumptions. However, the present study shows that the aeroelastic phenomena due to rotor rotation dramatically changes the character of aerodynamic excitation and sets limitations on the applicability of OMA to operational wind turbines. The main purpose of the study is to warn the experimentalists about these limitations and discuss possible ways of dealing with them.

Keywords Automatic operational modal analysis · Wind turbine drivetrain · Harmonics · Machine learning · Noise vibration and harshness

30.1 Introduction

The continuously increasing demand of wind energy production has led the interest of the wind industry towards the effort of reducing the cost of produced energy. This has caused the so called up-scaling trend in the last decades: bigger turbines with increased height are being produced and higher capacity models are being developed [1]. Moreover, offshore farms are becoming increasingly popular: at sea, the wind is generally more stable and stronger and there are less limitations on the size and on the produced noise of the turbine due to the lack of interaction with the human habitation. The increase of the loads acting on the different components caused by this up-scaling trend however makes a robust design harder. Moreover, the increased machine size increases significantly the challenge of installing offshore wind turbines. From a design point of view, a big challenge is that the loads acting on the different components of the machines are strongly dependent on the conditions at which the machines operate. Therefore, they are difficult to predict and simulate. A pressing issue in this context is that there is no complete understanding of the dynamics of the different machine components. For this reason, the design of machines solely based on simulated models cannot be considered adequate. Additional experimental tests must thus take place to have a better insight in the loads acting on the machines and to improve the design of the components. What is currently missing in the industrial design process is a continuous insight in the modal behavior of machines during their overall lifetime and under each operating condition [2]. The current industrial design process comprises of component-level-testing and full-scale machine testing, both in laboratory environments and in the field, aimed to observe the new

N. Gioia · P. J. Daems · T. Verstraeten · P. Guillaume · J. Helsen (✉)
Vrije Universiteit Brussel (VUB), Brussel, Belgium
e-mail: jan.helsen@vub.be

prototypes over short periods in which specific operating conditions are captured. This approach can however result in non-optimally designed machines and premature components failures, as not all operating conditions are being tested. With the advent of the era of the Internet of Things, a solution for overcoming this limitation is offered by the possibility of observing fleets of machines that are already operational in the field. This allows to capture long-term data coming from a machine going through all the possible operating conditions it is going to face during its lifetime. The capability of extracting design parameters (i.e. modal parameters) for the most important resonances from long-term data allows to gain insights in their changes over time. Particularly unveiling the links between these modal parameters (frequency, damping and mode shapes) and the operational parameters (e.g. rotor speed, temperature, pressure, yaw and pitch angle...) of the machine helps in further understanding turbine NVH behavior. Achieving this goal however requires different steps. First, there is the need of a scalable database capable of acquiring, storing and retrieving the needed information. Once the database is built and the data is stored on a server, methodologies able to automatically and continuously process the data must be available. Finally, a set of smart algorithms capable of post-processing the results must be available.

Concerning the processing of vibration data, Operational Modal Analysis (OMA) represents a powerful approach: it allows to extract modal parameters from the dynamic response of the structure to unmeasured operational forces, allowing to estimate the values of the natural frequencies and damping ratios of an operating turbine. OMA is however based on assumptions that are violated in case of wind turbines. First of all, OMA assumes time invariance of the system. This is not the case since a wind turbine consists of subsystems moving with respect to each other. Secondly, OMA assumes excitation forces that are randomly distributed, both temporally and spatially. This does not hold true in case of wind turbines; although the excitation coming from the wind turbulence is ideal for OMA, the effects of the rotor rotation dramatically change the characteristics of the aerodynamic force, making it periodic in time [3]. In this work, these two problems affecting OMA when applied to a wind turbine are faced. In order to solve the problem of the time-variant behaviour of the system, the data is automatically classified in order to cluster them in group of data for which the properties of the system can be considered invariant. Concerning the problem of the deterministic nature of the excitation source, a method to reduce the influence of harmonics component is implemented and automatized. Once these two problems are addressed, an automatic modal analysis algorithm described in previous works [4] is used to extract the modal parameters. The latter are then tracked in order to show their evolution over time using a set of clustering and classifying algorithms. By performing this analysis for different operating regimes of the machine, a qualitative assessment of how the modal parameters are influenced by the operating conditions can take place.

30.2 Theoretical Background

In literature, there are several examples of OMA techniques tailored to deal with harmonic disturbances. These methods however either assume the frequency of the harmonic disturbances to be known or identify the frequencies of the harmonic content from the data via noise poles on the unitary circle [2]. These methods are based on the assumption that the harmonic frequencies are stationary (i.e. they are constant in amplitude, frequency and phase). In case of rotating machines running in their real operating conditions, the speed cannot be considered constant. Therefore, the harmonics are smeared in the spectrum of the signals, resulting in them influencing broader frequency bands. For this reason, the fundamental assumption of the mentioned methodologies is violated and they fail. One possibility for making OMA applicable on rotating machines in operation is to use classical OMA algorithms after having filtered the harmonic components from the raw data during a pre-processing step. A list of signal processing techniques for removing harmonics from the vibration signals is given in [5]. In this work, cepstrum-based time-domain signal editing procedure is adopted. Cepstrum analysis is a procedure that brings the signal from the time domain to the quefrequency domain by means of a double application of the Fourier algorithm.

$$C_c(\tau) = \mathcal{F}^{-1} \log(\mathcal{F}(X(t))) = \mathcal{F}^{-1} \ln(A(f)) + j\phi(f) \quad (30.1)$$

where $X(t)$ is the original signal in the time domain, and $A(f)$ and $\phi(f)$ are respectively the amplitude and the phase of the frequency domain signal. By setting the phase to zero in Eq. (30.1), the formulation of the real cepstrum can be obtained (30.2):

$$C_r(\tau) = \mathcal{F}^{-1} \ln(A(f)) \quad (30.2)$$

This ensures the possibility of going back to the time domain. After having realized that there are many situations in which the editing can be carried out by modifying the amplitude only, the cepstrum has started to be considered a powerful signal editing tool: in the quefrequency domain, families of harmonics are concentrated in single lines (*rhamonics*). By setting the amplitude of rahmonics equal to zero in the quefrequency domain, the influence of the corresponding family of harmonics in the time domain is also reduced.

The success of the use of the cepstrum for OMA applications finds its reason in the fact that the information about the modes is concentrated at low quefrequency values [6]. The application of a low-pass lifter (e.g. an exponential window) on the real cepstrum greatly enhances the modal information with respect to anything else: it allows to remove all the components at higher quefrequencies, while keeping the modal information of the signal. The only distortion introduced at lower quefrequencies (thus on the interesting part of the signal) is the addition of a known amount of damping, that can be easily removed from the damping value estimated by an OMA procedure by means of the following equation:

$$\xi_r = \xi_m - \frac{1}{2\pi f_r \tau} \quad (30.3)$$

where, for each estimated mode, ξ_r is the real damping [%], ξ_m is the measured damping [%], f_r is the real frequency [Hz] and τ is the time constant of the exponential window [s].

Concerning the modal parameter estimation, the *poly-reference least-square complex frequency-domain* (p-LSCF) estimator is selected amongst the available ones due to its computational speed and the generation of a clearer stabilization diagram even in case of high modal density and/or highly damped modes. These characteristics make the algorithm suitable for automation and the continuous running of it in a big data infrastructure. The p-LSCF estimator is a frequency-domain modal analysis method that requires as primary data the output spectra of the system under analysis [7]. Assuming the excitation to be a white noise spectrum signal, this method models the output spectra in exactly the same way as frequency response functions (FRFs):

$$H(\omega) = \sum_{i=1}^n \frac{\{v_i\} \langle l_i^T \rangle}{j\omega - \lambda_i} + \frac{\{v_i^*\} \langle l_i^H \rangle}{j\omega - \lambda_i^*} \quad (30.4)$$

Where n is the number of complex conjugate mode pairs, $*$ is the complex conjugate operator, T is the transpose of a matrix, H is the complex conjugate transpose (Hermitian) of a matrix, v_i is the mode shape vector of the mode i , l_i^T the modal participation factors of the mode i and λ_i are the poles of the system (occurring in complex conjugate pairs). The poles are linked to the resonance frequencies and the damping ratios of the system by means of the following relation:

$$\lambda_i, \lambda_i^* = \xi_i \omega_i \pm j\sqrt{1 - \xi_i^2} \omega_i \quad (30.5)$$

The relationship between the input spectra [$S_{UU}(\omega)$] and the output spectra [$S_{YY}(\omega)$] of a system represented by the FRF $H(\omega)$ is described by:

$$[S_{YY}] = [H(\omega)][S_{UU}(\omega)][H(\omega)]^H \quad (30.6)$$

In case of output-only analysis, the auto-spectra are the only available information. The most important consequence of assuming the input signal as a white noise excitation is that the power spectrum of the input signal is constant; therefore $S_{UU}(\omega) = S_{UU}$ [7]. By considering this assumption and combining Eqs. (30.4) and (30.6), it is possible to write the modal decomposition of the output spectrum matrix as following:

$$S_{YY}(\omega) = \sum_{i=1}^n \frac{\{v_i\} \langle g_i \rangle}{j\omega - \lambda_i} + \frac{\{v_i^*\} \langle g_i^* \rangle}{j\omega - \lambda_i^*} + \frac{\{g_i\} \langle v_i \rangle}{-j\omega - \lambda_i} + \frac{\{g_i^*\} \langle v_i^* \rangle}{j\omega - \lambda_i^*} \quad (30.7)$$

where g_i are the operational reference factors, which replace the participation factors in case of output-only analysis. A right matrix model (Eq. 30.8) is then used to fit the measured FRFs data.

$$[H(\omega)] = [B(\omega)][A(\omega)]^{-1} \quad (30.8)$$

where $H(\omega) \in \mathbb{C}^{l \times m}$ is the FRF matrix containing the FRFs between the m inputs and the l outputs, $B(\omega) \in \mathbb{C}^{l \times m}$ is the numerator matrix polynomial and $A(\omega) \in \mathbb{C}^{m \times m}$ is the denominator matrix polynomial.

The results of the fitting of the measured FRFs by means of a parametric model are represented in the stabilization diagram [8]. The measured FRFs data are fitted with increasing model order models and the poles estimated for a certain model order are compared to the poles estimated for the lower model order. If their differences are within pre-set limits, the pole is labelled as stable one. The spurious numerical modes will not stabilize at all during this iterative procedure and they can be then easily sorted out of the modal parameter estimates. The stabilization diagram shows how the poles stabilize for increasing model orders and it allows the analyst to distinguish the physical modes from the spurious ones.

30.3 Methodology

30.3.1 Use of Big Data Analysis and Tailored Database

Due to the variability of the wind, turbines are not always operating at nominal conditions. Several transient events occur during control actions and several important loading cases act on the wind turbine (start-up, coast-down, emergency stop and grid loss related events). The load cases cover different operating conditions, and the most unfavorable load effects govern the design of the machine. However, during the design process, it is important to observe how the machines globally respond to the different loading conditions. In this way, it is possible to optimize the design of future prototypes and predict which is the modal behavior of the machine in case of critical loads. Long-term analysis and monitoring of the turbines leads to the need of dealing with a huge amount of data. An automatic approach able to tackle the described challenges is therefore required. In addition to the implementation of autonomous algorithms for advanced signal processing, a key issue is having a system available able to deal with these big amounts of data. Our integrated approach comprises three main steps [9]. (1) Data-acquisition system that allows to capture all the data within one consistent dataset: each machine has its own sensor and data acquisition network consisting of machine embedded sensors and custom monitoring system. (2) Scalable data-warehouse in order to be able to deal with large amount of data non-equally sampled and heterogeneous for nature: a no-SQL database is used to tackle problems of scalability and to increase the reliability in case of node failure. (3) Distributed computing since the analysis of large amount of data is computationally expensive. No-SQL architectures distribute the data across the cluster; it is possible to couple it with parallelized querying and data analysis. This architecture allows to combine machine learning algorithms with advanced vibration signal processing techniques. This allows to gather new insights in the modal behavior of the machine in different operating conditions and to make predictions on how it will respond in the future using data-driven prognostic techniques. This gives the opportunity to designers to construct data-driven models and to improve new prototypes based on physical system knowledge and experimental information.

30.3.2 Signal Classification

Wind turbines do not always operate at nominal operating conditions and different operating conditions imply different loading on the components of the machine. This phenomenon, combined with the fact that wind turbines are complex systems that comprise several rotating and reciprocating part moving with respect to each other, makes them time-variant systems. Since OMA assumes a time-invariant system, this problem has to be tackled. The method adopted in this work consists of dividing the data in short time blocks (i.e. 1 min datasets). Each dataset is then classified as a function of its operating conditions and grouped with datasets showing similar characteristics. This process is made automatically by implementing machine learning algorithms that observe parameters representative of the operating conditions. These are generally available from dedicated measurement systems (e.g. encoders for measuring the rotating speed) and/or from the controller of the machine (SCADA and status logs). Once the signals have been classified, OMA can be performed on the datasets. The estimates (frequency, damping and mode shapes) are then given as input to an automatic *tracking algorithm* [10] that observes how the modal parameters evolve along different datasets within the same cluster. The comparison amongst the estimates of each dataset is performed using poles and MAC values, in order to measure in which extend the estimates are coherent in terms of frequency/damping values (represented by the poles values) and mode shapes (represented by the MAC value). In this work, a completely automatic procedure based on machine learning that does not require the definition of a reference dataset is implemented.

30.3.3 Automation of Modal Analysis for Rotating Machines

A cepstrum-based time-domain signal editing procedure and a p-LSCF algorithm (described in Sect. 30.2) have been combined in order to be able to automatically perform OMA on a stream of vibration data coming from rotating machines. To make the p-LSCF estimator automatic, the main algorithm-analyst interaction has been eliminated by substituting the classical stabilization diagram [11] with a clustering method that autonomously interprets the information collected in the stabilization diagram. In this work, a clustering analysis has been used in order to group the poles showing stable characteristics (i.e. representative of the same mode). The physical modes are then selected automatically by exploiting the statistical characteristics of the generated clusters. The realized methodology is based on the works of other authors [12–15], and it has been implemented in such a way that it can run completely automatically by selecting the parameters required for the clustering algorithm autonomously based on the physical and statistical properties of the signal.

Concerning the cepstrum editing procedure, an algorithm that automatically selects the parameters required for the analysis (i.e. the *cut-off quefrequency*, the time constant of the low pass filter applied in the cepstrum domain) is implemented. This method is based on analyzing the effect of this signal editing procedure in certain frequency bands identified as the ones containing the harmonics. What is particularly observed, is the reduction of the energy as a consequence of using the lifter.

30.4 Results

To demonstrate the performance of the different implemented algorithms, vibration data acquired on an offshore wind turbine drivetrain is analyzed. The choice of studying this component is linked to the fact that its design is critical for avoiding NVH problems. Moreover, it is a complex structure in terms of modal density and presence of harmonics in the excitation signal.

Twenty hours of data in which several events and different operating conditions are present, have been selected. This allows to test the automatic event detection and classification of the data. Events such as run-ups and coast-downs have been removed from the groups of data to be analyzed. The remaining datasets have been clustered based on the rotor speed, generating three groups of data: standstill data (~3 h 30 min), data from the turbine rotating at an intermediate speed (~5 h 30 min), and data from the turbine rotating at its nominal speed (~10 h). The output of the automated tracking procedure is shown in Fig. 30.1.

For standstill data, the highest modal density is retrieved. It can moreover be seen that several modes are no longer stably retrieved in some operating conditions (e.g. pink and yellow mode for the turbine operating respectively at intermediate and nominal speed). This difference in dynamic behaviour illustrates the need of acquiring insights during all the different operating regimes of the turbine, as this change can be closely intertwined with NVH issues (e.g. tonality problems) appearing in certain conditions.

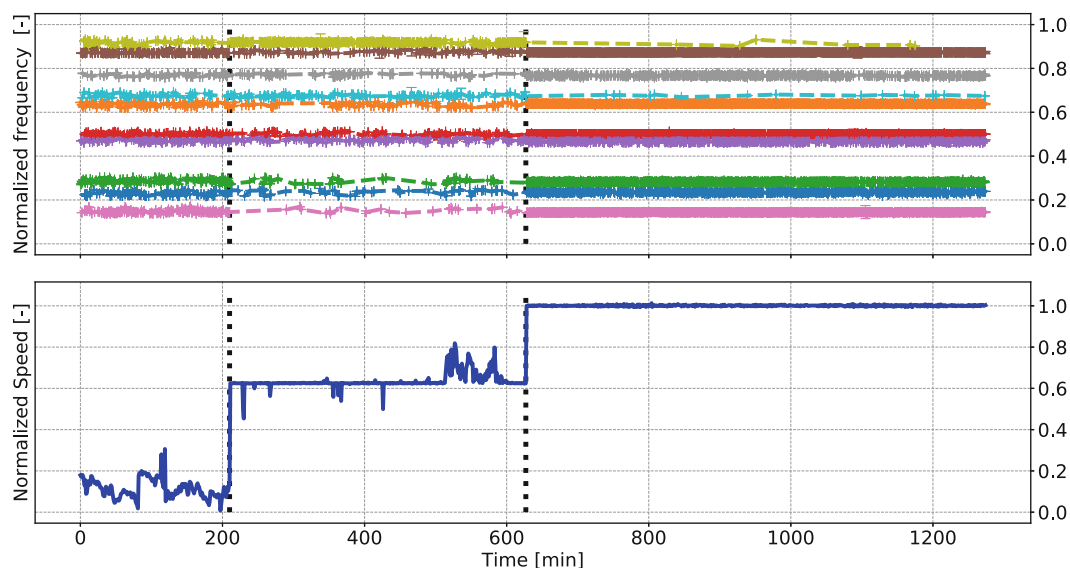


Fig. 30.1 Results of the tracking procedure for the three investigated operating conditions (axis values normalized for confidentiality reasons)

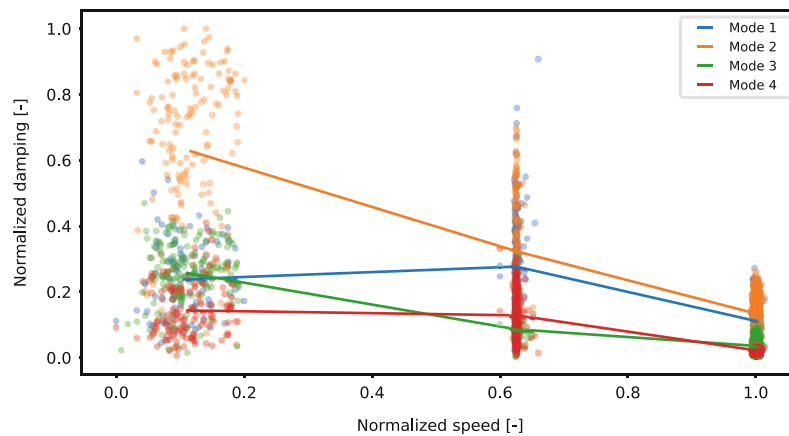


Fig. 30.2 Evolution of the damping ratio as a function of the operating speed of the turbine for four different modes. The solid lines represent the connection between the different cluster centroids (axis values normalized for confidentiality reasons)

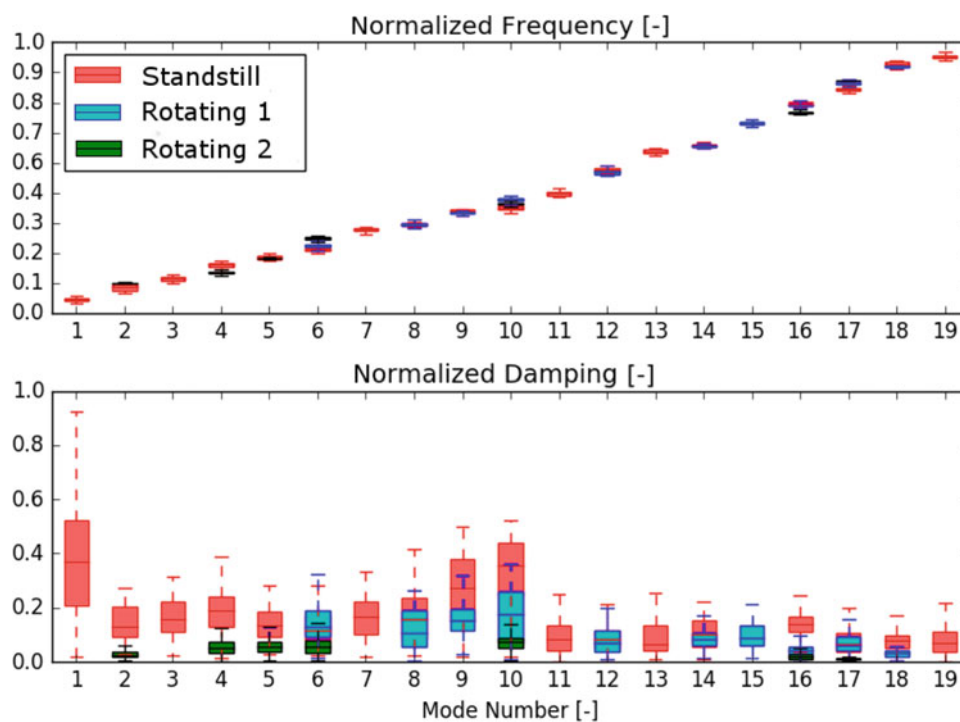


Fig. 30.3 Comparison of the tracking procedure applied on data coming from the same machine acquired with the machine operating at standstill, intermediate speed (Rotating 1) and nominal speed (Rotating 2) (axis values normalized for confidentiality reasons)

Not only the extracted resonance frequencies are subject to variations. A significant change in the estimated damping ratios can also be seen. This is illustrated in Fig. 30.2 for four different modes that are retrieved in the three investigated operating conditions. It can be noted that the estimated damping values fluctuate significantly, even when the average speed is nearly identical. This is expected, as the damping ratio of modes is influenced by several other operating parameters such as the wind speed and the pitch and yaw angle of the turbine [16]. Nevertheless, a general trend for the four different modes is the fact that the damping ratio decreases when the operating speed of the turbine increases.

In order to have a final comparison of the estimates obtained for the different operating conditions, the results of each tracking procedure have been processed in order to obtain punctual values and error bands of the modal parameters in each operating regime. The results of this comparison in terms of both resonance frequencies and damping ratio are shown in Fig. 30.3.

30.5 Conclusions

This paper has investigated a completely automated operational modal parameter estimation scheme, tackling the main challenges of performing OMA on complex rotating systems like wind turbine gearboxes. The implemented approach has been validated by processing vibration data of an offshore wind turbine drivetrain.

The main challenges introduced by the methodology used for the modal parameter estimation have been already investigated in previous works. With this research, emphasis has been given to the automation of the procedure and the implementation of it in a big data infrastructure that allows to parallelize the needed steps in order to save analysis time. It has been shown that the automatic procedure gives promising results, consistent with the ones obtained with a manual procedure and the ones shown in previous works. This automated approach moreover ensures that the outcome of the analysis is objective and less dependent on the analyst decisions, opening the doors to further long-term investigations.

The obtained results show that the operating speed of the turbine has an important influence on its dynamic behaviour. The future work consists of further coupling the tracking results with SCADA in order to gain a better insight in which set of operating parameters significantly influences the modal behaviour of the machine. To this end, signal modeling techniques and correlation investigation could be performed.

Acknowledgements The authors would like to acknowledge the financial support of VLAIO (Flemish Agency for Innovation & Entrepreneurship) through the SBO project HYMOP and the SIM project MaSiWEC.

Furthermore, the authors would like to acknowledge FWO for their support through the SB grant of N. Gioia and T. Verstraeten.

The authors also thank their partners for delivering the monitoring data.

References

- Helsen, J., Vanhollenbeke, F., Vandepitte, D., Desmet, W.: Some trends and challenges in wind turbine upscaling. In: Proceedings of ISMA International Conference on Noise and Vibration, September 2012, pp. ID-593 (2012)
- Pintelon, R., Peeters, B., Guillaume, P.: Continuous-time operational modal analysis in the presence of harmonic disturbances. *Mech. Syst. Signal Process.* **22**(5), 1017–1035 (2008)
- Tcherniak, D., Chauhan, S., Hansen, M.H.: Applicability limits of operational modal analysis to operational wind turbines. In: Proulx, T. (ed.) *Structural Dynamics and Renewable Energy*, vol. 1, pp. 317–327. Springer, New York (2011)
- Gioia, N., Daems, P.J., Guillaume, P., Helsen, J.: Long term operational modal analysis for rotating machines. *J. Phys. Conf. Ser.* **1037** (2018). *Measurement and Experimental Techniques*
- Randall, R.B., Sawalhi, N., Coats, M.: A comparison of methods for separation of deterministic and random signals. *Int. J. Cond. Monit.* **1**(1), 11–19 (2011)
- Randall, R.B.: A history of cepstrum analysis and its application to mechanical problems. *Mech. Syst. Signal Process.* **97**, 3–19 (2017)
- Peeters, B., Van der Auweraer, H.: PolyMAX: a revolution in operational modal analysis. In: 1st International Operational Modal Analysis Conference (IOMAC), Copenhagen, April (2005)
- Peeters, B., Lowet, G., Van der Auweraer, H., Leuridan, J.: A new procedure for modal parameter estimation. *Sound Vib.* **38**(1), 24–29 (2004)
- Helsen, J., Peeters, C., Doro, P., Ververs, E., Jordaens, P.J., Wind farm operation and maintenance optimization using big data. In: 2017 IEEE Third International Conference on Big Data Computing Service and Applications (BigDataService), April 6, pp. 179–184. IEEE, Piscataway (2017)
- El-Kafafy, M., Colanero, L., Gioia, N., Devriendt, C., Guillaume, P., Helsen, J.: Modal parameters estimation of an offshore wind turbine using measured acceleration signals from the drive train. In: *Structural Health Monitoring and Damage Detection*, vol. 7, pp. 41–48. Springer, Cham (2017)
- Van der Auweraer, H., Peeters, B.: Discriminating physical poles from mathematical poles in high order systems: use and automation of the stabilization diagram. In: Proceedings of IMTC 2004, the IEEE Instrumentation and Measurement Technology Conference, Como (2004)
- Magalhaes, F., Cunha, A., Caetano, E.: Online automatic identification of the modal parameters of a long span arch bridge. *Mech. Syst. Signal Process.* **23**(2), 316–329 (2009)
- Chauhan, S., Tcherniak, D.: Clustering approaches to automatic modal parameter estimation. In: Proceedings, International Modal Analysis Conference (IMAC) (2008)
- Goethals, I., Vanluyten, B., De Moor, B.: Reliable spurious mode rejection using self learning algorithms. In: Proceedings of the International Conference on Noise and Vibration Engineering (ISMA 2004), September 2004, Leuven, pp. 991–1003 (2004)
- Devriendt, C., Elkafafy, M., De Sitter, G., Guillaume, P.: Continuous dynamic monitoring of an offshore wind turbine on a monopile foundation. In: ISMA2012 (2012)
- Devriendt, C., Weijtjens, W., El-Kafafy, M., De Sitter, G.: Monitoring resonant frequencies and damping values of an offshore wind turbine in parked conditions. In: *IET Renewable Power Generation 2014*, pp. 433–441 (2014)

Chapter 31

Modal Test-Analysis Correlation Using Left-Hand Eigenvectors



Robert N. Coppelino

Abstract Over many years, members of the experimental modal analysis community have been challenged over the use of modal orthogonality and cross-orthogonality criteria for validation of experimental modal vectors and for assessment of test-analysis correlation, respectively. At the heart of the challenge is the role played by the potentially inaccurate TAM mass matrix, which is derived from a mathematical model. Recent work that exploits left-hand eigenvectors, estimated by the SFD technique, provides a promising way out of the TAM mass matrix impasse. Modal orthogonality, defined as the product of left- and right-handed experimental eigenvectors (real or complex) is mathematically an identity matrix. This guarantees that SFD estimated modes are always perfectly orthogonal. Modal cross-orthogonality, defined by product of analytical left-hand eigenvectors and experimental right-hand eigenvectors (after consistent “mass” normalization of both sets) does not possess the desired “unit maximum coefficient magnitude” property. Therefore, an alternative cross-orthogonality definition, based on weighted complex linear least-squares analysis, is evaluated and found to possess the desired property. Employment of (1) the left- and right-handed experimental eigenvector based orthogonality matrix and (2) the weighted complex linear least-squares based cross-orthogonality matrix represents a “game changer” that potentially frees the experimental modal analysis community from the potentially inaccurate TAM mass matrix.

[Test FEM Correlation Left Eigenvectors]

31.1 Introduction

Verification and validation of modern aerospace systems, particularly NASA’s Space Launch System (SLS), is a particularly challenging endeavor due to a variety of complicating factors including (1) high modal density in the important 0–50 Hz (primary structural loads) frequency band, (2) associated pronounced parametric uncertainty and sensitivity, and (3) the presence, in some components, of non-negligible nonlinearities. The first and second complicating factors are generally addressed today by modern finite element analysis methods [1], systematic experimental modal analysis [2], and U.S. Government standards [3, 4]. Specific SLS challenges and solutions were documented in a recent NASA contractor report [5], which should be regarded as a “progress report”. The present paper, which is closely associated with ongoing work on experimental mode verification (EMV) [6], offers a new perspective on the subject of modal test-analysis correlation employing left-hand eigenvectors. The weighted complex linear least-squares method [7] provides a rigorous alternative to correlation based on left-hand eigenvectors.

The Integrated Spacecraft Payload Element (ISPE) modal test experience led to introduction of experimental modal analysis and test-analysis correlation tool enhancements designed to deal with particularly difficult modal testing challenges. Exploitation of experimental left-hand eigenvectors produced the following results:

1. The left-hand, right-hand eigenvector based state-space orthogonality matrix for “valid” (complex) experimental modes automatically satisfies NASA STD-5002 and USAF SMC-004 requirements. The orthogonality matrix for experimental modes is mathematically perfect by definition, and it is independent of the approximate TAM mass matrix.
2. Employment of state-space orthogonality opens the possibility for evaluation of more general experimental dynamic systems including (a) aeroelasticity, (b) structure-control interaction, and (c) launch vehicle POGO applications.

R. N. Coppelino (✉)
Measurement Analysis Corporation, Torrance, CA, USA
e-mail: rcoppelino@macorp.net

3. Employment of the weighted complex least-squares formulation for test-TAM correlation and modal coherence appears to be an appropriate enhancement for incorporation in NASA STD-5002 and USAF SMC-004 test-analysis correlation standards. It is recognized that the task of modal correlation does not specifically require perfectly orthogonal, real modes; weighted complex least-squares, which employs the TAM mass matrix, represents a “minor” enhancement for modal test-TAM correlation evaluations.
4. Introduction of the weighted complex least-squares formulation for test-TAM correlation and modal coherence opens the opportunity for inclusion of damping in correlation and update endeavors, e.g., structures with non-negligible modal complexity due to localized, non-proportional damping mechanisms (joints).
5. The weighted complex least-squares formulation for test-TAM correlation and modal coherence automatically accounts for phase-shifted experimental modes that are the result of test excitation cross-talk.

The developments influenced by the ISPE test experience offer potential enhancements to U.S. Government modal testing standards that must undergo wider studies and critiques before establishment of general acceptance in the structural dynamics technical community.

31.2 Nomenclature

Symbol	Definition	Symbol	Definition
[A]	State Variable Plant Matrix	[Φ]	Modal Matrix
[B]	Viscous Damping Matrix	[Φ _L]	Left-Hand Modal Matrix
COR	Cross-Orthogonality Matrix	[Ψ]	Guyan Reduction Transformation
COH	Modal Coherence	α	Proportionality factor
{F}	Excitation Force	γ	Generalized Force Allocation Matrix
[H]	Frequency Response Function	η	State-Space Generalized Displacement
[K]	Stiffness Matrix	[φ]	Eigenvectors for a 2nd order system
[M]	Mass Matrix	λ	Eigenvalue
[OR]	Orthogonality Matrix	ω	Frequency (rad/sec)
[R]	Residual Error Matrix	ξ(f)	SVD Generalized Displacement
[Γ]	Excitation Force Allocation Matrix		
[U]	Physical Displacement Matrix	Subscript	Definition
[V]	SVD Trial Vector Matrix	() _C	Pertains to complex-least squares
f	frequency (Hz)	() _{FEM}	FEM
[h]	Generalized Frequency Response	() _{TAM}	TAM
{q}	Modal Displacement	() _{TEST}	Test
		() _η	State-Space
Superscript	Definition	() _A	Analytical
[~]	Effective Dynamic System Matrix	() _E	Experimental

31.3 Test Mode Orthogonality and Test-Analysis Correlation

The present discussion offers a review of (a) currently accepted U.S. aerospace community test mode orthogonality and test-analysis correlation practices, and (b) promising emerging practices influenced by the recent ISPE modal test experience.

31.3.1 Modal Test-Analysis Correlation (Established U.S. Government Standards)

The relationship between (real) test modes, [Φ_{TEST}], and their (real, undamped) analytical counterparts, [Φ_{FEM}], is described by the transformation,

$$[\Phi_{TEST}] = [\Phi_{FEM}] [COR] + [R]. \quad (31.1)$$

$[\Phi_{\text{FEM}}]$ is the partition of the FEM modes corresponding to the “test” instrumented DOF set, $[\text{COR}]$ is the cross-orthogonality matrix and $[\text{R}]$ is the residual error matrix. Employing $[\text{M}_{\text{TAM}}]$ as a weighting matrix, the least squares solution for cross-orthogonality is,

$$[\text{COR}] = [\text{OR}_{\text{TAM}}]^{-1} \left[\Phi_{\text{FEM}}^T \text{M}_{\text{TAM}} \Phi_{\text{TEST}} \right], \quad (31.2)$$

where the TAM mode orthogonality matrix is,

$$[\text{OR}_{\text{TAM}}] = \left[\Phi_{\text{FEM}}^T \text{M}_{\text{TAM}} \Phi_{\text{FEM}} \right] \approx [\text{I}]. \quad (31.3)$$

It should be noted that $[\text{OR}_{\text{TAM}}]$ is exactly an identity matrix only if the FEM modes are the unit mass normalized modes of a Guyan reduced structural dynamic model (consistent with the “test” instrumented DOF set).

An additional useful modal coherence matrix, $[\text{COH}]$, is defined as follows,

$$[\text{COH}] = \left([\text{I}] - [\text{OR}_{\text{TEST}}]^{-1/2} \left[\text{R}^T \text{M} \text{R} \right] [\text{OR}_{\text{TEST}}]^{-1/2} \right) = [\text{I}] - [\text{OR}_{\text{TEST}}]^{-1/2} \left[\text{COR}^T \text{OR}_{\text{TAM}} \text{COR} \right] [\text{OR}_{\text{TEST}}]^{-1/2}. \quad (31.4)$$

It should be noted that (a) TAM mode orthogonality, (b) test mode orthogonality, (c) test-TAM mode cross-orthogonality matrices, along with (d) corresponding test-analysis natural frequency differences, represent the accepted test-analysis correlation metrics in the U.S. aerospace industry. Modal coherence, $[\text{COH}]$, is employed by some investigators to judge the degree to which test and analysis modal clusters are linear combinations of one another; however, this metric is not widely recognized.

The following standards are imposed on space systems contractors by U.S. government agencies:

NASA [3]

For all significant modes, test mode orthogonality (unit mass normalized).

$$| \text{OR}_{\text{TEST},ij} | \leq 0.10 \text{ (10\%)} \quad \text{for } i \neq j \quad (31.5)$$

Test-Analysis mode cross-orthogonality (both sets unit mass normalized).

$$| \text{COR}_{ij} | \geq 0.90 \text{ (90\%)} \quad \text{for } i = j \quad \text{and} \quad | \text{COR}_{ij} | \leq 0.10 \text{ (10\%)} \quad \text{for } i \neq j \quad (31.6)$$

Difference between corresponding test and analysis modal frequencies must be less than 5%.

Air Force Space Command [4]

For all spacecraft modes up to 70 Hz, test mode orthogonality (unit mass normalized).

$$| \text{OR}_{\text{TEST},ij} | \leq 0.10 \text{ (10\%)} \quad \text{for } i \neq j \quad (31.7)$$

Test-Analysis mode cross-orthogonality (both sets unit mass normalized).

$$| \text{COR}_{ij} | \geq 0.95 \text{ (95\%)} \quad \text{for } i = j \quad \text{and} \quad | \text{COR}_{ij} | \leq 0.10 \text{ (10\%)} \quad \text{for } i \neq j \quad (31.8)$$

Difference between corresponding test and analysis modal frequencies must be less than 3%.

31.3.2 Modal Test Data Resulting from Estimated State-Space Models

Among the variety of experimental modal analysis techniques, there is a general class of methods that estimate an effective state-space dynamic system as part of the process. The SFD method [6], representative of the broader class of state-space estimation methods, employs singular value decomposition (SVD) to estimate (real) trial vectors, $[\text{V}]$, and generalized acceleration FRFs, $[\ddot{\xi}(f)]$, associated with measured physical DOF FRFs, $[\ddot{\text{U}}(f)]$, as follows:

$$[\ddot{\text{U}}(f)] = [\text{V}] [\ddot{\xi}_1(f)], \quad [\text{V}]^T [\text{V}] = [\text{I}]. \quad (31.9)$$

Assuming the generalized DOF follow the effective dynamic system form,

$$[\ddot{\xi}(f)] + [\tilde{\mathbf{B}}][\dot{\xi}(f)] + [\tilde{\mathbf{K}}][\xi(f)] = [\tilde{\Gamma}][F(f)], \quad \text{where} \quad [\tilde{\mathbf{B}}] = [\mathbf{M}^{-1}][\mathbf{B}] \quad \text{and} \quad [\tilde{\mathbf{K}}] = [\mathbf{M}^{-1}][\mathbf{K}], \quad (31.10)$$

The effective state-space system modes are computed by solution of the eigenvalue problem,

$$\begin{Bmatrix} \ddot{\xi} \\ \dot{\xi} \\ \xi \end{Bmatrix} = \begin{bmatrix} -\tilde{\mathbf{B}} & -\tilde{\mathbf{K}} \\ \mathbf{I} & 0 \end{bmatrix} \begin{Bmatrix} \dot{\xi} \\ \xi \end{Bmatrix}, \quad \text{which is of the general type,} \quad \{\dot{\eta}\} = [\mathbf{A}_\eta]\{\eta\}. \quad (31.11)$$

Complex eigenvalue analysis of the effective dynamic system produces the following results:

$$\begin{aligned} \{\eta\} &= [\Phi_\eta]\{q\} \quad \text{where the "left-hand" generalized eigenvectors are} \quad [\Phi_{\eta L}] = [\Phi_\eta]^{-1}, \\ [\Phi]_{\text{TEST}} &= [\mathbf{V}][\Phi_\eta], \quad [\Phi_L]_{\text{TEST}} = [\Phi_{\eta L}][\mathbf{V}^T], \quad \text{and} \quad [\Phi_L]_{\text{TEST}}[\Phi]_{\text{TEST}} = [\mathbf{I}]. \end{aligned} \quad (31.12)$$

The state-space eigenvectors resulting from experimental modal analysis using SFD are exactly orthogonal to one another, essentially eliminating the need for satisfaction of NASA and/or USAF test mode orthogonality criteria! Moreover, orthogonality of state-space experimental eigenvectors is not dependent on the TAM mass matrix, $[\mathbf{M}_{\text{TAM}}]$.

31.3.3 Theoretical System Modes in State-Space Form

Modes associated with an undamped or damped theoretical model may be formulated in a manner similar to the considerations employed in the previous discussion. If one substitutes the Guyan (or other suitable) reduction transformation for SVD trial vectors,

$$\{U\} = [\Psi_{\text{TAM}}]\{U_{\text{TAM}}\}, \quad (31.13)$$

the reduced-order TAM modal dynamic equations become,

$$[\mathbf{M}_{\text{TAM}}]\{\ddot{U}_{\text{TAM}}\} + [\mathbf{B}_{\text{TAM}}]\{\dot{U}_{\text{TAM}}\} + [\mathbf{K}_{\text{TAM}}]\{U_{\text{TAM}}\} = \{0\}. \quad (31.14)$$

Converting the above system to a state-space description, the following state-space eigenvalue problem is posed:

$$\begin{Bmatrix} \ddot{U}_{\text{TAM}} \\ \dot{U}_{\text{TAM}} \\ U_{\text{TAM}} \end{Bmatrix} = \begin{bmatrix} -\mathbf{M}_{\text{TAM}}^{-1}\mathbf{B}_{\text{TAM}} & -\mathbf{M}_{\text{TAM}}^{-1}\mathbf{K}_{\text{TAM}} \\ \mathbf{I} & 0 \end{bmatrix} \begin{Bmatrix} \dot{U}_{\text{TAM}} \\ U_{\text{TAM}} \end{Bmatrix}. \quad (31.15)$$

The (generally complex) right- and left-eigenvectors for the state-space TAM automatically satisfy perfect orthogonality in the same manner as the test eigenvectors, i.e.,

$$[\Phi_L]_{\text{TAM}}[\Phi]_{\text{TAM}} = [\mathbf{I}]. \quad (31.16)$$

It should be noted that in the special case of an undamped theoretical model in which the eigenvalues (in diagonal matrix form) are,

$$[\lambda_n] = [i\omega_n] \quad (\text{positive value natural frequencies}), \quad (31.17)$$

and the state-space right- and left-eigenvectors are of the form,

$$[\Phi]_{\text{TAM}} = \begin{bmatrix} \varphi_{\text{TAM}} \\ \varphi_{\text{TAM}} \lambda_{\text{TAM}}^{-1} \end{bmatrix}, \quad [\Phi_{\text{L}}]_{\text{TAM}} = \begin{bmatrix} \varphi_{\text{TAM}}^{\text{T}} \mathbf{M}_{\text{TAM}} & \lambda_{\text{TAM}} \varphi_{\text{TAM}}^{\text{T}} \mathbf{M}_{\text{TAM}} \end{bmatrix}. \quad (31.18)$$

Note that the real eigenvalues and eigenvectors are solutions of the undamped system eigenvalue problem,

$$[\mathbf{K}_{\text{TAM}}] [\varphi_{\text{TAM}}] = [\mathbf{M}_{\text{TAM}}] [\varphi_{\text{TAM}}] \left[\omega_{\text{n}}^2 \right]. \quad (31.19)$$

Results of both experimental and theoretical state-space modal analyses automatically satisfy NASA and USAF modal orthogonality criteria. Most relevant is the fact that experimental mode orthogonality does not require a TAM mass matrix.

31.3.4 Correlation of Experimental and Theoretical Modes (Left-Hand Eigenvectors)

After scaling experimental and theoretical eigenvectors to common normalization (unit lengths), it appears reasonable to hypothesize the following cross-orthogonality formulation:

$$\begin{aligned} [\Phi]_{\text{TEST}} &= [\Phi]_{\text{TAM}} [\text{COR}] + [\mathbf{R}], \\ [\Phi_{\text{L}}]_{\text{TAM}} [\Phi]_{\text{TEST}} &= [\Phi_{\text{L}}]_{\text{TAM}} [\Phi]_{\text{TAM}} [\text{COR}] + [\Phi_{\text{L}}]_{\text{TAM}} [\mathbf{R}] = [\text{COR}] + [0], \\ [\text{COR}] &= [\Phi_{\text{L}}]_{\text{TAM}} [\Phi]_{\text{TEST}}. \end{aligned} \quad (31.20)$$

The desired property of cross-orthogonality, [COR], namely absolute value of all coefficients $\leq 100\%$, is not guaranteed by Eq. (31.20). This is borne out by the following example, employing the hypothetical case of “real” test and TAM eigenvectors and eigenvalues of the form,

$$[\Phi]_{\text{TEST}} = \begin{bmatrix} \varphi_{\text{TEST}} \\ \varphi_{\text{TEST}} \lambda_{\text{TEST}}^{-1} \end{bmatrix}, \quad [\Phi_{\text{L}}]_{\text{TAM}} = \begin{bmatrix} \varphi_{\text{TAM}}^{\text{T}} \mathbf{M}_{\text{TAM}} \lambda_{\text{TAM}} & \varphi_{\text{TAM}}^{\text{T}} \mathbf{M}_{\text{TAM}} \end{bmatrix}. \quad (31.21)$$

If the TAM and test eigenvectors are identical and the eigenvalues differ by a uniform factor (occurs if $[\mathbf{K}_{\text{TEST}}] = \alpha [\mathbf{K}_{\text{TAM}}]$, and $\alpha \neq 1$, $(\lambda_{\text{TEST}}) = \alpha^{1/2} (\lambda_{\text{TAM}})$), then the state-space cross-orthogonality matrix is,

$$[\text{COR}] = [\text{COR}] = \left(\varphi_{\text{TEST}}^{\text{T}} \mathbf{M}_{\text{TAM}} \varphi_{\text{TEST}} \right) + \lambda_{\text{TAM}} \left(\varphi_{\text{TEST}}^{\text{T}} \mathbf{M}_{\text{TAM}} \varphi_{\text{TEST}} \right) \lambda_{\text{TEST}}^{-1}. \quad (31.22)$$

When the conventional “real” eigenvectors are normalized to a value of 1/2, the state-space cross-orthogonality is.

$$[\text{COR}] = \left(1 + \alpha^{-1/2} \right) / 2 \cdot [\mathbf{I}]. \quad (31.23)$$

Therefore, there is no guarantee that the absolute values of the terms in [COR] are bounded by 100%. Clearly the above cross-orthogonality definition does not necessarily behave like the more common form for real eigenvectors. This is attributed to the fact that Eq. (31.20) do not define a rigorous linear least-squares process.

31.3.5 Correlation of Experimental and Theoretical Modes (Complex Least Squares)

Systematic correlation of two sets of complex vectors (with identical DOF designations) is defined in a manner analogous to the case of real vectors (see Eqs. 31.1–31.4), wherein the transpose operator, is replaced by the complex conjugate transpose [7]. Focusing on the upper (“velocity”) partition of the state-space eigenvectors (see Eq. 31.11), the weighted least-squares formulation for the corresponding complex eigenvector partitions is defined below.

The relationship between (real) test modes, $[\varphi_{\text{TEST}}]$, and their (real, undamped) analytical counterparts, $[\varphi_{\text{TAM}}]$, is described by the transformation,

$$[\varphi_{\text{TEST}}] = [\varphi_{\text{TAM}}][\text{COR}] + [\text{R}]. \quad (31.24)$$

Employing $[\text{M}_{\text{TAM}}]$ as a weighting matrix, the least squares solution for complex cross-orthogonality (or complex correlation matrix) is,

$$[\text{COR}] = [\text{OR}_{\text{TAM,C}}]^{-1} [\varphi_{\text{TAM}}^* \text{M}_{\text{TAM}} \varphi_{\text{TEST}}]. \quad (31.25)$$

The TAM mode orthogonality matrix is,

$$[\text{OR}_{\text{TAM,C}}] = [\varphi_{\text{TAM}}^* \text{M}_{\text{TAM}} \varphi_{\text{TAM}}] \neq [\text{I}] \text{ (not necessarily a diagonal or an identity matrix)}. \quad (31.26)$$

The complex modal coherence matrix, $[\text{COH}]$, is defined as follows,

$$\begin{aligned} [\text{R}] &= [\varphi_{\text{TEST}}] - [\varphi_{\text{TAM}}][\text{COR}], \quad [\text{OR}_{\text{TEST,C}}] = [\varphi_{\text{TEST}}^* \text{M}_{\text{TAM}} \varphi_{\text{TEST}}], \\ [\text{R}^* \text{M}_{\text{TAM}} \text{R}] &= [\text{OR}_{\text{TEST,C}}] - [\text{COR}^*][\text{OR}_{\text{TAM,C}}][\text{COR}], \\ [\text{COH}] &= [\text{I}] - [\text{OR}_{\text{TEST,C}}^{-1}][\text{COR}^*][\text{OR}_{\text{TAM,C}}^*][\text{COR}]. \end{aligned} \quad (31.27)$$

Extensive evaluation of the complex (weighted) least squares process indicates that both the complex correlation and coherence matrices behave in a manner that parallels the behavior of their real eigenvector counterparts (Eqs. 31.1–31.4), specifically, when the vectors are normalized such that,

$$\{\varphi_{\text{TEST}}\}_n^* [\text{M}_{\text{TAM}}] \{\varphi_{\text{TEST}}\}_n = \{\varphi_{\text{TAM}}\}_n^* [\text{M}_{\text{TAM}}] \{\varphi_{\text{TAM}}\}_n = 1, \quad (31.28)$$

$$|\text{COR}_{m,n}| \leq 100\%, \quad |\text{COH}_{m,n}| \leq 100\% \text{ (for all "m and n" indices)}. \quad (31.29)$$

Therefore, the issues of complex modal orthogonality and test-analysis mode correlation may be separated into two distinct sub-tasks, namely:

1. Complex mode orthogonality is perfectly satisfied by left-hand eigenvector counterparts to state-space complex eigenvectors for test and TAM eigenvector sets.
2. Complex mode cross-orthogonality (correlation) and complex modal coherence are defined based on the weighted complex least-squares process.

31.4 ISPE Test-TAM Correlation

The Integrated Spacecraft Payload Element (ISPE), depicted in Fig. 31.1, was subjected to systematic modal testing at NASA/MSFC in the fall of 2016. Measured FRF data was quite extensive, and the NASA team had a great deal of difficulty in estimation of modal parameters in the 0–65 Hz frequency band. These challenges led to development of the present complex modal test-analysis correlation methodology.

Due to (a) the presence of many closely-spaced shell breathing modes of the test article and (b) non-proportional damping (which is a basic reality of all built-up structural dynamic systems), the test article's modes are generally complex (and are not readily approximated as "real" modes).

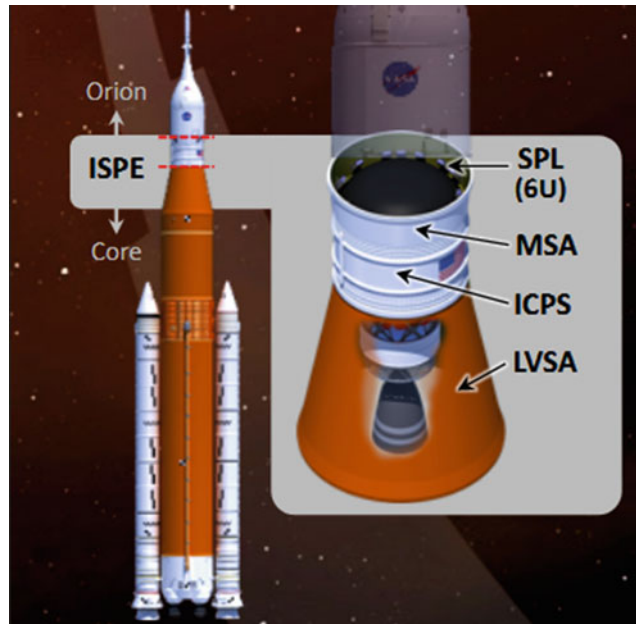


Fig. 31.1 Integrated spacecraft payload element (courtesy of NASA)

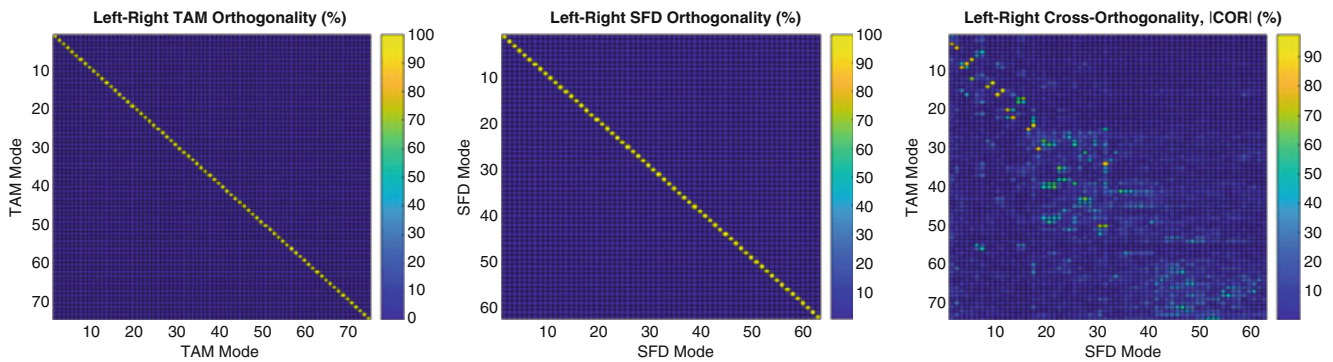


Fig. 31.2 Orthogonality and cross-orthogonality of TAM and test complex state-space eigenvectors (absolute values)

31.4.1 Orthogonality and Test-TAM Correlation (Using Left-Hand Eigenvectors)

The ISPE TAM model is described by 265 accelerometer DOF and 75 real, undamped modes in the 0–65 Hz frequency band, computed from the reduced TAM model. Processed ISPE modal test data consists of 63 complex modes in the 0–65 Hz frequency band, based on (a) the SFD experimental mode estimation algorithm and (b) mode selection process described in “Experimental Mode Verification (EMV) using Left-Hand Eigenvectors”, IMAC XXXVII. State-space orthogonality and cross-orthogonality of the TAM and test modes, employing the left-hand eigenvector method (Sects. 31.3.2–31.3.4 of this paper), are summarized below in Fig. 31.2.

31.4.2 Orthogonality and Test-TAM Correlation (Using Complex Least Squares)

Orthogonality, cross-orthogonality and modal coherence of the TAM and test modes, employing the complex least-squares method (Sect. 31.3.5 of this paper), are summarized below in Fig. 31.3.

While the TAM mode orthogonality matrix is a perfect identity, and the test mode orthogonality matrix is diagonal-dominant (much like expected for test modes that are adjusted, “forced” to be “real”). The cross-orthogonality matrix appears

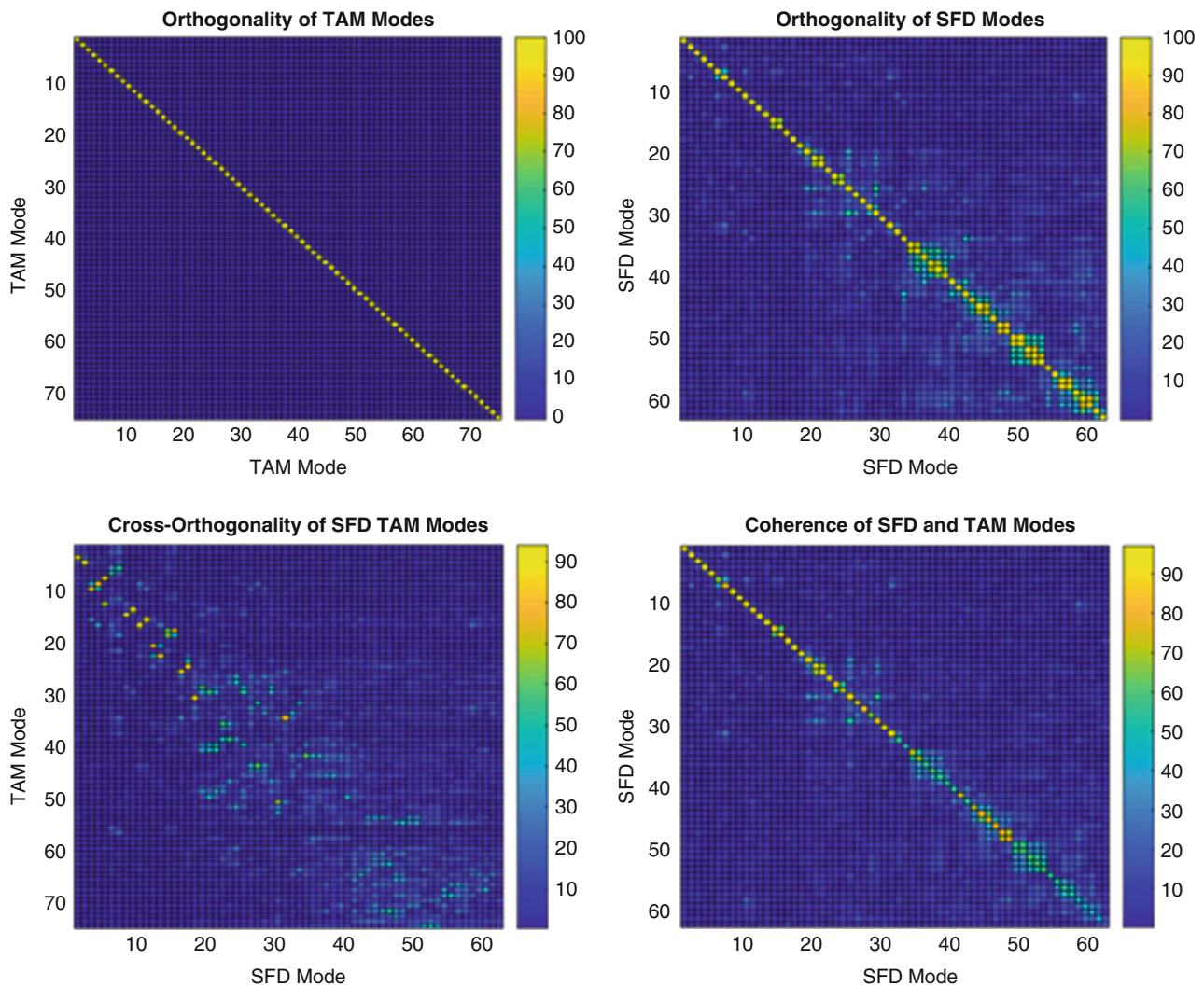


Fig. 31.3 Orthogonality, cross-orthogonality coherence of TAM and test complex eigenvectors (absolute values)

similar in form to its state-space counterpart (see Fig. 31.2), and the modal coherence matrix indicates that the majority of lower frequency ($\sim 50\%$) of test modes are strong linear combinations of the TAM modes.

31.5 Complex Least-Squares Test-TAM Correlation Study Based on Simulations

Qualities of the complex least-squares test-TAM correlation option were studied extensively using simulated modal data sets. Among the various case studies, one particular set employing a 5-DOF model is quite revealing. The stiffness, mass, and damping matrices for this model are provided below in Table 31.1.

Parametric variations of the above model produced three modal data sets, namely real, undamped modes (Model-0), complex, damped modes (Model-1), complex, damped modes associated with half the baseline damping (Model-2). A fourth modal data set (Model-1S) was included corresponding to the baseline, Model-1 complex modes with imposed phase shifts of 45° , 90° and -45° in modes 2, 3, and 4, respectively. This fourth set is used to evaluate ability to “rectify” test modes that are associated phase-shifted test eigenvectors due to off-axis excitation cross-talk. Eigenvalues associated with the first three sets are provided below in Table 31.2.

Cross-orthogonality and modal coherence results associated with various eigenvector sets are provided below in Table 31.3.

Table 31.1 5-DOF illustrative example matrices

Stiffness, [K]				
2000	-1000	0	0	0
-1000	2000	-1000	0	0
0	-1000	2000	-1000	0
0	0	-1000	2000	-1000
0	0	0	-1000	1000
Mass, [M]				
1	0	0	0	0
0	1	0	0	0
0	0	1	0	0
0	0	0	1	0
0	0	0	0	2
Damping, [B]				
2	-1	0	0	0
-1	2	-1	0	0
0	-1	2	-1	0
0	0	-1	2	-1
0	0	0	-1	10

Table 31.2 5-DOF illustrative example eigenvalues

Mode	Model 0: Undamped		Model 1: Damped [B]		Model 2: Perturbed [B]/2	
	Freq (Hz)	Zeta (%)	Freq (Hz)	Zeta (%)	Freq (Hz)	Zeta (%)
1	1.22	0.00	1.21	16.95	1.22	8.36
2	3.76	0.00	3.75	3.88	3.76	1.94
3	6.24	0.00	6.23	2.60	6.24	1.30
4	8.28	0.00	8.27	2.77	8.27	1.38
5	9.61	0.00	9.60	3.05	9.60	1.52

Table 31.3 5-DOF illustrative example cross-orthogonalities and modal coherences

	Magnitude (%)					Phase (deg)					Magnitude (%)					Phase (deg)				
	[COR ₀₁]					[COR ₀₁]					[COH ₀₁]					[COH ₀₁]				
	100	8	3	1	1	1	-85	95	-86	94	100	11	4	1	1	0	-90	93	-87	92
Model 1 vs Model 0	3	100	3	1	0	101	2	-85	94	-86	11	100	5	2	1	90	0	-94	86	-94
	1	2	100	1	0	-80	100	0	-86	94	4	5	100	2	1	-93	94	0	-93	87
	0	1	1	100	1	100	-81	97	0	-87	1	2	2	100	1	87	-86	93	0	-91
	0	0	0	0	100	-81	99	-83	95	0	1	1	1	1	100	-92	94	-87	91	0
Model 2 vs Model 1	100	4	2	1	0	-1	95	-89	89	-92	100	6	2	1	0	0	-90	92	-89	91
	1	100	2	1	0	-76	-1	97	-86	93	6	100	3	1	0	90	0	-92	88	-92
	0	1	100	1	0	108	-78	0	97	-84	2	3	100	1	0	-92	92	0	-91	89
	0	0	0	100	0	-71	102	-81	0	96	1	1	1	100	0	89	-88	91	0	-91
	0	0	0	0	100	109	-78	99	-83	0	0	0	0	0	100	-91	92	-89	91	0
Model 1S vs Model 1	100	0	0	0	0	0	-146	98	-41	0	100	11	4	1	1	0	-45	-177	-132	92
	0	100	0	0	0	100	45	75	94	-168	11	100	5	2	1	45	0	-49	-4	-139
	0	0	100	0	0	-178	142	90	-45	163	4	5	100	2	1	177	49	0	132	-3
	0	0	0	100	0	4	58	93	-45	-2	1	2	2	100	1	132	4	-132	0	-46
	0	0	0	0	100	-172	-135	92	-42	0	1	1	1	1	100	-92	139	3	46	0

The following observations are made from the above results:

1. Cross-orthogonality and modal coherence associated with baseline undamped “TAM” modes (Model-0) and “test” modes (Model-1), indicate proper, comprehensible behavior of the metrics.
2. Cross-orthogonality and modal coherence associated with baseline damped “TAM” modes (Model-1) and “test” modes (Model-2), indicate proper, comprehensible behavior of the metrics. This suggests that complex, damped eigenvectors may be employed in test-TAM evaluations.
3. Cross-orthogonality and modal coherence associated with baseline damped “TAM” modes (Model-1) and phase-shifted “test” modes (Model-1S) indicate proper accounting of test mode phase shifts in the phase of cross-orthogonality. This suggests that complex, “test” eigenvector phase shifts due to excitation cross-talk can be appropriately handled without the need for specialized “phase compensation corrections”.

31.6 Conclusions

The Integrated Spacecraft Payload Element (ISPE) modal test experience led to introduction of experimental modal analysis and test-analysis correlation tool enhancements designed to deal with particularly difficult modal testing challenges. Discrimination of valid and spurious experimental modes was addressed in a related paper [6]. Test-analysis correlation challenges associated with complex, closely-spaced experimental modes are addressed in the present paper. Conclusions associated with test-analysis correlation are as follows:

1. The left-hand, right-hand eigenvector based state-space orthogonality matrix for “valid” (complex) experimental modes automatically satisfies NASA STD-5002 and USAF SMC-004 requirements. The orthogonality matrix for experimental modes is mathematically perfect by definition, and it is independent of the approximate TAM mass matrix.
2. Employment of state-space orthogonality opens the possibility for evaluation of more general experimental dynamic systems including (a) aeroelasticity, (b) structure-control interaction, and (c) launch vehicle POGO applications.
3. Employment of the weighted complex least-squares formulation for test-TAM correlation and modal coherence appears to be an appropriate enhancement for incorporation in NASA STD-5002 and USAF SMC-004 test-analysis correlation standards. It is recognized that the task of modal correlation does not specifically require perfectly orthogonal, real modes; weighted least-squares, which employs the TAM mass matrix, represents a “minor” enhancement for modal test-TAM correlation evaluations.
4. Introduction of the weighted complex least-squares formulation for test-TAM correlation and modal coherence opens the opportunity for inclusion of damping in correlation and update endeavors, e.g., structures with non-negligible modal complexity due to localized, non-proportional damping mechanisms (joints).
5. The weighted complex least-squares formulation for test-TAM correlation and modal coherence automatically accounts for phase-shifted experimental modes that are the result of test excitation cross-talk.

The developments influenced by the ISPE test experience offer potential enhancements to U.S. Government modal testing standards that must undergo wider studies and critiques before establishment of general acceptance in the structural dynamics technical community.

References

1. Coppelino, R.: Chapter 23: Finite element methods of analysis. In: Piersol, A., Paez, T. (eds.) *Harris’ Shock and Vibration Handbook*, 6th edn. McGraw-Hill, New York (2010)
2. Allemang, R., Brown, D.: Chapter 21: Experimental Modal Analysis. In: Piersol, A., Paez, T. (eds.) *Harris’ Shock and Vibration Handbook*, 6th edn. McGraw-Hill, New York (2010)
3. *Load Analyses of Spacecraft and Payloads*. NASA-STD-5002 (1996)
4. *Independent Structural Loads Analysis*. Air Force Space Command, SMC-S-004 (2008)
5. Coppelino, R.: *Methodologies for Verification and Validation of Space Launch System (SLS) Structural Dynamic Models*, NASA CR-2018-219800/Volume I (2018)
6. Coppelino, R.: *Experimental Mode Verification (EMV) using Left-Hand Eigenvectors*, IMAC XXXVII (2019)
7. Miller, K.: Complex linear least squares. *SIAM Rev.* **15**(4), 706–726 (1973)



Chapter 32

A Theoretical Study on the Generation and Propagation of Traveling Waves in Strings

Isil Anakok, V. V. N. Sriram Malladi, and Pablo A. Tarazaga

Abstract The goal of this work is to understand the generation and propagation of one-dimensional steady state traveling waves in a finite medium with a two-force excitation methodology. The solution to the second order partial differential equation describing the equation of motion for a string is theoretically solved considering a fixed-fixed boundary condition. The parameters that affect the generation and propagation of waves should be well understood to control and manipulate the desired system's response. The string equation is solved by rearranging it based on linear wave components and phase difference components needed to generate steady-state traveling waves in a string. Two excitation forces are applied to a string near the boundaries to understand the generation and propagation of traveling waves at various frequencies. Determining the quality of the traveling waves and understanding the parameters on the wave propagation of a string can lead to further understand and leverage various engineering disciplines such as mechanical actuation mechanisms, propulsion of flagella, and the basilar membrane in the ear's cochlea.

Keywords Traveling waves · Vibration · Cost function · Strings · Two force excitations

32.1 Introduction

In previous works, Gabai et al. studied how multiple forces can be applied to one-dimensional structures as to develop and characterize traveling waves [1, 2]. Malladi et al. studied non-reflective waves in beams analytically and experimentally and in such studies a cost function (CF) is introduced to understand the quality of the traveling waves generated in a beam with free-free boundary condition [3–7]. The theoretical study of generating traveling waves for one-dimensional beams and higher-dimensional structures were further developed to great detail in [8]. Earlier work by the authors studied applied a two-force excitation and a cost function approach to generate and propagate steady-state travelling, standing, and hybrid waves in a string under fixed-fixed boundary conditions in [9]. The work was later extended by studying a string at different boundary conditions and adapting their cost functions to generate traveling waves at various frequencies [10]. Furthermore, the analytical study of a fixed-fixed string was validated by an experiment in [10]. This work analyzes and widens the simplified theory of generating traveling waves in strings. The solution to the second order partial differential equation describing the motion for a string is studied analytically and the direction of generation of traveling waves is discussed based on the effect of phase difference between two applied forces.

32.2 Analysis of the One-Dimensional Equation of Motion for Strings

The homogeneous solution of the second order partial differential equation describing a string can be found in [9]. A fixed-fixed string of length L excited by two forces ($F_1 = \cos(\omega t)$ and $F_2 = \cos(\omega t + \Phi)$) with a phase difference between the forces of Φ , is studied. F_1 and F_2 are applied at equal distance from both ends of the string (l_1 and l_2). The location

I. Anakok (✉) · V. V. N. S. Malladi · P. A. Tarazaga
Vibration, Adaptive Structures and Testing Lab (VAST), Department of Mechanical Engineering, Virginia Polytechnic Institute and State University, Blacksburg, VA, USA
e-mail: ianakok@vt.edu

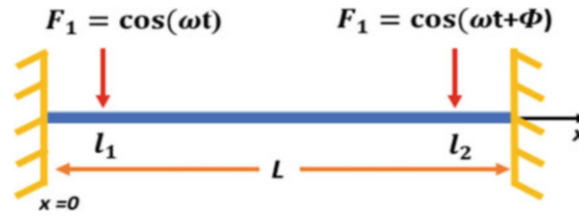


Fig. 32.1 The schematic of a string with two excitation forces and a fixed-fixed boundary condition

of the applied forces on the string, are shown in Fig. 32.1. The generation of traveling waves is highly dependent on the phase difference between two harmonic forces [10]. The equation of motion of a string subject to two external forces near its boundaries is given by,

$$\frac{\partial^2 w(x, t)}{\partial t^2} - c^2 \frac{\partial^2 w(x, t)}{\partial x^2} = \frac{F_1}{\rho A} \cos(\omega t) \delta(x - l_1) + \frac{F_2}{\rho A} \cos(\omega t + \Phi) \delta(x - l_2), \quad (32.1)$$

where $c (\sqrt{\tau/\rho A})$, τ is the tension, A is the cross-sectional area of the structure, ρ is the density of the structure, l_1 is the distance to the first force from the first end and l_2 is the distance to the second force from the second end.

The boundary condition at both ends are given by $w(0, t) = w(L, t) = 0$. A standard separation of variables approach is used to solve the equation of motion [11]. Thus, the response can be expressed as,

$$w(x, t) = \sum_{n=1}^{\infty} X_n(x) T_n(t), \quad (32.2)$$

where $X_n(x)$ is the spatial solution and $T_n(t)$ is the temporal solution. The two-force solution of a string is simplified by superposition as,

$$w(x, t) = \sum_{n=1}^{\infty} \frac{X_n(x) [f_1 \cos(\omega t) X_n(l_1) + f_2 X_n(l_2) \cos(\omega t + \Phi)]}{\omega_n^2 - \omega^2}, \quad (32.3)$$

where ω_n is the n th natural frequency given by $\omega_n = (n\pi/L) \sqrt{\tau/\rho A}$, and ω is the driving frequency. The solutions of the spatial component, $X_n(x)$, is given by the mode shapes (eigenfunctions) of the string as $\sin((n\pi/L)x)$, for $n = 1, 2, 3, \dots, \infty$ and $x \in [0, L]$.

Malladi et al. introduced the two-mode approximation as a summation of the response of the string at two modes that are symmetric and anti-symmetric [8]. Two response of the string yields

$$w_T(x, t) = w_{m1} + w_{m2} = \frac{X_{m1}(x) [f_1 \cos(\omega t) X_{m1}(l_1) + f_2 X_{m1}(l_2) \cos(\omega t + \Phi)]}{\omega_{m1}^2 - \omega^2} + \frac{X_{m2}(x) [f_1 \cos(\omega t) X_{m2}(l_1) + f_2 X_{m2}(l_2) \cos(\omega t + \Phi)]}{\omega_{m2}^2 - \omega^2}, \quad (32.4)$$

where subscripts $m1$ and $m2$ represent the first and second mode contribution. To simplify further, it is assumed that the applied forces, f_1 and f_2 , the mass normalized forces, are equal. Since both forces are applied from equal distances from the ends the spatial solution $X_n(l_1) = X_n(l_2)$ for the symmetric mode ($m1$) and $-X_n(l_1) = X_n(l_2)$ for the asymmetric mode ($m2$). By considering these conditions, substituting the determined spatial solutions, and grouping products of Eq. (32.4) that are not dependent on time and space, Eq. (32.4) is rearranged as,

$$w_T(x, t) = \sqrt{2} C_1 \left[(\cos(\omega t) X_{m1}(x) + \cos(\omega t + \Phi)) + (C_2 \cos(\omega t) X_{m2}(x) - \cos(\omega t + \Phi)) \right], \quad (32.5)$$

where $C_1 = \frac{f X_{m1}(l_1)}{\sqrt{2(\omega_{m1}^2 - \omega^2)}}$ and $C_2 = \frac{X_{m2}(l_1)(\omega_{m1}^2 - \omega^2)}{X_{m1}(l_1)(\omega_{m2}^2 - \omega^2)}$. According to [8], the string response can be written as a linear combination of four waves ($W_1 - W_4$) and four coefficients ($C_a - C_d$) that only carry the phase difference information shown in Eqs. (32.6) and (32.7).

$$w_T(x, t) = \sqrt{2} C_1 [C_a W_1 + C_b W_2 + C_c W_3 + C_d W_4] \quad (32.6)$$

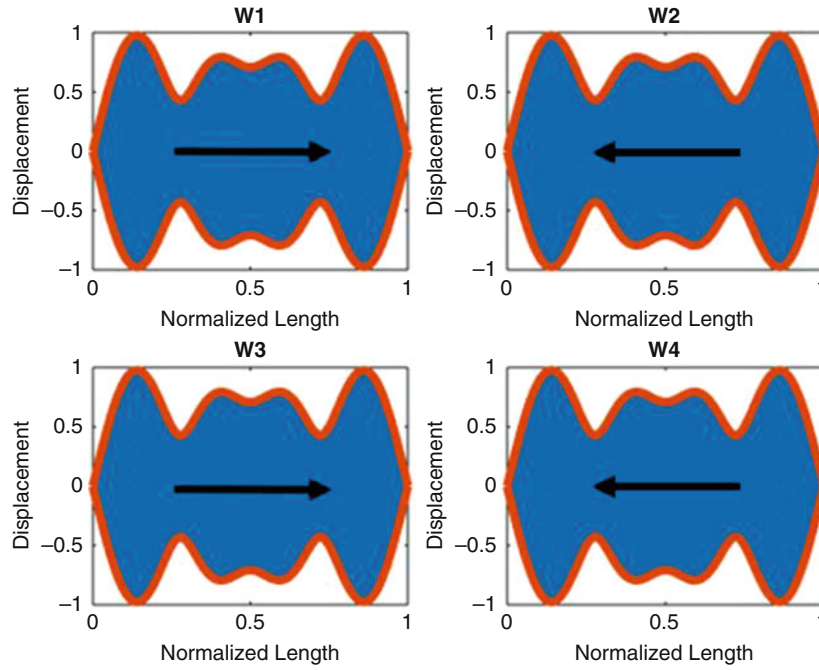


Fig. 32.2 The swept area of four linear waves of the response of a string

where

$$\begin{aligned}
 W_1 &= \frac{1}{\sqrt{2}} \left[X_{m1}(x) \cos \left(\omega t - \frac{\pi}{4} \right) + X_{m2}(x) \cos \left(\omega t + \frac{\pi}{4} \right) \right] \\
 W_2 &= \frac{1}{\sqrt{2}} \left[X_{m1}(x) \cos \left(\omega t + \frac{\pi}{4} \right) + X_{m2}(x) \cos \left(\omega t - \frac{\pi}{4} \right) \right] \\
 W_3 &= \frac{1}{\sqrt{2}} \left[X_{m1}(x) \cos \left(\omega t + \frac{\pi}{4} \right) - X_{m2}(x) \cos \left(\omega t - \frac{\pi}{4} \right) \right] \\
 W_4 &= \frac{1}{\sqrt{2}} \left[X_{m1}(x) \cos \left(\omega t - \frac{\pi}{4} \right) - X_{m2}(x) \cos \left(\omega t + \frac{\pi}{4} \right) \right]
 \end{aligned} \tag{32.7}$$

and

$$\begin{aligned}
 C_a &= (1 + C_2) + (1 - C_2) \cos \Phi + (1 + C_2) \sin \Phi \\
 C_b &= (1 + C_2) + (1 - C_2) \cos \Phi + (1 + C_2) \sin \Phi \\
 C_c &= (1 - C_2) + (1 + C_2) \cos \Phi + (1 - C_2) \sin \Phi \\
 C_d &= (1 - C_2) + (1 + C_2) \cos \Phi - (1 - C_2) \sin \Phi
 \end{aligned}$$

where $X_{m1}(x) = \sin \left(\left(\frac{(m1)\pi}{L} \right) x \right)$ and $X_{m2}(x) = \sin \left(\left(\frac{(m2)\pi}{L} \right) x \right)$. To visualize the characteristic of the linear waves in MATLAB, the 3rd and 4th modes are considered. Figure 32.2 shows each wave's swept area by time including the directions they travel.

While W_1 and W_3 travel to the right, W_2 and W_4 travel to the left. The swept areas of the summation of two linear waves are shown in Fig. 32.3. It is shown that $W_1 + W_4$ and $W_2 + W_3$ generate standing waves and that it can also be observed that traveling waves can be generated when the following combinations occur: $W_1 + W_3$ and $W_2 + W_4$. Additionally, each combination generates traveling waves at opposite direction.

Furthermore, Fig. 32.4 shows that $W_1 - W_3$ and $W_2 - W_4$ generate traveling waves at the opposite direction with $W_1 + W_3$ and $W_2 + W_4$, respectively. Thus, the combination to generate traveling waves affect the direction of the generated wave. Each combination has a CF value of 0.057 which is ideally expected to be zero for the traveling waves.

According to [8], the phase difference between the two forces can be calculated as

$$\Phi = \tan^{-1} \left(\frac{2C_2}{C_2^2 - 1} \right) + n\pi \quad \text{and} \quad \Phi = \tan^{-1} \left(\frac{-2C_2}{C_2^2 - 1} \right) + n\pi, \tag{32.8}$$

where C_2 is independent from time(t) and space(x). According to Eq. (32.8), the phase angle that minimizes the cost function of the traveling waves at various driving frequencies between 3rd and 4th modes is plotted in Fig. 32.5.

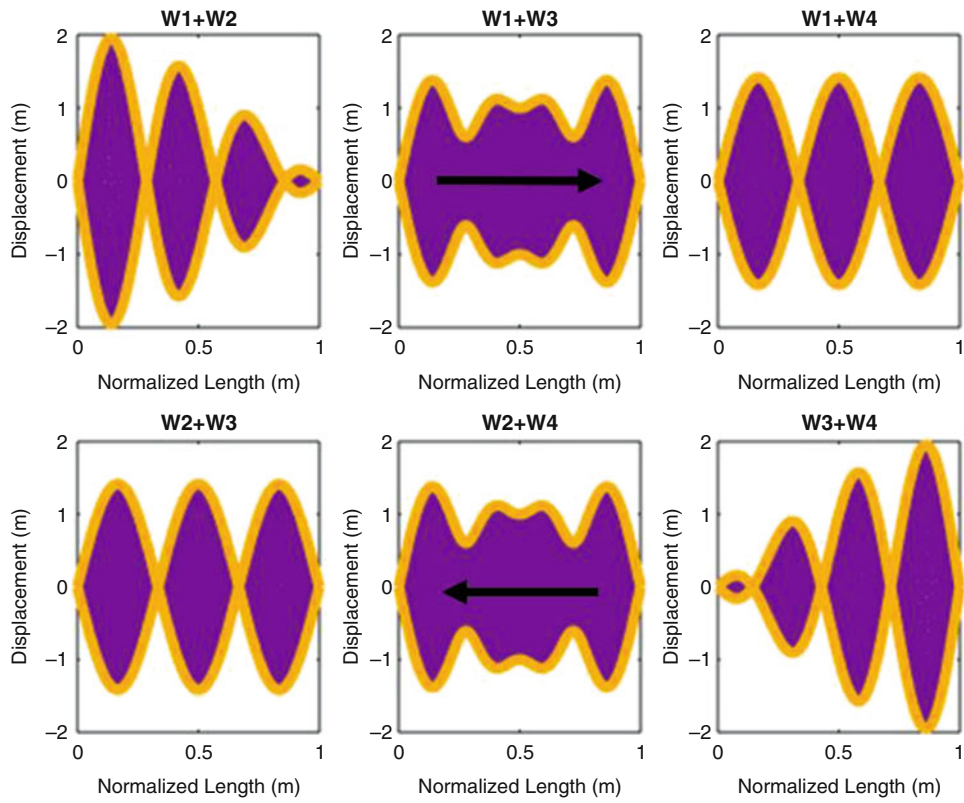


Fig. 32.3 The combinations of the swept areas of the summation of two linear waves

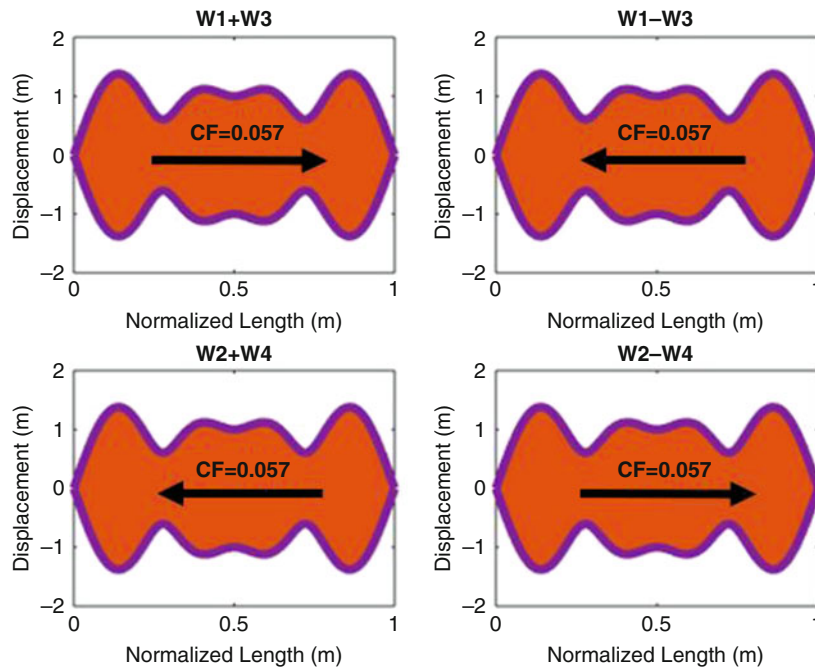


Fig. 32.4 The swept areas of the summation and subtraction of two linear waves along with their directions and the values of the CFs

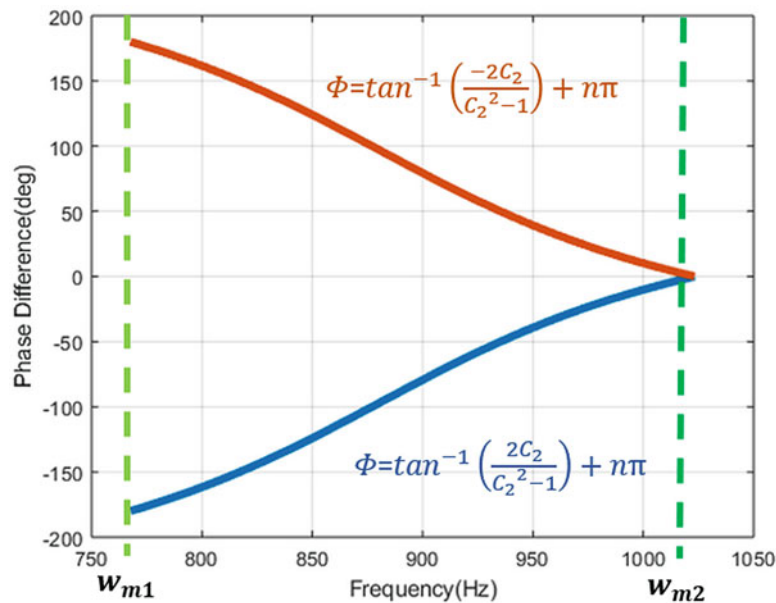


Fig. 32.5 The optimal cost function graph for a fixed-fixed string's traveling wave at various frequencies versus the phase difference from -180° to 180°

When Φ in Eq. (32.8) is chosen between 0° and 180° C_a and C_c are equal to zero and the traveling waves are the combination of the linear waves W_2 and W_4 . Similarly, if Φ is between -180° and 0° C_b and C_d are equal to zero and the traveling waves are the combination of the linear waves W_2 and W_4 . Thus, the direction of traveling waves can vary by changing the sign of the phase difference.

32.3 Conclusion

In this work, string equation is analyzed theoretically to generate steady-state traveling waves. The response is simulated in MATLAB for a fixed-fixed boundary condition. The two-force excitation approach is applied and the response of the second order partial differential equation is solved by using two-mode approach similar to previous studies. The relation between frequency and phase difference for traveling waves is extended to strings from the previous work developed in beams. Based on the preliminary theoretical study and simulations, the direction of the traveling waves in a string can be manipulated by addressing the phase angle used. The work has shown that steady state waves can be generated using this two-force approach in different directions via a careful understanding of the phase angle.

Acknowledgment VVNS Malladi and P Tarazaga would like to acknowledge the support of the Air Force Office of Scientific Research through the Young Investigator Program (FA9550-15-1-0198). Dr. Tarazaga would also like to acknowledge the support obtained through the John R. Jones III Faculty Fellowship.

References

1. Gabai, R., Bucher, I.: Spatial and temporal excitation to generate traveling waves in structures. *J. Appl. Mech.* **77**(2), 021010 (2010)
2. Gabai, R., Bucher, I.: Excitation and sensing of multiple vibrating traveling waves in one-dimensional structures. *J. Sound Vib.* **319**(1), 406–425 (2009)
3. Malladi, V.V.N.S., Avirovik, D., Priya, S., Tarazaga, P.A.: Travelling wave phenomenon through a piezoelectric actuation on a free-free beam. In ASME 2014 Conference on Smart Materials, Adaptive Structures and Intelligent Systems, p. V001T03A017-V001T03A017 (2014)
4. Malladi, V.V.N.S., Avirovik, D., Priya, S., Tarazaga, P.: Characterization and representation of mechanical waves generated in piezo-electric augmented beams. *Smart Mater. Struct.* **24**(10), 105026 (2015)
5. Malladi, V.V.N.S., Albakri, M., Tarazaga, P.A.: An experimental and theoretical study of two-dimensional traveling waves in plates. *J. Intell. Mater. Syst. Struct.* **28**(13), 1803–1815 (2017)

6. Malladi, V.V.N.S., Albakri, M., Musgrave, P., Tarazaga, P.A.: Investigation of propulsive characteristics due to traveling waves in continuous finite media. In *SPIE Smart Structures and Materials+ Nondestructive Evaluation and Health Monitoring*, International Society for Optics and Photonics, pp. 101620O-101620O (2017)
7. Malladi, V.V.N.S., Albakri, M.I., Gugercin, S., Tarazaga, P.A.: Application of projection-based model reduction to finite-element plate models for two-dimensional traveling waves. *J. Intell. Mater. Syst. Struct.* **28**(14), 1886–1904 (2017)
8. Malladi, V.V.N.S.: Continual traveling waves in finite structures: theory, simulations, and experiments. PhD thesis, Virginia Tech (2016)
9. Anakok, I., Malladi, V.V.N.S., Tarazaga, P.A.: A study on the generation and propagation of traveling waves in strings. In: Mains, M.L., Dilworth, B.J. (eds.) *Topics in Modal Analysis & Testing*, vol. 9, pp. 257–261. Springer, Cham (2019)
10. Anakok, I: A study on steady state traveling waves in strings and rods. MS thesis, Virginia Tech (2018)
11. Inman, D.J., Singh, R.C.: *Engineering Vibration*, vol. 3. Prentice Hall, Upper Saddle River (2001)



Chapter 33

Shaping the Frequency Response Function (FRF) of a Multi-Degree-of-Freedom (MDOF) Structure Using Arrays of Tuned Vibration Absorbers (TVA)

Campbell R. Neighborgall, Karan Kothari, V. V. N. Sriram Malladi, Pablo Tarazaga, Sai Tej Paruchuri, and Andrew Kurdila

Abstract Tuned vibration absorbers (TVA) provide passive energy dissipation from their primary structure but are limited to only having significant impact on a single frequency. Many researchers have theoretically determined optimal TVA parameters to build an array of varied sized TVAs to absorb a range of frequencies and ultimately flatten an entire peak of a structure's frequency response function (FRF). These theoretical approaches often only considered the primary structure to have a single degree-of-freedom and did not consider material and spatial constraints that would normally arise in physical implementation. This study provides the method and results of designing and implementing multiple arrays of TVAs to flatten the FRF at and around both modal frequencies of a two-degree-of-freedom (2DOF) structure. The host 2DOF structure is comprised of two small wooden blocks supported by four thin aluminum posts in a two-story setup with base excitation. A total of 20 TVAs were attached to each primary mass—ten targeting frequencies around the low-frequency mode and ten targeting frequencies around the high-frequency mode. The TVAs were cantilever beams made of varied length dry fettuccini pasta with some including modeling-clay tip masses. The final design successfully reduced the original 2DOF structure's first natural frequency response by more than 9 dB and second natural frequency response by more than 19 dB for both primary masses.

Keywords Vibration absorbers · Pasta · Multiple degrees-of-freedom · Demo · Tuning

33.1 Introduction

Tuned Vibration Absorbers (TVAs) are widely used to minimize the response of structures. However, TVAs are most useful when the frequency of operation is fixed. Furthermore, the addition of a TVA to a host structure adds another degree-of-freedom, which creates an additional peak to the frequency response of the system. Tunable piezoceramic vibration absorbers have been proposed to overcome this shortcoming. By changing the parameters of the shunt circuit attached to the piezoceramic, the vibration absorber can be tuned for different frequency of operation [1, 2]. However, active control techniques are necessary for tuning the piezoceramic vibration absorber. Vibrations researchers approached this problem from a different perspective and investigated ways to eliminate the peaks from the frequency response of a system. Attaching an array of linear TVAs to a host structure was shown to be an effective method to reduce the resonant peaks of the system, thus increasing the range of operation [3–6]. The application of multiple absorbers for broadband frequency attenuation complicates the design process. Vignola et al. [3] showed that the design process could be simplified by assigning distribution functions to the structural parameters of the oscillator array. They also studied the effect of the mass ratio for a given oscillator array and showed that a flat frequency response function could be achieved at mass ratios as low as 1%. Zuo and Nayfeh [4] formulated the model of an array of substructures attached to a single-degree-of-freedom primary structure as a decentralized feedback controller problem and developed a method to optimize the system parameters. Despite these benefits, tuned vibrations absorber arrays are very sensitive to uncertainties in structural parameters [7]. Hence piezoelectric oscillator arrays are being studied to develop tunable oscillators arrays. Paruchuri et al. [8, 9] modeled Piezoelectric Subordinate Oscillator Arrays (PSOAs) attached to a single degree of freedom host structure and proposed PSOA design techniques

C. R. Neighborgall · K. Kothari · V. V. N. Sriram Malladi (✉) · P. Tarazaga · S. T. Paruchuri · A. Kurdila
Vibrations, Adaptive Structures and Testing Laboratory, Department of Mechanical Engineering, Virginia Polytechnic Institute and State University, Blacksburg, VA, USA
e-mail: sriram@vt.edu

based on the selection of non-dimensional frequency distribution. The literature found on TVA arrays have primarily focused on the vibration attenuation of a single-degree-of-freedom structure. Kitis et al. in [10] proposed a numerical approach to minimize the response of a cantilever beam, a multi-degree of freedom structure, attached to multiple TVAs. However, each TVA was optimized to reduce each resonant peak of the multi-degree of freedom structure. This paper presents a case study on the effectiveness of using multiple TVA arrays in broadband frequency vibration attenuation over two resonant peaks. A model of four TVA arrays attached to a two-degree-of-freedom host system is presented, and the parameters selection methods are discussed. Finally, numerical and experimental results are compared.

33.2 Experiment Setup and Testing Procedure

The 2DOF host structure is made of two wooden blocks supported by four aluminum posts. Each wooden block is fitted with one accelerometer and bolted with three aluminum angles used to mount the TVAs, resulting in a total mass of 272 g for the primary mass 1 and 276 g for the primary mass 2. The total mass of the four aluminum posts is 127 g. Each TVA was a dry fettuccini pasta of specific length, with some of the TVAs including modeling clay tip masses. The TVAs were fixed to the aluminum angles via hot-melt adhesives. Figure 33.1 below displays the complete structure with both high and low-frequency TVA arrays. Only the low-frequency TVAs included tip masses.

The combined stiffness of the posts between each mass was estimated from geometric dimensions and material properties. These values were later tuned in the numerical model to best fit the 2DOF model's response to experimentally measured FRF of the 2DOF structure before applying the TVAs. Additionally, two damping ratios were applied to the model after collecting the experimental results, one for all TVAs and one for all aluminum posts. From the final tests, the 2DOF host structure had resonant frequencies at 3.34 and 9.39 Hz. With such low resonant frequencies, choosing the TVA material and geometry was crucial to effectively attenuate the 2DOF host structure's displacement response over a bandwidth around each resonant frequency. A variety of materials with a range of cross-section geometries were considered before selecting the final TVA material as dry fettuccini pasta. Despite the pasta being much less dense than some considered metals (about 1400 kg/m^3 for pasta contrast to 2700 kg/m^3 for aluminum and 8050 kg/m^3 for steel), the dry pasta is substantially less stiff than either metal (Young's Modulus of about 5 GPa for dry pasta contrast to 69 GPa for aluminum and 200 GPa for steel), giving it a lower first mode frequency than either metals with similar geometry. Fettuccini's cross-section allowed it to have a lower first resonant frequency compared to other dry pasta of equal length while also providing more surface area to adhere to our structure for secure mounting.

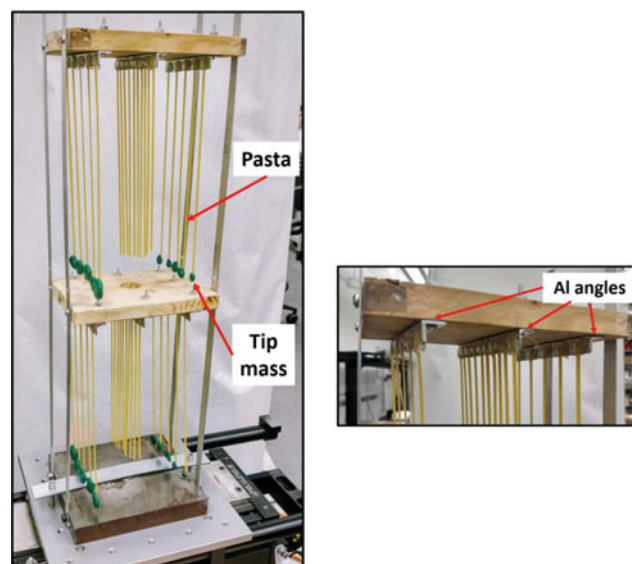


Fig. 33.1 Pictures of a physical system with low and high-frequency TVAs on both primary masses. The pasta TVAs were glued to the aluminum angles which were then bolted to the primary masses to minimize energy losses in the TVA mounts

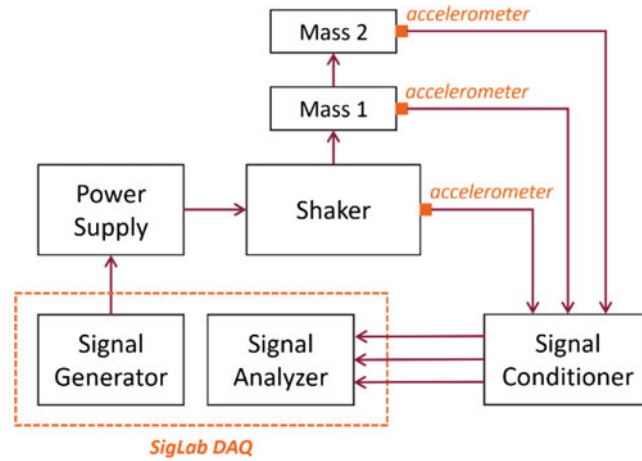


Fig. 33.2 Diagram of experiment setup and flow of signals

The experimentation setup used a SigLab[®] for signal generation and for the data acquisition (DAQ). A power amplifier magnified the signal to move the APS Electro-SIES shaker, providing base motion to the structure. Three high-sensitivity (~ 10 g/V) PCB[®] accelerometers were used in the tests—one at the base and one at each primary mass—and were routed to the SigLab[®] DAQ through a PCB[®] signal conditioner. SigLab[®]'s signal analyzer then calculated and plotted the frequency response function for each of the primary masses' displacement with respect to the base's displacement from the voltages received from the signal conditioner. The schematic setup used in all experiments is illustrated by Fig. 33.2.

33.3 Modeling

All components of the system were assumed to be linear and time-invariant to produce a lumped-parameter model (LPM) of the entire physical system. Using an LPM provided quick and straight-forward manipulation to address various TVA properties and adapt to different numbers of TVAs targeting each mode individually. The lumped-parameter model of the entire structure with $N1$ low-frequency TVAs targeting the host structure's first mode and $N2$ high-frequency TVAs targeting the host structure's second mode is illustrated as Fig. 33.3. Notice the system is under base excitation x_0 which is only connected directly to the first primary mass, m_1 .

To convert the cantilever beam TVAs into lumped-parameter models, each TVA was modeled as a spring-mass-damper with an undamped natural frequency equal to the first mode of vibration of an undamped Euler-Bernoulli beam of the same material and geometric properties. A Euler-Bernoulli beam's transverse vibration is governed by

$$\frac{\partial^2 w(x, t)}{\partial t^2} + c^2 \frac{\partial^4 w(x, t)}{\partial x^4} = 0, \quad \text{where } c = \sqrt{\frac{EI}{\rho A}} \quad (33.1)$$

which has a general spatial solution

$$X(x) = a_1 \sin \beta x + a_2 \cos \beta x + a_3 \sinh \beta x + a_4 \cosh \beta x \quad (33.2)$$

where $x = 0$ at the fixed end and $x = l$ at the free end [11]. Applying boundary conditions to the general spatial solution results in four equations to solve for the four coefficients a_1 , a_2 , a_3 , and a_4 . Setting the determinant of the coefficient matrix for these four equations equal to zero results in the characteristic equation

$$\cos(\beta_n l) + \cosh(\beta_n l) = -1, \quad (33.3)$$

where $\beta_n l$ is the n th weighted frequency of the Euler-Bernoulli cantilever beam. Equation (33.3) has an infinite number of weighted frequency solutions, but the first weighted frequency ($\beta_1 l = 1.8751$) provides the beam's first resonant frequency according to

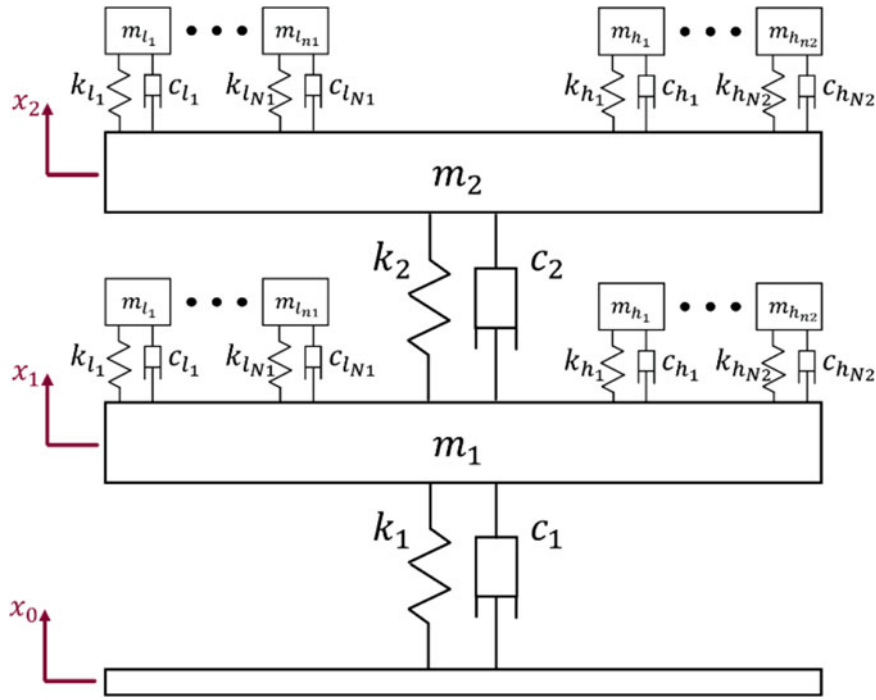


Fig. 33.3 Lumped-parameter model of the complete system under base excitation x_0 with N_1 low-frequency TVAs and N_2 high-frequency TVAs

$$\beta_1^4 = \frac{\omega_{n_1}^2}{c^2} \rightarrow \omega_{n_1} = \beta_1^2 \sqrt{\frac{EI}{\rho A}}. \quad (33.4)$$

Each cantilever beam's known mass and first resonant frequency was used to find its equivalent stiffness. This neglected the beam's second and higher order modes' contributions to its vibration, reducing the model's accuracy when the TVAs are excited at frequencies equal to or near their higher order mode frequencies. Because the lowest frequency TVA has a second resonant frequency well above the host structure's second resonant frequency, this neglect was acceptable.

With known material properties and geometry of a cantilever beam, the Euler-Bernoulli beam length, l , can be written as an equation of its first resonant frequency by

$$\beta_1 l = 1.8751 = B_1 \rightarrow l = \sqrt{\frac{B_1^2 c}{\omega_{n_1}}}. \quad (33.5)$$

The mass of each TVA was found from its density, cross-section area, and length, and the equivalent stiffness for the lumped-parameter model of each beam was found from its first mode frequency and mass as described by

$$m = \rho A l \quad (33.6)$$

$$k_{eq} = \omega_{n_1}^2 m \quad (33.7)$$

Equations (33.5), (33.6), and (33.7), provided a means to determine each TVA cantilever beam's length by its target resonant frequency while also providing the mass and stiffness parameters for the LPM. Damping ratios were later applied to the model's TVAs, and host structure supports after comparing the experimental and undamped numerical model FRFs. As such, the damping coefficients for the TVAs and host structure, respectively, are

$$c_{TVA} = \frac{\zeta_{TVA}}{2\sqrt{k_{TVAeq} m_{TVA}}} \quad (33.8)$$

and

$$c_p = \frac{\zeta_p}{2\sqrt{k_{peq}m_p}}. \quad (33.9)$$

The LPM for the entire system was then modeled by the mass (\mathbf{M}), damping (\mathbf{C}), and stiffness (\mathbf{K}) matrices described by

$$\mathbf{M} = \begin{bmatrix} m_1 & & & 0 \\ & m_2 & & \\ & & \text{diag} \{m_l\} & \\ 0 & & n=1 \dots N1 & \\ & & & \text{diag} \{m_h\} \\ & & & n=1 \dots N2 \end{bmatrix} \quad (33.10)$$

$$\mathbf{C} = \begin{bmatrix} c_1 + c_2 + \sum c_l + \sum c_h & -c_2 & -c_l & 0 \\ -c_2 & c_2 + \sum c_l + \sum c_h & 0 & -c_h \\ -c_l & 0 & \text{diag} \{c_l\} & 0 \\ 0 & -c_h & 0 & \text{diag} \{c_h\} \end{bmatrix} \quad (33.11)$$

$n=1 \dots N1$ $n=1 \dots N2$

$$\mathbf{K} = \begin{bmatrix} k + k_2 + \sum k_l + \sum k_h & -k_2 & -k_l & 0 \\ -k_2 & k_2 + \sum k_l + \sum k_h & 0 & -k_h \\ -k_l & 0 & \text{diag} \{k_l\} & 0 \\ 0 & -k_h & 0 & \text{diag} \{k_h\} \end{bmatrix} \quad (33.12)$$

$n=1 \dots N1$ $n=1 \dots N2$

where \mathbf{m}_l , \mathbf{m}_h , \mathbf{c}_l , \mathbf{c}_h , \mathbf{k}_l , and \mathbf{k}_h , are vectors of the masses (m), damping coefficients (c), and equivalent stiffnesses (k) of the low (l) and high (h) frequency TVAs, respectively.

33.4 Results and Discussion

The following subsections discuss the results associated with the experiments as well as a discussion and comparison with the model.

33.4.1 Experimental Results

TVAs were sized such that their first resonant frequencies equaled a linear distribution within a ± 1.5 Hz bandwidth around the low and high resonant frequencies of the original 2DOF host structure. This bandwidth was determined by the original 2DOF structure's FRF where the peaks fell below 10 dB when no TVAs were attached. This same bandwidth and number of TVAs for the two arrays attached to each primary mass was also included in the numerical model. The 2DOF structure's first and second resonant frequencies were 3.34 Hz and 9.39 Hz, respectively, making the low-frequency TVA array target frequencies between 1.84 and 4.84 Hz and the high-frequency TVA array target frequencies between 7.89 and 10.89 Hz. Each primary mass held two arrays of ten TVAs with 0.33 Hz spacing between each TVA. Due to fabrication inaccuracies, the lowest frequency TVA resonated just above 2 Hz. To minimize testing duration while also capturing all TVA frequencies, the testing frequency range was 2–13 Hz with a 0.045 Hz frequency step in a stepped-dwell excitation. The higher frequency tests were kept to see if the experimental FRF was less than the model FRF, where cantilever beams would vibrate at their higher order resonance which was not captured by the model.

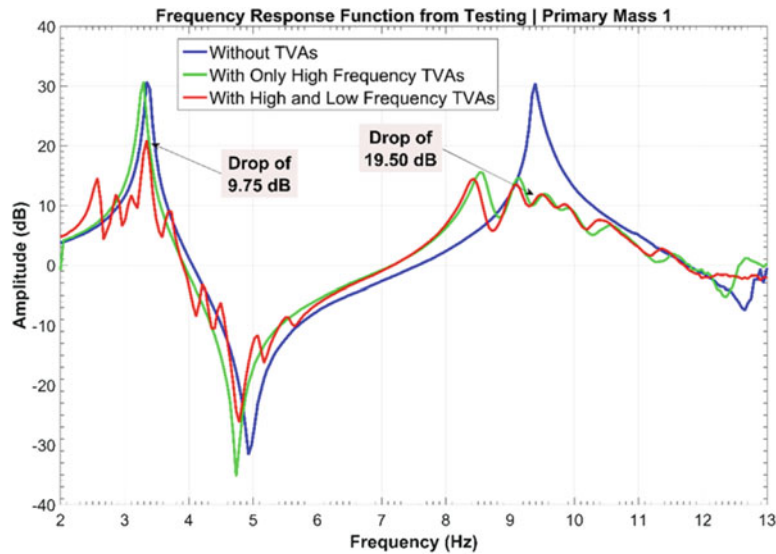


Fig. 33.4 Primary mass 1 displacement amplitude response with respect to base displacement vs. frequency from experimentation

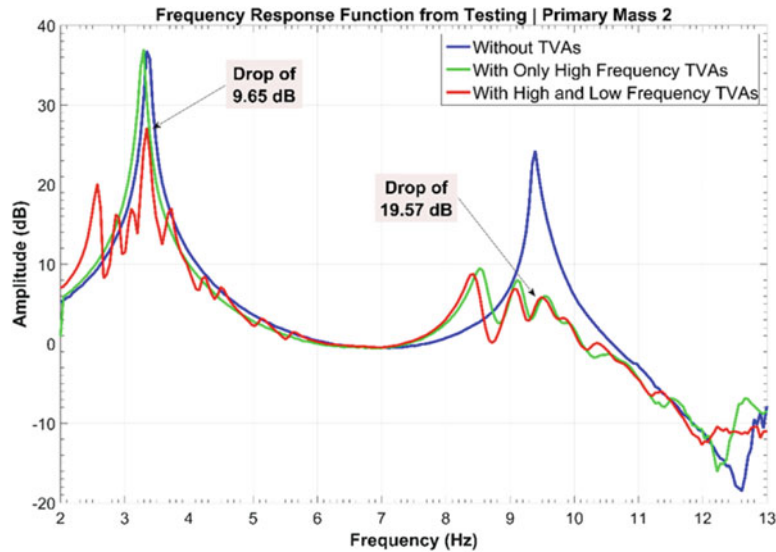


Fig. 33.5 Primary mass 2 displacement amplitude response with respect to base displacement vs. frequency from experimentation

Primary Mass 1 Figure 33.4 displays the experimental frequency response function of primary mass one displacement with respect to the structure's base displacement. For the case with both high and low-frequency TVAs, the magnitude response of the first peak observed at 3.34 Hz was attenuated by 9.75 dB, while the second peak, observed at 9.39 Hz, was attenuated by 19.50 dB. Figure 33.4 also shows that by using only the higher frequency TVAs with the primary structure isolates and damps the second mode of primary mass one without having a significant effect on its first mode's magnitude.

Primary Mass 2 Figure 33.5 shows the experimental frequency response function obtained for primary mass 2 with respect to the base of the structure. The magnitude response of the first peak observed at 3.34 Hz was attenuated by 9.65 dB due to the addition of the TVAs to the structure, while the second peak observed at 9.39 Hz was attenuated by 19.57 dB. Much like in the case of the primary mass 1, Fig. 33.5 also shows that using only the higher frequency TVAs with the primary structure does not have a significant impact on the magnitude of the primary structure's first mode, but lowers that frequency by 1.4% due to the increased mass of the total system.

33.4.2 Lumped-Parameter Model Results

The lumped-parameter model (LPM) of the system was used for basic understanding of how the TVAs affect the primary masses' FRFs. The LPM neglected gravitational effects, assumed the transverse vibrations in the cantilever TVAs behaved linearly, and neglected the cantilever TVAs second and higher order modes' contributions to the TVAs vibration.

The model's simulated frequencies ranged from 2 to 13 Hz to match the experiment's bandwidth. Comparisons of the FRF of the structure with both the high and low-frequency TVAs attached to both primary masses are shown with the baseline results (primary 2DOF structure without any TVAs). Also shown are the primary masses' responses when only high-frequency TVAs were attached to both primary mass.

The numerical modeling provided a proof-of-concept by showing that the two arrays of ten TVAs each could successfully and significantly attenuate the magnitude response of the 2DOF host structure's modes.

Primary Mass 1 As seen from Fig. 33.6, the variable length fettuccini pasta TVAs successfully damped the two primary modes of vibration of the 2DOF structure. The magnitude response of the first peak observed at 3.34 Hz was attenuated by 27.44 dB while the second peak, observed at 9.39 Hz, was attenuated by 23.19 dB.

Figure 33.6 also shows that when using only the high-frequency TVAs, the primary mass 1's vibration was successfully attenuated at the host structure's second mode without significantly influencing the first mode's magnitude.

Primary Mass 2 Similar to the results shown in Fig. 33.6, Fig. 33.7 shows that only implementing high-frequency TVAs successfully attenuates the vibration of primary mass two at the host structure's second mode without significant impact on the first mode's magnitude. Mass 2's vibration at both of the primary structure's modes is significantly attenuated when both low and high frequency TVAs were attached. Specifically, the magnitude response of the first peak observed at 3.34 Hz was reduced by 26.52 dB, while the second peak observed at 9.39 Hz was reduced by 23.18 dB when including both low and high frequency TVAs. For both primary masses, the first mode's frequency decreases by 2.7% due to the added mass of the TVAs. This is especially noticeable by the first peak of the system with no TVAs and first peak with only high-frequency TVAs.

33.4.3 Comparing Experimental and Modeling Results

The comparisons for each of the two primary masses has been made for four cases: the model's FRF and experiment's FRF for each primary structure without any TVAs, and the model's FRF and experiment's FRF for each primary structure with both high and low-frequency TVAs. The model's simulation and experiment's tests involving only high-frequency TVAs are excluded from this comparison because they did not provide any additional insight than discussed in the previous sections. Figures 33.8 and 33.9 illustrate the FRF of the four mentioned cases for primary mass 1 and primary mass 2, respectively. The

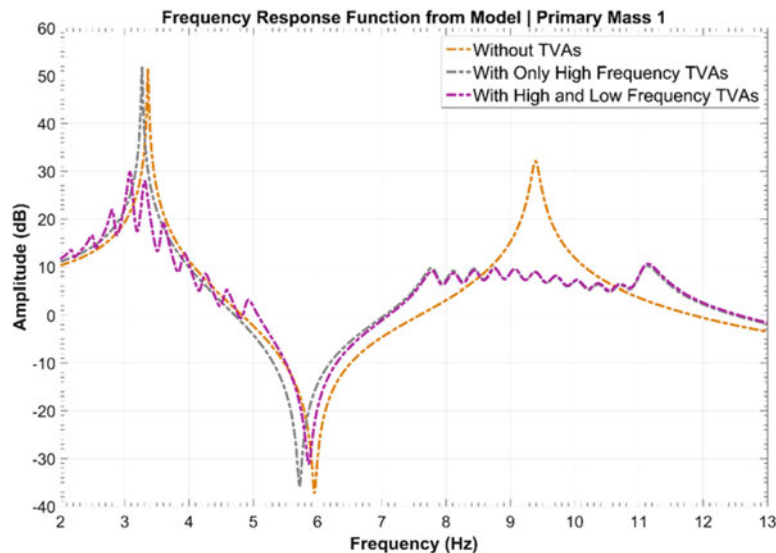


Fig. 33.6 Primary mass one displacement amplitude response with respect to base displacement vs. frequency from LPM

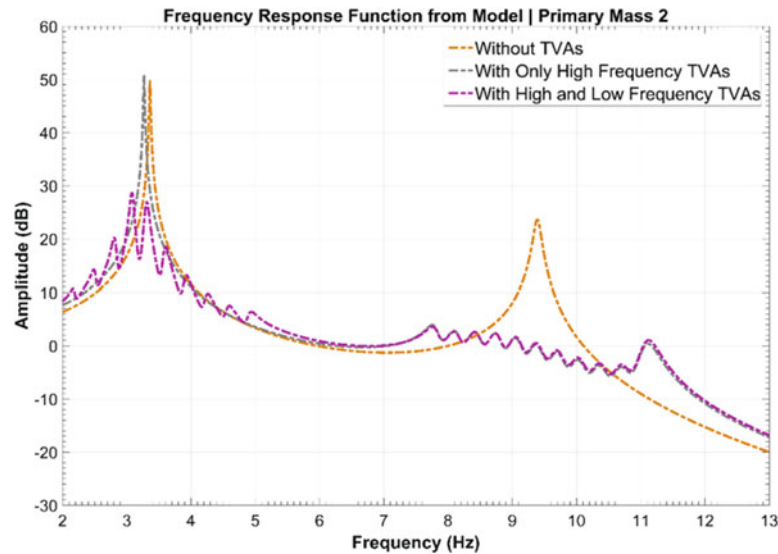


Fig. 33.7 Primary mass 2 displacement amplitude response with respect to base displacement vs. frequency from LPM

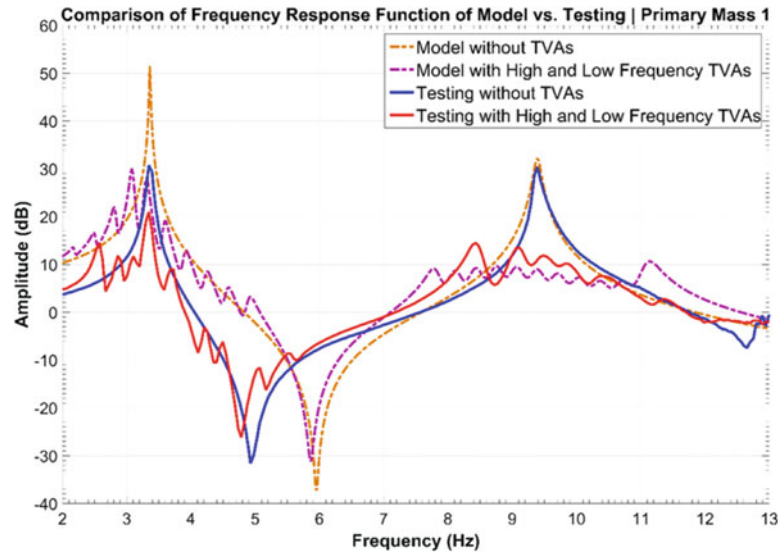


Fig. 33.8 Comparison of the model's FRFs and experiment's FRFs for primary mass 1

overall shape of the model's FRFs fit the experiment's FRFs well, as designed by fine-tuning the stiffness coefficients and damping ratios of the model after collecting the experimental data for the 2DOF structure. For the original 2DOF structure, the large difference in peak magnitude for both resonant frequencies, 3.34 and 9.39 Hz, is largely due to the difference in frequency resolution. The model's frequency resolution was 0.010 Hz, whereas the experiment's frequency resolution was 0.045 Hz, resulting in larger gaps between data points.

The direct comparison between the model and experimental data suggests that the lumped-parameter model is a straightforward and sufficient means of a first-order approximation for predicting how much attenuation can be achieved with arrays of specific counts of cantilever beam TVAs with known geometric and material properties. The deviations are most likely caused by (in order of most to least influential):

1. Neglecting the primary structure's four posts' mass which equate to about 24% of the host structure's two primary masses combined
2. Fabrication inaccuracies and mounting methods of TVAs including use of tip masses instead of longer cantilever beams for low-frequency TVAs

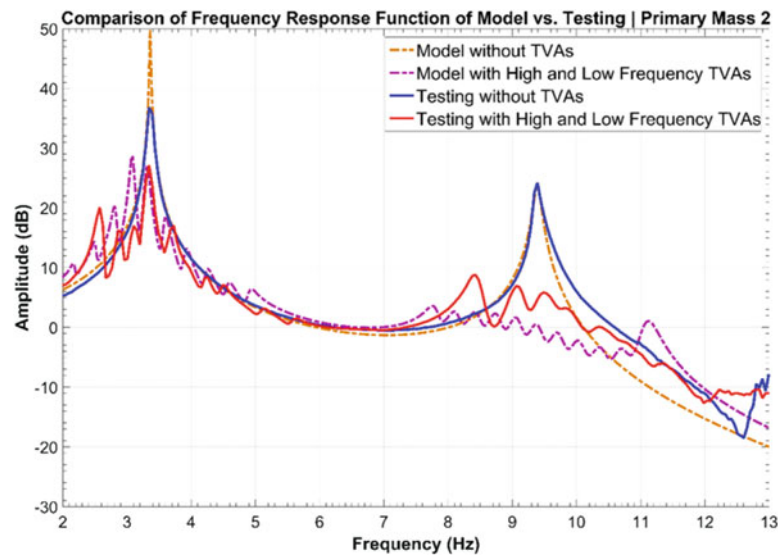


Fig. 33.9 Comparison of the model's FRFs and experiment's FRFs for primary mass 2

3. Assumptions made to convert distributed-parameter beams into a lumped-parameter model from the first weighted frequency of an Euler-Bernoulli fixed-free beam
4. Negligence of gravitational effects and other nonlinearities

Inconsistencies between pasta TVAs and their mountings to each primary mass is the most probable cause to the large peaks and valleys around the first and second mode in contrast to the small fluctuations in the model's FRFs. This is because some of the experimental TVAs may resonate at the same, or nearly the same frequency, whereas the LPM's TVAs resonated at unique, equally spaced, frequencies.

33.5 Conclusion

This study has successfully demonstrated that arrays of tuned-vibration absorbers (TVA) can significantly attenuate the host structure's vibration displacement magnitude over bandwidth and ultimately flattening the primary masses' frequency response functions (FRF). These TVAs were cantilever beams made of dry fettuccini pasta of varied length. The lumped-parameter model (LPM) created for each cantilever beam TVA via the first mode frequency of an Euler-Bernoulli beam with same material properties and geometry as the pasta proved to be a straight-forward and effective means for designing the TVA sizes and predicting the host structure's response once TVAs were attached. The LPM is readily scalable for any number of TVAs targeting each of the primary structure's modes individually. The total TVA arrays' mass was approximately 16.6% of the primary masses, which fell well below the targeted 25% mass ratio rule of thumb for TVAs.

The final TVA designs resulted in more than 9 dB attenuation for the first natural frequency and more than 19 dB attenuation for second natural frequency for both primary masses 1 and 2. After applying both the high and low-frequency TVAs, the modeled and experimental FRFs fell below 30 dB for the target bandwidth around the first mode and fell below 10 dB for the target bandwidth around the second mode.

The study has also shown that it is possible to design TVAs to target and reduce the magnitude response of a single mode of the primary structure independently, such that it affects the other modes insignificantly for the LPM. Further testing would be required to investigate how modeling distributed-parameter TVAs with multiple modal frequencies influences the host structure's response when the host structure's multiple natural frequencies align with multiple of the TVAs' modal frequencies. Other future studies of interest should also apply the same principles from this study to a host structure with 3 or more degrees-of-freedom and investigate how the variation of TVA mass ratio can influence the system's response.

Acknowledgments Tarazaga would like to acknowledge the support offered through the John R. Jones III Faculty Fellowship.

References

1. Davis, C.L., Lesieutre, G.A., Dosch, J.J.: Tunable electrically shunted piezoceramic vibration absorber. *Proc. SPIE*. **3045**, 51–59 (1997)
2. Kurdila, A.J., Lesieutre, G.A., Zhang, X., Prazenica, C., Niezrecki, C.: Averaging analysis of state-switched piezoelectric structural systems. *Proc. SPIE*. **5760**, 413–422 (2005)
3. Vignola, J.F., Judge, J.A., Kurdila, A.J.: Shaping of a system's frequency response using an array of subordinate oscillators. *J. Acoust. Soc. Am.* **126**(1), 129–139 (2009)
4. Zuo, L., Nayfeh, S.A.: Optimization of the individual stiffness and damping parameters in multiple-tuned-mass-damper-systems. *J. Vib. Acoust.* **27**, 77 (2005)
5. Akay, A., Xu, Z., Carcaterra, A., Koc, I.M.: Experiments on vibration absorption using energy sinks. *J. Acoust. Soc. Am.* **118**(5), 3043–3049 (2005)
6. Carcaterra, A., Akay, A., Bernardini, C.: Trapping of vibration energy into a set of resonators: theory and applications to aerospace structures. *Mech. Syst. Signal Process.* **26**, 1–14 (2012)
7. Vignola, J., Judge, J., Sterling, J., Ryan, T., Kurdila, A., Paruchuri, S.T., Glean, A.: Structural Acoustics and Vibration (others): Paper ICA2016-798. On the use of shunted piezo actuators for mitigation of distribution errors in resonator arrays. *Mitigation of Distribution Errors in Subordinate Oscillator Arrays*
8. Paruchuri, S.T., Sterling, J., Kurdila, A., Vignola, J.: Thermodynamic variational formulations of subordinate oscillator arrays (SOA) with linear piezoelectrics, *Proceedings of the ASME 2017 International Design Engineering Technical Conferences (IDETC) & Computers and Information in Engineering Conference* (2017)
9. Paruchuri, S.T., Sterling, J., Kurdila, A., Vignola, J.: Piezoelectric composite subordinate oscillator arrays and frequency response shaping for passive vibration attenuation. In: *2017 IEEE Conference on Control Technology and Applications (CCTA)*, pp. 702–707. IEEE (Aug 2017)
10. Kitis, L., Wang, B.P., Pilkey, W.D.: Vibration reduction over a frequency range. *J. Sound Vib.* **84**(4), 559–569 (1983)
11. Inman, D.J.: *Engineering Vibration*, 4th edn. Undergraduate and Graduate Level Textbook for Vibrations of Mechanical Systems (2014)

Chapter 34

Experimental Study on Tire Vibrations and Induced Noise



Sterling McBride, Seyedmostafa Motaharibidgoli, Mohammad Albakri, Ricardo Burdisso, Pablo Tarazaga, and Corina Sandu

Abstract Tire-pavement induced vibrations are among the main sources of vehicle exterior noise. Its dominant spectral content is approximately within 500–1500 Hz. For these frequencies, previous studies have proposed the existence of travelling waves along the tire's circumferential direction, as opposed to a modal behavior. This distinctive structural response generates acoustic waves that propagate into the environment. Unfortunately, no noise measurements above 500 Hz that can be used to validate this assumption have been conducted. In this work, a methodic measurement approach for tire vibrations and noise within the frequency range of interest is presented. Two tires of different size and construction were horizontally suspended over a test rig inside an anechoic room. In order to avoid the interference with the rig's rigid body modes, they were hanged with low stiffness cords. The tires were then excited with an impulse input by using an impact hammer. Noise was measured using a 19 microphone arc array. The array formed a semi-circle around the tire's cross section, thus providing noise levels induced by both sidewall and tread band vibrations. The arc was then rotated around the tire in order to capture tire noise directivity patterns. On the other hand, vibrations measurements were performed by using accelerometers on a set of 35 equally spaced points along the mid-tread line of the tires. A chirp signal was implemented as an input in order to fully characterize the tire response within the frequency range of interest. Noise measurements show the expected levels decay along the circumferential direction, whereas structural tire responses suggest the existence of waves that propagate along this direction.

Keywords Tire-pavement interaction noise · Tire wave-propagation · Tire noise directivity · Tire vibrations · Tire response

34.1 Introduction

Tire-pavement interaction noise (TPIN) is one of the most significant urban noise pollutants near highly populated areas, especially where vehicles travel at speeds above 50 km/h [1]. For this reason, research on tire-induced noise characterization and reduction is of great importance. Since the 1970s multiple TPIN generation mechanisms have been identified [2]. These involve propagating waves along the circumferential direction of the tire. A significant increase in response when waves are cut-on has been observed, with a dominant spectral content within 500–1500 Hz [3]. Currently, physically-based prediction tools implement either numerical or analytical methods to compute tire vibration and noise. For low frequencies, numerical models typically rely on finite element approaches. However, for higher frequencies, other models simulate waves propagating along the circumferential direction of the tire [4, 5]. These analytical methods are usually computationally more efficiency and provide improved physical insight. Still, they need to be validated against experimental data.

Initial evidence of propagating wave behavior in a tire was found during the 1980s, as presented in [6], where overall sound intensity contours around rolling truck tires were measured. In this case, the contours showed a steady intensity levels decay from the contact area towards the circumference of the tire. Other studies have shed more light into this behavior by measuring tire vibrations with laser vibrometers [7, 8]. However, studies where noise and vibration measurements are performed under consistent conditions (i.e., similar excitation methods, boundary conditions, etc.) seem to be scarce. Thus, the primary objective of this work is to measure tire vibrations and noise within the dominant TPIN frequency ranges, under similar conditions. In order to do so, noise and vibrations were measured for a horizontally suspended tire inside an anechoic environment. Results for both measurement cases are presented, as well as a brief analysis of their correlation.

S. McBride (✉) · S. Motaharibidgoli · M. Albakri · R. Burdisso · P. Tarazaga · C. Sandu
Department of Mechanical Engineering, Virginia Tech, Blacksburg, VA, USA
e-mail: sterling.mcbride@vt.edu; mostafa4@vt.edu; malbakri@vt.edu; rburdiss@vt.edu; ptarazag@vt.edu; csandu@vt.edu

34.2 Test Set-Up

All tire noise and vibrations measurements were carried out at Virginia Tech's anechoic room. Its inside dimensions (wedge tips to wedge tips) is $5.4 \times 4.1 \times 2.4$ m and has a cutoff frequency of 100 Hz, i.e. the room is designed to provide a normal-incidence sound absorption coefficient greater than 0.99 for all frequencies down to 100 Hz. A rig was built and positioned inside the room (see Fig. 34.1). The test tire was then hanged using low-stiffness chords. The reason to do this was to avoid contaminating the tire dynamics with those of the rig. A microphone array was attached to the sides of the rig. The microphone array formed a semi-circle around the tire. This set-up also allowed rotating the microphone 180° around the tire. The arch array contained 19 Panasonic model WM-64PNT electret microphones and had a diameter of 2.8 m.

Two different tires were tested under these conditions. A treaded tire of size 215/60R16 and a slick tire of size 225/45R17. In addition, two types of excitation methods were implemented. First, a Bruel and Kjaer Type 8208 impact hammer was used to excite the system with an impulse force, as shown in Fig. 34.2. The hammer had an incorporated a load cell on its tip that provided the amplitude and frequency content imparted to the test tire. The tire was hit multiple times at the center of the belt by a person standing inside the anechoic chamber. In addition, a hard tip was implemented in order to impart the highest possible impulse amplitude to the system.

The potential limitation of this approach is that the person standing in front of the tire may affect noise measurements because of acoustic reflections. Secondly, it is important to mention that due to human error, the input force magnitude of the impulses is not fully consistent for all hits. However, visual inspection on the measurements did not show much variation. Furthermore, an average value of these inputs was used for all frequency domain calculations in order to reduce this uncertainty.



Fig. 34.1 Experimental set-up inside Virginia Tech anechoic chamber

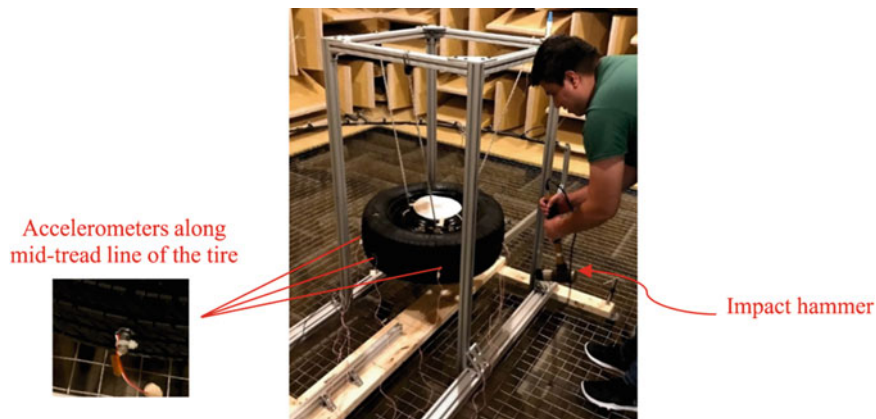


Fig. 34.2 Impact hammer excitation on the test tire

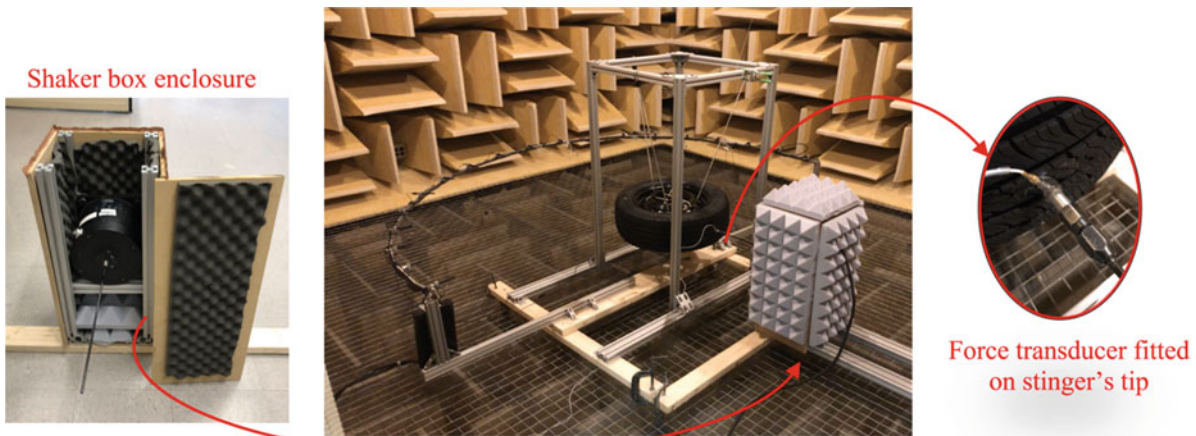


Fig. 34.3 Shaker set-up for tire testing inside anechoic room

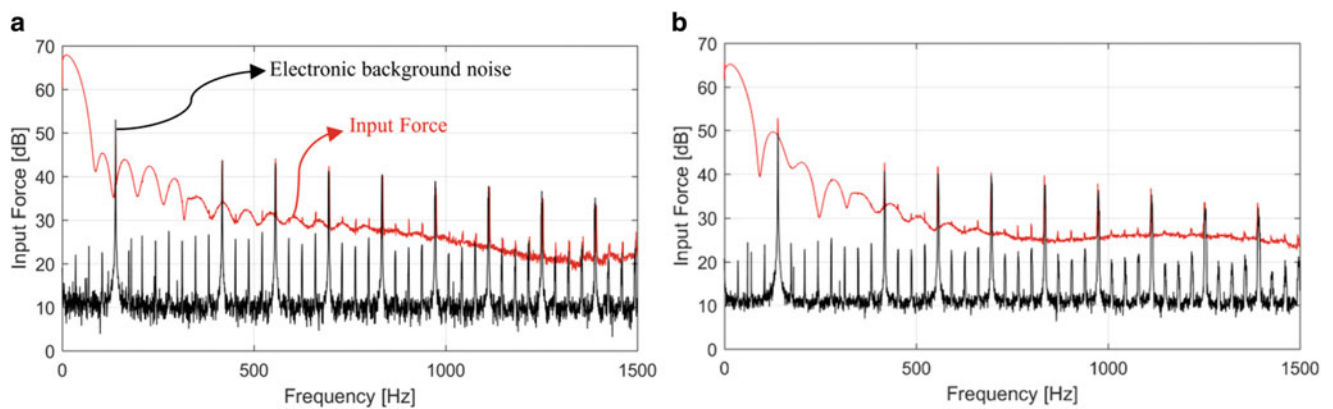


Fig. 34.4 Input forces for (a) treaded tire and (b) slick tire hammer tests (dB ref: 0.01 N)

The second tire-excitation method was performed using an electrodynamic shaker. Figure 34.3 shows how the shaker was set-up in front of the tire by using a separate base. A force transducer was fitted to the tip of the stinger in order to measure the actual force that is input into the tire. The shaker was enclosed into a wooden MDF box fitted with acoustic foam on the inside. The purpose of doing this was to isolate the noise emitted by the shaker during operation. Acoustic foam was also attached to the outside walls of the shaker-box. This was done in an effort to reduce the effects of reflections on the shaker box's surface. An estimated noise reduction of 30 dB at approximately 50 cm away from the shaker box was achieved. However, the effort to isolate the shaker's noise was not successful since shaker noise still contaminated all tire noise signals. Therefore, the hammer test was used solely for the purpose of exciting the tire and recording its produced noise, while the shaker test was used only to estimate the tire's vibrational response.

In order to measure tire vibrations, seven PCB U352C67 accelerometers were attached on the tire's mid-tread-line, as shown in Fig. 34.2. The accelerometers were initially spaced every 50° from each other along the tire's circumference. In order to be able to cover more measuring points, measurements were recorded five times. Each time, after moving all the accelerometers by 10° so that a total of 35 points are covered.

34.3 Measurement Results

The spectral content of the input force imparted during the impact hammer test on both the treaded and slick tires is shown in Fig. 34.4. The actual force signals are in red, while the electronic background noise in black.

Figure 34.4 shows that the electronic background noise contaminates the input force signals for both tires at well-defined discrete frequencies. It is also observed that the amount of energy imparted to the slick tire is higher. This is more noticeable

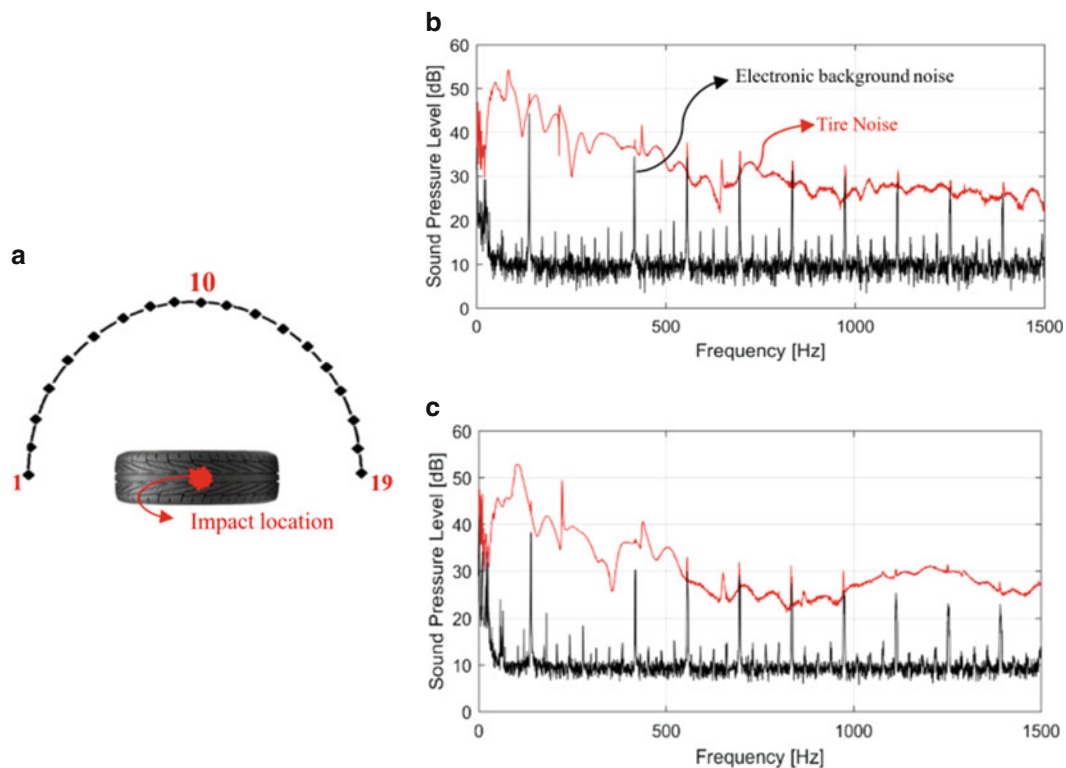


Fig. 34.5 (a) Sketch of microphone array location and corresponding measured noise spectra for both (b) treaded tire and (c) slick tire impact hammer tests

on the higher frequency range (above 1000 Hz), where the force signal for the treaded tire shows a decaying behavior. This is not the case for the slick tire. It is suspected that this phenomenon occurs because the tread acts as a damper that generates losses on the system. Since the slick tire does not have a tread, less energy is lost during the impact hammer test.

On the other hand, Fig. 34.5 shows the noise spectrum recorded by microphone 19, produced during the impact hammer test from both tires. This is for the case when the microphone array was at 90° with respect to the floor plane, as shown in the sketch in Fig. 34.5a. Both noise spectrums are shown in Fig. 34.5b, c. They show the same behavior as for the input forces, where energy losses are higher for the treaded tire.

The signal-to-noise ratio of the signals shown in Fig. 34.5 is better than that of the input force signals in Fig. 34.4. However, the background noise still contaminates the tire noise at localized frequencies. In order to address this issue, the tire noise spectra was interpolated at the location of the contaminating peaks, e.g. see the contaminating peak at approximately 600 Hz in Fig. 34.5c. Even though this procedure artificially eliminates energy from the spectrums, it still provides a good approximation. The reason is that the removed energy comes from electronic noise and not the actual acoustic wave's energy produced by the vibrating tire.

The overall sound pressure levels (OSPL) produced around the tire and captured by the rotating microphone array are shown in Fig. 34.6. Here, a sketch of a $1/8$ of a sphere around the horizontally hanged slick tire is shown. In this case, the highest noise levels occurred closest to the location where the impact hammer struck the tire. Along the circumferential direction of the tire, the OSPL decay. This confirms the tire noise decaying behavior reported by other investigators. On the other hand, it can also be observed that the OSPL directly above the horizontally hanging tire are the lowest. The reason is that the rim does not vibrate (i.e., has a rigid behavior) and does not produce any noise when the tire is struck with the impact hammer.

Additional results for measured A-weighted sound pressure levels along the circumferential direction of the tire are shown in Fig. 34.7. These are presented as an effort to correlate the decaying noise behavior along the circumferential direction of the tire and its corresponding vibrational response within the frequency range of interest (500–1500 Hz). Figure 34.7a shows how the microphone array was located for these measurements (array's circumference parallel to hanging tire's circumference). Figure 34.7b shows the noise levels for three $1/3$ rd octave frequency bands as a function of the angle \varnothing , around the tire's rotational axis. All results in Fig. 34.7 are for noise produced by the slick tire.

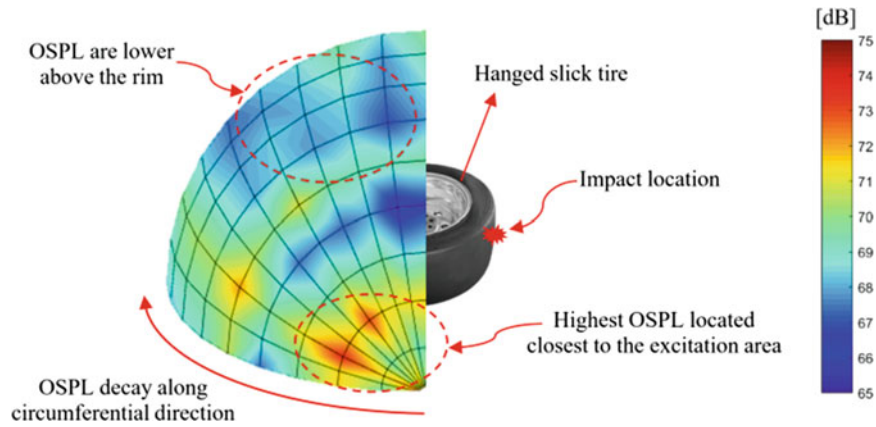


Fig. 34.6 Measured OSPL on surface located at 2.8 m from the center of the hanging slick tire

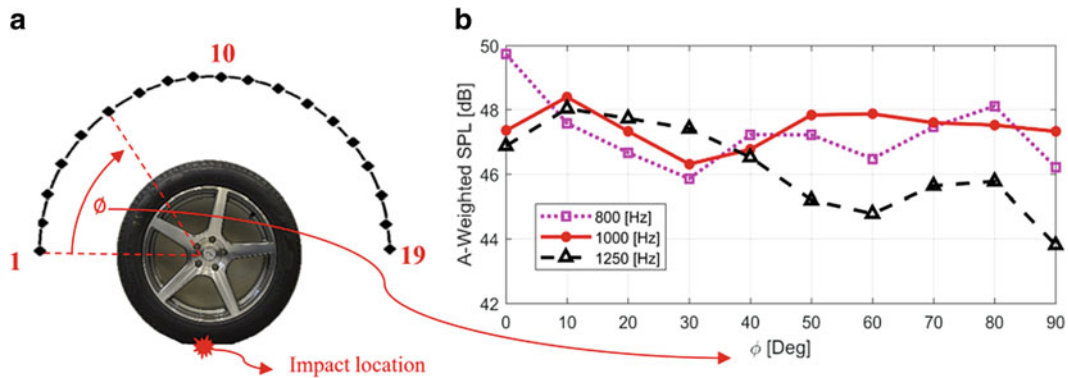


Fig. 34.7 (a) Sketch of measurement set-up and (b) measured A-weighted sound pressure levels along circumferential direction of the slick tire

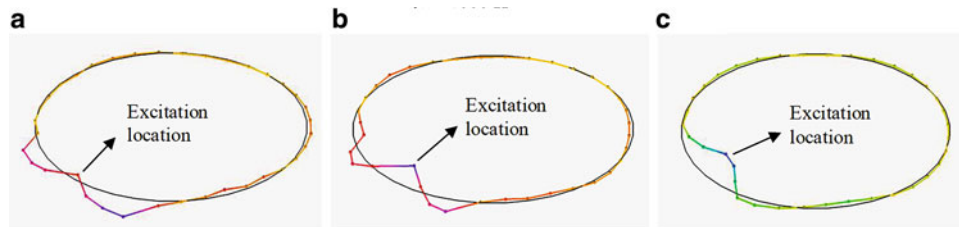


Fig. 34.8 Normalized acceleration amplitudes measured along the mid-tread line of the slick tire at (a) 836 Hz, (b) 1000 Hz, and (c) 1279 Hz

Figure 34.7b shows that for the frequency ranges of interest, there is a decay on noise levels along the tire’s circumferential direction. This decay is the most prominent for the 1250 Hz frequency band and less for 1000 Hz and 800 Hz. These results can be directly compared to the vibrational response of the tire. Figure 34.8 depicts the acceleration amplitudes normalized by their largest value, along mid-tread line of the slick tire for three different frequencies (exaggerated for visualization purposes). It can be observed that at 1279 Hz, the tire response decays more rapidly along its circumferential direction than at 1000 Hz. These results show that the tire vibrations and noise responses are correlated to each other and consistent with a wave propagation assumption for the frequency ranges of interest.

34.4 Conclusions

The conducted experimental campaign on tire vibrations and noise has uncovered the behavior of tire vibrations and noise within the mid frequency range (500–1500 Hz). Both noise and vibrational response of the tested tires reflect a decaying behavior, thus providing further evidence of the existence of propagating waves along the tire’s circumference. These results

can be used to validate existing analytical and numerical models used to predict tire noise and vibrations. Future work in this area could be done by improving the resolution of vibrations measurements using laser vibrometers. In addition, tire excitation methods for noise measurements could be improved. For example, by constructing a mechanism to release the impact hammer without the need of having a person hitting the tire inside the anechoic room. This would eliminate uncertainties on the experimental procedure.

Acknowledgements This work has been partially supported by the Center for Tire Research (CenTiRe), an NSF-I/UCRC (Industry/University Cooperative Research Centers) program led by Virginia Tech. The authors hereby wish to thank the industrial advisory board (IAB) of CenTiRe for their kind support and guidance. The authors also would like to thank Hankook Tire for providing the tires used for this test. The acoustic array and DAQ system used in the experimental tests was provided by AVEC, Inc., which is greatly appreciated. The authors would also like to acknowledge the efforts made by Lucas Spies, graduate student at Virginia Tech, for his assistance during the experimental set-up.

References

1. Sandberg, U.: Tyre/road noise – Myths and realities. The 2001 International Congress and Exhibition on Noise Control Engineering (2001)
2. Kuijpers, A., Van Blokland, G.: Tyre/road noise models in the last two decades: A critical evaluation. Proceedings of Inter-Noise, Hague, Holland. p. 2494 (2001)
3. Bolton, J.S.: The wave number decomposition approach to the analysis of tire vibration. Proceedings of Noise-Con, Ypsilanti, MI, 5–8 April 1998
4. McBride, S., Burdisso, R.: A comparison between modal and wave propagation models for simulation of tire-pavement interaction noise. Proceedings of Inter-Noise, Chicago, IL, 26–29 August 2018
5. Nilsson, C.M.: Waveguide finite elements applied on a car tyre. PhD dissertation, Royal Institute of Technology, Stockholm, Sweden (2004)
6. Donavan, P.R., Oswald, L.J.: The identification and quantification of truck tire noise sources under on-road operating conditions. In: General Motors Research Laboratories, no. GMR-3380, pp. 253–258 (1980)
7. Bernhard, R.: Observations of the structural acoustics on automobiles. Proceedings of Inter-Noise, Nice, France, 27–30 August 2000
8. Klos, J., Han, F., Bernhard, R.: Response measurement of rolling tires using Doppler vibrometry. Proceedings of Inter-Noise, Dearborn, MI, 19–21 August 2002

Chapter 35

On the Adaptive Vibration Suppression on a Flexible Spatial Structure



Oscar A. Garcia-Perez, Luis G. Trujillo-Franco, and Gerardo Silva-Navarro

Abstract This work deals with the application of a robust adaptive vibration control scheme on a flexible crane-type structure, which is based on Positive Feedback Control and on-line algebraic identification strategies of the most important modal parameters of the mechanical structure submitted to changes on mass, viscous damping and/or stiffness, common under variable payloads, as well as the estimation of exogenous excitation forces. For active vibration control the flexible structure employs a PZT stack actuator. Moreover, the modal parameters are estimated using on-line algebraic identification algorithms, which lead to fast estimations of those critical natural frequencies and modal damping on a given frequency range. This information is then used to synthesize and tune an adaptive Positive Position Feedback control scheme, for robust active damping injection tasks on certain specific mode shapes of the flexible structure. Some experimental results are provided to describe the fast and effective vibration attenuation on an experimental setup.

Keywords Vibration control · Flexible structures · Adaptive control · Algebraic identification · Modal control

35.1 Introduction

Cranes are quite used systems in different areas of the industry. However, this type of systems due to their large dimensions and high load capacity are very susceptible to the presence of vibrations. In the last decades, several works have been presented that seek to minimize the oscillations in the suspension point of the cranes. Although, the integrity of the mechanical structure has neglected in these works. There are many reports of faults in the structure of the cranes due to external forces as such wind, movement at the base, oscillations in the load, among others. The effect that external forces produce on the crane's dynamics is hardly controlled by applying some control strategy on the actuated joints found on the cranes.

There are different vibration control schemes that have been implemented in different types of mechanical structures such as Positive Position Feedback (PPF), Direct Velocity Feedback (DVF), Active Tuned-Mass-Damper (ATMD) and Integral Force Feedback (IFF) [1–3]. Positive Position Feedback proposed has been popular for vibration control on structures, due to many advantages, such as reduction on spillover effects as well as its easy design and tuning [1]. In this work, the problem of the attenuation of the undesirable vibrations that occur in the mechanical structure of the tower cranes is addressed by means of the injection of damping by means of active control using a PZT stack actuator.

In most structures the natural frequencies remain unchanged or their change occurs in after a long period of time. However, cranes are systems where the load varies constantly and also the weight of the load in most cases is quite significant with respect to the total mass of the overall system. Therefore, it is expected that the natural frequencies of the total system are constantly changing, so implementing a compensator with a fixed tuning frequency could bring a low performance or not at all attenuate none of the vibration modes of interest. There are works in which adaptive control schemes have been applied for vibration attenuation. In different works we have worked with adaptable PPF compensators, where identification has been done by processing off-line large datasets or, in other cases, using least squares techniques to perform the identification of the natural frequencies of the dynamic systems, these works assume that the change of the modal parameters of the structure change in a considerably slow way, this claim is true in many types of structures. However, the dynamic response of a crane is a function of the position of the load attached to the structure that constitutes the arm of the crane, therefore, the natural

O. A. Garcia-Perez (✉) · L. G. Trujillo-Franco · G. Silva-Navarro
Seccion de Mecatronica, Departamento de Ingenieria Electrica, Centro de Investigacion y de Estudios Avanzados del I.P.N., Ciudad de Mexico, Mexico
e-mail: ogarciap@cinvestav.mx

frequencies of this vibrating mechanical system change fast. As a solution of this situation, we propose an on-line algebraic modal parameter identification scheme for adaptive tuning of PPF compensators.

35.2 Description and Modal Model of the System

The system consists a space structure like rotary crane structure is mounted on a revolute type servomechanism as shown in Fig. 35.1. A DC motor provides a torque $\tau(t)$ to realize the rotational displacements of the structure and the load $W(t)$, the rotational displacements with respect to Z_0 are denoted by $\theta(t)$. One of the elements of the structure is replaced by a piezoelectric stack actuator which serves for vibration control purposes as shown in Fig. 35.1.

The placement of PZT stack actuator was selected using Gawronski approach that consists in evaluating all possible places for the collocation of the sensors and actuators and choosing the best for the application. The structure of the crane is a distributed system, so its dynamics is represented by an infinite number of degrees of freedom. However, it is possible to represent the dynamics of the structure by means of a mathematical model in modal coordinates so that it is possible to obtain models of lower order. Hence, the dynamics of the structure is represented using a modal model where the first five vibration modes are used. Also, the influence of the PZT stack actuator, the influence of the rotational displacements, and endogenous forces on the dynamics of the structures can be represented by the following expression.

$$I\ddot{Q}_m + 2Z\Omega\dot{Q}_m + \Omega^2 Q_m = B_{cm}u_{PZT}(t) + B_{am}\ddot{\theta}(t) + F_{mr} \quad (35.1)$$

$$y_s = C_{sm}Q_m, \quad y_t = C_{tm}Q_m, \quad C_{sm}, C_{tm} \in \mathbb{R}^{1 \times 5} \quad (35.2)$$

where $I, Z, \Omega \in \mathbb{R}^{5 \times 5}$ are modal mass, modal damping and modal stiffness matrices of the flexible structure, respectively. Also, $Q_m, B_{cm}, B_{am}, F_{mr} \in \mathbb{R}^{5 \times 1}$ represent modal coordinates, the influence vector of the PZT stack actuator, influence of rotational displacements and endogenous forces on the flexible structure. The control input for the PTZ stack actuator is denoted by $u_{PZT} \in \mathbb{R}$. The modal stiffness and modal damping in matrix form is given by

$$\Omega = \begin{bmatrix} \omega_1 & \cdots & 0 \\ \vdots & \ddots & \vdots \\ 0 & \cdots & \omega_5 \end{bmatrix}, \quad Z = \begin{bmatrix} \zeta_1 & \cdots & 0 \\ \vdots & \ddots & \vdots \\ 0 & \cdots & \zeta_5 \end{bmatrix} \quad (35.3)$$

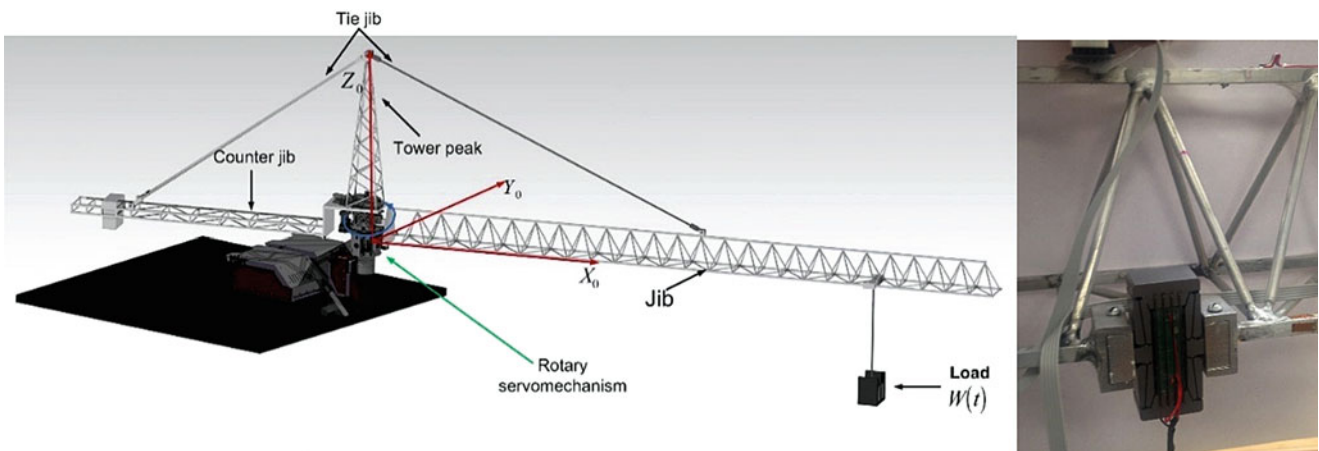


Fig. 35.1 Schematic diagram of the overall system

Table 35.1 Modal parameters of the first five vibration modes of the flexible structure of rotary tower crane

Mode	Natural frequency ω_i [Hz]	Modal damping ζ_i
1	4.4557	0.0185
2	9.7964	0.0221
3	13.8481	0.0186
4	15.8391	0.0374
5	43.3821	0.0096

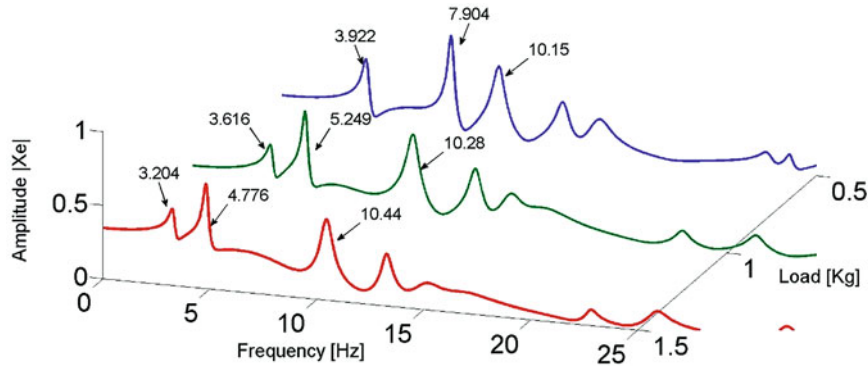


Fig. 35.2 Frequency response of overall system as a function to the load at suspension point of the arm structure

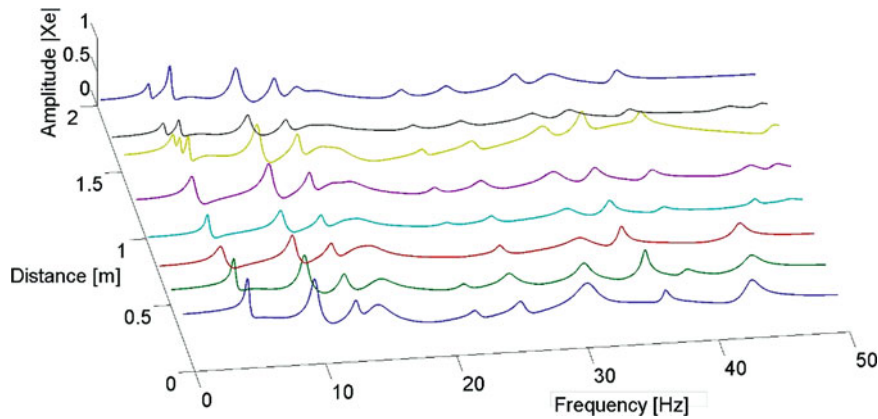


Fig. 35.3 Frequency response of the overall system as a function of the load along position on arm structure of rotary crane

Here, ω_i, ζ_i are the natural frequency and modal damping of the i -th vibration mode of the spatial structure. Moreover, y_s, y_t represent the displacements that are presented on sensor position and tip position of structure jib where the row vectors C_{sm}, C_{tm} can be represented as follow

$$C_{sm} = [c_{sm_1} \cdots c_{sm_5}], \quad C_{tm} = [c_{tm_1} \cdots c_{tm_5}] \tag{35.4}$$

The influence vectors B_{cm}, B_{am} can be obtained as. Hence, B_{cm} represent cosines directors the active element where PZT stack actuator is placed, and PTZ forces are represented using two axial forces actuating along the active element.

In Table 35.1 are shown the modal parameters of the first 5 vibration modes of the structure without load, which were obtained by means of experimental modal techniques and peak picking.

In most structures the modal parameters are fixed, so the dynamics of the structure remains unchanged. However, in a rotary crane due to load changes it is to be expected that these modal parameters are changing as a function of the load and its position along the arm structure of the crane. In Fig. 35.2 are shown the results obtained when the load is modified at the point of suspension near to the tip of the structure, while in Fig. 35.3 are shown the natural frequencies as a function of the position along the structure. The experimental results shown that the natural frequencies of the system change in a fast manner, affecting the dynamic response of the system so the vibration control technique must be robust and fast enough to detect and overcome those changes.

35.3 On-Line Algebraic Modal Parameter Identification Approach

As reported in previous works (see [4, 5]), the algebraic on-line system identification techniques are attractive and adequate to be applied on vibrations absorption control schemes due principally to their fast estimation of the principal modal parameters of multiple degrees of freedom mechanical systems like natural frequencies and modal damping ratios in an online and time domain fashion. The on-line algebraic identification approach used here to estimate the modal parameters of the mechanical system implies the on-line estimation of the coefficients \hat{a}_k of the system's characteristic polynomial as reported in [4]. In this work we are using only strain or acceleration measurements of the most significant points of the structure, according to the Gawronski approach to perform the adaptive identification of natural frequencies and modal dampings of the system. The application of the online algebraic identification scheme is performed using cumulative trapezoidal numerical integration with fixed sampling time of 1 ms. The algebraic identification scheme applied here is described on detail in [4, 5], where it is shown that, by solving the algebraic equation (35.5) also detailed in [4–6], one obtains the parameter vector θ as:

$$\theta = \mathbf{A}^{-1}\mathbf{B} = \frac{1}{\Delta} \begin{bmatrix} \Delta_1 \\ \Delta_2 \\ \vdots \\ \Delta_{n-1} \\ \Delta_n \end{bmatrix} \quad (35.5)$$

Then, the algebraic identifiers to estimate the coefficients a_k of the characteristic polynomial without problems of singularities when the determinant $\Delta = \det(\mathbf{A}(t))$ crosses by zero:

$$\hat{a}_k = \frac{\int |\Delta_{k-1}|}{\int |\Delta|}, \quad k = 1, 2, \dots, 2n - 1 \quad (35.6)$$

Thus, one could implement the algebraic identifiers (35.10) using only any available acceleration measurements \ddot{x}_i of any specific floor or degree of freedom. From the estimated coefficients \hat{a}_k , one can obtain the roots of the characteristic polynomial:

$$\hat{\lambda}_i = \hat{\sigma}_i + j\hat{\omega}_{di}, \quad \hat{\lambda}_i^* = \hat{\sigma}_i - j\hat{\omega}_{di}, \quad i = 1, 2, \dots, n \quad (35.7)$$

where $\hat{\sigma}_i$ and $\hat{\omega}_{di}$ are estimates of the damping factors and damped natural frequencies of the mechanical system, respectively. Hence, the estimates of the natural frequencies and damping ratios are given by

$$\hat{\omega}_{ni} = \sqrt{\hat{\sigma}_{ii}^2 + \hat{\omega}_{di}^2}, \quad \hat{\zeta}_i = \frac{\hat{\sigma}_i}{\sqrt{\hat{\sigma}_{ii}^2 + \hat{\omega}_{di}^2}} \quad (35.8)$$

Remark: We would like to mention that, once we identify the modal parameters or even the complete eigenstructure of the system, we can identify, if necessary, the excitation force and, thus, counteract it, for vibration absorption schemes or simply characterize this unknown excitation force. A descriptive block diagram of the online identification scheme used in shown in Fig. 35.4, where the natural frequencies $\hat{\omega}_{ni}$ are used to tune the adaptive vibration control scheme.

35.4 Adaptive-Like Multi Positive Position Feedback Control Scheme

The concept of Adaptive-Like Multi Positive Position Feedback (AMPPF) is based on conventional PPF control technique [1, 7]. A PPF is in essentially a second order compensator where the position signal is fed to a compensator that has large damping as compared to the flexible structure, and the output of the compensator is multiplied by a control gain and is positively fed [1]. Multiple PPFs compensator can be used in order to control more than one of vibration modes. In the rotary

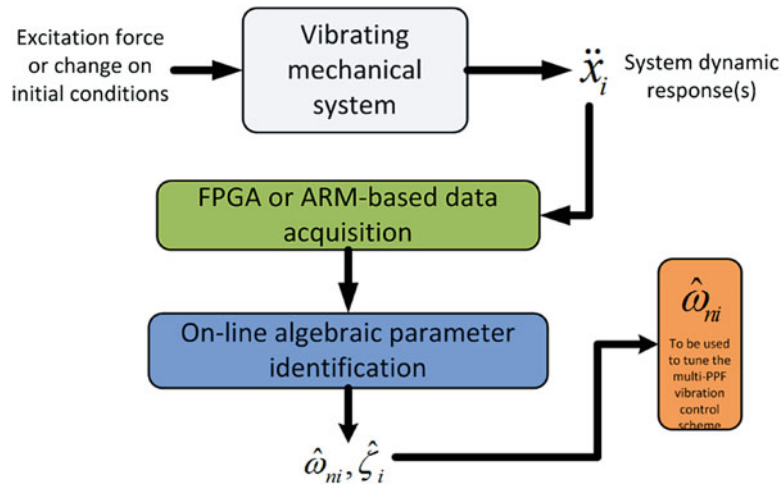


Fig. 35.4 Schematic diagram of the identification scheme

crane structure two PPF compensators are used which are designed to control the first two vibration modes of the overall system which are shown in the following expression

$$\begin{aligned}
 I_c \ddot{N} + 2Z_f \hat{\Omega}_f \dot{N} + \hat{\Omega}_f^2 N &= \hat{\Omega}_f^2 G y_s \\
 u_{PZT}(t) &= G^T \hat{\Omega}_f^2 N(t) \\
 N &= \begin{bmatrix} \eta_1 \\ \eta_2 \end{bmatrix}, \quad I_c = \begin{bmatrix} 10 \\ 01 \end{bmatrix}, \quad \hat{\Omega}_f = \begin{bmatrix} \hat{\omega}_{f1} 0 \\ 0 \hat{\omega}_{f2} \end{bmatrix}, \quad Z_f = \begin{bmatrix} \zeta_{f1} 0 \\ 0 \zeta_{f2} \end{bmatrix}, \quad G = \begin{bmatrix} g_1 \\ g_2 \end{bmatrix}
 \end{aligned} \tag{35.9}$$

where η_i denote the general coordinate of the i -th compensator, while $\hat{\omega}_{f_i}, \zeta_{f_i}$ represent frequency and modal damping of i -th PPF, respectively. The natural frequency of the compensator is chosen the same as the natural frequency of the structure. Hence, if $\hat{\omega}_{f_i} = \hat{\omega}_{n_i}$ the AMPPF control could be tuned until natural frequencies of the structure are changing. The values of gains of compensator are selected to guarantee the close loop stability of the AMPPF compensator and the system that is represented by Eq. (35.1). Hence, the closed loop stability of is guaranteed if stiffness matrix of the overall system in closed-loop K_f is positive definite as [8].

$$K_f = \begin{bmatrix} \Omega^2 & -B_{cm} G^T \hat{\Omega}_f \\ -\hat{\Omega}_f G C_{sm} & \hat{\Omega}_f \end{bmatrix} \tag{35.10}$$

35.5 Experimental Setup and Results

Our experimental setup consists of a flexible structure featuring a rotary crane as shown in Fig. 35.5. We use a data acquisition card Sensor Ray model 626 to measure the output signal of strain gauge and send back the corresponding analog control signal to the amplifier which drives the PZT stack actuator with the corresponding voltage. MATLAB/Simulink is used to compute the vibration control signals and online identification of the modal parameters of this vibrating mechanical system where the strain gauge signal is measured and processed to compute both AMPPF control signal and modal parameters identification.

As a first experiment, we evaluate the performance of the proposed control scheme when we add a load of 500 g at the tip of the crane. The performance of the AMPPF control is shown in Fig. 35.6 where the compensators are tuned to mitigate the effects of the first two vibration modes. We can observe the dynamic response of the structure with no vibration control scheme and, surrounded by the dashed box, the dynamic response of the flexible structure when the proposed control



Fig. 35.5 The experimental setup

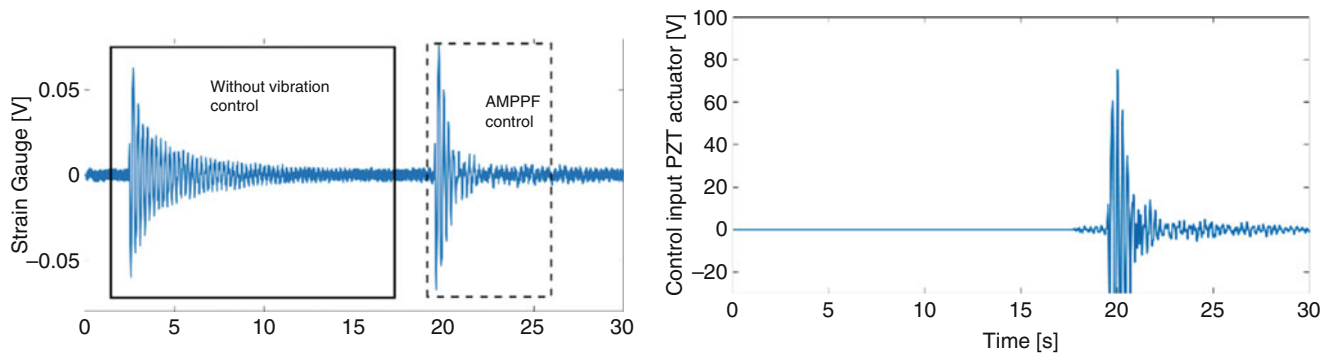


Fig. 35.6 System response with a load of 500 g

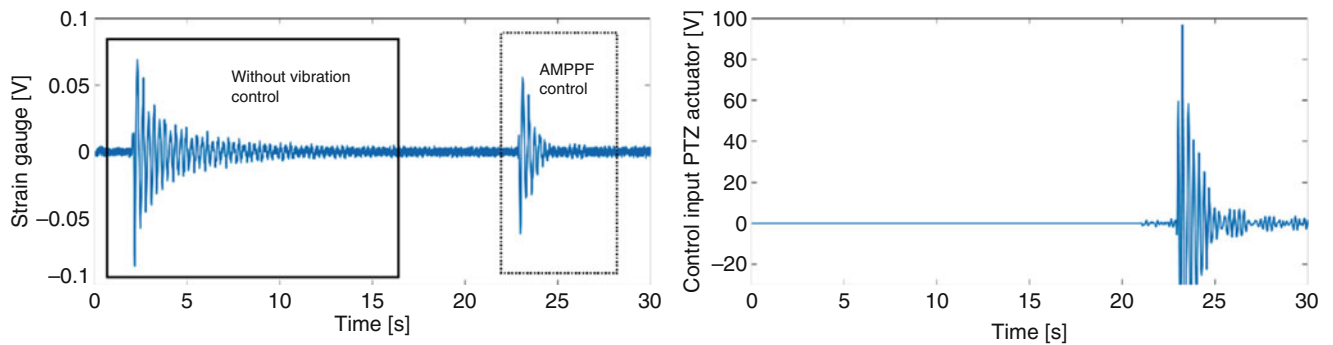


Fig. 35.7 System response with a load of 1 kg

scheme is applied. The time domain graphs show a modal damping injection to the system; as a result we obtain a faster free decay response. The control effort signal is also shown in order to highlight the reasonable voltages needed to counteract the undesirable vibrations. In Figs. 35.7 and 35.8 we show similar results for the cases of loads of 1 kg and 1.5 kg respectively, and the control effort in volts needed to achieve the attenuation of the undesired vibrations.

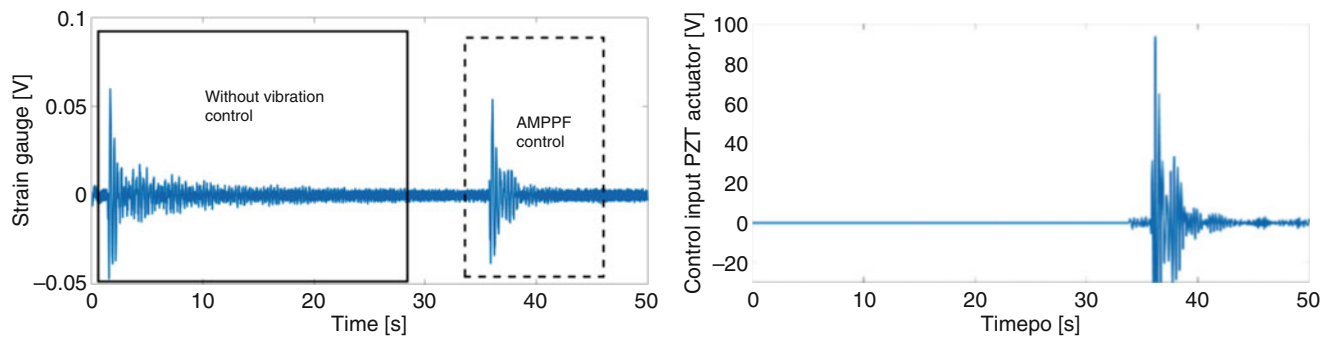


Fig. 35.8 System response with a load of 1.5 kg

35.6 Conclusions

It is proposed an adaptive-like vibration absorption scheme based on Multiple Position Feedback (AMPPF) using time domain algebraic identification techniques for on-line estimation of the natural frequencies for a flexible-crane structure. We show that the variable loads applied to the crane result in important changes on the modal parameters of the flexible structure, those changes are so fast that it is not possible to apply traditional identification schemes based on the FFT or least squares approaches. In general, the simulation and experimental results show a satisfactory performance of the proposed identification approach with robust estimations and good attenuation properties using the estimated natural frequencies to mitigate the undesired effects of the two first vibration modes of the flexible structure.

References

1. Goh, C.J., Caughey, T.K.: On the stability problem caused by finite actuator dynamics in the collocated control of large space structures. *Int. J. Control.* **41**(3), 787–802 (1985)
2. Fanson, J.L., Caughey, T.K.: Positive position feedback control for large space structures. *AIAA J.* **28**(4), 717–724 (1990)
3. Baz, A., Hong, J.-T.: Adaptive control of flexible structures using modal positive position feedback. *Int. J. Adapt. Control Signal Process.* **11**(3), 231–253 (1997)
4. Beltran-Carbajal, F., Silva-Navarro, G., Trujillo-Franco, L.G.: Evaluation of on-line algebraic modal parameter identification methods. In: *Proceedings of the 32nd International Modal Analysis Conference (IMAC XXXII)*, vol. 8, pp. 145–152 (2014)
5. Beltran-Carbajal, F., Silva-Navarro, G., Trujillo-Franco, L.G.: Adaptive-like vibration control in a three-story building-like structure with a PZT stack actuator. In: *Proceedings of the 33rd International Modal Analysis Conference (IMAC XXXIII)*, vol. 10, pp. 123–131 (2015)
6. Beltran-Carbajal, F., Silva-Navarro, G.: Adaptive-like vibration control in mechanical systems with unknown parameters and signals. *Asian J. Control.* **15**(6), 1613–1626 (2013)
7. Nima Mahmoodi, S., Ahmadian, M., Inman, D.J.: Adaptive modified positive position feedback for active vibration control of structures. *J. Intell. Mater. Syst. Struct.* **21**(6), 571–580 (2010)
8. Garcia-Perez, O.A., Silva-Navarro, G., Peza-Tapia, J.F.: Trajectory tracking and active vibration suppression on a flexible tower crane. In: *Proceedings of the 35th International Modal Analysis Conference (IMAC XXXV)*, vol. 6, pp. 159–166 (2017)



Chapter 36

Evaluation of the Human-Structure-Soil Interaction on a Two-Wheel Tractor Using Modal Analysis Techniques

E. Velazquez-Miranda, G. Silva-Navarro, J. Bory-Reyes, O. A. Garcia-Perez, and L. G. Trujillo-Franco

Abstract This work considers the experimental evaluation on a two-wheel tractor, employed for small agricultural practices, to characterize the human-structure-soil interaction under typical activities into small greenhouses (e.g., tillage). First, the two-wheel tractor is evaluated to get its modal parameters and, then, the machine is tested for endogenous excitation due to different engine speeds and for several working scenarios (operational modal analysis). In particular, the modal testing is focused on the human-structure-soil interaction to verify how the vibrations and noise affect to the human operator and, thus, propose passive solutions to reduce adverse effects caused on humans via passive damping injection and/or proper structural modifications. The results are used to evaluate the overall dynamic performance in a system-theoretic approach for decision-making during the design and evaluation of this machinery.

Keywords Two-wheel tractor · Experimental modal analysis · Operational modal analysis · Human-machine interaction

36.1 Introduction

Two-wheel tractors are used as principal source of mechanical power in small-scale farming in developing countries for land preparation, cultivation, harvesting, weed control, and transportation. Its operation, unlike conventional tractors, requires the command of the farmer, either seated or standing behind the machine, depending on the type of two-wheel tractor and agricultural activity to be performed. In agriculture the use of machinery, such as the two-wheel tractor, involves the interaction between the engine of the machine, implement and soil, which can generate different levels of undesirable vibrations and noise that are directly transmitted to the farmer, which can cause them some physical disorder.

For this reason, the dynamic analysis of this type of machinery leads to the improvement of both, the machine functionality and farmer's working conditions in a holistic context. In previous works, the holistic context of the relevant factors for the design of agricultural machinery was presented in [1], particularly, general structural analysis and evaluation of a two-wheel tractor, under the focus of the experimental and operational modal analysis was presented by the authors in [2].

In this work, the dynamic evaluation of a two-wheel tractor is performed focusing on the human-soil interaction to verify the levels of vibrations transmitted to the farmer through the handlebar. Thus, the machine modal parameters are identified, and then the vibrations due to endogenous excitation at different speeds and working scenarios are tested. Finally, the results are used to propose passive solutions to reduce adverse effects caused on farmers via passive damping injection and/or proper structural modifications.

36.2 Background

In the literature the analysis of mechanical vibrations in agriculture and its effects on the human being can be identified in two categories due to the direct human-machine interaction: (1) whole body vibration when humans are sitting or standing on vibrating surfaces, and (2) hand-transmitted vibration when the farmer pulls or holds a device or machine. In particular, the two-wheel tractor is associated with hand-transmitted vibration through the handlebar. The effects of hand-transmitted

E. Velazquez-Miranda (✉) · J. Bory-Reyes

Seccion de Estudios de Posgrado e Investigacion, ESIME-ZACATENCO, Instituto Politecnico Nacional, Ciudad de Mexico, Mexico

G. Silva-Navarro · O. A. Garcia-Perez · L. G. Trujillo-Franco

Seccion de Mecatronica, Departamento de Ingenieria Electrica, Centro de Investigacion y de Estudios Avanzados del I.P.N., Ciudad de Mexico, Mexico

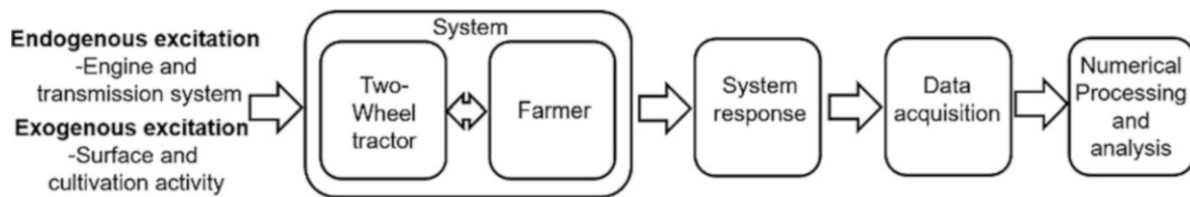


Fig. 36.1 Schematic diagram of the mechanical system under evaluation

vibration can lead to disorders in bones, joints, muscles, and even circular and neurological disorders. Therefore, standards and regulations have been developed for the measurement of vibrations in humans due to these effects, such as the ISO 2231-5 on *Mechanical Vibration and Shock-Evaluation of Human Exposure to Whole-Body Vibration*, and the ISO 5349 on *Mechanical Vibration-Measurement and Evaluation of Human Exposure to Hand Transmitted Vibration* [3, 4].

The vibrations in agricultural equipment have been widely studied by various authors. However, the evaluation of small-scale machinery has been carried out mainly in countries where the agricultural sector is predominant. For example, the structural analysis of equipment for the preparation of germinative beds has been studied by [5] with the objective of analyzing the frequencies at which resonances occur in working conditions. On the other hand, the evaluation of vibrations in a mini-tiller, with an analysis in different speed ranges, finding that the vibration comes from the unbalanced forces of the engine, was reported by [6]. Also, considering different modes of operation, [7] describes the characteristics of hand-transmitted vibration of a hand tractor making an analysis of variance to identify the effects of different directions of vibration acting on the human being. The structural optimization of a tiller handheld was made by [8] through the results of a computational and experimental modal analysis, whose results were evaluated by the analysis of variance to determine the appropriate dimensions of the handrail to reduce vibrations. With this same purpose, [9] proposed the use of damping materials to reduce hand transmission vibrations to the operator such as polyurethane and synthetic rubber, finding that the latter was the best option during the transportation, tilling and rota-tilling modes of the machine.

Previous studies characterize and study the transmission of vibrations in agricultural machines. Considering a systemic approach, the handlebar of the two-wheel tractor is the medium that transmits to the human being the vibrations of the machine (endogenous excitation) and the soil-machine interaction (exogenous excitation). The importance of human-machine interaction is that the human being is an articulated mechanism composed of rigid bars (bones) joined by joints so a human can be considered as an open kinematic chain that is exposed to excitement through the handlebar.

For this reason, it is essential to know the frequency ranges that influence the discomfort and physical damage of the human being. The frequency ranges present in human hand-arm has been studied by [10] through finite element analysis and operational modal analysis with the aim of understanding the mechanisms of injury in the hand-arm system. In this work the transmissibility of the vibrations was in a range of 2.6–244 Hz, finding that the frequencies related to effects on the wrist, elbow, and shoulder are in the order of 12.36 and 97 Hz.

In this context, the analysis of the vibrations present in the human being due to the excitation of agricultural machinery such as the two-wheel tractor is an aspect that must be addressed, since agricultural work requires exposure of the farmer to the effects of vibrations for extended periods of time. Likewise, the minimization of the acceleration components at the point of contact with the farmer reflects the importance of the redesign of the handlebar through the design of passive or semi-active systems adaptable to existing machinery since being a simple machine at a technological level and used by small farmers, it is necessary to consider the economy-functionality relation of the machine. For this purpose, and in the framework of a systemic approach, Fig. 36.1 shows the evaluation system and the variables involved in the study of human-structure-soil interaction on the Two-Wheel tractor.

36.3 Modal Analysis of a Two-Wheel Tractor Handlebar

The mechanical system used in the analysis consists of a 6.5 hp commercial two-wheel tractor used in greenhouse agriculture. The modal analysis of the two-wheel tractor is focused on the analysis of the handlebar, since it is the point where there is a direct interaction with the human (farmer). Figure 36.2 shows the main components of the machine used in the analysis.

The modal analysis to estimate the natural frequencies of the two-wheel tractor was carried out by means of a computational modal analysis and the experimental modal analysis. The 6.25 kg handlebar structure was modeled using the finite element method (FE) considering that the handlebar material is a structural steel AISI 1020 with Young Modulus



Fig. 36.2 Main components of the two-wheel tractor

Table 36.1 First 6 natural frequencies of the two-wheel tractor handlebar

Mode i	Frequency ω_i [Hz]
1	14.707
2	20.352
3	31.728
4	108.23
5	132.07
6	134.42

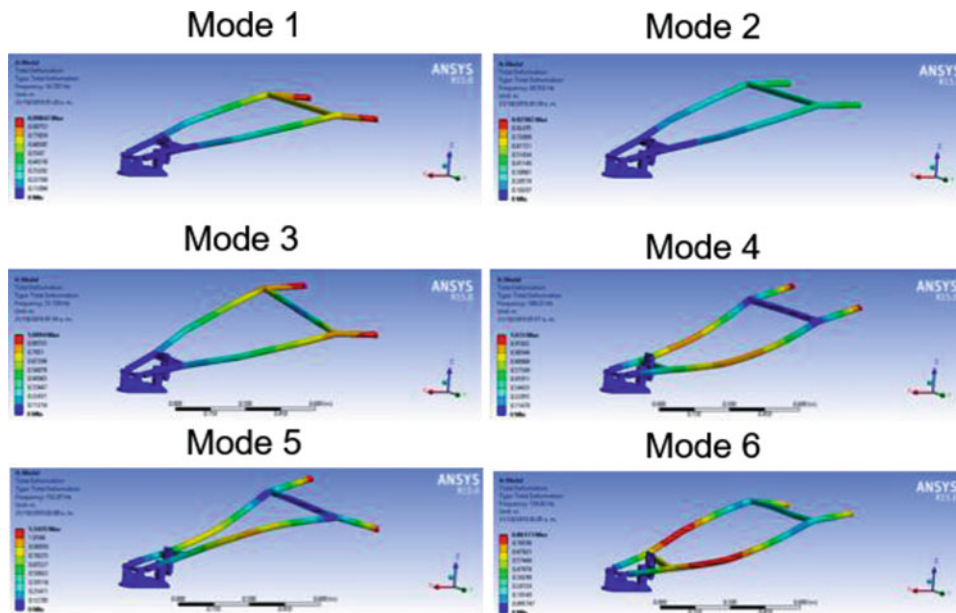


Fig. 36.3 First 6 dominant mode-shapes of the two-wheel tractor handlebar

of 186 GPa, poisson ratio of 0.29, and a density of 7870 kg/m³. The modal analysis was performed in Ansys Workbench with 41,646 nodes and 21,081 elements, placing fixed supports in the handlebar flange.

In Table 36.1 and Fig. 36.3 are shown the first 6 dominant mode-shapes identified during the numerical modal analysis of the handlebar.

According to the values of the natural frequencies and the mode-shapes of the handlebar, it can be observed that the first mode (14.707 Hz) and second mode (20.352 Hz) correspond to the bending of the structure in the vertical and horizontal direction, respectively, while the third (31.728 Hz), fourth (108.23 Hz) and fifth (134.42 Hz) modes denote a combination of bending and torsion in the handlebar. The first two mode-shapes are important because these are closely related to a typical Frequency Response Function (FRF) of the human wrist.

36.4 Experimental Modal Analysis of a Handlebar

The experimental modal analysis was carried out by placing three single axis accelerometers on the handlebar structure, to measure the vertical vibrations using an impact hammer for low frequencies as shown in Fig. 36.4. The natural frequencies and damping ratios were estimated using classical Peak Picking techniques.

The corresponding FRF of the accelerometer located on the handlebar grip A_2 is presented in Fig. 36.5, which denotes higher amplitudes below the 200 Hz range, while the related natural frequencies found via Peak Picking techniques are presented in Table 36.2, showing a comparison between the natural frequencies of the vibration modes obtained from the experimental modal analysis performed and those found in ANSYS.

As can be seen, the frequencies of 14.707, 20.352, and 108.23 Hz of the FE model evaluated in ANSYS suggest a correspondence with the experimental modal analysis performed with the impact hammer. This reveals that the frequencies



Fig. 36.4 Location of accelerometers on the handlebar structure

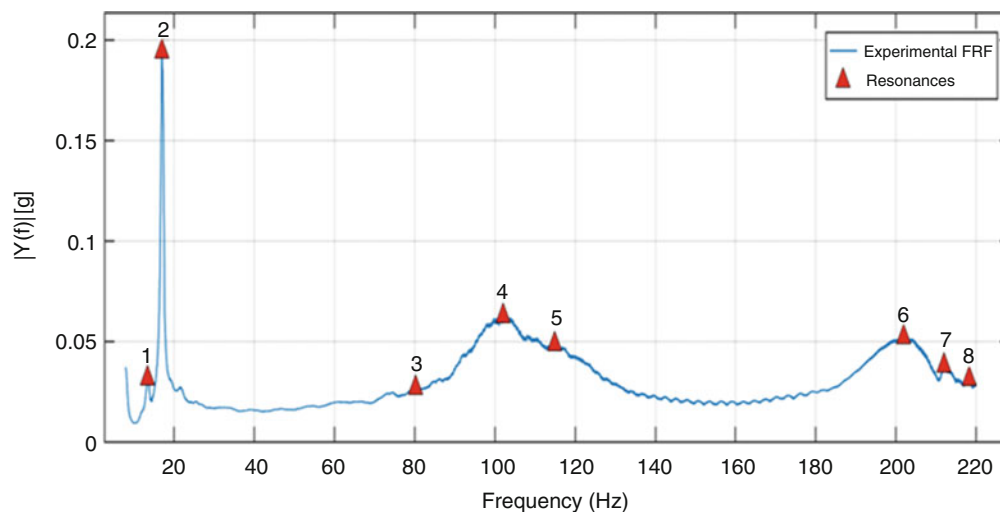


Fig. 36.5 Experimental FRF of the two-wheel tractor handlebar

Table 36.2 Comparison of natural frequencies

Mode	Frequency ω_i [Hz] (experimental modal analysis)	Modal damping ξ_i	Frequency ω_i [Hz] (ANSYS)
1	13.4468	0.0416	14.707
2	17.0350	0.0199	20.352
3	80.2876	0.4973	31.728
4	102.1149	0.1174	108.23
5	114.9657	0.1531	132.07
6	201.9767	0.0427	134.42
7	212.0380	0.0808	–
8	218.3203	0.1725	–

relative to the lateral vibrations were not precisely identified by the accelerometers, since they were arranged to acquire the signals only in the vertical direction, which can be directly coupled with a farmer.

36.5 Operational Modal Analysis

The operational modal analysis of the two-wheel tractor was carried out with the same experimental setup of the impact hammer test considering four scenarios to identify the influence and interaction of the human being in the frequency response of the handlebar under the two engine speeds, the low at 783 rpm and the high-speed at 1800 rpm. The first test was carried out with the machine in neutral (belt) transmission, then, in the same condition but with a person holding the grip of the handlebar, then the test was done with the machine in neutral transmission and the operation of the implement without touching the soil, and finally the interaction engine-implement-human was tested.

In the first scenario, the frequency response of the handlebar measured with the A_2 accelerometer (on the handlebar grip) with the engine on neutral position shows the existence of peaks with high amplitude at frequencies below 100 Hz at the low speed of the two-wheel tractor. These frequency ranges are the ones with the highest sensitivity for the human when he holds the grip of the handlebar. It is also observed that, at high speed no significant peaks are identified at low frequencies, but there is an increase in amplitude accelerations (about 27 times greater) due to the high speed of the machine, as illustrated in Fig. 36.6. From Tables 36.3 and 36.4, it can be noted the first dominant modes have very low damping (below 1%), which would be interacting with the farmer, causing possible physical damage.

On the second scenario, the results of the FRF derived from the human-engine-handlebar interaction at the low and high-speed in accelerometer A_2 show the presence of the same peaks in the frequencies than those without interaction with the operator. However, it is perceived a significant decrease of half in the amplitude of these peaks due to human energy absorption when pressing the grip of the handlebar, which leads to higher vibration transmission to the operator, since the

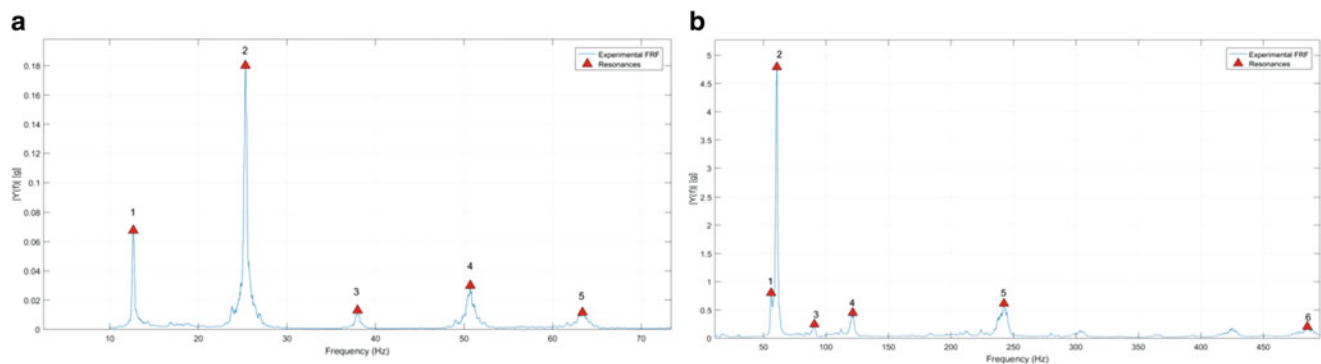


Fig. 36.6 FRF of the handlebar during neutral operation (a) at low-speed, and (b) at high-speed

Table 36.3 Frequency response of the handlebar during neutral operation in A_2 at low-speed

Mode i	Frequency ω_i [Hz]	Modal damping ξ_i
1	12.6601	0.0095
2	25.3201	0.0051
3	37.9802	0.0041
4	50.7118	0.0044
5	63.3719	0.0062

Table 36.4 Frequency response of the handlebar during neutral operation in A_2 at high-speed

Mode i	Frequency ω_i [Hz]	Modal damping ξ_i
1	56.1001	0.0139
2	60.7016	0.0107
3	90.6948	0.0101
4	121.4270	0.0088
5	242.3534	0.0060
6	485.0406	0.0038

force to hold the grip increases the stiffness in the human hand. Besides, it is important to highlight the presence of a peak about 2 Hz, which appears at low speed, which can be caused by the interaction of the human as is shown in Fig. 36.7, and Tables 36.5 and 36.6.

Finally, in the third and fourth scenarios, the FRF resulting from the interaction of the engine with the implement in A_2 shows an attenuation of the vibration amplitudes for both the low and high speeds as can be observed in Table 36.7 and Fig. 36.8. However, once the human interacts, a reduction of the damping is reflected when the implement works at high speed with respect to the previous FRF where the human-machine interaction led to higher damping as Tables 36.8 and 36.9 show.

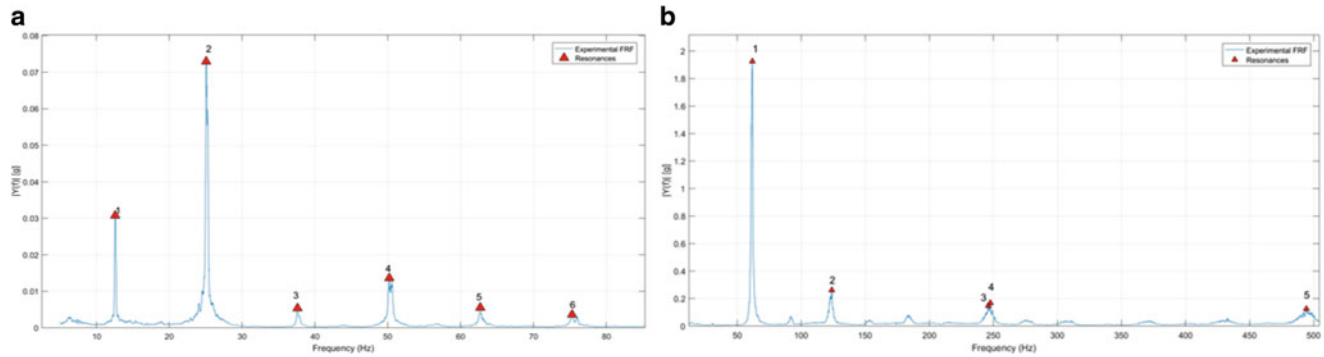


Fig. 36.7 FRF during human-engine-handlebar interaction (a) at low-speed, and (b) at high-speed

Table 36.5 Frequency response during human-engine-handlebar interaction in A_2 at low-speed

Mode i	Frequency ω_i [Hz]	Modal damping ξ_i
1	12.5766	0.0047
2	25.0698	0.0065
3	37.6106	0.0026
4	50.2110	0.0030
5	62.7042	0.0016
6	75.3047	0.0022

Table 36.6 Frequency response during human-engine-handlebar interaction in A_2 at high-speed

Mode i	Frequency ω_i [Hz]	Modal damping ξ_i
1	61.8697	0.0089
2	123.8468	0.0080
3	245.9769	0.0057
4	247.6339	0.0016
5	494.2188	0.0024

Table 36.7 Frequency response during engine-implement interaction in A_2 at low-speed

Mode i	Frequency ω_i [Hz]	Modal damping ξ_i
1	12.6481	0.0068
2	14.8893	0.0065
3	17.4523	0.0099
4	19.8126	0.0042
5	22.2803	0.0047
6	25.2486	0.0042
7	37.9086	0.0041
8	50.5568	0.0036
9	63.2287	0.0041
10	75.8411	0.0027

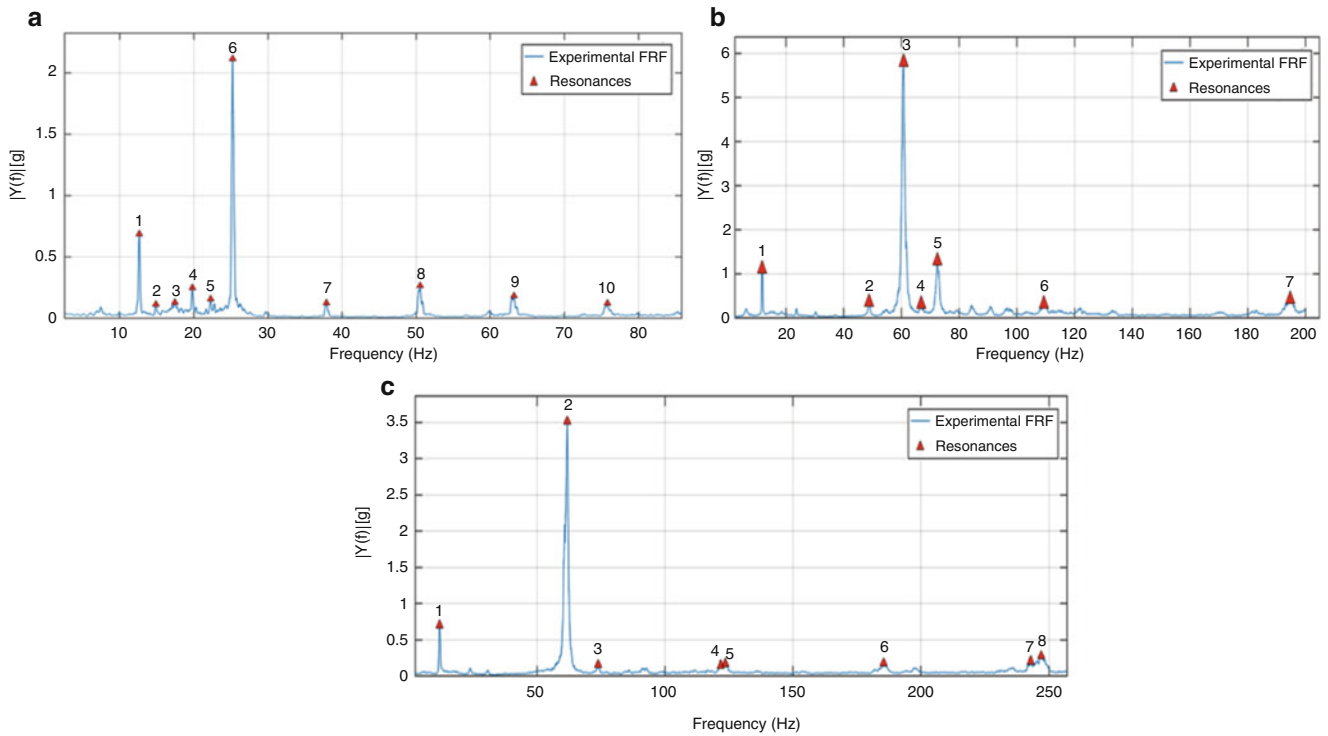


Fig. 36.8 FRF of engine-implement interaction (a) at low-speed, (b) at high-speed, and (c) human-engine-implement interaction at high-speed

Table 36.8 Frequency response during engine-implement interaction in A_2 at high-speed

Mode i	Frequency ω_i [Hz]	Modal damping ξ_i
1	11.8256	0.0169
2	48.8760	0.0056
3	60.8685	0.0059
4	66.9482	0.0043
5	72.5511	0.0060
6	109.4345	0.0070
7	194.7887	0.0055

Table 36.9 Frequency response during human-engine-implement interaction in A_2 at high-speed

Mode i	Frequency ω_i [Hz]	Modal damping ξ_i
1	11.9687	0.0224
2	61.8699	0.0061
3	73.9339	0.0047
4	121.8562	0.0141
5	123.6443	0.0056
6	185.4904	0.0023
7	243.0210	0.0019
8	247.0980	0.0048

36.6 Discussion

The results obtained from the structural analysis and experimental modal analysis of the handlebar of a two-wheel tractor, are important to evaluate its dynamic performance and the interaction of engine, implement and human. It was found that the vibrations present in the human, handlebar, two-wheel tractor, implement and soil are randomly and harmonically transmitted, with amplitudes depending on the selected machine-speed, implement and soil-type. It was also found that the range of the frequencies that affect the human, when operating the machine, is in the range below 200 Hz, as it has been found in the literature.

According to the study in [10], where the main natural frequencies of the human arm were analyzed, and comparing those results with the present analysis, it was confirmed that the frequencies found about 12, 25, 37 and 50 Hz, during the human interaction with the machine at low speed, are transmitted and closely related with physical disorders with palm, wrist and elbow. Thus, a human experience repetitive compression and tension movements that can trigger joint or muscular problems. On the other hand, when the two-wheel tractor was switched to high speed and the implement was put into operation, frequencies in a range of 61–122 Hz were identified, which are associated with effects at a shoulder level.

Therefore, to reduce these undesirable vibrations and noise transmitted to the human being, it is necessary to incorporate a low-cost passive or semiactive suspension system, by integrating an arrangement of springs and dashpots to the main base of the handlebar support, which can be fixed on the flange and fastening bolts. This can be complemented by elastomeric isolators between the flange and the lower handlebar supports.

36.7 Conclusion

In this work, we analyzed the vibrations of a commercial two-wheel tractor and its interaction with the human under different operating scenarios. Thus, the modal parameters of the machine were identified through FE methods, and the results were validated from experimental modal analysis. Likewise, an operational modal analysis was carried out focusing on the structure of the machine handlebar, and based on this, it is proposed a low-cost passive or semi-active suspension system capable to minimize harmful vibrations on humans and improve the farmer's comfort.

References

1. Velazquez-Miranda, E., Silva-Navarro, G., Bory-Reyes, J.: On the design methodologies for agricultural machines in Mexico. In: 14th International Conference on Electrical Engineering, Computing Science and Automatic Control (CCE), Mexico City, pp. 1–6 (2017)
2. Velazquez-Miranda, E., Bory-Reyes, J., Silva-Navarro, G., Garcia-Perez, O.A., Trujillo-Franco, L.G.: On the dynamic analysis, evaluation and functional design of a two-wheel tractor. In: 25th International Congress on Sound and Vibration (ICSV25), Hiroshima, Japan (2018)
3. Crocker, M.J.: Handbook of Noise and Vibration Control. Wiley, New Jersey (2007)
4. Braun, S., Ewins, D.J., Rao, S.S.: Encyclopedia of Vibration. Academic, San Diego (2002)
5. Gheorghe, G.V., Persu, C., Gageanu, I., Cujbescu, D.: Structural and modal analysis in SolidWorks of basic structure of equipment to prepare germinative bed in strips. In: 17th International Scientific Conference Engineering for Rural Development, Jelgava, Romania (2018)
6. Guo, L., Jian, C., Hangjia, X., Shimeng, W.: Vibration test and analysis of mini-tiller. *Biol. Eng.* **9**, 97–103 (2016)
7. Dewangan, K.N., Tewari, V.K.: Characteristics of hand-transmitted vibration of a hand tractor used in three operational modes. *Int. J. Ind. Ergon.* **39**(1), 239–245 (2009)
8. Niu, P., Yang, M.J., Chen, J., Yang, L., Xie, S.Y., Chen, X.B.: Structural optimization of a handheld tiller handrail by vibration modal analysis. *INMATEH.* **52**, 91–98 (2017)
9. Chaturvedi, V., Kumar, A., Singh, J.K.: Power tiller: vibration magnitudes and intervention development for vibration reduction. *Appl. Ergon.* **43**(5), 891–901 (2012)
10. Adewusi, S., Thomas, M., Vu, V.H., Li, W.: Modal parameters of the human hand-arm using finite element and operational modal analysis. *Mech Ind.* **15**(6), 541–549 (2014)



Chapter 37

Reproducible Modal Testing Using a Flexure-Based Impact Excitation System

Shivang Shekhar and O. Burak Ozdoganlar

Abstract Impact excitation is a common technique used for modal testing of structures. The quality and bandwidth of the dynamic model of a structure obtained through impact testing directly depends on the characteristics of the impact excitation. However, applying optimal, or even satisfactory, impact excitation to structures manually (using impact hammers) requires considerable experience. Indeed, even experienced personnel may have much difficulty in applying single-impact, repeatable (force magnitude, impact location, impact orientation) excitations with a required frequency bandwidth. As such, impact testing can become very time consuming, necessitating very large number of repetitions to obtain acceptable coherence values and an accurate dynamic model of the structure in the form of frequency response functions (FRFs).

To address these challenges, in this work, an impact excitation system (IES) is implemented, where the excitation is provided by a flexure-based system. In this system, the motion of the instrumented hammer is controlled by a custom-made flexure. By modifying the flexure geometry, initial displacement of the hammer (dictated by an electromagnet), the initial distance between the hammer tip and the sample surface, and the added mass at the hammer tip, a broad range of impact forces and frequency bandwidths can be obtained in a highly reproducible fashion. To demonstrate the repeatability and reproducibility of the presented system, impact testing is performed on a solid cast iron block with different force levels. The results between the automated and manual testing are compared by doing several repetitions. Finally, the given system is used in testing of a turbine blade to obtain its dynamics in the form of FRFs. As a result, it is concluded that the flexure-based impact excitation system enables applying controllable force levels and required frequency bandwidth to obtain accurate dynamic models of structures.

Keywords Impact excitation system · Modal testing · Frequency response functions · Dynamic model · Broadband excitation

37.1 Brief Introduction

High bandwidth dynamic characterization of structures is critical to their design and functionality. Modal testing is a common method to obtain the dynamics of structures. In modal testing, a known dynamic excitation is given to the structure and the resulting vibrations are measured. The dynamics is then obtained in the form of Frequency Response Functions (FRFs). For modal testing of structures, an impact hammer is used to excite the structure for a short duration which facilitates broadband excitation, i.e. multiple modes of the structures are excited simultaneously [1, 2]. During impact testing, the dynamic model of the structure is directly dictated by the quality of impact. Typically, impact testing is done manually, i.e. using a hand-held impact hammer. However, manual testing using a hammer suffers from various challenges. First, avoiding multiple hits is very difficult, especially for compliant structures. This results in poor coherence in the FRFs. Second, there is poor force control which may result in damage, while testing fragile structures. Finally, manual hits provide insufficient frequency

S. Shekhar

Department of Mechanical Engineering, Carnegie Mellon University, Pittsburgh, PA, USA
e-mail: shivangs@andrew.cmu.edu

O. B. Ozdoganlar (✉)

Department of Mechanical Engineering, Carnegie Mellon University, Pittsburgh, PA, USA

Department of Biomedical Engineering, Carnegie Mellon University, Pittsburgh, PA, USA

Department of Materials Science and Engineering, Carnegie Mellon University, Pittsburgh, PA, USA

e-mail: ozdoganlar@cmu.edu

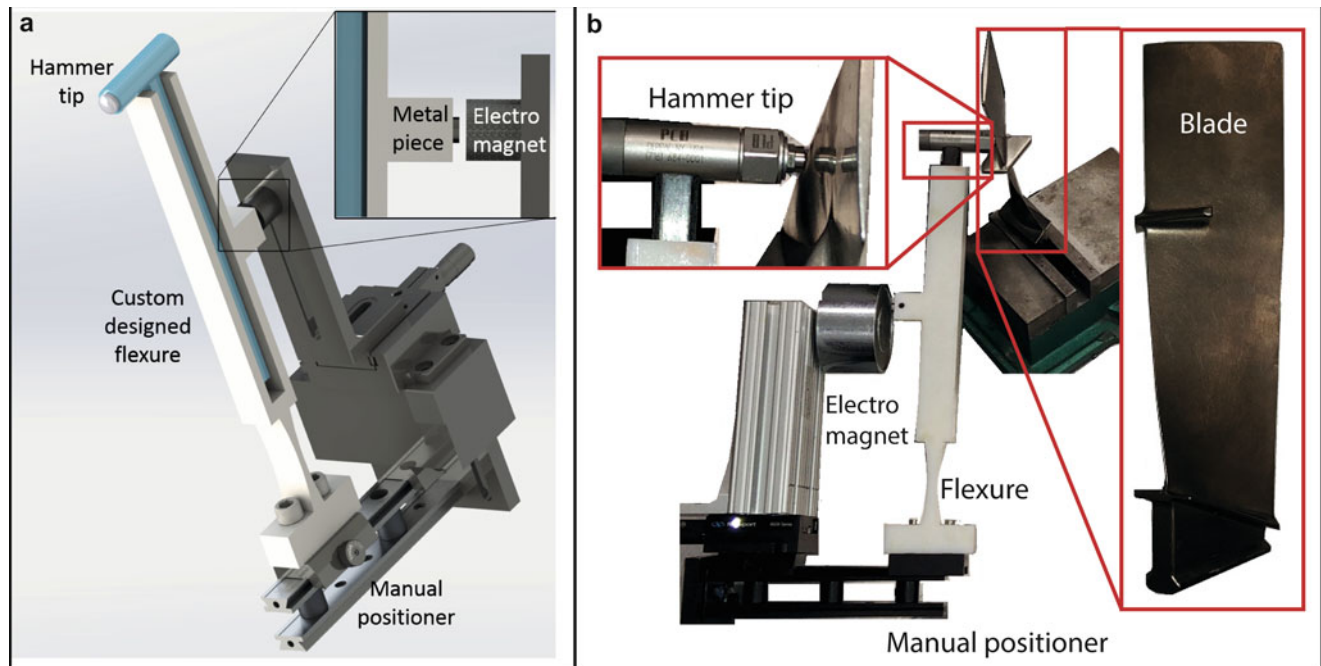


Fig. 37.1 (a) CAD model of the impact excitation system (IES) and (b) experimental testing of the turbine blade using the system

bandwidth and hence hinder high bandwidth characterization of structures [3]. Hence, there is a need of impact excitation systems to enable precise control over the force and bandwidth of excitation.

In the current work, an impact excitation system (IES) is designed and implemented for modal testing of structures to facilitate controlled impulsive excitation similar to [4]. A brief description of this system is included in Sect. 37.2 which describes different components of the IES. Section 37.3 includes preliminary results using the IES which are compared with the manual testing method in terms of repeatability and bandwidth.

37.2 Impact Excitation System

Figure 37.1a shows the design of the IES. The IES includes a flexure-based body, a commercially available impact hammer and an electromagnet. The impact hammer (PCB 086B03) is held into the flexure-based body. The hammer has a load cell at the tip to measure the force applied during impact. A metal piece is attached to the flexure body. An electromagnet is used to pull the hammer using the metal piece and to provide required initial deflection. This initial deflection (d_0) is controlled by the gap between the electromagnet and the metal piece. Thus, the electromagnet (ELMATU067040) facilitates automated and repeatable motion of the flexure based body. When the electromagnet is switched off, the flexure undergoes motion because of its own dynamics and hits the test structure. The force and the bandwidth provided to the test structure can be controlled by dictating the gap between the test structure and the hammer tip (g_0). Hence, given the initial momentum of the IES, the impact force and bandwidth can be controlled by changing this gap.

37.3 Preliminary Results

Using the system described above, some preliminary results are presented here to demonstrate its effectiveness. Impact tests are performed on a solid cast iron block. To compare the repeatability of excitation, experiments are done using the automated system and using the manual testing method. The variations for the two cases are then quantified and compared statistically. For each of the two cases, 15 repetitions are done. To have a good comparison, only the single hit cases are used in the analysis.

As shown in Fig. 37.2, the given system helps in providing highly repeatable excitations compared to the manual testing method in terms of impact force. The bandwidth also shows better performance compared to manual hitting though the difference is less. The given system also facilitates three different levels of precise force control as seen in Fig. 37.2. Table 37.1 includes the mean and standard deviation values of the impact force and bandwidth obtained for the difference cases.

Following the repeatability tests, the IES is used for dynamic testing of a jet engine blade as shown in Fig. 37.1b. Figure 37.3 shows the forces and bandwidth obtained and shows that the IES enables good quality single hit with high bandwidth of 4.7 kHz. Manual testing on the jet engine blade results in multiple hits. This results in highly non-uniform bandwidth which is reflected as poor coherence in the obtained FRFs (see Fig. 37.4). The comparison of FRF magnitude between the IES and manual testing shows significant differences, especially at higher (more than 2 kHz) frequencies.

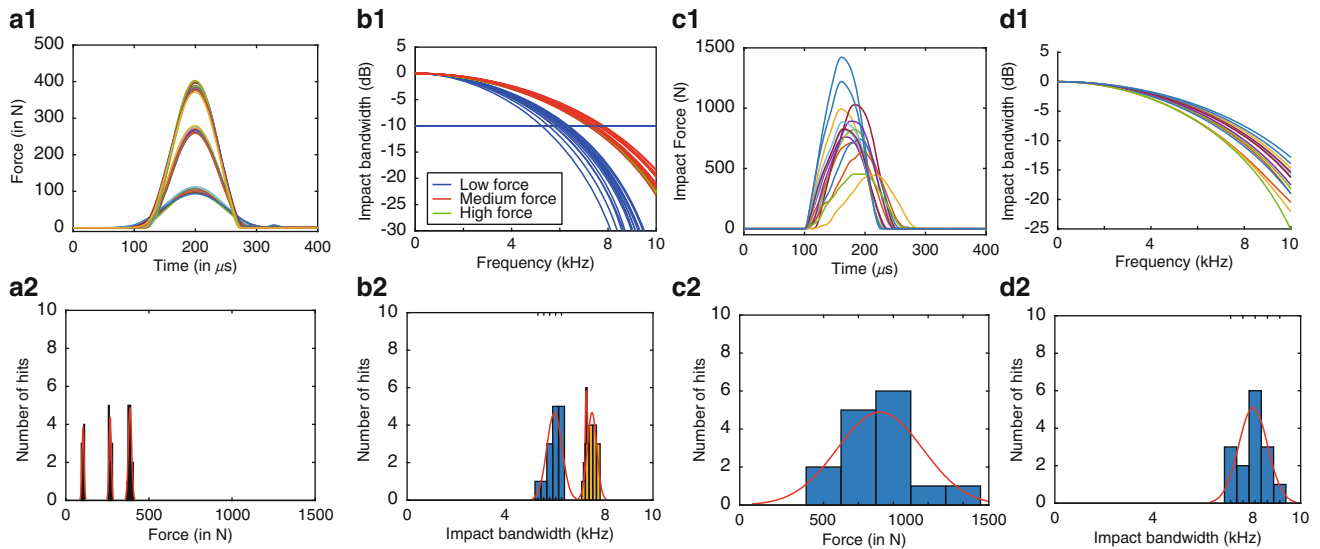


Fig. 37.2 Impact force and excitation bandwidth variability comparison between automated and manual hits (a) force using IES (b) bandwidth using IES (c) force using manual testing (d) bandwidth using manual testing

Table 37.1 Impact force and bandwidth data obtained from repeated testing on cast iron block

	Impact force (N)		Impact bandwidth (Hz)	
	Mean	Standard deviation	Mean	Standard deviation
IES (low force)	103.3	6.1	5991.3	307.5
IES (medium force)	266.7	6.8	7291.6	51.3
IES (high force)	386.1	9.8	7518.8	192.3
Manual testing	844.86	256.91	8065.5	586.5

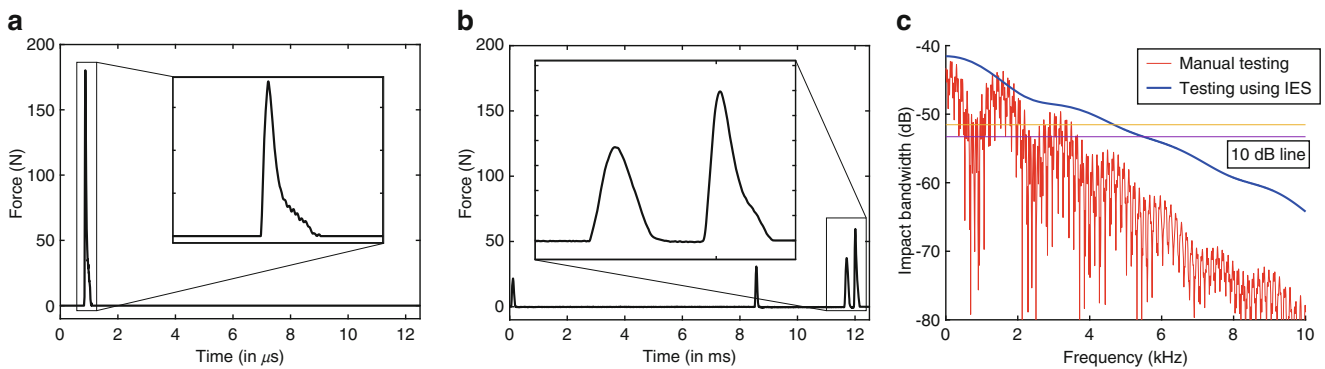


Fig. 37.3 Impact force obtained from (a) automated and (b) manual testing, on the jet engine blade, (c) comparison of impact bandwidth shows higher and more uniform bandwidth obtained using the presented system

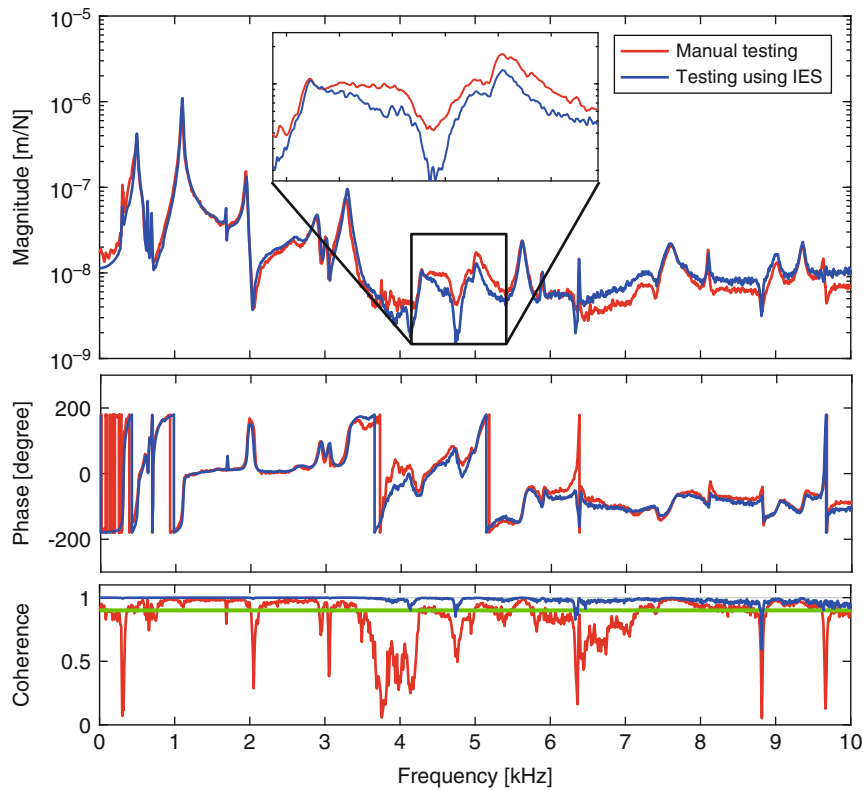


Fig. 37.4 Frequency response functions of the jet engine blade obtained using the automated IES and manual testing

37.4 Conclusions

The proposed Impact Excitation System (IES) is useful in providing repeatable impact testing of structures. Results obtained from repeated testing on a solid Cast Iron block show that the IES can be used to provide controlled excitations at different force levels while manual testing shows large variations in the force magnitude. Although the variations in bandwidth are quite similar in automated and manual testing, the IES has better control at all force levels.

The testing on jet engine blade shows that the presented flexure-based system enables getting good quality dynamic data in the form of frequency response functions. The obtained coherence is significantly better as compared to manual testing, especially at higher (more than 2 kHz) frequencies.

References

1. He, J., Fu, Z.-F.: Frequency response function measurement. In: *Modal Analysis*, pp. 140–158. Butterworth-Heinemann, Oxford (2001)
2. Baqersad, J., Poozesh, P., Niezrecki, C., Avitabile, P.: Comparison of modal parameters extracted using MIMO, SIMO, and impact hammer tests on a three-bladed wind turbine. In: *Topics in Modal Analysis II*, vol. 8, pp. 185–197 (2014)
3. Brown, D.L., Allemang, R.J.: Forty Years of Use and Abuse of Impact Testing: A Practical Guide to Making Good FRF Measurements, *Experimental Techniques, Rotating Machinery, and Acoustics*, vol. 8, pp. 221–241. Springer International Publishing, (2015)
4. Bediz, B., Korkmaz, E., Ozdoganlar, O.B.: An impact excitation system for repeatable, high-bandwidth modal testing of miniature structures. *J. Sound Vib.* **333**(13), 2743–2761 (2014)



Chapter 38

Modal Analysis and Characterization of Mounting Cart Used for Testing in the Combined Environment Acoustic Chamber

Melissa A. Hall

Abstract The ability to simulate the aeroacoustic and thermoacoustic loading typically experienced by space access vehicles and hypersonic flight vehicles is accomplished through the use of a progressive wave tube (PWT) housed in the Combined Environment Acoustic Chamber (CEAC). Simulating these types of acoustic loading requires the test article be mounted flush with the wall of the PWT, exposing the test article to the propagating pressure wave. This mounting capability is achieved through the use of a strong-back fixture, referred to in this work as a test cart, whose initial design was to withstand static pressure loading on the front face where a test article is mounted. However, this test cart experiences dynamic loading during these acoustic tests. Preliminary modal evaluations of test articles mounted to the cart have indicated that the test cart has several natural frequencies in the testing frequency range of interest (0–1000 Hz). The interaction between the test cart and test article is undesirable because it contradicts the analytical rigid boundary conditions and could also lead to unrealistic failure as a result of over excitation of the specimen if the same mode exists in the test cart and test article. The goal of this work is to characterize the test cart using experimental modal analysis and evaluate the need for modification or complete redesign of the test cart to eliminate modes below 1000 Hz and maintain the intended functionality of the cart.

Keywords Modal analysis · Impact testing · Test fixture · Structures · Interaction

38.1 Introduction

The intent of this work is to characterize the dynamic response of a testing support structure through experimental modal analysis. This characterization will be achieved using a roving hammer impact test to determine the structural modes of a steel, strong-back fixture (test cart), used in the Combined Environment Acoustic Chamber (CEAC). There are two different test cart configurations which are used on a regular basis. The first is a more rigid lattice weldment and the second is an open face, “picture frame” front mounting face. The picture frame cart allows for better line of sight access for non-contacting optical measurement systems. The picture frame cart is the main focus of this work. While there are numerous modal analysis methods that are well understood, impact testing is an easy and inexpensive multiple reference method that requires minimal setup, shorter testing time, and can be applied to many facilities and test structures. Upon completion of the impact test the resulting experimental data will be used to perform modal parameter estimation. Modal frequencies, damping estimates, and mode shapes will be analyzed with the future intent of this work to be the development of a modification or complete redesign of the test fixture.

38.2 Background

The CEAC test cart was designed for strength based on static loading. However, during acoustic tests, it encounters dynamic loading. In recent test programs being conducted within the Structural Validation Branch of the Air Force Research Lab, which were meant to verify new analytical techniques, response data from test articles has indicated a great deal of interaction from the test cart. Further investigation, via modal evaluations of test articles conducted while mounted to the test cart, indicated that the test cart displays a strong modal response in the frequency range of interest (typically 0–1000 Hz). The resulting modal evaluation data revealed that the test cart has numerous natural frequencies in this range.

M. A. Hall (✉)

Structural Validation Branch, Air Force Research Lab, Dayton, OH, USA

e-mail: melissa.hall.7@us.af.mil

Modal response of the test cart in the frequency range of interest poses a big problem, because it causes unforeseen and undesirable interaction with the test article. For analytical purposes, the test fixture is intended to provide a rigid boundary condition or at least a known boundary condition for modeling the test article. In the current testing configuration, this rigid or known boundary condition is not reachable. Additionally, and more importantly, if a mode of the test cart were to occur at the same frequency as a mode of the test article, the test article could be greatly over excited at this frequency and an unrealistic failure could occur. These reasons are why an understanding of the modal response behavior of this test cart will improve the predictions and understanding of the dynamic response of future test articles in the testing condition.

38.3 Analysis

The impact test was conducted using a PCB Piezotronics calibrated impulse-force hammer, model 086C03, for a total of 293 impact point location and direction combinations and 30 PCB Piezotronics triaxial accelerometers, model 356A16, whose locations on the structure are annotated by the pink nodes shown in Fig. 38.1a. This number of impact and measurement points provides the necessary spatial information to be able to fully characterize the structure. The picture frame test cart is shown in Fig. 38.1b in the standard testing condition within the CEAC.

The data acquisition system used National Instruments (NI) PXIe based hardware consisting of a PXIe-1085 chassis connected to the control computer via a PXIe-PCIe-8381 card and a custom m+p International software package to configure response and excitation channels and view real-time response functions and time history data. Impact data was collected using the m+p signal analyzer, with the data acquisition parameters shown in Table 38.1. Modal parameter estimation was completed using UC-SDRL X-modal III. The z-domain rational fraction polynomial (RFP-Z) modal parameter estimation algorithm was used for processing all experimental data groups.

There were more than 250 structural modes of the test cart found over the 0–1000 Hz frequency range with 25 modes present within the first 150 Hz. Figure 38.2 provides the Modal Vector Complexity Plots (MVCPs) for this first set of modes up to 150 Hz. Each MVCP includes the corresponding modal frequency, the mean phase correlation (MPC) value, and the Modal A scale factor and phase of each of the vectors. In each individual plot of Fig. 38.2, the scaled modal vectors are plotted; the more scattered each of the modal vectors are along the real axis the more complex the mode. Each mode below 150 Hz has an MPC value above 0.8 (or 80.0%) where an MPC value of 1.00 indicates a normal mode of the system [1]. Since

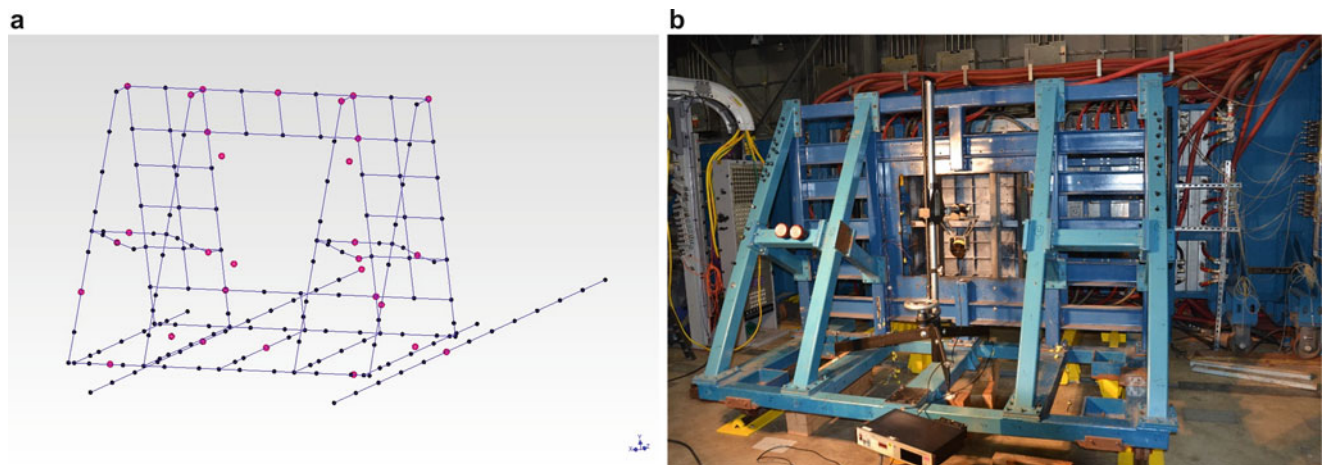


Fig. 38.1 (a) (Left) Wireframe model of the test cart with the triaxial accelerometer locations annotated by bold pink nodes (b) (Right) Currently used picture frame test cart installed in the acoustic chamber

Table 38.1 Data acquisition parameters defined in m + p signal analyzer software

Sample rate [Hz]	2560
Block size	16,384
Useful bandwidth [Hz]	1000
Frequency resolution [Hz]	0.15625
Number of averages	5
Window type	Force/exponential

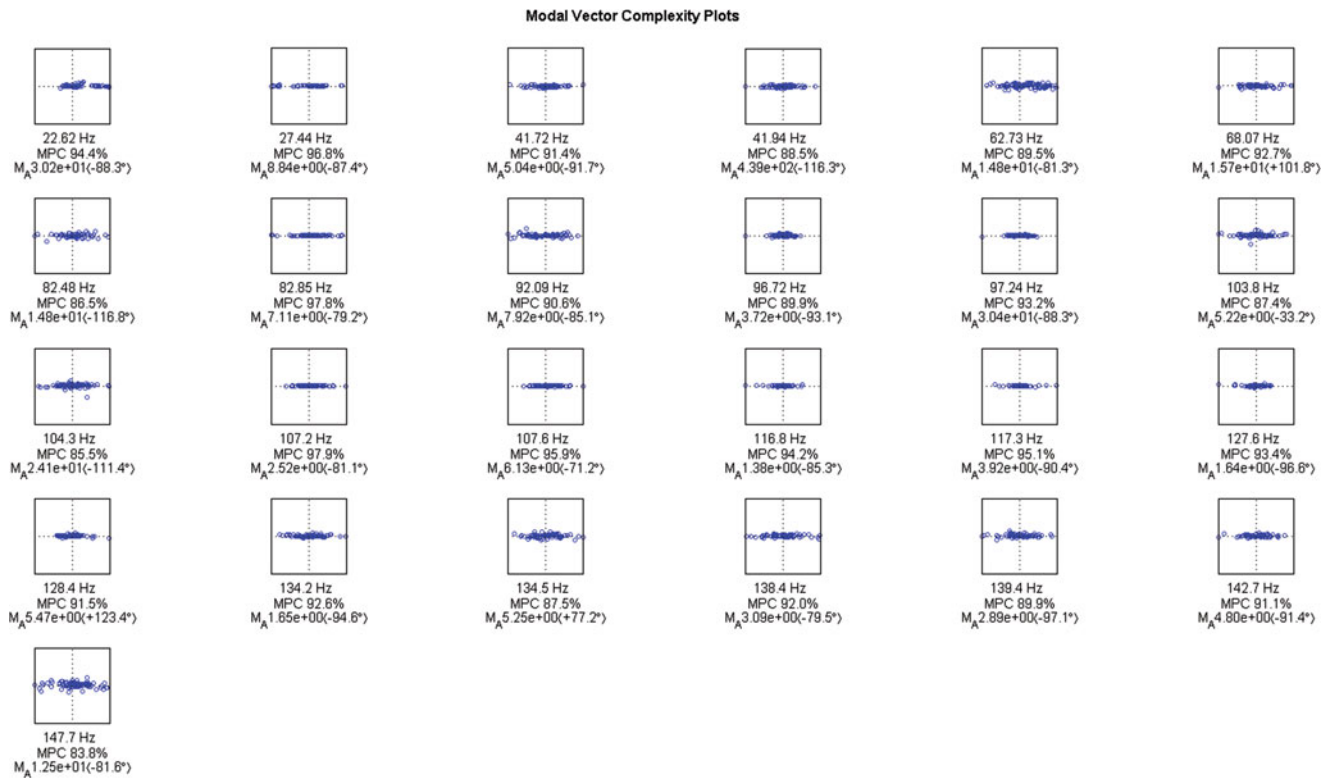


Fig. 38.2 Modal Vector Complexity Plots for all structural modes up to 150 Hz

these lower frequency modes tend to have significantly more displacement than the higher frequency modes, preventing the interaction of the cart face with the test articles is much more critical.

38.4 Conclusion

The purpose of this work was to characterize the CEAC test cart through the use of a roving impact modal test. The test resulted in the identification of more than 250 structural modes. Based on the presence of such a high number of structural modes within the 1000 Hz frequency range of interest for this test cart, multiple potential solutions exist. The first potential solution includes structural dynamic modification to the existing test cart structure. While several modification tools exist, adding mass or other damping materials to the structure could aid in shifting the modes away from the frequency range of interest. Any structural dynamic modification would need to be modeled and evaluated analytically and experimentally for the optimal solution. Another potential solution to this problem would be a complete redesign of the testing fixture. Currently, the design and use of a concrete inertial frame is being investigated.

Acknowledgements This work could not have been completed without the knowledge and support of the Structural Validation Branch Dynamics Team, Air Force Research Laboratory, Wright-Patterson AFB, OH.

Reference

1. Phillips, A.W., Allemang, R.J.: Application of modal scaling to the pole selection phase of parameter estimation. In: Proceedings of International Modal Analysis Conference (IMAC), UC Structural Dynamics Research Laboratory, Cincinnati, OH (2010)

Chapter 39

Effects of Sensor Count on Damping Estimates from Operational Modal Analysis



Esben Orlowitz

Abstract For fatigue estimation of many large structures the damping coefficients of the first couple of modes are the most essential. These modes can often be identified, by Operational Modal Analysis (OMA), by using a low number of sensors. However, it is not well known how the number of sensors and their locations are affecting the damping estimates provided from OMA. In this paper it is investigated how the damping estimates from OMA depend on the number of sensors and their locations. In addition, the so-called reference-based OMA methods using quadratic Hankel matrix, where only a few DOFs are used for calculations of the non-parametric functions (e.g. correlation functions), is compared to using the squared (full) Hankel matrix. All the results are presented based on experimental data.

Keywords Operational modal analysis · Damping estimation · Experimental data · System identification strategy

39.1 Introduction

For large structures operating in complex environments the structural dynamic properties are often observed to depend on the condition of operation, with relatively large variances as a result. These structures could for example be wind turbines[1] or ships[2].

To get the needed data for model validation, structural health or lifetime assessment of such structures, high requirements on the measurement strategy will be present. For instance, it may require a long measurement campaign and likely measurements on several samples from a population of structures, in order to get reliable structural dynamic properties under conditions of interest. Finally, the number of measurement points, or measured Degrees-Of-Freedoms (DOFs), and their locations will give many practical challenges for structures in operation. The damping properties of the first couple of modes are often the most essential, for instance, in fatigue estimation. However, the damping is often found to be a parameter which can show high dependency on the conditions and furthermore, damping is generally seen as the most difficult dynamic property to estimate.

To deploy the estimation of damping continuously and grab its dependencies to the condition, as said, the requirement to the measurement strategy becomes crucial. The cost and complexity of a monitoring (Data Acquisition) system could quickly be extensive and difficult to implement in operating structures, especially if retrofitting is needed. Using a low number of sensors, potentially already existing for other purposes, is therefore of high interest in the industry. As an example, typical fleet wind turbines are equipped with a single (triaxial)-accelerometer to measure the two horizontal directions of turbine top (Nacelle). Therefore, it could be of interest to investigate to which extent these could be used for proper validation of damping.

Theoretical it can be shown that the number of measured DOFs should give the modal parameter estimation method the ability to properly identify all significant sources of noise and physical responses. Hence, theoretically the number of DOFs measured should not limit the rank of the problem. The rank of any matrix $N \times N$ estimated based on the N measured DOF can never be larger than the smallest dimension of that matrix N . Based on this it is suggested in [3] that one should never assume a rank of structural dynamic problem to be smaller than four and that a good rule of thumb is always to use at least 5–6 measured DOFs. To fulfill these requirements and the practical wish for a low as possible amount of measured DOFs an alternative strategy than standard OMA is needed. Such a strategy could be to make a few short/non-permanent measurement campaigns with a large sensor setup to validate the mode shapes, assuming this to be representative. This could

E. Orlowitz (✉)
Siemens Gamesa Renewable Energy, Brande, Denmark

be done just after commission (or for ships during test-trial). Following, a smaller number of permanent sensors will be used for damping estimation under different condition and possible for tracking purposes.

In the present work an initial study of this strategy of using a small amount of measured DOFs for damping estimation on a known structure. The work is based on an experimental study of a free-free plate (two dimensional) with a close-spaced mode pair as the first two. The case is from a lab test, to minimize the unknown variables and ensure time in-variance to affect the results. In addition, the work includes finally a section with a small study of the consequences of using the reference-based methods in OMA, instead of using all measured DOFs as ‘references’. This corresponds to using rectangular and squared Hankel matrices and input to the modal parameter estimation method.

39.2 Method

The methodology applied in the present work to investigate the influence of the number of utilized DOFs in an OMA are based on a ‘high quality’ measurement. Such a ‘high quality’ measurement contains sufficient amount of measured DOFs to give a good spatial resolution for the modes of interest and a sufficient long measurement time, to avoid effect from these factors, as this is outside the scope of the present work.

This ‘full’ measurement is then used in a OMA and the result of it is used as a baseline for comparison with the ‘reduced’ measurements. The ‘reduced’ measurement are created by taking out selected DOFs of the ‘full’ measurement and performing OMA. The modal parameter estimation (MPE) is performed by the multi-reference Ibrahim time domain (MITD) method for modal parameter extraction [4]. The MITD method is in principle equivalent to the more well known stochastic subspace identification (SSI) method [5] and are using a Hankel matrix of the correlation functions as its non-parametric input. The methodology described above is then applied by ignoring selected entrances in the correlation function matrix used for OMA. The estimation of poles (natural frequency and damping) is evaluated along the stabilization diagram up to a stated model order. The results are then presented as the mean value of poles from different order, after stabilization is established. Even if ‘destabilization’ occurs after initial stabilization the estimates are included in the mean value. In addition the variance is calculated as the normalized random error, $\frac{\hat{\sigma}}{\hat{\mu}}$.

As mentioned, the primarily focus is in the present work is on comparisons of the damping estimates from the ‘full’ and ‘reduced’ measurement. Because of the reduction down to a lower number of measured DOFs than modes of interest there are no point in looking at mode shapes.

39.3 Setup and Analysis

The Plexiglas (PMMA) plate that has been experimentally tested is shown in Fig. 39.1a. The dimensions of the plate are $533 \times 321 \times 20$ mm. The plate is similar to the so-called IES-Plate proposed in [6], although, for practical reasons, the plate thickness was chosen slightly different from the IES-Plate, by choosing 20 mm thickness, which is a standard thickness in

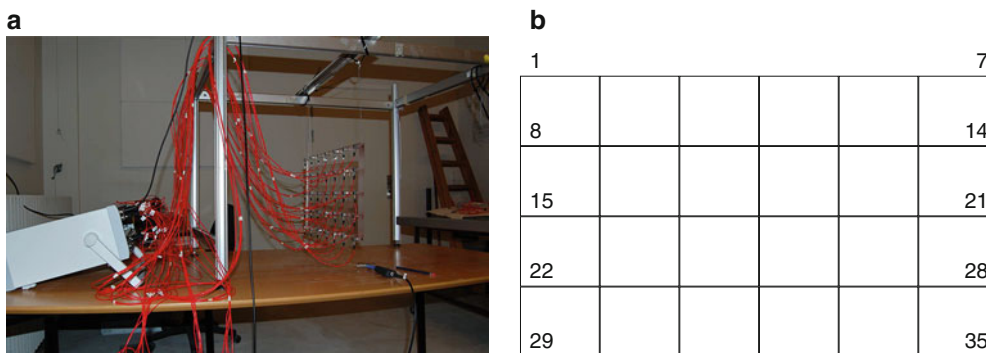
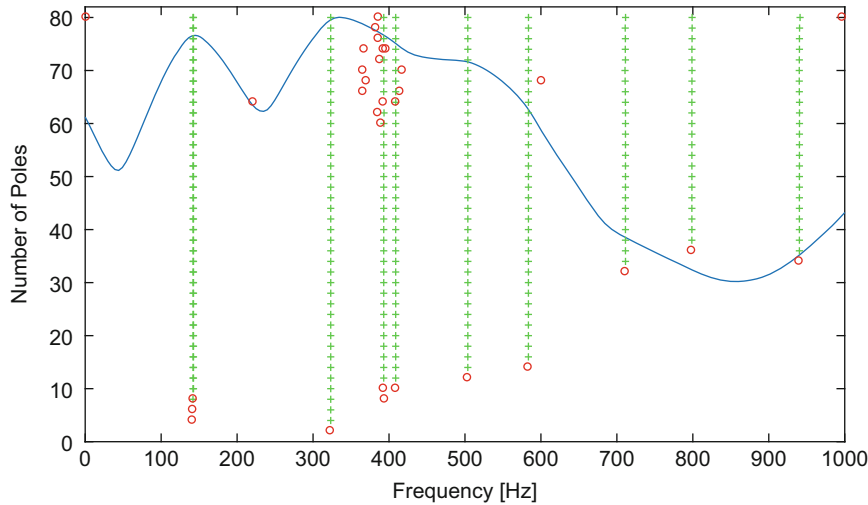


Fig. 39.1 (a) The Experimental setup: Plexiglas plate suspended vertically by two springs, and instrumented with 35 accelerometers. The impact hammer seen in the photo was not used for the present data. (b) Measurement grid on the plate consisting of 35 measurement points with a separation of 75×85 mm. The full dimensions of the plate are 533×321 mm and thickness 20 mm

Table 39.1 Analysis cases studied for the plate

Analysis #	DOF-#'s	#-of-DOFs	Legend
1	1:2:35	35	'all DOF'
2	1:2:35	18	'DOF 1:2:35'
3	2:2:34	17	'DOF 2:2:34'
4	1, 7, 29, 35	4	'DOF 1, 7, 29, 35'
5	1, 7	2	'DOF 1, 7'
6	1, 29	2	'DOF 1, 29'

**Fig. 39.2** Stabilization diagram using all 35 DOFs. Markers are interpreted as: 'open circle' unstable and 'plus symbol' stable pole

Europe. The present experimental measurement of the plate was originally a part of an experimental comparison of OMA and EMA reported in [7] and only the first ten modes are evaluated in this work. The mode shapes are shown in Fig. 39.7.

The measurement grid consisted of 35 DOFs distributed uniformly out of plane on the plate as shown in Fig. 39.1b and responses from all DOFs were measured simultaneously with a sampling rate of 5 kHz. The accelerometers and cables significantly mass-load the structure, and it is also possible that there will be additional damping added. The present experiment is, however, designed so that it is the combined structure together with the instrumentation that is investigated.

For all analysis, a measurement duration of 600 s are used. The estimated correlation functions are used in the MITD by ignoring the first 5 lags, in order to remove the influence of broad band noise [8], and a total of 200 lags have been applied in the analysis. The modal parameter estimation is performed up to an order of 80, allowing 40 modes in the identification.

The analysis cases for the plate are presented in Table 39.1. It should be interpreted as; the full correlation function matrix has 35×35 entrances and for analysis 3, as an example, only every second entrance, starting from 2 are included in the MPE. Hence analysis 3 ignores the all odd numbered measurement DOFs.

Two examples of the stabilization diagram, are presented in Fig. 39.2 using all 35 DOF and in Fig. 39.3 using only DOF 1 and 29. In the present stabilization diagrams the stability criteria was set to deviations from one order to the next of of 0.1% for natural frequencies, 2% for damping ratios and having modal assurance criterion (MAC) values exceeding 0.95.

39.4 Results

The average estimated damping ratios for the ten first modes are presented in Fig. 39.4 for the six different analysis cases. The corresponding normalized random errors are shown in Fig. 39.5 and the number of include estimates shown in Fig. 39.6.

From the average values of the damping, Fig. 39.4, it can be observed that there are only small differences between the different cases. As one could expected the most significant differences is seen then using only two measured DOFs. It should be noted that for mode #4 a sufficient stabilization could not be established using only DOF 1 and 29, see also Fig. 39.3 around 400 Hz. The major effect on the damping estimates are found when looking at the random error associated with the 'stabilized' poles, see Fig. 39.5. (Note: all poles after initial stabilization is include in the presented results, hence the

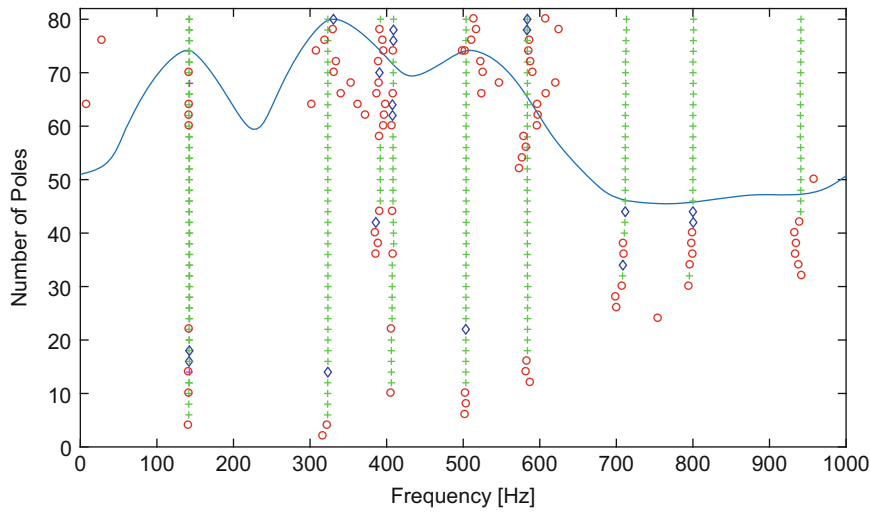


Fig. 39.3 Stabilization diagram using only DOF 1 and 29. Markers are interpreted as: ‘open circle’ unstable and ‘plus symbol’ stable pole, and ‘open diamond’ a pole that is stable in frequency, but not in damping

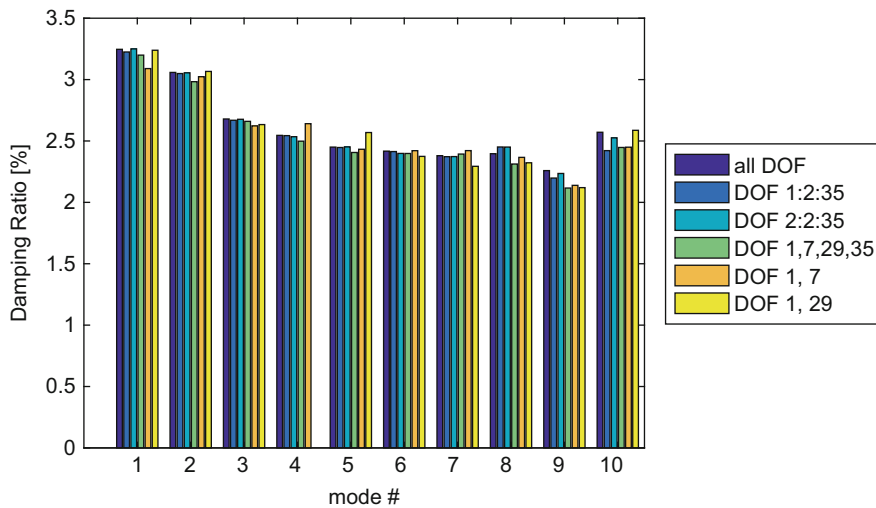


Fig. 39.4 Average damping ratio, (along stabilization diagram), for the ten first plate modes. It can be observed that mode #4 is not sufficient estimated, using only DOF 1 and 29, to give an average value

errors exceeds the stabilization criteria.) With a smaller number of measured DOFs a ‘de-stabilization’ is often observed, e.g. compare the two stabilization diagrams in Figs. 39.2 and 39.3.

When looking at the two first modes, that in this cases are close in frequency, it is interest to the which damping estimates can actually be reached using only two DOFs, but at the same time, the importance of where these two DOFs are located. (In the case of using DOF 1 and 29, actually the cross-MAC between the two close modes, around 140 Hz, is as low as 0.025.) (Fig. 39.7).

The natural frequencies are estimated with significant less influence of the number of measured DOFs. This both include on the mean value and the random errors, see Figs. 39.8 and 39.9, respectively.

39.5 Reference Based Estimation: The Size of the Hankel Matrix

Another interesting topic related to the measured DOFs of a structure is the common usage of reference-based OMA. Up until now in the present work the modal parameters have been estimated based on the use of the full Hankel Matrix with quadratic CF matrices, that is, the CFs have been calculated between all the measured responses. This is not common in the

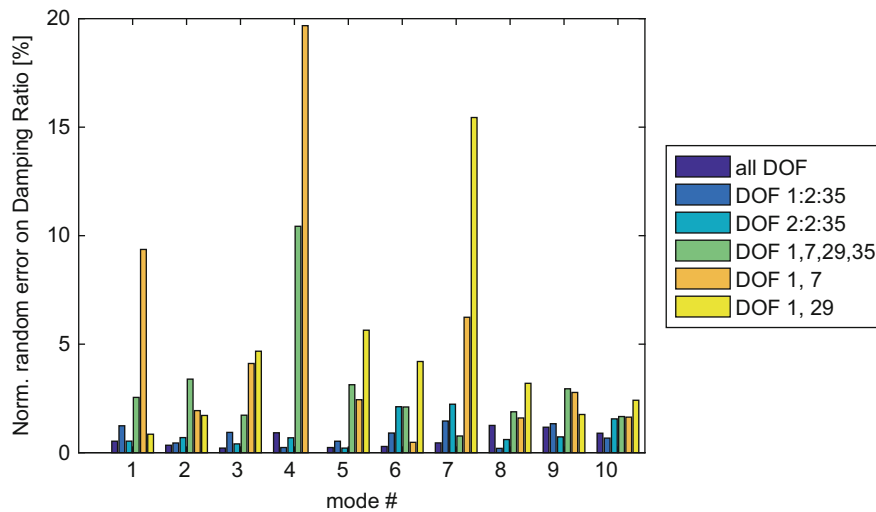


Fig. 39.5 Normalized random error on damping ratios, (along stabilization diagram), for the ten first plate modes. It can be observed that mode #4 is not sufficient estimated, using only DOF 1 and 29, to give an average value

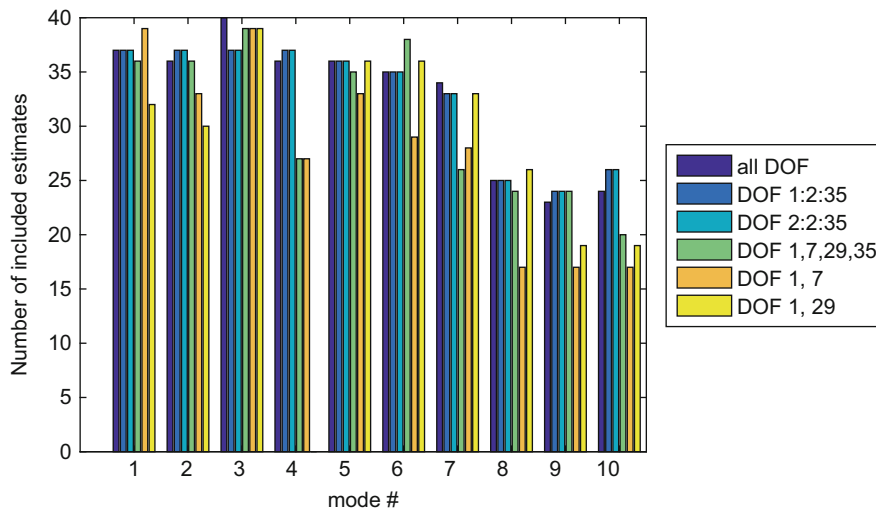


Fig. 39.6 Number of estimated poles used for calculation of average values and random errors

published literature on OMA, where instead so-called reference-based methods are common, see e.g. [5]. For the reference-based methods only a few of the responses are selected as references between which all CFs are calculated. The CF matrices of the Hankel matrix thus being of rectangular shape. The obvious advantage for applying reference-based methods is for computational speed, both a reduction in number of CFs that need to be calculated and the size of the ‘SVD problem’—for the SSI and the MITD methods. However, a reference-based method also means a reduction of the data used which in general is a poor decision from a statistical point of view.

In [5] the reference-based (correlation-driven) SSI method was compared to the ‘classical’ (full Hankel matrix) and found to give equivalent modal parameters. The reference-based algorithm showed an advantage by increasing the computational speed by a factor approximately equal to the ratio of references and the total amount of measured channels.

In this section the full data set from the plate using the full CF matrix is compared to the usage of selected DOFs as references (rectangular matrices). Normally the selection of reference DOFs demands an analysis itself. Basically the demand for a good reference DOF is that all modes of interest are well excited there. For structures of closely spaced modes the number of references must be at least equal to the number of closely spaced modes, as it is the case for classical EMA, where multiple-inputs are needed for closely spaced modes.

For the present plate it is known that there exists two closely spaced modes (mode 1 and 2) and thus two DOFs, as references, are at least needed for the MPE [7]. The plate is suspended as to be closely free-free, therefore its corner DOFs

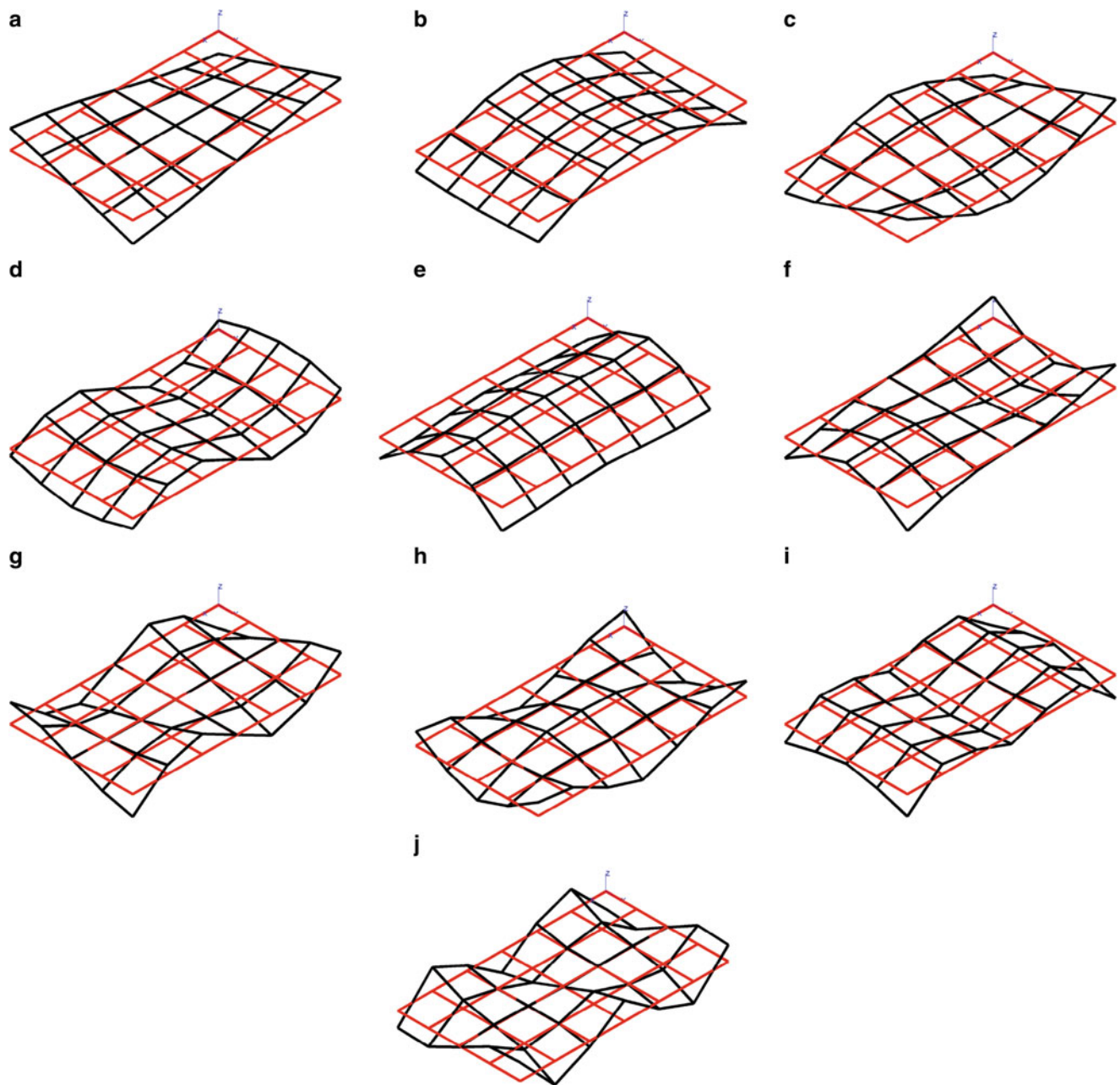


Fig. 39.7 Mode shapes of the plate. (a) Mode 1. (b) Mode 2. (c) Mode 3. (d) Mode 4. (e) Mode 5. (f) Mode 6. (g) Mode 7. (h) Mode 8. (i) Mode 9. (j) Mode 10

will contain all modes of interest at their maximum vibration levels. In this study only the usage of two reference DOFs and only combinations of the corner DOFs (1, 7, 29 and 35, see Fig. 39.1b) are investigated.

In Fig. 39.10a the estimated damping ratios is shown using different combinations of the corner DOFs. When using the DOFs diagonal to each other (29 + 7 and 1 + 35) the two closely spaced modes (mode 1 and 2) were badly estimated. They did not stabilize and only a single estimate was extracted (no mean value). Besides this exception, the mean values of the damping ratios are found very similar, independent of the use of reference-based or full matrix approach. In Fig. 39.10b the normalized random errors corresponding to the mean values of Fig. 39.10a are shown. Here it is found that for most of the modes the random error is significantly smaller when using the full Hankel matrix. However for mode 6 and 8 this is not the case, but the levels of the random errors are equivalent.

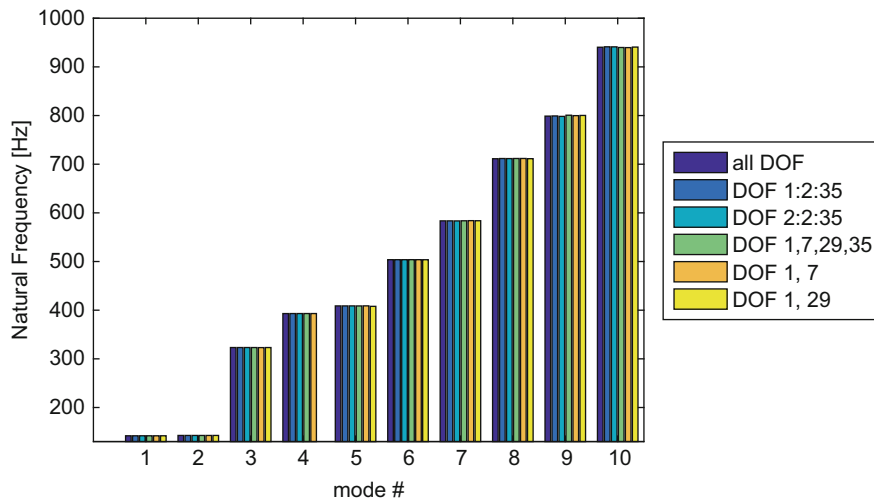


Fig. 39.8 Average natural frequency, (along stabilization diagram), for the ten first plate modes

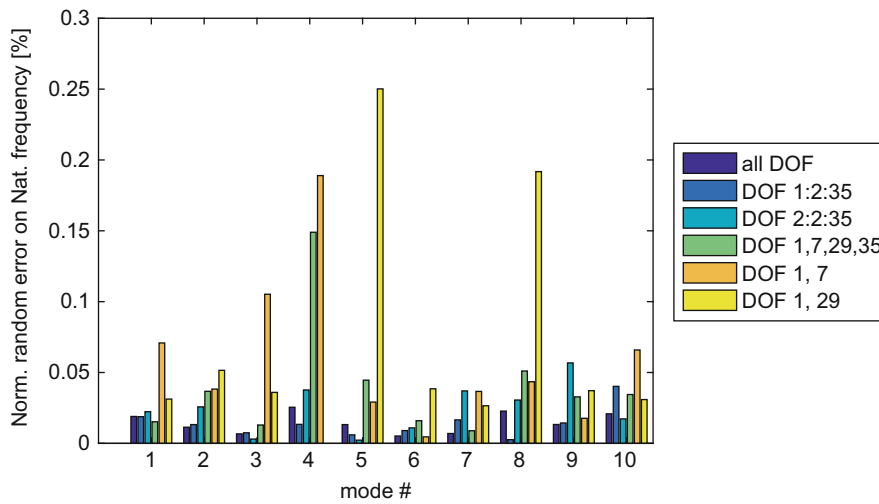


Fig. 39.9 Normalized random error on natural frequency estimates, (along stabilization diagram), for the ten first plate modes

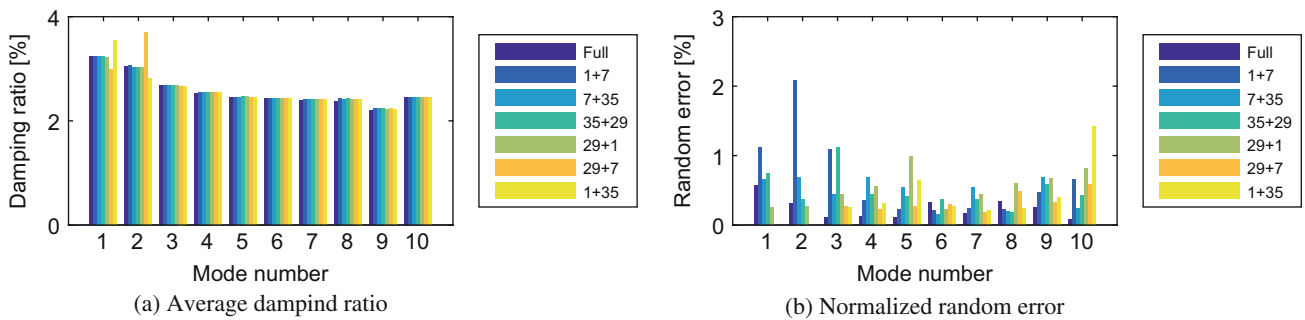


Fig. 39.10 Estimated damping ratios for the ten modes using reference-based estimation, (a) is the mean value evaluated from the stable modes in the stabilization diagram and (b) the corresponding normalized random errors. The ‘Full’ estimation using all channels as references is shown for comparison with the usage of selected references (corner DOFs), DOF: 1 + 7, 7 + 35, 35 + 29, 29 + 1, 29 + 7, 1 + 35

39.6 Discussion and Conclusions

It has been shown that for estimation of poles only, hence frequency and damping, an acceptable level of the estimate can be obtained using a relatively low number of measured DOFs. At least when looking at the lowest modes, which are often of highest interest. However, the variance of the damping estimates can be significant when the number of measured DOFs are small. This might be a challenge when automated methods are to be applied for monitoring purposes.

For the present plate under investigation using only its four corners, as measured DOFs, gave a random error below 5% for the first ten modes, except for one mode, mode #4. This exception also points out the interesting observation that the estimation of a mode, here mode #4, is not proper when using a low number of measured DOFs, even though higher order modes does not share this behavior. This illustrates the risks that one must be aware on when using a low number of sensors.

In the present work an uncommon procedure for the estimation method has been applied, using the full block Hankel matrix with quadratic CF matrices. This contrasts with the commonly used reference-based estimation procedure using a rectangular block Hankel matrix, created by choosing reference DOFs from the measurement from which CFs between all DOFs are used. The two procedures, reference-based and full matrix, were compared and it was found that the reference-based procedure gives no systematic difference in the estimates compared to the usage of the full block Hankel matrix. However, it was found that the random error in general was much lower when using the full block Hankel matrix. Another advantage of the usage of the full block Hankel matrix is that the possibility of choosing a bad combination of reference DOFs is less likely.

References

1. Weijtjens, W., Verbelen, T., Capello, E., Devriendt, C.: Vibration based structural health monitoring of the substructures of five offshore wind turbines. *Procedia Eng.* **199**, 2294–2299 (2017). X International Conference on Structural Dynamics, EURO-DYN 2017
2. Orlowitz, E., Brandt, A.: Operational modal analysis for dynamic characterization of a Ro-Lo ship. *J. Ship Res.* **58**, 216–224 (2014)
3. Brincker, R., Ventura, C.: *Introduction to Operational Modal Analysis*. Wiley, London (2015)
4. Allemang, R., Brown, D.: *Experimental modal analysis and dynamic component synthesis – vol 3: Modal parameter estimation*. Technical report, USAF (1987)
5. Peeters, B., De Roeck, G.: Reference-based stochastic subspace identification for output-only modal analysis. *Mech. Syst. Signal Process.* **13**, 855–878 (1999)
6. Smallwood, D., Gregory, D.: A rectangular plate is proposed as an IES modal test structure. In: *Proceedings of International Modal analysis IV*, Los Angeles, California (1986)
7. Orlowitz, E., Brandt, A.: Comparison of experimental and operational modal analysis on a laboratory test plate. *Measurement* **102**, 121–130 (2017)
8. Orlowitz, E., Brandt, A.: Influence of noise in correlation function estimates for operational modal analysis. In *Proceedings of International Modal Analysis Conference* (2018)



Chapter 40

Ambient Vibration Tests and Modal Response Analysis of an Old Age High-Rise Building in Downtown Vancouver, Canada

M. Motamedi, C. E. Ventura, P. Adebar, and R. A. Murugavel

Abstract This paper describes a series of ambient and forced vibration tests conducted on an old 44 story reinforced concrete building; Empire Landmark Hotel, located in Downtown Vancouver, Canada. The structure of the building consisted of reinforced concrete frames with concrete core walls, shear walls and concrete slabs. Three series of sensors were used to measure the ambient and forced vibrations of the building in multiple locations. Modal response analysis was performed to identify the dynamic properties of the building. As results, the natural frequencies, damping ratios and mode shapes of the building were presented.

Keywords Ambient vibration test · Modal analysis · Reinforce concrete building · Empire landmark hotel · Frequency

40.1 Introduction

Ambient Vibration Tests (AVT) and Forced Vibration Tests (FVT) are widely used for system identification and damage detection in the structures [1]. The recorded data from the instrumented buildings can be especially helpful for a better understanding of the true behavior of the structures. The vibration data obtained by sensors located in several locations of a building is used for the calibration and validation of its finite element model. In the current study, a series of AVT and FVT were conducted at the Empire Landmark Tower located at Downtown Vancouver to determine the dynamic properties of the structure. Various types of sensors were used for the measurements. A custom made shaker system was used to generate Force Vibration in the building. Modal response analysis technics were used to estimate the mode shapes, natural frequencies and damping ratios of the structure [2].

40.2 Building Description and Test Plan

The Empire Landmark Hotel was a 44-storey reinforced concrete shear wall tower which was 120 m tall. The building was completed in 1973 and is being demolished for replacement. Figure 40.1a shows the perspective view of the building.

The building consisted of six parking levels with storey height of 3.2 m, one lobby at ground level, 34 typical levels with story height of 2.61 m, one revolving restaurant at level 42 and two mechanical levels at top. Tower was constructed with the slab thickness of 150 mm and several shear walls and core walls in both directions with 200, 250 and 400 mm thickness. From the typical storey plan, it was found that the structure is stiff in E-W direction in comparison with N-S direction. In addition, cladding of the structure is made of precast concrete wall which also contributed to the lateral stiffness of the structure [3].

Three series of sensors were used to carry out the vibration tests: (1) Tromino[®] velocity/acceleration wireless sensors [4]; (2) EpiSensor force-balanced wired accelerometers (FBA-Model EpiSensor) [5]; and (3) CX1 network accelerometer. The EpiSensors were used at level 42 and in the basement whereas the Tromino sensors were distributed along the height of the building. The collected Tromino records were time synchronized with external GPS antenna in each sensor to allow the synchronization of the recordings both within each measurement setup and between setups. An electromagnetic custom made shaker was also fabricated and installed on Level 42 for exciting the building and performing the Force Vibration Tests. The sensor's location and their alignment are shown in Fig. 40.1b. Table 40.1 describes the location of sensors along the

M. Motamedi (✉) · C. E. Ventura · P. Adebar · R. A. Murugavel
Department of Civil Engineering, University of British Columbia, Vancouver, BC, Canada
e-mail: mmotamedi@civil.ubc.ca

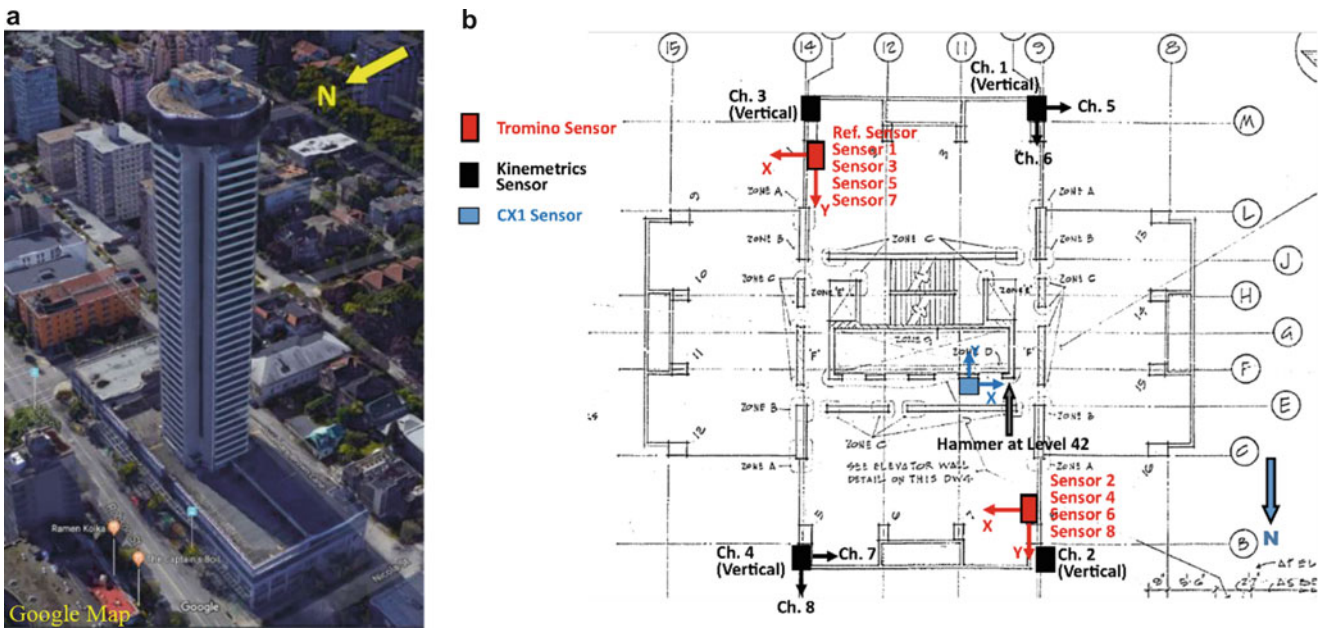


Fig. 40.1 Empire Landmark Tower-Downtown Vancouver: (a) Perspective view, (b) Plan view and sensors' location for vibration tests

Table 40.1 Location of the sensors along the height of the building

Sensors	Tromino sensors				EpiSensors		CX1 sensor
	Setup 1 and 2	Setup 3	Setup 4	Setup 5	Setups 1, 2 and 3	Setups 4 and 5	
Sensors' location	Level 44	Level 42 (ref)	Level 42 (ref)	Level 42 (ref)	Level 42	Basement	Level 42
	Level 43	Level 24	Level 5	Level 5			
	Level 42 (ref)	Level 19	Lobby	Lobby			
	Level 40	Level 14	Parking P3				
	Level 37	Level 8	Parking P2				
	Level 28		Basement				

height of the building. The sampling frequency of the recordings at each test was 512 samples per second. The total recording duration for each setup was about 30 min.

40.3 Modal Analysis

The computer program ARTeMIS Version 4, was used to perform the modal analysis of the specimen [6]. The software allows developing a 3D model of the structure and test points; the resulting mode shapes are displayed using this geometry. Two different techniques were used for modal identification: the Enhanced Frequency Domain Decomposition (EFDD) and the Stochastic Subspace Identification (SSI). These two modal identification techniques were used to cross-validate the results. The joint analysis of the signals measured in various strategic points of the structure made it possible to identify the modal configurations and the corresponding natural frequencies. The Power Spectra Densities obtained from ambient vibration measurements are illustrated in Fig. 40.2 where the peak values show the natural frequencies of the building.

40.4 Results and Conclusion

All measurement setups and sensor systems were employed to perform modal analysis where showed similar results for dynamic properties of the building for the first ten modes. The natural frequencies, damping ratios and corresponding mode shapes of the building are presented in Table 40.2. The frequency numbers obtained by different sensor systems matched accurately for the first seven modes and in the later modes there was a very slight deviation. The problem of unclear mode

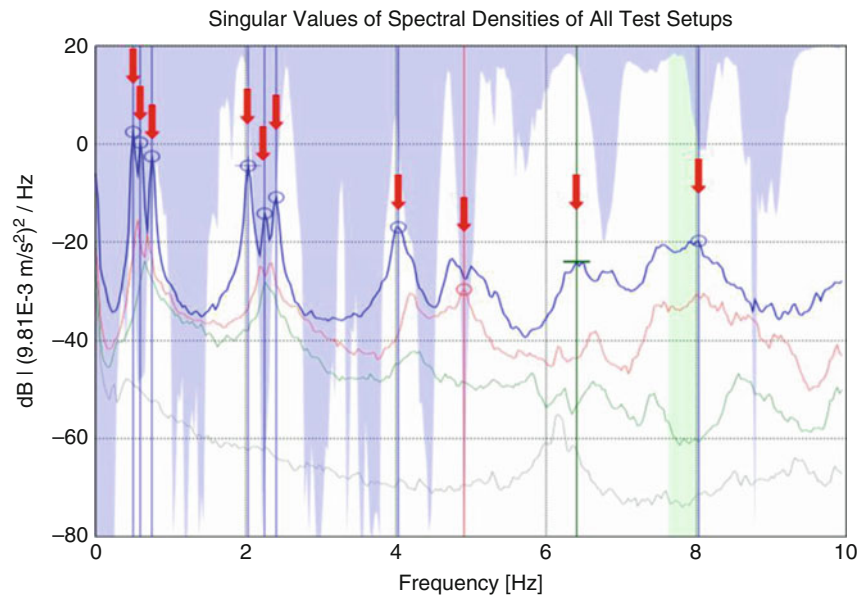


Fig. 40.2 Power Spectral Densities obtained from ambient measurements using EpiSensors at Level 42

Table 40.2 Mode shapes and frequencies of the building obtained from modal analysis

Mode #	Frequency (Hz)	Time period (s)	Damping ratio (%)	Mode shape and direction
1	0.500	2.000	3.474	1st lateral mode in N-S direction
2	0.594	1.684	3.367	1st lateral mode in E-W direction
3	0.750	1.333	2.506	1st torsional mode
4	2.031	0.492	1.202	2nd lateral mode in N-S direction
5	2.250	0.444	1.093	2nd torsional mode
6	2.406	0.416	1.070	Torsion + lateral E-W
7	4.031	0.248	–	3rd lateral mode in N-S direction
8	4.906	0.204	–	Lateral E-W
9	6.188	0.162	–	3rd torsional mode
10	6.781	0.147	–	4th lateral mode in N-S direction

shapes associated with the Tromino[®] sensor's data was resolved from the results of EpiSensors's data. So, analysis from the different types of sensor's data provided a good validation to the results obtained. However, the damping ratios in higher modes were ambiguous and are not reported here.

As shown, the first and second modal frequencies of the building were 0.5 and 0.594 Hz in North-South and East-West direction, respectively. The third mode was torsional with frequency of 0.75 Hz. From the measurements conducted in the basement, it was found that the frequency of soil-structure interaction was 5.062 Hz in up-down direction. The damping ratio of this mode identified through Enhanced Frequency Domain Decomposition (EFDD) was 4.5%. Also, the first and second pure base rocking frequency of the building were 13.031 Hz about E-W direction and 19.375 Hz about N-S direction, respectively.

Acknowledgements The tests were conducted by using the instruments and equipment of the Earthquake Engineering Research Facility (EERF) of the University of British Columbia with collaboration of its technicians and students. Their contribution and technical support is gratefully acknowledged.

References

1. Peeters, B.: System identification and damage detection in civil engineering. Ph.D. Thesis, Katholieke University of Leuven, Belgium (2000)
2. Brincker, R., Ventura, C.E.: Introduction to Operational Modal Analysis, 1st edn. Wiley, New York (2015)
3. Read Jones Christoffersen: Empire Landmark Hotel Drawings and Documents, RJC Consulting Engineering, Canada (1971)

4. Micromed: Tromino: Portable Ultra-Light Acquisition System for Seismic Noise and Vibration- User's Manual", Macromed, Italy (2012)
5. Kinometrics, Inc.: EpiSensor Force Balance Accelerometer, Model FBA ES-U2 User Guide, Kinometrics, USA (2005)
6. Structural Vibration Solutions, A/S: ARTeMIS Modal Software, Version 4, Denmark, Copyright 1998-2014



Chapter 41

System Identification of a Full Scale Wood Frame Building Specimen Subjected to Shake Table Tests

M. Motamedi and C. E. Ventura

Abstract This paper describes a series of ambient vibration tests conducted on a full scale wood frame building specimen to determine the dynamic properties of the typical wood frame school buildings in British Columbia, Canada. The specimen was subjected to the shake table tests to simulate the magnitude 8.8 earthquake and its aftershocks on the building. A set of sensors were used to measure the ambient vibration of the specimen before and after the main shock and after the sequent aftershocks. Modal response analysis was performed to identify the dynamic properties of the specimen. As the results, the natural frequencies, damping ratios and mode shapes of the specimen before and after each shake table test were presented.

Keywords System identification · Modal analysis · Shake table test · Wood frame building · Frequency and damping

41.1 Introduction

Ambient vibration tests are widely used for system identification and damage detection in the structures [1]. The recorded response data from the instrumented buildings can be especially helpful for a better understanding of the true behavior of the structures. The vibration data obtained by sensors located in several different locations of a building is used for the calibration and validation of its finite element model. In the current study, a full scale wood frame specimen which represented a typical school building in British Columbia was subjected to a series of shake table tests by a ground motion with different level of shaking as main shock and aftershocks. Ambient vibrations of the building in multiple locations were measured before the main shock, after the main shock and after each aftershock to identify the modal properties of the healthy specimen before the earthquake and the damaged specimen after the earthquakes. Modal response analysis techniques were used to estimate the mode shapes, natural frequencies and damping ratios [2].

41.2 Building Description and Shake Table Tests

The test specimen had a plan dimension of 7.62 m × 6.10 m and the height of 3.0 m and represented typical school building constructed in the city of Victoria, British Columbia, according to National Building Code of Canada. The structure consisted of two identical walls in the direction of shaking. Both walls were designed as exterior walls and each included two blocked shear walls to provide the lateral resistance [3]. Figure 41.1a shows the general view of the specimen prior to shake table test.

The large uniaxial shake table with dimensions of 6 m × 7.5 m at the Earthquake Engineering Research Facility of the University of British Columbia was used for earthquake motions simulation. The table itself can displace ±450 mm, with a maximum velocity of 75 cm/s. The dynamic actuator has a maximum pushing force of 260 kN.

The ground motion used for shake table tests was selected from Maule earthquake in Chile, 2010. The east-west component of this event was selected from STL station in Cerro Santa Lucia, Santiago as ground motion record. Table 41.1 presents the characteristics of the selected ground motion. The record was scaled to the Uniform Hazard Spectrum for Vancouver Island, and feature very large displacement at long periods. Test 1 was conducted by 100% intensity as main shock. Test 2, 3, and 4 were conducted by 100%, 125%, and 125% intensity, respectively as aftershocks.

M. Motamedi (✉) · C. E. Ventura
Department of Civil Engineering, University of British Columbia, Vancouver, BC, Canada
e-mail: mmotamedi@civil.ubc.ca

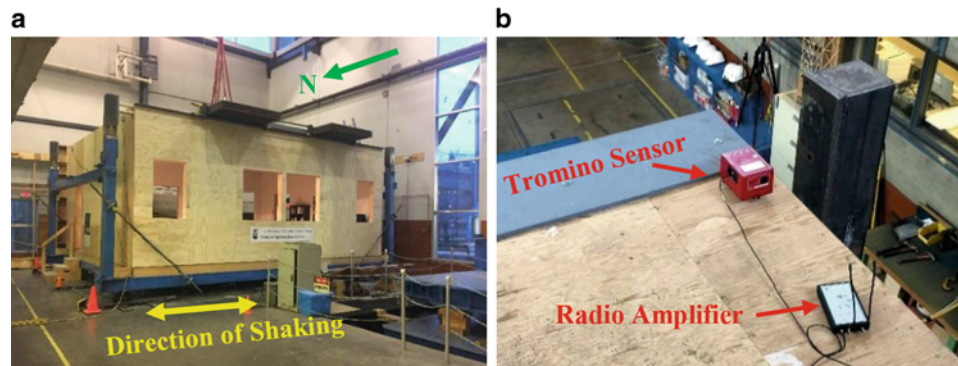


Fig. 41.1 Full scale wood frame specimen on shake table: (a) General view, (b) Wireless sensor installed at top for ambient vibration test

Table 41.1 Characteristics of the ground motion used for shake table tests

Ground motion	Magnitude (Mw)	Distance (Km)	Focal depth (Km)	PGA (g)	PGV (cm/s)	PGD (cm)	Soil type
Maule, Chile—2010	8.8	317	35	0.287	42.6	25.3	Intermediate soft

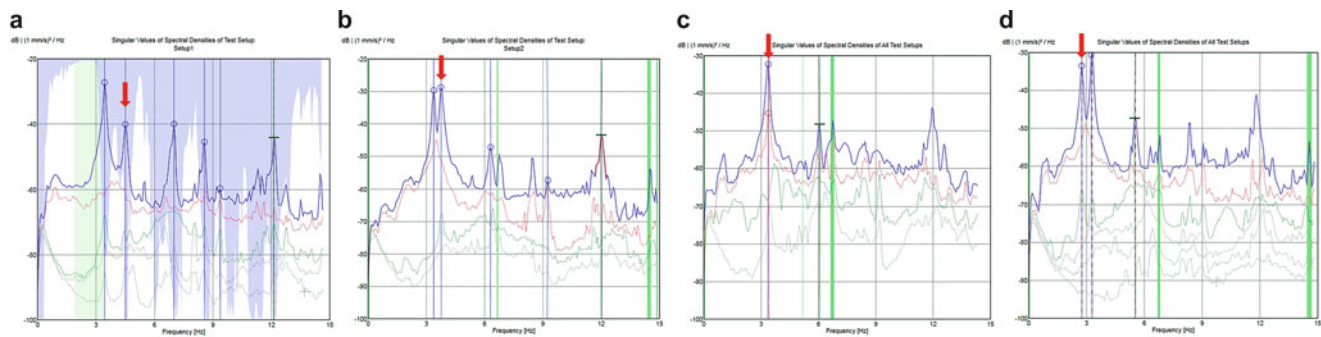


Fig. 41.2 Power Spectral Densities obtained from ambient measurements: (a) Before test 1, (b) After test 1, (c) After test 2, (d) After test 3

Tromino[®] velocity/acceleration sensors were used to carry out the ambient vibration tests. The Tromino sensors are suitable for high-resolution ambient vibration tests as they are fully portable, wireless, compact, and light instruments. Each sensor is equipped with two sets of three orthogonal high-resolution electrodynamic sensors (high gain and low gain velocity meter) and one set of three orthogonal digital accelerometers with a frequency range of 0.1–300 Hz [4]. For these tests the high-gain velocity data was used for the modal identification process. The collected records were time synchronized with a radio antenna and amplifier attached to each sensor. This allowed the synchronization of the recordings both within each measurement setup. The north component of the Tromino sensors were oriented parallel to north direction of the site. The sampling frequency of the recordings at each test was 128 samples per second. The total recording duration for each setup was about 20 min.

41.3 Modal Analysis

The computer program ARTEMIS Version 4, was used to perform the modal analysis of the specimen. The software allows developing a 3D model of the structure and test points; the resulting mode shapes are displayed using this geometry. Two different techniques were used for modal identification: the Enhanced Frequency Domain Decomposition (EFDD) and the Stochastic Subspace Identification (SSI). These two modal identification techniques were used to cross-validate the results. The joint analysis of the signals measured in various strategic points of the structure made it possible to identify the modal configurations and the corresponding natural frequencies [5]. The Power Spectra Densities obtained from ambient vibration measurements before and after shake table tests are illustrated in Fig. 41.2. The peak values show the natural frequency of the specimen in each level of damage.

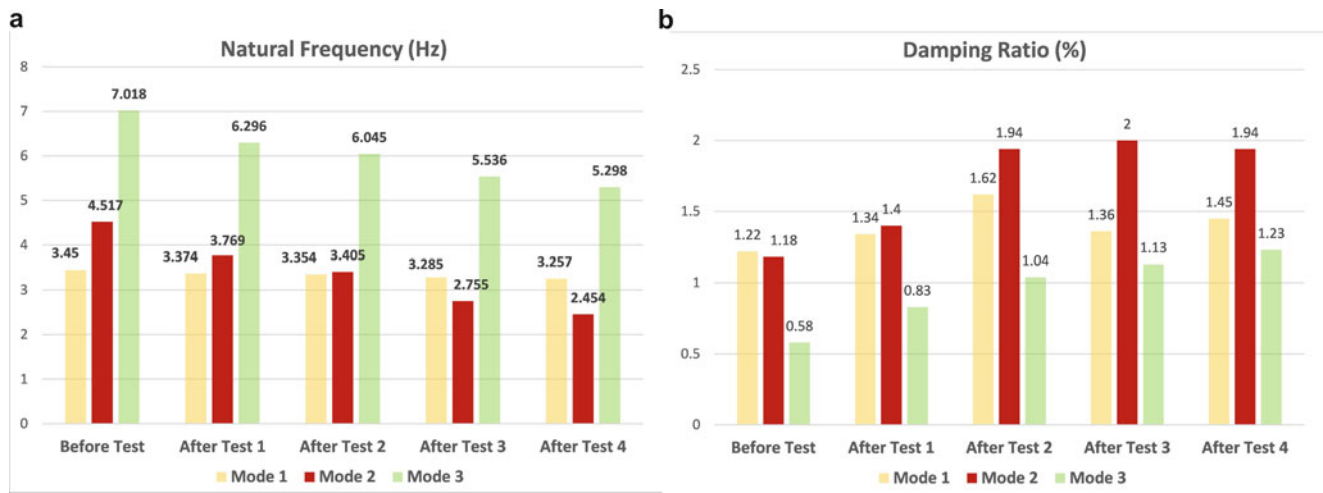


Fig. 41.3 Modal properties of the specimen before and after sequent tests: (a) Modal frequencies, (b) Modal damping ratios

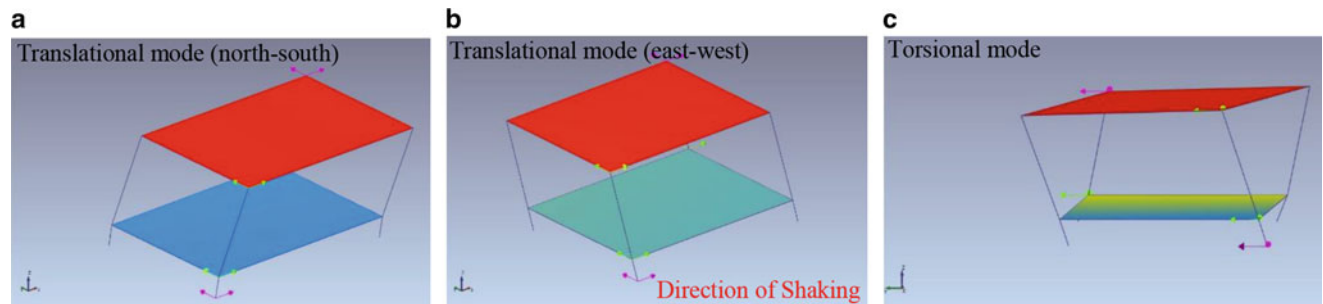


Fig. 41.4 Mode shapes of the specimen: (a) Mode 1, (b) Mode 2, and (c) Mode 3

41.4 Results and Conclusion

The natural frequencies, damping ratios and corresponding mode shapes are presented in Figs. 41.3 and 41.4, respectively. As shown, the frequency of the second mode decreased significantly after each shock (in direction of shaking). However, the frequency of the third mode decreased slightly (torsion of the specimen) while there was no frequency reduction in the first mode (perpendicular to direction of shaking). This shows the stiffness degradation of the shear walls due to shaking of the specimen in east-west direction. Furthermore, damping ratio increased by level of damage in the sequent tests. Damping ratio in second mode increased by 70% when the specimen subjected to main shock and some aftershocks.

Acknowledgements Funding of this research project was provided by the Ministry of Education of British Columbia, Canada. The tests were conducted at the Earthquake Engineering Research Facility (EERF) of the University of British Columbia with collaboration of its technicians and students. Their contribution and technical support is gratefully acknowledged.

References

1. Peeters, B.: System identification and damage detection in civil engineering. Ph.D. Thesis, Katholieke University of Leuven, Belgium (2000)
2. Brincker, R., Ventura, C.E.: Introduction to Operational Modal Analysis, 1st edn. Wiley, New York (2015)
3. APEGBC: Seismic Retrofit Guidelines, 3rd edn. Structural Engineering Guidelines for the Performance-Based Seismic Assessment and Retrofit of Low-Rise British Columbia School Buildings, Burnaby, BC, Canada. Association of Professional Engineers and Geoscientists (2017)
4. Micromed: Tromino: Portable Ultra-Light Acquisition System for Seismic Noise and Vibration- User’s Manual, Macromed, Italy (2012)
5. Structural Vibration Solutions, A/S: ARTEMIS Modal Software, Version 4, Copyright 1998-2014

Chapter 42

Estimating Rotor Suspension Parameters from Runout Data



Brian Damiano

Abstract Determining the dynamic characteristics of rotor suspensions is needed to make accurate predictions of rotor behavior. If direct measurements are unavailable, a method for estimating them is needed. This paper describes a method for estimating suspension characteristics from rotor runout data measured by proximity probes in a rotor test stand. Comparison of measured critical speeds with values predicted using the estimated rotor suspension parameters for a test rotor show good agreement, indicating that the method is valid.

Keywords Rotor dynamics · Rotor suspensions · Runout · Parameter estimation · Rotor models

42.1 Introduction

Recent work at Oak Ridge National Laboratory has led to the development of a method for extracting suspension dynamic characteristics (damping and effective mass) from runout data. This method may be useful for estimating suspension dynamic characteristics if direct measurements are unavailable or could be used to check suspension characteristic measurements obtained from a suspension test stand. The runout measurements used in the method are obtained from an instrumented rotor test stand with basic instrumentation and data acquisition hardware and software. A model-based approach is used to estimate the suspension dynamic characteristics from the measured runout data.

42.2 Method for Estimating Rotor Suspension Dynamic Characteristics from Runout Data

Required test stand instrumentation includes proximity probes and a key phasor measurement. The number of required proximity probes is determined by the rotor dynamics of the rotor being tested. A simple subcritical rotor is considered ideal because it minimizes rotor dynamic model complexity as well as the number of proximity probes needed to completely characterize the steady-state rotor deflection. Three proximity probes are needed when testing a subcritical rotor, with one probe being located near each end of the rotor and a third located midway between the rotor ends. Measurements from the probes located near the rotor ends are used to characterize the rigid-body modes, and measurements from all three probes are used to characterize the build into the rotor's first flexural mode. The key phasor is used to provide a speed measurement and an angle reference between the proximity probe measurements and the rotor.

Runout is rotor deflection at rotational speed. Working in the frequency domain, rotational speed is obtained from the largest magnitude peak in the key phasor spectrum, runout magnitudes are obtained from the proximity probe measurement magnitudes at the rotational speed, and proximity probe phases are obtained from the phase differences between the key phasor signal and the proximity probe signals at the rotational speed. Because the key phasor signal is related directly to

This manuscript has been authored by UT-Battelle, LLC under Contract No. DE-AC05-00OR22725 with the U.S. Department of Energy. The United States Government retains and the publisher, by accepting the article for publication, acknowledges that the United States Government retains a nonexclusive, paid-up, irrevocable, worldwide license to publish or reproduce the published form of this manuscript, or allow others to do so, for United States Government purposes. The Department of Energy will provide public access to these results of federally sponsored research in accordance with the DOE Public Access Plan (<http://energy.gov/downloads/doe-public-access-plan>).

B. Damiano (✉)

Dynamic Systems Analysis Group, Electrical and Electronics Systems Research Division, Oak Ridge National Laboratory, Oak Ridge, TN, USA
e-mail: damianob@ornl.gov

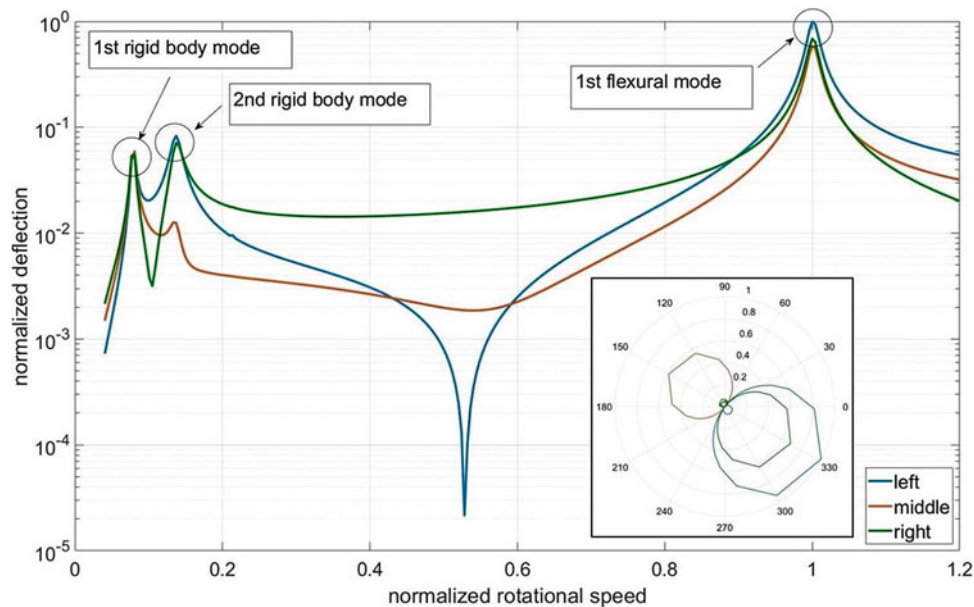


Fig. 42.1 Runout example shown as function of rotational speed and in polar coordinates

optical stripe on the rotor, runout measurements can also be related to an angle on the rotor. Runout calculations are typically performed by standard vibration measurement software packages, making them nearly transparent to the user.

The end result of the runout calculation is a complex rotation speed-dependent measurement of the synchronous rotor deflection as the rotor accelerates. Figure 42.1 shows calculated runout for an example rotor. Similar runout data collected as a rotor accelerates is used to estimate the suspension properties.

The method for estimating the suspension dynamic characteristics uses a rotor dynamic model to estimate the suspension characteristics required to produce measured runout for a known applied imbalance. Runout data are obtained by using a procedure identical to that used to obtain a balance weight influence coefficient:

- A reference run is performed to obtain baseline runout data. Runout data are obtained over the entire speed range of the reference run.
- A trial weight (or weight set) is applied to the rotor, and a second run—the trial run—is performed to obtain trial runout data. Runout data are obtained over the entire speed range of the trial run. The speed range of the reference run and the trial run should be the same; but, if not, the minimum overlapping speed range is used.
- Runout data from the baseline runout are subtracted from the trial runout data at each rotational speed. Assuming linear rotor response to the balance weights, the runout difference is the runout caused by the application of the trial weight to a perfectly balanced rotor.
- A rotor dynamic model is used to predict the runout that would be caused by the application of the trial weight to a perfectly balanced rotor. The suspension characteristics of the model are adjusted to provide the best match between the measured and predicted runout at each measured rotational speed. These best-match suspension characteristics estimate those of the tested suspension.

The reference run is typically performed by using a well-balanced rotor capable of successfully running to the highest target speed. The trial run is performed after applying a trial weight or a trial weight set. The largest trial weight that still allows the rotor to reach the target speed should give the best results because it gives the largest runout change; larger runout changes provide the best estimate of the suspension parameters.

If possible, runout data for the reference and trial runs should be collected at identical rotational speeds. If doing so is not possible, the data will need to be interpolated to a common set of rotational speeds. The lowest rotational speed used in the parameter estimation is the higher of the minimum rotational speeds in the reference and trial runs. Similarly, the highest rotational speed used in the parameter estimation is the lower of the maximum rotational speeds in the reference and trial runs.

A slow-roll correction is applied to the reference and trial run runout data to account for geometric offsets or other static deformities. If runout data are available for very low rotational speeds—defined here as approximately 20% of the first rigid-body mode critical speed, the first several runout data points for each proximity probe can be averaged and this average used

to perform the slow-roll correction. If very low speed data are not available, the probe data can be fit to the first rigid-body mode critical speed and then extrapolated to 0 Hz to estimate the slow-roll correction for each probe.

After performing the slow-roll correction, the reference run runout is subtracted from the corresponding trial run runout for each probe over the rotational speed range. The resulting data set approximates the runout that would be obtained for a linear system if the only rotor imbalance were the trial weight.

After the runout data are obtained from the reference and trial runs, the following steps are used to estimate the suspension parameters:

1. Determine the lowest rotational speed at which the suspension is expected to control rotor runout. This speed is normally the lowest measurable rotational velocity but may be different in certain cases.
2. Form an initial estimate of the suspension parameters at the lowest rotational speed of the runout.
3. Using a rotor dynamics code, calculate the estimated runout for the trial weight (or weight set) at the given rotational speed.
4. Form an error measure from the difference between the measured and calculated runouts.
5. Adjust the suspension parameter estimates based on the error measure.
6. Repeat steps 2–4 until the error measure meets some stopping criteria. The final suspension parameters used in the rotor dynamic model are estimates of the true suspension parameters at the given rotational speed.
7. Increment the rotational speed and repeat steps 1–6 until the suspension parameters are estimated for the entire rotational speed range of interest.

Initial estimates for the suspension parameters are often based on previous experience and engineering judgment. During the iterative process in which the suspension properties are estimated for a range of rotational speeds, current suspension properties are usually good choices for initial estimates for suspension parameters at the next rotational speed increment.

The error measure selection is also based on engineering judgment. In the simplest case, the error measure is the sum of the absolute values of the differences between the measured and predicted runout values for all the proximity probes. Experience in applying the method may show that more sophisticated error measures need to be used to get acceptable results.

Adjusting the suspension properties to minimize the error measure is best performed by a prewritten optimization code. Engineering analysis codes such as MATLAB, PTC Mathcad, and ANSYS simulation software have built-in functions to perform function optimization.

42.3 Estimating the Dynamic Characteristics of a Rotor Suspension

The method for estimating suspension dynamic characteristics from runout data was applied to a test rotor and suspension system. A subcritical rotor was used as the test article for estimating the suspension parameters. This test rotor/suspension system had a soft suspension on its left end and a relatively stiff suspension on the right end.

This suspension combination results in two rigid-body modes. The first rigid-body mode shape has an antinode on the left end and a node on the right end. The second rigid-body mode has antinodes on each end and a node located approximately 20% of the rotor length from the left end.

The dynamics of this system are such that the soft (left) suspension primarily determines the characteristics of the first rigid-body mode and the runout at low frequencies, while the stiffer (right) suspension primarily determines the characteristics of the second rigid-body mode and the runout at higher frequencies (about 42% of the second rigid-body critical speed and higher). In this example, the dynamic characteristics of the right suspension are estimated from runout data for frequencies above 42% of the second rigid-body critical speed.

The stand used in this test has three proximity probes and an optical key phasor. One proximity probe is located near the left side of the rotor, the second is near the rotor midspan, and the third is near the right side of the rotor. The runout data from these proximity probes and the key phasor were the only data used to estimate the suspension parameters.

Figures 42.2, 42.3, 42.4, and 42.5 show the normalized runout data for the reference and trial runs over the entire frequency range. In all the plots, the runouts are normalized to the maximum runout from the reference run and the frequencies are normalized to the second rigid-body critical speed. The trial weight is a single weight of 0.1-g magnitude placed at 120° and approximately three-fourths of the rotor length from the left side of the rotor. The data show a magnitude peak corresponding to the first rigid-body mode at approximately 17% of the second rigid-body critical speed and a magnitude shift at 1, which, by definition, corresponds to the second rigid-body mode.

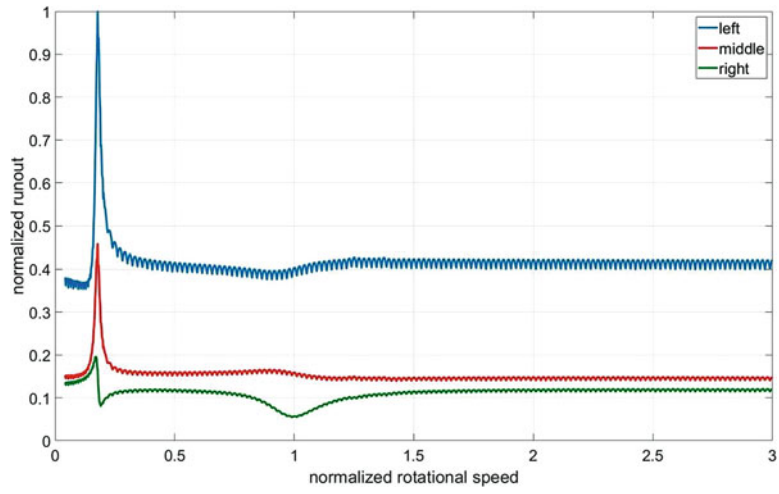


Fig. 42.2 Runout magnitudes—reference run

Fig. 42.3 Runout in polar coordinates—reference run

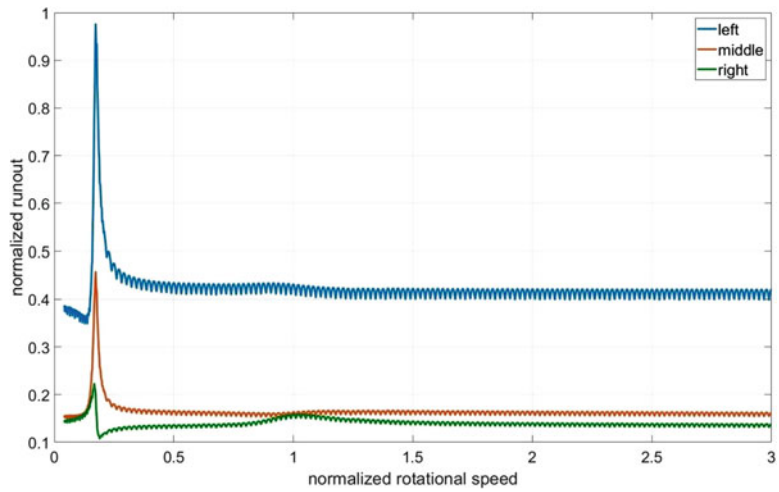
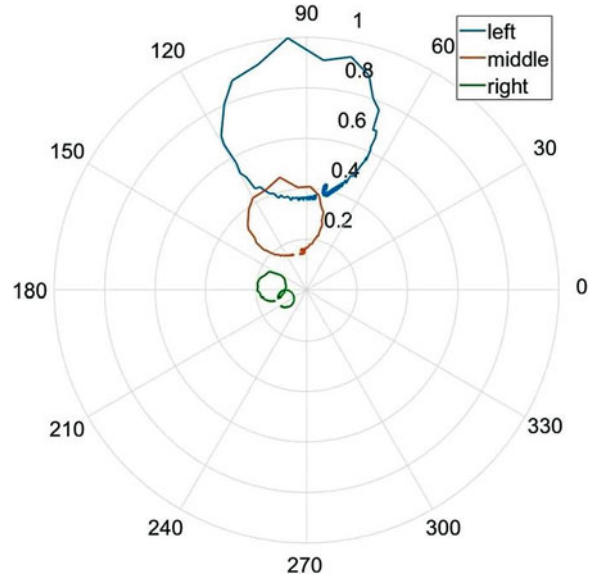


Fig. 42.4 Runout magnitudes—trial run

Fig. 42.5 Runout in polar coordinates—trial run

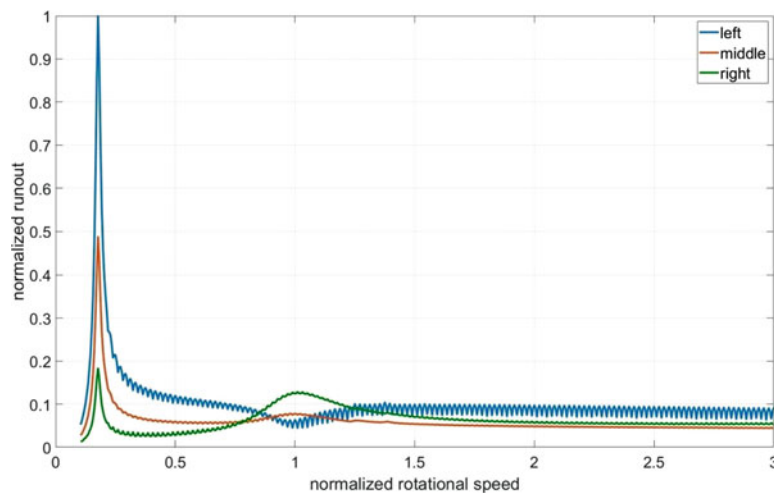
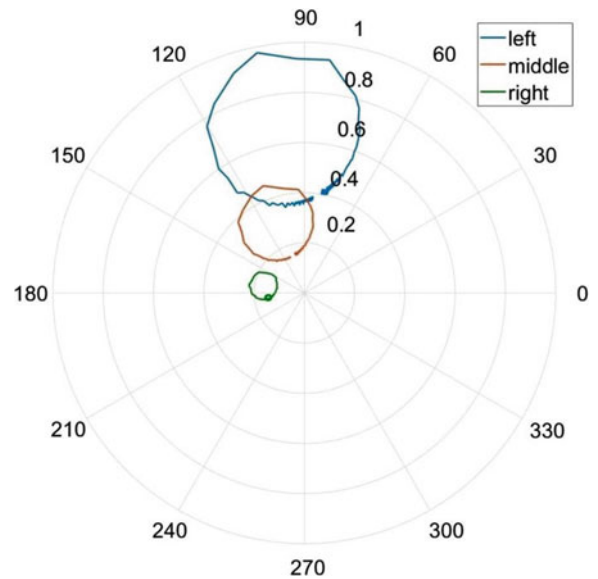


Fig. 42.6 Slow-roll-corrected runout magnitudes—reference run

A slow-roll correction is applied to the probe data. The average of the first five data points for each probe is used as the slow-roll correction. Figures 42.6, 42.7, 42.8, and 42.9 show the runout data after performing the slow-roll correction. Note that after the slow-roll correction, the runout data at low frequencies have a magnitude near 0 for the magnitude plots or begin near the origin for the polar plots.

After performing the slow-roll correction, the trial-run runout data are subtracted from reference run data. The resulting runout difference is the runout that would be expected for a perfectly balanced rotor with only the trial weight applied.

Figures 42.10 and 42.11 show the difference between the slow-roll-corrected runouts for each probe. In these plots, the runout is limited to values above 42% of the first rigid-body critical speed. This limitation is imposed to avoid calculating suspension parameter values at frequencies where the left suspension dynamic characteristics significantly affect rotor runout.

The simple rotor suspension model used here is a complex, frequency-dependent spring with only direct stiffness and damping. The concepts of effective mass and damping are used to express the frequency-dependent stiffness, $Z(\omega)$ of the suspension:

$$Z(\omega) = M(\omega)\omega^2 + iC(\omega)\omega \quad (42.1)$$

Fig. 42.7 Slow-roll-corrected runout in polar coordinates—reference run

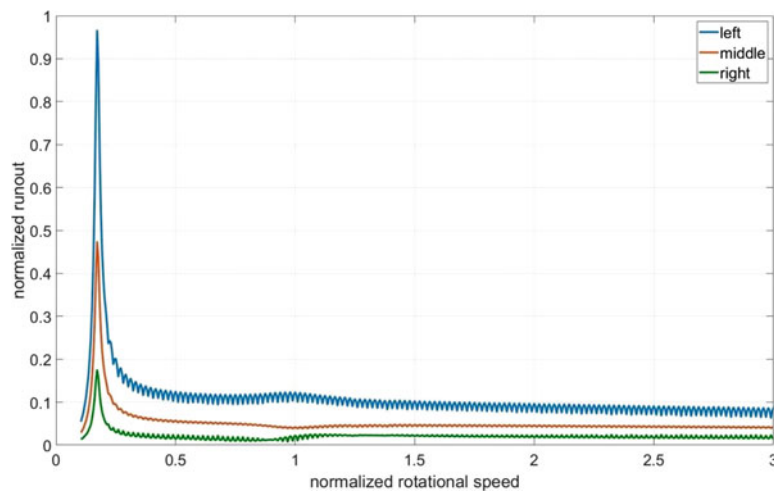
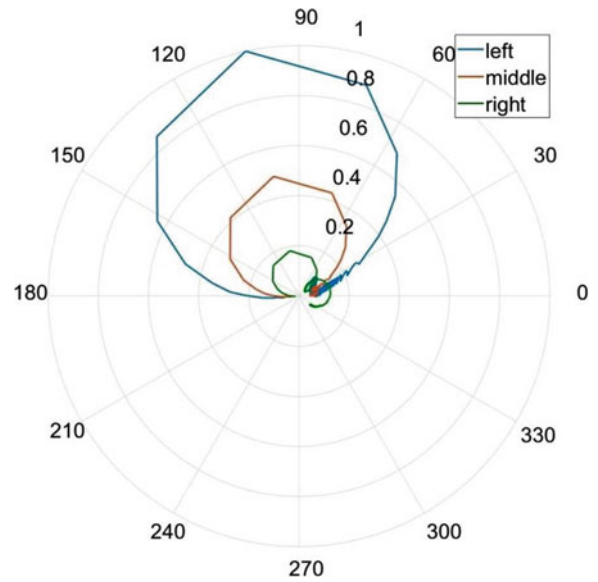


Fig. 42.8 Slow-roll-corrected runout magnitudes—trial run

where

$M(\omega)$ is the frequency-dependent effective mass,
 $C(\omega)$ is the frequency-dependent effective damping, and
 ω is the vibration frequency.

A MATLAB function was written to perform the optimization used to estimate the suspension parameters. At each rotational speed, an ORNL-developed rotor dynamics code was used to calculate the runout for the applied trial weight, assuming effective mass and damping values. The error measure used in the optimization is simply the sum of the absolute values of the differences between the calculated and measured runouts. The MATLAB function *fminsearch* was used to adjust the effective mass and damping values to minimize the error measure, giving the best match between the measured and calculated runout. This process was repeated for each rotational speed, resulting in a frequency-dependent estimate of the right end suspension parameters.

Figure 42.12 shows the estimated values of effective damping and effective mass for the tested suspension. These values were smoothed manually before being used in the rotor dynamic models.

Fig. 42.9 Slow-roll-corrected runout in polar coordinates—trial run

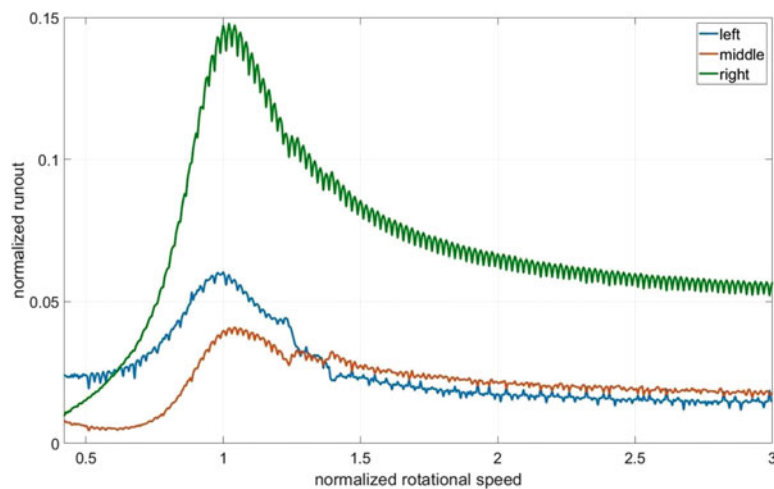
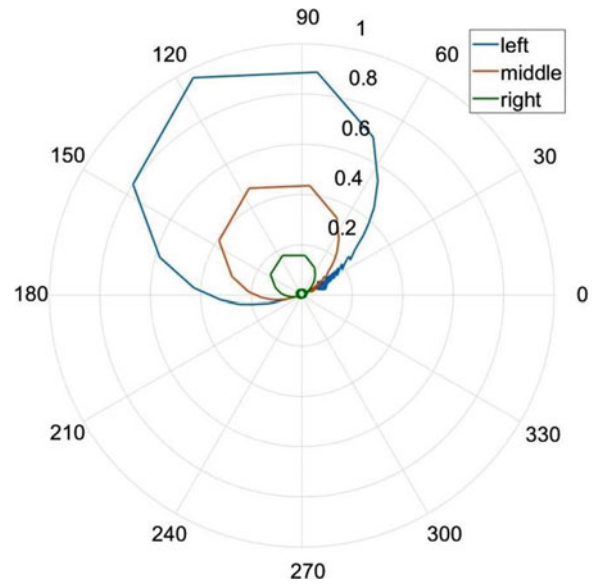


Fig. 42.10 Difference in slow-roll-corrected runout magnitude values

The results show that the tested suspension has negative values of effective mass at low frequencies. The effective damping peaks near 1.8 times the second rigid-body mode natural frequency and then rapidly drops in magnitude, apparently approaching an asymptotic value near 0 at higher frequencies. The effective mass also appears to approach 0 at higher frequencies.

Because actual suspension system stiffness values are unknown, there is no way to directly compare the estimated values of the tested suspension with known values. Some indication of the validity of the estimated suspension values can be obtained by comparing the calculated and measured second rigid-body critical speed and Q values of the tested rotor/suspension.

Using the estimated suspension properties in the rotor dynamics model gives a $\sim 2\%$ error in the frequency estimate and a $\sim 7\%$ error in the Q-value estimate. This agreement between the measured and predicted critical speeds and Q values indicates, but does not confirm, that the method described in this report for estimating suspension parameters from runout data is valid.

Fig. 42.11 Difference in slow-roll-corrected runout values shown in polar coordinates

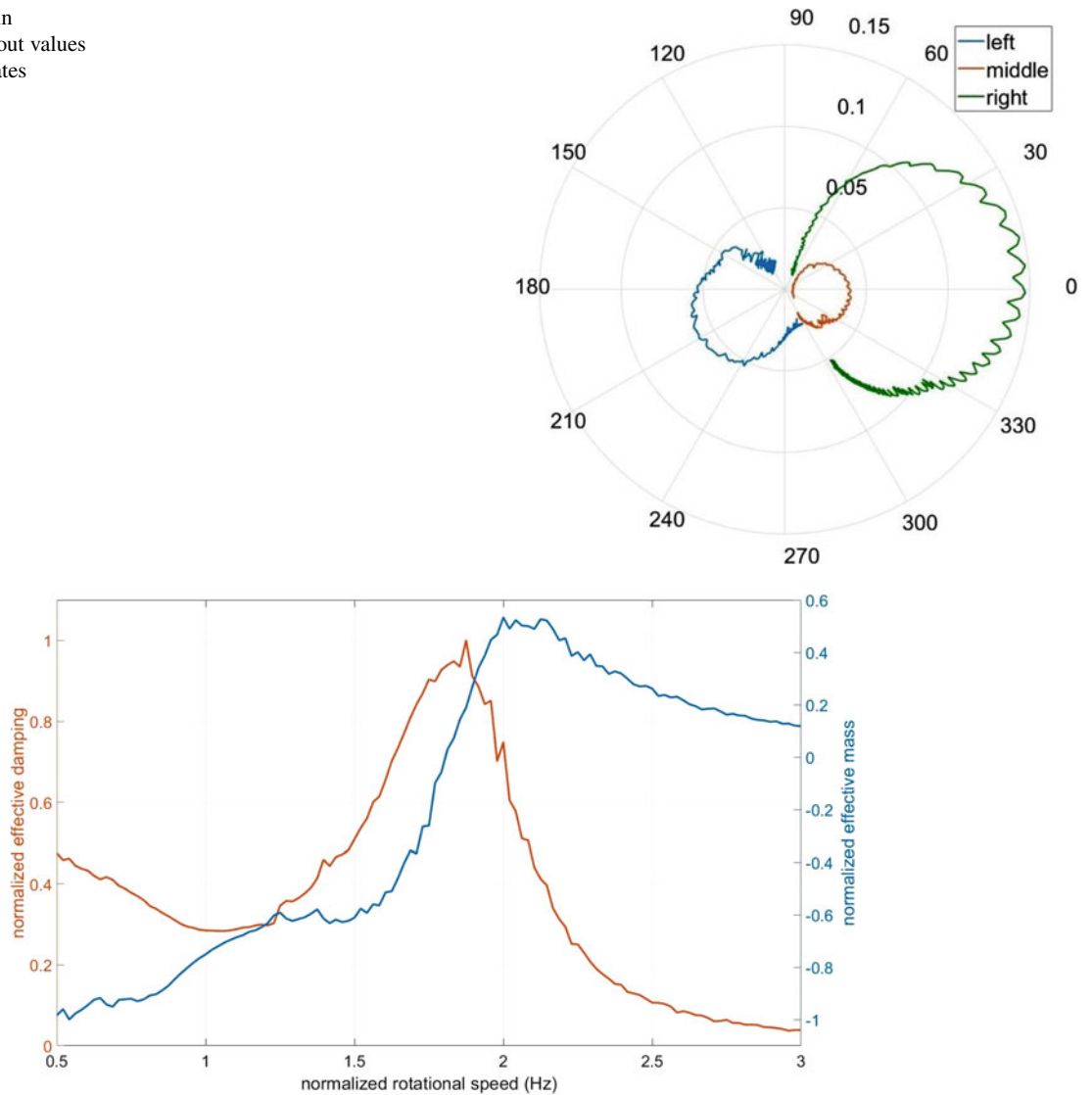


Fig. 42.12 Estimated rotor suspension properties

42.4 Conclusion

A method for estimating rotor suspension parameters from runout data has been developed and demonstrated. Comparison of measured critical speeds with values predicted using the estimated rotor suspension parameters for a test rotor show good agreement, indicating that the method is valid.